

# **Petrophysical properties of fault rock-Implications for petroleum production**

**Abdul Majeed shar**

Submitted in accordance with requirements for the degree of

**Doctor of Philosophy**

**The University of Leeds**

**School of Earth and Environment**

**May 2015**

## **Declaration of Authorship**

The candidate confirms that the work submitted is his/her own, except where work which has formed part of jointly-authored publications has been included. The contribution of the candidate and the other authors to this work has been explicitly indicated below. The candidate confirms that appropriate credit has been given within the thesis where reference has been made to the work of others.

This copy has been supplied on the understanding that it is copyright material and that no quotation from the thesis may be published without proper acknowledgement.

*I have no special talent. I am only passionately curious.*

— **Albert Einstein**

## **Acknowledgement**

Firstly, I would like to express my heartfelt gratefulness and gratitude to my supervisors Professor Quentin J. Fisher and Piroska Lorinczi who guided and assisted me in every step of my work, their level of support was beyond my expectations. This thesis would never be possible without their support; they assisted me in many aspects of my work and the feedback that they have provided on this thesis. Professor Quentin, I am extremely thankful for providing financial support which was a huge step for me. Indeed, it was a privilege to be one of your students.

I would like to thank to Dr. Carlos Grattoni for sharing knowledge and providing support during conduct of experiments at Wolfson multiphase flow laboratory. Thanks also for his supervision with experimental set-up and providing technical support. I would like to thank Mr. Phil Guise and John Martin for monitoring safety issues during experimental work. I thank various oil and gas companies from North Sea fields for the use of their core samples. I am also thankful of Dr. Mohammad Ahmed reservoir engineer from Schlumberger United Kingdom for his support in answering every question related to fault modelling in Eclipse software.

I would like to acknowledge the support from NED University towards tuition fees at University of Leeds. I would like to acknowledge the Ian Hillier Award 2013 received from London petrophysical society.

All my dedications go to my father and my mother who always valued education and steered me towards right directions. Thanks to my wife Asma for your patience and support towards the completion of this thesis. She has been very considerate as I could not give her much time after marriage. I thank God for blessing with son Jawad, my dearest son you made us happy.

I am thankful of all my professors for giving me the best of their knowledge and to empower me with the best tools and techniques that lead to this degree. I would like to

thank all my friends, Javed Haneef, Tom Lynch, Muhammad Yameen and all others who I have not mentioned individually, all of you have been there and supported.

## Abstract

Faults can have significant impact on reservoir productivity. Understanding the factors that controls the fluid flow properties of fault rocks provides a sound basis to assess the impact of faults on reservoirs productivity. So, different aspects that affect the fluid flow within siliciclastic fault formations were investigated in this research project. Fault rock samples from a number of locations were analysed including: (i) core samples from central and southern North Sea fields; (ii) and outcrop samples from the 90 Fathom fault, Northumberland, UK and Miri airport road exposure, Malaysia as well as the Hopeman fault from Invernesshire, UK. The impact of faults on fluid flow was assessed by integrating the data from QXRD analysis, microstructural examination, X-ray tomography, mercury porosimetry for pore size distribution, absolute and relative permeability measurements as well as capillary pressure tests. Single phase and multiphase flow properties which were conducted at a range of stresses are the most comprehensive collection of high quality fault rock data.

The permeability measurements made using gas gave higher values than with brine, which in turn gave higher values than when measured using distilled water permeability. The differences in permeability could be the results of clay particles swelling; mobilisation and retaining within the confined pore throats, although these effects depend on the rock mineralogy and pore fluid composition. Moreover, the permeability stress sensitivity was investigated. The results showed that at low confining stresses the permeability of the fault rock core samples showed high sensitivity to stress, whereas at higher confining stresses the permeability was less pronounced to stress. This might be due to the core damage effects and the microfractures formed due to stress release, which were observed from SEM images. The pore radius calculated from gas slippage parameters at low confining pressures was in the same order of magnitude as the micro fracture width. The micro cracks could be easily closed due to stress increase hence resulted in reduction of permeability. Overall, the stress sensitivity of fault rocks from outcrop is less than that from core. This is consistent with the idea that stress sensitivity is mainly the result of the presence of grain boundary microfractures formed as core is brought to the surface. This indicates that permeability measurements made on outcrop samples may be more reliable. Another key finding was that the published permeability

data (e.g. Fisher and Knipe, 2001) compared with present study data which is obtained at in-situ stress using formation compatible brines showed that the published data may not be inaccurate as the use of distilled water gives lower permeability than brines and low stresses resulted in higher permeability than in-situ stress measurements. Therefore, the results indicate that two different laboratory practices used in previous studies partially cancel each other out so that the existing data is yet valuable.

The effective gas permeability were also measured at a range of stresses and it was observed that the samples with lower absolute permeabilities were more stress sensitive to stress than high permeable samples. The relative permeability results obtained were incorporated into a specific example of synthetic reservoir model. These suggested that faults formed within low permeability sands might act as a barrier to fluid flow.

# Table of contents

<b>1</b>	<b>INTRODUCTION.....</b>	<b>1</b>
<b>1.1</b>	<b>Introduction.....</b>	<b>1</b>
<b>1.2</b>	<b>Impact of faults on fluid flow: an overview .....</b>	<b>2</b>
<b>1.3</b>	<b>Issues related to current fault rock petrophysical properties data .....</b>	<b>4</b>
1.3.1	Effect of stress on petrophysical properties of fault rocks.....	4
1.3.2	Fluid-rock chemical interactions.....	5
<b>1.4</b>	<b>Faults treatment in simulation and modelling .....</b>	<b>6</b>
<b>1.5</b>	<b>Research objectives .....</b>	<b>8</b>
<b>1.6</b>	<b>Thesis outline .....</b>	<b>9</b>
<b>2</b>	<b>PETROPHYSICAL PROPERTIES OF FAULT ROCK: A LITERATURE REVIEW .....</b>	<b>11</b>
<b>2.1</b>	<b>Introduction.....</b>	<b>11</b>
<b>2.2</b>	<b>Faults and their classification based on siliciclastic sediments .....</b>	<b>11</b>
2.2.1	Disaggregation zones .....	13
2.2.2	Cataclastic faults .....	14
2.2.3	Phyllosilicate-framework fault rocks .....	15
2.2.4	Clay smears .....	16
2.2.5	Cemented fault rocks.....	16
<b>2.3</b>	<b>Petrophysical properties of fault rocks: a review.....</b>	<b>17</b>
2.3.1	Single phase flow properties .....	17
2.3.1.1	Permeability of fault rocks obtained from reservoir core .....	18
2.3.1.2	Fault rocks from outcrop .....	19
2.3.1.3	Fault rocks formed during experiments .....	23
2.3.1.4	Analogue fault rocks.....	23
2.3.2	Multiphase flow properties .....	27
2.3.3	Two-phase flow properties (Relative permeability and capillary pressure) of fault rock .....	35
<b>2.4</b>	<b>Empirical estimation of fault rock properties .....</b>	<b>39</b>
2.4.1	Shale gouge ratio estimation .....	39

2.4.2	Empirical estimate of single phase fluid flow properties of fault rock .....	40
2.4.3	Empirical estimates of two phase flow properties of fault rock.....	44
<b>2.5</b>	<b>Significance of fault rock flow properties to model cross-fault flow .....</b>	<b>46</b>
<b>2.6</b>	<b>Factors affecting fluid flow properties of fault rocks .....</b>	<b>48</b>
2.6.1	Effect of pore fluid salinity on fault rock permeability.....	49
2.6.2	Stress sensitivity of rock permeability .....	50
<b>2.7</b>	<b>Examples of faults found within the petroleum reservoirs .....</b>	<b>53</b>
2.7.1	Faults as a barrier in petroleum reservoirs .....	54
2.7.1.1	Brent Province: UK and Norwegian North Sea .....	54
2.7.1.2	Rotliegend UK and Dutch North Sea .....	55
<b>2.8</b>	<b>Summary .....</b>	<b>56</b>
<b>3</b>	<b>MATERIALS AND METHODS .....</b>	<b>58</b>
<b>3.1</b>	<b>Introduction .....</b>	<b>58</b>
<b>3.2</b>	<b>Material studied .....</b>	<b>58</b>
3.2.1	Central North Sea .....	59
3.2.2	Southern North Sea .....	60
3.2.3	90 Fathom Fault, Northumberland, UK .....	61
3.2.4	Fault rock from Miri airport road exposure Malaysia.....	63
3.2.5	Fault rock from Clashach Quarry, Hopeman, Invernesshire.....	64
<b>3.3</b>	<b>Methodology .....</b>	<b>64</b>
3.3.1	Sample preparation, cleaning and preliminary measurements.....	65
<b>3.4</b>	<b>Microstructural structure examination .....</b>	<b>67</b>
3.4.1	X-ray tomography .....	67
3.4.2	SEM examination.....	68
3.4.3	Quantitative X-Ray diffraction (Q-XRD) .....	69
<b>3.5</b>	<b>Petrophysical analysis: single-phase properties .....</b>	<b>70</b>
3.5.1	Porosity .....	70
3.5.2	Steady-state gas permeability analysis.....	72
3.5.3	Steady-state liquid permeability analysis.....	74
3.5.4	Gas pulse-decay permeametry .....	75
3.5.5	Liquid pulse decay permeametry .....	77

3.5.6	Deconvolution of fault rock permeability .....	79
<b>3.6</b>	<b>Petrophysical analysis: two-phase flow properties .....</b>	<b>79</b>
3.6.1	Pore size measurement and threshold pressure determination.....	80
3.6.2	Relative Humidity chambers.....	81
3.6.3	Ultracentrifuge .....	83
3.6.4	Breakthrough Experiments .....	84
<b>3.7</b>	<b>Uncertainties and issues related to experimental work .....</b>	<b>84</b>
<b>4</b>	<b>SINGLE PHASE FLUID FLOW PROPERTIES OF FAULT ROCK.....</b>	<b>87</b>
<b>4.1</b>	<b>Introduction.....</b>	<b>87</b>
<b>4.2</b>	<b>Mineralogy and Microstructural properties .....</b>	<b>88</b>
4.2.1	Central North Sea reservoir cores .....	88
4.2.1.1	Microstructure and mineralogy of the host sandstone .....	89
4.2.1.2	Microstructure of the fault rocks .....	89
4.2.2	Southern North Sea reservoirs .....	92
4.2.2.1	Microstructure and mineralogy of the host sandstone .....	92
4.2.2.2	Microstructure of the fault rock .....	93
4.2.3	90 Fathom Fault, Northumberland.....	94
4.2.3.1	Microstructure and mineralogy of the undeformed sandstone.....	94
4.2.3.2	Microstructure of the fault rocks .....	94
4.2.4	Miri airport road outcrop exposure Malaysia .....	95
4.2.4.1	Microstructure and mineralogy of the undeformed sandstone.....	95
4.2.4.2	Microstructure of fault.....	95
4.2.5	Summary of microstructural analysis .....	96
4.2.6	X-ray tomography analysis .....	96
<b>4.3</b>	<b>Experimental overview: Single phase gas and liquid permeability.....</b>	<b>98</b>
4.3.1	Central North Sea reservoir samples.....	99
4.3.1.1	Host sandstones .....	99
4.3.1.2	Fault rock.....	100
4.3.2	Southern North Sea reservoir samples .....	104
4.3.2.1	Host sandstone.....	104
4.3.2.2	Fault rock.....	104
4.3.3	90 Fathom Northumberland, UK samples .....	105
4.3.3.1	Fault rock.....	105

4.3.3.2	Host sandstones .....	106
<b>4.4</b>	<b>Discussion.....</b>	<b>107</b>
4.4.1	Fault rock permeability: impact of fluid chemistry.....	107
4.4.2	Impact of clay content on fault rock permeability .....	122
4.4.3	Comparison of the fault rock permeability data with existing empirical models 127	
4.4.4	Implications of results for fault seal analysis.....	130
4.4.4.1	Estimation of fault permeability from clay content .....	130
4.4.4.2	Implications for estimation of fault rock permeabilities .....	131
<b>4.5</b>	<b>Conclusions .....</b>	<b>132</b>
<b>5</b>	<b>FAULT ROCK GAS AND LIQUID PERMEABILITY STRESS SENSITIVITY .....</b>	<b>135</b>
<b>5.1</b>	<b>Introduction.....</b>	<b>135</b>
<b>5.2</b>	<b>Gas flow mechanisms.....</b>	<b>136</b>
5.2.1	Slip flow (Klinkenberg model) .....	137
<b>5.3</b>	<b>Methodology .....</b>	<b>139</b>
<b>5.4</b>	<b>Results .....</b>	<b>141</b>
5.4.1	Central North Sea reservoir, UK.....	142
2.8.1.1	Stress dependent single phase gas permeability .....	142
1.6.1.1	Stress dependent brine permeability .....	143
5.4.2	Southern North Sea reservoir .....	146
2.8.1.2	Stress dependent gas permeability.....	146
2.8.1.3	Stress dependent brine permeability .....	146
5.4.3	Fault samples from 90 Fathom Fault, UK and Miri exposure, Malaysia.....	148
2.8.1.4	Stress dependent gas permeability.....	148
2.8.1.5	Stress dependent brine permeability results.....	149
<b>5.5</b>	<b>Discussion.....</b>	<b>152</b>
5.5.1	Influence of confining pressure on fault rock gas permeability.....	152
5.5.2	Klinkenberg slip factor.....	162
5.5.3	Comparison between fault rock and tight gas sand permeability stress sensitivity .....	166
5.5.4	Influence of confining pressure on liquid permeability .....	168
5.5.5	Integration of ambient and in-situ stress permeability.....	172

5.5.6	Implications of the results .....	174
2.8.1.6	Implications for the use of published data .....	175
<b>5.6</b>	<b>Conclusion.....</b>	<b>176</b>
<b>6</b>	<b>MULTI-PHASE FLOW PROPERTIES OF FAULT ROCKS .....</b>	<b>178</b>
<b>6.1</b>	<b>Introduction.....</b>	<b>178</b>
<b>6.2</b>	<b>Experimental overview: two-phase flow properties.....</b>	<b>179</b>
<b>6.3</b>	<b>Results .....</b>	<b>181</b>
6.3.1	Central North Sea Group-A fault rocks .....	182
6.3.1.1	Relative permeability.....	182
6.3.1.2	Capillary pressure .....	183
6.3.2	Central North Sea Group-B fault rock .....	186
6.3.2.1	Relative gas permeability .....	186
6.3.2.2	Capillary pressure .....	186
6.3.3	Central North Sea host sandstone .....	189
6.3.4	Southern North Sea .....	190
6.3.4.1	Gas relative permeability.....	191
6.3.4.2	Capillary pressure .....	191
6.3.5	Fault rock from Hopeman outcrop UK .....	194
6.3.5.1	Gas relative permeability.....	194
6.3.5.2	Capillary pressure .....	194
<b>6.4</b>	<b>Discussion.....</b>	<b>196</b>
6.4.1	Stress sensitivity of effective and relative gas permeability .....	196
6.4.2	Gas relative permeability controls and differences .....	203
6.4.3	Capillary pressure.....	210
6.4.4	Comparison of result with published two-phase flow properties of fault rock 213	
6.4.5	Implications.....	215
<b>6.5</b>	<b>Conclusion.....</b>	<b>217</b>
<b>7</b>	<b>MODELLING THE INFLUENCE OF FLUID FLOW ACROSS FAULT ..</b>	<b>218</b>
<b>7.1</b>	<b>Introduction.....</b>	<b>218</b>
<b>7.2</b>	<b>Methods of fault modelling.....</b>	<b>220</b>
<b>7.3</b>	<b>Incorporating host and fault rock properties into flow simulation model</b>	<b>224</b>

<b>7.4</b>	<b>Model set-up .....</b>	<b>227</b>
7.4.1	Simulation modelling results (Oil-water Model).....	230
7.4.2	Simulation modelling results (Gas-water model).....	235
<b>7.5</b>	<b>Discussion.....</b>	<b>248</b>
<b>7.6</b>	<b>Conclusions .....</b>	<b>250</b>
<b>8</b>	<b>CONCLUSIONS AND RECOMMENDATIONS FOR FUTURE WORK... 252</b>	
<b>8.1</b>	<b>Introduction.....</b>	<b>252</b>
<b>8.2</b>	<b>Summary of experimental results.....</b>	<b>253</b>
8.2.1	Conclusions from single phase permeability experiments (ambient stress) .	253
8.2.2	Conclusions from fault rock permeability stress sensitivity experiments.....	254
8.2.3	Two-phase flow properties.....	256
8.2.4	Modelling the impact of fault rock properties.....	256
<b>8.3</b>	<b>Implications of the results for fault seal analysis .....</b>	<b>257</b>
<b>8.4</b>	<b>Recommendations for future work .....</b>	<b>258</b>
8.4.1	Experimental work.....	258
8.4.2	Capillary end effects .....	259
8.4.3	Field scale fault modelling.....	259
8.4.4	Pore network modelling.....	260
	<b>REFERENCES.....</b>	<b>261</b>

# Table of Figures

## Chapter 1

Figure 1.1 Schematic diagram showing the difference between a juxtaposition seal (top) and a fault rock seal (bottom) (from Fisher, pers. com.2012).....	3
Figure 1.2 The above diagram is showing a 280 bar pressure difference that built up across faults in the Rotliegend reservoir from southern North Sea field as a result of petroleum production (from van der Molen et al., 2003).....	4
Figure 1.3 Workflow to build fault reservoir models incorporating fault rock properties. Input data comprises mapping of faults, outcrop analogues, seismic interpretation, estimating and measuring fault rock properties in laboratory (from Fisher, pers. com.2013).....	8
Figure 2.1 Conceptual illustrations of the faults formed within poorly lithified sediments and its components shows how they might affect the fluid flow (taken from Caine et al.,1996 and 2007).....	12
Figure 2.2 Illustration is the fault rock classification based on clay/phyllosilicate content shows important control of fault rock development (from Fisher and Knipe, 1998,2001) .....	13
Figure 2.3 BSEM images of (A) a disaggregation zone and (B) the adjacent undeformed sandstone. C) Hand specimen containing two disaggregation zones – arrows (from Fisher, 2005). .....	14
Figure 2.4 BSEM images of (A) an undeformed Rotliegend sandstone and (B) the adjacent cataclastic fault. C) Hand specimen containing a zone of cataclastic faults (from Fisher, 2005) .....	15
Figure 2.5 BSEM images of (A) an undeformed impure Brent sandstone and (B) the adjacent phyllosilicate-framework fault rock. (C) Hand specimen containing a several phyllosilicate-framework fault rocks (from Fisher, 2005). .....	15
Figure 2.6 (a) A field example of a clay smear (arrow) from near Miri, Sarawak, Malaysia (b) BSEM of typical clay smear fault rock (SEM image taken from Yang Pie, 2013 PhD thesis) .....	16

Figure 2.7 BSE micrographs showing: (A) a calcite vein in a calcite cemented sandstones; (B) a dolomite and anhydrite vein in a lithified sandstones; (C) an anhydrite cemented reactivated cataclastic fault; d) a microcrystalline quartz-cemented water-escape structure,(Fisher and Knipe, 1998). .....	16
Figure 2.8 Summary of the fault rock permeability data from the North Sea and Norwegian Continental Shelf Permeability is plotted against clay content for the various fault rock types. (from Fisher and Knipe 1998). .....	18
Figure 2.9 Summary of published fault rock permeability data on variety of different fault rock types collected.....	24
Figure 2.10 illustration of the steady state flow condition .....	27
Figure 2.11The illustration shows the drainage and imbibition capillary pressure curves.(taken from Tiab and Donaldson, 2011).....	30
Figure 2.12 A typical relative permeability curve for high permeability rock (from Fekete-2014). .....	34
Figure 2.13 Relative permeability curves for high and low permeability rock samples (taken from Shanley et al., 2004).....	35
Figure 2.14 Gas relative permeability (left) and capillary pressure (right) of the Hopeman fault rock (from Al-Hinai et al. 2008). .....	36
Figure 2.15 Gas relative permeability (left) and capillary pressure (right) from 90 Fathom Fault (from Tueckmantel et al. (2012) .....	37
Figure 2.16 Gas relative permeability from The data left side is presented on linear scale and right side present on logarithmic scale. (Cluff and Byrnes, 2010) equations used to construct the relative permeability curve. (after Tueckmantel et al., 2012).....	38
Figure 2.17 Gas relative permeability and water saturation data from published sources on tight gas sandstones (from Byrnes et al. 2009.) .....	39
Figure 2.18 Shale gouge ratio (SGR) algorithm commonly applied: (a) SGR from Yielding et al. (1997) (b) Clay Smear Potential from Fulljames et al. (1997) (c) Shale Smear Factor (Lindsay et al.,1993) (from Jolley et al., 2007).....	40
Figure 2.19 Relationships between shale versus log of permeability (mD). The large data points are plug permeability from core and outcrop of different locations (Gibbson1998). Filled circles cataclastic deformation bands; open circles are solution deformation band and the filled squares are clay gouge.Small data points	

are probe permeability measurements of deformation bands(open circles) and slip-surface(crosses) (Antonellini and Ayadin, 1994). The large boxes of gray colour are summaries of the data from Sleipner Field (Ellevset et al., 1998):(i)Cataclastic deformation bands, (ii) Phyllosilicate-framework fault rocks, (iii) Clay smear. The line labeled with K represents the average values based on core samples from Heidrun field,(Knai,1996). The curves given represent  $d=1$  mm(dashed line),  $d=10$ cm,  $d=1$  m,  $d=10$ m and  $d= 1$ km (thickest line). After Manzocchi et al. (1999).  
 ..... 42

Figure 2.20 Showing fault rock permeability against fault rock clay content measured on faults in cores. The data are grouped according to maximum burial depth. Exponential least-squares regression lines are shown for each group of data, showing a systematic decrease in permeability both with fault rock clay content and with depth (from Sperrevik et al., 2002). ..... 43

Figure 2.21 The relation between permeability versus clay content, the host rock permeability is represented by symbols and permeability of fault rock with solid lines as a function of clay content and burial depth. (From Bense and Person 2006) ..... 44

Figure 2.22 (a) Relative permeability and (b) capillary pressure for 0.01 mD dashed lines and 10mD solid lines fault rock. On graph of the  $P_c$  curve, the dark circles are the threshold pressure on drainage capillary pressure curve.( from Manzocchi et al., 2002) ..... 46

Figure 2.23 The diagram shows the properties of the fault rock used for simulation model (a) is the example of fault rock thickness relationship used for successful history matching (b)Fault rock permeability used for history matching in simulation model (taken from Manzocchi et al. 2010). ..... 48

Figure 2.24 The above conceptual model of multi-phase flow in a petroleum reservoir shows. (a) The saturation within fault and reservoir (red for hydrocarbon, blue for water). (b) The capillary pressure curve. (c) The directional water-wet relative permeability curves for the fault rock. The fault has a higher capillary entry pressure than the reservoir (from Fisher et al.,2001). ..... 48

Figure 2.25 Water-sensitivity of the Spiney sandstone, Moray Firth Basin, Note the large decrease in permeability when the brine is changed to 1% NaCl (from Lever and Dawe, 1987). ..... 50

Figure 2.26 The conceptual cartoon shows the stress impact on rock fabrics. .... 52

Figure 2.27 Stress dependence of the absolute gas permeability (left) and relative permeability (right) of a tight gas sandstone (from Al-Hinai, 2007). Note that the relative permeability is far more stress sensitive – especially at high water saturations. ....	52
Figure 2.28 Stress dependence of the absolute gas permeability of tight gas sands. Note that the low permeability samples can have up to two orders of magnitude lower permeability when measured at reservoir stress conditions compared to 100 psi, (from Cluff and Byrnes, 2010).....	53
Figure 3.1 Sketch map of the central North Sea field location. The study area is shown by arrow on map (after Keller et al. 2005). ....	60
Figure 3.2 The southern North Sea area studied (source: Norwegian Petroleum directorate)	61
Figure 3.3 The Great Britain map with location highlighted with the black square indicates the position of 90 Fathom fault outcrop area (taken from GoogleMaps-2014). ....	63
Figure 3.4 The Location map of the fault rock from Miri airport road exposure Malaysia with inserted map detailing the location of the study area (GoogleMaps-2014).....	63
Figure 3.5the location map of the fault rock from Clashach Quarry, Hopeman, Invernesshir United Kingdom. ....	64
Figure 3.6 The workflow adopted during this study.....	65
Figure 3.7 The Dean stark distillation apparatus for sample cleaning (taken from vinci Tech catalogue). ....	67
Figure 3.8 Illustration of the Scanning Electronic Microscope used for samples microstructural observation (a) an outside view (b) inside view. ....	69
Figure 3.9 Schematic diagram of the helium porosimeter setup .....	72
Figure 3.10 The schematic diagram of steady state gas permeametry. ....	73
Figure 3.11 Diagrams showing the principle behind Klinkenberg corrections. ....	74
Figure 3.12 Simplified schematic diagram for steady-state flow tests. ....	75
Figure 3.13 Outline of gas pulse decay permeametry .....	76
Figure 3.14 Diagram for liquid pulse decay apparatus. ....	77
Figure 3.15 The illustration is the drainage experiment with centrifuge. ....	83

Figure 3.16 the experimental setup used in this study by introducing constant gas into upstream side.....	84
Figure 4.1 Photomicrograph (A) BSEM image of cataclastic rock formed in a clean sandstone with relatively small clay content; (B) BSEM image of host sandstone; (C) BSEM image of phyllosilicate framework fault; (D) BSEM image of host sandstone. All these samples were from the Central North Sea reservoir samples group. ....	92
Figure 4.2 Photomicrographs of (A) BSEM image of Cataclastic fault with small grain size reduction; (B) BSEM image of adjacent host sandstone; (C) BSEM image of cataclastic fault from same field with large grain size reductions; (D) BSEM image of adjacent host sandstone all are from same field of southern North Sea reservoir core.....	93
Figure 4.3 BSEM images of typical single deformation band zone host sandstone and its associated host sandstone (top) and slip-surface cataclasite and host sandstone it contains (bottom) from the 90 Fathom Fault.....	95
Figure 4.4 The phyllosilicate-framework-fault and the host sandstone it contains from Miri exposure Malaysia.....	96
Figure 4.5 CT images taken on central North Sea reservoir core samples containing deformation bands.....	97
Figure 4.6 CT image of one of the typical 90 Fathom fault sample from slip-surface cataclasite. The white patches are the heavy minerals with high densities. ....	98
Figure 4.7 Cross plot showing the relationship between gas, brine and distilled water permeability of fault rock (log-log plot). Note that in the figure legend $K_g$ , $K_b$ , and $K_d$ refer to gas, brine and distilled water permeabilities respectively.....	109
Figure 4.8 Cross plot of the distilled water permeability against brine permeability for fault rocks (log-log plot).....	110
Figure 4.9 The relationship of gas permeability to brine permeability ratio versus clay content of the host sediments (semi-log plot). In the figure legend $K_g$ , $K_b$ , and $K_d$ refer to gas, brine and distilled water permeability respectively. ....	110
Figure 4.10 Photomicrograph of a typical SEM image from one of the Southern North Sea reservoir core sample, showing the presence of kaolin and backscattered image of one of the central North Sea core sample shows the presence of illite clay mineral within the pore spaces. ....	112

Figure 4.11 Plots showing effects of clay minerals (Mica, Kaolinite, Illite-smectite and chlorite) on fault rock gas, brine and distilled water permeability ratio. In this figure $K_g$ , $K_b$ , and $K_d$ refer to gas, brine and distilled water permeability of fault rock, respectively. ....	114
Figure 4.12 Plot showing the relationship between the pore radius derived from Hg-injection data and from gas slip-radius followed Klinkenberg procedures (log-log plot) ...	116
Figure 4.13 Plots showing the relationship between fault rock gas, brine and distilled water permeability with Hg-pore throat radius (upper) and the slip-radius (lower). Note that the data from Armitage et al. (2011) was measured at 60MPa effective stress on cap rock samples. (log-log plot).....	117
Figure 4.14 Sketch of an example of adsorbed water-layer on the solid grain surfaces (taken from schlumberger course notes and Fekete, 2014).....	119
Figure 4.15 Plot is showing the fault rock permeability ratio of gas to brine and water permeability versus the slip-radius.....	121
Figure 4.16 The plot of fault rock permeability ratio of gas permeability to brine and distilled water permeability against Hg-pore radius (log-log plot).....	121
Figure 4.17 Plot of the fault rock permeability of gas, brine and distilled water versus clay content of the host sediment (semi-log plot).....	123
Figure 4.18 Plot showing effects of clay minerals (Mica, Kaolinite, Illite-smectite and chlorite) content on fault rock gas, brine and distilled water permeability. (semi-log plots).....	125
Figure 4.19 Plot of permeability of a sand-clay mixture as a function of clay content where the initial sands have different grain-sizes and grain-sorting, hence porosity and permeability (semi-log plot).....	126
Figure 4.20 Comparison of the permeability of fault rocks as a function of clay content obtained during the present study using the fault rock empirical relations of Sperrevik et al. (2002) and Manzocchi et al. (1999) (semi-log plot).....	128
Figure 4.21 Comparison of the permeability of fault rock as a function of clay content using the model of Revil and Cathles (1999) and empirical model proposed by Sperrevik et al. (2002) and Manzocchi et al. (1999).....	130

Figure 4.22 Plot of fault rock gas permeability against gas slippage factor. Data collected during present study are compared to those presented by the Discovery group data from Byrens et al. 2000.....	131
Figure 4.23 Comparison of gas permeability $K_g$ and brine permeability $k_b$ data measured during this study with published correlations. ....	132
Figure 5.1 Diagrams showing the principle behind Klinkenberg corrections. ....	138
Figure 5.2 Plot of the fault rock normalized gas permeability versus net confining stress; data are from Central North Sea reservoir core samples. ....	143
Figure 5.3 Plot of the fault rock gas permeability versus net stress; data are from Central North Sea reservoir core samples.....	144
Figure 5.4 Normalized single phase gas permeability versus confining stress, and gas permeability versus confining stress the samples are from southern North Sea reservoir core samples.....	147
Figure 5.5 Plot showing the relationship between normalized single phase gas permeability and net confining stress; the data are from 90 Fathom fault plugs and Miri exposure Malaysia fault samples.....	149
Figure 5.6 Plot of the 90 Fathom fault, UK and Miri exposure Malaysia fault plugs gas permeability (mD) versus net confining stress (psi). ....	149
Figure 5.7 Plot showing the influence of confining stress on plugs permeability.....	152
Figure 5.8 Plot showing the relationship between gas permeability measured at lowest stress (i.e. 500psi) and power law exponent. ....	155
Figure 5.9 Typical BSEM images showing the micro-cracks observed within the fault rock core samples. ....	155
Figure 5.10 Diagram is the illustration of rock sample representing parallel plate fracture and matrix system. ....	158
Figure 5.11 Plot is the permeability of sample based on experimental results. Micro fractures were observed within the thin section of samples. Permeability largely decreases as stress increases. ....	159
Figure 5.12 Illustration is the stress-dependent permeability of fault rock, (a) absolute gas permeability without Klinkenberg correction (b) is the gas permeability corrected for Klinkenberg effects.....	160

Figure 5.13 Crossplot of gas permeability of fault rocks measured at 500 psi confining stress against permeability measured at 5000psi confining stress. ....	161
Figure 5.14 The plot is showing the rock mineralogy and absolute gas permeability stress sensitivity from Central North Sea.....	162
Figure 5.15 Effect of confining stress on gas slippage factor during gas permeability experiments. ....	163
Figure 5.16 Plot of gas slippage radius vs confining stress for fault rock samples, derived from gas permeability results of central North Sea reservoir core samples (left-side). The Plot of slip- radius versus confining stress data is from 90 Fathom fault samples (right-side).....	164
Figure 5.17 SEM thin section images show the sample contains small scale (0.1 to 0.5 $\mu\text{m}$ ) wide fractures at grain boundaries. ....	164
Figure 5.18 Comparison between gas slippage factors (b-factor) of fault rock samples calculated and estimated using different published correlations. The estimated slip factor and slip factor obtained from experimental data are both plotted against measured absolute gas permeability.....	166
Figure 5.19 Cross plot of the fault rock in-situ absolute gas permeability and pore radius derived from gas-slippage. ....	166
Figure 5.20 Plot of the gas permeability of fault rocks at 500psi confining pressure against the permeability at 5000psi confining pressure for fault rock and tight gas sandstone samples, tight gas data is taken from Byrnes et al. (2009). ....	167
Figure 5.21 The change in liquid permeability caused by changing pore fluids and stress..	169
Figure 5.22 Gas and brine permeability of fault rock samples studied. ....	170
Figure 5.23 Plot showing the relationship between brine permeability measured at lowest stress (i.e. 500psi) and power law exponent.....	171
Figure 5.24 Plot of the brine permeability of fault rocks at 500psi confining pressure against the permeability at 5000psi confining pressure for fault rock. The data plotted is from 90 Fathom fault UK, Mirri airport road fault exposure and reservoir core samples from Central North Sea. ....	171
Figure 5.25 Illustration shows the relationship between power law exponent and fault rock gas and brine permeability data from both reservoir core samples and 90 Fathom fault UK, Mirri airport road outcrop fault. ....	172

Figure 5.26 Permeability of rectilinear fault samples measured at (70psi stress) and fault plug samples measured at different stress conditions.....	173
Figure 5.27 Plot of gas permeability vs confining pressure for a fault rock sample. Note that the low pressure measurement has the lowest permeability. This is rare and is an artefact resulting from using a different sample for the ultralow permeability measurement. The lower kg value reflects sample heterogeneity.....	174
Figure 5.28 Plot of the permeability measured to distilled water for fault rock at ambient stress against brine permeability measurements made at maximum stress. ....	174
Figure 5.29 Plot of permeability vs clay content for distilled water permeability from Fisher and Knipe (2001) at ambient stress and brine permeabilities from this study at in-situ stress. ....	175
Figure 6.1 Two-phase flow data from central North Sea Group-A reservoir sample. The data presented comes from variety of techniques used, such as the centrifuge, relative humidity and mercury injection method, different colors represent the different methods used for changing water saturations. For the comparison purpose all Hg-injection capillary pressure have been converted to air-water values assuming interfacial tension of 70 dynes/cm and 480 dynes/cm for air- water and Hg-vacuum respectively. Contact angles of 00 and 1400 were considered for air-water and Hg-vacuum respectively. Data in the right-hand side graphs are plotted using semi-log scales. Graphs on the left-hand side present the same data in linear scale to visualize the results. ....	184
Figure 6.2 The two phase fluid flow properties of all measured samples from central North Sea group-B reservoir core samples. The colour of symbols indicates the different methods used for changing saturations (see legends in graphs presented). For the comparison purpose, all Hg-injection capillary pressure has been converted to air-water values assuming interfacial tension of 70 dynes/cm and 480 dynes/cm for air-water and Hg-vacuum respectively. Contact angles of 0 <sup>0</sup> and 140 <sup>0</sup> were considered for air-water and Hg-vacuum respectively. Data in the right-hand side graphs are plotted using semi-log scales. Graphs on the left-hand side present the same data in linear scale to visualize the results. ....	187
Figure 6.3 Data of host rock samples capillary pressure and gas relative permeability from central North Sea Group-B. The centrifuge technique was employed to alter the water saturation and to obtain capillary pressure data. The data is presented on linear (left-side) and semi-log (right side) graphs. ....	190

Figure 6.4	The two phase fluid flow properties of all measured samples from southern North Sea reservoir core samples. The colour of symbols indicates the different plugs properties and the methods used for changing saturations (see legends in graphs presented). For the comparison purpose, all Hg-injection from capillary pressure have been converted to air-water values assuming interfacial tension of 70 dynes/cm and 480dynes/cm for air- water and Hg-vacuum respectively. Contact angles of $0^0$ and $140^0$ were considered for air-water and Hg-vacuum respectively. Data in the right-hand side graphs are plotted using semi-log scales. Graphs on the left-hand side present the same data in linear scale to visualise the results. ....	193
Figure 6.5	Gas relative permeability as a function of water saturation obtained from Hopeman fault rock samples. ....	195
Figure 6.6	The illustration shows the capillary pressure data corresponding to water saturation obtained from Hopeman fault rock. ....	195
Figure 6.7	The plot shows the stress sensitivity of effective gas permeability versus stress from present study samples. The higher the water saturation of samples more is the stress sensitive. Not that the sample which shows higher reduction of effective gas permeability has lower absolute permeability value. ....	197
Figure 6.8	Plot shows the normalized effective gas permeability versus confining stress from reservoir core samples obtained at various saturations. The saturations were altered by two different techniques i.e. the relative humidity chambers and centrifuge technique. ....	197
Figure 6.9	Stress sensitivity of relative permeability of samples with absolute gas permeability $k_g \Rightarrow >0.2$ mD. ....	200
Figure 6.10	Stress sensitivity of relative permeability of a samples with absolute gas permeability $k_g = <0.02$ mD. ....	200
Figure 6.11	Diagram showing gas relative permeability results. The relative permeability measurements made at different stress conditions for sample sections of core samples. ....	201
Figure 6.12	The illustration is the representation of water redistribution with increasing applied stress (taken from Al-Hinai et al. 2008). ....	202
Figure 6.13	Illustration is the combined gas relative permeability of samples versus water saturation from present study. ....	203

Figure 6.14 The illustration is the semi-log plot of gas relative permeability versus capillary pressure for all samples. Data subdivided based on the range of measured absolute gas permeabilities is given in brackets.....	204
Figure 6.15 Plot of the gas relative permeability versus water saturations of fault rock samples based on pore radius data. The data plotted is from this study and collected from published studies of Al-Hinai et al. (2008) and Tueckmantel et al. (2012) respectively; the data were plotted on linear graph (left side) and semi-log graph (right-side).....	206
Figure 6.16 Illustration is the gas relative permeability of fault rock samples versus water saturation; the different colours indicate different ranges of absolute gas permeability. The data plotted on linear graph (left side) and semi-log graph (right-side).....	207
Figure 6.17 Gas relative permeability as a function of water saturation. The data represented with symbols are measured data and curves represent the predicted data (taken from Cluff and Byrnes, 2010).....	207
Figure 6.18 Plot of the gas relative permeability and water saturation relationship on linear and semi-log graph, the different colours indicate different ranges of clay content of host sediments. ....	208
Figure.6.19 The relative gas permeability versus capillary pressure plotted on (a) linear graph (b) semi-log graph. The data presented is obtained during this study from North Sea fields core samples. The different colours indicate different techniques used for saturation alterations. ....	210
Figure 6.20 Plot is the capillary pressure versus water saturation. (a) The plotted data is on linear chart and (b)semi-log plot. The capillary pressure was obtained with three different techniques. ....	212
Figure 6.21 Plot of the fault rock gas relative permeability versus water saturation for all samples used during the present study as well as that obtained in the studies of Al-Hinai et al. (2008) and Tueckmantel et al. (2012) respectively (left side data are on linear graph). The same data of relative permeability versus water saturation are plotted on semi-log graphs (right-side plot).....	214
Figure 6.22 Plot showing the relationship between relative permeability and capillary pressure from this study, and collected from Al-Hinai et al. (2008) and	

Tueckmantel et al. (2012).The data is presented (a) linear graph and (b) semi-log graph.....	215
Figure 7.1 illustrations is the methods of representing the transmissibility multipliers within within faulted and unfluted cells of the reservoirs (taken from Zjilstra et al. 2007) .....	221
Figure 7.2 A reservoir model representing hydrocarbon saturation within fault zones. In this model the fault is divided into three different zones, below free water level the fault will be assigned TMs, which will be determined from fault rock and host rock single phase permeabilities. within the zone 2, fault is immediately above the free water level, where capillary threshold pressure could not be exceeded by hydrocarbon, that would be considered as sealing fault for hydrocarbon (TMs=0). The zone 3 represents that the fault rock entry pressure has been exceeded so it is essential to calculate the TMs to consider the relative permeability of the fault rock (taken from Al-Hinai PhD thesis). .....	223
Figure 7.3 Illustration is the relative permeability data used for reservoir modelling.....	227
Figure 7.4 Capillary pressure curve from mercury injection data used for simulation models and was fitted with Brooks and Corey empirical equation. The data was converted from laboratory to reservoir water-oil capillary pressure and is from central North Sea reservoir core samples. ....	227
Figure 7.5 The flow simulation model geometries and their configuration adapted during modelling. (a) Fault modelled by assigning TMs between juxtaposed faults (b) the fault modelling was performed discretely by assigning its own cells and properties as (LGR) local grid refinements.....	229
Figure 7.6 Simulation results and their comparison from <b>CP-oil-water model</b> that has one producer in right compartment with no injector. The results presented for different cases where there was no fault case, TM case and the fault was modelled by LGR by assigning high and low capillary pressure curves. The results show, the total production from field, the filed pressure, region pressures and difference of pressures in between compartmented.....	232
Figure 7.7 Illustrations are the oil saturation distribution of the model at the end of simulation runs. (a) Base case-no fault (b) TM transmissibility multipliers case and (c) is LGR case explicitly modelling fault rock by giving its own relative permeability and capillary pressures. The fault cuts the entire model splitting it into two compartments. ....	233

- Figure 7.8 The illustrations are the comparison of results from **HP model** case of simulation run, which has one injector and one producer in each compartment. The results presented are compares different cases, where the fault was modelled by assignning (TM=1) no fault case, the fault modelled by assigning transmissibility multipliers which were calculated from fault rock properties and the third model in that the fault was given its own properties relative permeability and capillary pressures curves of two different ranges of high and low caapillary pressures. The results from all simulation runs were compared are the cumulative production of oil, field pressures, compartmentpressures and pressure difference within the compartments as a fucntion of producing time of the reservoir..... 234
- Figure 7.9 Comparisons of simulation results from CS model, where fault rock properties were assigned by transmissibility multipliers and by giving fault its own relative permeability and capillary pressure. The results show that the both of the compartments are depleting at same rate, so the model response in all case is identical..... 234
- Figure 7.10 Illustrations are the gas saturation distribution of the model at the end of simulation runs. (a) Base case-no fault (b) TM transmissibility multipliers case and (c) is LGR case explicitly modelling fault rock by giving its own relative permeability and capillary pressures. The fault cuts the entire model splitting it into two compartments..... 237
- Figure 7.11 Comparisons of simulation results from BP model, different model cases were run, such as no fault as a base case, a TMs case where fault rock properties were assigned by transmissibility multipliers and LGR by giving fault its own relative permeability and capillary pressure. The simulations results resented compares the different responses such as cumulative field production, field pressures and water production as well as region one pressures..... 238
- Figure 7.12 GP simulation model results for the gas reservoir that has one injector and one producer which are opposite side to each other. Comparisons of different cases, in which there was a base case (no fault), a model in that the fault rock properties were assigned by TM and explicit model (LGR) in that the fault was assigned with its own two-phase flow properties..... 238
- Figure 7.13 Illustrations are showing the maps of gas saturation distribution of the GP model at the end of simulation runs in which there is a one injector and the producer is in the opposite side of injector. (a) Base case-no fault (b) TM transmissibility

multipliers case and (c) is LGR case explicitly modelling fault rock by giving its own relative permeability and capillary pressures. ....	239
Figure 7.14 Field cumulative oil production total from the LGR model.....	246
Figure 7.15 Illustration is the pressure in (LGR case) compartment 1 and compartment 2. The producer is in the compartment 1 and model results from pressure difference between compartment 1 and compartment 2 at the end of simulation period.....	246
Figure 7.16 Oil saturation map of the model containing water and oil in left and right compartments (LGR case) at the end of simulation run.....	247

# Table of Tables

## Chapter 2

Table 2.1 Summary of published permeability and capillary threshold pressure data of variety of fault rock types. It should be noted that (Table 2.1) gives only the ranges of values, but the collected data from each listed author is provided in Figure 2.8. ...	26
--	----

## Chapter 3

Table 3.1 Summary of the samples that have been obtained and analysed during present study .....	59
Table 3.2 Capillary pressure and relative humidity generated by different salt solutions.....	82

## Chapter 4

Table 4.1 Summary of mineralogy from QXRD results of host sandstone composition (wt. %) for specimen from group-A Central North Sea reservoir samples. ....	91
Table 4.2 Mineralogy from QXRD results of host sandstone composition in (wt. %), for the specimen from group-B Central North Sea reservoir samples.....	91
Table 4.3 The summary of the QXRD results of host sandstone, composition in (wt. %) of the specimen from Southern North Sea reservoirs.....	94
Table 4.4 Summary of the permeability results (gas, brine and distilled water measured at ambient stress) and mercury threshold pressure from central North Sea reservoir cores. The fault rock was recognized as cataclastic fault.....	102
Table 4.5 Summary of the permeability results (gas, brine and distilled water measured at ambient stress) and mercury threshold pressure from central North Sea reservoir cores. ....	103
Table 4.6 Summary of the rectilinear blocks permeability results from Southern North Sea reservoirs samples (gas, brine and distilled water permeability measured at ambient stress).....	105

Table 4.7 Basic properties, gas, brine and distilled water permeability, b-factor and mercury-air threshold pressures from 90 Fathom fault and host rock samples. a reflects the sealed/unsealed samples for mercury injection. ....	106
--	-----

## Chapter 5

Table 5.1 Overview of the existing Klinkenberg correlation factors; $K_{ap}$ is apparent permeability and $\phi$ is porosity. ....	139
Table 5.2 Summary of the number of samples analysed under different experimental conditions. ....	141
Table 5.3 Stress dependent gas and brine permeability of cataclastic fault core samples from Central North Sea reservoirs. ....	145
Table 5.4 Petrophysical properties of fault rock, slip factor, slip radius and gas, brine power law exponents from central North Sea data. ....	145
Table 5.5 Basic properties and stress dependent single phase gas and brine permeability (mD) from southern North Sea reservoir cores. ....	147
Table 5.6 Stress dependent gas and brine permeability of 90 Fathom fault rock samples and Miri exposure fault rocks, Malaysia. ....	150
Table 5.7 Petrophysical properties of fault rock, gas slippage factor, slip radius and gas, brine power law exponents from outcrop samples. ....	151
Table 5.8 Table summarizes the selected permeability stress sensitivity models of low permeability tight rocks from literatures. ....	156

## Chapter 6

Table 6.1 List of the total number of samples analysed and the conditions under which measurements conducted. ....	180
Table 6.2 Stress sensitivity of effective and relative gas permeability $k_{rg}$ of Group-A central North Sea reservoir samples. The effective permeability equals the absolute permeability at zero percent water saturation. The plugs water saturations were altered by humidity chambers and centrifuge technique. The effective and relative gas permeability as well water saturations presented here are average of the host and fault. ....	185

Table 6.3 The stress sensitivity of effective gas permeability and relative gas permeability, $k_{rg}$ of Group-B central North Sea samples. The effective permeability equals the absolute permeability at zero water saturation. The water saturation of samples was altered by centrifuge technique and by relative humidity chambers. The capillary pressure data and water saturation shown in red color were obtained using humidity chambers, all other saturations were changed by centrifuge method. ....	188
Table 6.4 Stress sensitivity of absolute, effective and relative gas permeability $k_{rg}$ of Central North Sea host reservoir samples. The effective permeability equals the absolute permeability at zero water saturation. The saturation of samples was altered by using only centrifuge technique. ....	189
Table 6.5 Two-phase flow properties (capillary pressure and relative permeability) from southern North Sea core samples. The effective permeability equals the absolute permeability at zero water saturation. The saturation was altered by using centrifuge technique and relative humidity chambers. The data presented with blue coloured rows were obtained by using relative humidity chambers. All other data was obtained using centrifuge techniques. ....	192
Table 6.6 Summary of the effective and relative permeability and capillary pressure data data from Hopeman fault rock samples obtained during present study. ....	194

## Chapter 7

Table 7.1 The absolute fault and host permeabilities and porosities assigned to simulation models that based on data presented in <b>chapter 5</b> .....	224
Table 7.2 The table below shows the input variables for generating fault and host rock relative permeability and capillary pressure curves using equation of Brooks and Corey (1964). ....	226
Table 7.3 The summary of the different case scenarios of water-oil simulations run during the study. ....	230
Table 7.4 The summary of the different case scenarios of gas-water system simulations run during the study. ....	235

# 1 INTRODUCTION

---

## 1.1 Introduction

Faults can act as fluid flow barriers dividing petroleum reservoirs into different compartments that might severely affect the distribution and the productivity of hydrocarbons within subsurface reservoirs (e.g. Gibson, 1998; Elleveset et al., 1998; Fowles and Burley, 1994; Knai and Knipe, 1998; Manzocchi et al., 1999; Fisher and Knipe, 1998, 2001; Faulkner and Rutter, 2000; Sperrevik et al., 2002; Crawford et al., 2002; Shipton et al., 2002; Manzocchi et al., 2002; Al-Hinai et al., 2008; Manzocchi et al., 2010; Tueckmantel et al., 2010 and 2012). As stated by Manzocchi et al. (2010) that fault rocks affect fluid flow in three different ways. First, they act as a complete barrier to fluid flow by juxtaposing permeable layers against impermeable layers. Second, fault rocks may have lower permeability than the host rock, resulting in a reduction in the rate of flow across the fault. Third, they could create fault-parallel pathways for fluid flow. The petroleum industry has long since argued that faults can act as barriers (e.g. Smith, 1966, 1980; Berg, 1975; Watts, 1987; Alexander and Handschy, 1998; Fisher et al., 2001) to fluid flow. Examples of fields containing such barriers have been presented by many authors (e.g. Jolley et al., 2007; Zijlstra et al., 2007; Al-Hinai et al., 2007). Understanding the impact of faults on fluid flow is important for predicting reservoir performance also planning and development strategies (Fisher and Jolley, 2007). For example, unexpected fault-related compartmentalization can lead to dramatic reserve write-downs or even project abandonment. On the other hand, un-swept compartments can be very profitable targets for in-fill drilling (Professor Fisher, pers. Com.).

The main focus of the current study is to obtain data on petrophysical properties of fault rocks found within the siliciclastic sediments. The impact of faults on cross-fault flow was analysed by integrating the microstructural examination, X-ray tomography and

laboratory measurements of single- and multi-phase properties of fluid flow that are necessary for accurate modelling of reservoirs so that the uncertainties can be minimized. The first part of this chapter gives a theoretical background about the effect of faults on fluid flow. The second part of this chapter provides the issues related to the current fault rock petrophysical properties that have been investigated and the objectives of the study. The chapter then ends with a brief overview of the outline of this thesis.

## **1.2 Impact of faults on fluid flow: an overview**

Fault compartmentalization due to sedimentary heterogeneity plays significant role in hydrocarbon reservoirs by acting as a barrier (Manzocchi et al. 1999; Caine et al., 1996). Faults within hydrocarbon reservoirs might act as a potential seal by juxtaposing the reservoirs against non-reservoir formations as shown in **Figure 1.1**, such faults are usually called as juxtaposition seals (Watts, 1987). Juxtaposition seals are extensively recognized as these provide an important barrier for fluid flow on geological and production time-scales (e.g. Knipe, 1997; James et al., 2004). There is no such evidence that show about juxtaposition seals, that have formed conduits for fluid flow or after self-sealing, would have never acted as a conduits for fluid flow (Watts, 1987). The process of faulting might result in producing a fault gouge (here referred to as the fault rock) that also potentially restricts the fluid flow; such faults are reported as fault seals *sensu stricto* (Watts, 1987). The impact of fault rocks on fluid flow is yet debatable, few studies argue that fault rocks are the main reason to trap hydrocarbons on both geological and production time-scales (e.g. Knipe et al., 1997). Others studies have reported that faults are most likely are very thin and are not continuous to behave as a major barrier to fluid flow on geological time-scales. So, it is not necessary to be considered when predicting the petroleum traps (e.g. James et al., 2004). However, there is more agreement that fault rocks could act as a barrier.

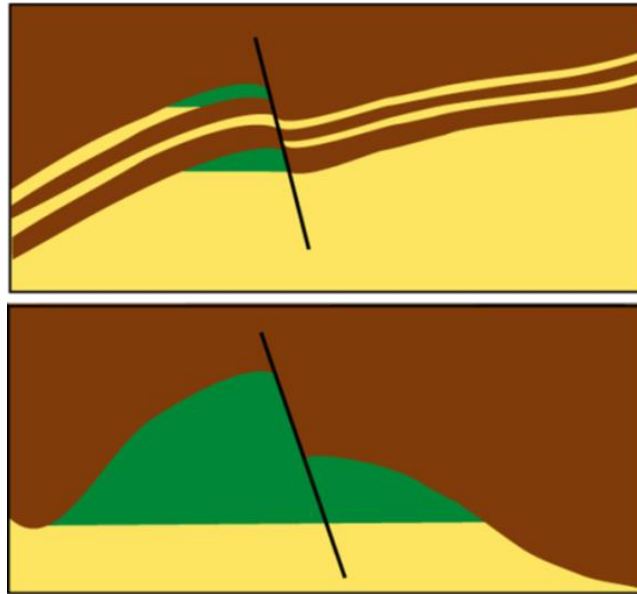


*Figure 1.1 Schematic diagram showing the difference between a juxtaposition seal (top) and a fault rock seal (bottom) (from Fisher, pers. com.2012).*

Moreover, the authors have reported that compartmentalization due to fault sealing could affect reservoir productivity and is important to take account of these effects into simulation and modelling (e.g. Jolley et al., 2007). There is evidence from many oil and gas fields currently being produced that have experienced significant productivity problems as a result of fault compartmentalization. Examples of such fields are Rotliegend reservoirs in the southern North Sea (e.g. Hulthen et al., 2010). Apart from that van der Molen et al., (2003) showed that a 280 bar pressure difference generated across a fault during production from a Rotliegend reservoir of offshore Netherlands (**Figure 1.2**). Al-Hinai et al. (2008) investigated the similar field which was reported by van der Molen et al. (2003) and found that the large pressure difference might not be explained based on the information of absolute permeability of fault rocks. However, they argued that the behavior of such compartmentalized reservoir could be explained by considering the two phase flow properties of the fault rocks by incorporating into simulation model. Moreover, Zijlstra et al. (2007) also conducted simulation and modelling studies of fault compartmentalized reservoir from Rotliegend reservoirs and he found that the fault were acting as barriers to production. Another example of fault modelling and history matching of the fault related reservoir comes from the work of Jolley et al. (2007). This thesis aims to investigate the extent to which fault rock impacts the fluid flow within petroleum reservoirs.

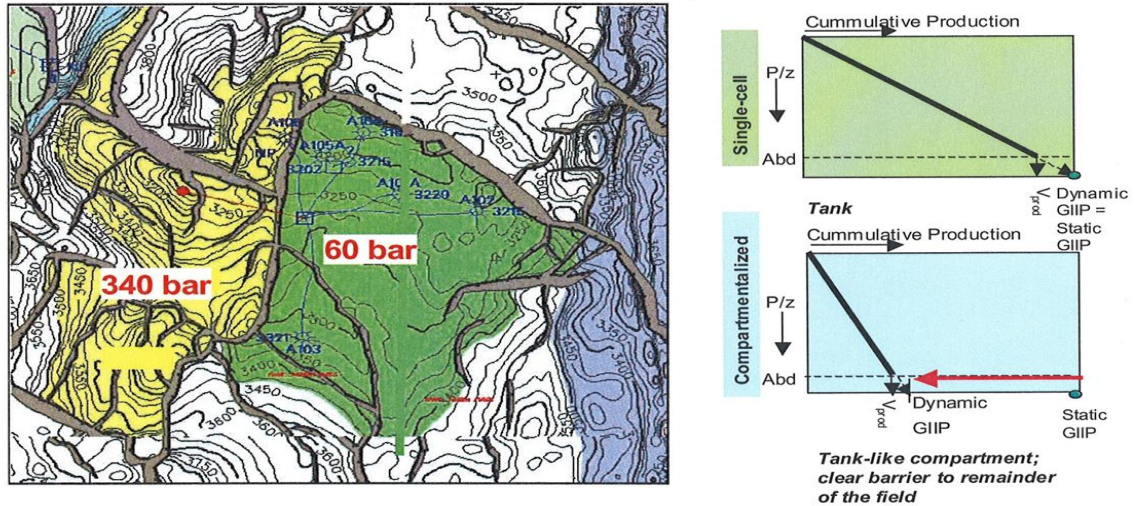


Figure 1.2 The above diagram is showing a 280 bar pressure difference that built up across faults in the Rotliegend reservoir from southern North Sea field as a result of petroleum production (from van der Molen et al., 2003).

### 1.3 Issues related to current fault rock petrophysical properties data

Faults act as major barriers to fluid flow within the compartmentalized reservoirs (e.g. Fisher and Jolley, 2007) therefore, it is necessary to accurately model the impact of faults on fluid flow. For accurate modelling behavior of such reservoirs it is necessary to have accurate fluid flow properties. The following section outlines the impact of confining stress as well as the impact of brine composition on fault rock flow properties that will be addressed in this thesis.

#### 1.3.1 Effect of stress on petrophysical properties of fault rocks

An important aspect investigated in this thesis was the stress sensitivity of permeability of fault rock. The fault rock permeability measured at ambient stress conditions are well documented (e.g. Gibson et al., 1998; Ellevset et al., 1998; Knai and Knipe, 1998; Fisher and Knipe, 1998; 2001; Sperrevik et al., 2002; Tueckmantel et al., 2011, 2012). However, it is well known that laboratory measurements of the permeability of tight rocks are very stress sensitive (e.g. Morrow and Brower, 1986; Byrnes and Castle, 2000). For example, routine core analysis permeability measurements made on tight gas sandstones may be several orders of magnitude lower than measurements made at in situ stress conditions (e.g. Byrnes et al., 2010). If this is the case for fault rocks, the

most commonly used workflow (e.g. Fisher and Knipe, 2001) to calculate fault transmissibility multipliers to incorporate fault rock properties into simulation models could be based on measurements that underestimate fault permeability. The single-phase permeability values are routinely used by industry to calculate transmissibility multipliers that are incorporated into production simulation models to account for the impact of faults on fluid flow (e.g. Fisher and Jolley, 2007). To assess the extent to which the measurements conducted at low stresses might affect the results of fault seal analysis. The present study has conducted experiments to examine the stress sensitivity of the absolute permeability of fault rock samples obtained from reservoir core samples from North Sea fields and outcrops samples supplied from 90 Fathom fault and from Mirri airport road exposure Malaysia.

### **1.3.2 Fluid-rock chemical interactions**

The permeability of sandstone samples containing clays is sensitive to brine composition (e.g. Khilar and Fogler, 1984; Lever and Dawe, 1987). The clays minerals are the main reason to influence the permeability of sandstones reservoirs when exposed to water (e.g. Wilson and Pittman, 1977). As a result understanding the influence of clay mineralogy and pore fluid sensitivity on permeability is necessary to investigate the extent to which it affects the fault rock permeability. The physiochemical interactions between water and clay minerals severely impact the sample permeability (e.g. Byerlee, 1999). Israelachvili et al. (1992) demonstrated that the influence of water interacting with rock surfaces might result in formation of layer of bound water on mineral surfaces. Fault rock samples if they contain clay mineral fractions such as those generated within the clay bearing fault gouges or phyllosilicate framework, fine grained clays might exist in between pore spaces of such faults (e.g Rutter et al. 1986). If permeability of such samples measured with distilled water might be affected due to swelling clay minerals and fine particles mobilization, as a result the effective pore throat size of rock can be reduced due to swelling clay minerals or by creating a layer of immobile bound water which coats the mineral surfaces (e.g. Faulkner, 2004).

The impact of faults on fluid flow within production simulation could be modelled by applying transmissibility multipliers to the face of grid blocks adjacent to faults that has become a routine in industry (e.g. Manzocchi et al., 2002). Actually, there are several software packages that allow transmissibility multipliers to be easily calculated for

gridblocks adjacent to faults. Unfortunately, much of the fault permeability data used in TMs calculations is of questionable quality having been measured under inappropriate experimental conditions (e.g. using distilled water (Fisher and Knipe, 2001) instead of the reservoir brines. The experiments were conducted to measure the sensitivity of the absolute gas and liquid permeability of fault rocks. The experiments were performed using brine of different compositions to assess the extent to which the measurements conducted using different brine composition could affect the results for fault seal analysis. In addition, distilled water permeability was also measured that could be used to compare and correct the existing fault rock permeability data (e.g. Fisher and Knipe, 2001) though the data can be used with confidence for fault modelling.

## **1.4 Faults treatment in simulation and modelling**

Fault rocks often impact the reservoir productivity by reducing the rate of fluid flow, the rate of reduction of fluid flow across fault could be modelled by the use of simulations. Reservoir simulation is a well-established tool to analyze the productivity of petroleum reservoirs and to estimate the reservoir's capacity (e.g. Durlofsky, 2004). Authors have argued that the impact of fault rock would not only be described based on their absolute permeability but it is essential to take account of their relative permeability and capillary pressures of fault rock (Manzocchi et al., 2002). There are many papers on single phase (e.g. Fisher and Knipe, 1998, 2001; Sperrevik et al., 2002) but far less on fault rock two-phase (e.g. Al-Hinai et al., 2008; Tueckmantel et al., 2011) flow properties (e.g. capillary pressure and relative permeability) have been published. Therefore, an important aspect investigated in this thesis was the two-phase flow (relative permeability and capillary pressure) behavior of fault rocks. The two phase flow properties were measured in the laboratory was used for simulation and modelling to analyse the cross fault flow behaviour.

In literature, there are many examples that have been published to demonstrate the production history match by simulation modelling that were achieved using absolute permeability of fault rocks (e.g. Knai and Knipe, 1998; Jolley et al., 2007). In some cases the history match was improved by reducing the transmissibility multipliers below the calculated values (Fisher, 2005). To reduce transmissibility multipliers by several orders of magnitude might not be justifiable, however the possible explanation of

aforementioned approach of reducing transmissibility multipliers those based on absolute permeability values could be the ignoring of two-phase flow that should be considered for fault rock flow modelling. Authors, such as Manzocchi et al. (2002) have explained potential importance of incorporate the two-phase flow (relative permeability and capillary pressure) properties into simulation models. In addition, few recent publications has also provided that history matching could be significantly improved by incorporating the two-phase flow instead the predictions made using the transmissibility multipliers that were calculated based on single phase permeability values (e.g. Al-Hinai et al., 2007; Zijlstra et al., 2007).

A complete fault seal analysis workflow to build fault reservoir model from mapping to dynamic modelling is presented in **Figure 1.3**. It should be noted that mapping of faults is easy; however, the measurements of petrophysical properties of fault rocks within laboratory are difficult, due to many reasons such as the friable nature of many fault-related rocks within field and the difficulty of drilling and retrieving core samples from fault section. Petroleum industry avoids drilling and coring fault sections due to complications (i.e. drilling hazards). Drilling in fault sections might result in mud losses and there might be over pressured reservoir formations. Moreover, the measurements within laboratory are time consuming and difficult because of the most of the fault rocks exhibits low permeability, which needs longer time to be performed.

The data from cataclastic and phyllosilicate-framework fault were obtained from cores samples of different fields from North Sea and Hopeman outcrop faults. These data sets of two-phase flow (relative permeability and capillary pressure) were incorporated into Eclipse2013.1 simulation software to model the impact of faults on fluid flow. The flow across fault was modelled by based on the (TMs) multipliers calculated from single phase permeability and using LGR by assigning fault rock their own relative permeability and capillary pressure curves.

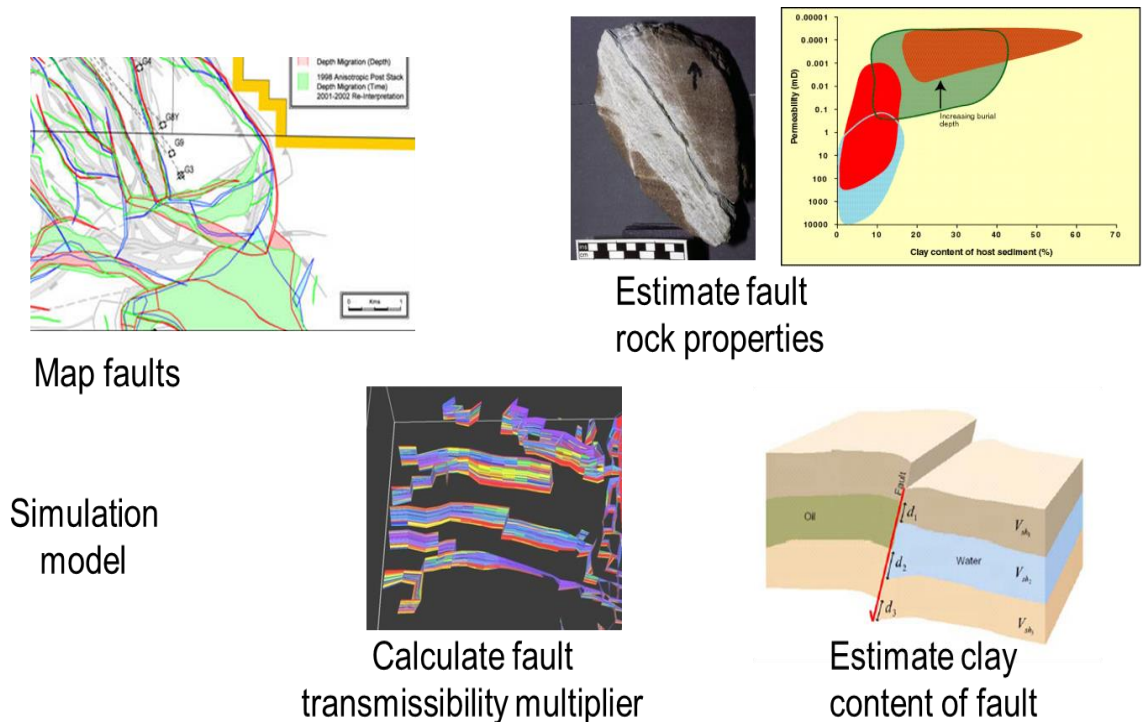


Figure 1.3 Workflow to build fault reservoir models incorporating fault rock properties. Input data comprises mapping of faults, outcrop analogues, seismic interpretation, estimating and measuring fault rock properties in laboratory (from Fisher, pers. com.2013).

## 1.5 Research objectives

This study aims to explore the impact of brine composition on permeability of fault rock, stress sensitivity of fault rocks and to examine the factors that affect the fault rock permeability stress sensitivity. There is evidence from the laboratory experiments that the permeability of tight rocks is sensitive to stress than high permeable samples (Byrnes et al. 2010). If this is the case for fault rocks, the permeability of fault rock might be lower by many orders of magnitude at in-situ conditions. Although, this might be due to experimental artefact or core damage effects as core is brought to surface, that might show different stress sensitivities than the in-situ reservoir conditions (Holt and Kenter, 1992). To investigate the extent to which permeability changes due to increase in stress, the measurements were made at a range of stress conditions from ambient to in-situ stress. This will help to accurately predict fluid flow behavior across fault rock and to reduce the uncertainty in modelling fluid flow within fault compartmentalized reservoirs. In addition, a key aim was to assess the implications of these properties for petroleum production. In terms of the former aims, the project aims to assess both the

accuracy of data currently available on fault rock permeability (e.g. Fisher and Knipe, 2001).

Another aim was to obtain data on relative permeability and capillary pressure of fault rocks because the fault rock two-phase flow data is in sparse. The large amount of time was spent on running experiments, collecting and analysing the data, in addition to that attempts were also made to model the data by simple synthetic reservoir simulation model to investigate the implications of the results.

## **1.6 Thesis outline**

**Chapter 2** is aimed at introducing the reader to the relevant literature covering the subject of fault rock petrophysical properties by presenting a review of these properties (single phase and multiphase flow) of faults. The fault rock properties reviewed based on the knowledge of outcrop and reservoir cores studied during the exploration and appraisal of petroleum reservoirs. In addition, few examples from North Sea fields observations are presented to increase understanding that how faults affect the fluid flow.

**Chapter 3** describes the materials studied and the methodologies adopted during this research. Firstly, it provides a gives an overview of the fields studied then provides detailed description of the single phase flow experimental setup used during this research work. In addition to single phase flow experiments, multi-phase flow experiments were conducted, the experimental procedures are also described in this chapter.

**Chapter 4** presents experimental results (e.g. single phase Klinkenberg corrected gas, brine and distilled water permeability and mercury air threshold pressures). The mineralogy and microstructural properties of samples studied during this research are also presented in this chapter. In, particular this chapter provides the gas and liquid permeability differences, controls and the impact of brine composition on fault rock permeability.

**Chapter 5** provides the details about the stress sensitivity results of fault rock permeability (single-phase gas, brine and distilled water permeability). The results obtained on stress sensitivity were also analysed and discussed in this chapter. This

chapter analyzes and explores the combined effects of changing confining stress and pore pressure on slippage parameters and absolute permeability. The samples were obtained from North Sea reservoirs cores and outcrops were collected from Miri airport road exposure Malaysia as well as 90 Fathom fault.

**Chapter 6** presents laboratory results on two-phase flow properties (gas relative permeability and capillary pressure) of fault rocks. The effective gas permeability stress sensitivity is also discussed in this chapter. The relative permeability data obtained were compared with published data sets of fault rock.

**In Chapter 7** laboratory results provided in **Chapter 6** are incorporated into the industry standard Eclipse 2013.1 simulation software to model the flow across faults to investigate the implications of the results.

**Chapter 8** summarizes the conclusions derived from each chapter that form the main findings from this thesis. Furthermore, aspects in which the results of this thesis could be applied have been identified and presented. The chapter concludes with recommendations on possible further work.

# 2 Petrophysical properties of fault rock: a literature review

---

## 2.1 Introduction

This thesis assesses the key controls on the fluid flow properties of fault rock found within the subsurface reservoirs by integrating microstructural and petrophysical property analysis. In the following chapter, previous work on these aspects is reviewed. The chapter begins by providing a classification of fault rocks found within siliciclastic sediments. The chapter then reviews previous studies on the petrophysical properties of fault rocks. Finally, some examples are provided on how faults impact fluid flow in the petroleum reservoirs from the North Sea.

## 2.2 Faults and their classification based on siliciclastic sediments

Several studies have shown that faults can have a significant impact on fluid flow within petroleum reservoirs acting either as barriers or conduits (e.g. Fisher and Knipe, 1998; Fisher and Jolley, 2007). The microstructure and petrophysical properties of fault rocks are controlled by a number of deformation and diagenetic processes including: grain fracturing, grain contact quartz dissolution, cementation as well as the mixing and smearing of clay minerals along the fault (Fisher and Knipe, 2001). There are generally three ways by which faults are thought to compartmentalize or affect the reservoir behavior (e.g. Manzocchi et al., 2010). First; they may juxtapose permeable and impermeable layers. Second, fault rocks may have lower permeability than the host rock, resulting in a reduction in the rate of flow across the fault. Third, they can act fault-parallel pathways for fluid flow. In fact; fault rock architecture is highly variable; therefore there is no simple way to

predict the fluid flow behavior of such reservoirs with explicit models (e.g. Manzocchi et al., 2010). Faulting of rocks might result in several different components that include a core where most of the stress is accommodated (**Figure 2.1**) that is associated with damage zone and supposed to be interrelated to the other different fault entities such as fractures and small displacement faults. The fault formed due to rock deformation exhibits thickness of few meters to centimetres that result into reduction in porosity and permeability due to cataclasis (e.g. Shipton et al., 1998).

Over the past two decades significant amounts of research has focused on assessing the microstructure and measuring the petrophysical properties of fault rocks at low stress conditions that have been found within surface outcrops or the core recovered from petroleum reservoirs (Antonellini and Aydin, 1994; Gibson, 1998; Ellevset et al., 1998; Knai and Knipe, 1998; Fisher and Knipe, 1998,2001; Sperrevik et al., 2002; Al-Hinai et al., 2007; Tueckmantel et al., 2010).

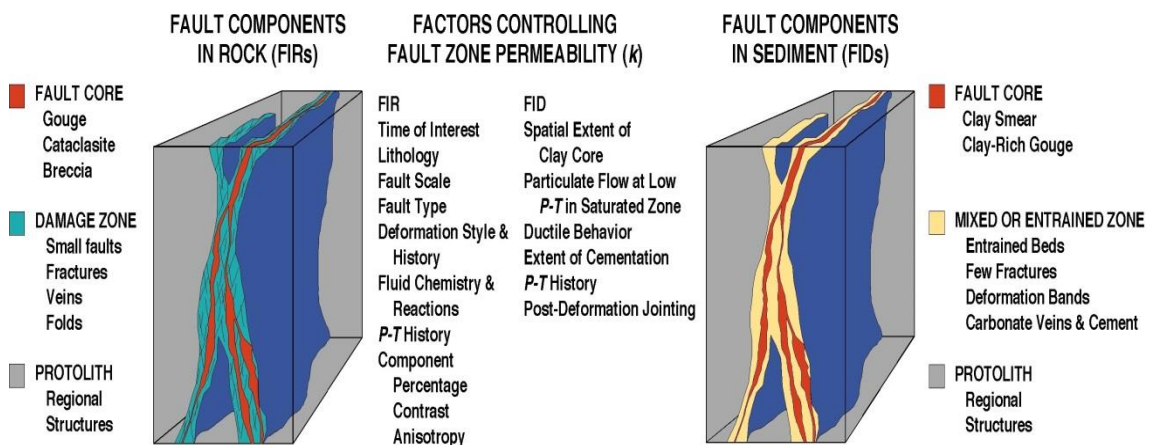


Figure 2.1 Conceptual illustrations of the faults formed within poorly lithified sediments and its components shows how they might affect the fluid flow (taken from Caine et al., 1996 and 2007).

In general, the petroleum industry has been quite successful at avoiding drilling, or at least coring, major seismic-scale faults. Faults that are present in core, therefore, tend to have a relatively small throw (usually <10 cm) (e.g. Fisher and Knipe, 1998). So the analysis of fault rocks collected from outcrop provides the method of directly investigating the microstructural and petrophysical properties of fault rocks along seismic-scale faults. According to Fisher and Knipe (1998, 2001) the petrophysical properties of faults are controlled by various processes such as:-

- The amount of clay minerals present within the sediment during faulting;
- Stress and temperature history during pre-, syn- and post deformation;
- The porosity due to cataclasis at the time of faulting;
- The sediments grain size and sorting.

Faults found within hydrocarbon reservoirs and surface outcrops based on their clay content and amount of cements can be classified into different types such as disaggregation zones, phyllosilicate-framework fault rocks, cataclasites, clay smears, and cemented faults (**Figure 2.2**) (e.g. Fisher and Knipe, 1998, 2001). Aforementioned types of fault rocks are discussed below.

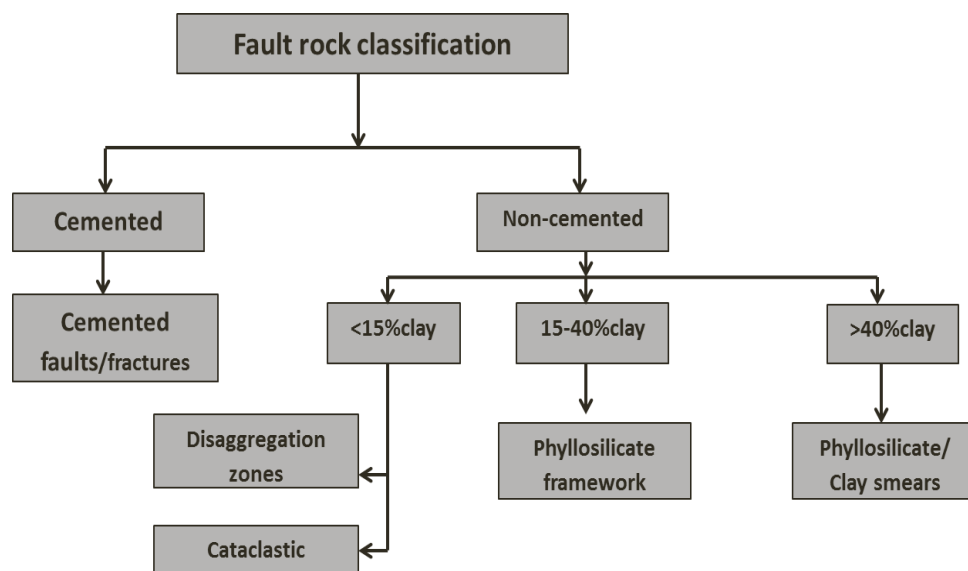


Figure 2.2 Illustration is the fault rock classification based on clay/phyllsilicate content shows important control of fault rock development (from Fisher and Knipe, 1998,2001)

### 2.2.1 Disaggregation zones

Disaggregation zones (**Figure 2.3**) are formed at poorly lithified clean sands (<15% clay) at low stresses. Faulting occurs by independent particulate flow without grain fracturing (e.g. Knipe et al. 1997, Fisher and Knipe 1998; Ottesen and Ellevest, 1998). The lack of grain fracturing and the low clay content means that these faults rocks do not act as barriers to fluid flow (Fisher and Knipe, 2001).

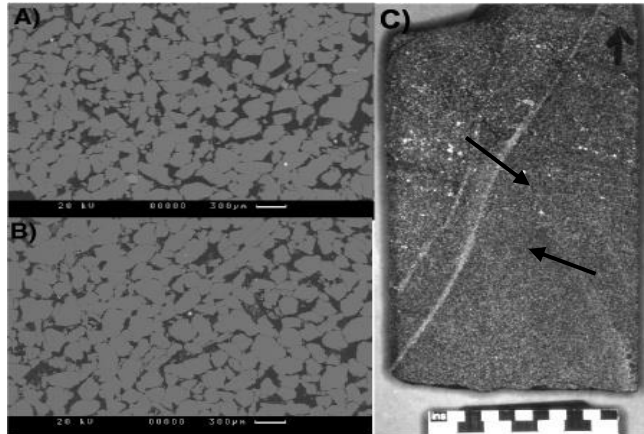


Figure 2.3 BSEM images of (A) a disaggregation zone and (B) the adjacent undeformed sandstone. C) Hand specimen containing two disaggregation zones – arrows (from Fisher, 2005).

### 2.2.2 Cataclastic faults

Cataclastic faults (**Figure 2.4**) form under higher effective stress, which in porous, clean (<15% clay) sandstone results in grain fracturing and porosity collapse. Cataclastic fault rocks have been extensively studied by various researchers (e.g. Engelder, 1974; Knipe et al., 1989; Antonellini and Aydin, 1994, 1995). Cataclastic faults in clean sandstones usually have reduced permeability and increased capillary threshold pressure compared to their associated host sediments (Fisher and Knipe, 1998). The reduction in permeability occurs because:

- i. The size of grains reduces during the deformation resulting in a collapse of macroporosity. In addition, grain sorting gets worse allowing the grains fragments to be compacted in an efficient way (e.g. Antonellini and Aydin, 1994, 1995).
- ii. Quartz cementation is often enhanced within the fault following deformation. This occurs because of two reasons. Firstly, the rate of quartz cementation is proportional to the surface area and the cataclastic faults usually have large surface area than the surrounding host sandstone (Fisher and Knipe, 1998). Secondly, faulting removes clays coats the surface of quartz grains (Fisher et al., 1999).

The research done on this type of faults suggests that the permeability, porosity and capillary threshold pressure varies significantly depending on factors such as the

stress, porosity and grain size at the time of faulting and the post deformation thermal history (Knipe et al. 1997; Fisher and Knipe, 1998).

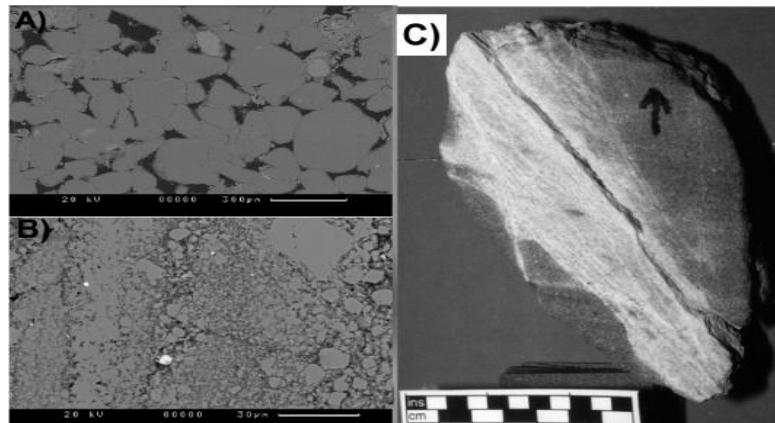


Figure 2.4 BSEM images of (A) an undeformed Rotliegend sandstone and (B) the adjacent cataclastic fault. C) Hand specimen containing a zone of cataclastic faults (from Fisher, 2005)

### 2.2.3 Phyllosilicate-framework fault rocks

Phyllosilicate-framework fault rocks (**Figure 2.5**) are developed in impure sands (15 to 40% clay) (Fisher and Knipe, 1998). These faults have lower permeability and increased threshold pressures compared to their undeformed sands because of two processes. First, clay becomes mixed with framework grains resulting in replacement of macropores with the clay and micro-porosity. Second, following faulting, these fault rocks experience enhanced grain-contact quartz dissolution if the reservoir temperature rises above  $>90^{\circ}\text{C}$  (Fisher and Knipe, 1998). Fisher and Knipe (2001) published data that indicates that phyllosilicate-framework fault rocks act as significant barriers with permeabilities in range from  $<0.1$  to  $<0.0001$  mD having Hg-threshold pressures of 50 to 3000 psi (0.345-20.68 MPa).

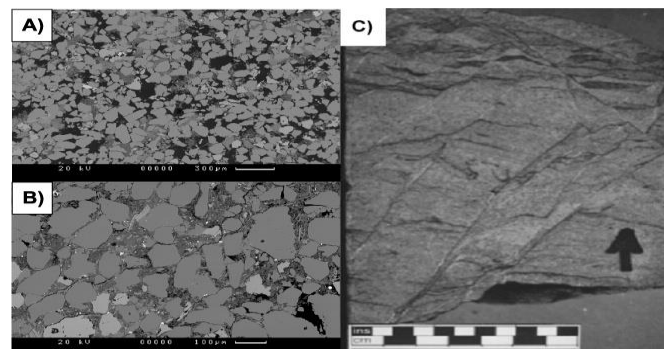


Figure 2.5 BSEM images of (A) an undeformed impure Brent sandstone and (B) the adjacent phyllosilicate-framework fault rock. (C) Hand specimen containing a several phyllosilicate-framework fault rocks (from Fisher, 2005).

## 2.2.4 Clay smears

Faulting of clay-rich sediments (>40%) results in the smearing of clay along the fault plane resulting in clay smear faults as shown in **Figure 2.6**, which are extremely effective barriers to fluid flow (Knipe et al., 1997; Fisher and Knipe, 2001). Several other studies have described the processes of faulting of mudstones and shale layers resulting as clay smears (e.g. Bouvier et al., 1989; Yielding et al., 1997, 2002; Jolly et al., 2007; Solum et al., 2009).

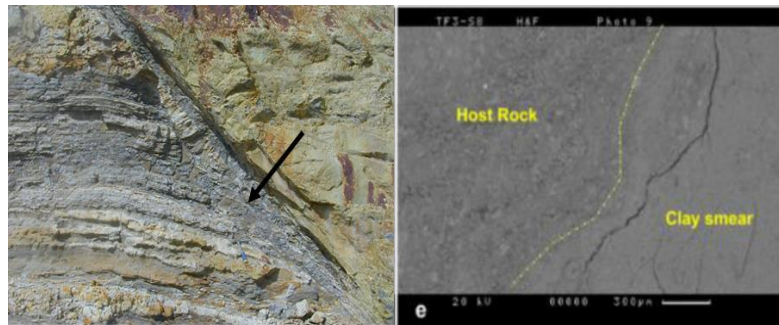


Figure 2.6 (a) A field example of a clay smear (arrow) from near Miri, Sarawak, Malaysia (b) BSEM of typical clay smear fault rock (SEM image taken from Yang Pie, 2013 PhD thesis)

## 2.2.5 Cemented fault rocks

In addition to the fault rock types discussed above, some faults that experience dilation during faulting become cemented (**Figure 2.7**). Cemented fault rocks are particularly common along faults that have experienced movement after they have been uplifted significantly above their maximum burial depth (e.g. Rotliegend reservoirs). Common cements include anhydrite, barite, ferroan dolomite, microcrystalline quartz and siderite. (Fisher and Knipe, 1998)

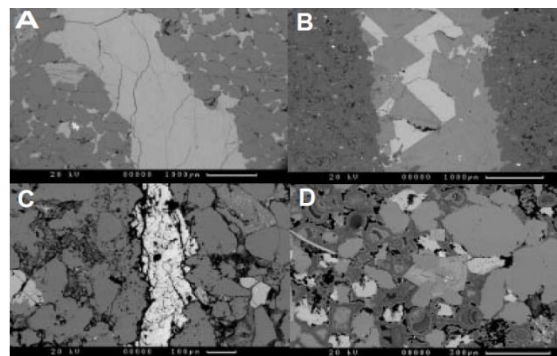


Figure 2.7 BSE micrographs showing: (A) a calcite vein in a calcite cemented sandstones; (B) a dolomite and anhydrite vein in a lithified sandstones; (C) an anhydrite cemented reactivated cataclastic fault; (D) a microcrystalline quartz-cemented water-escape structure, (Fisher and Knipe, 1998).

## **2.3 Petrophysical properties of fault rocks: a review**

To accurately model the impact of faults on fluid flow within petroleum reservoirs information is needed on their absolute permeability, relative permeability and capillary pressure (e.g. Manzocchi et al. 2002). In this section a review is provided on published (single phase and two phase properties) petrophysical properties of fault rock. A large amount of data is available on the single phase permeability of fault rocks (e.g. Antonellini and Aydin, 1994; Gibson, 1998; Ellevset et al., 1998; Knai and Knipe, 1998; Fisher and Knipe, 1998, 2001; Sperrevik et al., 2002; Al-Hinai et al., 2007; Tueckmantel et al., 2011). However; there are only few studies found in literature about fault rock relative permeability (e.g. Al-Hinai et al., 2008; Tueckmantel et al., 2011). In the following sections, all three properties were reviewed to increase understanding about the fault rock properties and their impact on fluid flow within fault compartmentalized reservoirs. In particular, this section provides the description of experimental procedures adapted during fault rock permeabilities measurements and discusses how experimental design can bias measurements and hence bias the fault rock permeabilities. The majority of experiments on fault rocks permeability measurements have solely focused single phase measurements at ambient stress, although very few attempts were made to measure the relative permeability and capillary pressure of because the relative permeability measurements adds the complexity, time and cost to experiments. Experiments are typically carried out on cylindrical and rectangular samples of reservoir cores and outcrops. The pore fluids were typically constitutes of distilled water and gas (Fisher and Knipe, 2001; Faulkner and Rutter, 2000). The issues and the conditions under which measurements were made are described below.

### **2.3.1 Single phase flow properties**

The fault rock petrophysical properties, which have been found in literature comes from a number of sources including measurements made: (i) on faults present in cores recovered from petroleum reservoirs (e.g. Fisher and Knipe, 1998, 2001; Ogilvie and Glover, 2001; Sperrevik et al., 2002) (ii) on fault rocks collected from outcrops (e.g. Antonellini and Aydin, 1994; Gibson, 1998; Evans et al., 1997; Faulkner and Rutter, 1998; Shipton et al., 2002; Flodin et al., 2005; Al-Hinai et al., 2007; Fossen and Torabi, 2009; Tuekmantel et al., 2011 ) (iii) on fault rocks

generated during rock deformation experiments (e.g. Englander, 1974; Zoback and Byerlee, 1976; Crawford, 1998; Bernard et al., 1998) and (iv) sand-clay mixtures produced as analogues to clay-rich fault gouges (Crawford et al., 2002; Al-Hinai et al., 2007). The measurements vary significantly in terms of fluid, stress conditions under which they were made and type of the fault rock.

### 2.3.1.1 Permeability of fault rocks obtained from reservoir core

The most extensive number of fault rock properties published is based on measurements conducted by (Fisher and Knipe; 1998, 2001; Sperrevik et al., 2002). The analyses were made on cores which were obtained from a wide range of reservoirs in the North Sea and Norwegian Continental Shelf. The difficulty in drilling core plugs containing faults meant that the rectilinear blocks containing the faults were cut. These were placed in a core-holder at a confining pressure of ~70psi and permeability measured using the steady-state method with deionised water as the permeant. A summary of the absolute permeability data in relation to clay content is presented (**Figure 2.8**).

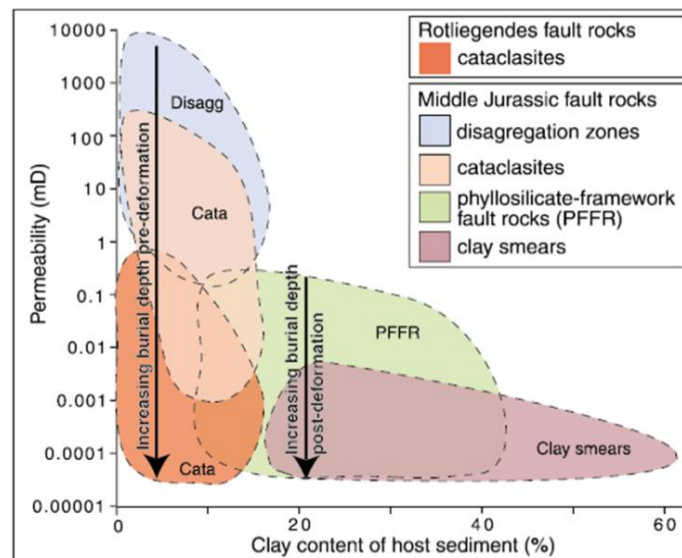


Figure 2.8 Summary of the fault rock permeability data from the North Sea and Norwegian Continental Shelf Permeability is plotted against clay content for the various fault rock types. (from Fisher and Knipe 1998).

Based on the fault rock classification presented in **Section 2.2**, Fisher and Knipe (1998) suggested that the disaggregation zones typically have similar flow properties to the un-deformed reservoir and do not significantly affect fluid flow. Cataclastic faults have permeability of  $>1$  to  $<0.0001$  mD and Hg-threshold pressures of 10 to

2000 psi. Phyllosilicate-framework fault rocks that have been analysed and reported have permeability in range of  $<0.1$  to  $<0.0001$  mD and Hg-threshold pressures of 50 to 3000 psi and the clay smears have permeability of  $<0.0001$  mD and Hg-threshold pressures of  $>3000$  psi.

#### 2.3.1.2 **Fault rocks from outcrop**

Due to difficulty in drilling and coring subsurface fault structures, surface outcrops of deformation bands have received considerable attention by various investigators to delineate the fault rock fluid flow properties. Antonellini and Ayadin (1994) obtained cataclastic deformed fault rock samples of low clay content from Navajo Entrada sandstone of National park Utah USA. The permeability at ambient stress measured under mini-permeameter using gas as a pore fluid. The measured values for fault were ranging from 0.10mD to 100mD and the host sandstones permeability was 600mD. The deformation band permeability on average was three orders of magnitude lower than the host sandstones.

Morrow et al. (1984) made permeability measurements on clay-rich fault gouge from the San Andreas Fault. The measurements were made under confining stress conditions of 800 to 29000psi (5MPa to 200MPa). The permeability results obtained ranges from 0.1md to 1 Darcy. It appears that the values presented were representing the entire plug, the plugs were composed of both fault rock and undeformed sandstone. So any permeability measurements on such samples will represent an average permeability of the fault rock and host sandstone. It is, however, possible to de-convolve the fault rock permeability by assuming that the measured value is the thickness-weighted harmonic mean of the fault rock and the host sediment permeability (Cardwell and Parsons, 1945).

Fowles and Burley (1994) presented the permeability of cataclastic deformation bands collected from the Penrith sandstone in NW England and SW Scotland. The samples permeability was measured with gas and was corrected for Klinkenberg gas slippage effects. The measurements were made at a confining pressure of 220 psi. The permeability of deformation bands ranged from 0.04mD to 2000mD. The helium porosity was also measured on these samples that were in range of 0.045 to 0.31. The permeability results obtained for whole plugs and were not deconvolved to get true value of fault rock permeability. Many measurements were also made

parallel to the fault structure and are therefore dominated by the host sandstone permeability.

Evans et al. (1997) collected two types of outcrop fault samples (i.e. clay rich gouge and damage zone of fine grained cataclastic rock) of East fort thrust fault in Woming USA. Nitrogen gas was used as the permeant for the permeability measurements and the steady state method employed. The rectangular blocks were prepared for measurements. The permeability of rectangular blocks was measured at ambient temperature and single confining stress of 3.5MPa (~500psi) and the plugs were subjected to different confining stress ranging from 3 to 50 MPa (~400 to 7000psi). The damage zone permeability measured was in range of 10mD and 0.1mD. Evans et al. (1997) concluded that damage zone permeability of usually affected by fractures faults yielded a value  $10^4$  times greater in comparison to fault core and protolith. The reported permeability of fault samples were representing to the entire plug permeability and was not deconvolved for true fault rock permeability as discussed above faults are thin volumes of deformation bands and are mixture of host sediments.

Faulkner and Rutter (1998) reported permeability of clay-bearing fault gouge samples, which were collected from an outcrop of the Carboneras fault zone SE Spain. The measurement methods employed were transient and pore pressure oscillation using pore pressure of 4MPa (~500psi) and effective pressure of 160 MPa (~23000psi). The reported permeability was measured by applying different pressure cycles and keeping pore pressure constant to 40MPa (~5000psi). Later, Faulkner and Rutter (2000) measured permeability of the samples which were collected from same location as discussed above using two different pore fluids, the argon gas and water. The measurements were made by applying confining stress of 200MPa. The pore pressure oscillation technique was used to measure the permeability. They reported one order of magnitude reduction in permeability when they changed pore fluid from argon gas to water. The fault sample analysed were composed of clay bearing gouge which they argued that did not react with gas as a pore fluid. On the other hand, water may react with the clayey sands and reduces rock permeability due to clay swelling or movement of fines (e.g Khilar and Fogler, 1984). The measured permeability results were corrected for Klinkenberg slip effects but no attempt was made to de-convolve to get true value of fault rock permeability.

Ogilvie and Glover (2001) studied the petrophysical properties of cemented and uncemented cataclastic faults from the Hopeman sandstone NE Scotland and Southern North Sea reservoir core. The permeability was measured with probe permeametry as well as pressure decay and was corrected for gas slippage effects. The porosity was estimated through volumetric measurements of core samples using two different techniques helium pycnometry and image analysis. The measured fault rock permeability values were in range of 0.009mD to 6.7mD. They reported reduction in permeability of four orders of magnitude in cataclastic deformation relative to their host sandstones and noted a less severe reduction of two orders of magnitude for faults in clay-rich sandstone. The reported permeability reduction values vary from sample to sample, and the values were not de-convolved for fault rock, represents the entire plug permeability.

Flodin et al. (2005) measured the permeability of cataclastic deformed fault rocks from the Aztec sandstone in Nevada. Most measurements were steady-state measurements conducted in a Hassler-type core holder at ~400 psi using helium gas. Six samples were measured at higher pressures (up to 60 MPa – 8700 psi). The porosity measured for host samples was in range of 16.6 and 24.4%. By increasing confining stress up to (60MPa-8700psi), the reduction range in porosity was around 1.7% and 3.2%. The measured permeability of deformed rock was ranging from ~0.28mD to 38.6mD. The measurements were not Klinkenberg corrected and no attempt was made to de-convolve the values for fault rock permeability. The samples ran at higher stresses showed remarkably stress sensitivity (permeability reduction ratios of 0.26 to 0.7).

Shipton et al. (2002) reported permeability of of cataclastic deformation bands recovered from ~60m depth of Navajo sandstones central Utah outcrop. They measured permeability at three different scales, the probe permeametry, whole core and permeability at confining stress levels. The values were in range of 0.4mD to about 3000 mD. The reported permeability values were based solely on the whole plug no attempt was made to deconvolve the permeability.

Al-Hinai et al. (2008) reported permeability data for seven fault plugs from the Clashach fault, Scotland. The fault was 20m minimum displacement and its host rock was medium-grained sandstone. Fault and host rock both were affected by

quartz cementation. The absolute gas permeability reported by Al-Hinai et al. (2008) for the seven plugs were in range of 0.001mD and 0.006mD with its associated host sandstone permeability in range of 10mD to 700mD.

Rotevatn et al. (2008) also reported permeability data on cataclastic deformation bands while investigating a sub-type of deformation band from outcrop of western Sinai, Suez rift, Egypt. The reduction in permeability reported was 2 to 4.5 orders of magnitude to its associated host sandstone. Rotevatn et al. (2013) stated that there is a less significance of deformation band thickness on fluid flow through faulted reservoirs and aquifers. The studied area was an outcrop from Orange, France, and the conclusion was based on number of simulations ran.

Torabi and Fossen (2009) estimated permeability from image processing technique based on the cataclastic and phyllosilicate deformation bands recovered from few core samples of Central North Sea fields and various outcrops of different localities around the globe. As their analysis was based on different deformed bands of cataclastic and phyllosilicate-framework fault rocks from different outcrops therefore they found large variation in estimated values of permeability as a result of large reduction in grain size and were deformed. Although, the grain size reduction was varying along the deformation bands compared to host sands. For example, in one phyllosilicate sample the estimated porosity and permeability was 11% and 0.46mD respectively. Furthermore they estimated host sandstone permeability of 210mD with low clay content and coarse grained sediments. The deformed band permeability was around four orders of magnitude lower than host rock permeability.

Tuekmantel et al. (2011) extensively studied seismic and small scale cataclastic faults. The faults for petrophysical properties analysis were collected from outcrop sandstones in Suez rift Egypt and 90 Fathom UK. The studied faults were of different categories consisting the single deformation band, deformation band zone and slip-surface cataclasite. The permeability measurements were made with steady state (slip corrected) as well as with pulse decay methods using helium gas. The permeability was also deconvolved to get true fault rock permeability value. Tuekmantel et al. (2011) reported that the arithmetic mean of permeability for deformation band is 20mD and 3mD for slip surface cataclasites. Tuekmantel et al.

(2010, 2011) reported only gas permeability; no attempt was made to measure liquid permeability.

#### **2.3.1.3 Fault rocks formed during experiments**

Crawford (1998) measured permeability in the laboratory conducting experiments using tri-axial cell to create cataclastic shear bands in the Hopeman sandstone from the Clashach Quarry, NE Scotland. Permeability was measured using a pulse decay transient technique with mineral oil as a pore fluid. The experiments were conducted at confining pressures of up to around 60 MPa. The permeability of cataclastic fault measured was in range of 0.43mD to 2.50mD. The reported permeability was 2.5 to 3.5 orders lower than host rock due to cataclasis. Bernard et al. (1998) measured the permeability on deformation experiments from the Still Water fault zone Nevada USA; the measurements were made with pulse decay and the maximum effective stress applied was 90 MPa (~13050 psi). They reported two orders of magnitude difference in permeability of fault cores at effective stress of 90MPa. The results represent the entire plug permeability and were not deconvolved for true fault rock permeability. Takahashi (2003) measured permeability on fault rocks generated in laboratory using triaxial cell by creating artificial deformation band of clay smeared category fault. The permeability measured by oscillation techniques. The samples used for measurements were interlayered siltstone and sandstone with permeability values of 0.000001 mD and 0.001mD respectively.

Cuisiat and Skurtveit (2010) reported permeability on artificially generated fault samples comprising a sand-clay sequence under different stress conditions. The experiments were performed and results reported on multilayered sand-clay mixtures. The permeability measurements were made at different stresses, the initial sand permeability reported at 500psi effective stress was 3350mD.

#### **2.3.1.4 Analogue fault rocks**

Crawford et al. (2008) measured permeability on producing sand-clay (kaolinite-quartz) mixtures as an analogue fault gouge. The permeability measurement made by pore pressure oscillation technique by continuous increase in confining pressure from 10 to 55 MPa. The reported permeability in between two extremes of mixtures of sand-clay was ranging from 0.001mD to 1000mD, which was varying over six

orders of magnitude depending on the composition of sand–clays mixture and applied stress range. The reported permeability data were not de-convolved and were measured through the entire plug.

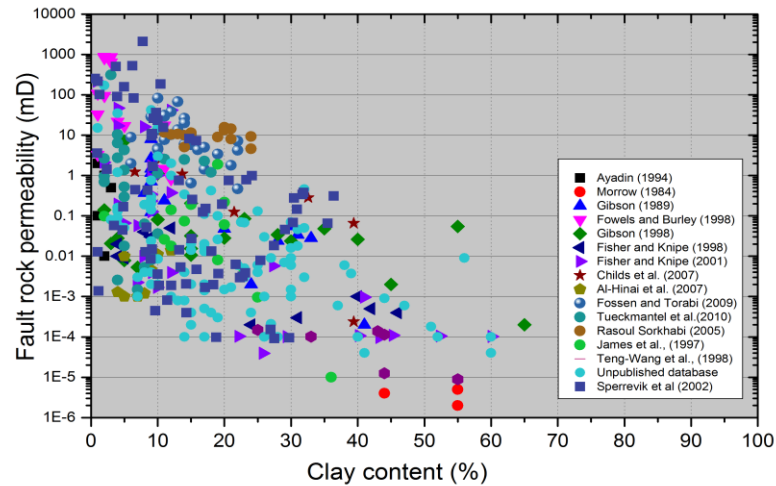


Figure 2.9 Summary of published fault rock permeability data on variety of different fault rock types collected.

The fault rock properties discussed above are now widely used to predict and model the impact of faults on fluid flow. This does not, however, mean that the properties are accurate. Indeed, close inspection of the analytical methods used to collect the fault rock petrophysical data as well as the values themselves give reasons to suspect that the published values could be in error. In particular,

- Most measurements of fault rock permeability (e.g. Fisher and Knipe, 1998, 2001) were made at ambient stress (~70 psi). However, recent measurements have shown that the permeability of fault rocks and tight gas sandstones (e.g. Al-Hinai et al., 2007) are highly sensitive to stress.
- Most measurements of fault rock permeability (e.g. Fisher and Knipe, 1998, 2001) were conducted using de-ionised water despite the fact that the rocks usually contain clay and that makes their permeability very sensitive to brine composition.
- The clay smears are often quoted as having a permeability of <0.0001 mD (e.g. Fisher and Knipe, 2001). This value is far higher than often quoted for shales.

To better parameterise fault sealing behaviours by performing simulation studies and increase confidence in evaluating the cross fault fluid flow behaviour the

experimental work is needed to be conducted under realistic reservoir stress conditions. Emphasis should be given to conduct measurements on samples representative of the subsurface reservoirs and usage of the formation compatible fluids, as these have been selected for present study. Therefore, these results could be used with confidence for evaluating cross fault flow behaviour within fault compartmentalized reservoirs.

Table 2.1 Summary of published permeability and capillary threshold pressure data of variety of fault rock types. It should be noted that (Table 2.1) gives only the ranges of values, but the collected data from each listed author is provided in Figure 2.8.

Author	Fault rock type	Core/Outcrop/synthetic	Permeability Fault (mD)	Permeability Host (mD)	Clay content (%)	Threshold pressure (psi)	Pore fluid	Max: Conf. stress(psi)	Method
Ayadin (1994)	Cataclastic	Outcrop	0.001—2.5	1000	2-3	—	Gas		SS
Morrow et al.,(1981)	Clay fault gouge	Core	0.0002-0.000002	—			water	7255	PDP
Gibson (1989)	Cataclastic	Outcrop	0.0002—8.02	2—3175	5—41	—		3000	SS
Antonellini and Aydin (1994)	Cataclastic	Outcrop				—	Gas		
James et al. (1997)	Cataclastic	Core	0.0001—3.0		—	—	Gas	7250	PDP
Fowles, and Burley (1994)	Cataclastic	Outcrop	0.1—1158		—	—	Gas		
Gibson (1998)	Cataclastic	Outcrop	0.0002—7.20	0.3—3362	—	—			SS/PDP
Fisher and Knipe (1998)	Cataclastic/PFR <sup>1</sup> / Clay	Outcrop	0.0002—0.05		4—46		Water	70	SS
Crawford (1998)	Sand-clay	Synthetic	0.43—2.50	234—473			Oil	14993	PDP
Faulkner and Rutter (1998)	Cataclastic	Outcrop	4-1.6x10 <sup>-6</sup>	—	60—80	—	Gas	5800	PDP
Ogilvie and Glover (2001)	cataclastic	Core/Outcrop	0.009—6.7	—			Gas		PDP/ SS
Fisher and Knipe (2001)	Cataclastic/ PFR <sup>1</sup> / Clay smear	Core	0.0001—41	—	4—60		Water	70	SS
Faulkner and Rutter(2001)	Cataclastic	Outcrop	0.00003—0.0001		60—80		G/W	24000	PDP
Shipton (2002)	Cataclastic	Outcrop	0.3—1.44	168—620				2900	SS
Sperrevik et al (2002)	Cataclastic/ PFR <sup>1</sup> / Clay smear	Core	0.00001—2109		2—36		Water	—	SS
Childs et al. (2007)	Phyllosilicate	Core	0.0002—2.6	0.002—489	4—79				
Al-Hinai et al. (2007)	Cataclastic	Outcrop	0.0012—0.20		4—12	—	Gas		SS/PDP
Fossen and Torabi (2009)	Cataclastic	Outcrop/core	0.65—654		6—22	—	Image analysis		Image analysis
Rotevan et al (2008)	Cataclastic	Outcrop	0.001—575	—	—		Image analysis		Image analysis
Tueckmantel et al.(2010 , 2012)	Cataclastic	Outcrop	0.001—10.50		2—17	15—13000	Gas		SS/PDP

<sup>1</sup> Phyllosilicate-framework fault rock

### 2.3.2 Multiphase flow properties

Since the early twentieth century much has been written about multiphase flow through porous media (e.g. Muskat and Meres, 1936; Dullien, 1992; Pinder and Gray, 2008). Here we highlight some of the important issues and understanding that are relevant to the discussion about fault rock relative permeability and capillary pressure. The flow of a single phase fluid in a porous media (**Figure 2.10**) is generally obtained using Darcy's Law:

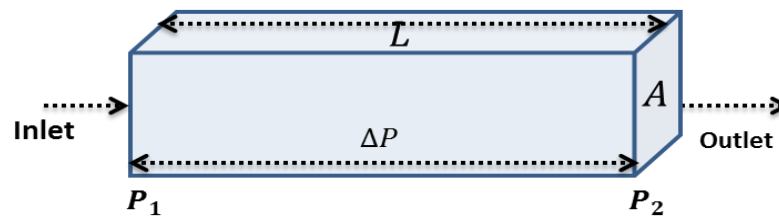


Figure 2.10 illustration of the steady state flow condition

$$q = -\left(\frac{K}{\mu}\right)\left(\frac{A}{L}\right)(\Delta P) \quad (2 - 1)$$

Where:  $q$  = rate of fluid flow through porous media ( $\text{cm}^3/\text{s}$ )

$A$  = flow area perpendicular to flow ( $\text{cm}^2$ )

$\mu$  = Dynamic viscosity of fluid flowing through porous medium (cp)

$\Delta P$  = pressure drop across the porous media (atm)

$L$  = flow path length (cm)

$K$  = Permeability (D)

The "-" sign shows that the direction of fluid flow is from higher pressure to low pressure. When there are two or more fluids flowing through the porous medium, capillary pressures also plays a significant role and an impact on fluid flow.

In reservoir simulation, petroleum engineers are concerned with simultaneous flow of more than one phase. In reservoirs, where there is a two phase system the fluids present will be in immiscible and there will be no mass transfer among phases. One phase will be wetting phase, other will be non-wetting depending the rock wetting conditions. Multiphase flow from reservoir engineering point is the movement of immiscible fluids (oil, water and gas) through porous medium (reservoir). The fluid phases are non-reactive. In this type of fluid flow system, the fluids moves together,

leading to a distinct interfaces. As an example, during enhanced oil recovery process, the gas or water is injected into petroleum reservoir to displace the oil in which one phase is immiscible that is displaced from reservoir pores by another fluid phase. That is the objective of reservoir engineer to study and understand fluid movement/transport within the reservoir and to acquire information to predict, control and manage hydrocarbon production. Such type of study involves building a reservoir simulation model that could provide actual reservoir flow behaviour.

Darcy's law could be extended to multiphase flow, it relates to the total volumetric flow rate of each phase through a porous rock to its pressure gradient, the properties of fluid viscosity and the rock effective permeability,

$$q_w = -k_w A \Delta p_w / \mu_w \Delta x_1$$

$$q_o = -k_o A \Delta p_o / \mu_o \Delta x_1$$

In terms of Darcy's velocity to phases,

$$u_w = -k_w \Delta p_w / \mu_w \Delta x_1$$

$$u_o = -k_o \Delta p_o / \mu_o \Delta x_1$$

In terms of 3D two-phase flow the differential form of Darcy's law could be presented as,

$$u_a = -\frac{1}{\mu_a} k_a (\nabla p_a - \rho_a \nabla z) \quad a=w, o, \text{ equation 2.5}$$

Where,  $K_a$ ,  $p_a$ , and  $\mu_a$  are the effective permeability, pressure and viscosity of phase  $a$ . In reservoirs the two-phase flow could interfere with each other, therefore the effective permeability of phase in presence of other immiscible fluid will always be less than absolute permeability. The relative permeability is widely considered in reservoir simulation and is expressed as,

$$K_a = K_{ra} K, \quad a=w, o$$

### **Formulations in terms of phase pressure and saturations:-**

using  $p_o$  and  $S_w$  as a main variables, equation 2.5 can be written as,

$$\nabla \left( \frac{\rho_w}{\mu_w} k_w (\nabla p_o - \frac{dp_c}{dS_w} \nabla S_w - \rho_w \Delta z) \right) = \partial(\phi \rho_w S_w) / \partial t - q_w,$$

$$\nabla \left( \frac{\rho_o}{\mu_o} k_o (\nabla p_o - \rho_o \nabla \Delta z) \right) = \partial(\phi \rho_o (1 - S_w)) / \partial t - q_o,$$

Carrying out the time differentiation, in equation above (2.5), and diving with  $\rho_o$  and  $\rho_w$ , adding the resulting equation final result would be,

$$\frac{1}{\rho_w} \nabla \left( \frac{\rho_w}{\mu_w} k_w (\nabla p_o - \frac{dp_c}{dS_w} \nabla S_w - \rho_w \Delta z) \right) + \frac{1}{\rho_o} \nabla \left( \frac{\rho_o}{\mu_o} k_o (\nabla p_o - \rho_o \nabla \Delta z) \right)$$

$$= \frac{S_w}{\rho_w} \partial(\phi \rho_w) / \partial t + \partial(\phi \frac{\rho_o(1-S_w)}{\partial t} \cdot \frac{1}{\rho_o} \frac{q_w}{\rho_w} - \frac{q_o}{\rho_o})$$

Note if the saturation is explicitly evaluated than this equation could be used to solve for p. this is IMPES scheme and is mostly used to exploit reservoir two phase flow system.

Capillary pressure plays a significant role if there is two-phase system. The capillary pressure,  $P_c$  is the difference of pressures among two immiscible fluids which are in contact with each other in porous rocks. So, the pressure difference between wetting and non-wetting fluid is the result of the interfacial tension which exists across the interface separating two immiscible fluids. The difference due to capillary pressure could be represented by,

$$P_c = P_{nw} - P_w$$

In equation above the  $P_{nw}$ , is the pressure of the non-wetting phase and  $P_w$ , is pressure of wetting phase.

The difference of pressure in case of two immiscible fluids such as oil and water could be,

$$P_c = P_o - P_w$$

The **Figure 2.11** shows the typical capillary pressure curve that is the example of drainage and imbibition capillary pressure as a function of phase saturation obtained on water- wet samples. The point A on curve represents that the sample is initially fully saturated with water as a wetting fluid, if oil (no-wetting fluid) is injected to

displace water that process would result in a draining process. Furthermore, it would be observed from curve that at point **B**, there will be no more fluid displaced, and the saturation of wetting phase (water) at this point will be irreducible saturation. Conversely, if wetting phase is displaced by injecting non-wetting (oil) that will result in imbibition curve. When the wetting fluid phase that injected to displace non-wetting phase, when it reaches to its maximum value ( $S_w=1-S_{nw}$ ), at that saturation point, there will be zero capillary pressure(C point on the curve).

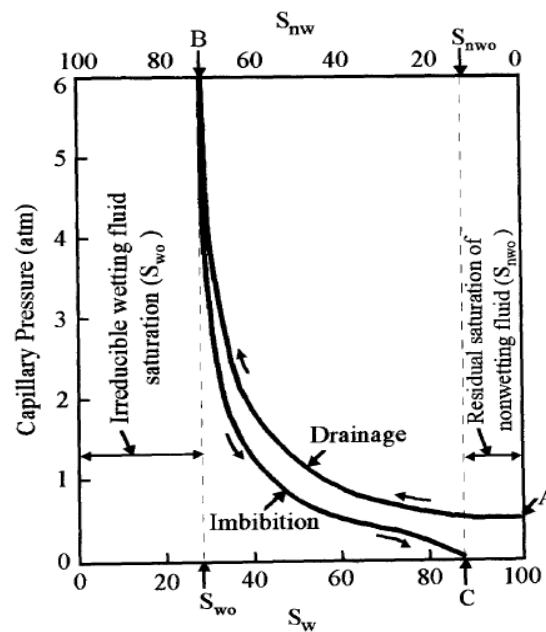


Figure 2.11 The illustration shows the drainage and imbibition capillary pressure curves. (taken from Tiab and Donaldson, 2011)

In fault sealing system, the main parameter that controls the flow of two-phases is the capillary entry pressure (e.g. Shipton et al., 2005). In a two phase system, for a non-wetting fluid to flow through a porous rock pore throat, it is important that its phase pressure must exceed than the phase pressure of the wetting fluid phase by at least its capillary threshold pressure. The capillary flow (i.e. capillary leakage) across fault rock takes place when the net pressure applied by the wetting phase overcomes the threshold pressure or capillary entry pressure that is explained as the minimum pressure which is required to initiate the displacement of brine present within the fault rock acting as seal. Washburn's (1921) equation could be used to estimate the capillary entry pressure  $P_c$ , from the knowledge of rock pore throat size and the interfacial tension between wetting and non-wetting fluids as given below,

$$P_c = \frac{2\sigma\cos\theta}{r} \quad (2 - 2)$$

where:  $P_c$  is the capillary pressure and is in  $\text{dynes/cm}^2$ ;  $\sigma$  is the interfacial tension between wetting and non-wetting fluid as hydrocarbon and water ( $\text{dynes/cm}$ );  $\theta$  is the contact angle between the fluids and rock surface, and  $r$  is pore throat radius ( $\mu\text{m}$ ). According to Berg (1975) the contact angle is a measure of the wettability of fluids and the wettability is the preferential adherence/spreading on solid surface of one fluid in presence of two immiscible fluids (e.g. Mercer and Cohen, 1990). In case of strongly water-wet rock contact angle is equals  $0^\circ$ , for a strongly oil-wet rock that would be  $180^\circ$ . The rocks with intermediate wettability have contact angles of between  $0^\circ$  and  $180^\circ$ .

A porous sedimentary rock consists of a variety of different sizes of pore throats, the minimum pressure that is needed for a non-wetting fluid such as oil or gas to entirely/completely flow through the pore system is controlled by the smallest pore throat radius across the path that is connecting to the largest pore throats. This pressure is usually called as the entry pressure or threshold pressure,  $P_{th}$  (Katz and Thompson, 1986, 1987). The capillary entry pressures are dependent on the pore throat radius and at corresponding capillary entry pressure the pore throat radius could be obtained by empirical relations provided by Pittman (1992). Moreover, the pressure difference between wetting and non-wetting phases could be generated due to buoyancy effects. These effects occur due to the density difference of two immiscible fluids such as hydrocarbons fluid has a lower density than water/brines. The difference in pressure because of the buoyancy forces,  $P_b$ , exerted by a hydrocarbon column can be linked to the density of hydrocarbon column,  $\rho_h$ , and the density of water phase  $\rho_w$ , therefore, the height exerted by hydrocarbon column,  $h$ , and the acceleration due to its gravity,  $g$ , that could be represented by the following equation:

$$P_b = gH(\rho_w - \rho_h) \quad (2 - 3)$$

or, in terms of field units:

$$P_b = 0.433H(\rho_w - \rho_h) \quad (2 - 4)$$

In above equation, the constant 0.433 is a unit conversion, which takes into account the effect of gravity, densities have unit in  $\text{g/cm}^3$ , and  $H$  measured in feet

(Schowalter, 1979; Watts, 1987). In water-wet reservoirs, hydrocarbon fluids can only flow if buoyancy forces  $P_b$  exceeds the threshold pressure  $P_{th}$ . The maximum column height of petroleum fluids that could hold under a seal supported by combining Equations 2-2 and 2-4 in the situation for which  $P_b = P_{th}$  there will be balance between two forces to hold the fluids. Thus,

$$H_{cp} = \frac{P_c}{0.443(\rho_w - \rho_h)} \quad (2 - 5)$$

Several authors have attempted to calculate the pore radius corresponding to entry pressures. Such as, Gibson (1998) reported that pore radius of  $13.3\mu m$  which corresponds to the height of only 2m hydrocarbon column. The pore radius of  $0.18\mu m$  corresponding to petroleum reservoir column of  $137m$  has been reported by Ogilvie and Glover (2001). These data suggested that fault rocks could be barrier to hydrocarbons flow. Moreover, Shipton et al. (2005) argued that poorly sorted fine grained smaller pore throat fault could be capillary barrier to two phase flow but to fully quantify more work is required to understand in what situations it could be barrier. Therefore, for fault rock sealing potential evaluation, it is essential to investigate the two phase flow of fault rocks by collecting the more data that could be calibrated with known hydrocarbon columns/heights found within the hydrocarbon reservoirs (e.g. Fisher and Knipe, 2001).

If fault seal breaches and the threshold pressure of a fault rock exceeds, then the rate of the fluids transfer through the rock would be explained/determined based on an *alternative derivatives of Darcy's law. After seal breaches, two or more fluids start flowing through the porous medium, each individual phase has its own relative permeability which depends upon the number of factors. Such as pore structure and pore throat radius, rock wettability and fluid phases present within the reservoirs (e.g. Dandekar, 2006). The following Darcy's flow equation can be used in case of presence of more than one phase flowing through the porous media,*

$$q_f = - \left( \frac{KK_{rf}}{\mu_f} \right) \left( \frac{A}{L} \right) (\Delta P_f) \quad (2 - 6)$$

where the subscript  $f$  represent a fluid phase flowing through the porous medium;  $Kr$  represents the fluid relative permeability (i.e. the ratio of the effective permeability to absolute permeability of the porous medium).

In case of two-phase flow, the relative permeability of the system would be plotted as function of water saturation (**Figure 2.12**). It can be inferred from **Figure 2.12** that each phase at some stage reaches a point where it becomes immobile and cannot flow. The point at which water flow ceases is called irreducible water saturation. The point where oil becomes immobile is called residual oil saturation. Although, initially it was thought that relative permeability is a unique function of saturations of the fluids flowing through the porous medium, later research showed that there are lots of other factors affecting this. Such traditional relative permeability experiments are difficult to conduct and interpret even for high permeability samples. However, the low permeability experiments are even more difficult to be undertaken. There are not many published data on such measurements of low permeability fault rock samples. Several authors has argued that the tight-rocks within low permeability reservoirs have very complex nature of pore system that is dominated by different shapes of pores such as slotted pores and sheet-like pore throats and higher overburden stresses could result to specific issues concerning multiphase flow. The existence of such a complex pore structure might result in reduced rate of effluent production, such as phase trapping. The explanations about favourable and unfavourable pore structures related to the phase trapping could be found in (e.g. Bachu and Bennion, 2008). Who demonstrates that a pore structure in which the majority of the effective permeability is controlled in a moderately small size of the pore space, which comprises of interconnected meso- or macropores or little cracks and would not be sensitive to water-based trapping. These might be slightly more able to store the water without obstructing the major pores. A pore structure of a more uniformly distributed of micro-pores (1-10  $\mu\text{d}$ ) could be by a slight increment in water saturation might stop flow by clogging the pores with water and in this manner a reduction in effective gas permeability occurs through the entire pore structure. Further he argues that this phenomenon of phase trapping might occurs in pore structures which are very small with narrow pore throats.

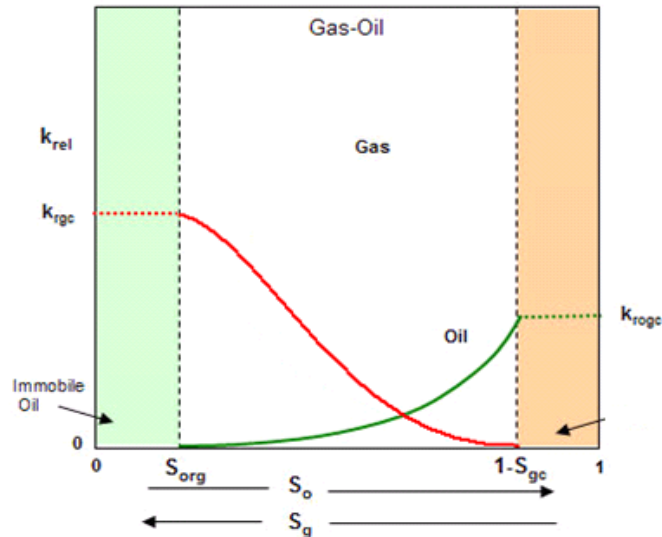


Figure 2.12 A typical relative permeability curve for high permeability rock (from Fekete-2014).

Apart from tapping of phase within confined pore throats, relative permeability could be severely affected by overburden stress. There will be significant difference in behaviour of high relative permeability rock to low permeability and the classical methods and theories of relative permeability analysis might not be applicable. Shanley et al. (2004) used the term ‘permeability jail’ to describe a saturation range within low permeability rocks in which the relative permeability to both the wetting and non-wetting phases were essentially zero (**Figure 2.13**). This contrasts with results from higher permeability rocks in which the relative permeability of one of the phases is always significant (e.g. **Figure 2.13**). However, in low quality rock having very low absolute permeabilities could result in poor relative permeability which is called ‘relative permeability jail’ and it could not be thought as a typical drainage relative permeability functions such as those found within the conventional relative permeability curves. However, several authors have agreed that the permeability jail is an extremely important for reservoir and petrophysical assessment of quality of hydrocarbon resources (e.g. Britt and Schoeffler, 2009). Blasingame (2008) mentioned that aspect as a challenging study with respect to the concept of capillarity controlled flow through porous media. The significance of the “permeability jail” is that rocks with even moderately low permeable (i.e. 0.1mD) may act as efficient barriers to fluid flow (e.g. Fisher et al., pers. comm.). This concept also holds significance regarding fault rock sealing behaviour within multiphase flow systems. As in water-wet reservoirs the cross fault flow of

hydrocarbons occurs when capillary pressure goes beyond the capillary threshold pressure, or when the capillary threshold pressure exceeds (e.g. Manzocchi et al., 2010).

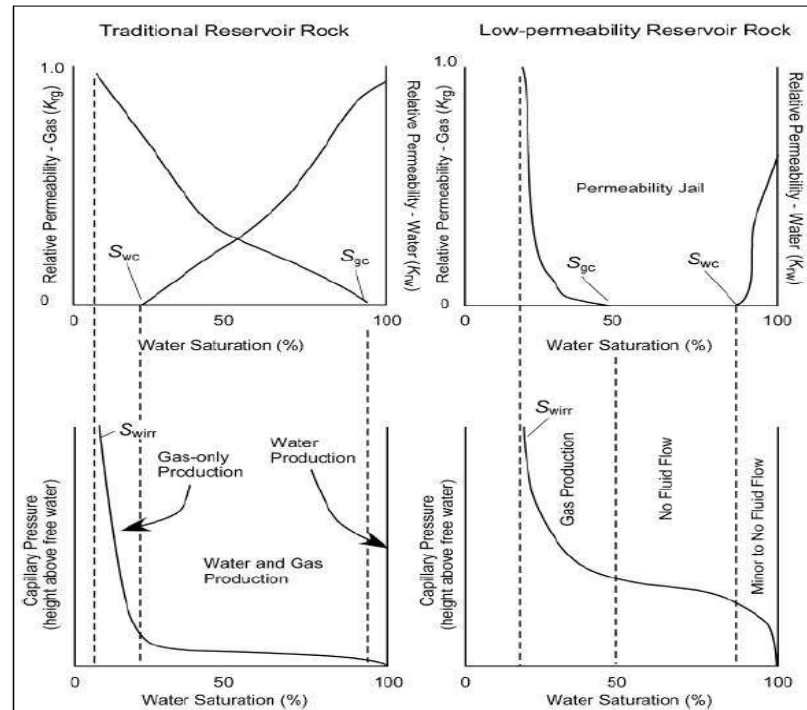


Figure 2.13 Relative permeability curves for high and low permeability rock samples (taken from Shanley et al., 2004)

### 2.3.3 Two-phase flow properties (Relative permeability and capillary pressure) of fault rock

Conventionally, the fault rock simulations and modelling were performed by calculating the fault transmissibility which were solely based on single phase permeability of fault rocks (Manzocchi et al., 1999). However, recently several authors have highlighted the potential importance of incorporating the multiphase flow properties (relative permeability and capillary pressure) of fault rocks into production simulation models (e.g. Fisher and Knipe, 2001; Manzocchi et al., 2002; Al-Busafi et al., 2005; Zijlstra et al., 2007; Al-Hinai et al., 2008; Tueckmantel et al., 2011). Far less data is available on the relative permeability and capillary pressure of fault rock (e.g. Al-Hinai et al., 2008; Tueckmantel et al., 2011) but the data on two-phase flow is small that need to be increased so the data could be used with confidence for modelling the fault compartmentalized reservoir behaviour.

Al-Hinai et al. (2008) published the first data on the gas relative permeability and capillary pressure of the Hopeman fault found in the Clashach Quarry, Hopeman, Invernesshire (**Figure 2.14**). The fault analysed was quartz cemented cataclastic. This increased the importance of the fault related reservoir flow behaviour in dynamic modelling. This measured data were used for modelling of southern North Sea field Rotliegendes reservoir. Al-Hinai et al. (2008) found that neglecting relative permeability and capillary of fault rock can lead to an overestimation of flow through fault by several orders of magnitude.

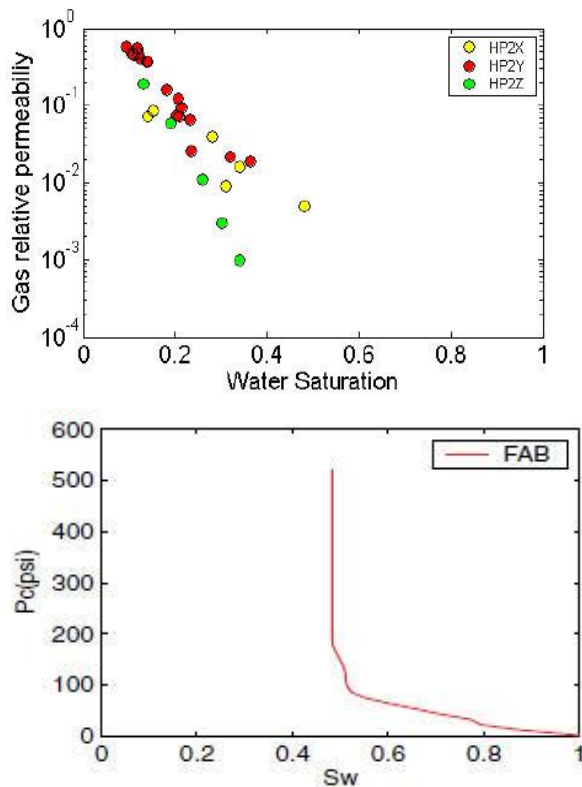


Figure 2.14 Gas relative permeability (left) and capillary pressure (right) of the Hopeman fault rock (from Al-Hinai et al. 2008).

In addition to above, the gas relative permeability on cataclastic fault rock from 90 Fathom Fault was published by Tueckmantel et al. (2011). The reported data were measured on a slip surface cataclasite, deformation band zones, and a single deformation band as well as host rocks (**Figure 2.15**). Tueckmantel et al. (2011) pointed out that there is significant difference in fluid flow properties of fault rocks along small and large scale faults. In particular, the grain size reductions are noticeable in the slip surface cataclasites and the cataclastic porosity variations also influence the cross-fault fluid flow.

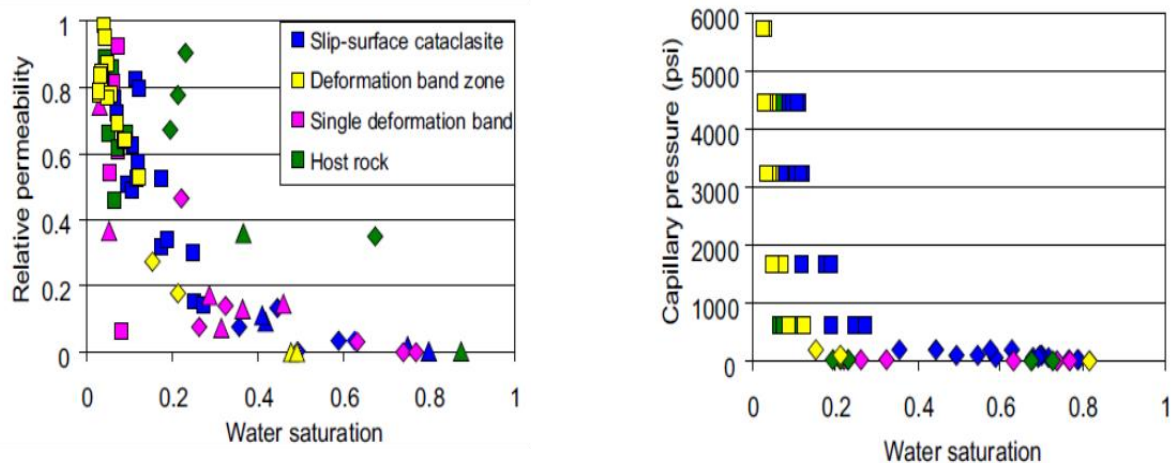


Figure 2.15 Gas relative permeability (left) and capillary pressure (right) from 90 Fathom Fault (from Tueckmantel et al. (2012))

Tueckmantel et al. (2012) attempted to model fault rock relative permeability (**Figure 2.15**) using the equation of Cluff and Byrnes (2010) to assess whether there is any similarity with the two phase flow behavior of tight gas sandstone and cataclastic faults. Zijlstra et al. (2007) model the fluid flow behavior of fault rock reservoirs in Rotliegend sandstones by using the tight gas sandstone data as analogue. In fact, there is a large amount of data exists within the published database on tight gas reservoirs (e.g. Thomas and Ward 1972; Byrnes et al., 1979 and Cluff and Byrnes 2010). Cluff and Byrnes (2010) used a Corey type equation on tight gas sandstone to fit relative permeability curves on his data. As seen in **Figure 2.16**, using Cluff and Byrnes (2010) equation fault rock relative permeability was modeled by Tueckmantel et al. (2012). They modelled fault rock relative permeability by considering two different ranges of absolute permeabilities to fit the curves based on Cluff and Byrnes (2010) equation. The upper absolute gas permeability value was considered 10mD and lower was 0.001mD. The two dashed curves as can be seen in **Figure 2.16** highlights that the tight gas sands exhibits higher relative permeability very few fault rock relative permeability data points are falling under the curves generated. The solid line shows the exponents were increased from its original value of 1.7 to 3 to the fit the experimental data. As the exponent was modified then the more experimental data came under the curve generated shown as solid line in **Figure 2.16**. Tueckmantel et al. (2012) concluded the data does not fit well with model based on tight gas could possibly be due to fault rock heterogeneity. The fault rock is composed of variety of grain sizes, because of this tight gas relative

permeability as an analogue to fault rock relative permeability is less applicable in predicting the behavior of fault compartmentalized reservoir rocks. It should also be noted that the previous measurements of fault rock relative permeability are often derived from outcrops samples (e.g. Tueckmantel et al., 2012; Al-Hinai et al., 2008). However, the question remains that the reservoir cores samples could be appropriate to measure the multiphase phase flow properties and analyze the impact on fault compartmentalized reservoirs. For comparison purpose the samples from fault outcrops of different locations were also used for petrophysical property measurement.

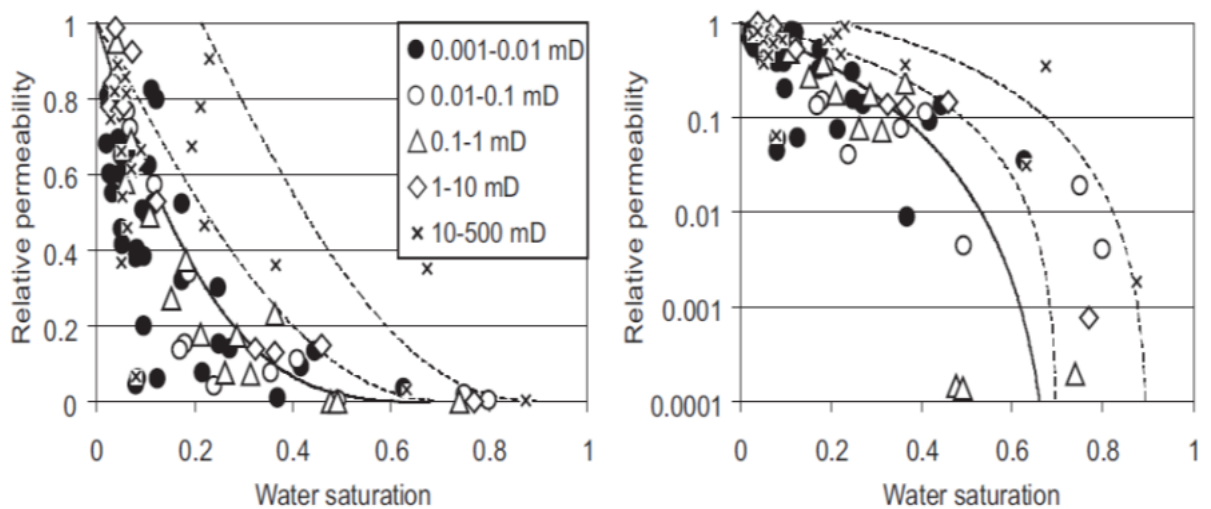


Figure 2.16 Gas relative permeability from The data left side is presented on linear scale and right side present on logarithmic scale. (Cluff and Byrnes, 2010) equations used to construct the relative permeability curve. (after Tueckmantel et al., 2012).

Furthermore, it has been argued that there is a lack of data on fault rock relative permeability various authors used relative permeability of tight rock samples as an analogue (e.g. Zijlstra et al. 2007). The data on relative permeability of tight gas sands are summarized in **Figure 2.17** and is collected from various published sources by Byrnes et al. (2009). This is presented here to increase the understanding about the low permeability homogenous sands two-phase flow properties. Furthermore, in subsequent chapters the petrophysical data of tight gas sands will be compared with the fault rock data collected during present study to see whether there is similarity with tight rocks petrophysical property trends.

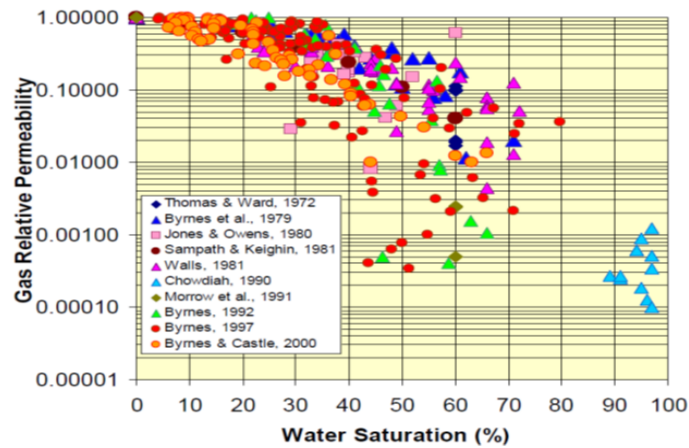


Figure 2.17 Gas relative permeability and water saturation data from published sources on tight gas sandstones (from Byrnes et al. 2009.)

## 2.4 Empirical estimation of fault rock properties

The link between fault rock types and clay content has led to the development of several algorithms to predict the clay content along faults and estimate permeability. Many authors attempted to predict the amount of clay content present within host sediments and developed algorithms to relate with permeability of fault rock in order to assess the fault seal. On the basis of clay content information many studies have also attempted to provide with fault rock permeability estimation by use of algorithms (e.g. Manzocchi et al., 1999; Sperrevik et al., 2002; Bense and Person, 2006; Childs et al., 2007). In this section the review of estimation of SGR using algorithm for fault seal assessment is provided.

### 2.4.1 Shale gouge ratio estimation

The fault rock permeability is partly controlled by clay content (Fisher and Knipe, 2001). The literature contains number of algorithms to predict clay content along fault rock. For example, algorithms such as Shale Gouge Ratio (SGR) from Yielding et al. (1997) Clay Smear Factor (CSF) from Lindsay et al.(1993) effective shale gouge ratio (ESGR) from Knipe et al. (2004) Clay Smear Potential (CSP) from Bouvier et al. (1989) all aim to predict the clay distribution along faults. Outcrop and core observations from faults have shown that the main fault zone or ‘core’ contains a highly variable distribution of rock types rather than a uniformly mixed rock type, as modelled using the SGR algorithm (e.g. Child et al., 2007). Often sand and shale

units within the faults are not well mixed. Parts of the sand units are entrained within the fault and preserved as floating blocks, clasts or large intact lenses of stratigraphy, whereas the majority of the more clay rich lithology tend to be more mixed. Therefore, the algorithm may not be the effective way for estimation of properties for such a heterogeneous fault rock. The SGR estimation algorithms used are listed below:

$$SGR = \frac{\sum(V_{cl} \cdot \Delta Z)}{\text{throw}} \times 100\% \quad (2 - 7)$$

Clay smear potential can be estimated by: (Bouvier et al., 1989)

$$CSP = \sum \frac{\text{thickness}^2}{\text{distance}} \quad (2 - 8)$$

Shale smear factor empirical equation is given by: (Lindsay et al., 1993)

$$SSF = \frac{\text{throw}}{\text{thickness}} \quad (2 - 9)$$

where SGR is the shale gouge ratio,  $V_{cl}$  is clay volume fraction in the zone and  $\Delta Z$  is the thickness of each bed, as seen in **Figure 2.18**. The discussion about the shale gouge ratio is kept limited in here, as it is beyond the scope of this research.

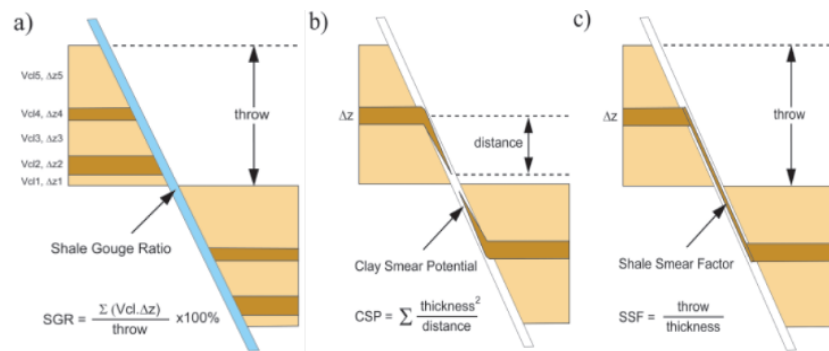


Figure 2.18 Shale gouge ratio (SGR) algorithm commonly applied: (a) SGR from Yielding et al. (1997) (b) Clay Smear Potential from Fulljames et al. (1997) (c) Shale Smear Factor (Lindsay et al., 1993) (from Jolley et al., 2007).

## 2.4.2 Empirical estimate of single phase fluid flow properties of fault rock

The significance of predicting fault rock permeability has been highlighted in earlier discussion of this chapter. Manzocchi et al. (1999) established an empirical relation

of fault rock permeability estimation as a function of clay fractions and fault displacement based on published data of plugs and probe permeametry measurements which they collected from various sources of reservoir and outcrop fault rock data (e.g. Antonellini and Aydin, 1994; Gibson, 1998; Ottesen Ellevset et al., 1998; Knai and Knipe, 1998). Although, the empirical relation did not take account of the various clay mineral types those might be associated within rock formations, such as swelling and non-swelling clays minerals (Crawford et al., 2008). Therefore, the empirical equation might not be appropriate for accurate fault rock permeability predictions. **Figure 2.19** shows the permeability data from plugs and probe permeametry obtained from several reservoirs and outcrops. Manzocchi et al. (1999) based on the knowledge of (SGR) shale gouge ratio and fault displacement, attempted to estimate the permeability  $k_f$  (in mD) of the fault rocks providing an empirical equation;

$$k_f = -4SGR - \frac{1}{4} \log(D) (1 - SGR)^5 \quad (2 - 10)$$

where  $K_f$  = the fault permeability in (mD)

$D$  = fault displacement in (m),

$SGR$  = shale gouge ratio

This data set shows a decreasing trend of fault permeability with increasing clay content; however; it does not specify the clay types. The main drawback of this empirical equation is that it does not take into account of the multiphase flow properties of fault rocks which could result in an overestimation of the rate of cross-fault flow; particularly if low permeability (<0.1 mD) fault rocks (i.e.  $SGR > 0.2$ ) are dominant (Fisher et al. 2001). Another consequence of the model estimates is that it does not account for the cementation effects of fault rock permeability. It was also pointed out by Manzocchi et al. (1999) that this method does not provide any reliable fault rock permeability estimates at low values of SGR. Walsh et al. (2008) argues that apart from clay fractions, the permeability of fault rock could be affected by various other factors, such as burial depth and types of the various clay minerals. Fisher and Knipe (2001) demonstrated that the correlation in between clay content and fault rock permeability is scattered that could be due to variations in diagenesis between different sandstones. Fault rocks formed in impure sandstones, whose clay

content ranges between ~15-25%, could be affected by quartz dissolution and those having >25% clays could be more affected by mechanical compaction. Chemical compaction in the latter could be suppressed by the presence of phyllosilicates on quartz surfaces reducing the rate of quartz cementation (Fisher and Knipe, 1998). Therefore, in predicting fault rock permeability from clay fractions all other aspects related to faulting should be considered to evaluate fault seal behavior accurately.

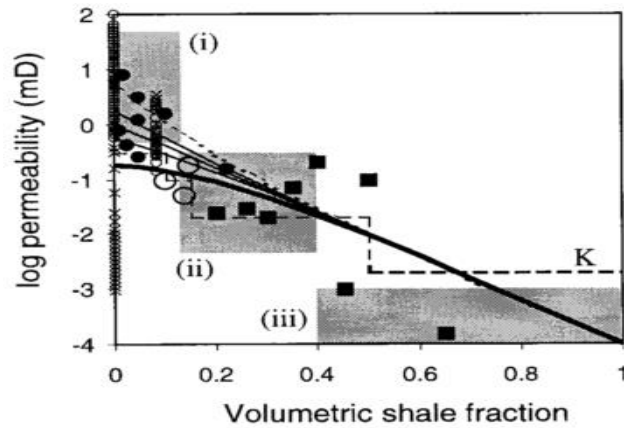


Figure 2.19 Relationships between shale versus log of permeability (mD). The large data points are plug permeability from core and outcrop of different locations (Gibson1998). Filled circles cataclastic deformation bands; open circles are solution deformation band and the filled squares are clay gouge. Small data points are probe permeability measurements of deformation bands (open circles) and slip-surface (crosses) (Antonellini and Ayadin, 1994). The large boxes of gray colour are summaries of the data from Sleipner Field (Ellevset et al., 1998): (i) Cataclastic deformation bands, (ii) Phyllosilicate-framework fault rocks, (iii) Clay smear. The line labeled with K represents the average values based on core samples from Heidrun field, (Knai, 1996). The curves given represent  $d=1$  mm (dashed line),  $d=10$  cm,  $d=1$  m,  $d=10$  m and  $d=1$  km (thickest line). After Manzocchi et al. (1999).

More quantitative assessments have attempted to relate the permeability of fault rocks to the clay content of the host sediment at the time of faulting. For example, (Figure 2.20) shows typical permeability values of fault rocks from the Middle Jurassic and Rotliegend reservoirs of the UK North Sea. Sperrevik et al. (2002) provided an even more quantitative, but empirical, approach by conducting multiple regression analysis on clay-permeability-burial depth -depth of deformation data, the resulting regression was:

$$k_f = a_1 \exp\{-[a_2 V_f + a_3 z_{\max} + (a_4 z_f - a_5)(1 - V_f)^7]\} \quad (2 - 9)$$

where,  $k_f$  is the fault permeability,  $V_f$  is the fault zone clay content (fraction)  $z_{\max}$  is the maximum burial depth (m),  $z_f$  is the depth at the time of deformation (m) and the constants are:  $a_1 = 80000$ ,  $a_2 = 19.4$ ,  $a_3 = 0.00403$ ,  $a_4 = 0.0055$ ,  $a_5 = 12.5$ . Although

this model is widely used in industry, the correlation coefficients using this model are quite poor.

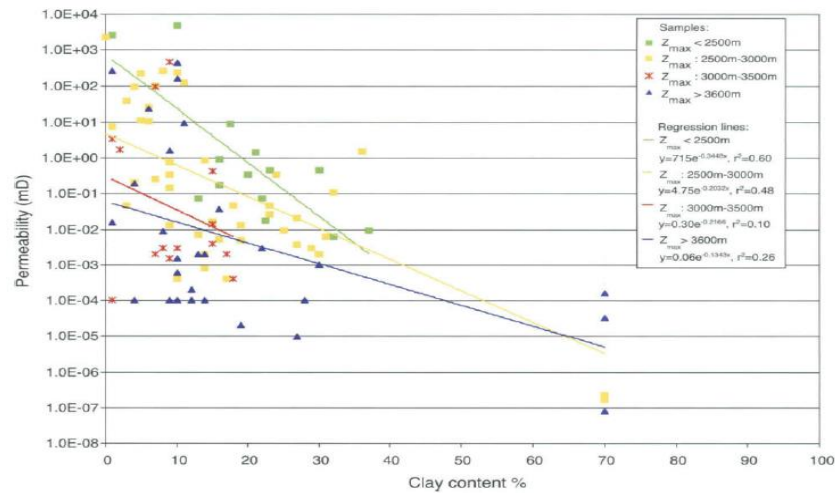


Figure 2.20 Showing fault rock permeability against fault rock clay content measured on faults in cores. The data are grouped according to maximum burial depth. Exponential least-squares regression lines are shown for each group of data, showing a systematic decrease in permeability both with fault rock clay content and with depth (from Sperrevik et al., 2002).

Also, great care must be taken applying the model to reservoirs other than those on which the regression analysis is based because: (i) the permeability of fault rocks is controlled by chemical processes (e.g. quartz cementation and grain-contact quartz dissolution) once mechanical compaction has finished (i.e. 1000-2000 m) and these processes are controlled by temperature history and not effective stress; (ii) kaolin is the main clay mineral in many of the reservoirs which this correlation is based and this may not be the case in other areas. A way to partially overcome the first problem in areas with differing geothermal gradients to the North Sea is by substituting  $Z_{max}$  for a depth value that has the same temperature as the North Sea (Fisher and Knipe, 2001).

Bense and Person (2006) provided an algorithm for siliciclastic type sedimentary rock to assess whether the fault present in hydraulic zone acts as a conduit or barrier. The estimation of the fault zone permeability was based on clay content and fault throw. Basically, the Bense and Person (2006) approach was based on the empirical relation of Bethke (1985) used a linear regression of the form of equation,

$$\log K = a\phi - b \quad (2 - 10)$$

Where  $a$  and  $b$  are empirical coefficient of equation. After fitting data it was found that  $a= 16.3$ , and  $b=-16.3$  for sandstone, but for shales the coefficients were  $a=9.1$ , and  $b=-22.1$ . Bense and Person (2006) stated that if sandstone is 5% and shale are 70%, and then Equation (2-10) can be interpolated in between two end members for constructing the permeability and porosity relation for clay rich sandstones. To consider the clay content of fault rock the Equation (2-10) was modified by Bense and Person (2006) to provide permeability estimation of siliciclastic fault rock ( $K_f$  in mD)

$$\log K_f = (a\phi - b - cz \cdot e^{-d \cdot v_{clay}}) \quad (2 - 11)$$

Where  $c$  and  $d$  are emprical coefficients and  $z$  is depth of burial at the time of faulting. The parameters  $c$  and  $d$  were set to  $3.1 \times 10^{-3}$  and  $3.1 \times 10^{-2}$  respectively. The two parametres ( $c$  and  $d$ ) were approximately fitted with field data (Figure 2.21) from Sigda et al. (1999); Rawling et al. (2001) and Sperrevik et al. (2002). The equation (2-10) used for host sediments permeability estimation and fault rock permeability  $K_f$  ( $m^2$ ) were estimated using Equation (2-11). This empirical relation does not take account of two-phase flow through fault rock and is less applicable to modelling petroleum reservoirs, because the fault rocks are heterogeneous, consisting of distinct amount of clay and sands and more than one fluid flowing.

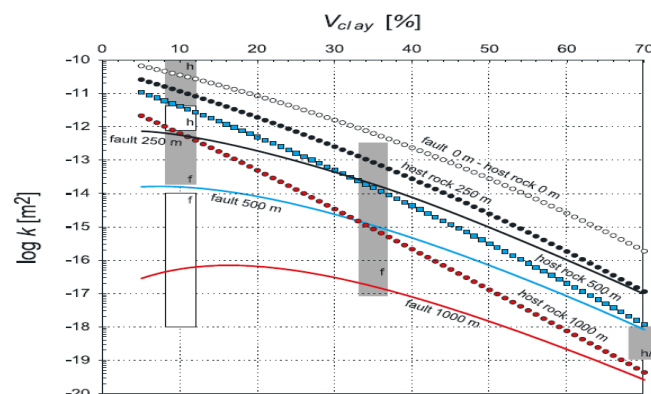


Figure 2.21 The relation between permeability versus clay content, the host rock permeability is represented by symbols and permeability of fault rock with solid lines as a function of clay content and burial depth. (From Bense and Person 2006)

### 2.4.3 Empirical estimates of two phase flow properties of fault rock

It is generally believed that fault rock properties have a strong influence on the dynamic behaviour of the fault compartmentalized reservoirs. The measurement of the two-phase flow properties (relative permeability and capillary pressure) of fault

rock is technically challenging. At present a limited amount of data on two-phase flow of fault rock is available (e.g. Al-Hinai et al., 2008; Tueckmantel et al., 2011). It would be highly desirable to provide with empirical relationships to predict these properties based on single phase flow properties, (e.g. absolute permeability and mercury injection data. In fact significant effort is required to establish reliable empirical relations to predict these properties. Manzocchi et al. (2002) provided with empirical relations to model multiphase flow based upon Ringrose et al. (1993) approach:

$$Pc = CS_e^{-2/3}(\phi/K)^{0.5} \quad (2 - 12)$$

where  $Pc$  is capillary pressure in bars,  $C = 3$ ;  $\phi$  is the porosity,  $K$  is absolute permeability in mD and  $S_e$  is an effective wetting phase saturation which is defined as:

$$S_e = (S_w - S_{wc}) / (S_{wor} - S_{wc}) \quad (2 - 13)$$

where  $S_w$  is water saturation,  $S_{wc}$  denotes the connate water saturation, and  $S_{wor}$  denotes the water saturation at irreducible oil.

Fault rock porosity was determined using an empirical equation:

$$\phi = 0.5K^{0.25} \quad (2 - 14)$$

Manzocchi et al. (2002) did some modifications to the above defined relations for modelling purposes; they derived fault rock porosity as function of the single phase permeability, and then attempted to modify  $S_{wor}$  values from 0.6 to 0.85, they also changed the connate water saturation functions to

$$S_{wc} = 0.85 - 10^{(-0.6 \exp(-0.5 \log(k)))} \quad (2 - 15)$$

In addition to above the drainage capillary pressure curve could be defined by providing empirical estimates using the following relationship:

$$P_c = C(1 - S_e^5)S_e^{-2/3} \left( \frac{\phi}{k} \right)^{0.5} \quad (2 - 16)$$

The relative permeability and oil relative permeabilities empirical relation were also defined similar to the Ringrose et al. (1997) approach, namely:

$$K_{rw} = 0.3S_e^3 \quad (2 - 17)$$

$$K_{ro} = 0.85(1 - S_e)^3 \quad (2 - 18)$$

They generated a synthetic capillary pressure and relative permeability curves (**Figure 2.22**) for absolute permeability values of 0.01 mD and 10 mD.

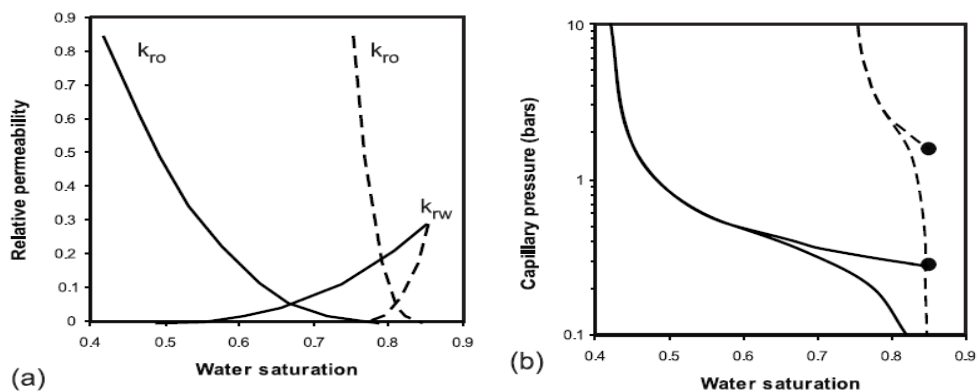


Figure 2.22 (a) Relative permeability and (b) capillary pressure for 0.01 mD dashed lines and 10mD solid lines fault rock. On graph of the  $P_c$  curve, the dark circles are the threshold pressure on drainage capillary pressure curve. (from Manzocchi et al., 2002)

## 2.5 Significance of fault rock flow properties to model cross-fault flow

Conventionally, the numerical modelling and simulation of hydrocarbon reservoirs was based on discretizing the domain on coarse grid scale typically of hundreds of meters. The fault rocks are variable in thickness. The thickness of faults varies from meter to cm scale. The modelling based on conventional techniques was not effective to capture the fault properties accurately. Recently lot of effort has been made to develop appropriate algorithms for transmissibility calculations to model fault compartmentalized reservoirs performance (e.g. Manzocchi et al., 1999, 2002, and 2010). The transmissibility is “the volume weighted average of the permeability of two grid cells connected in a simulation model” (e.g. Myers et al., 2007). In **Figure 2.23** the examples are presented that has been adopted in previous studies to model fault rock properties. Several authors attempted different approaches to

include fault rock flow properties in flow simulation models (e.g. Ringrose and Corbett 1994; Manzocchi et al., 1998, 2002; Rivenæs and Dart 2002; Al-Busafi et al., 2005a; Bergand Øian 2007). For details about the methods to incorporate faults in simulation models the reader is referred to Manzocchi et al. (1999, 2002, and 2010).

There are several published examples that have been adapted to history match the data by use of simulation modelling that were achieved using absolute permeability of fault rocks (e.g. Knai and Knipe, 1998; Jolley et al., 2007). However, some studies have found that to yield a history match of data of Brage and Oseberg Fields, it is required to reduce the transmissibility multipliers by several orders of magnitude (e.g. Rivenæs and Dart, 2002). Nonetheless, the reduction in TMs without any strong justification is not recommended because history matches are inherently non-unique and by arbitrarily changing a property to achieve a history match may mean that one is not correctly modelling another important control on production. For example, Sverdrup et al. (2003) achieved history match to data of oil reservoir using TM, which were calculated based on single phase flow properties of fault but did not succeed in history matching of gas reservoir. They argued that two phase flow should be considered for modelling of gas reservoirs. Zijlstra et al. (2007) initially attempted to history match data by assigning transmissibility multipliers but did not achieve a matching of the data. However, they achieved history matching of data by incorporating two-phase flow that lead to the better results. It is also important to have correct fault rock thickness and permeability information based on the realistic geology interpretations, so the transmissibility multiplier must be accurately calculated and assigned for input to reservoir simulations for accurate predictions (e.g. Al-Busafi et al., 2005a).

A conceptual model based on work of Fisher et al. (2001) to model multi-phase flow across a fault reservoir presented in **Figure 2.24** that demonstrates the case in which the fault has a high capillary threshold pressure than the reservoir. Close to the Free Water Level (FWL) (**Figure 2.24** points 1 and 2) the buoyancy pressure in the petroleum column is not adequate to exceed the capillary threshold pressure of the fault rock. This shows that at this point hydrocarbon has zero relative permeability, which was not accounted in conventional simulation and modelling (Fisher et al.,

2001). Therefore, this concept suggests that fault rock relative permeability must be considered when modelling compartmentalized reservoirs.

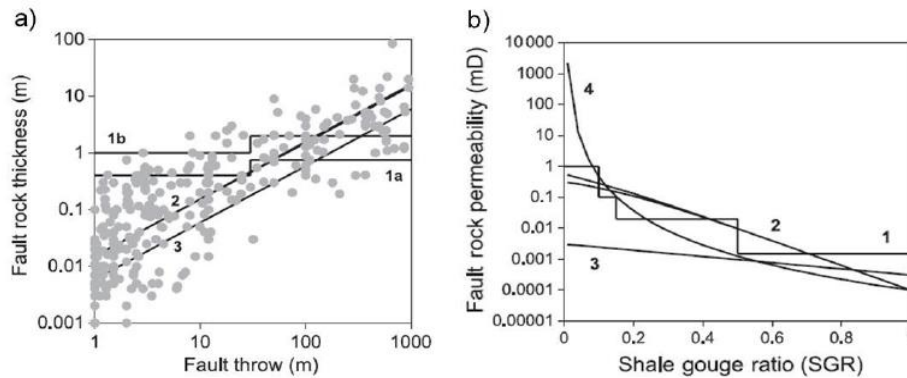


Figure 2.23 The diagram shows the properties of the fault rock used for simulation model (a) is the example of fault rock thickness relationship used for successful history matching (b) Fault rock permeability used for history matching in simulation model (taken from Manzocchi et al. 2010).

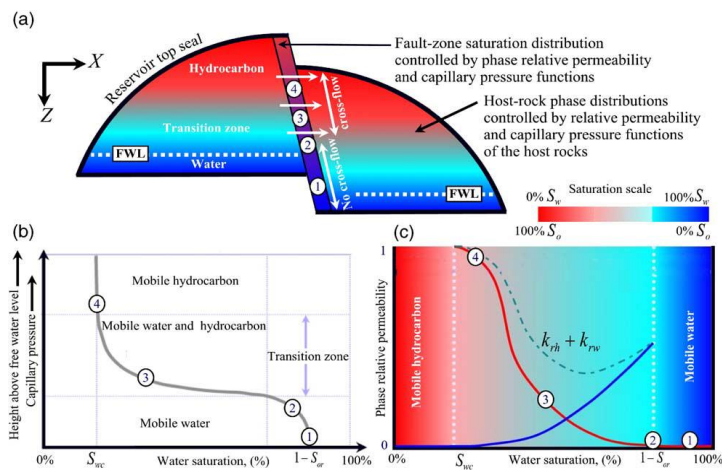


Figure 2.24 The above conceptual model of multi-phase flow in a petroleum reservoir shows. (a) The saturation within fault and reservoir (red for hydrocarbon, blue for water). (b) The capillary pressure curve. (c) The directional water-wet relative permeability curves for the fault rock. The fault has a higher capillary entry pressure than the reservoir (from Fisher et al., 2001).

## 2.6 Factors affecting fluid flow properties of fault rocks

Faults are one of the main causes of reservoir compartmentalization (e.g. Jolley et al., 2007). Understanding their impact on fluid flow is important for predicting reservoir performance and planning strategies. The fluid flow properties of fault rocks are mainly affected by pore fluid, amount of clay content, the overburden stress and the amount of

cements present within the rock (e.g. Fisher and Knipe, 2001). In following section each of these are discussed.

### **2.6.1 Effect of pore fluid salinity on fault rock permeability**

This section provides the discussion about the combined effect of particles retention and movement during permeability measurement in association with the pore morphology. In rocks containing clay such as fault rocks, the permeability can be dependent upon fluid salinity, (e.g. **Figure 2.25**). Numerous studies have been conducted in understating the effect of pore fluids, fines particles mobilization and their impact on rock permeability alteration (Khilar and Fogler, 1948; Lever and Dawe, 1987), since these effects will be investigated for fault rock permeability by changing brine compositions. The clay is one of the causes of permeability reduction (e.g. Verwey and Overbeek, 1948) and authors have provided with theories to predict these effects related to particle mobilization (e.g. Khilar and Fogler, 1948; Kia et al., 1987; Rosenbrand et al., 2014). Most of the fault rock formed within the clayey sands or phyllosilicate environment requires knowledge of the amount of shales or clays present within these formations and to know the extent how they affect the fault rock permeability measurements. The most common types of clay minerals found in sedimentary rocks are kaolinite, chlorite, illite and smectite (e.g. Nesham, 1977). The major effects of clays on fault reservoirs are the reduction of pore size and permeability; fine particles migrations when there is loose clay mineral present within sands; these have tendency to migrate and plug the pore throats that could be the potential reason of reduction in permeability and clays are sensitive to distilled that hydrate after contacting with water which in turn causes reduction in rock permeability (Richard and Dawve, 1984, Khilar and Fogler, 1948).

Clay minerals of fine grained particles deposited in sandstones, particularly it is associated in phyllosilicate and clay rich fault sequences. As reported by Nesham (1977) clays could be found within the sandstone in three different ways; (1) laminar clay, where it could be found in form of laminae between layers of clean sands; (2) structural clays, where it could be associated with sand grains or nodules within the sandstones and the third is the dispersed clay minerals, where clay might be dispersed throughout the sand, to some extent exist in between the intergranulars or possibly be coating the sand grains. Each of these have tendency to affect the fault rock permeability either by creating a layer of bound water or by movement of fine particles

and these fine particles might get trapped within the confined pore throats. The fine particles are supposed to be the loosely attached particles surrounded with quartz grains (Khilar and Fogler, 1984; Kia et al. 1987) and depends upon the mineral compositions, also upon the permeability of the rock and pore network (Hibbeler, 2003). The way the fine particles impair permeability is: when loosely attached particles within porous medium starts flowing, moving towards the pore throat locations where these fine particles might get trapped and reduces the flow paths (Muecke et al. 1979) consequently the reduction in permeability could be observed.

Authors have argues that the differences in gas permeability to brine and water could be the result of layer of bound water on the mineral surface that reduces the pore throat radius (Heid et al. 1950; Luffel et al. 1993; Solymar et al. 2003; Andreassen & Fabricius 2010). Therefore, in this thesis attempts will be made to investigate the extent to which the gas and liquid permeability of fault rocks affected due to changing brine composition. This will be performed by conducting laboratory experiments and the results would be integrated with microstructural analysis.

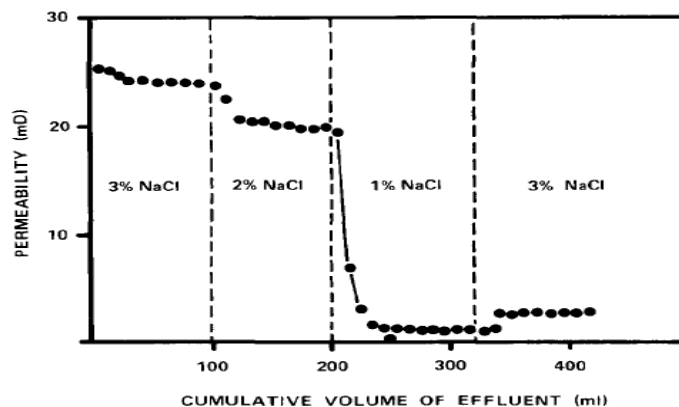


Figure 2.25 Water-sensitivity of the Spiney sandstone, Moray Firth Basin, Note the large decrease in permeability when the brine is changed to 1% NaCl (from Lever and Dawe, 1987).

## 2.6.2 Stress sensitivity of rock permeability

It is generally well understood that the properties of porous sedimentary rock can alter with change in the depth and change in the subsurface overburden stress. Since, the early 1950s, there has been a continuous debate over the influence of stress on permeability of porous sandstones. The permeability of tight sandstones are often sensitive to the stress and pore pressure under which these are measured (e.g. Jones and Owens, 1980; Sampath and Keighin, 1982; Brower and Morrow, 1985; Warpinski and Teufel, 1992; Rushing et al., 2003). Several other researchers (e.g. Thomas and Ward,

1972; Sampath and Keighin, 1982; Walls et al., 1982) performed number of laboratory experiments on permeability of sandstone. These studies concluded that the absolute permeability of samples reduced significantly with the increase in confining stress. On the other hand, the relative permeability did not show any significant reduction with the application of overburden stress. Others (e.g. Al-Qureshi and Khairy, 2005; Chierici et al., 1967; Davis and Davis, 1999; and Jones et al., 2001) concluded that permeability can significantly be altered with impact of overburden or net stress due to the fact that pore network, pore geometries and pore throats changes by applying overburden stress, even if there is more than one phase is flowing. The absolute permeability generally decreases with increasing confining stress  $\sigma_c$  and decreasing pore pressure  $P_p$ , it can be expressed as a function, of the effective stress, (e.g. Warpinski and Teufel, 1992; Zoback and Byerlee, 1975; Al-Wardy and Zimmerman, 2004; Li et al., 2009):

$$\sigma' = \sigma_c - n_k P_p \quad (2.19)$$

where  $n_k$  is the effective stress coefficient for permeability, which measures the effect of a pore pressure change on the effective stress.  $\sigma_c$  is confining stress and  $P_p$  is the pore pressure applied for permeability measurement.

Authors have reported that the reduction in permeability at higher stresses, in particular the low permeability sandstones might be affected due to grain boundary micro cracks formation as a result of stress release, but not by intergranular pores of the rock (e.g. Ostensen, 1983; Brower and Morrow, 1985, Farrell et al., 2014). The laboratory experiments might show permeability stress sensitivity by increase in confining stress due to closing of micro-cracks that could be possible reason of the permeability stress sensitivity in low permeability sandstones (e.g. Ostensen, 1983). The effect of changing stress on permeability could be modelled by simple relation of power law as given below (e.g. Keaney et al., 2004).

$$k = k_\infty [\sigma_c - n_k \bar{P}]^{-\gamma} \quad (2.20)$$

where, in above equation (2.20)  $K_\infty$  is the permeability of the samples extrapolated to zero stress and  $\gamma$  is the stress exponent. This equation will be used in chapter five to model the fault rock permeability stress sensitivity.

**Figure 2.26** shows how stress impacts on the rock pores structure. When stress acts on porous rock the grain to grain contact gets closer to each other, due to this effective size of the pore throats decreases eventually the movement of fluids is restricted consequently the permeability (e.g. Walls, 1982; Davis and Davis 1999). A summary of the tight gas data shown in **Figure 2.28**, which shows that as permeability decreases it becomes more sensitive to stress. Similarly the fault rocks are low permeability their permeability might be sensitive to stress.

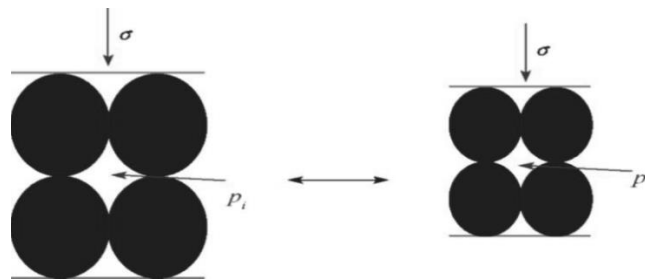


Figure 2.26 The conceptual cartoon shows the stress impact on rock fabrics.

In past, a lot of research has been done on different fault rock types, most of the data collected was measured at ambient stress conditions of 70 psi (e.g. Antonellini and Aydin, 1994 Gibson, 1998; Fisher and Knipe 2001, Teuckmantel et al., 2010). There is very little experimental work has previously been undertaken on the stress sensitivity of fault rock petrophysical properties (e.g. Al-Hinai et al., 2007). The fault rock relative permeability is also stress sensitive and it could be lower several orders of magnitude (e.g. Al-Hinai et al., 2007).

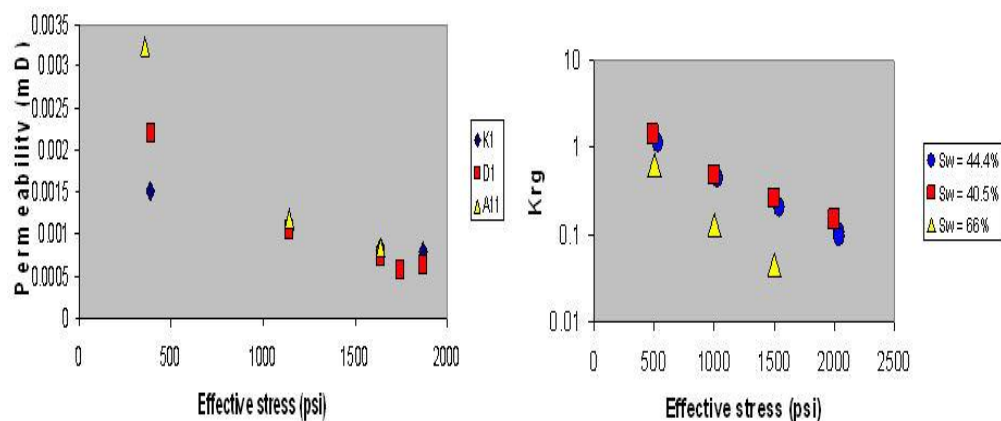


Figure 2.27 Stress dependence of the absolute gas permeability (left) and relative permeability (right) of a tight gas sandstone (from Al-Hinai, 2007). Note that the relative permeability is far more stress sensitive – especially at high water saturations.

It has become industry standard to calculate transmissibility multipliers to incorporate into production simulation models to account for the impact of faults on fluid flow (Fisher et al., 2005; Jolley et al., 2007). In majority of cases, transmissibility multipliers are calculated using permeability of fault rocks were measured under low confining pressures <70psi, if this is the case then calculation of the fault rock transmissibility and incorporating into simulations models could be based on measurements that underestimate fault permeability. Therefore the stress sensitivity of fault rock permeability is still not well understood, far less data on fault rock stress sensitivity is available (**Figure 2.27**); so significant effort is required to conduct experiments at *in-situ* stress conditions to understand and evaluate the fault flow properties at various stress conditions. Data is required on variety of fault rock particularly the poorly lithified cataclastic faults that are quite common in deep water reservoirs (e.g. as seen in Gulf of Mexico) and phyllosilicate-framework fault rocks with differing degrees of sediment lithification; so the impact of fluid flow on fault compartmentalized reservoirs can be delineated.

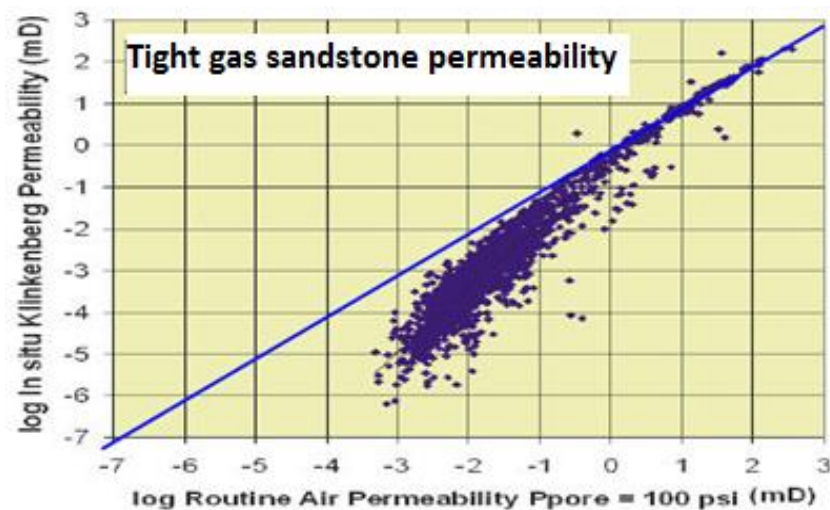


Figure 2.28 Stress dependence of the absolute gas permeability of tight gas sands. Note that the low permeability samples can have up to two orders of magnitude lower permeability when measured at reservoir stress conditions compared to 100 psi, (from Cluff and Byrnes, 2010).

## 2.7 Examples of faults found within the petroleum reservoirs

Here a review of fault-related barriers in petroleum reservoirs is presented by providing the evidence from published papers.

## **2.7.1 Faults as a barrier in petroleum reservoirs**

The main evidence on fault sealing provided here comes from the Brent Province, UK and Norwegian North Sea, and Rotliegend, UK and Dutch North Sea.

### **2.7.1.1 Brent Province: UK and Norwegian North Sea**

The most productive reservoir unit in the North Sea is Middle Jurassic, Brent Group, of the UK and Norwegian North Sea that is sand-dominated and is largely deltaic sequence (e.g. Fisher et al., 2013; Leveille et al., 1997). In reality, the Brent Group was key producing province because of its exploration and development history means that huge amount of data have been collected over the past 45 years, that has become an important area to investigate the impact of faults on fluid flow based on geological and production time-scales (Fisher et al., 2013). Fisher and Knipe (1998, 2001) have gathered petrophysical a large amount of data, comprises the microstructural and petrophysical property analysis studies on these faults, which were found in the Brent Group. The studies conducted on these fault such as, microstructural examination which has suggested that the faulting occurred at a shallow depths, the main deformations processes involve are the particulate flow( movement and sliding of grain particles without grain fracturing ) and sometimes a minor amount of cataclasis is observed (e.g. Fisher and Knipe, 1998). The investigation made by Fisher and Knipe (1998 and 2001) on these reservoirs has suggested that the main fault types occurs includes, the disaggregation zones those formed in clean sandstones where these is less than 5% of clay; the phyllosilicate-framework fault rocks which were formed in impure sandstones, in which the clay content ranges from 15% to 40% and the third type of fault are the clays smears formed due to the faulting of shale-rich sediments having greater than 40% clay. There was no evidence for cemented faults and no any indication of the later fault reactivation has been reported from any of the samples analysed (e.g. Fisher and Knipe, 2001).

Harris et al. (2002) provided evidence about the fault and reported that there is lack of communication across fault between the upper and lower Brent Group. The study presented by Harris et al. (2002) showed that up to 650 psi (4.48 MPa) pressure difference built up across a fault separating the Upper and Lower Brent Group in the Strathspey Field. Another example comes from work of Jolley et al. (2007) they

presented fault seal analysis studies on many of the fields from the Brent Province also from the Brent and North Cormorant Fields. The study demonstrated that how faults act as barriers on a production time-scale and the study also demonstrated that production history matches to simulation models could be achieved by incorporating realistic fault rock properties (i.e. permeability values).

Generally, it seems that in Brent Group fields where there is juxtaposition of clean sand (no any clays) against clean sand (within high permeable faults) in these conditions fault have less impact on fluid flow (e.g. Fisher and Jolley, 2007). Because, these fault rock formed in disaggregation zones (Fisher and Knipe, 2001) and these faults have same fluid flow properties (permeability and capillary threshold pressures) to their associated undeformed sandstone. In contrast, the faults that were formed in sediments within the clay rich sequences appears to act as a major barriers to fluid flow over production time-scales. This shows that the fault exist are the clay smears or phyllosilicate-framework fault rocks (Fisher and Knipe, 2001).

#### **2.7.1.2 Rotliegend UK and Dutch North Sea**

The significant production of gas that is coming from the Rotliegend reservoir of the UK and the Dutch southern North Sea and is the most important source of natural gas for United Kingdom which is producing over the last 40 years (Fisher et al., 2013). The reservoirs are composed of mostly the aeolian, fluvial, sabkha and lacustrine sediments, and most likely have a high net to gross ratio and lower clay content. The faulting of reservoirs occurred due to two periods, the Jurassic and Early Cretaceous as a result of basin extension (e.g. Arthur, 1993) and the Late Cretaceous due to basin inversion (e.g. Arthur, 1993). Fisher and Knipe (1998, 2001) had gathered a large amount of data on microstructural and petrophysical properties of fault rocks from Rotliegend reservoirs in the southern North Sea. They suggested within these reservoirs two types of fault rocks are dominating. The first types of faults are the cataclastic faults that have been generated due to the grain-fracturing, post-deformation and quartz cementation. The permeability of these fault rocks reported by Fisher and Knipe (2001) ranges from ~0.1mD to <0.0001 mD. Other types of fault formed include the cemented faults/fractures that resulted after wide range of mesodiagenetic alteration such as quartz and illite precipitation. The most common cements found within this type of faults include anhydrite, ankerite, siderite and barite (e.g. Fisher and Knipe, 1998, 2001). Most

likely the cataclastic faults formed at a depth of one to three kilometres during Jurassic to Early Cretaceous, these latter become cemented faults during basin inversion, due to the uplifting of a sedimentary basin. (e.g. Leveille et al., 1997).

There is significant indication about the influence of fault rock that has impacted reservoirs productivity within the Rotliegend reservoirs of the southern North Sea. Van der Molen et al. (2003) presented that there is a 250 bar (~3627 psi) difference of pressure which was generated across a fault for the period of production from a Rotliegend reservoir of offshore Netherlands. Another example comes from Al-Hinai et al. (2007) who investigated similar field as described by van der Molen and proposed that the large pressure difference within the reservoir studied might not be described based simply on the information of absolute permeability of fault rocks. Although, they claimed that the pressure difference could be explained if the two phase flow properties of the fault rocks considered for incorporation into the simulation model. Al-Hinai et al. (2007) in their study stated that it is necessary to incorporate the relative permeability characteristics of faults rocks in the production simulation models to history match the production data; ignoring the two phase flow properties into account can overestimate cross fault flow. Moreover, Zijlstra et al. (2007) also reported that fault rocks in Rotliegend reservoirs were acting as barriers to fluid flow during production.

## **2.8 Summary**

This chapter has attempted to review the current knowledge regarding the impact of faults on fluid flow within fault compartmentalized reservoirs. It was also attempted to present with few field examples from fault compartmentalized reservoirs that were reported within North Sea fields. The review has paid particular attention by describing the evidence that is used by the petroleum industry to assess how faults have affected fluid flow. Even though there is a large amount of data on deformed rock are present within the published data base, achieving economic flow rates through such compartmentalised reservoir is a challenge. Despite the concern about the permeability, deformed rocks has a large effect on estimates of productivity of reserves. Within laboratory measurements the permeability stress-sensitivity of fault rock samples were often overlooked however it is essential during compartmentalized reservoirs analysis as well as during calculation of transmissibility multipliers to input into reservoir simulation and modelling. Current study has attempted to measure and gather

petrophysical properties of fault rocks at ambient and in-situ stress conditions. In addition, the measured petrophysical properties data were integrated with mineralogical and microstructural examination to delineate the controls and differences of fault rock properties. Obviously, a better understanding of the processes that control the fault rock petrophysical properties would improve the value of fault-seal predictions.

# 3 Materials and Methods

---

## 3.1 Introduction

The research presented in this thesis is mainly based on the measurement of the microstructural and fluid flow properties of fault rocks. Fluid flow through homogenous conduits, such as pipes, is easy to model. However, fine grained heterogeneous porous media, such as fault rocks have a complex pore structure that cannot be described explicitly, which makes modelling very difficult. The work conducted in this thesis therefore attempts to integrate data from laboratory experiments of the fluid flow properties of fault rocks (e.g. permeability, relative permeability etc.) with microstructural and mineralogical information obtained from scanning electron microscopy (SEM), quantitative X-ray diffraction (QXRD) and X-ray tomography.

This chapter describes the materials studies and the experiments conducted during the research project. Apart from this introductory section this chapter is divided into six sections. **Section 3.2** provides the overview about the fields and outcrops from where the samples were obtained. The next section (**Section 3.3**) provides details about the sampling, coring and cleaning techniques. The following section (**Section 3.4**) describes the techniques used to study and analyze the structure and mineralogy of the samples such as scanning electron microscopy (SEM), quantitative X-ray diffraction (QXRD) and X-ray tomography. **Section 3.5** starts with details about the experimental procedures and material (core samples and pore fluids) used during experiments. In addition to this, the two phase flow properties (capillary pressure and relative permeability) experimental methods are described in **Section 3.6**. At the end of this chapter issues and uncertainties related to measurements are discussed (**Section 3.7**).

## 3.2 Material studied

This section provides an overview about the fields studied. It mainly concentrates on the background information about the fields studied. A total of fifteen core sections were

provided by sponsor from Central and Southern North Sea reservoirs. The depth of Central North Sea core sections were 11724.0 to 13115.2 m. The Southern North Sea section was cored at a depth of 3111 to 3133.55 m. Apart from reservoir cores large blocks of outcrop from different fault structures were also provided during this study for the above mentioned properties analysis. The summary of the fields and number of the samples that have been obtained and analyzed during this study are given in **Table 3.1**. The reservoir cores supplied and outcrops collected are categorized as mainly cataclastic and phyllosilicate-framework fault rocks, but some disaggregation zones were also analyzed and are discussed in following sections. The samples from Mirri airport road Malaysia outcrop could be analogous to Miri oil field, Miri outcrop is located in the similar structure as the Miri oilfield that was producing from 1910 to 1979 (Van der Zee and Urai, 2005). The samples from Hopeman fault rock UK studied could be analogue to North Sea reservoirs.

*Table 3.1 Summary of the samples that have been obtained and analysed during present study*

<b>Summary of samples collected and analysed</b>					
<b>S.No</b>	<b>Location</b>	<b>Depth (m)</b>	<b>Fault rock type</b>	<b>Sample type</b>	<b>No. of samples analysed</b>
1	Central North Sea fields	11724-13115.2	Cataclastic/Phyllosilicate frame-work fault rock	Reservoir core	27
2	Southern North Sea	3111-3133.5	Cataclastic/Phyllosilicate-framework and Disaggregation zone	Reservoir cores	6
3	90 Fathom Fault UK	-	Deformation Band zone and slip-surface Cataclsite	Outcrop	10
4	Mirri airport Road fault Malaysia	-	Phyllosilicate framework	Outcrop	2

### **3.2.1 Central North Sea**

The area studied is indicated by an arrow in **Figure 3.1** and is part of NW–SE trending extension of the Forties–Montrose High, which is separating the eastern and western arms of the Central Graben (Keller et al., 2005). This has a NW-plunging structure surrounded by major NNW–SSE and WNW–ESE extensional fault with throws are more than 600 m and bounded by WNW- and NNW-striking faults which are linked to the Permian structures (e.g. Keller et al., 2005). The Central North Sea area contains a thick sequence of Triassic and Jurassic sediments and is underlain by a thin layer of salt (e.g. Fraser et al., 1993). The seismic information has shown the movement of

Zechstein salt from Early Triassic time and the pre-Triassic section is highly variable (Keller et al., 2005). According to Zenella and Coward (2003) the structural configuration of the central North Sea is basically the result of a Late Jurassic to Early Cretaceous rifting event, the rift alignment for the Permo-Triassic rift is thought to lie underneath the current Horda Platform.

The salt mobilization continued during the Triassic period but the influence was decreasing on the depositional architecture. As stated by Smith et al. (1993) the resulting structure consists of rotated grounded pods of Triassic age above salt where the Zechstein salt has been entirely evacuated. The main control on sedimentation of the Smith Bank and Skagerrak formations appears to be a combined effect of halokinesis (movement of salt and salt bodies in the sub-surface or flow of salts as well as the emplacement, structure and tectonic influence of salt bodies) and indirect basement fault movement (e.g. Hoiland et al., 1993). The reservoirs discovered in this area consist of different formations such as, the Triassic Skagerrak formation, the Upper Jurassic Fulmar Formation, the Upper Cretaceous chalk and Paleocene sandstone and is structurally complex (e.g. Archer et al., 2010). The compartmentalization of reservoirs plays a significant role which is demonstrated by differences in pressure between the West Limb and the Northern Terrace (Archer et al., 2010)

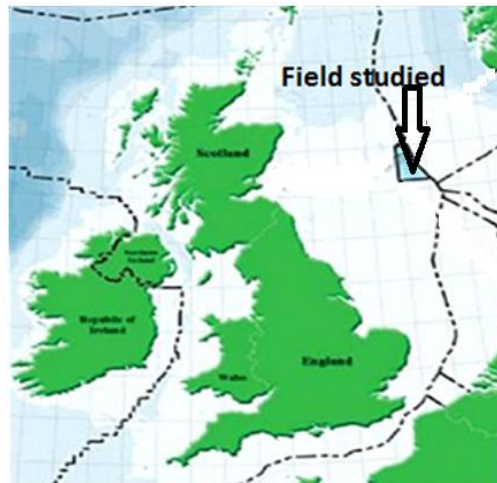


Figure 3.1 Sketch map of the central North Sea field location. The study area is shown by arrow on map (after Keller et al. 2005).

### 3.2.2 Southern North Sea

The southern North Sea field studied is shown in **Figure 3.2** that is yet an important petroleum province, and is producing since 40 years after production (Norwegian

petroleum directorate report). According to the report published by Norwegian petroleum ministry that fields from southern North Sea will be producing for another 40 years and around thirteen fields are producing in this part of the North Sea. The southern North Sea reservoirs are significantly compartmentalized and are linked to the structural development of the area and are also related to the tectonic activity; around 100m of fault throws are present and this might be the major reason of sealing capacity of several fields (e.g. Leveille et al., 1997). According to Gupta (2013) there is very limited pressure communication between these reservoirs.

A diagenetic process in these sandstones samples consists of an early shallow diagenesis, intermediate diagenesis, which includes burial and local uplift, and deep burial (e.g. Gaupp and Okkerman, 2011). The authigenic minerals that are found throughout the basin comprise quartz, carbonates, iron oxides, kaolin, illite and chlorite (e.g. Gaupp & Okkerman 2011). Most of the samples were in red colour which reflects the presence of hematite Torrent & Schwertmann (1987). According to Desbois et al. (2011) hematite and iron oxides could still be found in the form of small grains among clay minerals.



Figure 3.2 The southern North Sea area studied (source: Norwegian Petroleum directorate)

### 3.2.3 90 Fathom Fault, Northumberland, UK

According to Kimbell et al. (1989) the 90 Fathom fault commenced as E-W trending normal fault because of the early Carboniferous N-S extension and is part of E-W to ENE-WSW trending stublick normal fault. This has been previously be studied ( e.g. Jones and Dearman, 1967; Collier, 1989; De Paola et al., 2005; Tueckmantel et al.,

2011; Al-Hinai et al., 2008). The 90 Fathom fault system is down towards the north and southern part of the carboniferous Solway Basin, which covers area around 6500km<sup>2</sup> north England and southern part of Scotland (Chadwick et al., 1993). The fault is an extensional fault dipping to the north, and consists of three EW trending faults with an offset of around 15m in the Whitely Bay area (Jones, 1968). The fault can be traced inland as a linked segmented fault zone for more than 30 km and has a maximum throw of 260m.

The 90 Fathom fault collected from coastal section of Cullercoats Bay and Whitley Bay NE of Newcastle upon Tyne (**Figure 3.3**) the red square indicates the position of area studied. The fault at this location trends to E-W and juxtaposes Permian Yellow Sand against a footwall sequence of Carboniferous shale and mudstone to the south (Collier, 1989). As stated by Jones (1967) the fault throw at Cullercoats Bay is around 120m, the main fault constitutes of slip surface which is dipping with 40<sup>0</sup> towards NNE. Tueckmantel et al. (2011) stated that the slip surface contains 15 cm thick cataclasite without any interspersed host sediments. The sediments exposed to hanging wall consists of medium to fine grained with complex pattern of deformation bands. According to Collier (1989) and Knott et al. (1996) most of the deformation bands are trending towards E-W parallel to the main fault. The fault rock obtained for analysis consists of single deformation bands, deformation band zone thosed exposed into damaged zones; in additon to these the slip surface cataclasites fault present within the main fault also analysed.



Figure 3.3 The Great Britain map with location highlighted with the black square indicates the position of 90 Fathom fault outcrop area (taken from GoogleMaps-2014).

### 3.2.4 Fault rock from Miri airport road exposure Malaysia

The Miri Airport Road outcrop in Miri, Sarawak, Malaysia (**Figure 3.4**) has previously have been studied by (e.g. Burhannudinnur and Morley 1997; van der Zee and Urai 2005; Sorkhabi and Hasegawa, 2005). The Miri airport exposure outcrop had a combination of clay smear and deformation band (e.g. Sorkhabi and Tsuji, 2005). The exposure contains cyclic deltaic deposits composed of around 85% sand and 15% shale. The structure of the outcrop belongs to the Miocene Sands of the Miri formation. The thickness of the clay layers is 10 to 50 cm, most of these layers are very thin less than 10 cm forming a thin-bedded fault sequence with throw which is ten times the thickness of the sand layer (van der Zee and Urai, 2005). Previous studies have focused on describing the structural characteristics of the fault zone. A key exception is the study of Sorkhabi and Hasegawa (2005) is that who used a probe permeameter to suggest that deformation bands have unconfined gas permeabilities of 5 to 20mD compared to 10 to 300mD measured for the host sandstones. The current study differs in that it assesses fault rock permeability at a range of confining stress measured and analysed. It should be noted that no attempt was made to deconvolve the permeability; the reported permeability were an average of fault and its associated un-deformed rock.

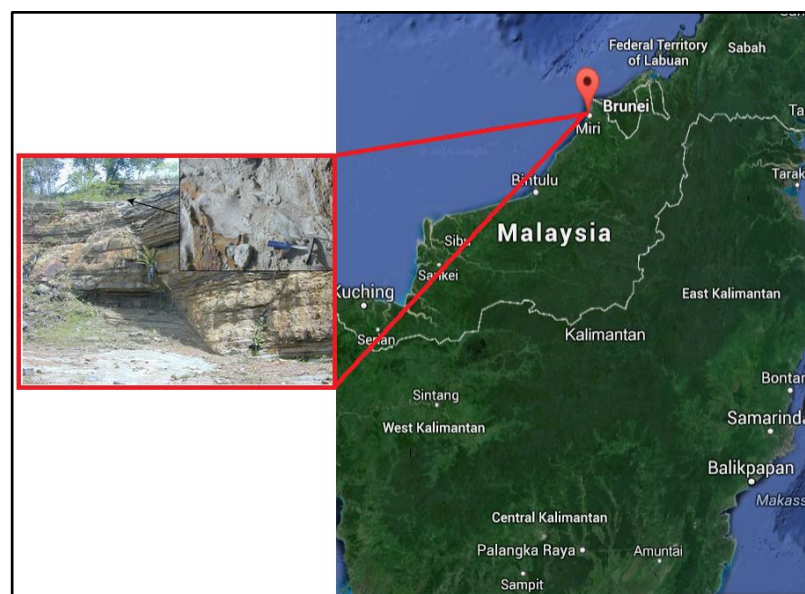


Figure 3.4 The Location map of the fault rock from Miri airport road exposure Malaysia with inserted map detailing the location of the study area (GoogleMaps-2014).

### 3.2.5 Fault rock from Clashach Quarry, Hopeman, Invernesshire

The samples used for study from Clashach fault within the Hopeman sandstones is located on the south part of the Moray Firth, the outcrops is on the shore about one kilometre to the east. The fault location map below shows area where from these were obtained (**Figure 3.5**). The Hopeman sandstone is clean with yellow-brown sandstone of mainly the aeolian origin, which lies unconformably on Devonian sediments of the Orcadian Basin of Hopeman. As reported by Benton et al. (2002) the Permo-Triassic basins of United Kingdom (UK) that follows the north-south linear rift system, which was strongly impacted through the underlying structure. Furthermore, they reported that different rift systems can be recognized those contain a large number of separate basins, those basins are filled 1 to 4 km of mostly continental red beds and evaporates. The tectonic plate movement was continuous from Late Carboniferous into Early Permian times (Benton et al., 2002).



*Figure 3.5 the location map of the fault rock from Clashach Quarry, Hopeman, Invernesshire United Kingdom.*

## 3.3 Methodology

To characterize the sealing potential of fault compartmentalized reservoirs, it is essential to have an integrated understanding of their microstructural analysis and petrophysical properties. The methods and techniques used to provide wide-range of petrophysical

description of fault rock samples such as microstructural analysis, porosity, permeability, fluid saturations, relative permeabilities, centrifuge, relative humidity chambers and mercury capillary pressures are presented in this chapter. To achieve the research objectives various types of experiments were carried out and attempt were also made to design some experiments. The work conducted, includes the preparation, cleaning, photographing and scanning of samples, followed by aforementioned petrophysical properties measurements at ambient and in-situ stress conditions as shown in **Figure 3.6**. Apart from experimental work, attempts were also made to a model the results using industry standard software.

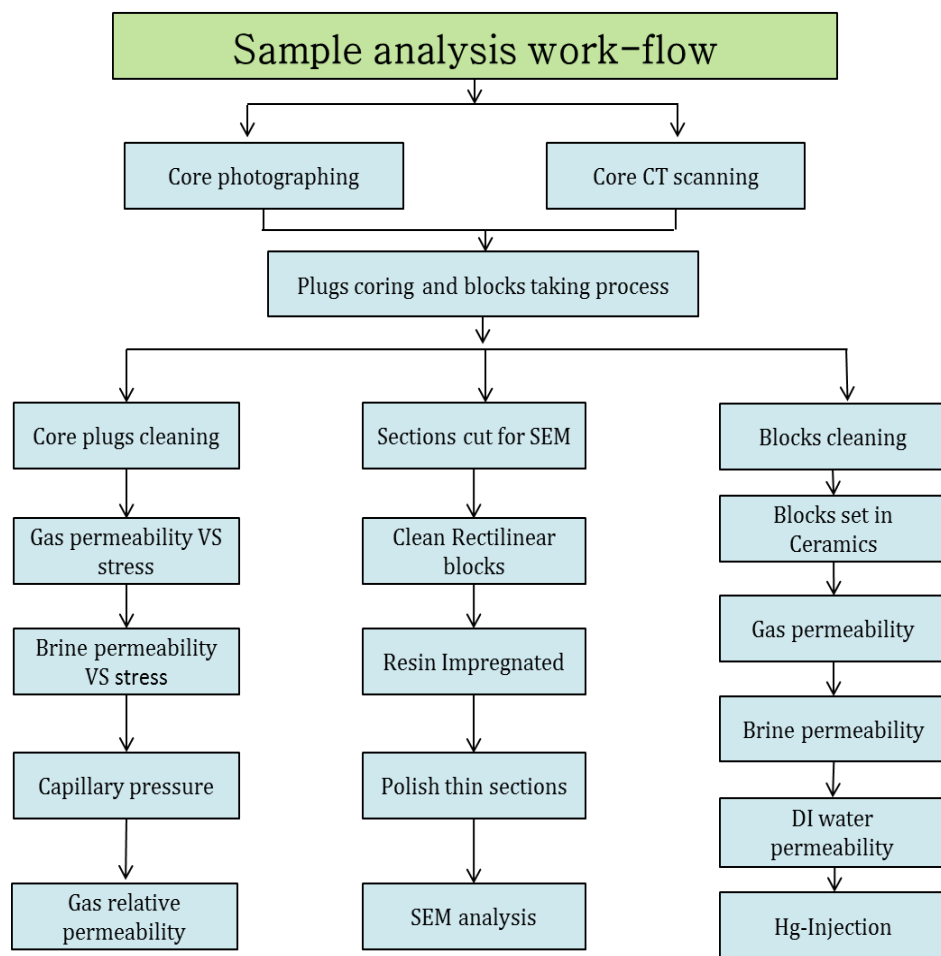


Figure 3.6 The workflow adopted during this study.

### 3.3.1 Sample preparation, cleaning and preliminary measurements

Once the samples were available for the study, the sampling of core was carried out. This was done by the available facilities in the laboratory. Two sizes of core holders

were available (1 inch and 1.5 inch) to accommodate the core plug. Therefore, both sizes of plugs were taken. The reservoir cores were taken by using 1 inch coring bit in order to avoid the full utilization of core section and the rest of the core section was used for mercury injection and SEM analysis. The outcrop plugs were taken with 1.5 inch size. Usually, water causes permeability alteration and clay swelling or contamination to core plugs, therefore air was used as a coring fluid. The deformation band plugs were taken perpendicular to the bedding and the host plugs were taken in horizontal direction. Once the core plugs were taken, it was necessary to trim and smooth them to give them a cylindrical shape to fit into the core holder. Therefore, these were trimmed and smoothed in order to place in core holder for permeability measurement. The plugs taken had an average diameter of 2.50 cm and lengths varying from 3 cm to 6 cm. It is worth noting that the total number of plugs taken was 47 and the same number of rectilinear blocks of host and faults were also carefully taken from the same core sections to generate quality data.

The core plugs were then cleaned with using Dean-stark apparatus (**Figure 3.7**) to remove any residual fluids and salts. After cleaning, the core samples were placed in oven at 60 °C to dry for about 24 hours. Once the plugs dried, these were taken out of the oven and their weights were recorded until their stabilization and were kept in a vacuum dessicator at room temperature for further measurements.

The rectilinear blocks were given cylindrical shape by putting them into ceramics in order to place them into core holders for permeability measurements. It should be emphasized that all host and fault core plugs permeability was measured at room temperature and at a range of confining stress conditions; the confining stress was increased in incremental steps up to maximum of 5000 psi. The permeability of rectilinear samples was measured at ambient conditions. The flow direction during permeability measurement was perpendicular to fault orientation in all fault plugs and was parallel to host plugs.

In total three different pore fluids were used to run the experiments. These include gas, brine and demineralized water. The brine flooded during experiments was dead brine i.e. with no dissolved gas and was prepared using an appropriate amount of 99.6% NaCl in the laboratory, using deionized water. Initially, gas was used as a pore fluid to measure the permeability of all faults and host rock samples. The reason for flooding

first with gas was that the gas cannot damage the pore fabrics of the rock, and then de-aerated brine permeability was measured using (NaCl) of different salinities. Finally the plugs permeability was measured by flooding with deionized water.



*Figure 3.7 The Dean stark distillation apparatus for sample cleaning (taken from vinci Tech catalogue).*

## **3.4 Microstructural structure examination**

The microstructure of all samples was examined to determine their overall structure, mineralogy, diagenetic history, fault rock types and the faulting relative to the diagenetic history and the deformation mechanisms. The rock internal structure was examined using X-Ray tomography, prior to SEM analysis. The mineralogy and diagenetic history of the rock were examined with a secondary electron microscope. The mineralogy of the rock was also examined by QXRD that provides samples quantitative assessments. The details about each of these techniques used during the study are described below.

### **3.4.1 X-ray tomography**

The internal structure of all cores was examined by a Picker PQ2000 dual energy computed tomography (CT) scanner system. This consists of an X-ray tube-system, a

core sample placing table, and a computer controlling system. A CT system produces thin cross-sectional images of the core samples. During this study, images were taken at a 1 cm interval through the samples prior to coring as well as the individual core plugs. The images recorded by X-ray tomography can be visualized with differences in material density; the differences in density are due to the degree of X-ray attenuation, and are dependent of material and energy. The key aims of collecting data on this were: to identify the best position to take the core plugs, to see whether the core is damaged and to identify the structural heterogeneities in the samples. The difference in fault and host material can be differentiable because of their density differences. Furthermore, fractures, heavy minerals and cemented surfaces can be recognized due to their density differences.

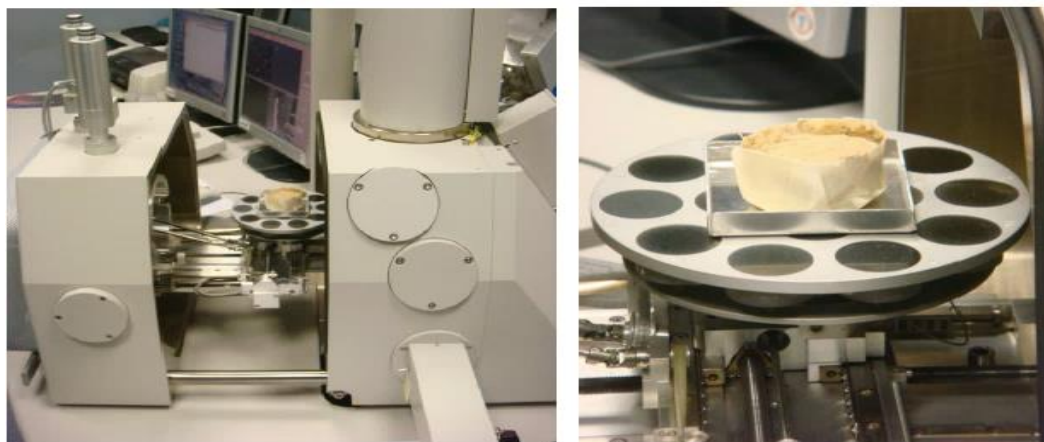
### **3.4.2 SEM examination**

The microstructure of deformed and their associated host rock were examined using scanning electron microscope (SEM). For SEM analysis the samples were first polished, resin impregnated and carbon coated. CAMSCAN CS44 SEM is used; this includes the secondary electron (SE) detector, a backscattered detector (BSE), a cathodoluminescence (CL) detector and an energy dispersive X-ray spectrometer (EDS). A view of the scanning electron microscope used is shown in **Figure 3.8**.

The secondary electron (SE) signal provides topographic information and is therefore extremely useful for investigating the relationship between detrital and authigenic components and establishing their relative timing. The backscattered electron (BSE) signal is directly proportional to the mean atomic number of the mineral; so phases of different mass have different brightness levels, therefore the heavy minerals appeared as a brighter and pores are as a dark area on the images. The CL detector is used to differentiate between minerals, and is sensitive to abundances of traces, such as quartz overgrowth is difficult to observe with BSE image, but it could be detected by using CL image. The images were stored as 8 bit TIFF files so that they could be loaded into the ImageJ for an image analysis. In particular, ImageJ was used to threshold the BSE images to provide estimates of porosity and mineral presence.



(a)



(b)

Figure 3.8 Illustration of the Scanning Electron Microscope used for samples microstructural observation (a) an outside view (b) inside view.

### 3.4.3 Quantitative X-Ray diffraction (Q-XRD)

The Phillips PW-1050 X-Ray diffractometer was used for the data collection, which consists of an X-ray tube, a sample holder and an X-ray detector. The Hilton Brooks HBX software package was used for the data analysis. A spray drier technique was used to produce samples for QXRD analysis that do not contain a significant preferred orientation even if there is significant amount of clay (Hillier, 1999). Each mineral have a distinct X-ray diffraction pattern based on their crystal structure. For mineral identification the QXRD can be used in both situations to either qualitatively or quantitatively analyse the sample sediments. However, during present study the mineralogy was identified by quantitative method to determine relative fractions of minerals. The samples were prepared by grinding and mixing with a standard (20 weight % corundum) and then spraying of slurry of the mixture through an air brush

into a tube furnace. The sphere-shaped aggregates were produced, which were about 25 to 30µm wide; these produced minerals have random orientation (Hillier, 1999). The samples were then loaded into a circular holder with a 20 mm diameter cavity. The holder was gently tapped to pack the sample without applying any pressure on the powder and the excess amount of powder was scrapped. The data was then collected and analysed; based on the technique mentioned by Hillier (1999), these results are accurate at 95% confidence level to  $\pm X0.35$ , where X is the concentration in weight %.

### 3.5 Petrophysical analysis: single-phase properties

The samples were analysed using standard experimental procedures and protocols. In particular, helium pycnometry, steady state gas permeability, steady state liquid permeability, gas pulse decay and liquid pulse decay permeametry were all used. All permeability tests were performed on a Hassler-type core-holder. For low permeability samples (<0.1 mD) the pulse decay technique has been used to measure permeability. For high permeability samples (>0.1 mD), permeability measurements were made using the steady-state method.

#### 3.5.1 Porosity

The porosity of rock is expressed as either absolute or effective, and is a measure of the storage capacity which retains the volume of fluids. Effective porosity is expressed as the ratio of interconnected pores to the bulk volume, while the absolute porosity is the ratio of total pore volume to bulk volume. The total, absolute porosity of the sample can be calculated with the following equation:

$$\phi = \frac{V_b - V_g}{V_b} \quad (3 - 1)$$

where;  $\phi$  is porosity;  $V_b$  is bulk volume and  $V_g$  is grain volume.

Helium porosimeter was used to measure the grain volume, which basically consists of two chambers based on the principle of Boyle's law (**Figure 3.9**). Helium gas was admitted for porosity measurement, which penetrates into small pores quickly, which is an inert gas does not react with sample surfaces (Dandekar, 2006). In order to obtain grain volume two steps were followed. The first step was to calibrate the system to know the volume of reference chamber  $V_1$  and sample chamber  $V_2$  by injecting helium

gas. After calibration the second step was to place a core plug into the sample chamber at a pressure  $P_1$ , and this was isolated from the second chamber (reference chamber). The helium gas was admitted to the second chamber at pressure  $P_2$ , after that valve was opened to flow helium into sample chamber which reaches pressure stabilization, this was read as final pressure  $P_f$ . A few minutes were allowed for pressure stabilization, usually 3 minutes or more, depending on how tight the sample is. The pore space of the core plug was penetrated by helium gas; therefore the difference of volumes between two tests is the grain volume. According to Boyle's law principle,

$$P_f V_f = P_1 V_1 + P_2 V_2 \quad (3 - 2)$$

Substituting the volumes for calculation of grain volume,

$$P_f (V_1 + V_2 - V_g) = P_1 (V_1 - V_g) + P_2 V_2 \quad (3 - 3)$$

Rearranging equation to grain volume,

$$V_g = \frac{V_1 (P_f - P_1) + V_2 (P_f - P_2)}{P_f - P_1} \quad (3 - 4)$$

where  $V_1$  and  $V_2$  are calibrated volume of two chambers respectively.

The bulk volume of cylindrical plug was determined by  $\pi r^2 L$ , where  $L$  is the length of the sample and  $r$  is the sample radius. The pore volume is the difference in grain volume and bulk volume. The procedure was repeated to get the porosity of each plug.

The porosity was measured for all fault and host samples; the measured porosity was the average porosity of the plugs. It should be noted that the fault porosity is not possible to measure because the fault has a small volume compared to the associated undeformed rock. Therefore the deformation band porosity was determined by image analysis technique.

It is important to know the precision of measured value (how much it deviates from the true value) of porosity with helium porosimeter. The porosity of 10 core plugs from Central North Sea UK was measured. The average porosity was determined 23.71%, the minimum was 20.9%, and the maximum was 26% with standard deviation of 1.73%. It should be noted that the values could be viewed as minimum level of precision. In fact

the plugs studied were heterogeneous. The overall error estimates could be within one to two porosity units.

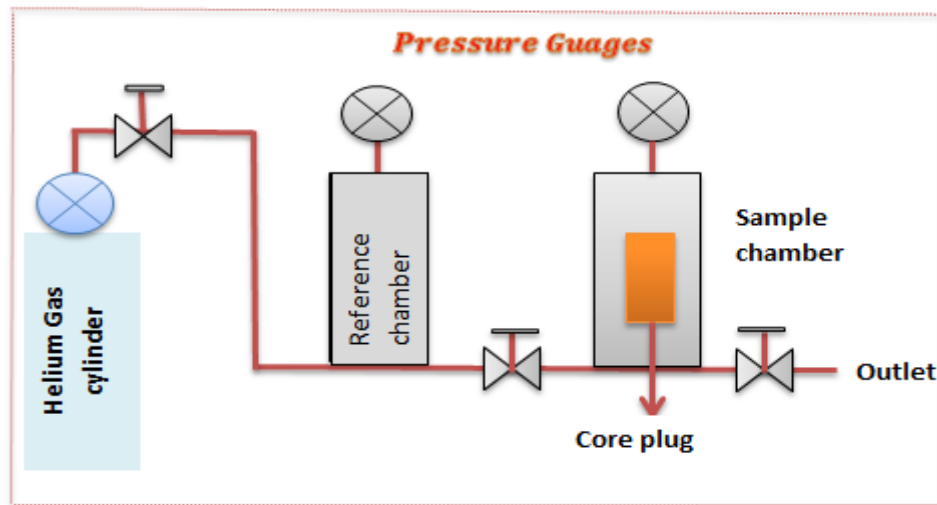


Figure 3.9 Schematic diagram of the helium porosimeter setup

### 3.5.2 Steady-state gas permeability analysis

The experimental arrangement consists of a cylindrical sample mounted in a high pressure core holder connected with gas supply and differential transducers of apparatus connected with computers for appropriate data logging and monitoring, as outlined in **Figure 3.10**. The maximum confining pressures that could be safely used were 5,000 psi for 1 inch samples and 10,000 psi for 1.5 inch samples. The confining pressure was safely applied with hand pump at the desired pressure level. Helium and nitrogen gas were used as flowing fluids. The permeability of the samples was measured by injecting gas through the core sample at a constant flow rate. The pressure drop across the sample was measured using a differential pressure transducers and the gas flow rate was measured by an Omega precision flow meter. Gases are compressible fluids; therefore their densities need to be considered while measuring the permeability. The permeability was obtained by using Darcy's equation:

$$K = \frac{2\mu QL}{A(P_2^2 - P_1^2)} \quad (3 - 5)$$

where:  $\mu$  = gas viscosity, (cp)

$L$  = sample length, (cm)

$Q$  = rate of fluid flow at ambient temperature conditions, (cm<sup>3</sup>/s)

$A$  = cross sectional area of the sample ( $\text{cm}^2$ )

$P_1$  = upstream pressure (atm)

$P_2$  = downstream pressure (atm)

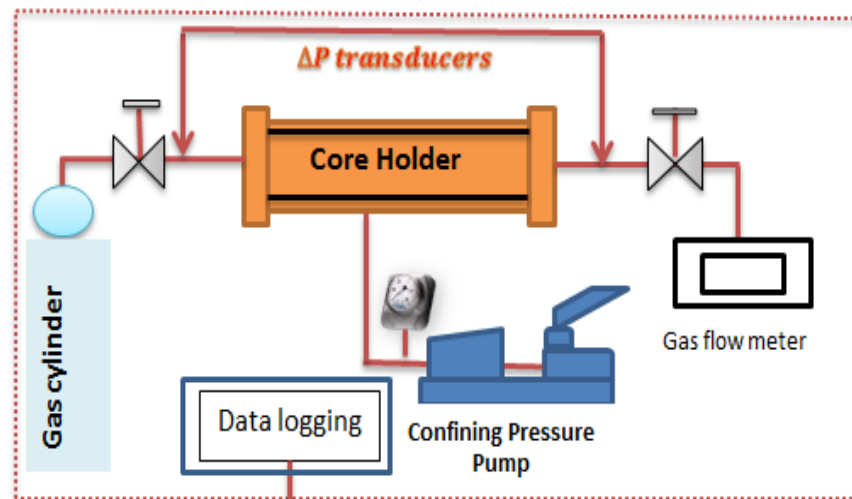


Figure 3.10 The schematic diagram of steady state gas permeametry.

### 3.5.2.1 Klinkenberg procedure

A key issue of using gas to measure permeability is the “gas slippage” effect, which creates a deviation from the actual permeability of the rock. If the mean pressure is increased, the mean free path for molecules of gas become smaller and the proportion of molecules colliding with each other increases in comparison to elastic collisions with the pore wall, which results in friction losses. Overall, the permeability measured at low pressures will be higher than at high pressures. Therefore, the gas slippage can becomes more important in low permeability rocks (Klinkenberg, 1941), so permeability measurements conducted at low pore pressures need to be corrected to obtain absolute permeability values. Gas relative permeability ( $k_{rg}$ ) measurements are also often made at low pore pressures so these too may need correcting to take into account of gas slippage effects. The effect of pore pressure correction is made based on the following formula from Klinkenberg (1941);

$$K_g = K_l \left( 1 + \frac{b}{\bar{p}} \right) \quad (4 - 1)$$

Where  $k_{ap}$  is the apparent gas permeability,  $k_{ab}$  is absolute gas permeability;  $b$  is the Klinkenberg b-value and  $\bar{P}$  is the average pressure. Flow tests are conducted at a range of pore pressures and then a plot of  $k_{ap}$  vs  $1/\bar{p}$  is then be extrapolated to  $1/\bar{p} = 0$ .

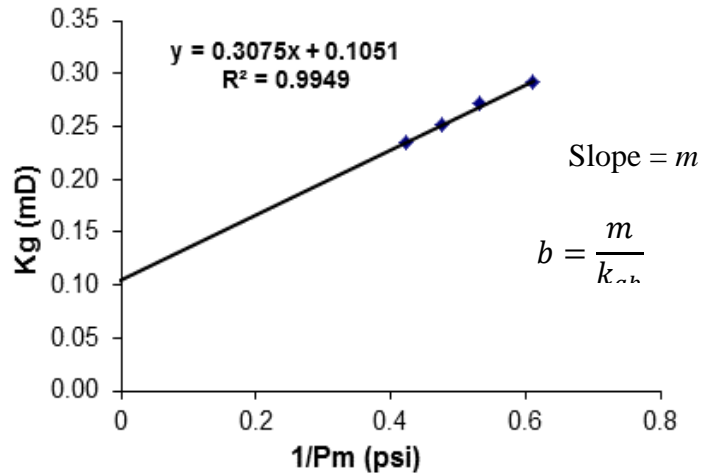


Figure 3.11 Diagrams showing the principle behind Klinkenberg corrections.

Klinkenberg (1941) was interested in obtaining liquid permeability from gas permeability measurements by plotting the results as a function of inverse of mean pore pressures. In the context of fault rock gas permeability the slippage factor gives the extent to which permeability will deviate as a function of pressure due to gas slippage effects.

### 3.5.3 Steady-state liquid permeability analysis

The experimental setup used during steady state permeability measurement consists of a core holder, two GDS (standard level pressure and volume controller) pumps, which pump fluid at constant rate and constant pressure, hydraulic pump to apply confining pressure and the data logging and monitoring computer. The experimental setup is outlined in **Figure 3.12**. Core holders were available for 1in and 1.5in diameter core plugs, a confining stress of 5000psi can be applied to 1 in core holder and up to 10,000 psi to 1.5in core holder; the experiments during this study were run up to maximum confining stress of up to 5000 psi. This setup measures the permeability down to 0.01mD.

The fully saturated samples were placed into a core holder to measure the permeability by allowing the constant flow rate of liquid to flow at room temperature. The fluid was pumped by GDS pumps with high accuracy. The pressure gradient across the sample

was recorded by the differential pressure transducers once it was observed that the inlet and outlet pressure through the core are invariant with time (i.e. the steady state flow has established). The permeability was then obtained by using Darcy's Law:

$$Q = - \left( \frac{K}{\mu} \right) \left( \frac{A}{L} \right) (\Delta P) \quad (3 - 10)$$

Where:  $Q$  = Rate of fluid flow through porous media ( $\text{cm}^3/\text{s}$ )

$A$  = Cross-section of the sample ( $\text{cm}^2$ )

$\mu$  = Dynamic viscosity of fluid flowing through porous medium (cp)

$\Delta p$  = Pressure drop across the porous media (atm)

$K$  = Permeability of the sample (D)

$L$  = Length of the sample (cm)

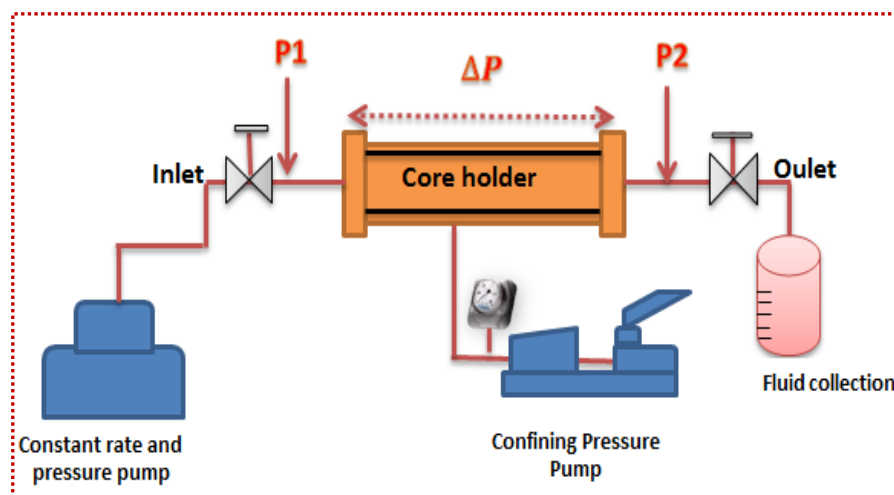


Figure 3.12 Simplified schematic diagram for steady-state flow tests.

### 3.5.4 Gas pulse-decay permeametry

It is difficult to apply conventional techniques to run experiments on very low permeable samples; these conventional methods of measurement are impractical and difficult to apply, as long periods of time are required to establish steady state flow. Brace et al. (1968) established a transient technique for permeability measurement. This technique was designed based on the concept of pressure transient method for measuring the permeability of granite which has a permeability down to 1 nD (Brace et al., 1968). This method of Brace et al., (1968) has been discussed by various researchers. Several mathematical models have been suggested for the transient pulse

test (e.g. Lin, 1982; Hsieh et al., 1981; Amaefule et al., 1986; Dicker and Smith, 1988; Jones, 1997).

The pulse decay experimental setup consists of cylindrical sample that is connected with two large fluid reservoirs, the volumes are  $V_0$  and  $V_1$ , a downstream volume  $V_2$  and  $V_3$  and a pressure differential transducer. It should be noted that these all valves have fixed volume. At the start of the experiment the pressure in upstream reservoir is suddenly increased, and a few minutes are allowed to achieve the thermal stability, then the upstream valve is suddenly opened to initiate the pressure pulse. As the upstream pressure has decayed, fluid starts flowing from upstream side to downstream side across the core sample. The data collection starts and is automatically recorded. In the Brace et al., (1968) procedure, the permeability of the sample is measured from upstream pressure decay curve. The permeability of the sample was calculated by mathematical solution of set of equations given in Brace et al., (1968). The experimental setup used consists of CoreLab200 PDP pulse decay permeameter. The layout of the setup is shown in **Figure 3.13**, which is an adaptation of Brace et al., (1968) design. This calculates the permeability of samples automatically. The measurements were made by applying a pore pressure of 1000 psi. The pore pressure for permeability measurement used was high, therefore the Klinkenberg effect was negligible; but this was done on all samples by changing mean pore pressure, in similar way for steady-state experiments. The confining stress applied was in range of 500 to 5000 psi.

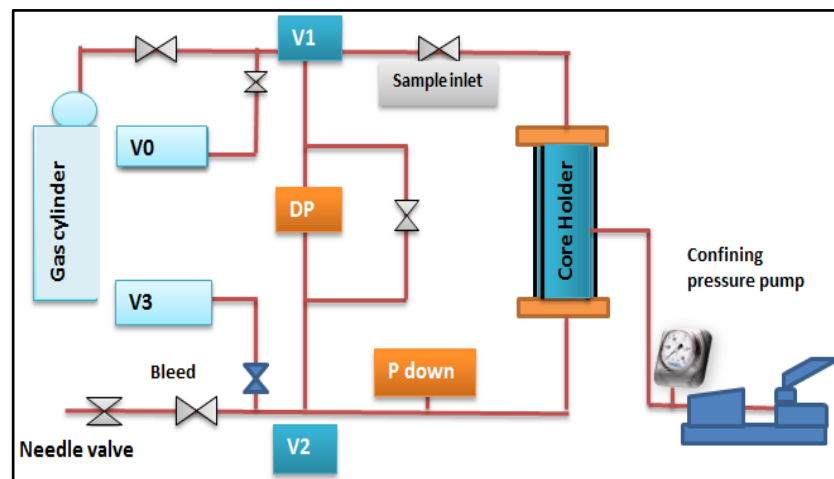


Figure 3.13 Outline of gas pulse decay permeametry

### 3.5.5 Liquid pulse decay permeametry

Recent research studies on low permeability rocks have argued that the gas permeability is lower than liquid permeability, slip corrected gas permeability could not be used as a substitute to liquid (Byrnes, 1997). Another consequence of measuring low permeability cores is that a high pore pressure and long-time for stabilization is required, this may change the pore network by fine particles migration (Soeder, 1988). Therefore brine permeability measured by liquid pulse decay setup, which basically based on the concept of Amaefule et al. (1986). The experimental set-up consists of a core holder, a confining pump and a GDS pump for upstream pressure application and a computer data logging and monitoring; the schematic diagram is shown in **Figure 3.14**. The core holder is connected with high pressure pump on its upstream side and the downside was connected with a large liquid vessel; this large size vessel is in fact considered as an infinite volume during the experiment with respect to upstream pressure.

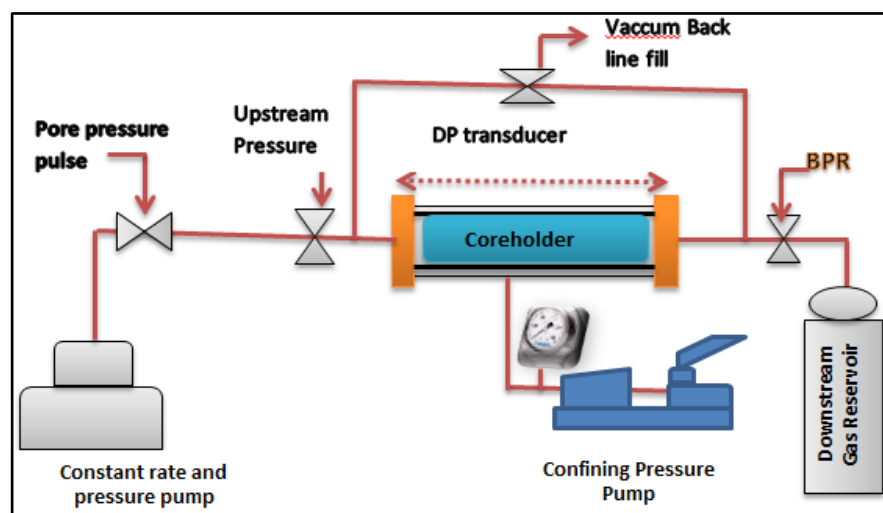


Figure 3.14 Diagram for liquid pulse decay apparatus.

A core plug of fully liquid saturated was place in a core holder at a confining stress to prevent the leakage through the rubber sleeve. Before starting the experiment, the pump started to pressurize the system to dissolve any trapped air in the system. If there is small volume of gas present in the system, it may flow through the core sample and may be trapped in the pore throat, which may affect the results. Therefore it becomes necessary to pressurize the system, to dissolve and remove any of the gas present. The compressibility measurement of the pore fluid is also important before analysing the data. During experiments the compressibility of pore fluid was measured independently and incorporated in equations for permeability calculations.

At the start of the experiment, the pressure in upstream side is increased; the upstream valve is suddenly opened to create a pressure pulse. As pressure pulse is generated, the liquid starts flowing across the sample and the pressure differential starts to decay. The upstream pressure, temperature and differential pressure are then automatically recorded. Then the data obtained was analysed from the solution of diffusivity equation, its derivation is based upon the combination of differential form of Darcy's equation together with continuity equation of Brace et al. (1968) and is given below:

$$\frac{\partial^2 p}{\partial x^2} = \frac{\mu\phi(\beta_s + \beta)}{K} \frac{\partial p}{\partial t} \quad (3-11)$$

Where,  $\beta$  is the fluid compressibility and  $\beta_s$  is the rock compressibility,  $\mu$  is the viscosity of fluid  $K$  is the permeability and  $\phi$  is the porosity,  $p$  is pressure and  $t$  is time. On the basis of assumption that  $\beta_s \ll \beta$ , Equation (3-9) was modified by Amaefule et al. (1986) to give the following relation:

$$\frac{\partial^2 p}{\partial x^2} = \frac{\mu\phi\beta}{K} \frac{\partial p}{\partial t} \quad \text{for } 0 < x < L; t > 0 \quad (3-12)$$

The pressure decay Equation (3-11), together with the corresponding initial and boundary conditions results in following Fourier series solution:

$$\Delta p_{x=L} = 2h\Delta p_i \sum_{n=1}^{\infty} \frac{\exp(-\sigma\alpha_n^2 t)}{[L(\alpha_n^2 + h^2) + h]} \quad (3-13)$$

where :

$$\sigma = \frac{K}{\phi\mu\beta}; h = \frac{A\phi}{V_1} \quad (3-14)$$

and  $\alpha_n$  are the roots of the transcendental equation (e.g. Amaefule et al. 1986):

$$\begin{aligned} \alpha L \tan \alpha L &= \alpha_n \tan \alpha_n \\ \alpha L \tan \alpha L &= hL = \frac{V_p}{V_1} \end{aligned} \quad (3-15)$$

The permeability of sample was obtained by using the following form of equation derived by Amaefule et al. (1986):

$$K = \left( \frac{\phi\mu\beta}{\alpha_1^2} \right)^m \quad (3-16)$$

Where,  $m$  is the slope of  $\ln\Delta p$  versus time.

To determine the precision level of permeability measurements the permeability of 10 core plugs was measured from Central North Sea reservoir samples. The average permeability measured was 1.1mD, the minimum 0.282 mD and maximum 2.77 mD, with standard deviation of 0.834mD. The results could be viewed as minimum level of precision, there might be uncertainty in measuring length and diameter of core plugs.

### 3.5.6 Deconvolution of fault rock permeability

It is not usually possible to obtain samples consisting solely of fault rock; instead all core plugs contain a mixture of fault rock un-deformed sandstone. So any permeability measurements on such samples will represent an average permeability of the fault rock and host sandstone. It is, however, possible to deconvolve the fault rock permeability by assuming that the measured value is the thickness-weighted harmonic mean of the fault rock and the host sediment permeability (e.g. Cardwell and Parsons, 1945). In which case the fault permeability,  $k_f$ , can be calculated using,

$$K_f = \frac{l_f}{\frac{l}{K_{avg}} - \frac{(l-l_f)}{K_h}} \quad (3-17)$$

Where,

$K_f$  = Fault rock permeability (mD)

$K_{avg}$  = Average permeability of the plug containing host and fault rock (mD)

$l_f$  = Fault rock width (cm)

$l$  = Sample length (cm)

$k_h$  = Host rock permeability (mD)

All fault rock permeability results calculated with above methods are analysed and discussed in subsequent chapters.

## 3.6 Petrophysical analysis: two-phase flow properties

The two-phase flow properties were measured for reservoir fault and host cores. The properties measured include gas-water relative permeability, air-brine capillary pressure

and saturations. Two techniques (imbibition and drainage) were used for measuring air-brine capillary pressure and brine saturation; each method has some limitation, therefore both were used to alter the saturation and to obtain capillary pressure.

The water saturation was altered by centrifuge and relative humidity chambers; once the equilibrium between capillary pressure and saturation was established, the effective gas permeability was measured using either steady state or pulse decay method (**Section 3.5**). The stress dependence of gas relative permeability of partially water saturated samples was also measured on these samples. In addition to above methods of effective gas permeability measurements, gas breakthrough experiments were run by putting samples in core holder at higher stresses, the experimental procedure is described in **Section 3.6.4**.

### **3.6.1 Pore size measurement and threshold pressure determination**

Mercury injection curves were measured for all fault and host rock samples using a Micromeritics mercury injection porosimeter. The rectangular samples were first cleaned and prepared with the maximum dimension of 12 mm x 12 mm x 10 mm for mercury analysis. The samples were sealed by araldite on five sides for fault specimen prior to inject the mercury; the reason for sealing the five sides and keeping one side open is that when mercury is intruded it should flow across the fault rock so that a threshold pressure can be identified.

Purcell (1949) was the first who introduced this technique. The mercury is a non-wetting fluid, it cannot invade spontaneously into the specimen; therefore it must be forced by applying pressure to invade into the specimen. The mercury was injected in cleaned samples at a pressure up to 60,000 psi. The equilibrated pressure required is inversely proportional to the pore size (Washburn, 1921); therefore, a small pressure is required to invade mercury into large pores, higher pressures are needed to force the mercury if the pore size is small. The injection pressure is then plotted against the mercury saturation to produce a curve for analysis. From the pressure versus mercury intrusion data the instrument generates the volume and pore size distributions using the expression given by the (Washburn, 1921);

$$D = -\frac{1}{p}4\sigma\cos(\theta) \quad (3 - 18)$$

where

$D$  = Pore diameter ( $\mu\text{m}$ )

$p$  = Applied pressure (psi),

$\sigma$  = Surface tension (dyne/cm)

$\theta$  = Contact angle (Degree)

The surface tension of mercury varies with purity. The usually accepted value is 484dyne/cm. The contact angle between mercury and solid containing the pores varies with solid composition.

As stated by Katz and Thompson (1987), the threshold pressure is the pressure at which mercury forms inter-connected pathways throughout the samples; this is the threshold pressure and corresponds to an inflection point on the mercury injection curve. It should be noted that the inflection point may not be defined clearly on mercury injection curves, therefore it becomes tedious to pick the threshold pressure as its interpretation varies and depends upon the interpreter. Quantification of errors related to threshold pressure picking from mercury injection curves is difficult.

### 3.6.2 Relative Humidity chambers

This method is based on the observation that if wetting and non-wetting fluids are present in a porous medium, they make a curvature due to their surface and interfacial forces (e.g. Kelvin 1871; Newsham et al., 2003). This method of capillary pressure measurement also reported by ( e.g. Calhoun Jr et al. 1949; Melrose 1987; Newsham et al., 2004) . A mathematical relation of capillary pressure to vapour pressure in a porous medium containing water in equilibrium with its vapours can be calculated using the following equation (Newsham et al., 2004);

$$P_c = -\frac{RT}{V_m} \ln\left(\frac{R_H}{100}\right) \quad (3 - 19)$$

Where;

$P_c$  = Capillary pressure

$R$  = Universal gas constant,

$R_H$  = Relative humidity,

$T$  = Absolute temperature,

$V_m$  = Molar volume of water,

Newsham et al. (2004) reported that the work of Melrose (1987) has established the validity of using the above equation for the calculation of capillary pressure at lower water saturations. Therefore the main advantage of using this method was to achieve lower saturation and higher capillary pressure. Newsham et al. (2004) reported that with the humidity chamber the water saturation of 5% can be achieved at a capillary pressure of 10,000 psi.

During the present study salt solutions as indicated in **Table 3.2** were used to measure the air-brine capillary pressure. The cleaned and dried samples were placed in humidity chambers. Initially these were put at highest capillary pressure to achieve the lowest saturation. The saturation of plugs was checked by weighing the sample with precision balance every three days. When sample weight was uniform, there was no change in sample weight for more than a week, it was assumed that the equilibrium between capillary pressure and saturation has been achieved. For some samples this took several days and even weeks to reach equilibrium. Once the equilibrium between capillary pressure and saturations was reached, the plugs were then taken out of the chambers and their effective gas permeability was measured. The equation for saturation calculations was obtained by using following equation,

$$S_w = \frac{(wt\ of\ core - wt\ of\ dry\ core)}{Pore\ volume} \quad (3 - 20)$$

Where,  $S_w$  is the water saturation in percent or it could be in fractions and  $wt$  is the weight of the core sample in gm. It should be noted that the pore volume of the sample was determined using helium porosimetry.

Salt Type	Relative humidity at 25 °C (%)	Equivalent capillary Pressure (psi)
Potassium sulphate	97	606
Potassium nitrate	92	1660
Potassium chloride	85	3236
Ammonium sulphate	80	4443
Sodium chloride	75	5728

Table 3.2 Capillary pressure and relative humidity generated by different salt solutions.

### 3.6.3 Ultracentrifuge

During this study the Optima L-100 XP ultracentrifuge was used to conduct drainage experiments. The principle of this method is based upon a centrifugal force (**Figure 3.15**) which is applied at certain revolving speed to expel the mobile fluids out of the sample (e.g. Slobod et al., 1951)

Brine saturated plugs were placed in centrifuge pre-calibrated cups, without applying confining pressure and were run at an initial speed of 1000 rpm. During centrifuge rotation the plug in-situ fluids displaced and the rate of fluid production with time at an assigned rotation speed were measured in calibrated cups. Sometime was allowed to established equilibrium at corresponding rotational speed of centrifuge. After a couple of days if there was no fluid displaced from any of the plugs, this shows that the equilibrium has been established; then samples were taken out of the centrifuge. Saturation was determined from the weight of the samples. The effective gas permeability was then measured at corresponding saturation by either the steady state or pulse decay method. Once the measurements on effective gas permeability were made, then the samples were replaced and the centrifuge was set at the next higher rotational speeds. The samples used took about six to seven days to reach equilibrium; the speed was then gradually increased to the next higher speed. The time required for establishing equilibration varies and depends upon sample. During this study the highest speed of rotation used was 8000 rpm. A mathematical model (Forbes, 1997) used to generate a capillary pressure curve.

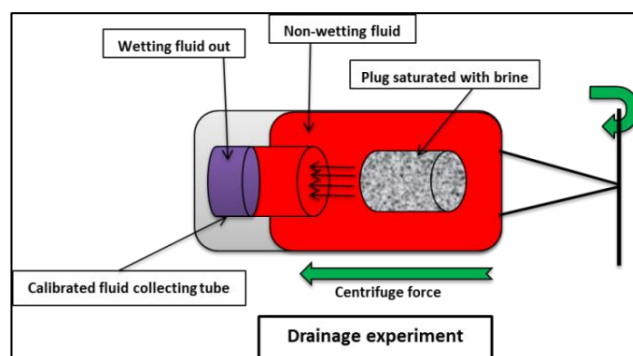


Figure 3.15 The illustration is the drainage experiment with centrifuge.

### 3.6.4 Breakthrough Experiments

The breakthrough experiments in this study were performed by imposing the constant flow rate of high pressure gas across the samples. The procedure is outlined in **Figure 3.16**. It consist of a gas supply, hassle-type core holder of 1inch, a hydraulic pump for applying confining pressure of maximum 5000 psi and a flow meter with high precision differential pressure transducers. The procedure follows by placing a partially brine NaCl saturated sample into core-holder, the gas injected at a constant rate upon the upstream side of the core and monitoring the pressure of the non-wetting fluid until breakthrough occurs. This method took a long period of time (almost two to three weeks) to result in gas breakthrough. The effective gas permeability was obtained using the Darcy's equation.

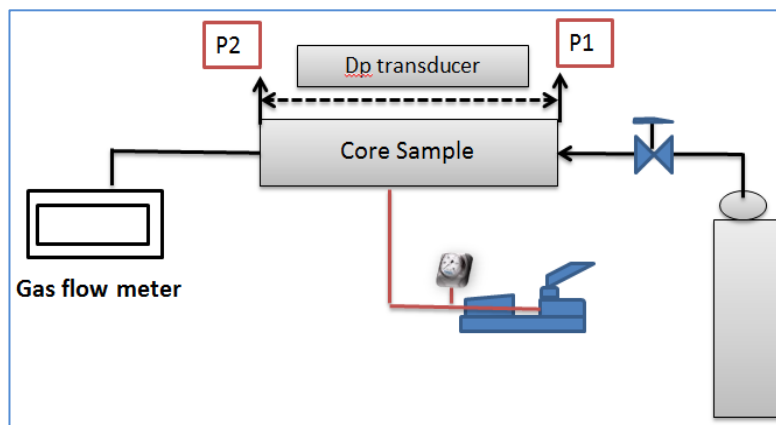


Figure 3.16 the experimental setup used in this study by introducing constant gas into upstream side.

### 3.7 Uncertainties and issues related to experimental work

To achieve the objectives of this research, experiments with different pore fluids were conducted. The basic concepts of permeability measurements were the same as mentioned earlier; the difference was changing the pore fluid and confining stress employed to investigate the consequences upon the fault rock permeability. The methodologies and experimental techniques are discussed in previous sections of this chapter, while in this section the issues and uncertainties related to experiments are discussed.

The importance of the experimental data has increased with the advancement of computing technology. Simulators are now available to incorporate the data into simulation for modelling purpose to analyse the dynamic behaviour of reservoirs. A lot of effort was also made to reduce uncertainties during conduct of experiments.

However, there are still a few doubts regarding the data measured in laboratory; the measurements made by instruments have a certain degree of uncertainty that must be accounted for precision. Therefore, it is important to understand, investigate and admit the uncertainties involved before conducting any experiment. Each of these is discussed below and maximum effort was put to pay proper attention in avoiding them.

For instance, one of the objectives of this research is to measure the petrophysical properties of the fault rocks, it is essential to have appropriate samples before doing any experiment. The next main thing in taking fault core plug is to consider its orientation towards the deformation band; fault plugs must be taken perpendicular to bedding. The plugs diameter and length may not parallel to their axis, so a single measurement can give an error. Therefore at least five measurements should be taken and an average of these could be used in calculations to minimize the error.

As the permeability setup is designed for very low permeability measurements, leak tightness for the apparatus is very important. Calibration for the leak test was conducted by putting a steel plug into the core holder and allowed for 24 hours to check pressure stability of the setup. For pressure tests, if there was no change in upstream pressure observed over the period of time then the setup is said to be leak free. The measurements were temperature sensitive, so the experiments must be conducted in the controlled temperature environment.

The experiments were conducted at high confining pressures to evaluate the permeability at reservoir stress state. The compressibility measurement of the pore fluid and the experimental setup is also important before analysing the data. The compressibility of the setup and pore fluid is measured independently and incorporated in analysis. Moreover, the experiments were also conducted at higher NaCl saturation, of 20 to 30%; therefore care must be taken in handling of the brine saturated samples, they must be left in vacuum chambers, and should not be left in an open environment, due to the fact that water in open space starts evaporating and NaCl brine will start precipitating, which may alter the pore structure of plug and eventually damage the pore network and may impair permeability of the rock.

Before start of experiments, when sample loaded into a core holder, one must ensure that the core plug fits perfectly between the two ends and then screw the end caps and

tight the threads, otherwise there might be chance of fluid leakage and damage to rubber sleeve of the core holder while applying confining stress.

In order to avoid aforementioned complications and uncertainties and to achieve the desired accuracy in the final results, care must be taken prior to conduct experiments and the standard procedures and protocols must be followed.

# 4 **Absolute permeability of fault rocks: impact of clay and pore fluid type**

---

## **4.1 Introduction**

Permeability is a fundamental property of any reservoir rock that controls fluid flow and is essential for modelling reservoir production (e.g. Fisher & Knipe 2001). The permeability data of fault rocks available within the public domain were measured using gas or distilled water as a pore fluid (e.g. Fisher and Knipe, 1998, 2001; Gibson, 1998; Fowels and Burley, 1998; Shipton, et al., 2002; Tueckmantel et al., 2010). However, hydrocarbon reservoirs also contain brines. Researchers have argued that permeability measured with gas could be up to several orders of magnitude higher than when measured with water for the same sample, especially for low permeability samples (e.g. Faulkner and Rutter, 2000; Tanikawa and Shimamoto, 2006; Byrnes et al., 2010). Other studies have found that gas and brine permeabilities are nearly identical (e.g. Chowdiah, 1987; Rushing et al., 2004). There is virtually no data available to indicate the impact that the composition of the permeant has on fault rock permeability. The following chapter aims to fill this knowledge gap. In particular, it aims to assess whether the fault rock permeability data presented in Fisher and Knipe (2001) could be in error due to the fact that measurements were made using distilled water as the permeant rather than formation compatible brines. To achieve the objectives, this research has focussed on integrating laboratory experiments on fluid flow properties of fault rocks with microstructural data obtained from SEM analysis. It is also essential to have an

integrated understanding of their microstructural analysis and petrophysical properties to characterize the sealing potential of faults.

The chapter starts by describing the microstructure and mineralogy of fault rock samples and their associated undeformed sandstone (**Section 4.2**); this is followed by the X-ray tomography of samples. The chapter then presents the results from experiments conducted to assess the impact of brine composition on fault rock permeability; the permeability to gas is also included for comparison (**Section 4.3**). Permeability of rock is often controlled by pore size, for this reason mercury (Hg) porosimetry tests were also conducted to examine the pore throat size distribution. In addition to derive pore size information from mercury porosimetry, it is also theoretically possible to estimate pore size from the Klinkenberg slip parameters that is often measured during steady-state gas permeability experiments. The following chapter presents such estimates as a comparison with the values obtained from Hg injection and also to provide potential information that could help explain the differences in permeability to brine, distilled water and gas. To the author's knowledge, no other study has attempted such a comparison on fault rock samples. Furthermore the implications of the results, as well as the significance of permeability measurement and proper utilization of measured data for fault rock transmissibility calculation to evaluate the cross fault fluid flow behaviour are discussed in **Section 4.4**. The main findings from results of this chapter are presented in **Section 4.5**.

## **4.2 Mineralogy and Microstructural properties**

Information on the mineralogical properties/composition and microstructure of samples is necessary to help understand laboratory flow experiments. In this study two techniques were used to obtain such information: QXRD analysis and SEM (these techniques are described in detail in **Section 3.3**). The fault rock microstructural properties were defined and classified based on their clay content following the classification introduced by Fisher and Knipe (2001).

### **4.2.1 Central North Sea reservoir cores**

The overview and geological settings of the field studied is provided in **Section 3.2**. The reservoir core samples studied were categorized into two groups, A and B, and

are discussed below separately. The host and fault rock of ten samples from group A and eleven from group B were analysed.

#### **4.2.1.1 Microstructure and mineralogy of the host sandstone**

The host sandstones from group A is medium to fine grained and is moderate to well-sorted (**Figure 4.1B**). The QXRD results (**Table 4.1**) indicate that these are composed of: quartz (38.1 to 25.9 %), microcline (22 % to 33%), chlorite (7.6 % to 31.7%), albite (9.9% to 16.3 %), pyrite (0.60% to 2.3%), mica (5.1% to 11%), illite-smectite (2.5% to 6.6%), and kaolin (0.3% to 6.5%) and has a porosity of 23.7% to 28%.

The main diagenetic processes to affect the sample were the precipitation of K-feldspar, chlorite, and quartz as well as the partial dissolution of feldspar. The K-feldspar occurs as up to 50  $\mu\text{m}$  wide overgrowths on detrital K-feldspar. The chlorite occurs as a grain coating clay. It is possible that it formed as a result of the recrystallization of early smectitic clay. Secondary pores, surrounded by K-feldspar overgrowths, are present. These probably formed as a result of feldspar dissolution. The authigenic quartz occurs as both overgrowths and outgrowths.

Group B sandstones (**Table 4.2**) are fine to medium grained, moderate to well sorted; a typical BSEM image is shown in **Figure 4.1D**. These samples are composed of quartz (26% to 49.4 %), albite (9 to 23%), illite-smectite (2.7 to 7.7%), dolomite (2.4% to 6.7%), mica (2.1% to 8.4%), chlorite (2.5% to 12%), and pyrite (0% to 2.4%). The porosity of these samples ranges from 12% to 22.0%. The main diagenetic processes to affect the sample were mechanical compaction, precipitation of dolomite, chlorite and small amounts of quartz and albite. The dolomite occurs as 50 $\mu\text{m}$  rhombs that are compositionally zoned with dolomite cores and thin ankerite rims. The chlorite occurs as a grain coating clay. It is possible that it formed as a result of the recrystallization of early smectitic clay. The authigenic quartz and albite occurs as outgrowths on detrital quartz and plagioclase respectively.

#### **4.2.1.2 Microstructure of the fault rocks**

The most common type of fault rock within these cores of “group A” are cataclastic faults (**Figure 4.1A**). These have a porosity of around ~5 to 9%, which is ~ 25 to

~30% that of the host sandstone. This reduction in porosity has occurred mainly as a result of deformation-induced grain-fracturing, which enhanced mechanical compaction. Faulting occurred after the precipitation of K-feldspar overgrowths and chlorite (or its precursor) but before quartz. The extent of the grain reduction experienced by these fault rocks varies, details about each individual sample are provided in **Appendix A**.

Group B fault rocks fall in between two categories: cataclastic and phyllosilicate-framework faults; the majority of faults formed within this were recognized as phyllosilicate framework faults (**Figure 4.1C**). The faults formed within this group reveal a heterogeneous microstructure. In some places, they have a very similar microstructure to that of the host sandstone. Other samples studied experienced a slight reduction in porosity due to the deformation-induced mixing of clays with framework grains leading to a replacement of macroporosity with clays and microporosity. Just like for group A, the extent of the grain-size reduction experienced by the fault rocks in group B varies; details about each individual sample are provided in **Appendix A**.

Table 4.1 Summary of mineralogy from QXRD results of host sandstone composition (wt. %) for specimen from group-A Central North Sea reservoir samples.

Mineralogy from QXRD analysis for Central North Sea reservoir -Group A samples										
Sample Name	Quartz	Albite	Microcline	Mica	Illite-smectite	Kaolinite	Chlorite	Pyrite	Porosity	Clay
CP1A	19.2	7.3	16.3	3.8	0.0	4.8	23.5	0.0	25.2	32.1
CP1B	24.5	8.7	20.8	7.0	2.2	2.9	11.0	0.0	22.9	23.1
CP1C	28.9	8.3	16.9	4.5	2.5	1.2	14.0	0.0	23.7	22.3
CP1D	28.7	10.9	20.0	4.7	5.3	2.6	6.8	0.0	21.0	19.4
CP2A	25.5	9.7	20.4	4.4	4.3	0.0	8.7	1.7	24.4	17.4
CP2B	23.9	8.2	21.6	6.9	2.0	0.8	7.7	0.5	28.4	17.5
CP2C	24.2	8.1	22.7	4.8	3.2	0.8	7.2	0.4	25.7	16.0
CP2D	27.2	8.2	25.9	6.2	0.0	0.2	7.5	0.5	23.4	14.0
CP2E	26.4	12.6	17.6	6.5	3.9	2.9	5.9	0.0	24.1	19.2
CP2F	24.5	10.7	22.4	8.8	1.7	2.7	8.1	0.0	21.1	21.3

Table 4.2 Mineralogy from QXRD results of host sandstone composition in (wt. %), for the specimen from group-B Central North Sea reservoir samples.

Mineralogy from QXRD analysis for Central North Sea -Group B samples											
Sample Name	Quartz	Albite	Microcline	Calcite	Dolomite	Mica	Illite-smectite	Chlorite	Pyrite	Porosity	Clay
5AF1	41.7	16.8	0.0	0.0	3.3	6.4	5.4	4.4	1.1	21.0	16.2
5BF1	40.5	17.0	0.0	0.0	4.1	8.4	7.5	4.7	1.8	16.0	20.6
5DF1	42.1	17.5	0.0	0.0	2.4	5.8	2.7	2.5	4.9	22.0	11.0
5EF1	42.2	19.1	0.0	0.0	3.5	3.9	6.0	3.1	0.1	22.0	13.1
7AF1	40.2	14.7	8.9	0.7	6.2	4.6	3.0	5.6	0.0	16.0	13.2
7BF1	37.4	13.7	10.0	0.5	6.7	4.2	6.1	4.4	0.0	17.0	14.7
7CF1	32.8	18.2	11.7	0.7	2.8	5.7	6.4	7.7	0.0	14.0	19.8
7DF1	32.0	23.5	7.8	0.5	5.4	2.3	7.7	8.9	0.0	12.0	18.9
7EF1	36.2	16.7	6.6	0.0	4.0	4.5	7.4	9.5	0.0	15.0	21.4
7FF1	31.0	21.8	6.2	0.4	4.8	3.4	4.0	12.5	0.0	16.0	19.8
3AF1	26.4	11.6	19.0	0.0	3.4	6.9	2.9	12.0	0.0	18.0	21.7
10/3A	49.4	15.8	7.4	0.0	2.7	2.7	3.7	6.3	0.0	12.0	12.8

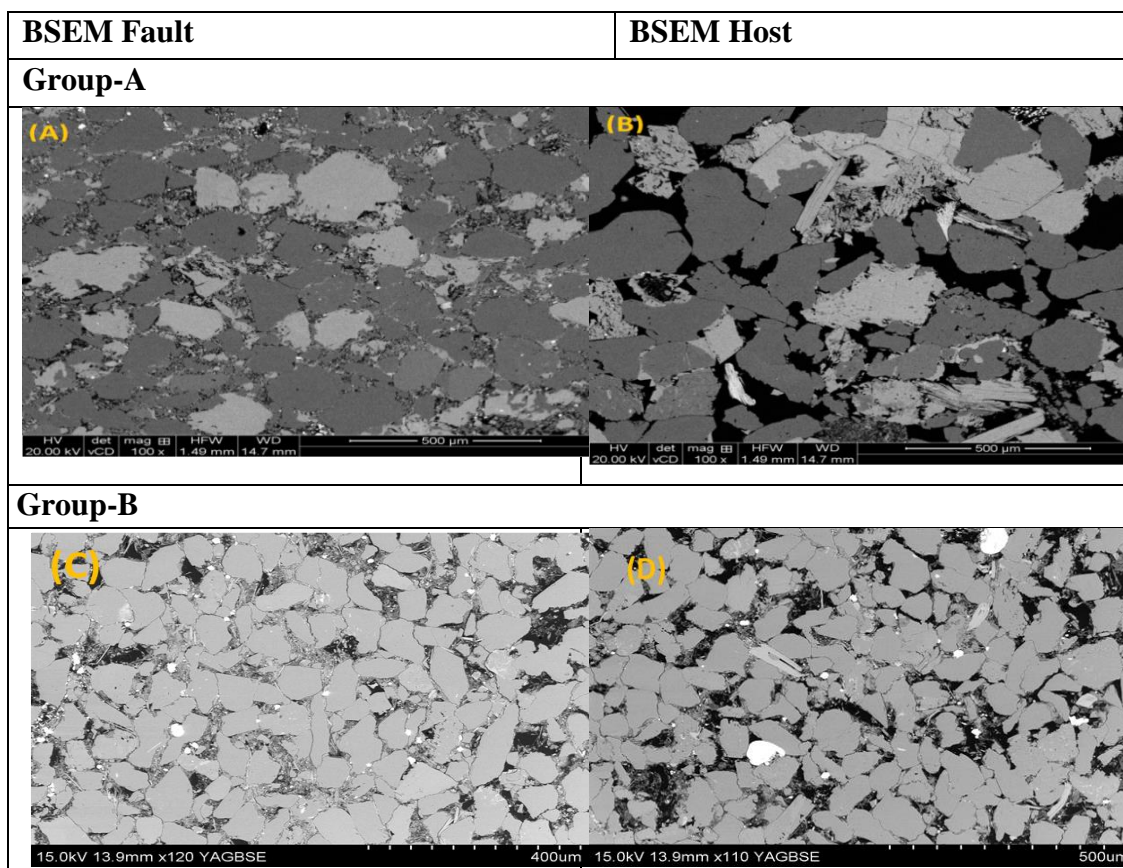


Figure 4.1 Photomicrograph (A) BSEM image of cataclastic rock formed in a clean sandstone with relatively small clay content; (B) BSEM image of host sandstone; (C) BSEM image of phyllosilicate framework fault; (D) BSEM image of host sandstone. All these samples were from the Central North Sea reservoir samples group.

## 4.2.2 Southern North Sea reservoirs

Three cores samples were supplied from a Triassic reservoir in the Dutch sector of the Southern North Sea.

### 4.2.2.1 Microstructure and mineralogy of the host sandstone

The undeformed sandstone is medium to fine grained, well sorted with a porosity of 9% to ~23% (**Figure 4.2B and D**). The QXRD analysis is reported in **Table 4.3**. This indicates that the samples are composed of quartz (28.2% to 63.4%), albite (4.2% to 7.5%), calcite (0.3% to 39.3%), dolomite (1.4% to 19.8%), mica (2.9% to 9.0%), illite-smectite (0.30% to 4.0%), kaolinite (13.9% to 29.6%), siderite (1.3% to 4.0%), anhydrite (1.7% to 3.4%) and barite (1.4% to 2.1%). The main diagenetic processes to affect the samples were the precipitation of kaolin and quartz; there are also the occasional secondary pores. The kaolin occurs as ~50 $\mu$ m booklets and appears to have precipitated during early burial but may have recrystallized. The

authigenic quartz occurs as outgrowths and can occasionally be observed overgrowing the kaolin.

#### 4.2.2.2 Microstructure of the fault rock

Examination of the hand specimen revealed the microstructure could be extremely heterogeneous so several samples were taken for SEM analysis. The faults have a porosity of ~4% to ~8%, which is <50% that of the host sandstone. This reduction in porosity has occurred mainly as a result of cataclastic deformation, which enhanced mechanical compaction (**Figure 4.2A and C**). Faulting occurred after the precipitation of kaolin and dolomite but before the quartz. Among three faults two were cataclastic and one was juxtaposition fault that had experienced dilation and had been cemented by anhydrite. It is possible that the fault formed relatively early and that the dilation occurred due to late stage reactivation. The extent of the grain reduction experienced by these fault rocks varies and details of each individual sample are provided in Appendix A.

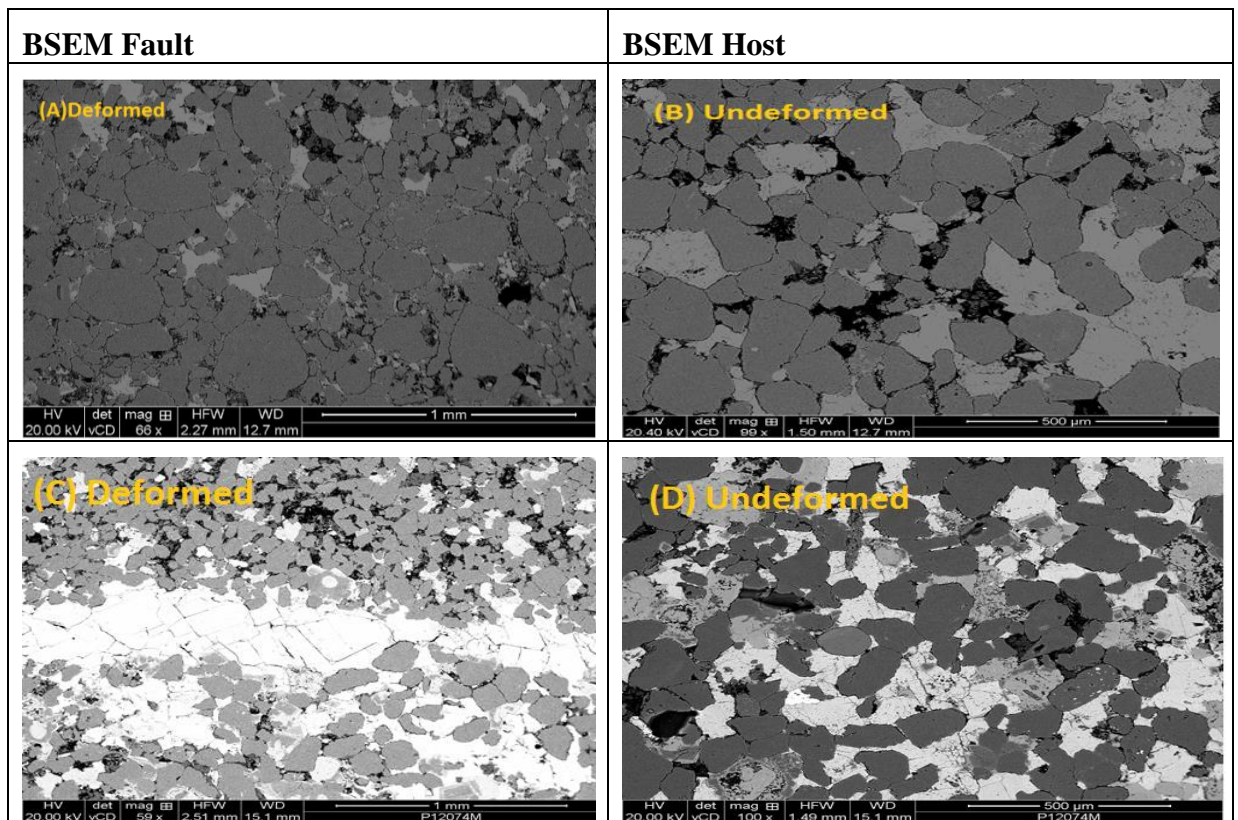


Figure 4.2 Photomicrographs of (A) BSEM image of Cataclastic fault with small grain size reduction; (B) BSEM image of adjacent host sandstone; (C) BSEM image of cataclastic fault from same field with large grain size reductions; (D) BSEM image of adjacent host sandstone all are from same field of southern North Sea reservoir core.

Table 4.3 The summary of the QXRD results of host sandstone, composition in (wt. %) of the specimen from Southern North Sea reservoirs.

Mineralogy from QXRD for Southern North Sea reservoir samples									
Sample Name	Quartz	Albite	Calcite	Dolomite	Mica	Illite-smectite	Kaolinite	Porosity	Clay
WIN1A	49	5.8	1.1	0	5.6	1.5	21.2	15.8	28.3
WIN2A	46	6.2	0.4	0	7.4	0.9	21.2	17.6	29.6
WIN1B	29	5.2	11.8	19.3	2.8	3.9	16.9	11	23.6
WIN2B	31	6.3	12.9	17.8	5.1	2.1	13.7	11.3	20.9
WIN1C	26	3.8	35.3	1.3	5.1	0	17.2	11.5	22.4

### 4.2.3 90 Fathom Fault, Northumberland

The host rock, single deformation band and slip-surface cataclasite were sampled from the hanging wall of the 90 Fathom Fault UK. In total, six samples were prepared from slip-surface cataclasite, four from single deformed zone for petrophysical properties analysis.

#### 4.2.3.1 Microstructure and mineralogy of the undeformed sandstone

The samples from undeformed sandstones are well sorted, fine to medium grained, containing well rounded grains. From image analysis the rock is composed of quartz (~56% to 65%), K-feldspar (7% to 10%), kaolin (~4% to 17%), calcite (0% to 1%), with detrital clay of ~3% and a porosity of 10% to 20% (**Figure 4.3**). The host sandstone has a simple diagenetic history involving the precipitation of kaolin, anhydrite and partial dissolution of K-feldspar. The K-feldspar exhibits in various dissolution textures; the kaolin occurs in clusters composed of 10µm pseudo hexagonal plates.

#### 4.2.3.2 Microstructure of the fault rocks

Microstructural and petrophysical property analysis was conducted on two types of fault rocks - slip-surface cataclasites and single deformation bands. Image analysis of BSE images suggests that the slip-surface cataclasites are composed of 60-75% quartz, 12 to 17% kaolin, and 9-12% K-feldspar. The fault rocks experienced cataclastic deformation, which reduced their porosity to ~ 5-7%, which is ~50% that of host sandstone. The single deformation band also experienced a grain size reduction and porosity collapse due to grain fracturing.

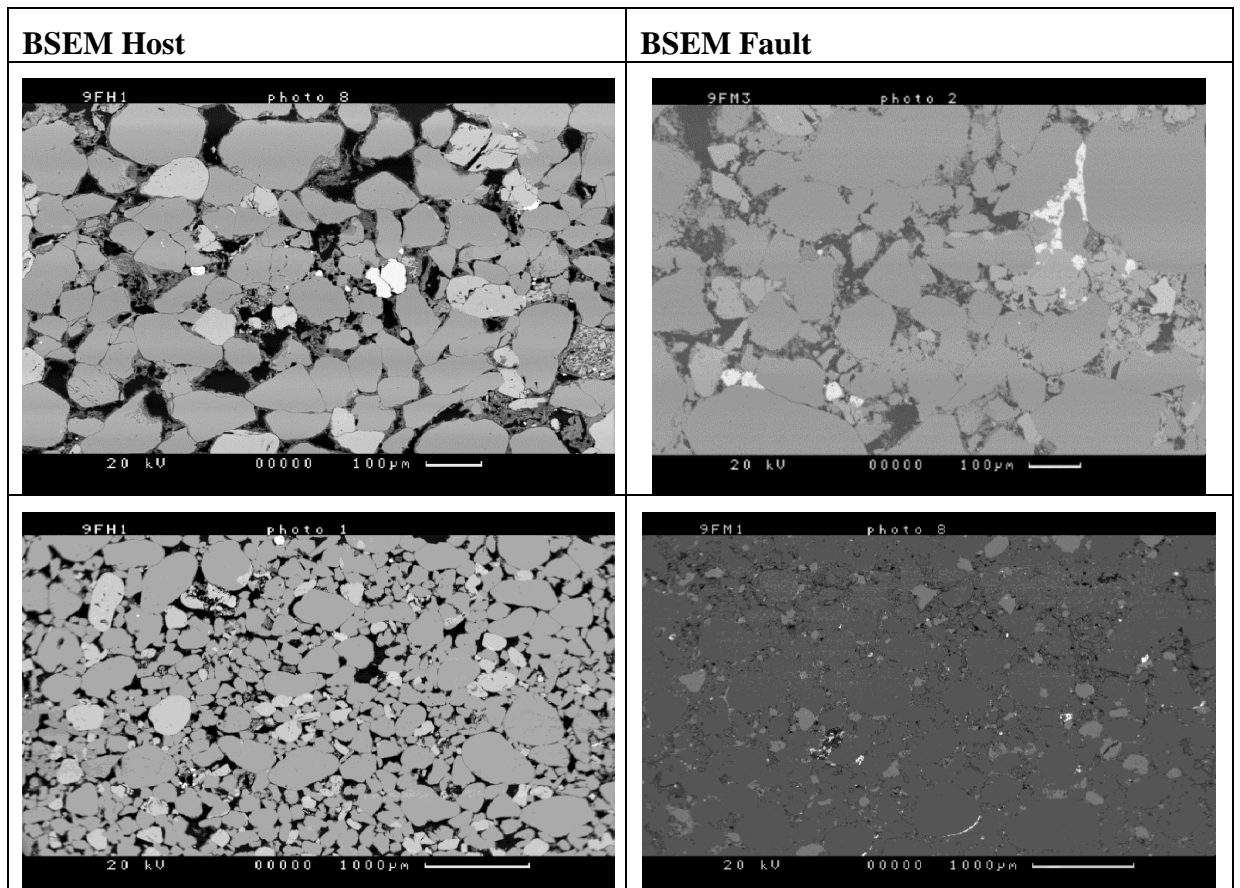


Figure 4.3 BSEM images of typical single deformation band zone host sandstone and its associated host sandstone (top) and slip-surface cataclasite and host sandstone it contains (bottom) from the 90 Fathom Fault.

#### 4.2.4 Miri airport road outcrop exposure Malaysia

Two samples were analysed from this outcrop, and their microstructure is discussed below. The permeability measured on these fault rock samples is discussed in Chapter 5.

##### 4.2.4.1 Microstructure and mineralogy of the undeformed sandstone

The samples from undeformed sandstones are moderately sorted, fine to medium grained. The image analysis shows that the rock contains mainly quartz and clay minerals. The only diagenetic processes that have affected the samples were the mechanical compaction.

##### 4.2.4.2 Microstructure of fault

The deformed rock examined has a variable microstructure; overall it appears to be a phyllosilicate-framework fault rock (**Figure 4.4**). The quartz grains within the samples have clearly undergone a small amount of cataclasis during faulting. The

extent of cataclasis would be consistent with deformation occurring at < 1km burial depth. A porosity of 16.1% was obtained from the samples analysed but it should be noted that the sample was composed of both fault rock and undeformed sediments.

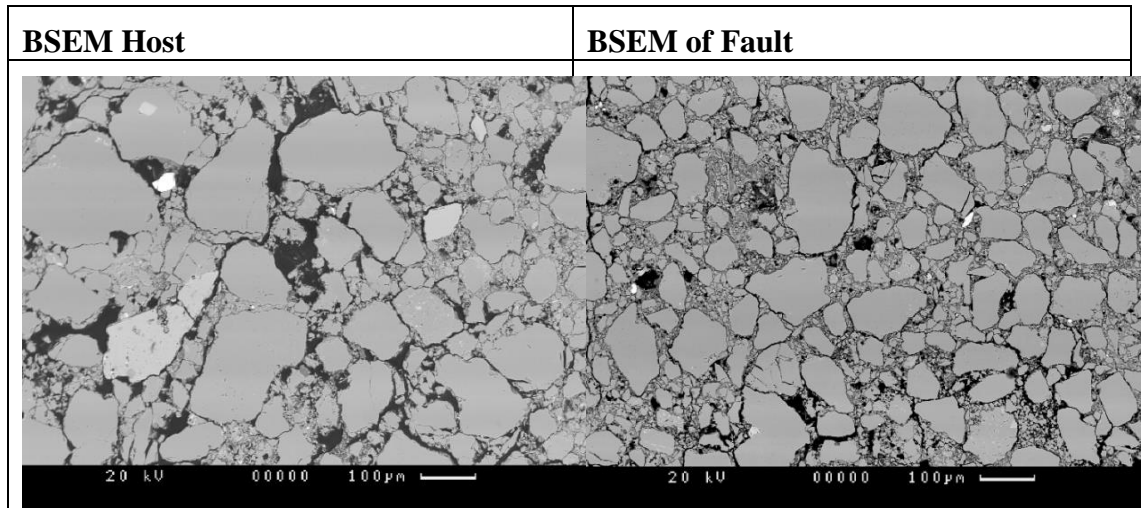


Figure 4.4 The phyllosilicate-framework-fault and the host sandstone it contains from Miri exposure Malaysia.

#### 4.2.5 Summary of microstructural analysis

Microstructural and QXRD analysis showed that the fault rocks can be subdivided depending on the clay content of their host sediment at the time of faulting and the stress during faulting (Fisher and Knipe, 2001). The majority of faults examined from the Triassic reservoirs of the central North Sea were categorized as cataclastic faults and few were recognized as phyllosilicate-framework faults. The faults from the southern North Sea were classified as cataclastic and cemented faults; anhydrite was the main cementing material found within these samples. QXRD analysis shows that kaolinite is the dominant clay mineral within southern North Sea core samples. On the other hand, QXRD analysis shows that chlorite is the dominant clay mineral within the central North Sea core samples.

#### 4.2.6 X-ray tomography analysis

The internal structure of all samples provided was determined using a Picker PQ2000 dual energy CT-scanner. The description of experimental technique used is provided in **Section 3.3.2**. The key aim of obtaining CT images was to identify whether the core is damaged prior to petrophysical properties measurement and the presence of open fractures and heavy mineral cements within the samples. This also permits us for recognition of different mineral components via their gray-dark scale

representation in a CT image. In general, the quartz and feldspars appears dark gray as in **Figure 4.5** one of the typical CT image taken from central North Sea core appeared as dark-gray colour that shows the quartz mineral. The quartz was the dominating mineral within the studied samples. The darker images on CT reveal that these are more porous than the brighter, the bright images reflects heavy minerals such as pyrites. **Figure 4.5** the bright colour streaks on both samples appears that these are very tightly packed and are low porous as well as low permeable. The white spots on CT image **Figure 4.5** appears to be cementing material such as pyrite, which has very high density and it has a high attenuation. Light gray colour on CT images represents medium density minerals such as illite-smectite. It is however very difficult to differentiate these clay minerals because the percentages of these minerals, as analysed by QXRD, were very low.

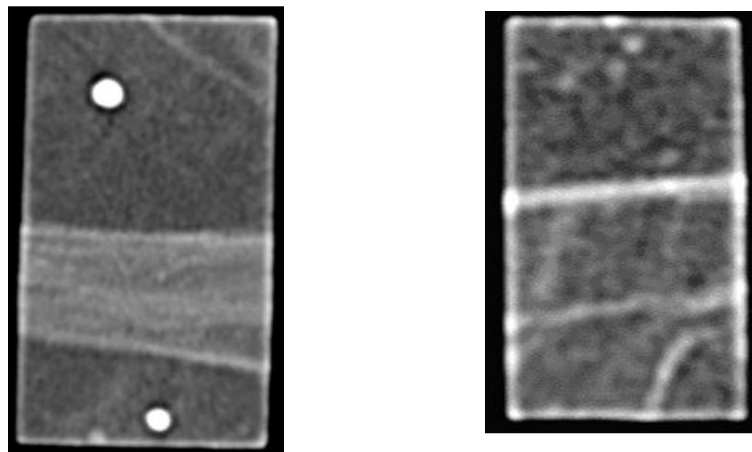


*Figure 4.5 CT images taken on central North Sea reservoir core samples containing deformation bands.*

In **Figure 4.6**, CT images taken from outcrop samples of a slip-surface cataclasite are shown. The CT image appears to be dark gray color which indicates that the sample contains higher quartz minerals. The homogenous density of host sample is evident from **Figure 4.6**. The slip-surface cataclasite sample indicates white color patches, which are evidence of iron minerals; these minerals have very high densities.

X-ray imaging is particularly useful for recognizing that how heterogeneous the samples are, identifying the deformed and undeformed rocks and differentiating heavy minerals such as calcite, pyrite, hematite or iron from other dominant minerals such as quartz was the dominant mineral in all of the samples studied. Subsequently,

the X-ray tomography enhances the understanding about lateral and horizontal changes in rock properties. However, the main use of CT-tomography within present study was to what position would be better to take fault and their associated host samples.

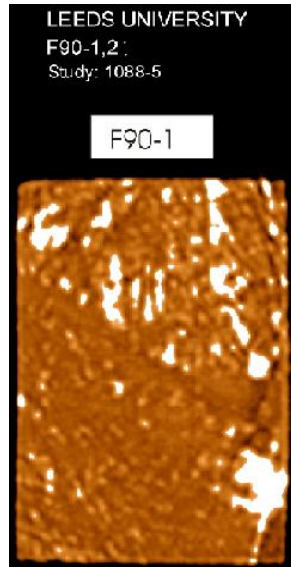


*Figure 4.6 CT image of one of the typical 90 Fathom fault sample from slip-surface cataclasite. The white patches are the heavy minerals with high densities.*

### **4.3 Experimental overview: Single phase gas and liquid permeability**

The Klinkenberg corrected single phase gas permeability as well as the permeabilities to brine and demineralized water was measured using steady-state and pulse decay methods. Details about the samples preparation and measurement methods are presented in **Section 3.3** and **Section 3.5** respectively.

Initially, gas permeability measurements were made on both host and fault rock at ambient conditions by flowing nitrogen or helium gas through the samples. After gas permeability measurements, all samples from the central North Sea were fully saturated with 30% NaCl brine and the permeability measured. The samples were then cleaned, dried and then saturated with 3.5% NaCl solution and then their permeability was measured. For all other samples following gas permeability measurements, permeability was measured using 20% NaCl brine (200,000 ppm) and distilled water. It should be noted that all samples liquid permeability measurements were made by decreasing brine concentrations. Initially the

measurements were made with higher brine (NaCl) concentrations then decreased to next lower (NaCl) concentration and then finally the permeability was measured using distilled water as a pore fluid.

In this study, a range of breakthrough pressures for each sample was estimated by collecting the mercury-injection capillary pressure data. In addition to that pore size distributions of all samples were derived from mercury porosimetry and the experimental details are given in **Section 3.5.2**.

All permeability measurements for fault rock samples were made perpendicular to the fabric as the study focuses on investigating the influence of cross-fault fluid flow. It should be noted that all deformation bands and slip-surface cataclasites studied contain host and fault rock; the measured permeability for these samples is therefore an average of host and fault. The true fault rock permeability ( $K_f$ ) values were deconvolved using the technique outlined in **Section 3.5.6**. All fault rock permeability results reported are deconvolved and the undeformed samples permeabilities are also presented for comparison.

The arithmetic mean permeability of fault samples is also reported, based on the approach provided by Manzocchi et al. (1999) who stated that the flow through heterogeneous rocks such as faults can be approximated as a function of harmonic mean of fault thickness and arithmetic-mean of fault rock permeability. The averaging of fault rock permeability basically comes from the concept that fault rock is heterogeneous, therefore the permeability varies significantly along the length of deformed zone.

### **4.3.1 Central North Sea reservoir samples**

The permeability measurements were made on host and fault of ten samples from group A and eleven from group B. The experimental results for all tests conducted are summarized in **Tables 4.4 and 4.5**.

#### **4.3.1.1 Host sandstones**

The group A host rock samples have the highest gas permeability values in the range from 49mD to 1820mD. The brine permeability ranges from 28mD to 1230mD. The average permeability to gas and 30% NaCl brine are 430mD and 280mD

respectively. The permeability to 3.5% NaCl brine ranged from 20mD to 850mD, with arithmetic mean of 178mD. The permeability to distilled water is the lowest ranging from 10mD to 397mD with an average of 97mD. The average ratio of 30% NaCl brine permeability to distilled water is a factor of two; which is lower than the deformed samples.

The peak pore diameter obtained using Hg-injection porosimetry that ranges from 8.7 $\mu$ m to 27 $\mu$ m and the threshold pressure ranges from 8psi to maximum of 25psi with an arithmetic-mean of 12psi (**Table 4.3**), for each individual sample's mercury curves refer to **Appendix A**.

The group B host sandstone samples permeability results are reported in Table 4.5; the gas permeability for the undeformed sandstones range from 29mD to 0.62mD with arithmetic-mean of 13mD. The brine permeability has values from 0.37mD to 22mD with an arithmetic average of 6mD. The permeability to distilled water is the lowest ranging from 0.19mD to 8.3mD with an average of 2.9mD. The gas permeability measurement was repeated on these samples after the distilled water permeability; it was same in both cases.

The peak pore diameter obtained from Hg-injection ranges from 2.2 $\mu$ m to 12.5 $\mu$ m and the threshold pressure ranges from 15psi to a maximum of 150 psi, with an arithmetic mean of 41 psi (**Table 4.3**).

#### **4.3.1.2 Fault rock**

The fault rock samples of group A have gas permeabilities that range from 0.28mD to 6.4mD with an arithmetic-mean of 1.6mD. The permeability to 30% NaCl brine was slightly lower than the permeability to gas, with an average value of 1.1mD, ranging from 0.054mD to 4.4mD. The permeability of these samples to 3.5% NaCl ranges from 0.005mD to 2.5mD with an arithmetic mean of 0.5mD. The distilled water permeability was the lowest, ranging from 0.003mD to 1.3mD, with an average of 0.26mD. This was around 10 fold lower than the gas permeability.

In addition to permeability measurements, the slippage factor was also calculated, the calculated *b*-factor values ranges from 3 to 18 psi. These calculations were

performed by fitting straight line on Klinkenberg tests. The results for each sample calculated are reported in **Table 4.4**

The peak pore size measured using Hg injection porosimetry ranges from 1.5 $\mu$ m to 21 $\mu$ m with arithmetic mean of 8.8 $\mu$ m. The threshold pressure ranges from 15psi to 300psi, with arithmetic mean of 63psi (**Table 4.4**). Only CP2D samples resulted in a higher threshold pressure of 300psi, whereas the other samples are in between 15 and 100psi. The highest threshold pressure could be the result of mica and chlorite observed from microstructural analysis and quantitative XRD.

The group B fault samples exhibited the lowest permeabilities; results are reported in **Table 4.4** together with the host samples. The gas permeability ranges from 0.002mD to 0.79mD with arithmetic mean of 0.12mD. The brine permeability has values from 0.001mD to 0.094mD with an arithmetic average of 0.016mD. The distilled water permeability on average is 0.007mD; it ranges from 0.00012mD to 0.057mD. The repeat of gas permeability was also performed, which on average was slightly higher than the initial value. The repeat of gas permeability ranges from 0.0014mD to 1.3mD with an average of 0.19mD. The slippage factor was also calculated, the calculated *b*-factor values ranges from 32 to 273psi and are reported in **Table 4.5**.

Group B fault samples have peak pore size ranges of 0.27 $\mu$ m to 8.7 $\mu$ m with arithmetic mean of 3.3 $\mu$ m, as determined by Hg-injection porosimetry. The threshold pressure ranges from 20 psi to 500psi with an arithmetic mean of 111psi (**Table 4.5**). The highest threshold pressure could be the result of mica and chlorite observed from microstructural analysis and Quantitative XRD.

Table 4.4 Summary of the permeability results (gas, brine and distilled water measured at ambient stress) and mercury threshold pressure from central North Sea reservoir cores. The fault rock was recognized as cataclastic fault.

Sample Name	Sample Length (cm)	Fault thickness (cm)	Central North Sea reservoir permeability (mD)-Group-A								Mercury -air threshold pressure (psi)		b-factor (psi)
			Gas		Brine ( NaCl 30%)		Brine (NaCl 3.5%)		DI water		Host	Fault	
			Host	Fault	Host	Fault	Host	Fault	Host	Fault	Host	Fault	Fault
CP1A	3.0	0.10	123	1.88	83	1.35	23	0.72	14	0.30	10	40	4
CP1B	2.4	0.40	110	1.59	102	1.35	90	0.74	29	0.27	25	40	3
CP1C	2.6	0.55	231	1.19	154	0.75	56	0.19	20	0.14	20	40	12
CP1D	2.1	0.30	243	6.42	142	4.38	68	2.5	41	1.34	15	15	10
CP2A	4.3	0.95	91	0.42	43	0.26	29	0.04	25	0.02	8	15	18
CP2B	3.4	0.49	290	2.78	91	2.30	86	0.82	71	0.38	10	20	3
CP2C	3.9	0.63	1823	0.54	1230	0.33	522	0.27	346	0.095	10	40	13
CP2D	2.6	0.85	1108	0.69	878	0.19	850	0.11	397	0.039	8	300	12
CP2E	2.2	0.20	171	0.28	57	0.054	35	0.005	20	0.003	10	20	18
CP2F	4.3	0.50	49.6	0.54	28	0.21	20	0.05	10	0.011	10	100	6
<b>Arithmetic-mean</b>		<b>0.5</b>	<b>424</b>	<b>1.6</b>	<b>281</b>	<b>1.1</b>	<b>178</b>	<b>0.5</b>	<b>97.2</b>	<b>0.26</b>	<b>12.6</b>	<b>63.0</b>	

Table 4.5 Summary of the permeability results (gas, brine and distilled water measured at ambient stress) and mercury threshold pressure from central North Sea reservoir cores.

Sample ID	Length (cm)	Fault thickness (cm)	Central North Sea Permeability (mD)-Group-B								Hg-air threshold pressure		b-factor (psi)
			Gas		Brine 20%		DI Water		Gas		Host	Fault	
			Host	Fault	Host	Fault	Host	Fault	Host	Fault	Host	Fault	
5AF1	2.2	0.5	3.6	0.004	1.0	0.045	0.5	0.0005	3.6	0.011	20	500	273
5BF1	2.5	0.8	0.6	0.056	0.4	0.004	0.2	0.0024	0.6	0.08	150	300	141
5EF1	2.2	0.3	29.2	0.20	16.7	0.023	8.3	0.016	29.2	0.41	15	40	153
5FF1	2.2	0.2	37.0	0.79	22.0	0.094	11.0	0.057	37.0	1.34	15	40	32
7AF1	2.3	0.5	16.0	0.09	9.0	0.0029	4.5	0.0011	16.0	0.04	8	20	69
7BF1	2.0	0.3	15.0	0.002	5.4	0.0017	2.2	0.0002	15.0	0.0014	20	45	137
7CF1	2.5	0.3	3.8	0.07	0.8	0.0015	0.4	0.0003	3.8	0.03	15	145	45
7EF1	2.1	0.2	2.5	0.07	0.6	0.0010	0.3	0.00012	2.5	0.10	40	40	82
7FF1	2.3	0.4	4.8	0.03	0.9	0.0021	0.5	0.0015	4.8	0.03	15	40	67
3AF1	2.1	0.7	22.0	0.02	7.7	0.0024	3.7	0.0014	22.0	0.02	75	25	138
10/3A	2.8	0.9	4.4	0.04	1.3	0.0014	0.7	0.0012	19.0	0.02	75	25	68
<b>Arithmetic mean</b>			<b>13</b>	<b>0.12</b>	<b>6.0</b>	<b>0.016</b>	<b>2.9</b>	<b>0.007</b>	<b>14</b>	<b>0.19</b>	<b>41</b>	<b>111</b>	

### 4.3.2 Southern North Sea reservoir samples

The permeability measurements were made on 6 samples of host and fault rock; the details of all experimental results are summarized in **Table 4.6**.

#### 4.3.2.1 Host sandstone

The permeability to gas ranges from 0.054mD to 7.8mD with an arithmetic-mean of 3.1mD. The brine permeability ranges from 0.0052mD to 1.1mD with an arithmetic mean of 0.42mD. The brine permeability on average was 7 factors lower than gas permeability. The permeability to distilled water was around 10 fold lower than gas, with an average value of 0.31mD; its values range from 0.0039mD to 1.02mD.

The peak pore size measured using Hg injection porosimetry ranges from 3.1 $\mu$ m to 14.5 $\mu$ m with arithmetic-mean of 4.8 $\mu$ m. The threshold pressure ranges from 15psi to 150psi, with arithmetic mean of 87psi (**Table 4.6**).

#### 4.3.2.2 Fault rock

The gas permeabilities to these fault rocks vary from 0.00071mD to 0.075mD with an arithmetic average of 0.026mD. The brine permeability ranges from 0.0002mD to 0.031mD with arithmetic mean of 0.0087mD, which on average was about three factors lower than gas permeability. The permeability to demineralized water was the lowest, ranging from 0.011mD to 0.00011mD with an arithmetic average of 0.0039mD, which on average was around an order magnitude lower than the gas permeability. Overall there was a large difference in permeability found within these samples, which reveals that these were highly heterogonous.

Furthermore, the b-factor values were also calculated from these samples permeability tests and are reported in **Table 4.6**. These were estimated from Klinkenberg tests where the straight line gave correlation coefficient of 0.95 or more for four data points.

The peak pore size measured using Hg injection porosimetry ranges from 0.7 $\mu$ m to 10.9 $\mu$ m with arithmetic mean of 4.8 $\mu$ m. The threshold pressure ranges from 40psi to 300psi with arithmetic mean of 155psi (**Table 4.6**).

Table 4.6 Summary of the rectilinear blocks permeability results from Southern North Sea reservoirs samples (gas, brine and distilled water permeability measured at ambient stress).

Sample ID	Sample Length (cm)	Fault thickness (cm)	Permeability (mD)						Hg-threshold pressure(psi)		b-factor (psi)
			Gas		Brine (NaCl 20%)		DI water		Host	Fault	
			K <sub>g</sub>		K <sub>b</sub>		K <sub>d</sub>				
Host	Fault	Host	Fault	Host	Fault	Host	Fault	Fault			
Win1A	3.5	0.1	7.2	0.028	0.90	0.0058	0.53	0.005	68	97	59
Win2A	3.4	0.1	7.8	0.075	1.1	0.031	1.02	0.011	68	97	25
Win3A	3.1	0.1	3.4	0.053	0.47	0.015	0.29	0.006	68	97	14
Win1B	2.7	0.1	0.03	0.001	0.024	0.0004	0.0096	0.0002	150	300	94
Win2B	2.4	0.1	0.09	0.001	0.009	0.0002	0.0095	0.0001	150	300	82
Win1C	2.6	0.3	0.05	0.002	0.005	0.0002	0.0039	0.0002	15	40	48
<b>K_arithmetic mean</b>			<b>3.1</b>	<b>0.027</b>	<b>0.42</b>	<b>0.009</b>	<b>0.31</b>	<b>0.004</b>	<b>87</b>	<b>155</b>	<b>54</b>

### 4.3.3 90 Fathom Northumberland, UK samples

The permeability measurements have been made from main slip surface and single deformation band of the 90 Fathom Fault, Northumberland, UK.

#### 4.3.3.1 Fault rock

The results show that slip-surface cataclasite fault rock samples have a lower permeability than the single deformation band. The gas permeability to slip-surface cataclasites samples ranges between 0.035mD and 0.0042mD with an arithmetic average of 0.018mD (Table 4.7). The brine permeability ranges from 0.0063mD to 0.0032mD with arithmetic mean of 0.004mD. The brine permeability was 4 factors lower than gas permeability. The permeability to distilled water was the lowest with arithmetic mean of 0.0028mD. The distilled water permeability of fault samples was around 5 fold lower than the gas permeability.

The single deformation band has a gas permeability ranging between 2mD and 13mD, with arithmetic mean of 8.2mD. The brine permeability ranges from 3.8mD to 7mD with arithmetic-mean of 4.5mD. The distilled water permeability was the lowest, ranging from 1.8mD to 0.20mD, with arithmetic mean of 0.66mD. The *b*-factor values were obtained from permeability measurements and are reported in Table 4.7 together with other petrophysical properties.

The slip-surface cataclasite showed the largest threshold pressure ranging from 650 to 5000psi with arithmetic mean of 6164psi. The single deformed band samples have threshold pressures of 15 to 75psi and peak pore diameters is of 0.12µm to 8.50µm.

### 4.3.3.2 Host sandstones

The permeability to gas ranges from 0.2mD to 175mD, with mean value of 55mD. The brine permeability ranges from 0.01mD to 77mD with an arithmetic average is 29mD, which is around 10 fold lower than gas permeability. The distilled water permeability is the lowest permeability, ranging from 0.015mD to 19mD with arithmetic-mean of 7mD.

Hg injection results suggest the host sandstones have pore diameters of 10 $\mu$ m pores and the threshold pressure ranges from 8 to 15psi with an arithmetic mean of 11 psi (Table 4.7).

Table 4.7 Basic properties, gas, brine and distilled water permeability, b-factor and mercury-air threshold pressures from 90 Fathom fault and host rock samples. a reflects the sealed/unsealed samples for mercury injection.

<b>(a) Slip-surface cataclasite</b>										
Sample ID	Sample Length (cm)	Fault thickness (cm)	90 Fathom fault permeability (mD)						Hg-threshold pressure (psi)	b-factor (psi)
			Gas		Brine (NaCl 20%)		DI water			
			Host	Fault	Host	Fault	Host	Fault	Fault	Fault
90FM1 F	2.6	1.2	0.3	0.012	0.05	0.003	0.03	0.002	1000.0	68
90FM4 F	2.9	1.3	0.7	0.017	0.05	0.004	0.02	0.003	3000 / 650a	48
90FM6 F	3.2	1.5	0.2	0.004	0.02	0.003	0.01	0.002	13000.0	63
90FM7 F	3.3	2.0	1.0	0.031	0.10	0.004	0.06	0.003	3250.0	94
90FM9 F	3.1	1.5	0.3	0.011	0.01	0.003	0.02	0.003	5000.0	76
90FM10 F	3.1	1.2	1.2	0.035	0.13	0.006	0.09	0.003	400 / 200a	72
<b>Arithmetic mean</b>		<b>1.4</b>	<b>0.6</b>	<b>0.018</b>	<b>0.061</b>	<b>0.004</b>	<b>0.037</b>	<b>0.003</b>		
<b>(b) Single deformation band</b>										
90FZB1	2.7	0.1	99	10	71	6.2	17	0.3	20	3.8
90FZB3	3.2	0.1	99	13	71	7.1	17	0.4	40	8.6
90FZ-5	2.9	0.1	175	2	77	1.0	19	0.2	15	5.9
90FZ-2	2.1	0.1	175	7	77	3.8	19	1.8	20	8.9
<b>Arithmetic mean</b>		<b>0.1</b>	<b>136.8</b>	<b>8.2</b>	<b>73.9</b>	<b>4.5</b>	<b>17.6</b>	<b>0.7</b>	<b>24</b>	

## 4.4 Discussion

This section starts by discussing the results from fault rock permeability measurements, such as the impact of pore fluid salinity on permeability and the relation between permeability and pore size. The section then discusses the interdependence between clay content and fault rock permeability. Moreover, the section provides a comparison of permeability and clay content results with empirical models. Finally the section provides with main implications from results.

### 4.4.1 Fault rock permeability: impact of fluid chemistry

The permeability of fault rocks was measured with three different pore fluids i.e. gas, brine and distilled water to assess the sensitivity of the absolute permeability of fault rocks to the composition of the permeant. This then provides an indication to the inaccuracies that could occur in fault seal analysis studies by applying published fault permeability data (e.g. Fisher and Knipe, 2001) in which distilled water was used as a permeant. It is often believed that the Klinkenberg corrected gas permeability should be the same as that of the liquid permeability (e.g. Rushing et al., 2004; Chowdiah, 1987). However, the permeability results obtained during the current study showed that the permeability measurements made using gas gave higher values than with brine, which in turn gave higher values than when measured using distilled water permeability (**Figure 4.7** and **Figure 4.8**). The deionized water permeability was lower than the gas permeability in all samples (**Figure 4.7**). The brine permeability on average was reduced by 35% and the distilled water permeability was around an order of magnitude lower than gas. Similar differences in permeability between gas and water have also been observed by other authors (e.g. Lovelock, 1977; Sampath and Keighin, 1982; Faulkner et al., 2000; Baraka-Lokmane, 2002). To assess the differences in gas, brine and distilled water permeability are important to consider as these provides the relative control of fluid flows within fault compartmentalized reservoirs. Crawford et al. (2008) reported differences in argon gas and water permeability of artificial kaolinite-quartz mixtures as an analogue to fault gouges. The differences in gas and distilled water permeability of sandstones might be due to the physiochemical interactions between distilled water and clay mineralogy (e.g. Lever and Dawe, 1987; Byerlee, 1999). Rutter et al. (1986) demonstrated that if sandstone samples contains the clay mineral

fractions which are very fine grained if surrounded within the pores spaces their interaction with water might significantly affect the effective pore throat size consequently the permeability of the rock samples (e.g. Faulkner, 2004).

The major effects of clay minerals on permeability could be: 1) the reduction of effective pore size; 2) fine particles migrations and plugging of the pore throats that could be the potential reason of reduction in permeability; 3) clays are sensitive to distilled water when they come into contact with water starts to hydrate and swell which in turn reduces the sample permeability (e.g. Richard and Dawe, 1984). Therefore, these mechanisms of permeability reduction suggests that if clay minerals exist within the samples studied, liquid permeability would be lower than the slip corrected gas permeabilities. Clay minerals are fine grained particles could be deposited within pore surface of sandstones (Baraka-Lokmane, 2002). Probably these clays might exist simultaneously in all different forms within the same rock formation (e.g. Khilar and Fogler, 1984). Each clay mineral have tendency to affect the fault rock permeability in some form either by swelling to reduce the pore throat size, or creating a layer of bound surface water or by movement and retention of fine particles within confined pores (e.g. Khilar et al., 1990). The authors attempted to provide with some conceptual models of fine particles retention that accumulate within the confined pores such as: particles deposition on the framework grains; formation of bridging; draining of larger grain particles towards confined pore throats resulting in blockage of smaller size pore throats (e.g. McDowell-Boyer et al., 1986; Sen and Khilar, 2006).

Most of the fault rock samples studied were from phyllosilicate framework and cataclastic fault category and these on some extent were associated with the clayey sands. Therefore, it was necessary to have knowledge of the quantities of these minerals (clays) present within the rock samples, so the controls on fault rock permeability could be quantified. The relative amounts of minerals were determined by performing QXRD experiments, results showed that the samples were containing variety of clay minerals such as kaolinite, illite-smectite and chlorite (**Table 4.1 and Table 4.3**). However, among all analysed samples few samples were not containing all different types of clay minerals. The existence of clay minerals could affect the permeability in different ways, such as kaolinites are not swelling minerals, fine particles migration and entrapment could block the smaller pore throats, (e.g. Mohan

and Fogler, 1997). On the other hand smectite could act as swelling clay mineral while interacting with distilled water (Lever and Dawe, 1987). Therefore, the reduction in liquid permeability observed could be due to two processes. Firstly, the clay particles surrounded within pore throats can swell reducing the effective size of the pore throats (e.g. Khilar and Fogler, 1984; Sampath and Keighin, 1982; Moore et al., 1982; Lever and Dawe, 1987). Secondly, the reduction in liquid permeability could be due to the detachment of authigenic clay minerals fine particles from pore walls and migration and entrapment of these fine particles, (e.g. Khilar et al., 1983; Baraka-Lokmane, 2002). Mesri and Olson (1971) reported higher permeability values for pure clays with non-reactive fluids than reactive fluids, which also indicated the importance of clay-water interactions particularly for low permeability formations.

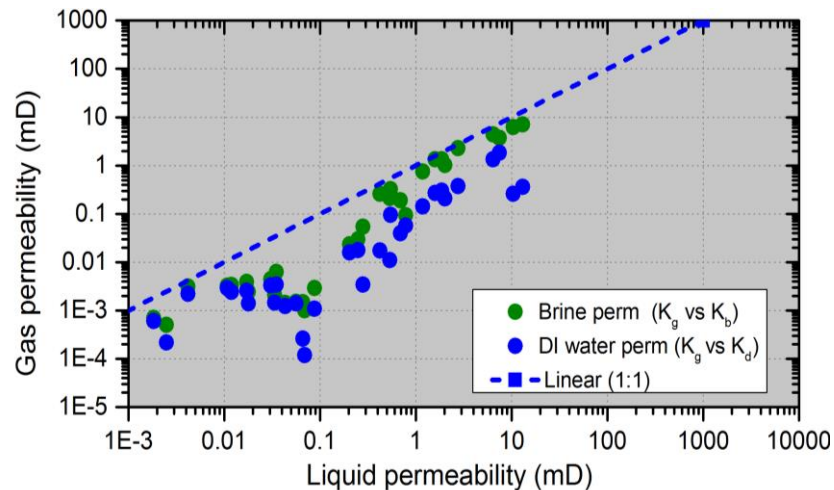


Figure 4.7 Cross plot showing the relationship between gas, brine and distilled water permeability of fault rock (log-log plot). Note that in the figure legend  $K_g$ ,  $K_b$ , and  $K_d$  refer to gas, brine and distilled water permeabilities respectively.

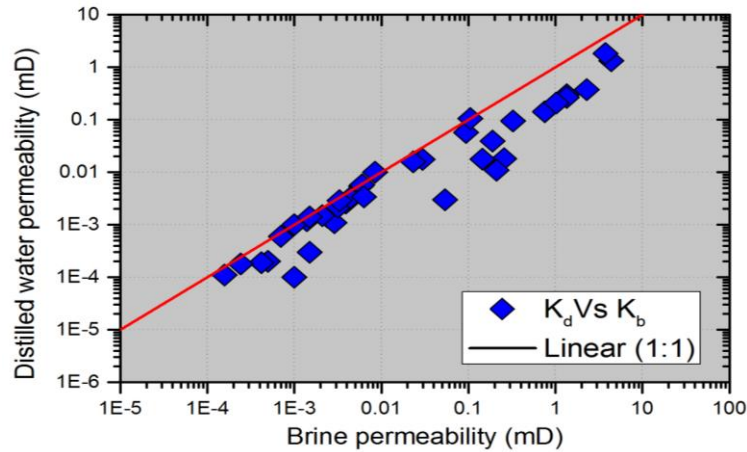


Figure 4.8 Cross plot of the distilled water permeability against brine permeability for fault rocks (log-log plot)

Furthermore, the permeability ratio and clay content plotted in **Figure 4.9** appears to be scattered. The **Figure 4.9** demonstrates that there is no relation between the permeability contrast (i.e. the ratio of gas to brine permeability, and brine to distilled permeability) and the clay content. Likewise the clay content and gas to distilled water permeability ratio did not show any trend. Although, the results plotted are in significant scatter. The scatter of permeability with clay content reflects the samples heterogeneity and another the possibility could be percentages of clay minerals varies from sample to sample. Few of the samples were not containing all different types of clay minerals and in other samples there were not all clay minerals.

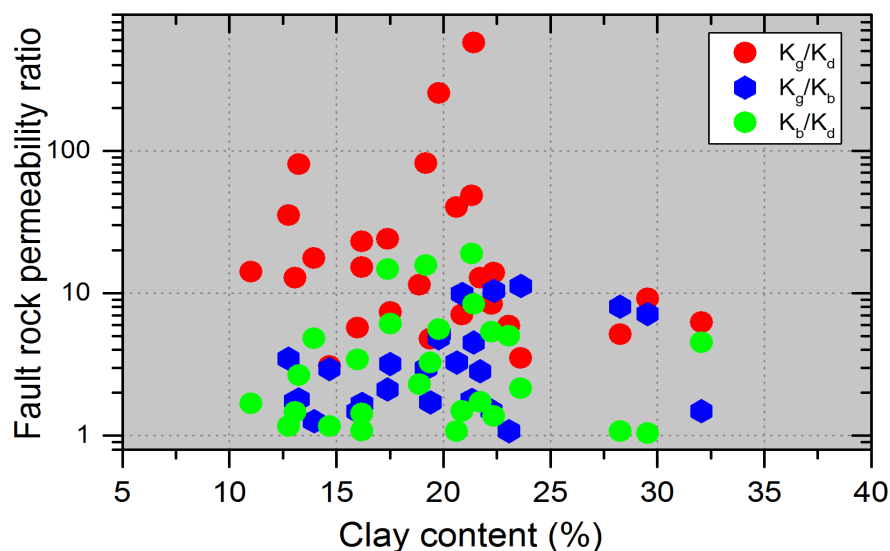


Figure 4.9 The relationship of gas permeability to brine permeability ratio versus clay content of the host sediments (semi-log plot). In the figure legend  $K_g$ ,  $K_b$ , and  $K_d$  refer to gas, brine and distilled water permeability respectively.

In **Figure 4.9** the permeability ratio is plotted against total clay content; which is the sum of all different clay mineral types. Observing the scatter in correlating permeability with the total amount of clay content, the permeability ratio plotted against each clay mineral separately (**Figure 4.11**) that also resulted in significant scatter. There is no relation in between fault rock permeability with any of the single clay mineral. The reason for this is not clear but this could be the result of clay minerals presence in variable quantities such as, few samples were not containing all different types of clay minerals while others were containing.

The clay minerals occur in variety of different forms within the rock pore spaces; such as grain coating and pore lining clays (e.g. Neasham, 1977). For example, kaolinite occurs as stacks of ‘booklets’ or as loose plates (Wilson and Pittman, 1977). SEM analysis (**Figure 4.10**) confirms the presence of kaolinite clay mineral that is the dominant clay mineral in sandstone. The Kaolinite has a tendency to detach from pore surface and migrate with fluid injected, possibly these fine particles could be trapped within the smaller size pore throats (e.g. Lever and Dawe, 1987; Khilar et al., 1990; Revil and Glover, 1998; Rosenbrand et al., 2013). The effect of fine particles movement on permeability has been investigated by several authors by conducting the filtration experiments (e.g. McDowell-Boyer et al., 1986; Sen and Khilar, 2006; Yuan and Shapiro, 2011). The fluid injected for permeability measurement, the fine clay minerals such as kaolinite and other fine particles could possibly be retained within the confined pore throats because of low permeable nature of samples. This might happen when particles that have mobilized along with pore fluid towards the pore constrictions and if pores have a smaller size than mobilized particles size; these will be then retained at the confined pore throats resulting in blocking of the pore throats. In contrast, if the size of pores is large enough and pressure gradient is higher than fine particles would be transported and possibly enhance the permeability (e.g. Candela et al., 2014).

Recently, Rosenbrand et al. (2013) has reported that fine particles that migrate through samples could be collected together with effluents produced during laboratory experiments (e.g.). Similarly, during present study, effluents were also collected and filtered through the 0.2 $\mu$ m filter paper however there was no indication of any of the fine particles production. This could be used as evidence that fines migration is not important mechanism in these samples to reduce permeability.

However, the clay swelling and fine particles entrapment within the confined pore throats could be the possible reason of reduction in liquid permeability of the fault rock samples studied (e.g. Lever and Dawe, 1987).

Apart from kaolinite clay minerals, the illite-smectite clay minerals were also observed from QXRD analysis. The illite-smectite appears like a thin hair, which usually occurs in between grain boundaries these clay minerals, could reduce the pore connectivity (e.g. Mondol et al. 2008; Bjorlykke, 2010). During fluid flow experiments, if low concentrated brines or distilled water as a pore fluid is injected for permeability measurement, the illite-smectite clay minerals possibly swell and might result in reduction of pore throat size because that have swelling tendency (e.g. Lever and Dawe, 1987) this could be the possible mechanism of permeability reduction especially in low permeability fine grained rocks. On the other hand, those samples which they were not containing clay minerals having higher absolute permeability would not be affected if their permeability measured using distilled water as a pore fluid.

The results of fault rock permeability examined showed that the clay minerals are not the only reason to show an obvious relationship. Although, these provides possible reasons of reduction of fault rock permeability due to their interaction with reactive pore fluids. The permeability reduction mechanisms discussed above might not be the exclusive due to the different fault rock types and the range of the existence of different minerals and mineral particle sizes.

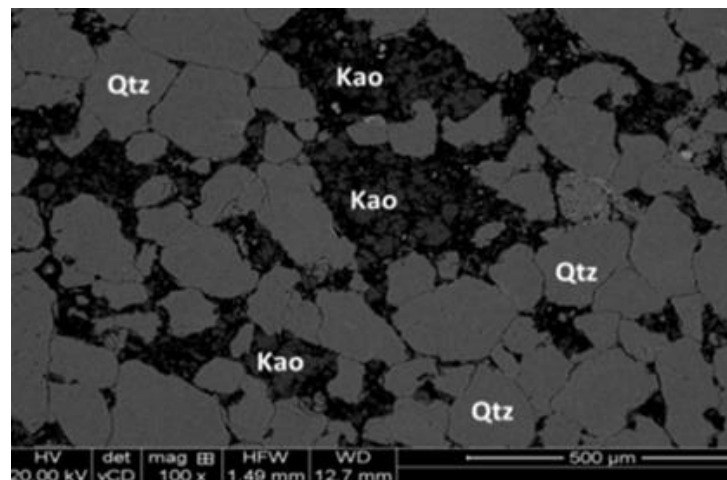


*Figure 4.10 Photomicrograph of a typical SEM image from one of the Sothern North Sea reservoir core sample, showing the presence of kaolin and backscattered image of one of the*

*central North Sea core sample shows the presence of illite clay mineral within the pore spaces.*

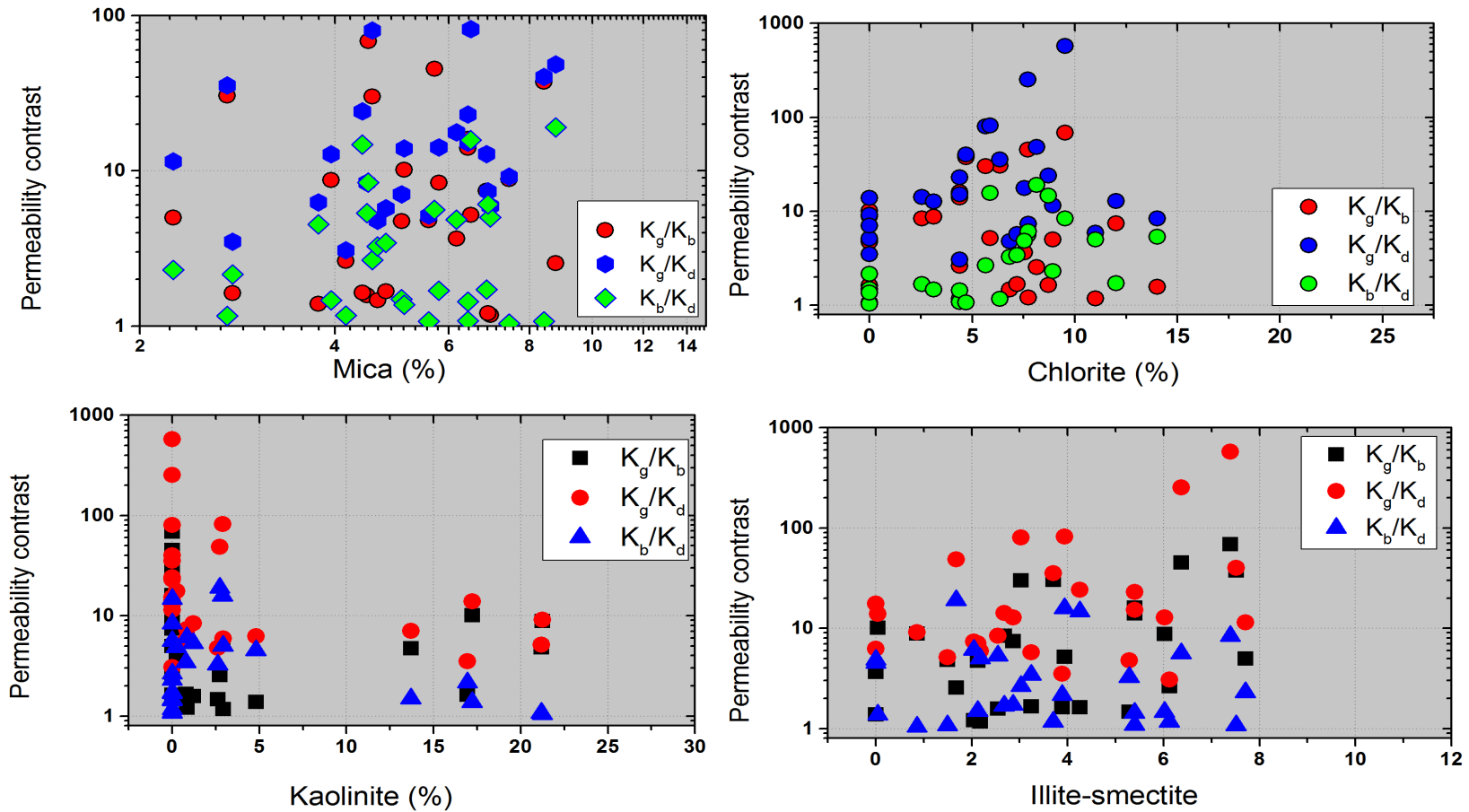


Figure 4.11 Plots showing effects of clay minerals (Mica, Kaolinite, Illite-smectite and chlorite) on fault rock gas, brine and distilled water permeability ratio. In this figure  $K_g$ ,  $K_b$ , and  $K_d$  refer to gas, brine and distilled water permeability of fault rock, respectively.

Apart from rock surface interactions with fluids, various investigations have suggested that the permeability of fine grained rocks could be controlled by more important factors such as pore geometry, pore size distribution and clay mineral distribution (Dewhurst et al., 1998). The pore throat size is often measured by mercury porosimetry. It is also theoretically possible to estimate pore size from the results of gas permeability experiments following Klinkenberg procedure. In particular, gas slippage becomes an increasingly important flow mechanism when the mean free path of a gas molecule approaches the pore throat radius (e.g. Loeb, 1927) (equation 4.1).

$$\lambda = \frac{\mu}{P} \sqrt{\frac{\pi R_g T}{2M}} \quad (4.1)$$

where  $\lambda$  is the mean free path of the gas at mean pressure,  $\mu$  is the gas viscosity,  $P$  is the mean pore pressure,  $R_g$  is the gas constant,  $T$  is temperature and  $M$  is the molar mass of the gas. The pore radius can be estimated from the  $b$ -value obtained during steady-state gas permeability tests using the formula,

$$b = \frac{4c\lambda P}{r_{eff}} \quad (4.2)$$

$$r_{eff} = 4c\lambda P / b_{slip} \quad (4.3)$$

where  $b$  is a gas slippage factor,  $c$  is constant and is equal to one.  $r_{eff}$  is the effective pore radius.

The slippage radius obtained from gas slip parameters using Equation (4.3) and Hg-radius derived from mercury porosimetry are plotted in **Figure 4.12** resulted in a scatter. The slippage derived radius was around an order of magnitude lower than mercury radius. Bloomfield and Williams (1995) measured permeability on number of tight sandstone sample of North sea reservoirs also reported one to two orders of magnitude lower slippage radius than mercury porosimetry derived pore radius. The reason for the difference in between two pore radius could be the presence of clay minerals within the pore space. Particularly the pore structure from mercury injection data could be controlled by various other factors such as the presence of deformed clay minerals. The rock pore structure could be altered by injection of mercury due to presence of delicate clay minerals, which in fact does not represent the true value

of pore size. In contrast, the gas injected through the sample during steady state experiments follow those pathways which only contribute gas flow. Therefore, the pore throats during gas permeability measurement could not be altered; rather mercury injection could be the possibility to alter pore size and result in higher values than slip radius.

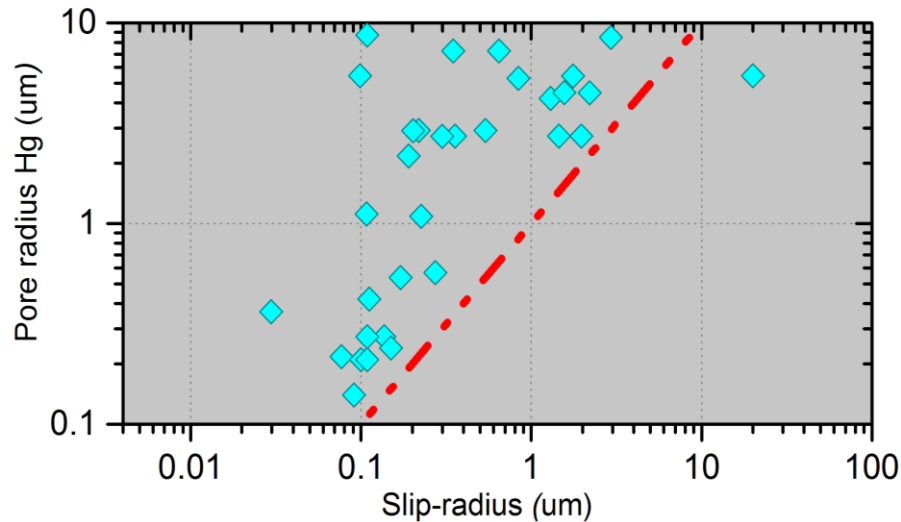


Figure 4.12 Plot showing the relationship between the pore radius derived from Hg-injection data and from gas slip-radius followed Klinkenberg procedures (log-log plot)

Furthermore, the permeability data plotted against mercury derived pore radius (**Figure 4.13a**) also resulted in a large scatter. The permeability of fine grained mudstone has been studied by Dewhurst et al. (1998, 1999). They proposed that scatter in permeability data with pore radius could be the result of variations in pore throat size due to sedimentary heterogeneity. Other authors have also argued that the scatter in permeability and pore throat radius could be experimental error (e.g. Heid et al., 1951; McPhee and Arthur, 1999). Recently, Armitage et al. (2011) measured the permeabilities on caprocks from the Krechba field, Algeria. The permeability results and pore radius from mercury porosimetry reported by Armitage et al. (2011) plotted together with the present study also resulted in scatter (**Figure 4.13a**). It should be noted that the permeability results from Armitage et al. (2011) appear lower than those of the present study shown in **Figure 4.13a**, as these were measured at effective stress of 60Mpa ~8000psi. Although the present study measurements are made at ambient stress condition. The findings of the current study based on relation of permeability and mercury derived pore radius are consistent with those previous studies reported by Armitage et al. (2011). They all reported that there is a scatter in

relating permeability and mercury porosimetry radius. Given the scatter of permeability data relating with mercury injection derived radius, the present study attempted to relate the permeability with gas slippage derived pore radius; apparently this resulted in a reasonable relation with slippage radius (**Figure 4.13b**). Therefore, this suggests that the slippage radius could be better to relate permeability than mercury porosimetry radius, because this provides the effective pore size of a rock. In other words, this gives the information of those pores which are connected to contribute gas flow through circular pores.

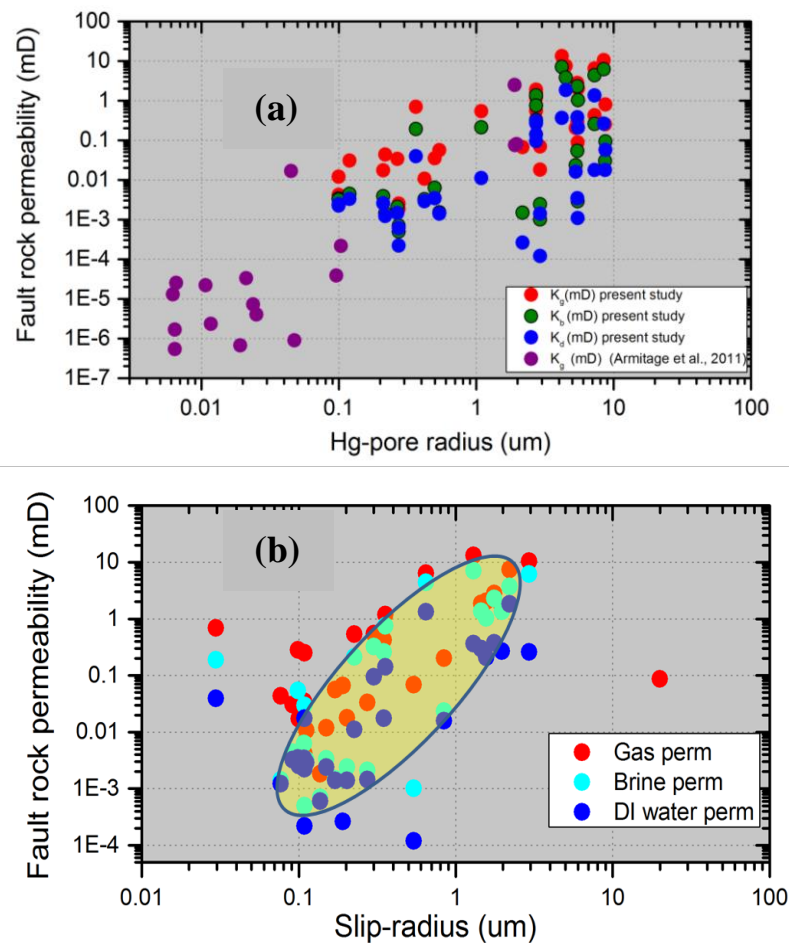


Figure 4.13 Plots showing the relationship between fault rock gas, brine and distilled water permeability with Hg-pore throat radius (upper) and the slip-radius (lower). Note that the data from Armitage et al. (2011) was measured at 60MPa effective stress on cap rock samples. (log-log plot)

The Klinkenberg corrected gas permeability is often higher in sandstone samples than brine or water permeabilities (e.g. Heid et al., 1950; Luffel et al., 1993; Solymar et al. 2003; Pinder and Celia, 2006) which suggest that different factors could affect this difference. The key parameter is the layer of immobile fluid on the solid-fluid

interface (e.g. Heid et al., 1950; Jones and Owens, 1980; Rutter, 1983; Faulkner and Rutter, 2000, 2003; Andreassen and Fabricius, 2010) which reduces the pore throat size available to liquid to flow (**Figure 4.14**). In samples which are very fine grained containing clay minerals are surrounded by the layer of clay bound water that affects the permeability of fault rock samples. That clay bound water itself could not be able to move when fluid is flowing through the rock hence this bounded water also reduces the pore throat size by coating the mineral surfaces (**Figure 4.14**). As the pore size reduces consequently the reduction in liquid permeability of samples will occur. Immobile bound water holds significance in the permeability of fine grained rocks such as fault rocks resulting in a thin layer of brines coating on pore surfaces. However, this assumption would not hold significance in high permeability sandstones (Grattoni pers. Comm.). The effect of clay bound water on permeability could be estimated by considering the reduction in effective size of the pore. The pore size could be obtained from gas slip parameter or from mercury injection data, although the reduction consideration could be done based on the information of thickness of immobile water layer. Several authors have attempted to estimate the size of the thickness of immobile water layer, Grim (1953) suggested that the layer thickness could range from 0.8nm to 4nm. It should be noted that the thickness of this layer increases as brine salinity decreases (Solymar et al. 2003). Behnsen and Faulkner (2011) found that the adsorption of water on clays might result in exaggeration of clay minerals within the pores of sandstones and this might cause the intergranular pore spaces reduction for liquid flow. Authors also argued that the layer of immobile water could also exist on the surfaces of other minerals such as quartz (e.g. Esther, 2014). The stern layer thickness is also considered as bound water layer thickness, which varies from 0.5nm to 2.5nm based on the work of Israelachvili and Adams (1978).

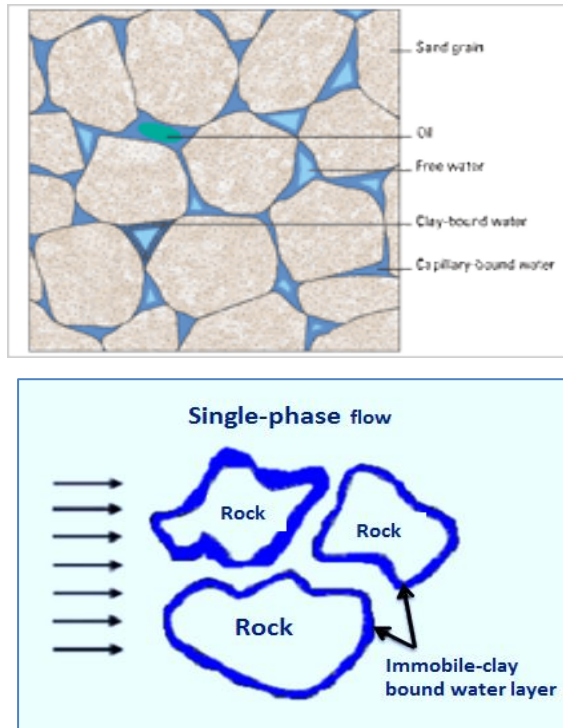


Figure 4.14 Sketch of an example of adsorbed water-layer on the solid grain surfaces (taken from schlumberger course notes and Fekete, 2014).

Based on the observations of impact of bound water layer and its impact on rock permeability, an attempt was made to estimate the difference in permeability due to the immobile fluid layer thickness on fault rock samples. This was performed by considering two scenarios of pores throats size the first was considered with clay bound layer thickness and second was without clay bound layer thickness. For this reason, to assess the impact due to immobile fluid layer on samples permeability, an assumption was made to consider an effective pore throat radius derived from Klinkenberg parameters. The calculations were performed by adding the thickness value that caused due to immobile layer thickness that resulted in reduction of pore throat size. The calculations were based on the principle of Poiseuille's equation that gives the flow through bundle of cylindrical pores. Assuming that there is no-slip flow at the boundary of the pore wall, flow through cylindrical tube is laminar flow that would lead to following Hagen-Poiseuille equation:

$$q = Q/A = \frac{n\pi r_p^4}{8} \times \frac{1}{\mu} \Delta p \quad (4.4)$$

Where,  $q$  is the flow rate,  $n$  is the number of capillaries  $r_p$  is the pore size and  $\mu$  is the viscosity of sample,  $\Delta p$  is the pressure drop through capillary. If sample porosity is the volume of the cylindrical capillaries normalised by bulk volume  $V_b$ ,

$$\phi = \frac{n\pi r_p^2}{v_b} = n\pi r_p^2 \quad (4.5)$$

The permeability in terms of the size of the pore throats and the porosity can be expressed by combining above equations,

$$k = \frac{1}{8} r_p^2 \phi \quad (4.6)$$

The flow through thin quartz capillaries indicates a bound water layer thickness of 0.40nm to 80nm (e.g. Newman, 1987; Solymar et al., 2003). The value of bound-water thickness of 80nm was assumed for permeability estimation using Poiseuille's equation during this study. The permeability calculated with layer of bound water resulted in a difference of about 50%, compared to the permeability calculated without layer of bound water.

The permeability ratio of gas to brine and gas to distilled water was also plotted with pore radius derived from gas slippage parameters and with mercury injection derived pore radius to see the whether these results in a relation but the data resulted into scatter (**Figure 4.16 and 4.17**). This might be the result of differences in gas and liquid permeabilities due to aforementioned mechanisms such that there was not unique mineral composition of samples. In some samples the relative proportions of higher clay minerals existing and in other it was not found.

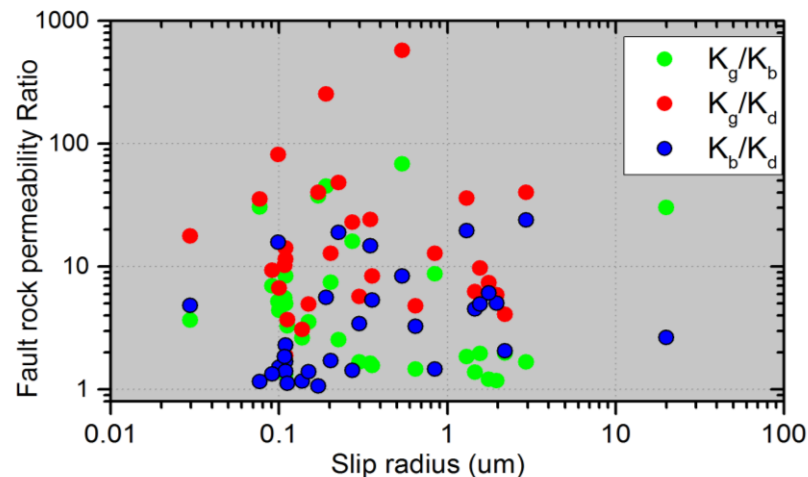


Figure 4.15 Plot is showing the fault rock permeability ratio of gas to brine and water permeability versus the slip-radius.

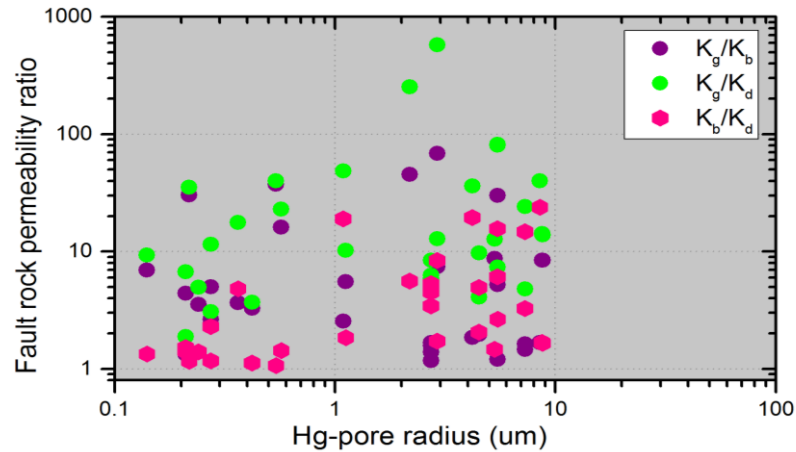


Figure 4.16 The plot of fault rock permeability ratio of gas permeability to brine and distilled water permeability against Hg-pore radius (log-log plot).

Experimental errors could be the cause of discrepancies in between gas and liquid permeability. Moreover, the presence of trapped gas during liquid permeability experiments possibly reduces the liquid permeability (e.g. Faulkner and Rutter, 2000). Although this should not be the case with the samples studied during present study, as before running liquid permeability experiments all samples were pressurized at 1500psi, the gas becomes dissolved into water at such a high pressure.

The discussion presented above indicates that the differences in gas and liquid permeability observed during laboratory experiments could possibly be explained by the interaction of water as a pore fluid with clay minerals (e.g. Faulkner and Rutter, 2000). The water adsorbed by the clay minerals surfaces possibly reduces the pore throat size due to interaction with swelling clays, hence reduces the permeability. Furthermore, it was thought that the differences in gas and liquid permeability could be due to layer of immobile fluid on mineral surfaces due to fluid mineral interaction. It is possible that permeability of fault rock is controlled by several factors including fines migration, the presence of micro-cracks and the complex interaction between these factors means that there is no simple way to predict relative controls to gas and liquid permeability. The differences and controls related to fault rock permeability discussed above might not be exclusive due to other reasons, as there are different fault rock types such as those formed within the clay-rich sediment sequences and their range of the minerals composition and their sensitivity to pore fluid might be different than cataclastic and phyllosilicates-

framework faults. The distributions of clay minerals within the pore spaces and the range of pore throat sizes might be different and the permeability could be different within different fault rock types. Therefore, these results of fault rock permeability reported cannot be directly generalized to all types of faults in different fields.

#### **4.4.2 Impact of clay content on fault rock permeability**

The results from fault rock permeability and clay content are plotted in **Figure 4.17**; these indicate that there is a large scatter in the permeability and clay content. The scatter between these two properties could be the fault rock heterogeneity and this has resulted into a poor relation between permeability and clay content. One reason of scatter could be the clays and sand grains are not well mixed at the time of faulting, the fractions of clays and sands could be in random proportions within the rocks. Faulting causes the crushing and reduction of grain particle sizes as a result of cataclasis which has been observed in most of the present study samples, these processes resulted in permeability reduction by several orders of magnitude which is lower than its associated host rocks (e.g. Fisher and Knipe, 1998). However, the most common feature found within the fault rock sequences is the phyllosilicates, hence these are main causes of reduction of fault rock permeability (Childs et al. 2002). Therefore, the differences in permeability of fault formed within different lithologies of fine grained clays sequences could be several orders of magnitude lower than the differences in permeability of fault rock in coarse sediments (e.g. Childs et al., 2002). The effect of phyllosilicates and clay smearing into faults are significant and these have a large impact in reducing the fault rock permeability than compared to other mechanism such as (i.e. cataclasis, porosity collapse (e.g. Fisher and Knipe, 2001). Although, these mechanisms provides the evidence about the causes of reduction of fault rock permeability, however it was attempted to find a link in between fault rock permeability and clay fractions but no relationship exist. Similarly, the scatter in permeability and clay content was also reported by Fisher and Knipe (2001). They argued that the poor relation in clay content and fault rock permeability could be the variations in diagenesis between different sandstones. Furthermore they reported that fault rocks formed in impure sandstones, whose clay content ranges between ~15-25%, could be affected by quartz dissolution and those having >25% clays could be more affected by mechanical compaction.

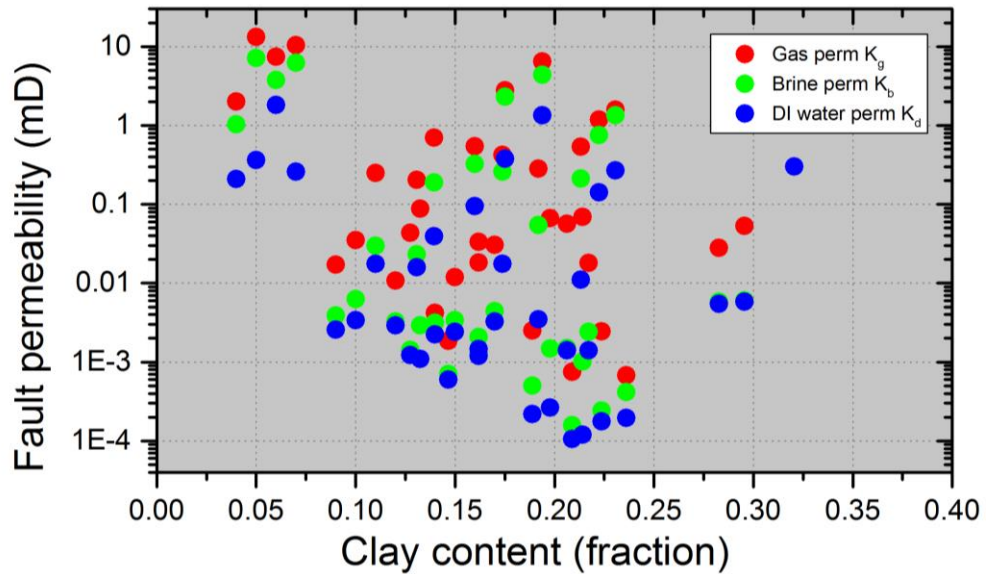


Figure 4.17 Plot of the fault rock permeability of gas, brine and distilled water versus clay content of the host sediment (semi-log plot).

In addition, to relate fault rock permeability with total clay content, an attempt have also been made to relate the permeability to each clay mineral separately, to see if there is any relationship exists between these minerals. Fault rock gas, brine and distilled water permeability were plotted against each clay mineral; however this also resulted in a poor relationship with each clay mineral (**Figure 4.18**). Overall, no correlation was found between permeability and any of the clay mineral. This could be due to the few samples were containing all different clay minerals and others were not, another reason could be the microfractures due to stress release resulted in higher permeability. The lack of correlation probably reflects the fact that each property is controlled by combination of different microstructural elements, diagenesis and burial depths. These results show that it is unsafe to correlate fault rock permeability with only clay fractions. There are several other factors which might affect the permeability of fault rocks such as the burial depths and clay minerals and their distributions within the pore spaces (e.g. Walsh et al., 2008). The fault rock permeability could be controlled by grain size and sorting (e.g. Morrow et al. 1984). The porosity and permeability of sand-clay mixtures (i.e. fault gouge) are often controlled by far more other factors than simply the clay content (e.g. Revil and Cathles, 1999; Revil et al., 2002).

Revil and Cathles (1999) presented a model for permeability of sand-clay mixtures; this model seems ideal for understanding potential controls on the permeability of

fault gouge. The model for the permeability of clay-sandstone mixtures  $k_m$ , presented by Revil and Cathles (1999) is given below:

$$K_m = K_{sd}^{1-\frac{V_{cl}}{\phi_{sd}}} \times K_{Cfs}^{V_{cl}/\phi_{sd}}, \quad 0 \leq V_{cl} \leq \phi_{sd} \quad (4.3)$$

$$K_m = K_{sh} V_{cl}^{3/2}, \quad \phi_{sd} \leq V_{cl} \leq 1 \quad (4.4)$$

where  $K_m$  is the permeability of sand clay mixtures,  $V_{cl}$  is the clay volume,  $\phi_{sd}$  and  $K_{sd}$  are the porosity and permeability of the sand end-member,  $K_{sh}$  is the permeability of the shale end-member and permeability of the clay-free sand is,

$$K_{Cfs} = K_{sh} \phi_{sd}^{3/2} \quad (4.5)$$

In Revil et al. (2002) model, the permeability and porosity of a sand-clay mixture (i.e. fault gouge) could be controlled by the porosity and permeability of the clay and sand matrix, (i.e. both the porosity of the sand, as well as the permeability of the sand and clay). Moreover, the critical porosity of the sand is controlled by grain sorting and its permeability is also controlled by both grain-sorting and grain-size.

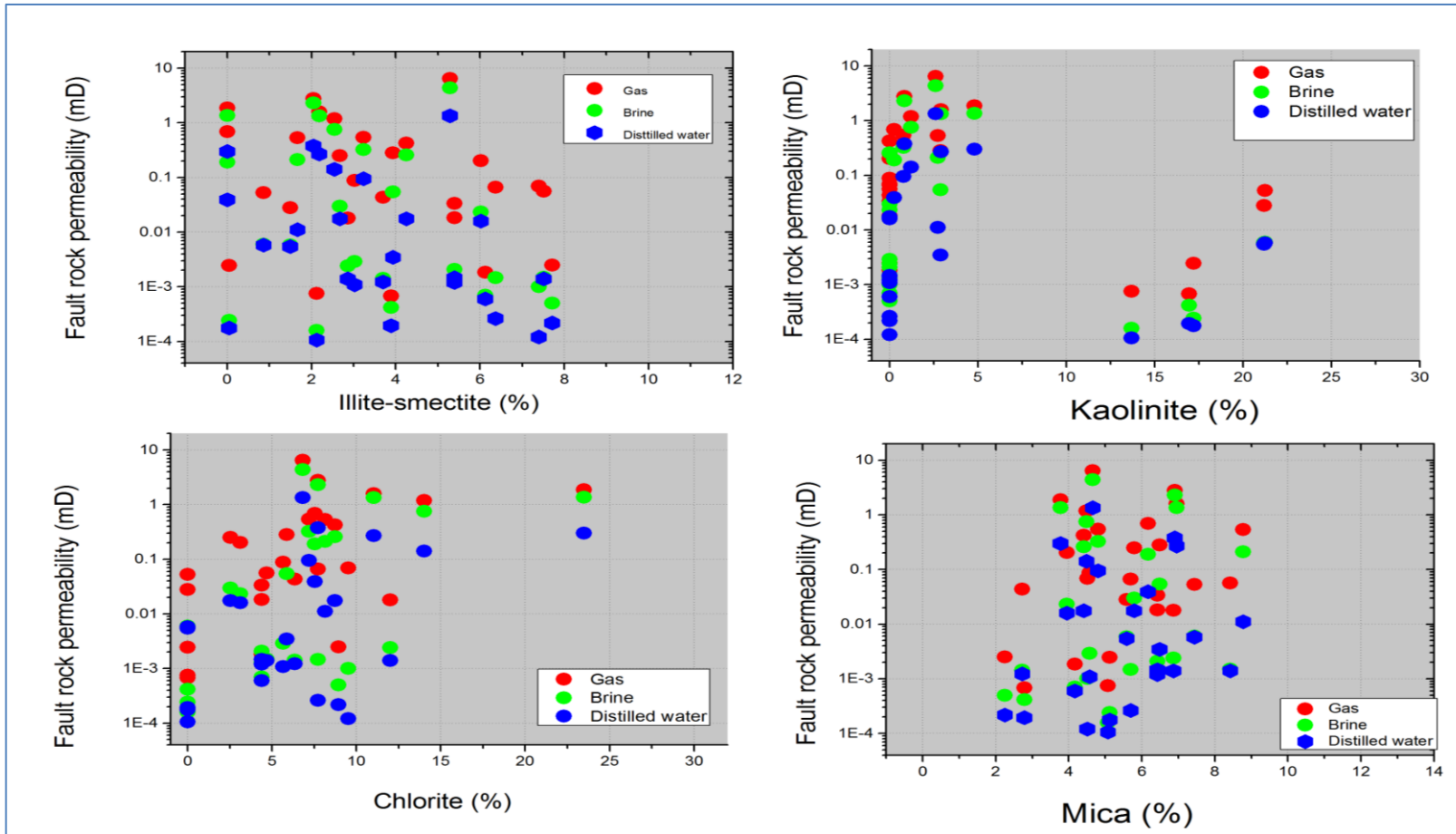


Figure 4.18 Plot showing effects of clay minerals (Mica, Kaolinite, Illite-smectite and chlorite) content on fault rock gas, brine and distilled water permeability. (semi-log plots)

To assess the implications of this model for fault rock permeability, the gas, brine and water permeability data of fault rock collected during present study was combined to compare with the model of Revil and Cathles (1999). For this purpose, three different ranges of sand-clay mixtures model estimations were made to capture the full range of data. The first sand considered coarse grained and well sorted sand, with a porosity of 42% and a permeability of 1000mD and with a clay end-member permeability of 0.0028mD. The second sand is fine-grained, poorly sorted sand with a porosity of 29% and permeability of 100mD, with clay end-member permeability of 0.01mD. The third sand was very poorly sorted, with a porosity of 15% and permeability of 0.01mD and the permeability of the clay end member of 0.0055mD. The results show that for given clay content the mixtures can have up to four orders of magnitude difference in permeability (**Figure 4.19**). These estimates provided with a reasonable agreement to the measured permeability values. Although few outliers is the reflection that the measure of clay content from QXRD analysis gives the total amount of clay content rather the clay might be distributed within the pore spaces. The permeability is also controlled by the distribution of clay content within the pore bodies not only the amount of clay.

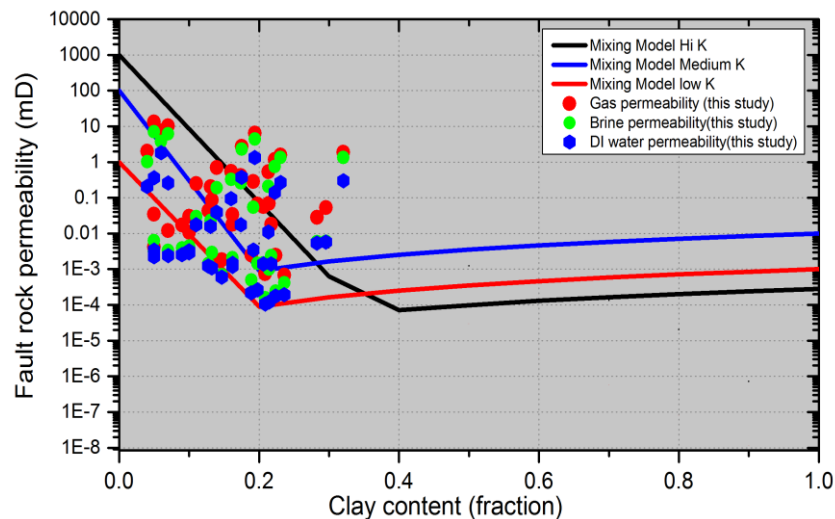


Figure 4.19 Plot of permeability of a sand-clay mixture as a function of clay content where the initial sands have different grain-sizes and grain-sorting, hence porosity and permeability (semi-log plot)

### 4.4.3 Comparison of the fault rock permeability data with existing empirical models

The sealing capacity of fault rocks could be assessed with empirical relations developed by (e.g. Sperrevik et al., 2002; Manzocchi et al., 1999). The empirical relations of Manzocchi et al. (1999) and Sperrevik et al. (2002) demonstrates that fault rock permeabilities decreases with increasing clay percentages (**Figure. 4.20**) and provide a direct relationships with clay fractions to predict fault rock permeabilities. It has been argued that the clay contents within the fault rocks are thought to be the same to the clay fraction of the sequence which has moved past a point on a fault (e.g. Walsh et al., 2008). Based on the assumptions of Manzocchi et al. (1999) if fault rock permeability estimated that might result in discrepancies due to various other factors, such as burial depth, diagenesis and types of the clay minerals and the extent of cementing materials present. Due to that reason, the model introduced by Revil and Cathles (1999) discussed above was applied to the data obtained during the present study for comparison with other two model of fault rock permeability estimation i.e. Manzocchi et al. (1999) and Sperrevik et al. (2002). It should be noted that fault rock permeability estimated using empirical equation of Sperrevik et al. (2002) considering the maximum depth of 3000m, which is similar to depth of the cores analyzed during the current study. The trend line generated based on Sperrevik et al. (2002) correlation plotted together with data obtained during present study of fault rock appears to be higher than measured data at lower clay content. However, most of the experimental data on fault rock permeability appears below the curve generated by Sperrevik et al. (2002) correlation (**Figure 4.20**).

In addition to Sperrevik et al. (2002) permeability estimation relation, the fault rock permeability was also estimated by using empirical equation of Manzocchi et al. (1999). The equation developed was based on the experimental data of Antonellini and Aydin (1994) and number of other fault rock data sets. Manzocchi et al. (1999) model uses fault displacement term ( $D$ ) that takes into account of the effect of deformation thickness similar thickness of fault displacement reported by Antonellini and Aydin (1994). The fault displacement thickness of 1mm used in Manzocchi et al. (1999) equation for fault rock permeability estimation. The reason of selecting 1mm fault displacement thickness is that the most of the studied deformation bands were in range of 1 to 2 mm. The estimated permeability appears higher than measured permeability at

even low clay content (**Figure 4.21**). Manzocchi et al. (1999) model is overestimating fault rock permeability at even lower clay fractions. The difference in estimated and measured permeability is around 3 orders of magnitude (**Figure 4.21**). The model estimates about 3 to 4 orders lower permeability particularly at low clay content than measured. Therefore, it could be argued that these empirical equations provide a poor representation of the fault rock permeability estimates based on the present study data..

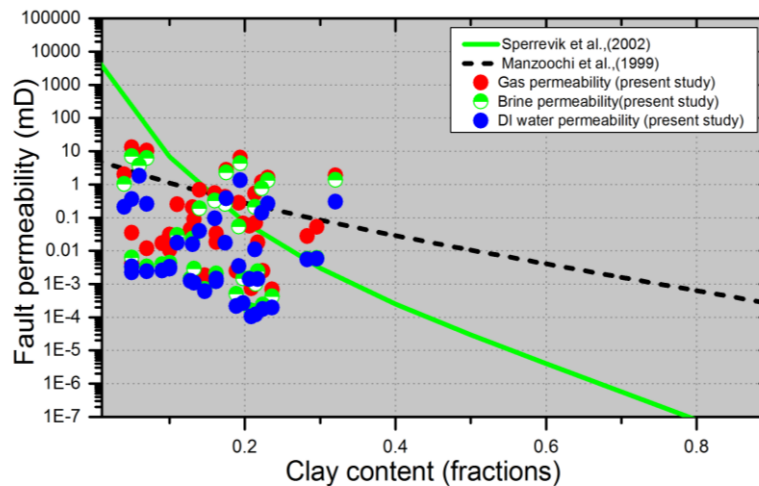


Figure 4.20 Comparison of the permeability of fault rocks as a function of clay content obtained during the present study using the fault rock empirical relations of Sperrevik et al. (2002) and Manzocchi et al. (1999) (semi-log plot).

The empirical relation reported Revil and Cathles (1999) and Revil et al. (2002) were applied to the present study data and the results of the measured fault rock permeability were plotted versus clay content and are shown in **Figure 4.21**. **Figure 4.21** presents that at higher permeability range the Revil and Cathles (1999) model results are very similar to those of Sperrevik et al. (2002) particularly at clay contents of <40%. This seems to be in contradiction with the concerns expressed above regarding the quality of the data on which the Sperrevik et al. (2002) paper was based. A potential reason for the results being similar to the Revil and Cathles (1999) model at higher range of permeabilities is that the laboratory measurements used in the Sperrevik et al. (2002) calculation were conducted at very low confining pressures using distilled water as permeant. A higher confining pressure would probably have reduced the permeability by several orders of magnitude for samples whereas the use of distilled water is likely to have given permeability values far lower than if formation-compatible brine had been used. In other words, the effects of using low stress and incompatible formation water

for measuring the fault rock permeability may have cancelled each other out. The Sperrevik et al. (2002) model predicts that permeabilities continues to decrease as the percentage of clay increases, whereas, the model of Revil et al. (2002) does not show any reduction at higher clay contents. It could be argued, that the Revil et al. (2002) model of permeability estimates could be more appropriate than that of Sperrevik et al. (2002) at higher clay contents because: (i) the data used by Sperrevik et al. (2002) for samples with very high clay contents was far lower, the predicted permeabilities by Sperrevik et al. (2002) was 0.001 nD. However, to the best of author's knowledge, no any laboratory technique has yet published such low permeability (i.e. 0.001nD) on core plugs. Therefore, the fault seal algorithms based on Manzocchi et al. (1999) and Sperrevik et al. (2002) empirical estimates does not take account of mixture of sand-clay rather they provide a direct relation in between two properties. However, apart from clay fractions, the fault rock permeability could be affected by various other factors, such as burial depth and types of the clay minerals (e.g. Walsh et al., 2008).

It is found that the data is totally consistent with the Revil et al. (2002) models and that a massive amount of scatter exists because of the differences in permeability of the sand and clay endmembers that are mixed in the fault. The sand endmember could vary between 10D and 0.001 mD depending on original grain size and sorting and the extent of diagenesis. The clay endmember could vary by orders of magnitude depending on clay type and level of compaction, therefore, it is probably the published empirical relationships that are too simplistic and that the clay vs permeability that have measured in the laboratory is more realistic and fits in better with theory.

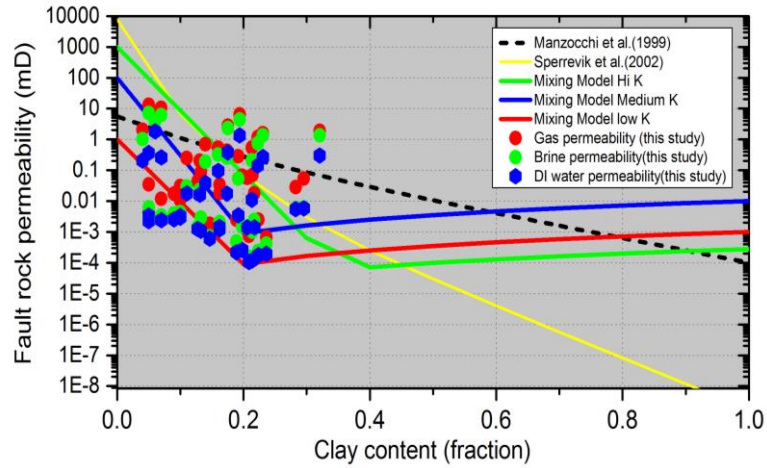


Figure 4.21 Comparison of the permeability of fault rock as a function of clay content using the model of Revil and Cathles (1999) and empirical model proposed by Sperrevik et al. (2002) and Manzocchi et al. (1999)

#### 4.4.4 Implications of results for fault seal analysis

##### 4.4.4.1 Estimation of fault permeability from clay content

The fault rock permeabilities are usually incorporated in reservoir simulation for modelling reservoir behaviour using transmissibility multipliers (Manzocchi et al., 1999, 2010). Most of these are derived from distilled water permeability based on work related to Fisher and Knipe (1998, 2001). However, many of the gas reservoirs are also compartmentalized due to fault processes (e.g. Zijlstra et al., 2007). The results of the present study suggest that permeability measured with distilled water permeability on average reduced by an order of magnitude than gas permeability. If the distilled water permeability is used in the place of gas permeability for transmissibility calculation that might result in underestimation of cross fault transmissibility (e.g. Fisher and Knipe 1998, 2001). Therefore, care must be taken in assigning proper value of fault transmissibility for predicting the gas recovery and analysing gas reservoir behaviour.

In addition, the oil and gas reservoirs are usually surrounded by aquifers. Aquifer permeability is important to control the rate of aquifer encroachment, which in turn impacts on gas trapping (i.e. ultimate recovery) and brine production. Therefore, it becomes important to determine the rate of aquifer encroachment so that gas and brine production can be modelled and production could be optimized (e.g. Hower et al., 1992). If this is the case then the brine permeability measured during present study will help to model aquifer encroachment. This could be better performed by assigning

transmissibility multipliers based on brine permeabilities rather than distilled water permeabilities to model accurately the aquifer encroachment. The fault rocks studied are based on cataclastic type and phyllosilicate-framework; although the clay rich sequences fault or clay smears type of fault rock permeability might affect in different way that needs to be investigated.

#### 4.4.4.2 Implications for estimation of fault rock permeabilities

There is lack of data on two-phase fault rock properties authors used tight gas sandstone as an analogue for the fault compartmentalized reservoirs modelling (e.g. Zijlstra et al., 2007). Similarly, present study assessed the controls on gas slippage effects within fault rock samples, the slippage factor data obtained plotted together from Byrnes et al. (2009) data of the tight gas sandstone, which resulted in a large scatter (**Figure 4.22**). The large amount of scatter in the  $b$ -value-permeability data means that either the  $b$ -values are calculated for each sample or the measurements should be made at very high pore pressure (>1000 psi) to reduce the magnitude of the slippage correction that needs to be applied.

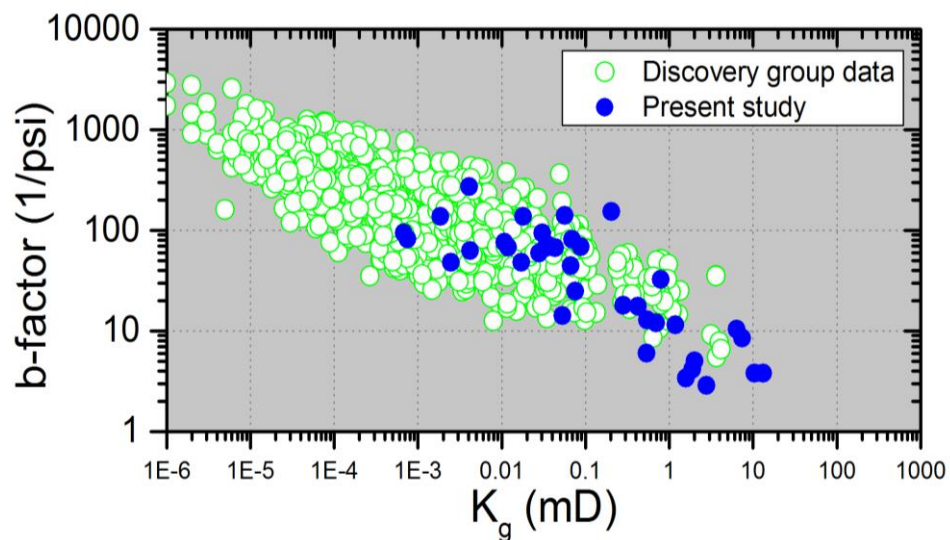


Figure 4.22 Plot of fault rock gas permeability against gas slippage factor. Data collected during present study are compared to those presented by the Discovery group data from Byrnes et al. 2000.

The brine permeability can be estimated from gas permeability based on empirical correlations (e.g. Jones and Owens, 1980; Chowdiah, 1987). In an attempt present study using above mentioned correlations estimated brine permeability. The estimated values of fault rock brine permeability based on empirical relations differ from the data

measured in laboratory (**Figure 4.23**). As, these estimated values using empirical relations and were compared with present study data of fault rock permeability suggested that the measured liquid permeability stays less than gas permeability even at higher  $>1\text{mD}$  gas permeability. Therefore, the estimated results based on above empirical correlations may result in overestimation of liquid permeability consequently the transmissibility multipliers for fluid flow modelling.

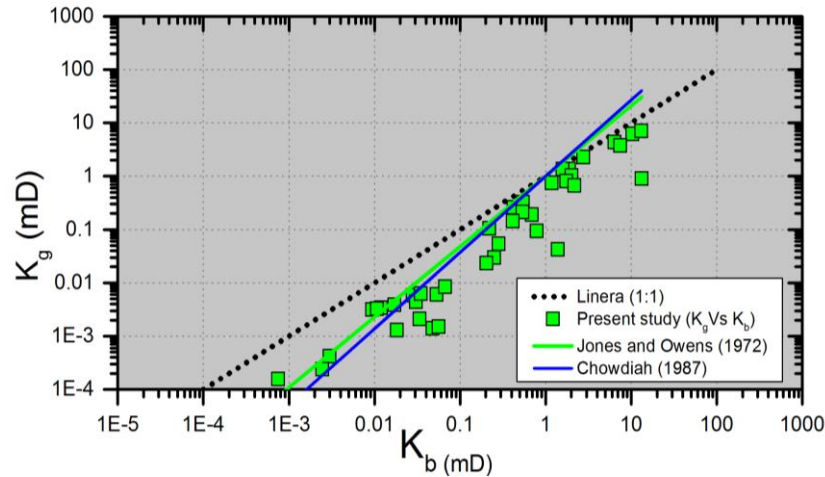


Figure 4.23 Comparison of gas permeability  $K_g$  and brine permeability  $k_b$  data measured during this study with published correlations.

## 4.5 Conclusions

This chapter integrates the results from microstructural analysis and experimental investigations to delineate the cross fault flow behaviour. The conclusions made from results are summarized below:

- Fault rock samples permeability was initially measured with gas as a pore fluid that reduced by one order of magnitude when measured with distilled water. The permeability to gas is around 30% that of NaCl brine, most of the fault rock gas permeability results were close to 20% NaCl brine permeability. The findings suggest that if gas permeability is used to calculate transmissibility multipliers instead of formation compatible fluids that could lead to an overestimation of cross fault fluid flow.
- The characteristic pore throat size of samples was estimated based on the Klinkenberg (1941) procedure and from mercury porosimetry data. Around an order of magnitude difference was observed in pore sizes. The pore throat size

from mercury injection data was higher than those estimated from Klinkenberg slip parameters because of the existence of delicate clay minerals. However, the effective pore size estimated following Klinkenberg procedure reflects that the gas only follows those paths which are open to flow without obstructing the pores.

- The microstructural observations from polished thin sections were studied to relate fault rock permeability to samples texture. In addition to that QXRD analyses of samples conducted which showed range of clay minerals, illite-smectite, kaolinite and chlorite. A lower permeability to distilled water was observed than brine and gas that might be due to interactions of water with clay mineral.
- It was attempted to evaluate the relation of gas slippage to permeability of fault rock samples. The results showed that there is a broad negative power-law correlation between b-value and permeability. Overall, there was a large amount of scatter in the b-value and permeability data which suggests that such correlations should not be used where accurate absolute permeability values of low permeability fault rock are needed. Instead, the b-value should be obtained for each sample or experiments should be conducted using high pore pressures to minimize the correction.
- An attempt was made to identify correlation between permeability and clay content. Overall, no relation was identified between fault rock permeability and clay content. The lack of correlation probably reflects the fact that clay minerals with different proportions exists within different samples. Fault rock permeability might be controlled by a combination of different microstructural elements. Results reported suggest that it is unsafe to correlate permeability simply with clay content.
- The comparisons of existing empirical estimates of permeability of fault rock samples were performed such as those of the Manzocchi et al. (1999); Sperrevik et al. (2002) and of Revil et al. (2002). It was observed that the model of Revil and Cathles (1999) resulted in scatter due to heterogeneity and other reasons such as microfractures. However, the Revil and Cathles (1999) model provides

reasonable estimates of permeability compared to above mentioned empirical relations. Although it also depends on the information of sand-clay fractions.

# 5 Fault rock gas and liquid permeability stress sensitivity

---

## 5.1 Introduction

Fault rock permeability measurements made at ambient stress conditions are well documented (e.g. Fisher and Knipe, 2001; Fowles and Burley, 1994; Gibson, 1998; Sperrevik et al., 2002; Tueckmantel et al., 2011, 2012). There is however very few published data on the permeability of fault rocks, that has been attempted to obtain data at in situ stress conditions (e.g. Al-Hinai et al., 2007). This could be a serious omission as laboratory measurements of the permeability of tight rocks are very sensitive to the confining stress (e.g. Thomas and Ward, 1972; Brower and Morrow, 1985; Byrnes et al., 2000). In particular, routine core analysis permeability measurements made at ambient low stress (~400 psi confining pressure) on tight sandstones may be several orders of magnitude lower than those made at in situ stress conditions (e.g. Byrnes et al., 2000). If this is the case for fault rocks, the most commonly used data (e.g. Fisher and Knipe, 2001) for calculating transmissibility multipliers to take into account the impact of faults on fluid flow in production simulations models could be wrong by several orders of magnitude because the measurements were made at ambient stress rather than the in- situ stress conditions. The present study attempts to assess the extent to which measurements conducted at low stresses could affect the results of fault seal analysis.

Fault rock samples obtained from outcrops are also commonly used to assess the impact of faults on fluid flow (e.g. Morrow et al., 1984; Fowles and Burley, 1994; Gibson, 1998; Al-Hinai et al., 2006). There are, however, concerns that weathering may have altered the properties of these samples relative to their subsurface values. So the question remains whether samples from reservoir cores could be more

appropriate for the derivation of fluid flow properties for fault rocks than those from the subsurface. Although, the stress relaxation may result in micro-fracturing, which could be observed in both outcrop samples and reservoir cores (e.g. Dong et al., 2010).

This chapter comprises five main sections. The chapter starts by reviewing the basic theory on low permeability tight rock samples in **Section 5.2**. The overview of experimental procedures is presented in **Section 5.3**. The experimental results of absolute gas and brine permeabilities measured at different levels of stress are presented in **Section 5.4**. The discussion about the permeability stress sensitivity of fault rock data is presented in **Section 5.5**. Klinkenberg procedures were performed on all samples at different net confining stresses to determine the gas slip parameters and thus enable a better comparative analysis of the stress sensitivity of the gas and brine permeability of fault rocks. The impact of brine composition on fault rock permeability is also discussed. The results from tight gas sandstones permeability and present study data on fault rock are compared and discussed. The implications of these results on fault seal workflow are then presented. Finally, the conclusions made based on the results, are summarized in **Section 5.6**.

## **5.2 Gas flow mechanisms**

Gas flow in tight rocks has remained of interest of many researchers and is extensively investigated because it plays a major role in gas reservoir engineering and it also has considerable importance for risking the flow properties of seals above gas storage sites. Permeability is a property of the porous medium and is often thought to be independent of the type of pore fluid present in the pore space. However, in a porous medium in which the pores with diameters similar to those of the mean free path of the gas molecules, the additional flux due to gas flow at the pore walls (i.e. the slippage flow of gas molecules) increases the flow rate of gas and hence the apparent permeability. In the following section the phenomenon of slip flow is discussed.

### 5.2.1 Slip flow (Klinkenberg model)

Klinkenberg (1941) presented a model representing a direct relationship between the measured gas permeability ( $K_g$ ) and the intrinsic permeability, with the inverse of the mean pressure ( $\bar{P}$ ) and the Klinkenberg  $b$ -factor, given by:

$$K_g = K_l \left( 1 + \frac{b}{\bar{P}} \right) \quad \text{Eq. (5 - 1)}$$

Where,  $K_g$  is the apparent gas permeability,  $K_l$  is the true absolute permeability of rock;  $b$  is the Klinkenberg  $b$ -value and  $\bar{P}$  is the average pressure. Flow tests are conducted at a range of pore pressures and then a plot of apparent gas permeability vs  $1/\bar{P}$  is then be extrapolated to  $1/\bar{P} = 0$ . The permeability measurements from the Klinkenberg tests were fitted using a straight line to estimate the  $b$  factor. As recommended by the API (1998), only tests where the data can be fitted to a straight line with a correlation coefficient greater than 0.98 for 4 or more data points should be considered (**Figure 5.1**). In Figure 5.1 three shows that the permeability measurements were taken at a 3 ranges of stress conditions and were corrected for slippage effects. The higher the stress lower permeability would be expected and higher slippage factor.

It is also theoretically possible to get the pore radius from  $b$ -factor values using following equation (Klinkenberg 1941):

$$b = \frac{4c\lambda P}{r_{eff}} \quad \text{Eq. (5-2)}$$

where,  $c$  is dimensionless parameter that depends on the geometry but is in the order of one, (Klinkenberg, 1941) and  $r_{eff}$  is the pore radius. The  $b$  factor is constant with pore pressure (Klinkenberg, 1941), when  $\lambda$  is expressed as: (Loeb, 1934)

$$\lambda = \frac{\mu}{P_p} \sqrt{\frac{RT\pi}{2M}} \quad \text{Eq. (5-3)}$$

where  $\mu$  is the gas viscosity,  $R$  the gas constant,  $T$  absolute temperature and  $M$  the molar mass of the gas.

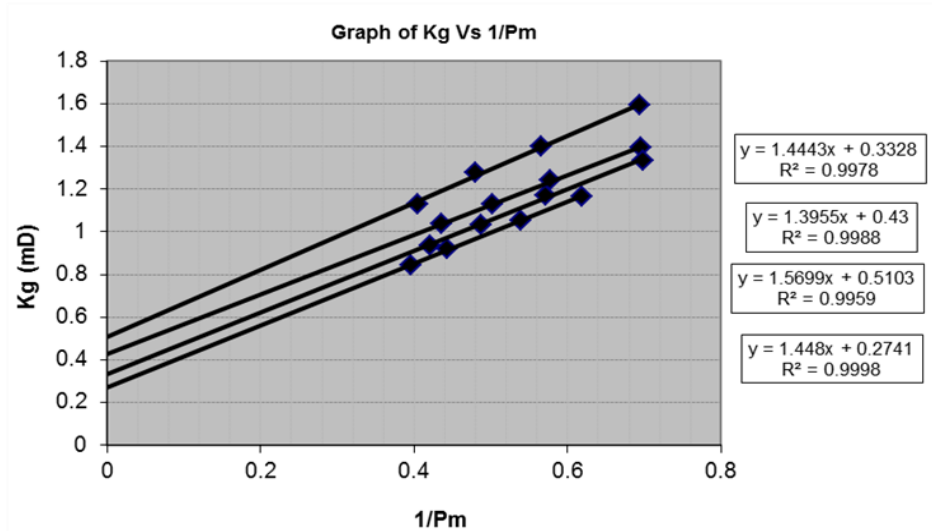


Figure 5.1 Diagrams showing the principle behind Klinkenberg corrections.

The gas slippage-factor is a function of the pore size, which is why the value varies with the type of rock. The  $b$ -factor has been the focus of various studies, that is used to relate with Klinkenberg gas permeability to estimate absolute gas permeability (e.g. Tanikawa and Shimamoto, 2006; McPhee and Arthur, 1991; Sampath and Keighin, 1982; Florence et al., 2007). A summary of the existing Klinkenberg factor correlations are provided in **Table 5.1**.

The Klinkenberg plots are usually constructed to derive accurate values of the gas slippage factor and apparent gas permeability. However, in petroleum industry it is common to make a single permeability measurement at a low gas pressure and then apply a Klinkenberg correction based on empirical relationships between the gas slippage factor and permeability, or gas slippage factor and porosity and permeability (e.g. Heid et al. 1951; Jones and Owens, 1980; Sampath and Keighin, 1982). Sampath and Keighin (1982) model the rock as a collection of cylindrical pores, where  $k_{\infty} \propto r^4$ , so that slippage radius  $r_{slip} \propto (k_{\infty} / \phi)^{1/2}$  and  $b \propto (K_{\infty} / \phi^{-0.5})$  (Sampath and Keighin, 1982). As the  $b$  factor depends on the gas, correlations would have to be corrected for the gas used (e.g. Florence et al., 2007). However, permeability measured with the same gas (Byrnes et al., 2009) resulted in a scatter. This has increased uncertainty when using such correlations to deduce to subsurface conditions. Therefore to save the time, and hence the operational costs to analyze the permeability of low permeability tight rock samples under in situ conditions transient

techniques such as pulse decay permeametry (e.g. Brace et al., 1968; Jones, 1997) are increasingly being used (e.g. Rushing et al., 2003). The pulse-decay experiments are conducted using gas at high pore pressures of up to 2000 psi (e.g. Jones, 1997) because the higher pore pressures reduce the gas slippage. Although, low permeability samples have small pore throat sizes, so it may still be necessary to perform Klinkenberg corrections to obtain accurate absolute permeability (e.g. Jones, 1997). This chapter, in addition to liquid permeability stress sensitivity presents experimental data on gas permeability stress sensitivity of fault rocks obtained under a range of pore pressure and confining stresses. The results will be used to analyze and to explore the combined effects of changing pore pressure on slippage and absolute permeability of fault rock.

Table 5.1 Overview of the existing Klinkenberg correlation factors;  $K_{ap}$  is apparent permeability and  $\phi$  is porosity.

S.N.o	Author	Sample	Equations
1	Heid et al. (1950)	Oil-field cores with permeability values of about 0.1 – 1000mD	$b = 11.419 (K_g)^{-0.39}$
2	Jones and Owens (1979)	Core samples (>100) ranging from 0.01 to 2500mD	$b = 12.639 (K_g)^{-0.33}$
3	Jones (1972)	Tight gas sand samples ranging from 0.10 – 100mD	$b = 6.9(K_g)^{-0.36}$
4	Sampath and Keighin (1981)	Cores obtained from North sea gas reservoir. (0.01 – 10mD)	$b = 13.851(K_g)^{-0.53}$
5	McPhee and Arthur (1991)	Ten core samples from tight gas sand field ( $10^{-15} - 10^{-17} \text{ m}^2$ )	$b = 0.0955(K_g/\phi)^{-0.53}$
6	Tanikawa and Shimamoto (2006)	Sedimentary rocks with permeability 0.001 – 10mD	$b = 11.2(K_g)^{-0.37}$
7	Florence et al. (2007)	Data in the literature and from industrial sources (0.01 - 0.01mD).	$b = 43.345(K_g / \phi)^{-0.5}$

### 5.3 Methodology

A rigorous investigation has been made on the stress dependent petrophysical properties of a variety of fault rocks. The samples were obtained from central and southern North Sea reservoir cores, and collected from different outcrops of 90

Fathom fault and Miri airport road fault rock exposure Malaysia. The permeability to gas, brine and distilled water has been determined for all of the aforementioned samples. Prior to permeability measurements all samples were cored and cleaned, in addition preliminary measurements were made on these samples such as their dimensions i.e. diameter and length were measured using a calliper. The details about how plugs were cored and cleaned are presented in **Chapter 3**.

The permeability of 47 fault rock rectilinear samples has been measured at ambient stress by changing pore fluids from gas to brine (20% NaCl), and finally measured with distilled water. In addition to ambient stress measurements the permeability of 10 fault plugs have been measured as a function of stress using 30% NaCl brine, 3.5% NaCl brine, distilled water and gas. A summary of the number of samples analysed under different experimental conditions is given in **Table 5.2**. Detailed microstructural results and petrophysical properties of these samples were presented in **Chapter 4**. All permeability tests were performed using a Hassler-type core-holder. The pulse decay technique has been used to measure permeability of tight samples ( $<0.1$  mD). For high permeability samples ( $>0.1$  mD), permeability measurements were made using the steady-state method. The experimental procedures adopted and measurement techniques employed are described in detailed in **Chapter 3**.

Helium gas and synthetic brines (NaCl) of different composition prepared in the laboratory were used for permeability stress sensitivity experiments. Initially, gas permeability measurements were made on all plugs at various stress conditions by flowing nitrogen and helium gas. After gas permeability measurements all samples of the central North Sea were fully saturated with 30% NaCl brine and the permeability was then measured. For all other samples, following gas permeability measurements, permeability was measured using 20% NaCl brine. Finally, the permeability of 10 plug samples from Central North Sea was measured with 3.5% NaCl and with distilled water. All brine 3.5%NaCl and distilled water permeability results are presented in **Appendix A**. It should be noted that permeability measurements were made at different levels of stress. Initially the experiments were conducted at lower stress of 500psi then this was gradually increased up to 5000psi. The experiments on Central North Sea group-A core samples were conducted at a

maximum confining stress of 2500psi, due to friable nature of samples. However, all other measurements were made at maximum net confining stress of 5000 psi.

The fault rock permeability values reported were deconvolved to get true fault rock permeability ( $K_f$ ) using the techniques provided in **Section 3.5.6**. The permeability measured at each confining stress was deconvolved. The arithmetic mean of the gas and brine permeability of plugs at each stress is also reported, which is based on the concept that the samples are heterogeneous (e.g. Manzocchi et al., 1999).

Table 5.2 Summary of the number of samples analysed under different experimental conditions.

Summary of fault rock samples analysed			
RCA Analysis	No. of Samples analysed	SCAL Analysis	No. of Samples analysed
SEM	69	Gas permeability vs stress	47
QXRD	53	Brine permeability vs. stress	35
Porosity	50	DI Water permeability versus stress	10
Hg-injection	57	Gas permeability vs load cycling	03
Ga permeability	47		
Brine Permeability	47		

## 5.4 Results

In the following section, the stress dependent petrophysical properties of central and southern North Sea reservoir core samples as well as the petrophysical properties obtained on outcrop samples collected from the 90 Fathom fault United Kingdom and Miri airport road Malaysia fault exposure are reported. The total number of samples analysed under different conditions are summarized in **Table 5.3**. The results of SEM and QXRD for studied samples are presented in **Appendix A** and are discussed in **Chapter 3**.

The absolute permeability of sandstone samples can be expressed as a function,  $F$  of the effective stress i.e.,  $k_{\infty} = F(\sigma')$ , where  $\sigma'$  can be represented as,  $\sigma' = \sigma_c - n_k P_p$ ,

where  $\sigma'$  is the effective stress  $P_p$  is the pore pressure and  $\sigma_c$  is confining stress (e.g. Warpinski and Teufel, 1992; Al-Wardy and Zimmerman 2004; Li et al., 2009). The absolute permeability drops as the stress is increased, and is fitted with a power law relationship (Ghabezloo et al., 2008)

$$k_{\infty} = K(\sigma_c - n_k P_p)^{-\gamma} \quad \text{Eq. (5-4)}$$

Where,  $\sigma_c$  is the net stress or confining stress,  $P_p$  is the pore pressure,  $n_k$  is the effective stress coefficient for permeability, assumed to be equal to one,  $K$  is the permeability extrapolated to zero net stress, and  $\gamma$  is the stress exponent. In addition, the reduction in permeability due to stress increase was calculated using the following equation,

$$D_k(\%) = [(K_{@500} - K_{in-situ})/K_{@500}] \times 100 \quad \text{Eq. (5-5)}$$

where  $D_k$  is the permeability loss in percentage,  $K_{@500}$  (mD) is permeability measured at low stress of 500 psi confining stress, and  $K_{in-situ}$  (mD) is permeability measured at in-situ stress conditions.

### 5.4.1 Central North Sea reservoir, UK

The following section provides details about the results obtained on stress dependent gas and brine permeability of fault rock samples.

#### 2.8.1.1 Stress dependent single phase gas permeability

The gas permeability measured at 500 psi confining stress ranges from 0.08mD to 5.2mD, with an arithmetic mean of 1.2mD. The permeability measured at 2500psi confining stress ranges from 0.06mD to 4.3mD, with an arithmetic mean of 0.93mD. The data on permeability obtained is reported in **Table 5.3**. The relationship between normalized gas permeability and confining stress is reported in **Figure 5.2**, which shows that the permeability of these samples are stress dependent over the range used. On average, the reduction in permeability falls around 22.5% as stress increased from 500psi to 2500psi. Overall, the stress sensitivity of permeability measurements increases with decreasing permeability.

The gas permeability results follow a power-law relationship to the stress (**Figure 5.3**), the data was fitted using Equation 5-4. The fitting parameters obtained from applying a power-law model to the stress dependent permeability data and are provided in **Table 5.4**. The slippage factor values were then used to estimate the pore radius using Equation 5-2. The results obtained on gas slippage factor are reported in **Table 5.4**.

### 1.6.1.1 Stress dependent brine permeability

The results show that the brine permeability ranges from 0.04mD to 3.52mD at net confining stress of 500psi, with an arithmetic average of 0.63mD (**Table 5.3**). Similarly, the brine permeability at confining stress of 2500psi ranges from 0.002mD to 2mD, with an arithmetic mean of 0.40mD. In other words, the permeability is on average reduced by 35% as stress is increased from 500 to 2500psi. This reduction in permeability can be classified as a moderate reduction (>35%) in comparison with the reduction that is experienced in the gas permeability of these samples. The power law trend line was also fitted with brine permeability results and the exponent for each sample is reported in **Table 5.4**.

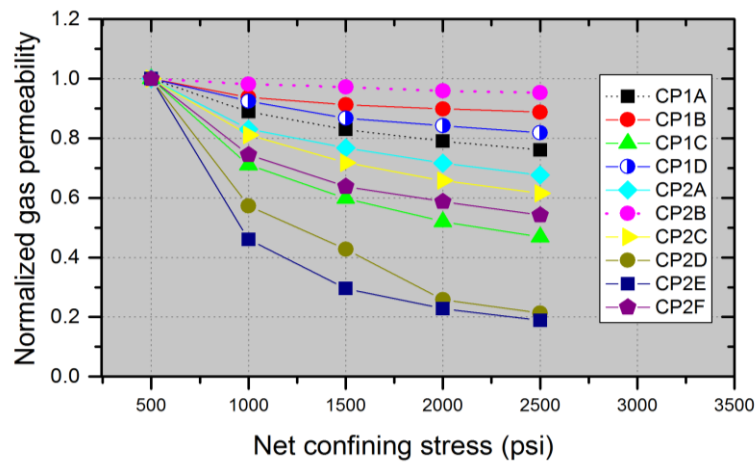


Figure 5.2 Plot of the fault rock normalized gas permeability versus net confining stress; data are from Central North Sea reservoir core samples.

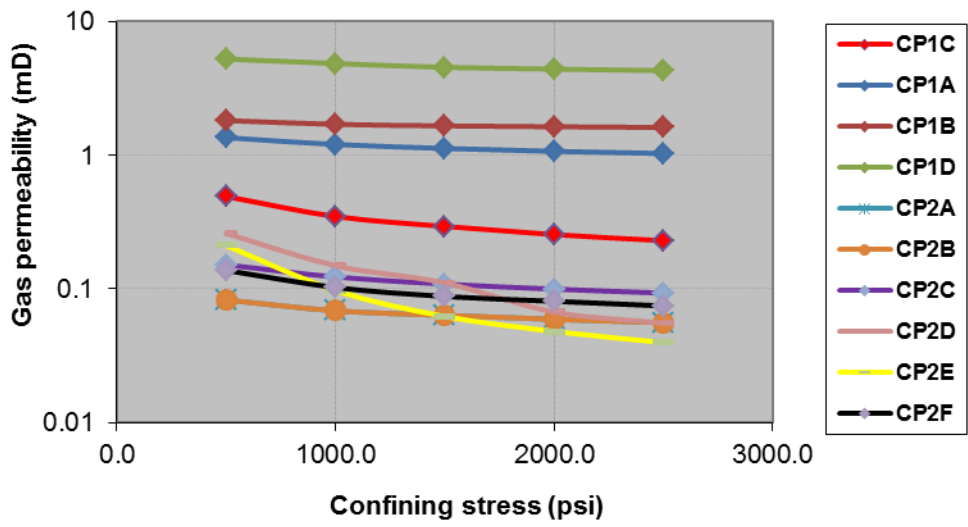


Figure 5.3 Plot of the fault rock gas permeability versus net stress; data are from Central North Sea reservoir core samples.

Table 5.3 Stress dependent gas and brine permeability of cataclastic fault core samples from Central North Sea reservoirs.

Central North Sea core samples permeability (mD)														
Sample ID	L (cm)	D (cm)	PV (cm <sup>3</sup> )	Mass (gm)	500		1000		1500		2000		2500	
					K <sub>g</sub>	K <sub>b</sub>								
CP1A	4.7	2.4	5.5	61	1.4	0.81	1.2	0.75	1.1	0.70	1.1	0.59	1.0	0.55
CP1B	3.1	2.4	3.2	28	1.8	1.14	1.7	1.05	1.7	0.88	1.6	0.84	1.6	0.79
CP1C	4.6	2.4	4.7	40	0.49	0.09	0.35	0.08	0.29	0.08	0.25	0.07	0.23	0.07
CP1D	4.6	2.4	4.4	42	5.2	3.52	4.8	2.53	4.5	2.30	4.4	2.2	4.3	2.0
CP2A	4.3	2.4	4.6	38	0.08	0.04	0.07	0.04	0.06	0.04	0.06	0.04	0.06	0.03
CP2B	6.4	2.4	8.4	57	1.9	0.55	1.9	0.53	1.9	0.52	1.8	0.51	1.8	0.51
CP2C	5.9	2.4	6.6	52	0.15	0.08	0.12	0.07	0.11	0.06	0.10	0.06	0.09	0.06
CP2D	4.1	2.4	4.4	38	0.26	0.007	0.15	0.0039	0.11	0.0037	0.07	0.0037	0.06	0.003
CP2E	5.5	2.4	5.9	49	0.21	0.05	0.10	0.04	0.06	0.023	0.05	0.015	0.04	0.011
CP2F	4.5	2.4	4.4	43	0.14	0.05	0.10	0.05	0.09	0.043	0.08	0.041	0.07	0.040
<b>Arithmetic- mean</b>					<b>1.2</b>	<b>0.63</b>	<b>1.05</b>	<b>0.51</b>	<b>0.99</b>	<b>0.47</b>	<b>0.95</b>	<b>0.44</b>	<b>0.93</b>	<b>0.40</b>

Table 5.4 Petrophysical properties of fault rock, slip factor, slip radius and gas, brine power law exponents from central North Sea data.

Sample ID	Power law exponent		500 (psi)		1000 (psi)		1500(psi)		2000 (psi)		2500 (psi)	
	Gas	Brine	b <sub>k</sub> (psi)	Slip-radius (μm)								
<b>CP1A</b>	-0.2	-0.2	4	1.8	5	1.48	4	1.7	5	1.5	5.3	1.5
<b>CP1B</b>	-0.1	-0.2	4	1.9	4	1.97	4	2.1	3	2.2	3.5	2.2
<b>CP1C</b>	-0.6	-0.1	12	0.7	22	0.36	24	0.2	-	-	-	-
<b>CP1D</b>	-0.2	-0.3	10	0.7	12	0.65	5	1.7	3	2.8	-	-
<b>CP2A</b>	-0.3	-0.1	18	0.4	19	0.40	21	0.4	22	0.3	-	-
<b>CP2B</b>	-0.04	-0.05	3	2.7	3	2.43	4	2.1	4	1.8	-	-
<b>CP2C</b>	-0.4	-0.2	16	0.5	20	0.39	23	0.3	24	0.3	25.5	0.30
<b>CP2D</b>	-1.4	-0.5	37	0.2	148	0.05	259	0.03	290	0.1	320.0	0.10
<b>CP2E</b>	-1.5	-1.0	18	0.4	34	0.23	48	0.2	64	0.2	77.7	0.15
<b>CP2F</b>	-0.55	-0.2	23	0.3	27	0.28	31	0.2	32	0.2	34.1	0.21

## 5.4.2 Southern North Sea reservoir

Three cores samples were supplied from a Triassic reservoir in the Dutch sector of the Southern North Sea. A total of five plugs were taken for measurement, the gas and brine permeability results are reported in **Table 5.5**.

### 2.8.1.2 Stress dependent gas permeability

Single-phase gas permeability measured on these plugs at confining stress of 1000psi ranges from 0.00059mD to 0.14mD with an arithmetic average of 0.032mD. The gas permeability at confining stress of 5000psi ranges from 0.00020mD to 0.11mD, with arithmetic average of 0.025mD. So overall, the arithmetic average reduction in permeability was 22%, similar to that experienced in gas permeability of Central North Sea reservoir core samples. The relationship between normalized gas permeability versus confining stress was plotted and is shown in **Figure 5.4**.

### 2.8.1.3 Stress dependent brine permeability

The results show that the arithmetic average brine permeability reduced from 0.012mD to 0.009mD as the effective stress was increased from 1000 to 5000psi. The permeability at confining stress of 1000psi ranges from 0.00009mD to 0.042mD. These samples have shown less stress sensitivity to brine permeability as compared to gas permeability stress sensitivity (**Table 5.5**). The permeability at 5000psi stress ranges from 0.000036mD to 0.035mD. The average reduction in brine permeability is ~25%, which is similar to that experienced in the gas permeability of these samples. The permeability results plotted versus stress are reported in **Appendix A**.

Table 5.5 Basic properties and stress dependent single phase gas and brine permeability (mD) from southern North Sea reservoir cores.

Southern North Sea core samples gas permeability (mD)														
Sample ID	L (cm)	D (cm)	PV (cm <sup>3</sup> )	Mass (gm)	1000		2000		3000		4000		5000	
					K <sub>g</sub>	K <sub>b</sub>								
Win1A	6.0	2.5	5.1	65	0.019	0.017	0.014	0.013	0.012	0.011	0.011	0.010	0.010	0.0093
Win3A	6.0	2.5	5.4	64	0.14	0.042	0.12	0.038	0.12	0.036	0.11	0.034	0.11	0.035
Win1B	6.7	2.5	2.8	82	0.00059	0.00009	0.00054	0.00009	0.00035	0.00006	0.00027	0.00006	0.00020	0.000048
Win2B	5.2	2.5	2.7	63	0.00067	0.00034	0.00055	0.00011	0.00035	0.00007	0.00026	0.00004	0.00021	0.000036
Win1C	6.7	2.5	3.1	79	0.0026	0.00018	0.0013	0.0001	0.00086	0.00012	0.00067	0.00012	0.00053	0.000086
<b>Arithmetic average</b>					<b>0.032</b>	<b>0.012</b>	<b>0.028</b>	<b>0.010</b>	<b>0.026</b>	<b>0.010</b>	<b>0.025</b>	<b>0.009</b>	<b>0.025</b>	<b>0.009</b>

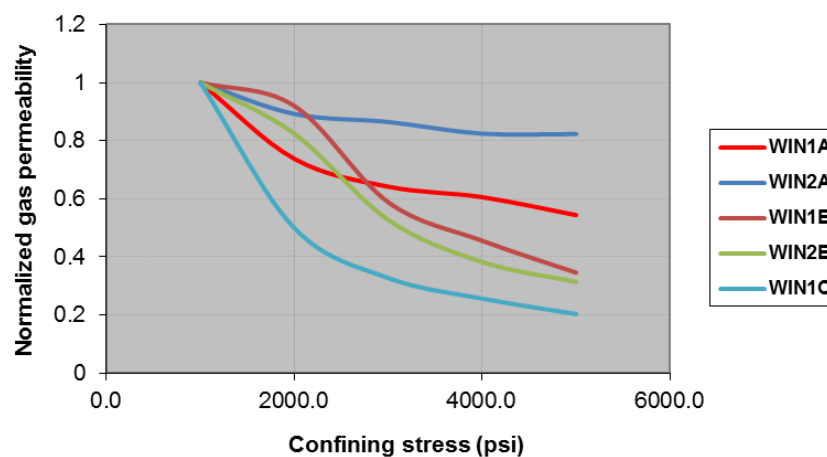


Figure 5.4 Normalized single phase gas permeability versus confining stress, and gas permeability versus confining stress the samples are from southern North Sea reservoir core samples.

### 5.4.3 Fault samples from 90 Fathom Fault, UK and Miri exposure, Malaysia

The stress dependence of gas and brine permeability of six plugs from the main slip surface cataclasite, four plugs from single deformed zone and two samples from Miri fault exposure were measured. The normalized gas permeability results from all samples are plotted in **Figure 5.5**. The gas permeability versus confining stress results are provided in **Figure 5.6**.

#### 2.8.1.4 Stress dependent gas permeability

The gas permeability measured on slip-surface cataclasite plugs at confining stress of 1000psi ranges from 0.0080mD to 0.08mD, with an arithmetic average permeability of 0.044mD (**Table 5.6**). The permeability measured at 5000psi ranges from 0.071mD to 0.005mD with an arithmetic average of 0.034mD. So, the average reduction in permeability experienced by these samples is 22.7% by increasing the confining stress from 1000psi to 5000psi. These samples have shown less stress dependency compared to reservoir core plugs permeability. The gas permeability of single deformation band plugs are also reported in **Table 5.6**, which shows that on average permeability reduces from 3.9mD to 2.6mD as stress changes from 1000psi to 5000psi. This reduction in permeability by increasing confining stress from 1000 to 5000psi is ~ 30%.

Miri exposure Malaysia fault samples were classified as moderately stress dependent (>60%) as compared to other outcrop samples from 90 Fathom fault. The permeability of these samples on average reduced from 0.5mD to 0.18mD as confining stress increases from 1000psi to 5000psi. The permeability results of these samples are also reported in **Table 5.6**. The Klinkenberg procedure followed on these measurements to obtain the slippage factor values. The pore size estimated from gas slippage factor using Equation (5-2) was also obtained and results are reported in **Table 5.7**.

### 2.8.1.5 Stress dependent brine permeability results

Laboratory measured results show that the slip-surface cataclastic permeability ranges from 0.011mD to 0.0014mD with the arithmetic mean of 0.051mD at 5000psi confining stress. These results suggest that the brine permeability is only slightly stress dependent. Whereas the Miri samples have shown more reduction than 90 Fathom samples when increasing confining stress from 500 psi to 5000 psi. The permeability measured at stress of 1000psi to 5000 psi, on average ranges from 0.01mD to 0.005mD.

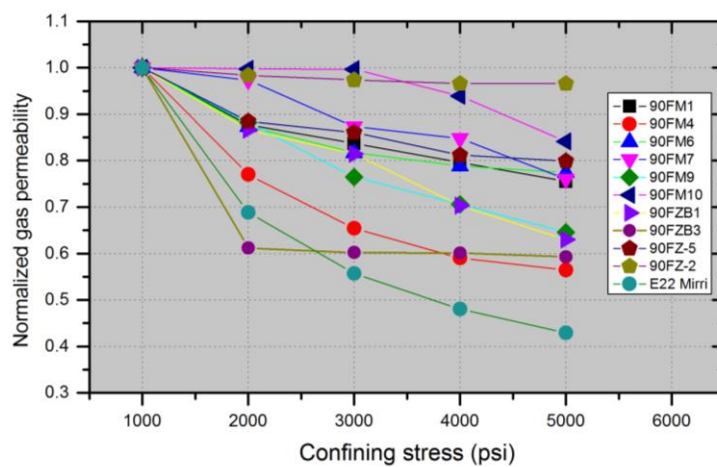


Figure 5.5 Plot showing the relationship between normalized single phase gas permeability and net confining stress; the data are from 90 Fathom fault plugs and Miri exposure Malaysia fault samples.

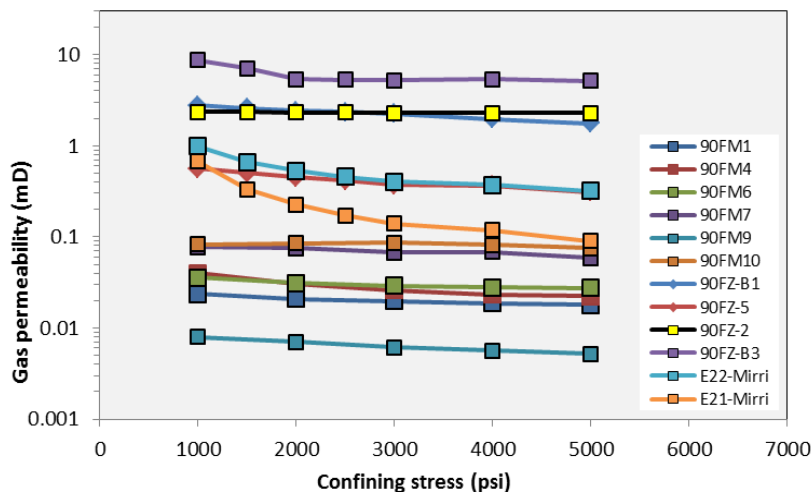


Figure 5.6 Plot of the 90 Fathom fault, UK and Miri exposure Malaysia fault plugs gas permeability (mD) versus net confining stress (psi).

Table 5.6 Stress dependent gas and brine permeability of 90 Fathom fault rock samples and Miri exposure fault rocks, Malaysia.

<b>(a) Slip-surface cataclas</b>														
Sample ID	L (cm)	D (cm)	PV (cm <sup>3</sup> )	Mass (gm)	1000 (psi)		2000 (psi)		3000 (psi)		4000 (psi)		5000 (psi)	
					K <sub>g</sub>	K <sub>b</sub>								
90FM1	6.2	3.6	7.8	153	0.024	0.0034	0.021	0.0022	0.020	0.0020	0.019	0.0018	0.018	0.0016
90FM4	6.1	3.6	6.8	153	0.040	0.0083	0.030	0.0061	0.026	0.0053	0.023	0.0047	0.022	0.0046
90FM6	5.9	3.6	6.4	148	0.036	0.0096	0.031	0.0083	0.029	0.0072	0.028	0.0070	0.028	0.0070
90FM7	6.8	3.6	8.4	168	0.08	0.084	0.08	0.073	0.067	0.067	0.068	0.061	0.059	0.0568
90FM9	5.3	3.6	4.8	135	0.008	0.0014	0.007	0.0013	0.006	0.0009	0.006	0.0009	0.005	0.0008
90FM10	6.2	3.6	7.4	153	0.080	0.020	0.082	0.016	0.084	0.014	0.079	0.013	0.071	0.013
<b>Arithmetic- mean</b>					<b>0.044</b>	<b>0.021</b>	<b>0.041</b>	<b>0.018</b>	<b>0.039</b>	<b>0.016</b>	<b>0.037</b>	<b>0.015</b>	<b>0.034</b>	<b>0.014</b>
<b>(b) Single Deformation band</b>														
90FZB1	5.6	3.6	11	127	2.8	0.54	2.4	0.50	2.3	0.44	2.0	0.4	1.8	0.38
90FZB3	5.6	3.5	9.8	112	8.7	—	5.3	—	5.3	—	5.4	—	5.2	—
90FZ-5	5.4	3.5	8.9	109	1.7	0.16	1.5	0.15	1.5	0.14	1.4	0.13	1.4	0.12
90FZ-2	5.9	3.6	9.5	113	2.4	0.58	2.3	0.50	2.3	0.47	2.3	0.45	2.3	0.44
<b>Arithmetic- mean</b>					<b>3.9</b>	<b>0.4</b>	<b>2.9</b>	<b>0.4</b>	<b>2.8</b>	<b>0.4</b>	<b>2.7</b>	<b>0.3</b>	<b>2.6</b>	<b>0.3</b>
<b>(C) Miri exposure Malaysia sample</b>														
E21 Mirri	5.3	3.1	14.8	124	0.33	0.0076	0.17	0.0048	0.12	0.0037	0.09	0.0031	0.07	0.0027
E22 Mirri	5.3	3.8	12.4	123	0.66	0.011	0.46	0.0096	0.37	0.0086	0.32	0.0080	0.28	0.0075
<b>Arithmetic- mean</b>					<b>0.50</b>	<b>0.010</b>	<b>0.31</b>	<b>0.007</b>	<b>0.24</b>	<b>0.006</b>	<b>0.20</b>	<b>0.006</b>	<b>0.18</b>	<b>0.005</b>

Table 5.7 Petrophysical properties of fault rock, gas slippage factor, slip radius and gas, brine power law exponents from outcrop samples.

		Slip parameters at different confining stress											
		Power law exponent		1000 (psi)		2000 (psi)		3000(psi)		4000 (psi)		5000 (psi)	
Sample ID	Gas	Brine	b <sub>k</sub> (psi)	Slip- radius (μm)									
90FM1 F	-0.17	-0.40	230	0.10	202	0.11	206	0.11	209	0.11	219	0.10	
90FM4 F	-0.37	-0.38	47	0.49	68	0.28	129	0.18	131	0.17	112	0.20	
90FM6 F	-0.16	-0.21	239	0.09	242	0.09	245	0.09	211	0.11	176	0.13	
90FM7 F	-0.15	-0.23	82	0.27	140	0.16	164	0.14	188	0.12	181	0.12	
90FM9 F	-0.27	-0.30	-	-	-	-	-	-	-	-	-	-	
90FM10 F	-0.09	-0.20	-	-	-	-	-	-	-	-	-	-	
90FZB1	-0.27	-0.23	8	2.94	17	1.30	14.44	1.56	26.33	0.86	35.73	0.63	
90FZB3	-0.31	-	16	1.4	70	0.32	68	0.3	62	0.36	65	0.34	
90FZ-5	-0.36	-0.18	7	3.09	14	1.67	12.50	1.52	9.63	2.35	16.03	1.41	
90FZ-2	-0.02	-0.19	42	0.54	38	0.60	37.38	0.60	35.49	0.64	28.44	0.79	

## 5.5 Discussion

This section starts with discussing the significance of stress on permeability of fault rocks. Then effects of confining stress on fault rock gas and liquid permeability are discussed. The section then provides a comparison in between published data on tight gas permeability and the fault rock permeability data collected during the present study. Moreover, the section integrates the permeability data measured at ambient stress and in-situ stress conditions. Finally, the section provides with main implications from results.

### 5.5.1 Influence of confining pressure on fault rock gas permeability

The stress sensitivity results of fault rock permeability are shown in **Figures 5.2 to 5.6**. These results indicates that the permeability decreases as the stress increases, the effect of changing confining stress on permeability is greater at lower confining stresses. A lower reduction in permeability is observed as the stress is increased to a higher stress level. This reduction in permeability is similar to that reported for tight sandstones (e.g. Brower and Morrow, 1985; Warpinski and Teufel, 1992; McPhee and Arthur, 1991; Evans et al., 1997; Rushing et al., 2003; Wibberley and Shimamoto, 2003; Byrnes et al., 2010). Ostensen (1983) investigated the tight rocks permeability and he argued that the reduction in permeability due to increase in confining stress is dominated by micro-fractures. Unloading of the samples could result in a widening of connected network of micro-fractures or the grain boundaries that provide a high permeability network. The higher stress sensitivity is observed at lower confining stresses (**Figure 5.7**) that could be the result of core damage effects due to stress relief following coring.

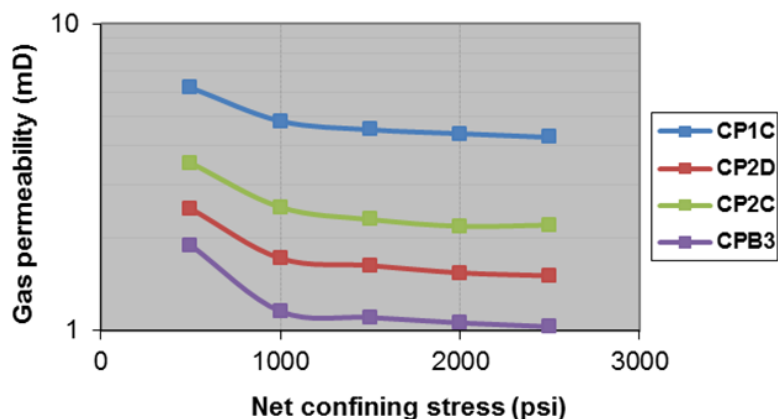


Figure 5.7 Plot showing the influence of confining stress on plugs permeability.

Core damage effects, where core samples are physically altered due to stress release during coring, has been reported by several authors (e.g. Holt and Kenter, 1992; Holt et al., 1992, 1994, 1998; Furre et al., 2007; Dong et al., 2010). The core samples alteration is possibly be the result of various processes such as overburden stress and pore pressure release, temperature decrease, exposure to drilling fluids, core plugs cutting and cleaning before performing laboratory experiments (e.g. Holt and Kenter, 1992). Holt and Kenter (1992) attempted to quantify core damage due to stress release by performing a number of experiments. Holt and Kenter (1992) created synthetic sandstone samples under stress in a tri-axial cell similar to reservoir stress. The specimen created was composed of similar grain size of reservoir sands. Holt and Kenter (1992) performed loading and unloading experiments and found that the pore volume decreases due to cement bond within the grains breaks during coring then grains reorientation occurs and micro cracks forms. This suggests that unloading of samples could result in changes to pore throat sizes and development of micro-cracks along the grain boundaries.

Some other studies, such as Carlson et al. (2011) also found that the decrease in permeability is higher at lower confining stresses, which could be the results of closure of micro-fractures. They also argued that one of the main causes of the micro-fracturing is stress-relief during coring and core sampling. Zoback and Byerlee (1974) reported that the effect of changing stress on permeability reduction in granite samples was due to the closure of micro-cracks. Moreover, Bai et al. (1997) found that the permeability of porous sedimentary rock is mainly related to the geometric dimensioning of grain particles and their arrangements.

The stress sensitivity of permeability could be characterized by stress exponents. The stress exponents calculated for each sample are summarized in **Table 5.4 and Table 5.7**. **Figure 5.8** shows the relationship between stress exponent and absolute gas permeability plotted on log-normal plot. This shows that the highest stress sensitivity of permeability refers to the highest stress exponent  $\gamma$ . For example the sample CP2E (**Table 5.3**) showed the highest stress exponent, micro fractures can be observed between grain boundaries of this sample, which resulted in large decrease in permeability due to stress increase samples. For this reason an unstressed thin sections of this sample was prepared for micro-fractures observation. The SEM images (**Figure**

5.9) showed the presence of grain-boundary micro-fractures. Therefore, the idea of effect of micro-fractures on rock permeability stress sensitivity is supported by the SEM image analysis.

Authors have also reported that the larger values of stress exponent correspond to the large decrease in permeability (e.g. David et al., 1994). Evans et al. (1997) performed laboratory experiments on outcrop fault from East Fork thrust fault Wyoming USA. They compiled stress exponents by curve fitting on permeability-stress data from the protolith, damaged zone, fault core and from clay-rich fault gouge permeability data (i.e. of those from Morrow et al., 1984). Evans et al. (1997) reported that exponents for damage zone and fault core were similar, while protolith resulted in larger stress exponent values, the samples which were observed with larger stress exponents were more likely sensitive to stress. These studies suggested that the permeability reduction that occurs in samples with large values of stress exponents might be the result of micro crack closure (e.g. David et al., 1994). Similarly the present study observed the micro-cracks formed within the grain boundaries which were in range of 0.1 to 2  $\mu\text{m}$  (Figure 5.9). The grain boundary micro cracks could easily be closed when stress is applied which is why these samples are more stress sensitive. It should be noted that different samples follow different stress sensitivity behaviour. The data plotted is derived from both reservoir cores from North Sea fields and samples from 90Fathom outcrop fault. It was observed (Figure 5.8) that the reservoir cores have a large negative exponent values than outcrop samples. This potentially reflects that reservoir cores are more sensitive to stress than outcrop samples possibly due to the core damage effects and formation of grain boundary microfractures.

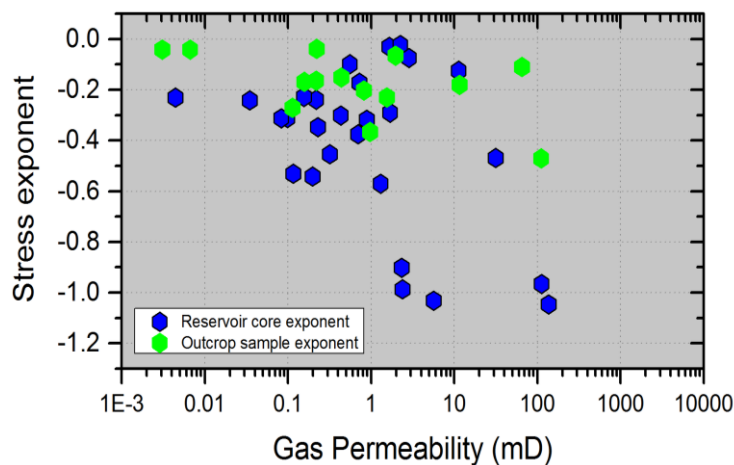


Figure 5.8 Plot showing the relationship between gas permeability measured at lowest stress (i.e. 500psi) and power law exponent.

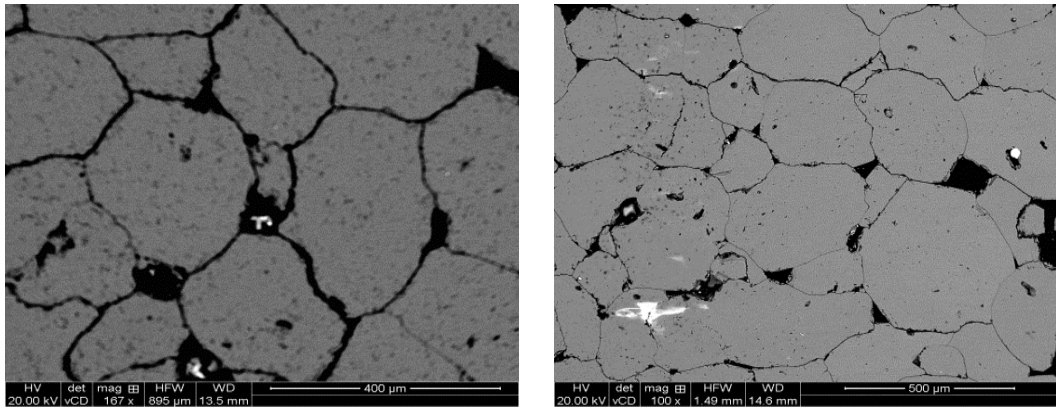


Figure 5.9 Typical BSEM images showing the micro-cracks observed within the fault rock core samples.

The permeability of rock samples depends upon the pore geometries, pore dimensions, flow conduits or cracks, connected pore networks (e.g. Gangi, 1976; Walsh and Brace, 1978; Ostensen, 1983; Yale, 1984; Thompson et al., 1987; Kwon et al., 2001). Relationships between permeability and effective stress have been developed based on flow through micro-cracks and cubic law of flow through fractures (e.g. Gangi, 1978; Walsh and Brace, 1978; Ostensen, 1983; David, 1993; David et al., 1994). A summary of selected models from literature are presented in **Table 5.8**. The differences in permeability stress sensitivity models (**Table 5.8**) are probably the difference in assumed shape of the cracks (e.g. Kwon et al., 2001). For example, Gangi (1978) model most likely fits well with nail-like crack shape and follow the power law trend with permeability and effective stress. Walsh (1981), as well as Brower and Morrow (1983), found that permeability stress sensitivity follows the exponential decline because the samples contain flat-cracks. Walls (1981) found that permeability decreases due to stress increase as a result of flat cracks closure. Sampath and Keighin (1982) reported that permeability is sensitive to stress because of presence of thin-film inter-granular cracks with an aperture in the order of  $\mu\text{m}$ . The micro cracks were observed from SEM image analysis and these micro fractures could easily be closed due to effective stress. Ostensen (1983) extensively studied permeability stress sensitivity of low permeability samples and believed that permeability could be controlled by micro cracks. He analysed SEM images and found small cracks separating the grain boundaries. Similarly the present study permeability reduces significantly due to the application of stress which suggests that flow was dominated by micro cracks. Davies and Davies (1999)

also found that the reduction in permeability due to increasing overburden stress is influenced to rocks with slotted pores. Although, the different microcrack shapes might explain the different stress sensitivities of sandstone samples (e.g. Tanikawa and Shimamoto, 2008). The fault rock permeability might be the more sensitive to stress due to grain boundary microfractures than the rock inter-granular pore volume.

Table 5.8 Table summarizes the selected permeability stress sensitivity models of low permeability tight rocks from literatures.

Summary of the selected permeability stress sensitivity Correlations		
S.No.	Author	Model /Correlation
1	Gangi, (1978)	$K/K_i = \left[1 - \left(\frac{\sigma}{\tau E}\right)^\xi\right]^3$
2	Walsh, (1981)	$\left(\frac{K}{K_o}\right)^{1/3} = 1 - \left(\frac{\sqrt{2h}}{a_o}\right) \ln\left(\frac{P}{P_o}\right)$
3	Ostensen, (1983)	$K^{1/2} = \ln(\sigma)$
4	Brower and Morrow, (1983)	$K = F_a F_b h^2 \phi / 18,$ $(K_p/K_o)^{1/3} = (1-8.01 \times 10^{-6}) p A_R$
5	David et al. (1994)	$K = K_o \exp[-\gamma(P_{eff} - P_o)]$
6	Evans et al. (1997)	$K = K_o \exp(-\gamma P_c)$

Moreover, to understand the effect of micro-fractures and overburden stress on permeability of fault rocks, it is essential to describe the equations and the changes of the parameters under different conditions. **Figure 5.10** shows an idealized diagram of parallel plate fracture model. The permeability relationship was generated based on a dual porosity-permeability model. In particular, it is assumed that the rock is composed of matrix porosity and fracture porosity. The total permeability from both fracture and matrix can be represented as:

$$k_T = \frac{k_m \phi_m + k_f \phi_f}{\phi_m + \phi_f} \quad \text{Eq. (5-6)}$$

where,  $k_m$ , and  $k_f$  are the matrix and fracture permeabilities respectively,  $\phi_m$  and  $\phi_f$  are the matrix and fracture porosities respectively.

The permeability of a set of fractures,  $k_{fs}$ , can be calculated using the cubic flow law:

$$k_{fs} = \frac{fn \times f_w^2}{12} \quad \text{Eq. (5-7)}$$

where  $f_w$  is the fracture width and  $f_n$  is the number of fractures. If fracture width is incorporated in  $\mu\text{m}$ ,  $k_{fs}$  will be in  $10^{-12} \text{ m}^2$  or 1 Darcy and  $f_n$  is:

$$f_w = \frac{A^{0.5} \phi_f}{fn} \quad \text{Eq. (5-8)}$$

where  $A$  is the cross sectional area of the sample. In addition to Equation (5-8) the fracture permeability could be obtained by using the following equation,

$$K_f = \frac{K_{av}A - K_m(A-w)}{wl} \quad \text{Eq. (5-9)}$$

where  $K_{av}$  is the average permeability of fracture and matrix that was obtained during flow experiments in the laboratory using fractured and un-fractured core samples,  $A$  is the crosssectional area,  $K_m$  is the matrix permeability and  $w$  is the width of fracture. The fracture permeability could be obtained by combining Darcy's flow equation and viscous forces assuming a parallel plate model,

$$K_f = 8.45 \times 10^9 w^2 \quad \text{Eq. (5-10)}$$

Combining above Equations (5-10) and Equation (5-11) to determine  $w$ :

$$8.45 \times 10^9 w^3 l - K_{av}A + K_m(A - w) = 0 \quad \text{Eq. (5-11)}$$

It is also important to find out the contribution of rate of flow from matrix as well as from fractures separately. The contribution of flow from matrix and fracture systems could be described based on the Darcys's Law,

$$q_m = \frac{K_m A \Delta p}{\mu L} \quad \text{Eq. (5-12)}$$

Where  $q_m$ , is the matrix flow rate,  $A$  is the crosssectional area,  $\Delta p$  is the pressure drop,  $\mu$  is the viscosity of flowing fluid and  $L$  is the length of the sample.

$$q_f = 9.86 \times 10^{-9} \frac{w^3 l \Delta p}{12 \mu L} \quad \text{Eq. (5-13)}$$

In above equation (5-13)  $q_f$  is the flow rate through fractures.

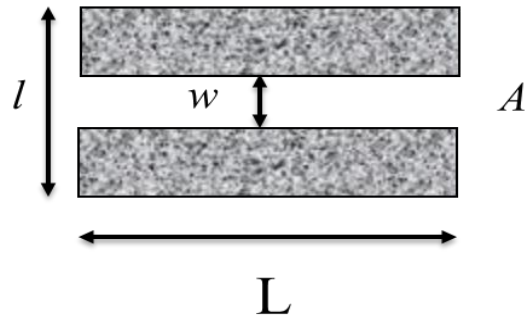


Figure 5.10 Diagram is the illustration of rock sample representing parallel plate fracture and matrix system.

Based on the above discussion, the permeability was modelled by considering number of fractures present within the samples. Two different cases were considered for permeability estimation, in which one sample contains the fractures width of  $1\ \mu\text{m}$  and second sample contains  $0.5\ \mu\text{m}$  wide fractures. The fracture spacing estimated from SEM micrograph was after every  $200\ \mu\text{m}$ , which is the average grain-size. It was considered that the fracture is open at ambient stress measurements and closed at in situ stresses. The permeability in both cases of open and closed fractures were modelled using the equations presented above and are plotted as a function of stress. The experimental results are also plotted together with the modelled data. The model results at ambient stress are nearly identical to the experimental results (**Figure 5.11**), which supports the idea that samples with microfractures could result in dominant part of flow of fluid at low stress, consequently the higher permeability values could be obtained at lower stress conditions. As the stress increased, micro-fractures become closed resulting in decreased permeability. The flow of fluid at higher stress of up to in-situ then will be only expected from intergranular pores, which might be equivalent to theoretically derived pores size from slip parameters. It was also observed from the experimental results that permeability at in-situ stress of  $5000\ \text{psi}$  is much lower (**Figure 5.11**) due to closing of the microfractures. These results suggest that the permeability and fracture width has a significant effect by changing stresses.

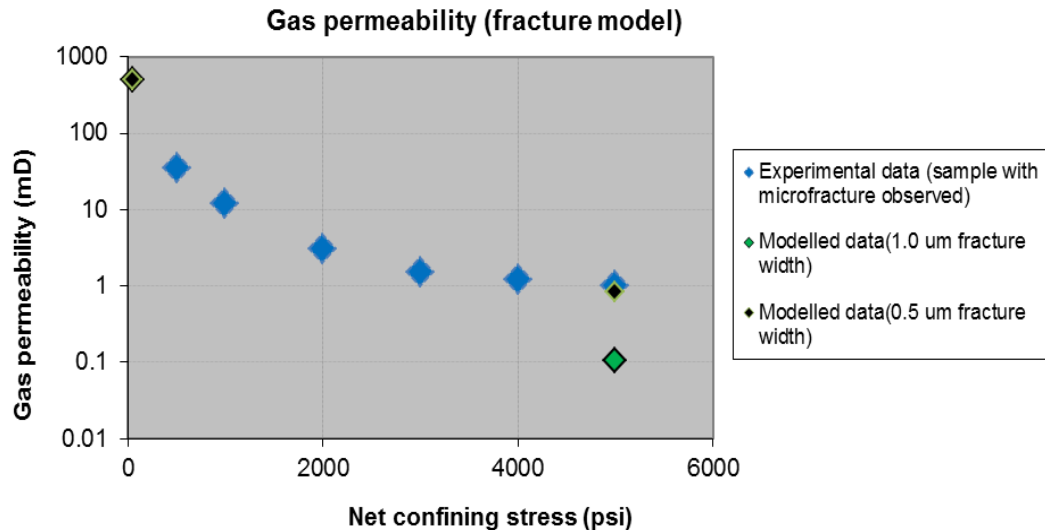


Figure 5.11 Plot is the permeability of sample based on experimental results. Micro fractures were observed within the thin section of samples. Permeability largely decreases as stress increases.

Much of the stress sensitivity observed in the laboratory is likely due to the core damage. However, experiments were conducted in which samples were placed under reservoir stress and pore pressure conditions. The results presented in **Figure 5.12a** are without corrected for slippage effects and **Figure 5.12b** are corrected for gas slippage effects. The measured permeability increases when the pore pressure was reduced at *in situ* confining stress, due to increased gas slippage (**Figure 5.12a**). In other words, the increase in gas slippage due to the pore pressure reduction at in-situ stress increases the apparent permeability for high net confining stress. Conversely, the Klinkenberg corrected permeability was reduced by the increasing net stress. The net effect is reduction in measured permeability with increasing net stress at low net stress levels, where slippage is low due to the high pore pressure, due to the reduction of slip corrected permeability. At lower pore pressures, higher net stresses, the increased flow due to slippage compensates the reduction of Klinkenberg corrected permeability and measured permeabilities increases.

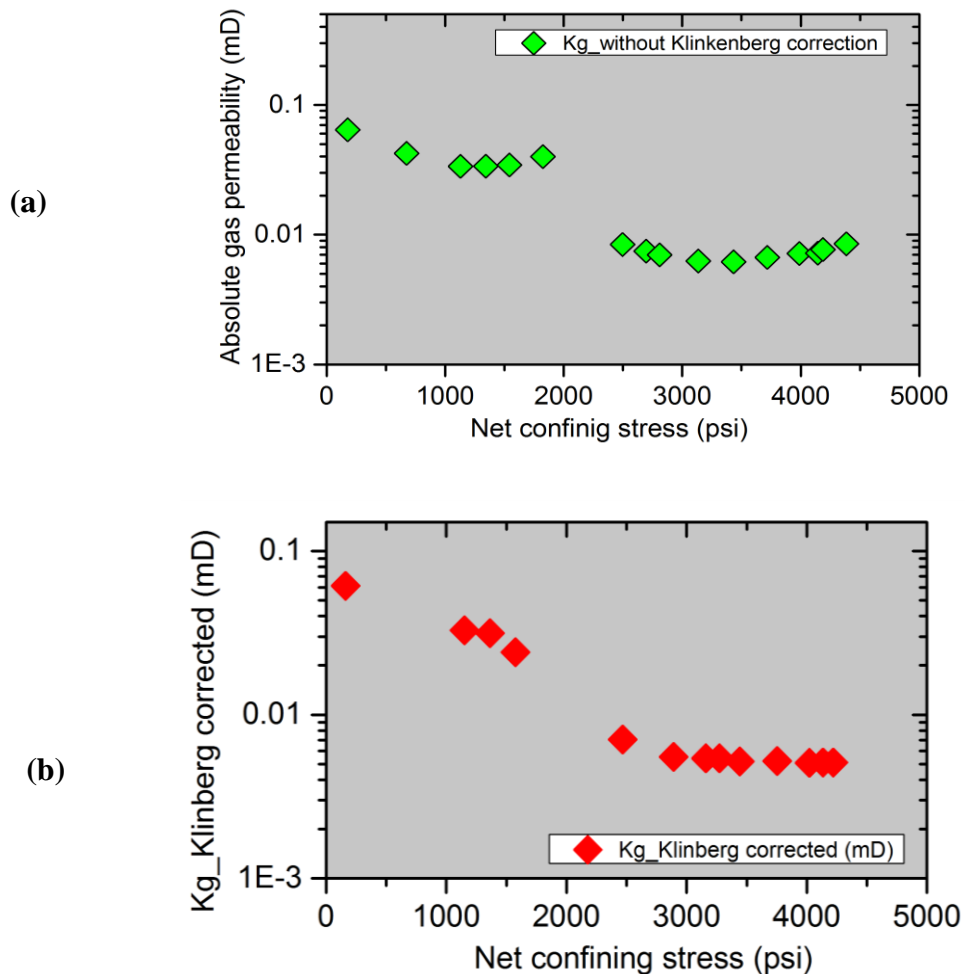


Figure 5.12 Illustration is the stress-dependent permeability of fault rock, (a) absolute gas permeability without Klinkenberg correction (b) is the gas permeability corrected for Klinkenberg effects.

**Figure 5.13** shows the permeability of outcrop samples from 90 Fathom Fault and Miri airport road fault samples plotted together with North Sea reservoir core samples. Measurements made at low stress i.e. 500 psi and high stress up to in-situ stress of 5000 psi. The permeability of the outcrop samples appears to be less stress sensitive than that of the reservoir core samples. This indicates that the stress sensitivity observed in the laboratory is likely due to the core damage effects. In general, the permeability to gas measured at 500psi is around double to that measured at 5000psi. These the results indicate that permeability derived from outcrop samples could still be reliable to use for reservoir modelling and analysis.

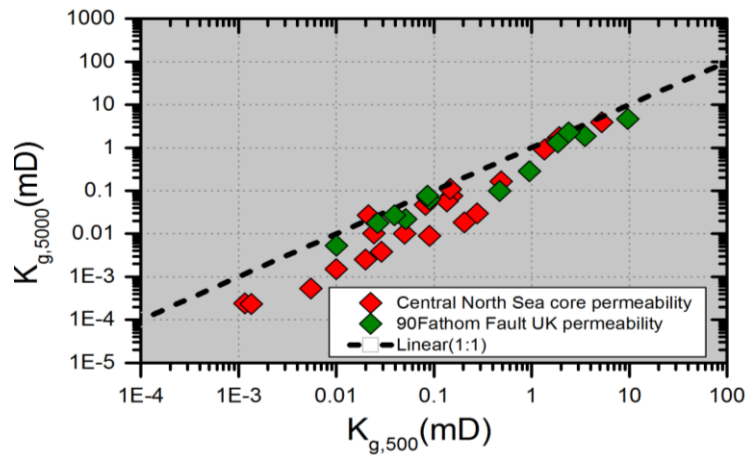


Figure 5.13 Crossplot of gas permeability of fault rocks measured at 500 psi confining stress against permeability measured at 5000psi confining stress.

**Figure 5.14** shows the rock mineralogy and permeability stress sensitivity, which indicates that there is no relation in between rock mineralogy and the fault rock permeability stress sensitivity. The samples even with similar amount of quartz and clays have shown different stress dependency behavior. Similar observations were also made by Pathi (2008) who investigated samples of organic-rich Woodford shale from western Canada and showed that there is no significant role of mineralogy in controlling the stress sensitive of the permeability. he. They also observed that the samples even with similar percentages of clay and quartz showed different stress sensitivity. Chalmers et al. (2012) suggested that the stress sensitivity to permeability could be related to rock heterogeneity. They found that the more the rock heterogeneous more will be the sensitive to stress. Therefore, it is clear from the results obtained that the mineralogy is not the only reason to describe the fault rock permeability stress sensitivity.

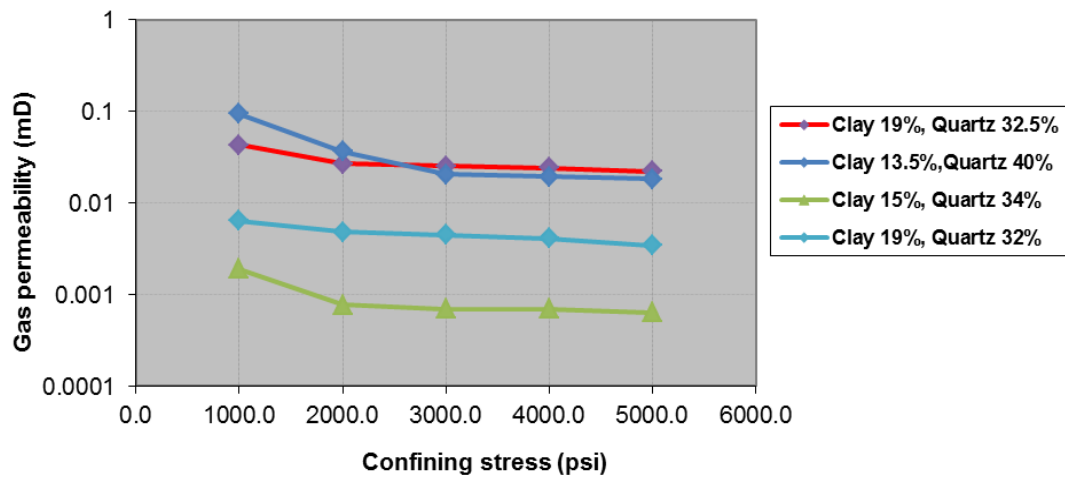


Figure 5.14 The plot is showing the rock mineralogy and absolute gas permeability stress sensitivity from Central North Sea.

Overall, the results suggests that the core samples permeability under in-situ stress conditions might be less sensitive to stress potentially due to the presence of microfractures formed as a result of stress release. Samples from outcrop are less stress sensitive than those from reservoir core potentially due to the presence of microfractures formed. An implication of this result is that the permeability of fault rocks is not likely to be significantly stress sensitive in the subsurface unless reactivated. It was observed that low permeability samples could be affected more due to core damage effects than high permeability samples. To reduce uncertainties related to laboratory measurements of permeability stress sensitivity core damage effects must be taken into account in interpreting the results. For example, the permeability measurements conducted in laboratory might be different than sub-surface (in-situ) reservoir conditions that may overestimate the actual permeability of reservoir at subsurface conditions. It should also be noted that every fault rock might experiences different damage and stress effects so each sample should be investigated separately.

### 5.5.2 Klinkenberg slip factor

The stress sensitivity of fault rock permeability could be related to the slip radius. Slip radius is an indication of pore dimension, as the gas flow model is based on flow in a rectangular duct with smooth walls (e.g. Beskok and Karniadakis, 1999). **Figure 5.15** shows the two different scenarios of slip factor at low and at high confining stress. This shows that as the confining stress increases gas slip factor increases which results in reduced size of the slippage-radius (e.g. Klinkenberg, 1941). In some cases, gas

slippage factor showed an unexpected increase with increasing stress. For example, the  $b$  factor of 90FBZ1 sample increased by 4 fold between 1000psi and 5000 psi. Whereas, the  $b$  factor of the sample 90FM4 increased by a 3 factors between 1000psi and 5000psi. This increase in gas slip factor is due to stress increase could be the experimental error.

The slippage radius was estimated from gas slip parameters at each confining stress. The calculated slip radius obtained from gas slippage parameters are plotted in **Figure 5.16**. The results show that as the confining stress increases the slippage radius decreases and is evident from **Figure 5.16**. The reduction in slippage radius due to stress could be the result of closing off the flow paths or flow channels (e.g. Sampath and Keighin, 1982). The values of slippage radius at low confining stress are similar in dimensions to the width of the micro-cracks found along the grain boundaries from SEM images **Figure 5.15**. At higher confining stress it is assumed that micro-fractures are completely closed consequently the rock pore size decreases. Therefore, the fluid flow through these pores reduces at in-situ stress resulting in permeability reduction.

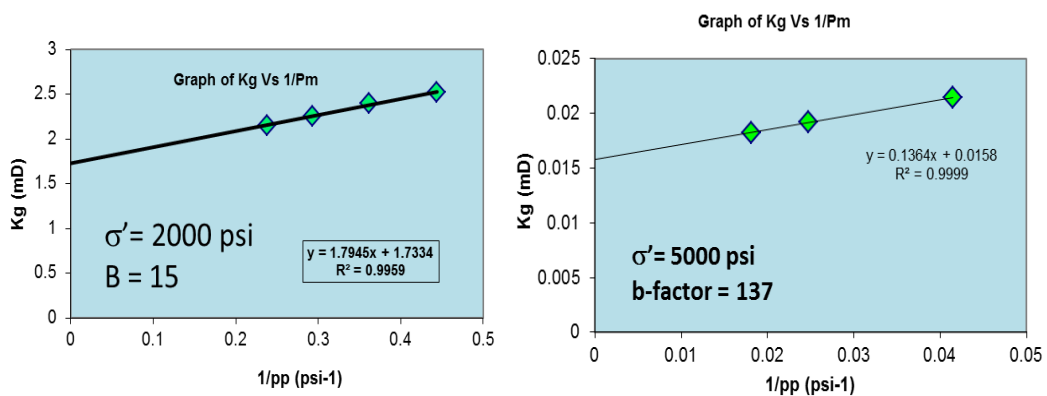


Figure 5.15 Effect of confining stress on gas slippage factor during gas permeability experiments.

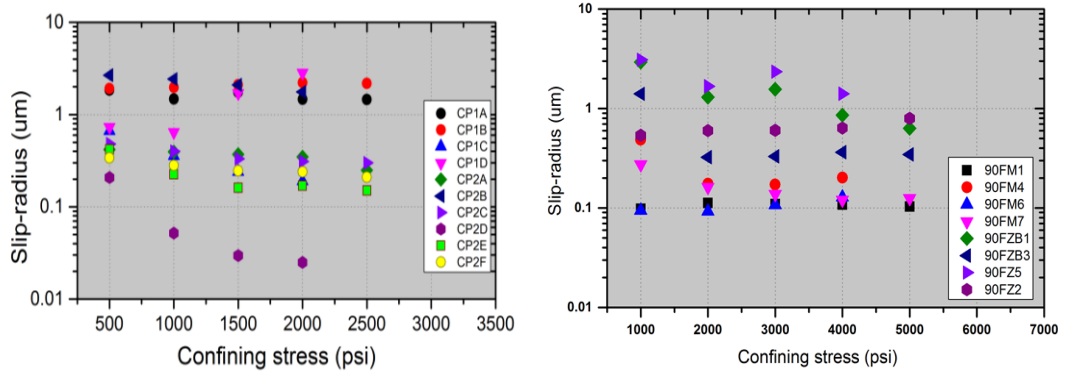


Figure 5.16 Plot of gas slippage radius vs confining stress for fault rock samples, derived from gas permeability results of central North Sea reservoir core samples (left-side). The Plot of slip-radius versus confining stress data is from 90 Fathom fault samples (right-side).

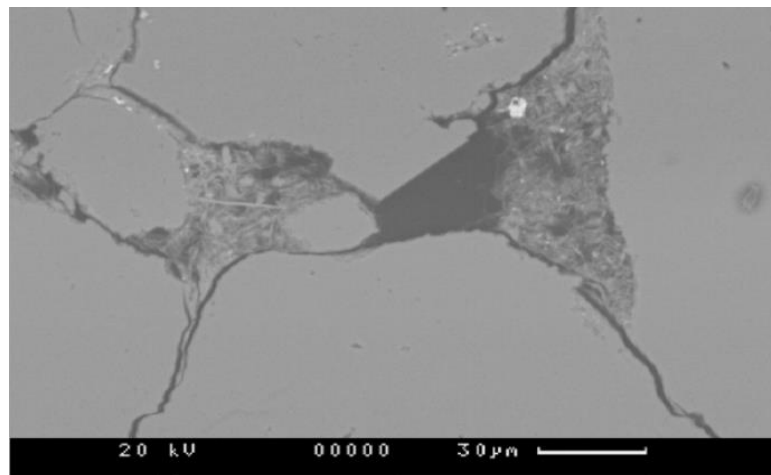


Figure 5.17 SEM thin section images show the sample contains small scale (0.1 to 0.5  $\mu\text{m}$ ) wide fractures at grain boundaries.

**Figure 5.18** shows the relationship between gas slippage factor and gas permeability – a general trend of decreasing gas slippage values with increasing gas permeability can be seen for fault rock data but there is a great deal of spread in the data, rendering it impractical for predictive purposes. The gas slippage factor data obtained during the present study were compared with those estimated from published models. The estimated slippage factor values from empirical models suggest that only few model predictions are consistent with experimental data (**Figure 5.18**). Therefore, it is clear that the models used for tight rocks predictions could not be applied for fault rocks one reason could be the fault rock heterogeneity.

Furthermore, there were some improved models published on gas slippage parameter estimation, such as McPhee and Arthur (1991) provided a model by incorporating porosity term. McPhee and Arthur (1991) correlation uses an exponent value (-0.53) which is close to that of theoretically derived correlation of Florence et al. (2007) which has an exponent value of (-0.50). Hence, the introduction of porosity term in model of McPhee and Arthur (1991) has not provided reproduction of experimental gas slippage factor for fault rock samples. The two empirical models of tight sands (e.g. Heid et al., 1952; Jones and Owens, 1980) provided estimations of the *b*-factor which are slightly close to the experimental data compared to the other empirical models. The scatter in empirical relationships between slippage factor and permeability (**Figure 5.18**) indicates that it is unsafe to use such correlations to correct permeability measurements conducted on low permeability fault sample at low pore pressures. It is therefore recommended that either *b*-values should be calculated for each sample at each stress point (ambient or in-situ stress in permeability experiments) or a very high gas pressure (>1000 psi) is used to reduce the magnitude of the slippage correction that needs to be applied.

The gas permeability of the fault rock was plotted against the slippage radius that follows a declining trend with decreasing pore radius as highlighted with shaded area. The data plotted also has shown some scatter (**Figure 5.19**). The scatter in data might reflect the permeability heterogeneity. Some authors (e.g. Heid et al., 1951; McPhee and Arthur, 1991) have suggested that the scatter in the relation between pore size and permeability could be the experimental errors. In carbonate rock samples having high permeability and high *b*-factor values, smaller pore radius has also been observed by Funk et al. (1989). They believed that high *b* factor was related to the presence pores with greater than average pore size in those samples. Similarly, the fault rocks are also heterogeneous and their permeability values could be scattered once plotted against their slip radius.

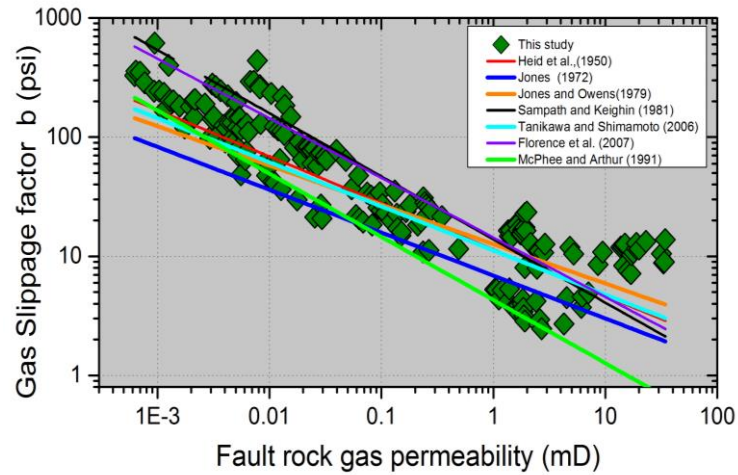


Figure 5.18 Comparison between gas slippage factors (*b*-factor) of fault rock samples calculated and estimated using different published correlations. The estimated slip factor and slip factor obtained from experimental data are both plotted against measured absolute gas permeability.

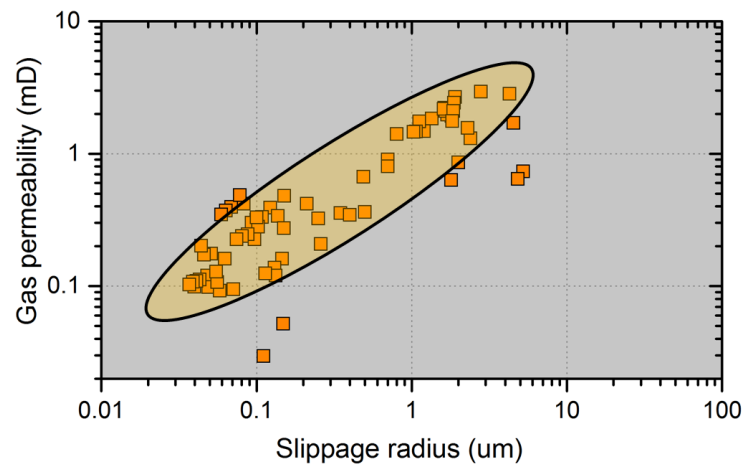


Figure 5.19 Cross plot of the fault rock in-situ absolute gas permeability and pore radius derived from gas-slippage.

### 5.5.3 Comparison between fault rock and tight gas sand permeability stress sensitivity

Moreover, the fault rock permeability stress sensitivity was compared to that of the permeability results of tight gas sandstones published by Byrnes et al. (2009). As discussed above, there is very small amount of data on stress dependent permeability of fault rocks, therefore the tight gas sandstones properties have been used as an analogue (e.g. Zijlstra et al., 2007).

The permeability of all samples tested reduced as confining pressure was increased. The permeability measured at in situ stress (~5000psi) was up to a factor of 10 lower than when measured at typical pressures (i.e. 500psi) (**Figure 5.20**). Measurements undertaken during the present study were conducted at high pore pressures or corrected for Klinkenberg slippage effects. So the present study data appears to show less sensitive to stress than the Byrnes et al. (2009) data (**Figure 5.20**) but this simply reflects that the low stress measurements performed by Byrnes et al. (2009) were not Klinkenberg corrected. The stress dependence of the permeability increases with decreasing absolute permeability of samples. Overall, it appears that the extent of stress dependence of fault rock permeability is slightly less than to that of the tight gas sandstone reservoirs.

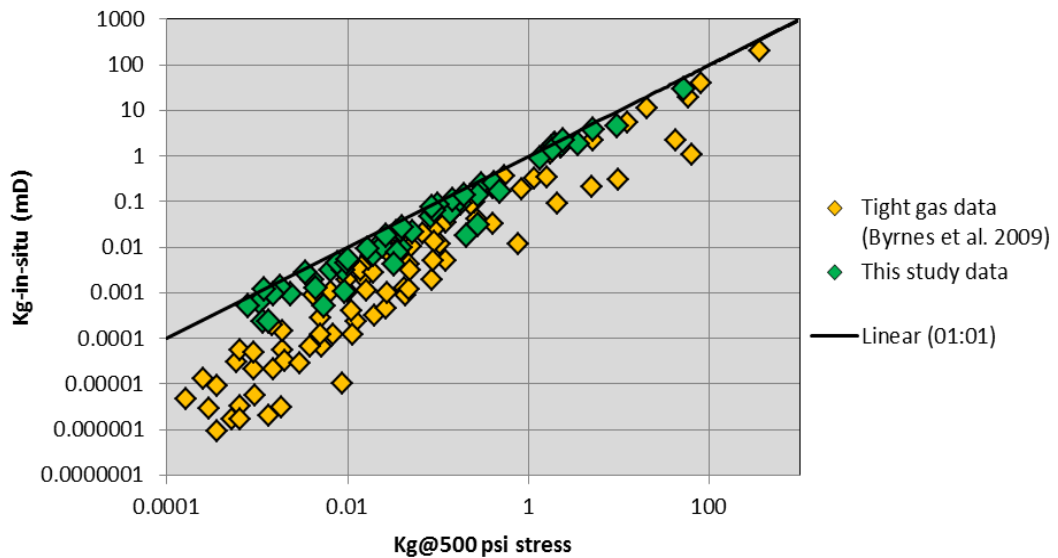


Figure 5.20 Plot of the gas permeability of fault rocks at 500psi confining pressure against the permeability at 5000psi confining pressure for fault rock and tight gas sandstone samples, tight gas data is taken from Byrnes et al. (2009).

#### 5.5.4 Influence of confining pressure on liquid permeability

Brine and distilled water permeability were conducted on the same samples as these were used previously for gas permeability measurements. **Figure 5.21** provides the liquid permeability decreases by increasing stress from samples analysed. The results showed that the liquid permeability for all fault rock samples decreases with increase of confining stress. The liquid permeability is lower than gas permeability for all studied fault rock samples (**Figure.5.22**). On average the liquid permeability reduced by an order of magnitude. The reduction in liquid permeability due to stress increase was also observed by other authors in tight rocks (e.g. Wei et al., 1986; Morrow et al. 1981, 1984; Jones, 1988; Jones et al., 2001). Similar to gas permeability stress sensitivity, most of the reduction in brine and distilled water permeability took place over the initial increase of stress (**Figure 5.21**). However, the characteristic nature of gas and liquid permeability stress sensitivity are different. This could be due to experimental errors or experiments on liquid permeability may require longer equilibration times (Grattoni, pers.com.). Morrow *et al.* (1981) conducted experiments on fault gouge also found that permeability of fault rocks reduced by increasing stress. The permeability studies previously been conducted on clay-bearing fault gouges from a borehole on the San Andreas Fault in California by Morrow *et al.* (1981). The mineralogy of the samples consists of montmorillonite, mixed-layer clays, illite, kaolinite and chlorite. The samples studied were crushed up and mixed into slurry with distilled water, due to mixing of slurry with water, samples did not retain original fabrics. Although, they performed measurements on a wide range of fault rock such as phyllosilicate-rich and non-phyllosilicate clastic samples as a function of effective pressure. The results reported showed that these were sensitive to stress under the stress applied for measurement.

The liquid permeability measured has shown decrease by changing NaCl concentrations (**Figure 5.21**). Apart from stress sensitivity differences in gas and liquid permeability there were few other mechanisms by which permeability of samples differs. One reason for the difference in gas and brine permeability could be a layer of bound water on the mineral surface that reduces the pore throat size (e.g. Heid et al. 1950; Luffel et al. 1993; Andreassen & Fabricius 2010). The reduction in distilled water permeability observed is more likely be due to physicochemical interactions of the

water with swelling clay minerals and dispersion of fine particles (e.g. Khilar and Fogler 1983; Wei et al., 1986). Generally, the flow of water through rock pore spaces exhibits Newtonian behaviour (Tanikawa and Shimamoto, 2008). However, if pore spaces are very small gas does not adhere to the pore walls as liquid does, due to this it causes additional pressure drop and lower flow rate as well as lower permeability (e.g. Tanikawa and Shimamoto, 2008). Faulkner and Rutter (2000) measured argon gas and water permeability on clay rich fault gouge and suggested that the permeability measured with gas is about one order of magnitude larger than water permeability. The present study data on fault rock samples in general is also consistent with that of the Faulkner and Rutter (2000) and Tanikawa and Shimamoto (2008). Faulkner and Rutter (2000) argued that the difference in liquid and gas permeability is due to reactions of distilled water with clay minerals caused adhesion of water molecules to the rock surfaces. There are several other reasons to describe the discrepancies between gas and brine permeability. As authors suggests that differences could be the results of quartz precipitation within narrow pores along cracks (e.g. Vaughan et al., 1986).

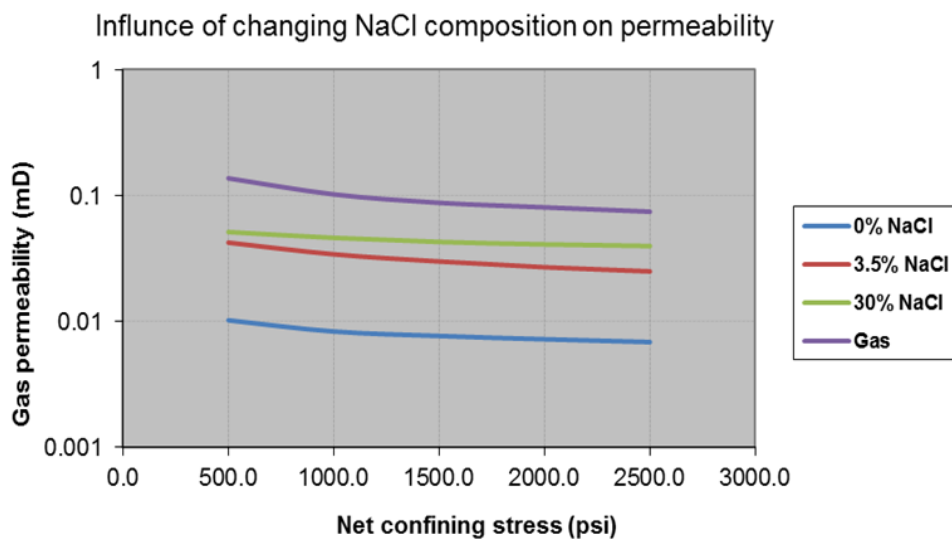


Figure 5.21 The change in liquid permeability caused by changing pore fluids and stress.

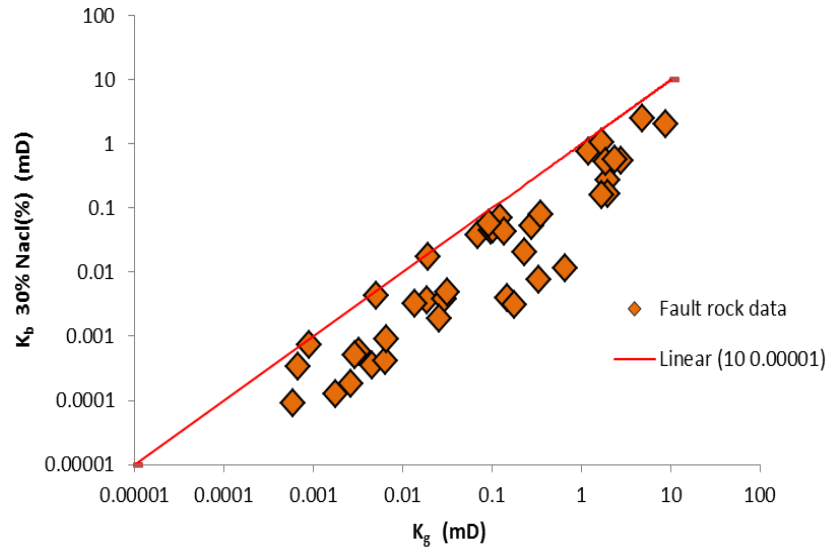


Figure 5.22 Gas and brine permeability of fault rock samples studied.

As discussed, the stress sensitivity of gas permeability could be characterized by stress exponent, similarly the brine permeability stress sensitivity could be related to stress exponent. The higher the stress exponent, larger will be the decrease in permeability due to increasing stress. The stress exponents plotted against brine permeability (**Figure 5.23**) the stress exponents are higher for reservoir core samples from central North Sea. Other the other hand samples from 90 Fathom fault outcrop are less stress sensitive than those from core potentially due to the presence of microfractures formed as a result of stress release (e.g. Holt and Kenter, 1992; Holt et al.,1998; Furre et al., 2007). The microfractures from SEM image analysis were observed in few samples that's why these samples appear to be more sensitive to stress and resulted in lager stress exponents. It has been argued that samples collected from outcrop may result in higher permeabilities than samples with same lithology collected from the subsurface reservoirs (Morrow and Lockner 1994).

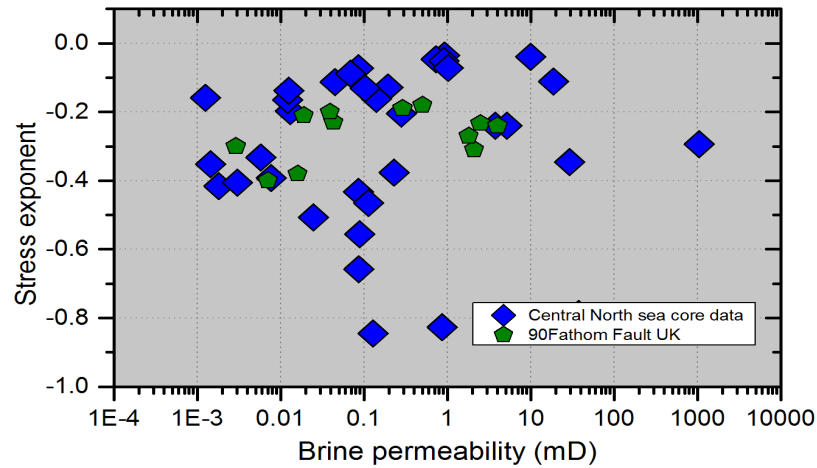


Figure 5.23 Plot showing the relationship between brine permeability measured at lowest stress (i.e. 500psi) and power law exponent.

The brine permeability measured at 500 psi stress plotted against the permeability measured at in-situ stress of 5000 psi appears to be stress sensitive (**Figure 5.24**). Similar to gas permeability, the brine permeability of reservoir core samples from central North Sea have shown slightly more stress sensitivity than outcrop samples of 90 Fathom fault UK, which reflects that core samples might have affected by core damage effects.

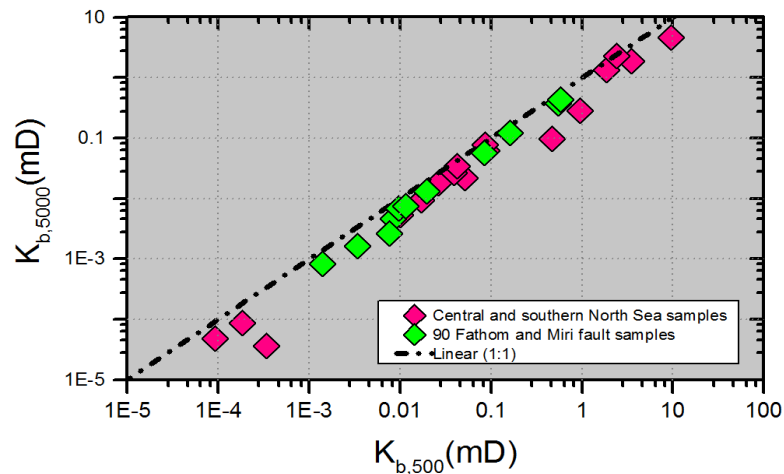


Figure 5.24 Plot of the brine permeability of fault rocks at 500psi confining pressure against the permeability at 5000psi confining pressure for fault rock. The data plotted is from 90 Fathom fault UK, Mirri airport road fault exposure and reservoir core samples from Central North Sea.

Gas and brine permeability stress exponents are plotted in **Figure 5.25** against their permeability at low stress of i.e. 500psi to see the difference in stress sensitivity. **Figure**

5.25 shows that gas permeability is slightly more sensitive to stress than liquid permeability because of the stress sensitivity exponents in gas permeability appears to be higher than liquid permeability.

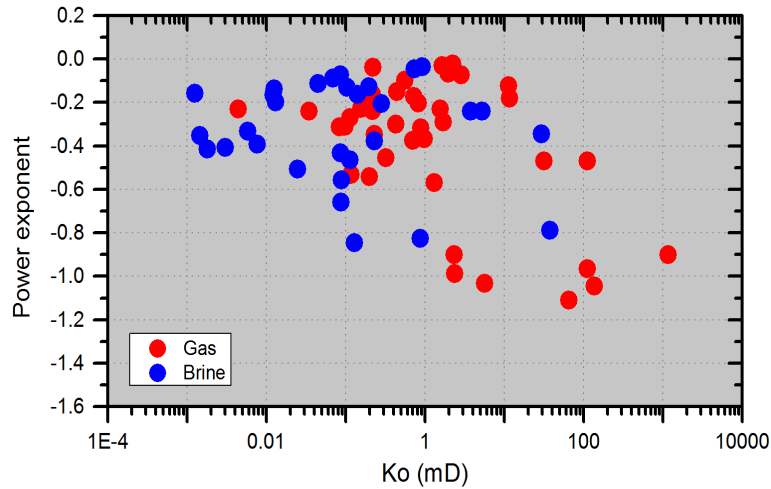


Figure 5.25 Illustration shows the relationship between power law exponent and fault rock gas and brine permeability data from both reservoir core samples and 90 Fathom fault UK, Mirri airport road outcrop fault.

### 5.5.5 Integration of ambient and in-situ stress permeability

This section incorporates the laboratory permeability results from this chapter and those presented in **Chapter 4** of fault rocks using two different types of samples i.e. rectangular blocks and plugs. The primary objective of this was to investigate the accuracy of the traditional technique of permeability measurements. This was performed by comparing results from plugs made at different stress levels and rectangular block samples permeability measured at ambient stress conditions.

The permeability of samples were measured on two different types of samples, the plugs permeability was measured at different levels of stress and fault rectilinear samples were permeability measured at ambient stress. The permeability of all samples were measured first with gas then gradually changing with brine of composition from 30% to 3.5% (NaCl). Finally, the distilled water was used to measure the permeability. The gas, brine and distilled water permeability results are presented in **Figure 5.26** from two different types of samples. These permeability results show that at lower stress, the permeability is higher, as stress increases the permeability has shown gradual reduction,

this is obvious and it was expected. However, in some case (**Figure 5.27**), it should be noted that permeability measurements conducted at very low stress (70 psi) were sometimes lower than those conducted at higher confining pressure (>500 psi). The reason for this counterintuitive result is that different samples were used for the very low permeability measurements so the differences probably reflect the heterogeneity of the structure of the fault rocks.

**Figure 5.28** shows the relationship between ambient stress distilled water permeability of fault rock against the in-situ stress brine permeability. The comparisons between distilled water permeability measurements made at ambient stress conditions and the formation compatible (NaCl) brine permeability measured at in-situ stress, these results suggests that permeability in both cases are nearly identical. The two bad laboratory practices partially cancel the effects of each other. Therefore the permeability data reported by Fisher and Knipe (2001) measured using distilled water as permeant and measured at ambient stress present within the published data base on fault rock is still useful for fault seal analysis.

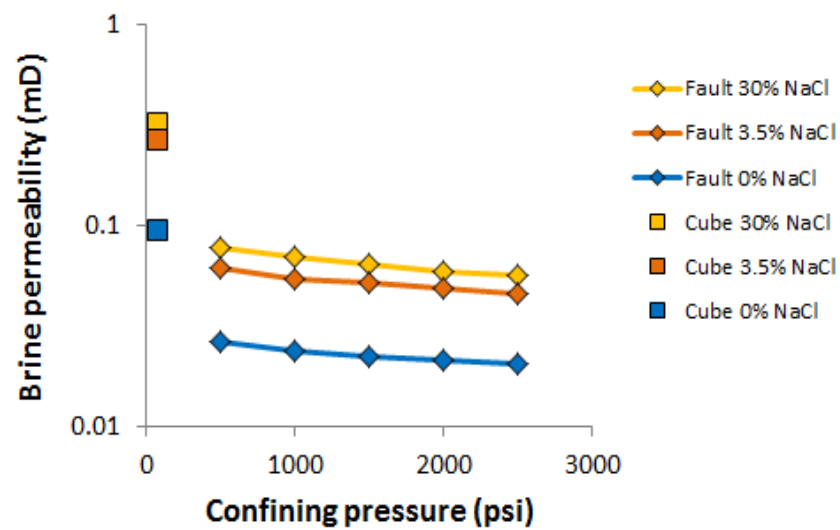


*Figure 5.26 Permeability of rectilinear fault samples measured at (70psi stress) and fault plug samples measured at different stress conditions.*

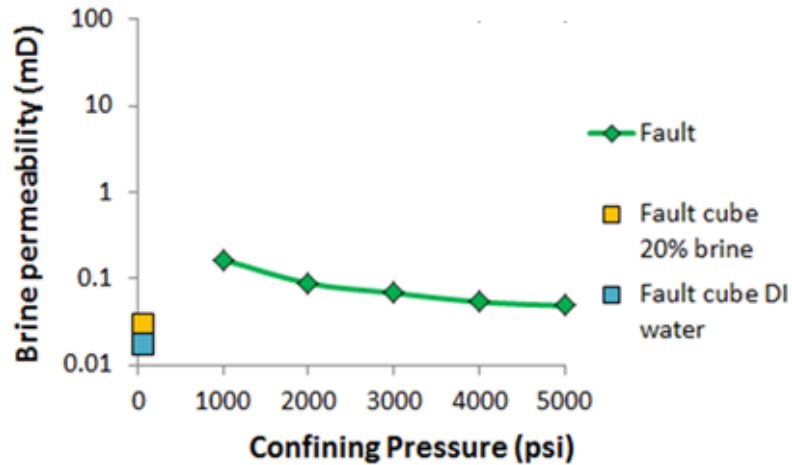


Figure 5.27 Plot of gas permeability vs confining pressure for a fault rock sample. Note that the low pressure measurement has the lowest permeability. This is rare and is an artefact resulting from using a different sample for the ultralow permeability measurement. The lower kg value reflects sample heterogeneity.

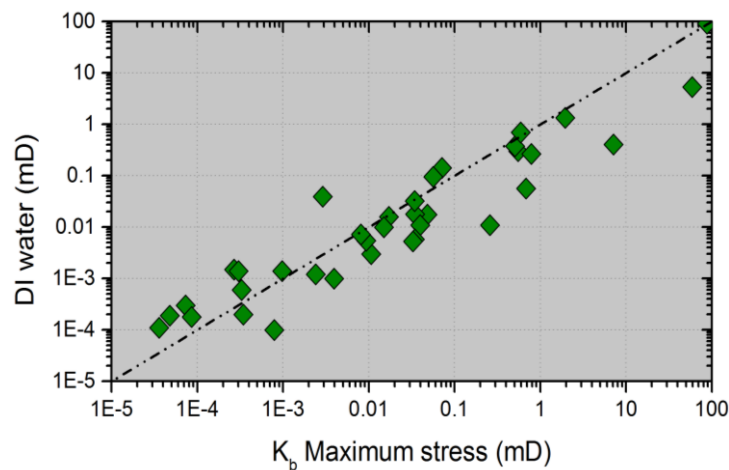


Figure 5.28 Plot of the permeability measured to distilled water for fault rock at ambient stress against brine permeability measurements made at maximum stress.

### 5.5.6 Implications of the results

The experiments conducted on fault rock permeability shows that the absolute permeability of fault rock samples is very stress dependent so care must be taken when applying results for simulation modelling purposes. The liquid permeability data obtained at low stress on average is ten times higher than measurements made at in-situ stress condition of reservoir. In contrast the gas permeability measured at ambient

conditions is on average 15 times greater than that measured at in situ stress for fault rock samples taken from reservoir cores. Moreover, the stress dependency of fault rocks samples taken from outcrop is less than those obtained from reservoir core samples. This suggests that the stress dependence of the permeability of faults from core is an artefact result of cooling or stress relaxation. This observation shows that outcrop data could still be reliable to use for reservoir modelling.

#### 2.8.1.6 Implications for the use of published data

A key aim of this chapter was to test how fault permeability measurements differ from those which are generally present within the published data (e.g. Fisher and Knipe, 2001) because these were measured under inappropriate experimental conditions i.e. measured at low stresses using distilled water as permeant. Therefore, the results obtained during present study were compared with those previously published by Fisher and Knipe (2001) (**Figure 5.29**). From **Figure 5.29**, it is observed that the permeability measured at ambient stress using distilled water gives lower permeability values, whereas the permeability measured at in-situ stress with formation compatible fluid i.e. brine NaCl also gives lower values, therefore the effect of low stress distilled water measurements and high stress brine permeability measurements partially cancel each other out. Consequently, it is observed from the present study analysis that the data reported by Fisher and Knipe (2001) still could be reliable to use for analysis of fault seal.

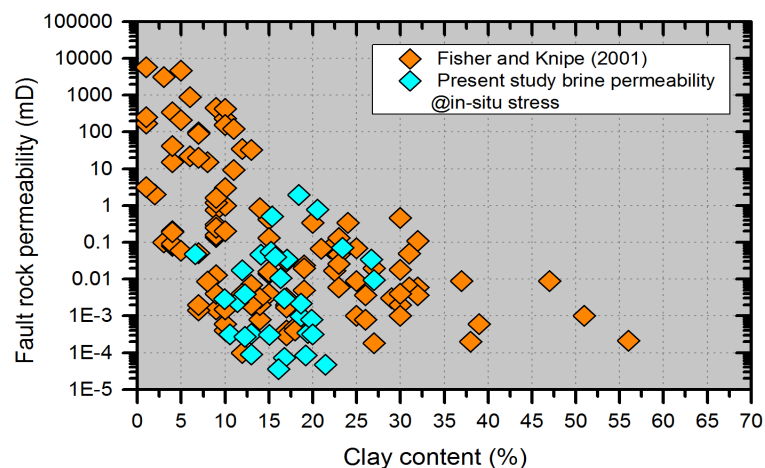


Figure 5.29 Plot of permeability vs clay content for distilled water permeability from Fisher and Knipe (2001) at ambient stress and brine permeabilities from this study at in-situ stress.

## 5.6 Conclusion

Experiments have been conducted to investigate the stress sensitivity of fault rock gas and liquid permeability; Klinkenberg corrections were applied to all gas permeability measurements. The combined effect of gas slippage and permeability reduction due to stress was analysed and following conclusions were drawn.

- At low confining stresses, the permeability of the fault rock core samples showed high stress sensitivity, whereas at higher confining stresses the permeability was less pronounced to stress. This might be due to the core damage effects, and the micro fractures formed due to stress release and were observed from SEM images of the samples. The pore radius calculated from gas slippage parameters at low confining pressures was in the same order of magnitude as the micro fracture width. The pore radius was reduced at higher confining stresses which reflect that micro fractures are closed due to stress application. The permeability estimated from simple fracture model also supported the idea that at ambient stress there was high flow as well as higher permeability due to microfractures.
- The absolute gas and liquid permeability of fault rocks obtained from core and outcrop is sensitive to the stress conditions under which it is measured. Overall, the stress sensitivity of fault rocks is similar to tight gas data of Byrnes et al. (2009). Although, some fault rocks have shown less stress sensitivity than tight gas sandstones.
- Samples from outcrop shown less stress sensitivity than those from reservoir core samples this potentially reflects the presence of microfractures formed as a result of stress release. The micro-fractures were also observed from thin sections of core samples.
- The published fault rock permeability data (e.g. Fisher and Knipe, 2001) may not be as wildly inaccurate because the use of distilled water (which gives lower permeability than formation water) and low stresses (which give higher permeability than high stress measurements) partially cancel one another out. Therefore it is still safe to use the data sets reported by Fisher and Knipe (2001) for modelling and making predictions for fault seal analysis.

- At *in situ* stress, the pore pressure reduction initially reduced the measured permeability by increasing the net stress and thus reducing the absolute permeability. As the pore pressure was reduced further, the increased contribution of gas slippage increased the measured permeability. This indicates that large drawdowns would enhance the rate of gas production within these reservoirs.
- It was attempted to discover the relation between permeability stress sensitivity and rock mineralogy. Although it was found that mineral composition is not the primary reason to control the permeability stress sensitivity, the samples even with similar mineral composition have shown different stress sensitivity.
- The scatter in permeability and slippage factor indicated that it is unsafe to use empirical correlations to correct permeability measurements conducted on low permeability fault sample at low pore pressures.

# 6 Multi-phase flow properties of fault rocks

---

## 6.1 Introduction

There is an increasing need to predict, quantify and model the impact of faults on fluid flow within fault compartmentalized reservoirs (e.g. Fisher and Jolley, 2007). In subsurface reservoirs, where there is more than one phase is present relative permeability plays significant part in controlling fluids movement and distribution (e.g. Dandekar, 2006). The effective and relative permeability as a function of water saturation and stress is required to understand the performance and productivity of reservoirs. There is very limited published data available on two-phase flow (relative permeability and capillary pressure) properties of fault rocks. There is far less data that have examined the stress sensitivity of relative permeability of fault rocks (e.g. Al-Hinai et al., 2006). Clearly, this dataset needs to be increased for accurate modelling of fault compartmentalized reservoir behavior. The main aim of this chapter is to establish a database on fault rock two-phase flow properties e.g. relative permeability and capillary pressure such that the fluid flow behavior within fault compartmentalized reservoirs can be accurately modelled.

Apart from this introductory section, this chapter comprises five sections. **Section 6.2** provides an overview of experiments conducted and the total number of samples used for two-phase flow measurement. In **Section 6.3** results obtained on effective and relative gas permeability data as well as the data from capillary pressure measurements using centrifuge, relative humidity chambers are reported. In addition, the mercury-air capillary pressure data was obtained using mercury injection measurements and were converted to air-brine capillary pressures, are also reported in **Section 6.3**. **Section 6.4** provides the discussion about the effective and relative

gas permeability stress sensitivity; also the relative permeability controls and differences are also discussed in this section. Finally, the main findings from the results presented in this chapter are summarized in **Section 6.6**. In chapter 7 the results of relative permeability are incorporated into synthetic reservoir model to show the effect of faults on cross fault flow.

## **6.2 Experimental overview: two-phase flow properties**

A full description of microstructural and basic petrophysical properties of the samples used is provided in **Chapter 4 Section 4.2**. Here a brief description about two-phase flow experiments conducted to obtain relative permeability and capillary pressure data is provided. A summary of the samples studied is provided in **Table 6.1**. Two different techniques for capillary pressure measurement were used: centrifuge and relative humidity chambers. In addition to above methods of capillary pressure measurement, the air-mercury capillary pressures data for each sample was obtained by mercury injection; the procedure is described in chapter 3 **Section 3.6.1**. Detail about the two phase flow experiments is given in **Section 3.6**.

The effective gas permeability was measured on samples that had their water saturation changed prior to experiments. The water saturations were changed by using humidity chambers and ultra-centrifuge as described in **Section 3.6**. Each technique provides a specific range of capillary pressures; combinations of techniques were used so that relative permeability measurements could be obtained over a wide saturation range. Initially, the samples were placed into relative humidity chambers for changing the water saturation. The plugs were then resaturated with brine NaCl and placed into an ultra-centrifuge to change the brine saturation of the sample. The aim of placing them into an ultra-centrifuge was to decrease the water saturation and to measure the capillary pressures. Once the equilibrium between water saturation and capillary pressures was established, the samples were taken for effective gas permeability measurement. The effective gas permeability of samples was measured using either steady state or pulse decay techniques described in **Section 3.3**. The relative permeability to gas was calculated by dividing the effective permeability by absolute permeability at the same stress conditions. In addition, at higher stress conditions of 4000psi, few of the partially saturated samples were used

to measure their effective gas permeability. This was performed by placing sample into a core holder for longer period of about five to six days to achieve steady state flow and the methodology employed is described in **Section 3.6**. It should be noted that the gas relative permeability results are reported are average of the fault and host plug for all samples from reservoir core plugs. However, the samples from Hopeman fault rock are all comprises as a deformed band sections, their relative permeability values corresponding to their saturation calculations are more appropriate. In this chapter, the term water saturation is used in place of brine saturation for simplification when presenting and discussing the results. Generally, the relative permeability is a concept that is used to express the decrease of the flow in the presence of other mobile fluids within the porous media (e.g. Honarpour and Mahmood, 1988). Several authors have highlighted that the permeability of core samples depends on brine composition; permeability decreases as salinity is reduced (e.g. Lever and Dawve, 1987). This might be the case for relative permeability and if so it would be more likely be affected because of the presence of fine grained clay minerals under varying proportions and their interactions with water (Faulkner, 2004). Therefore, prior to measurements the samples were saturated using NaCl brines to minimize the physiochemical reactions that might affect relative permeability. The results of capillary pressure and relative permeability are presented on two different types of plots i.e. Cartesian and semi-log plots.

*Table 6.1 List of the total number of samples analysed and the conditions under which measurements conducted.*

<b>Summary of fault rock samples analysed</b>		
<b>SCAL Analysis</b>	<b>No. of Samples analysed</b>	<b>Pore fluid used</b>
Gas relative permeability vs stress	47	Gas-water (Helium and Brine NaCl)
Capillary pressure (Relative humidity Chambers)	35	Distilled water and air
Air brine capillary pressure (centrifure)	40	Air-Brine Nacl 200,000ppm

### 6.3 Results

This section presents the fault rock two-phase flow properties (capillary pressure and relative permeability) results. The results from central North Sea fields studied are reported into two groups Group-A and Group-B.

The relative permeability results presented were obtained by diving effective gas permeability to absolute permeability at their corresponding confining stresses.

The Hg-air capillary pressures were related to gas brine capillary pressures by taking account of their contact angle and interfacial tension based on the work of Purcell (1949). Hg-injection capillary pressures have been converted to air-brine values assuming interfacial tension of 70 dynes/cm and 480 dynes/cm for air- water and Hg-vacuum respectively and the contact angles of  $0^0$  and  $140^0$  were considered for air-water and Hg-vacuum respectively. Following relation of Purcell (1949) used,

$$\frac{P_c H_g}{P_{c,a-b}} = \frac{\sigma H_g \cos \theta_{Hg}}{\sigma_{a-b} \cos \theta_{a-b}} \quad (6-1)$$

Where,  $P_c H_g$ , is a mercury capillary pressure,  $P_{c,a-b}$  air-brine capillary pressure.  $\cos \theta$  is angle between gas mercury and brine,  $\sigma$  is the interfacial between fluids.

The aforementioned equation for converting mercury injection capillary pressure to air-brine capillary was based on the higher ranges of absolute permeabilities (>10mD) by Purcell (1949). However, Wells and Amaefule (1985) conducted tests on core samples of Cretaceous tight sandstone of Western Alberta, Canada based on the method described by Purcell (1949) and showed a concern that there might be differences in converting mercury capillary pressures to air-brine in low permeability samples. They found that mercury capillary pressures above 50% of water saturations are about 10 factors larger than air-brine capillary pressure measured by centrifuge. This contradicts the previously reported difference of 5 factors by Purcell (1949). However, Wells and Amaefule (1985) did not provide reason about the difference between air-brine capillary pressure and mercury injection capillary data. They thought that air brine contact angles might be different in tight rocks and in high permeability sands. Though, this is not the case related to data reported in

this thesis as the most of data used for comparison was below 50% saturations. However, that might be taken into account while converting air-mercury capillary pressures to air-brine above 50% of saturations.

In addition to mercury injection, the capillary pressure was obtained by the centrifuge method. It is often required to have good estimates of fluid equilibrium during centrifuging to obtain the capillary pressure curve without any error at each rotational speed. The capillary pressure curve was calculated from the average production measurements and rotational speed of centrifuge by applying known approximate mathematical solutions (e.g. Forbes, 1997).

It should be emphasized that fault rock often comprises of small thickness as compared to its associated host sandstone therefore, the saturations calculations are inappropriate in terms of volumetric calculations. The saturation values throughout the chapter should be considered as an average of the rock samples.

### **6.3.1 Central North Sea Group-A fault rocks**

A total of ten samples were analysed to obtain relative permeability and capillary pressure data. The results obtained are presented in **Table 6.2** and **Figure 6.1**. It should be emphasized that there is a large variation of both the absolute and effective gas permeability as well as the level of heterogeneity of the samples examined. In particular, the cataclastic faults are highly heterogeneous being composed of bands of low permeability faults separated by regions of relatively high permeability undeformed sandstone.

#### **6.3.1.1 Relative permeability**

The relative gas permeabilities were measured at stresses from 500 psi to 2500 psi. The minimum water saturation value obtained by humidity chambers is 0.06 and the corresponding relative permeability value is 0.95. The maximum water saturation of 0.53 was achieved by employing centrifuge technique and the relative permeability to gas is 0.0092.

### 6.3.1.2 Capillary pressure

A combined capillary curve defined by several saturation points was obtained using three different techniques i.e. Ultracentrifuge, mercury injection and humidity chambers (**Figure 6.1**). Plug CP2B was cut to fit into the centrifuge. The capillary pressure obtained using relative humidity chamber varied between 9000 psi and 1660 psi. The water saturations ranged from 0.06 to 0.17. The maximum water saturation and lowest capillary pressure were achieved by using the ultracentrifuge; the capillary pressure obtained ranged from 50 psi to 210 psi.

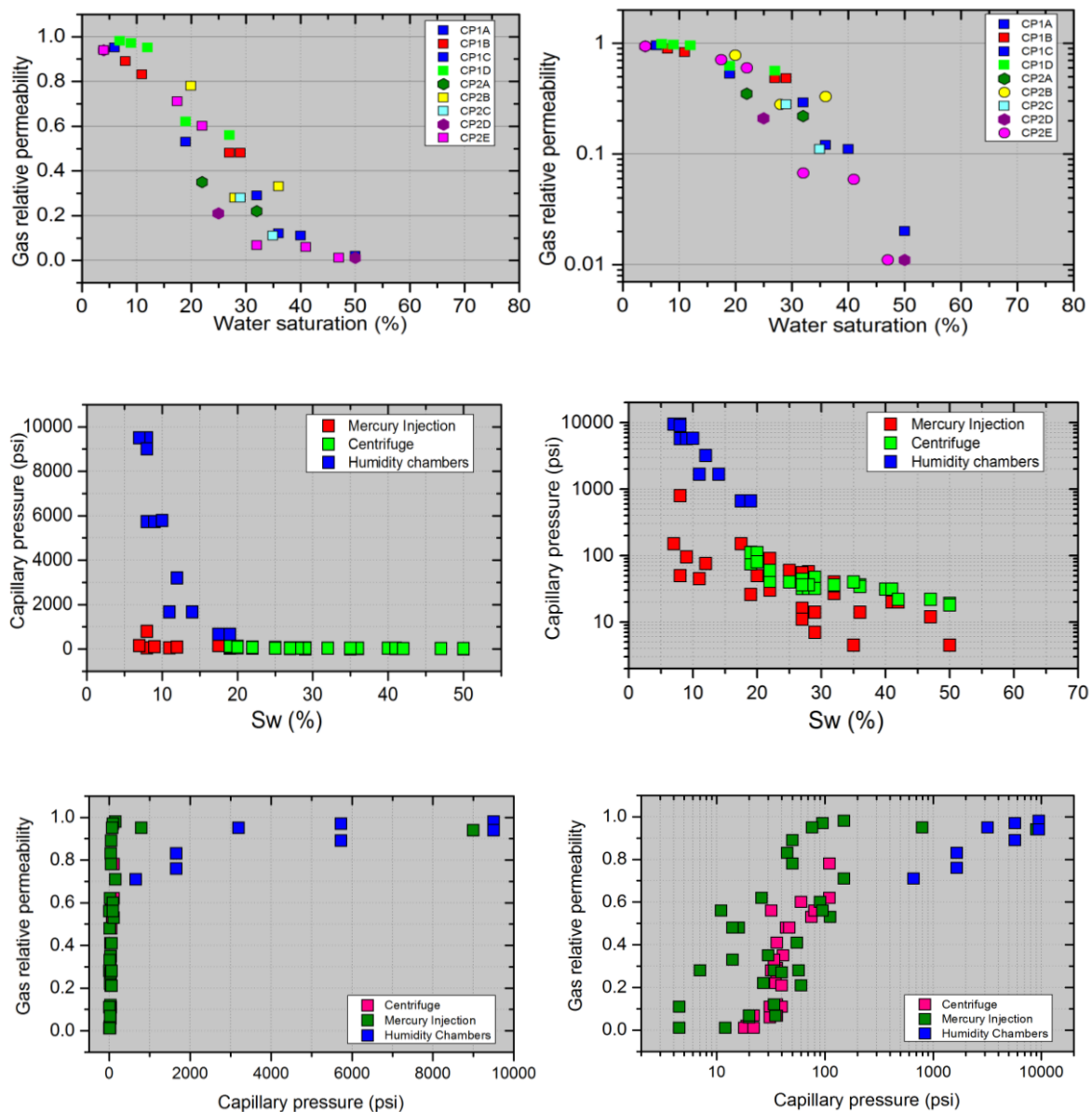


Figure 6.1 Two-phase flow data from central North Sea Group-A reservoir sample. The data presented comes from variety of techniques used, such as the centrifuge, relative humidity and mercury injection method, different colors represent the different methods used for changing water saturations. For the comparison purpose all Hg-injection capillary pressure have been converted to air-water values assuming interfacial tension of 70 dynes/cm and 480 dynes/cm for air-water and Hg-vacuum respectively. Contact angles of 00 and 1400 were considered for air-water and Hg-vacuum respectively. Data in the right-hand side graphs are plotted using semi-log scales. Graphs on the left-hand side present the same data in linear scale to visualize the results.

Table 6.2 Stress sensitivity of effective and relative gas permeability  $k_{rg}$  of Group-A central North Sea reservoir samples. The effective permeability equals the absolute permeability at zero percent water saturation. The plugs water saturations were altered by humidity chambers and centrifuge technique. The effective and relative gas permeability as well water saturations presented here are average of the host and fault.

Central North Sea Group-A gas relative permeability and capillary pressure data													
Sample ID	PC-air-brine	Sw	500 (psi)		1000 (psi)		1500 (psi)		2000 (psi)		2500 (psi)		Pc-Measurement method
			K	Krg	K	Krg	K	Krg	K	Krg	K	Krg	
CP1A	-	0	63.7	1	56.6	1	52.9	1	50.3	1	48.5	1	Centrifuge Centrifuge
	31	40	11.0	0.17	8.01	0.14	5.96	0.11	5.34	0.11	4.58	0.09	
	36	32	19.8	0.31	16.6	0.29	15.4	0.29	14.3	0.28	12.8	0.26	
CP1B	0	0	16.1	1.0	15.1	1.0	14.7	1.0	14.5	1.0	14.3	1.0	vapor chamber vapor chamber vapor chamber Centrifuge Centrifuge
	5728	6	15.4	1.0	14.2	0.9	13.3	0.9	13.0	0.9	12.7	0.9	
	3230	8	14.7	0.9	13.4	0.9	13.0	0.9	12.6	0.9	12.3	0.9	
	1660	11	13.5	0.8	12.5	0.8	12.1	0.8	11.9	0.8	11.6	0.8	
	44	27	8.2	0.6	7.5	0.6	6.2	0.5	6.0	0.5	5.9	0.5	
47	29	7.6	0.5	7.3	0.5	6.8	0.5	6.5	0.4	6.4	0.4		
CP1C	0	0	4.93	1.00	3.50	1.00	2.95	1.00	2.56	1.00	2.31	1.00	Centrifuge Centrifuge Centrifuge
	19	50	0.11	0.02	0.07	0.02	0.06	0.02	0.05	0.02	0.05	0.02	
	34	36	0.54	0.11	0.43	0.12	0.34	0.12	0.32	0.13	0.30	0.13	
47	19	2.56	0.52	1.89	0.54	1.57	0.53	1.38	0.54	1.25	0.54		
CP1D	0	0	120	1	111	1	104	1	101	1	98.2	1	vapor chamber vapor chamber vapor chamber Centrifuge Centrifuge
	5728	7	117.9	0.98	108.7	0.98	103.2	0.99	98.32	0.97	95.6	0.97	
	3230	9	116.8	0.97	107.85	0.97	101	0.97	98.05	0.97	95.3	0.97	
	1660	12	114.02	0.95	105.3	0.95	99.02	0.95	96.2	0.95	92.9	0.95	
	75	19	73.9	0.62	69.2	0.62	62.5	0.60	59.5	0.59	55.5	0.57	
50	27	65.5	0.55	61.7	0.56	61.3	0.59	61.2	0.61	61.1	0.62		
CP2A	0	0	1.76	1	1.46	1	1.35	1	1.26	1	1.21	1	Centrifuge Centrifuge
	35	32	0.308	0.18	0.305	0.21	0.302	0.22	0.301	0.24	0.30	0.25	
41	22	0.61	0.35	0.51	0.35	0.46	0.34	0.43	0.34	0.42	0.34		
CP2B	0	0	150.8	1.0	147	1.0	144.5	1.0	142.8	1.0	141.2	1.0	Centrifuge Centrifuge Centrifuge
	34	36	35.0	0.2	37.0	0.3	38.0	0.3	38.5	0.3	39.2	0.3	
	32	28	41.5	0.3	41.2	0.3	40.3	0.3	39.5	0.3	38.0	0.3	
110	20	120.0	0.8	114.0	0.8	112.0	0.8	110.0	0.8	110.0	0.8		
CP2C	0	0	1.83	1.00	1.48	1.00	1.25	1.00	1.18	1.00	1.11	1.00	Centrifuge Centrifuge
	40	35	0.20	0.11	0.17	0.12	0.16	0.13	0.15	0.13	0.13	0.12	
32	29	0.45	0.25	0.37	0.25	0.35	0.28	0.34	0.28	0.33	0.30		
CP2D	0	0	0.89	1.00	0.51	1.00	0.38	1.00	0.23	1.00	0.19	1.00	vapor chamber Centrifuge Centrifuge
	9000	2	0.86	0.97	0.48	0.94	0.36	0.95	0.22	0.96	0.18	0.95	
	40	25	0.19	0.21	0.11	0.21	0.08	0.22	0.05	0.21	0.04	0.20	
18	53	0.01	0.01	0.01	0.01	0.004	0.011	0.003	0.01	0.003	0.01		
CP2E	0	0	1.3	1	0.67	1	0.44	1	0.33	1	0.27	1	vapor chamber vapor chamber Centrifuge Centrifuge Centrifuge
	9000	4	1.25	0.96	0.632	0.94	0.419	0.95	0.309	0.94	0.252	0.93	
	1660	17.5	1.02	0.78	0.52	0.78	0.312	0.71	0.235	0.71	0.193	0.71	
	22	47	0.026	0.02	0.013	0.019	0.01	0.025	0.0082	0.025	0.008	0.029	
	60	22	0.762	0.59	0.402	0.60	0.26	0.58	0.191	0.58	0.156	0.58	
39	32	0.089	0.068	0.047	0.070	0.032	0.073	0.024	0.073	0.019	0.070		
CP2F	0	0	1.24	1	0.92	1	0.79	1	0.73	1	0.67	1	Centrifuge Centrifuge Centrifuge
	22	42	0.089	0.072	0.062	0.068	0.047	0.059	0.043	0.059	0.038	0.057	
	39	32	0.334	0.27	0.25	0.27	0.218	0.28	0.199	0.27	0.17	0.25	
80	20	0.63	0.51	0.47	0.51	0.443	0.56	0.438	0.60	0.41	0.61		

### **6.3.2 Central North Sea Group-B fault rock**

A total of fifteen fault plug samples were used for relative permeability and capillary pressure measurement. The results obtained are summarized in **Table 6.3** and **Figure 6.2**. Compared to Group-A fault samples, fault rock samples of Group-B are highly heterogeneous, being composed of bands of low permeability deformation bands separated by regions of relatively high permeability undeformed sandstone. These samples were also observed with very low absolute gas permeabilities.

#### **6.3.2.1 Relative gas permeability**

The effective and relative gas permeability was obtained at different stress conditions. The gas relative permeability measured varies largely from sample to sample and ranges from 0.00001 to 0.89. The maximum water saturation of 53% was obtained by the centrifuge technique and the minimum water saturation of 8% was achieved by employing the relative humidity chambers. The results of effective and relative permeability at corresponding water saturations are summarized in **Table 6.3**.

#### **6.3.2.2 Capillary pressure**

The capillary pressure was obtained by the techniques discussed above same techniques were applied for all samples capillary pressure determinations. The saturation of these samples are also average of both deformed and host sands. The calculations from centrifuge rotational speeds of were performed after reaching good estimation of equilibrium, using the Forbes (1997) method.

The highest capillary pressure of 9000 psi at the minimum water saturation of 8% was achieved by humidity chambers method and the lowest capillary pressure 20 psi was obtained by centrifuge at about 50% water saturations. The centrifuge method gave higher water saturation of 50% and higher capillary pressure of 112 psi. All capillary pressure measurement results are summarized in **Table 6.3**.

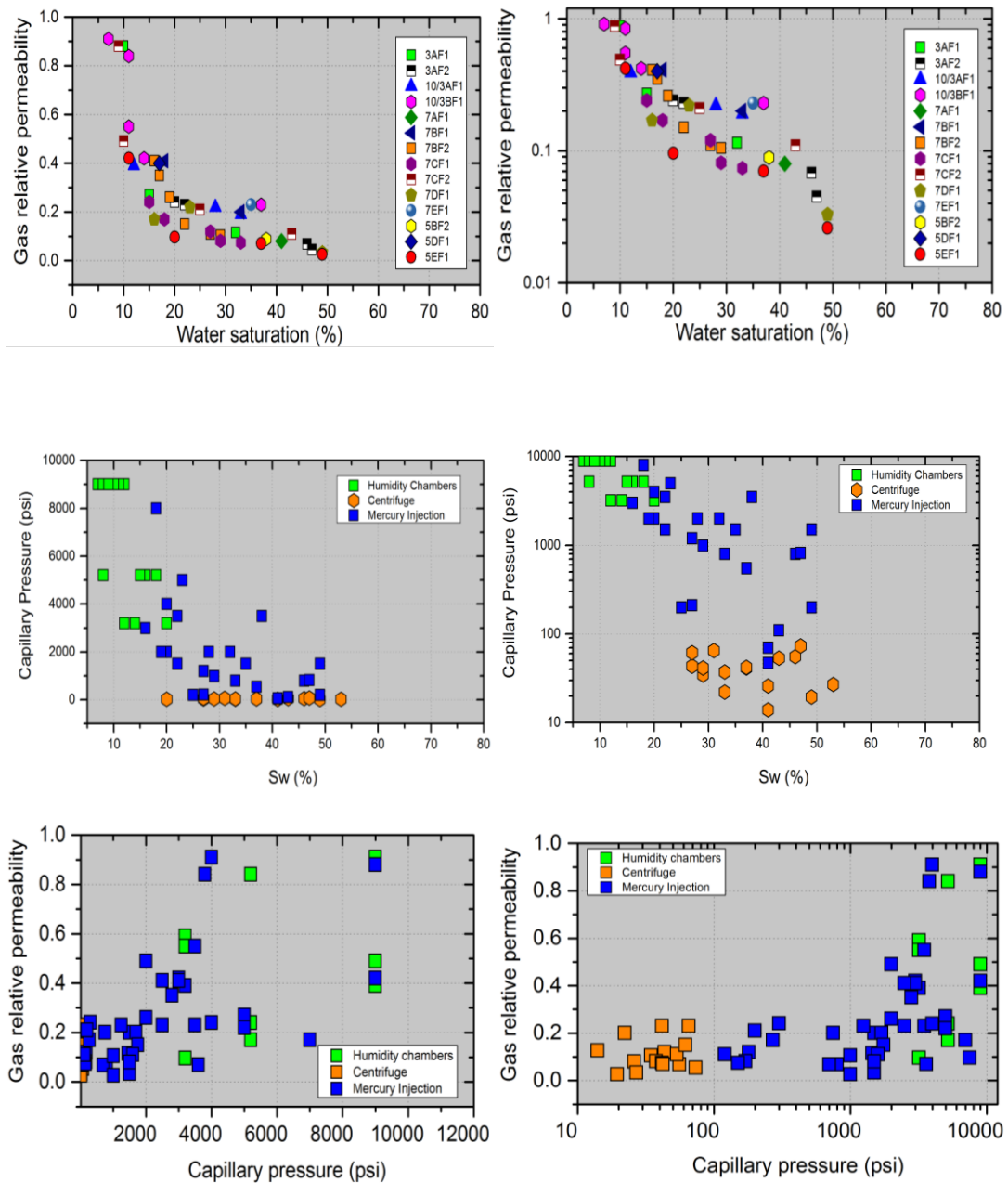


Figure 6.2 The two phase fluid flow properties of all measured samples from central North Sea group-B reservoir core samples. The colour of symbols indicates the different methods used for changing saturations (see legends in graphs presented). For the comparison purpose, all Hg-injection capillary pressure has been converted to air-water values assuming interfacial tension of 70 dynes/cm and 480 dynes/cm for air-water and Hg-vacuum respectively. Contact angles of  $0^{\circ}$  and  $140^{\circ}$  were considered for air-water and Hg-vacuum respectively. Data in the right-hand side graphs are plotted using semi-log scales. Graphs on the left-hand side present the same data in linear scale to visualize the results.

Table 6.3 The stress sensitivity of effective gas permeability and relative gas permeability,  $k_{rg}$  of Group-B central North Sea samples. The effective permeability equals the absolute permeability at zero water saturation. The water saturation of samples was altered by centrifuge technique and by relative humidity chambers. The capillary pressure data and water saturation shown in red color were obtained using humidity chambers, all other saturations were changed by centrifuge method.

Central North Sea-Group-B - Two-phase fluid flow properties												
Sample ID	PC (Psi)	Sw (%)	1000 (psi)		2000 (psi)		3000 (psi)		4000 (psi)		5000 (psi)	
			K_eff	K <sub>rg</sub>								
3AF1	-	0	0.06	1	0.04	1	0.039	1	0.036	1	0.033	1
	56	46	0.004	0.068	0.0003	0.006	-	-	-	-	-	-
	75	32	0.006	0.110	0.005	0.11	-	-	-	-	-	-
	112	22	0.01	0.23	0.01	0.22	-	-	-	-	-	-
	5782	15	0.02	0.27	0.01	0.26	-	-	-	-	-	-
	9000	10	0.05	0.88	0.04	0.86	-	-	-	-	-	-
3AF2	-	0	0.011	1	0.0095	1	0.0082	1	0.0074	1	0.0069	1
	73.5	47	0.001	0.054	-	-	-	-	-	-	-	-
	55.5	28	0.002	0.160	-	-	-	-	-	-	-	-
	110	20	0.003	0.240	0.002	0.20	-	-	-	-	-	-
10/3AF	-	0	0.06	1	0.05	1	0.04	1	0.03	1	0.03	1
	22.2	32	0.01	0.21	0.02	0.37	0.01	0.30	0.01	0.27	0.01	0.28
	9000	9	0.05	0.84	-	-	-	-	-	-	-	-
10/3BF	-	0	3.67	1	3.49	1	3.33	1	3.23	1	3.13	1
	41.5	37	0.87	0.24	0.76	0.22	0.65	0.19	0.54	0.17	0.51	0.16
	5728	11	3.34	0.91	3.07	0.88	-	-	-	-	-	-
	9000	8	1.54	0.42	1.43	0.41	-	-	-	-	-	-
7AF1	-	0	10.73	1	10.47	1	10.21	1	10.15	1	10	1
	26	41	0.87	0.08	0.57	0.05	0.33	0.03	0.25	0.02	0.13	0.012
	55	22	3.25	0.30	3.05	0.29	2.90	0.28	2.61	0.26	2.44	0.24
7BF1	-	0	0.0063	1	0.0054	1	0.0049	1	0.0045	1	0.0044	1
	22	33	0.001	0.21	-	-	-	-	-	-	-	-
7BF2	-	0	0.02	1	0.018	1	0.026	1	0.018	1	0.017	1
	35.5	22	0.003	0.15	0.00001	0.001	-	-	-	-	-	-
	5782	12	0.0019	0.11	0.0018	0.10	-	-	-	-	-	-
	9000	8	0.0153	0.89	0.0156	0.88	-	-	-	-	-	-
7CF1	-	0	0.082	1	0.06	1	0.029	1	0.021	1	0.019	1
	43.3	27	0.01	0.12	0.0009	0.01	0.0007	0.023	0.0004	0.02	0.0002	0.01
	5728	18	0.01	0.17	0.0097	0.16	-	-	-	-	-	-
	9000	15	0.02	0.24	0.01	0.22	-	-	-	-	-	-
7CF2	-	0	0.38	1	0.35	1	0.31	1	0.28	1	0.27	1
	53.5	43	0.065	0.17	0.045	0.13	0.038	0.12	0.034	0.12	-	-
	41.5	25	0.08	0.22	0.08	0.22	0.06	0.21	0.05	0.19	-	-
7DF1	-	0	0.01	1	0.0080	1	0.0065	1	0.0063	1	0.0059	1
	27	49	0.00032	0.033	-	-	-	-	-	-	-	-
	5728	16	0.0016	0.17	0.00120	0.15	-	-	-	-	-	-
7EF1	-	0	0.39	1	0.29	1	0.22	1	0.19	1	0.18	1
	65	39	0.09	0.23	0.00092	0.0031	-	-	-	-	-	-
	5782	12	0.23	0.59	-	-	-	-	-	-	-	-
5EF1	-	0	2.20	1	1.77	1	1.66	1	1.62	1	1.31	1
	19.5	49	0.06	0.03	0.05	0.03	0.04	0.02	0.04	0.02	0.03	0.02
	5728	20	0.21	0.096	0.16	0.09	-	-	-	-	-	-
5EF2	-	0	11.0	1	10.5	1	10.3	1	10.1	1	9.9	1
	42.2	37	0.77	0.07	0.72	0.07	0.64	0.06	0.53	0.05	0.50	0.05
	9000	11	0.92	0.42	0.71	0.40	-	-	-	-	-	-
5FF1	-	0	0.15	1	0.10	1	0.08	1	0.07	1	0.06	1
	14	41	0.03	0.17	0.02	0.18	0.012	0.15	0.009	0.13	0.0079	0.13
5BF2	-	0	0.06	1	0.05	1	0.05	1	0.04	1	0.04	1
	26.5	38	0.01	0.09	0.0047	0.096	0.0040	0.089	0.0032	0.078	0.0026	0.066

### 6.3.3 Central North Sea host sandstone

A total of eleven host rock samples were used from central North Sea group-B field to measure their relative permeability and capillary pressure at different stress conditions. The results obtained on relative permeability and capillary at corresponding water saturation obtained are summarized in **Table 6.4** and plotted in **Figure 6.3**. The capillary pressure for all these samples were obtained using only the centrifuge method. The minimum water saturation achieved was 0.26, with a corresponding relative permeability of 0.86. The capillary pressure ranges from 10 psi to 32.2psi.

*Table 6.4 Stress sensitivity of absolute, effective and relative gas permeability  $k_{rg}$  of Central North Sea host reservoir samples. The effective permeability equals the absolute permeability at zero water saturation. The saturation of samples was altered by using only centrifuge technique.*

Central North Sea reservoir undeformed samples												
Sample ID	Capillary pressure (psi)	Water saturation (%)	Conf. stress 1000Psi		Conf. stress 2000Psi		Conf. stress 3000Psi		Conf. stress. 4000Psi		Conf. stress 5000	
			K_eff	K <sub>rg</sub>	K_eff	K <sub>rg</sub>	K_eff	K <sub>rg</sub>	K_eff	K <sub>rg</sub>	K_eff	K <sub>rg</sub>
3AH1	-	0	17.6	1	17	1	17	1	15.9	1	14.6	1
	11	55	8.4	0.48	8.2	0.48	8.1	0.48	7.6	0.48	4.5	0.31
	20.5	31	14.4	0.82	14	0.81	13	0.79	12.5	0.79	12	0.79
10/3AH	-	0	2.9	1	2.8	1	2.6	1	2.5	1	1.9	1
	10	63	0.9	0.32	0.9	0.30	0.8	0.31	0.7	0.27	0.6	0.32
	20	50	1.3	0.46	1.3	0.45	1.1	0.43	1.1	0.43	0.9	0.46
10/3BH	-	0	101	1	95	1	92	1	89	1	85	1
	22.5	33	86	0.85	81	0.85	77	0.83	75	0.84	73	0.85
7AH1	-	0	15.0	1	15	1	14	1	14.2	1	14	1
	13.7	52	6.9	0.46	3.2	0.22	2.9	0.20	2.2	0.15	1.6	0.12
	25	29	12.5	0.83	12	0.81	12	0.82	11.3	0.80	11.0	0.80
7BH1	-	0	9.5	1	8.6	1	7.1	1	6.2	1	6.1	1
	16.8	35	5.8	0.61	5.9	0.68	5.7	0.80	5.4	0.87	5.2	0.85
7CH1	-	0	2.5	1	2.2	1	1.8	1	1.8	1	1.7	1
	11.26	58	0.7	0.29	0.6	0.29	0.5	0.28	0.4	0.25	0.4	0.24
	15.46	44	1.3	0.52	1.2	0.55	1.0	0.56	0.1	0.053	0.1	0.053
7EH1	-	0	1.8	1	1.8	1	1.7	1	1.5	1	1.4	1
	12.05	57	0.5	0.27	0.4	0.25	0.4	0.25	0.4	0.26	0.4	0.26
	16.4	40	1.1	0.62	1.1	0.63	1.1	0.62	0.9	0.58	0.8	0.57
5AH1	-	0	2.4	1	2.5	1	2.6	1	2.7	1	1.9	1
	9.5	43	1.1	0.45	1.0	0.38	0.9	0.34	0.9	0.33	0.7	0.37
	18	30	1.9	0.81	1.9	0.765	1.9	0.73	1.9	0.70	1.6	0.84
5BH1	-	0	0.5	1	0.4	1	0.4	1	0.4	1	0.4	1
	11.8	47	0.3	0.51	0.22	0.48	0.2	0.46	0.2	0.46	0.2	0.42
	22	32	0.4	0.74	0.3	0.75	0.3	0.75	0.3	0.72	0.3	0.71
5EH1	-	0	34	1	33.9	1	33.7	1	33	1	32	1
	12.6	43	17	0.49	4.6	0.14	3.6	0.11	3	0.10	3	0.10
	32.2	33	29	0.85	27.8	0.82	26.9	0.80	26	0.79	26	0.82
5FH1	-	0	34	1	33.9	1	33.7	1	33	1	32	1
	14.5	36	26	0.76	24.8	0.73	23.6	0.70	22	0.68	21	0.66
	21.5	26	30	0.86	27.9	0.82	26.5	0.79	26	0.79	25	0.80

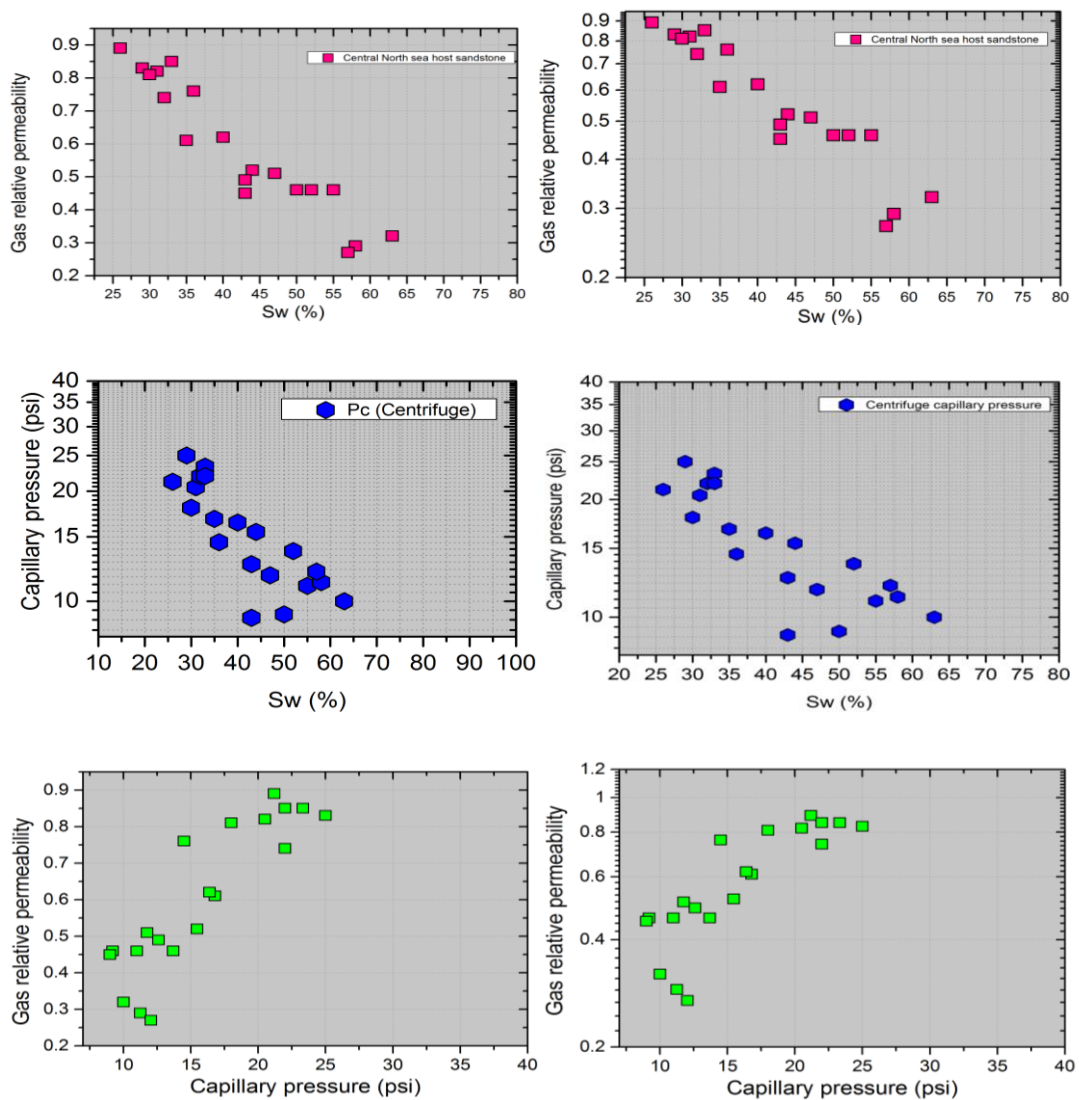


Figure 6.3 Data of host rock samples capillary pressure and gas relative permeability from central North Sea Group-B. The centrifuge technique was employed to alter the water saturation and to obtain capillary pressure data. The data is presented on linear (left-side) and semi-log (right side) graphs.

### 6.3.4 Southern North Sea

A total of three core samples were supplied, from these five plugs were taken for permeability and capillary pressure measurements. The results obtained on capillary pressure and relative permeabilities are reported in the following section.

#### **6.3.4.1 Gas relative permeability**

The relative permeability measured varies from sample to sample. The relative permeabilities at corresponding water saturations are summarized in **Table 6.5** and **Figure 6.4**. The minimum water saturation of 0.010 is achieved by employing the humidity chambers method. The corresponding relative permeability obtained for this minimum water saturation value and a confining stress of 1000 psi is 0.89.

#### **6.3.4.2 Capillary pressure**

The capillary pressure measurements were made by three different techniques, namely centrifuge, relative humidity chambers and mercury injection method. The combined capillary pressure results are summarized in **Table 6.5** for all samples. The highest capillary pressure and lowest water saturation are obtained by humidity chambers. The saturations obtained by humidity chambers technique ranges from 0.010 to 0.27 and capillary pressure ranges from 5728 psi to 9000 psi. The lowest capillary pressure and highest water saturations were achieved by employing the centrifuge technique. The measured capillary pressure by the centrifuge method ranges from 22 psi to 158 psi at corresponding saturations values of 0.39 to 0.52 respectively.

Table 6.5 Two-phase flow properties (capillary pressure and relative permeability) from southern North Sea core samples. The effective permeability equals the absolute permeability at zero water saturation. The saturation was altered by using centrifuge technique and relative humidity chambers. The data presented with blue coloured rows were obtained by using relative humidity chambers. All other data was obtained using centrifuge techniques.

Sample ID	Pc (psi)	Avg Sw	1000 (psi)		2000 (psi)		3000 (psi)		4000 (psi)		5000 (psi)	
			K <sub>eff</sub>	K <sub>rg</sub>								
WinA1F	-	0	3.9	1	3.6	1	3.5	1	3.4	1	3.3	1
	22.2	39	1.4	0.37	1.3	0.36	-	-	-	-	-	-
	52	32	2.6	0.7	2.7	0.74	-	-	-	-	-	-
	9000	10	3.4	0.89	3.1	0.88	3.1	0.87	-	-	-	-
WinA3F	-	0	9.6	1	9.2	1	8.7	1	8.5	1	8.4	1
	35	37	6.0	0.6	7.7	0.8	7.4	0.9	7.3	0.9	7.1	0.8
	34	31	4.2	0.44	3.3	0.35	3.1	0.35	2.9	0.33	2.6	0.3
	9000	12	8.16	0.85	7.56	0.82	7.16	0.82	7.00	0.82	-	-
win1BF	-	0	0.07	1	0.03	1	0.02	1	0.02	1	0.01	1
	136	52	0.0045	0.067	0.0018	0.06	0.0012	0.06	-	-	-	-
	6000	27	0.031	0.470	0.014	0.46	0.009	0.44	-	-	-	-
	9000	15	0.051	0.760	0.023	0.77	-	-	-	-	-	-
Win2BF	-	0	0.05	1.00	0.02	1.00	0.02	1	0.01	1	0.01	1
	136	54	0.0004	0.01	0.0002	0.0087	0.0001	0.0087	-	-	-	-
	164	47	0.0015	0.03	0.0002	0.01	0.0001	0.0083	-	-	-	-
	6000	23	0.020	0.41	0.0092	0.40	0.0062	0.41	-	-	-	-
win1C	-	0	0.05	1	0.03	1	0.020	1	0.02	1	0.01	1
	158	52	0.0045	0.08	0.0024	0.08	0.002	0.08	0.0013	0.08	-	-
	5728	22	0.03	0.55	0.016	0.54	-	-	-	-	-	-
	9000	12	0.043	0.79	0.023	0.78	0.015	0.77	-	-	-	-

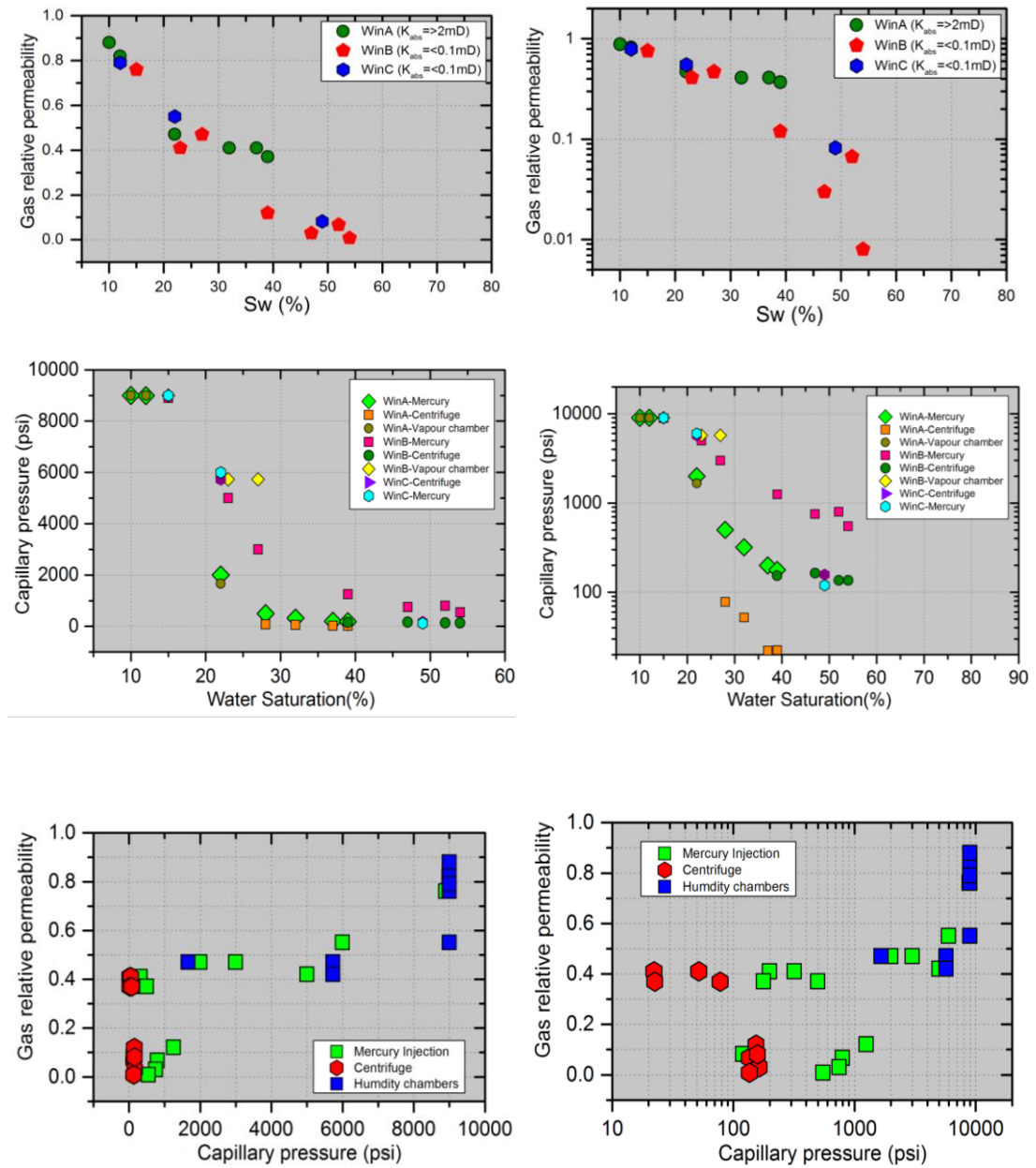


Figure 6.4 The two phase fluid flow properties of all measured samples from southern North Sea reservoir core samples. The colour of symbols indicates the different plugs properties and the methods used for changing saturations (see legends in graphs presented). For the comparison purpose, all Hg-injection from capillary pressure have been converted to air-water values assuming interfacial tension of 70 dynes/cm and 480dynes/cm for air- water and Hg-vacuum respectively. Contact angles of  $0^{\circ}$  and  $140^{\circ}$  were considered for air-water and Hg-vacuum respectively. Data in the right-hand side graphs are plotted using semi-log scales. Graphs on the left-hand side present the same data in linear scale to visualise the results.

### 6.3.5 Fault rock from Hopeman outcrop UK

A total of 5 samples were analysed to obtain effective gas permeability and capillary pressure data at different water saturations. The saturations of these samples were altered by using centrifuge technique and humidity chambers. The results obtained are presented in **Table 6.6** and are also presented as shown in **Figure 6.5** and **Figure 6.7**

#### 6.3.5.1 Gas relative permeability

The relative gas permeabilities of these samples were conducted at stress of 1500 psi. The minimum water saturation value obtained was 0.09 and the corresponding relative permeability value is 0.60. The maximum water saturation of 0.35 was achieved by employing centrifuge technique and the relative permeability to gas measured was 0.0195.

#### 6.3.5.2 Capillary pressure

A capillary curve defined by several saturation points was obtained using different measurement techniques. The capillary pressure obtained ranges from 189psi to maximum of 840psi. The maximum water saturation and lowest capillary pressure were obtained ranged from 0.35 to 189 psi respectively.

*Table 6.6 Summary of the effective and relative permeability and capillary pressure data data from Hopeman fault rock samples obtained during present study.*

<b>Sample ID</b>	<b>Pc (psi)</b>	<b>Avg S<sub>w</sub></b>	<b>L (cm)</b>	<b>D (cm)</b>	<b>K<sub>abs</sub> (mD)</b>	<b>K<sub>eff</sub> (mD)</b>	<b>K<sub>rg</sub></b>
HPB3	189	0.35	5.1	2.04	0.0033	0.00008	0.0195
HPB4	380	0.30	4.78	3.28	0.0048	0.00011	0.023
HPB8	520	0.26	4.06	3.72	0.0112	0.0004	0.037
HPX6	640	0.19	3.16	3.56	0.0041	0.0004	0.086
HPB2	750	0.13	4.79	3.72	0.0029	0.0006	0.191
HPX5	840	0.09	4.90	3.72	0.0012	0.0007	0.600
HPB8	840	0.11	4.06	3.72	0.0112	0.0088	0.783

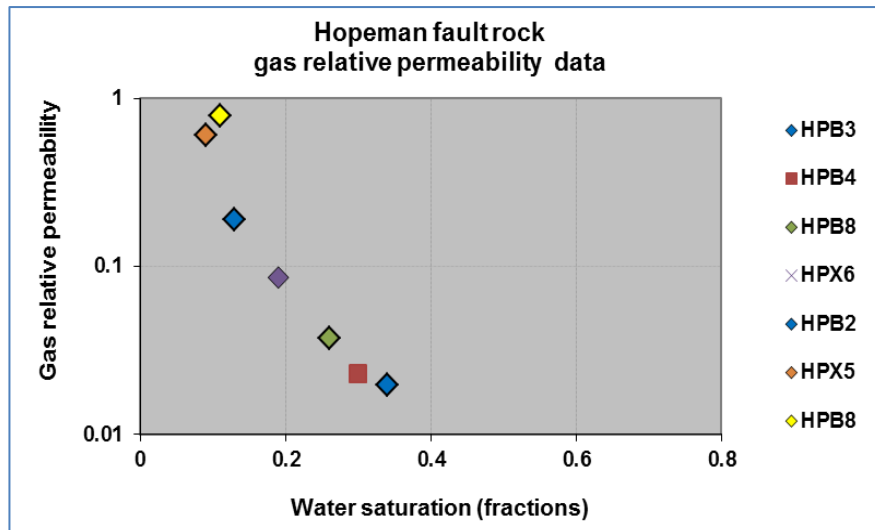


Figure 6.5 Gas relative permeability as a function of water saturation obtained from Hopeman fault rock samples.

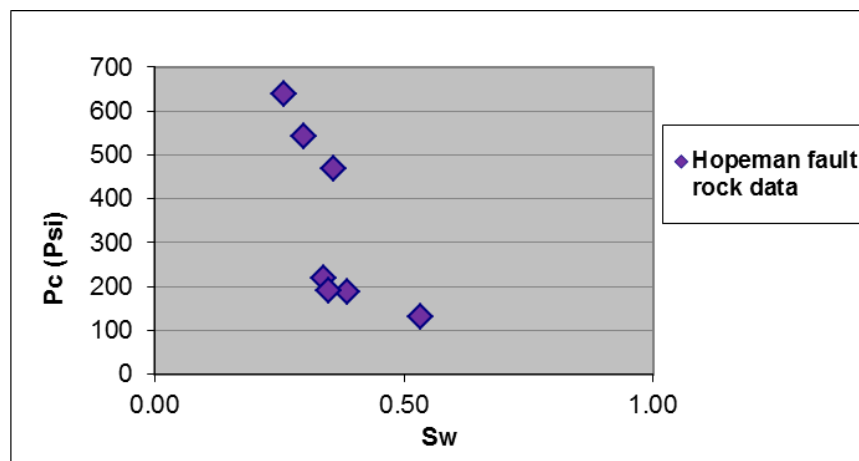


Figure 6.6 The illustration shows the capillary pressure data corresponding to water saturation obtained from Hopeman fault rock.

## 6.4 Discussion

This section starts by discussing the stress sensitivity of the effective and relative gas permeability. The section then discusses about the key controls on relative gas permeability of the samples. Moreover, the section compares the present study data on relative permeability and capillary pressure with the data collected from published studies. Finally the section addresses the main implications of the results presented for fault seal analysis.

### 6.4.1 Stress sensitivity of effective and relative gas permeability

It is often argued that the fault rock relative permeability is far more sensitive to stress (e.g. Al-Hinai et al., 2006). Much of the work is devoted to investigate the stress sensitivity of tight rocks (i.e. tight gas sands) relative permeability (e.g. Thomas and Ward, 1972; Shanley et al., 2004; Byrnes et al., 2001). However, far less data exists on the effective gas permeability stress sensitivity of fault rock and is essential for accurate modelling and analyses of stress sensitive reservoirs. Several authors have reported that the lower absolute permeability exhibits more stress sensitivity to relative permeability at a given water saturation (e.g. Cluff and Byrnes, 2010). The laboratory experiments conducted by Hildenbrand et al. (2002) reported that gas relative permeabilities at irreducible water saturation within very fine-grained porous media exhibits several orders of magnitude lower relative permeabilities than the coarse sandstones. The low-permeability sandstones samples pore throats might decrease up to 50–70% due to increase in overburden stress subsequently the permeability of these samples would be affected (e.g. Byrnes and Keighin, 1993, 1997).

The results from present study suggests that the stress sensitivity of the effective gas permeability of samples increases as the percentage of water saturations increases and the absolute permeability decreases (**Figures 6.7**). For example, the absolute permeability of dry cores at 1000psi of confining pressure is >2000 times larger than that of the cores with partially water saturated at 4000psi confining pressure. To better understand the changes in effective gas permeability magnitude due to stress increase, the results were normalized and are presented in **Figure 6.8**. This reduction in effective gas permeability is similar to that reported for tight gas sandstone samples (e.g. Cluff and Byrnes, 2010; Shanley et al., 2004). These results show that as the stress increases

the effective gas permeability reduces more than compared to dry gas permeability. However, this opposes to the study of tight rock samples reported by Thomas and Ward (1972) they stated that the absolute gas permeability is more sensitive to stress than relative permeability. Although, the results from the present study also contradict the findings of Fatt (1953) who suggested that the relative permeability of sandstones does not change by the application of overburden stress.

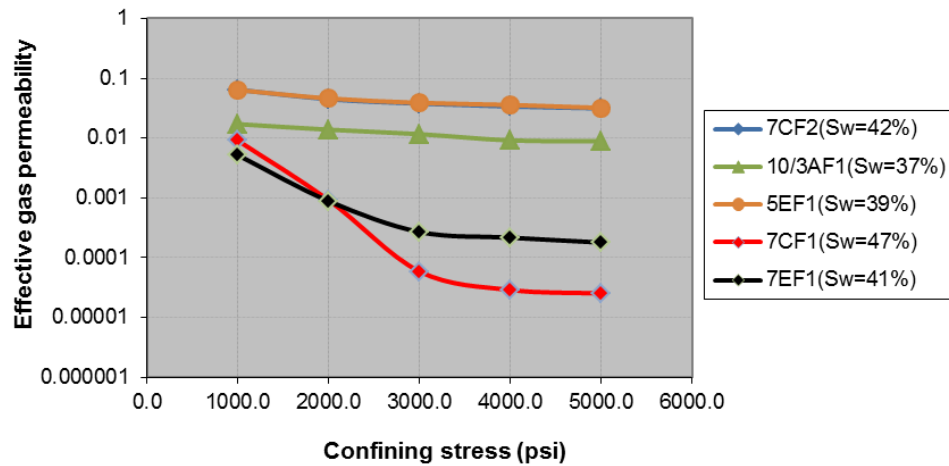


Figure 6.7 The plot shows the stress sensitivity of effective gas permeability versus stress from present study samples. The higher the water saturation of samples more is the stress sensitive. Not that the sample which shows higher reduction of effective gas permeability has lower absolute permeability value.

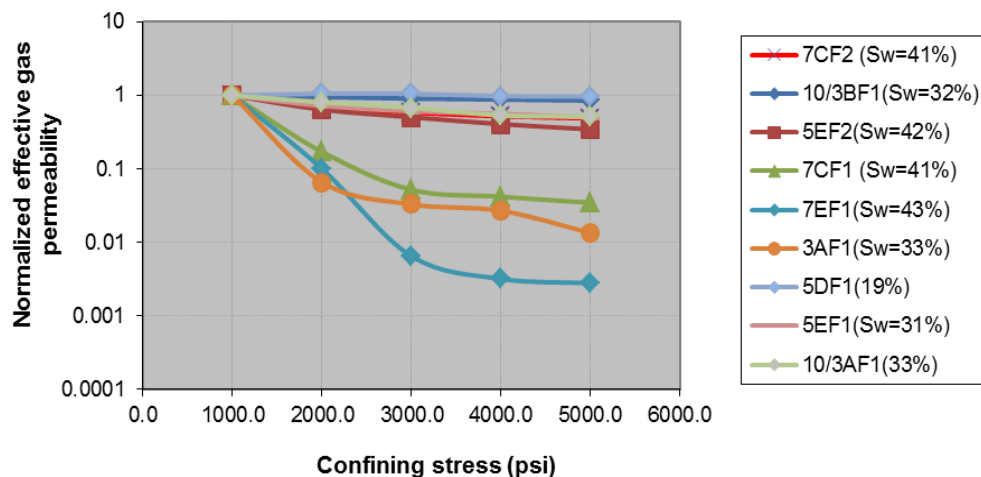


Figure 6.8 Plot shows the normalized effective gas permeability versus confining stress from reservoir core samples obtained at various saturations. The saturations were altered by two different techniques i.e. the relative humidity chambers and centrifuge technique.

Moreover, Wilson (1956) conducted drainage and imbibition experiments to obtain the relative-permeability of sandstone samples at confining pressures of up to 5000psi. They observed that the changes in effective permeability of oil at irreducible water saturations were very close to the single-phase permeability. Although, the author reported that the data showed slight stress effects on relative permeability and concluded that there was very less stress effect but is noticeable in terms of relative permeability, their findings of relative permeability stress sensitivity on some extent supports present study findings.

Dacy (2010) argued that gas relative permeability could not be sensitive to stress if relative permeability calculated from the effective gas and absolute gas permeabilities that were measured at the same stress conditions. Similar to that, present study calculated gas relative permeabilities using absolute gas permeability data points that were measured at the same confining pressure as the effective gas permeability measurements were made. However, two important observations were made from the relative permeability calculations. The first shows that (**Figure 6.9**) there is no significant decrease in relative permeability with stress increase. Although, the second observation appears that (**Figure 6.10**) that the stress sensitivity of gas relative permeability increases with both decreasing absolute permeability and increasing water saturations. The stress sensitivity of effective gas permeability observed within low permeability core samples could be the result of core damage effects. The core damage might be the result of grain boundary micro-cracks and are being more pronounced in low permeability samples than high permeability samples (Ostensen, 1983). Although, retrieving core samples from sub-surface reservoirs might cause core damage due to stress release (Holt and Kenter, 1992; Holt et al., 1994). At low stress conditions, the contribution of high flow rates might be expected from micro-cracks often this leads to higher permeabilities. As stress is increased grain boundary cracks are easily closed resulting in reduced effective permeability. Therefore, the effective gas permeability of samples is even more sensitive due to grain boundary micro-cracks than intergranular pores. Authors have reported that the different types of cracks exhibits different permeability stress sensitivity (e.g. Ostensen, 1983; Kwon et al., 2001). As a result, the stress release different shapes of cracks might generate and samples partially saturated with water might exhibit different stress sensitivity. Because of this the effective gas and relative gas permeability of some samples were more sensitive to stress, however

some sample are not so stress sensitive. Presumably, the water accumulations in the micro-cracks might exhibits varying proportions/ water fractions depending on micro-cracks shape. Some cracks are nail like some are thin sheet tubular like and slotted pores as reported within Ostensen (1983). So, due to this, different samples experiences different stress sensitivity behavior and permeability sensitivity follows different decline trends with increase in confining stress.

Several other authors have reported that the highest reduction in permeability due to increasing overburden stress takes place in those samples which are dominated by micro-cracks (e.g. Shanley et al., 2004). Jones and Owens (1980) supported the observation made by Thomas and Ward (1972) about the impact of stress on sandstone rock permeability. They reported that the influence of stress could be explained by the pore structure of rock such as thin tabular like pore throats might be closed due to stress increase hence the reduction in permeability could be observed. Byrnes et al. (2001) found that permeability decreases due to the closing of pore throats due to increase in confining stress. They linked this concept of reduction in permeability with the Klinkenberg slippage factors and reported that as the confining stress increases the gas slippage factor increases, which decrease the permeability due to the decrease of the cross-sectional area of the thin tabular pores. In these, situations it would be expected that the variances between laboratory permeability and the permeability at in-situ conditions of reservoirs at higher stress levels could be the result of closing of microfractures as a result of stress.

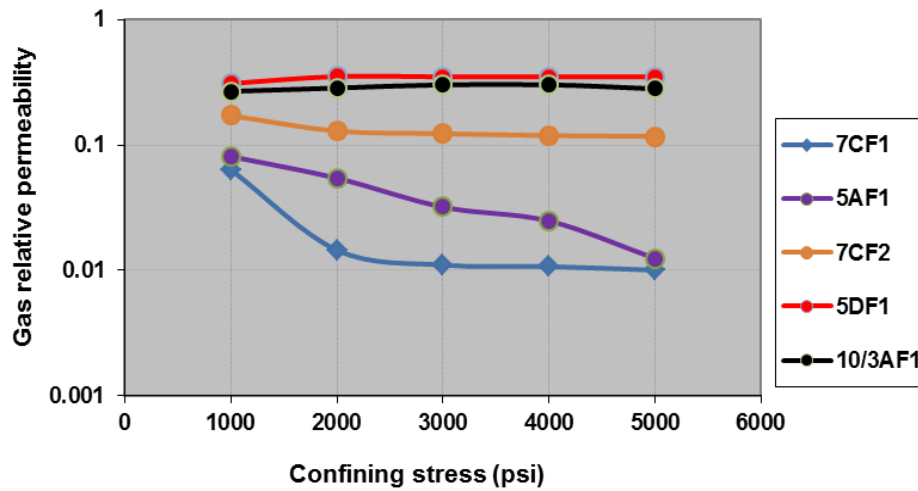


Figure 6.9 Stress sensitivity of relative permeability of samples with absolute gas permeability  $k_g \geq 0.2$  mD.

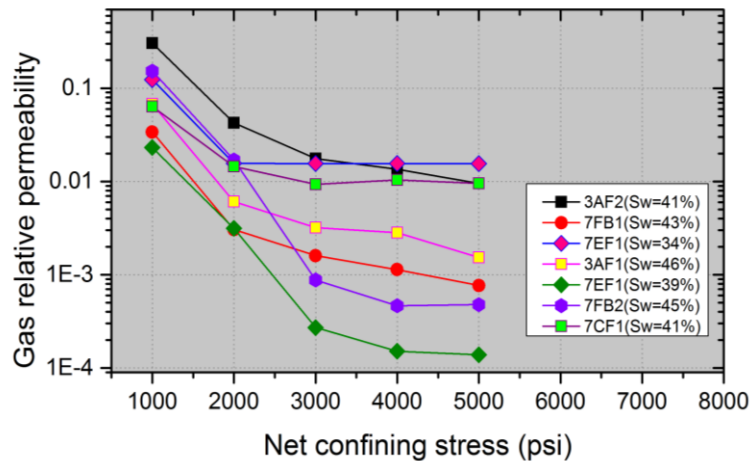


Figure 6.10 Stress sensitivity of relative permeability of a samples with absolute gas permeability  $k_g < 0.02$  mD.

Furthermore, the gas relative permeability was compared with low stress measurements at 1000psi and high stress gas relative permeabilities of samples which were obtained at confining stress of 4000psi. The high stress measurements were performed by the steady state permeability method by placing the samples into core holder at confining stress up to 4000psi. The gas was injected for longer period of time to measure the effective gas permeability. Although, the method was difficult as it was requiring longer stabilization time to reach steady state.

The effective gas permeability of samples is largely controlled by pore pressures (e.g. Walls, 1982). Water tends to accumulate in larger pores as a result of stress, which

restricts the flow of gas until unless there is a pressure gradient to displace water out of those pore spaces (e.g. Walls, 1982). Jones and Owens (1980) performed experiments on samples from Sprit River cores showed that to decrease water saturation from 100% to 40% experiments requires a pressure gradient of 391psi/cm. The present study experiments were about 20psi/cm therefore, water movement would not be expected within the studied samples. The higher pressures have also disadvantages that might alter the rock internal pore structure due to the small samples size that is why smaller pressures were applied. The relative permeability data analysed is summarized in **Figure 6.11**. The large difference can be seen in relative permeability data at low and high confining stress at similar saturations. The results shows that there is a downward shift in the samples relative permeability curve at higher stress compared to low stress relative permeability at similar saturations. There are several reasons that led to differences at high stress and low stress relative permeability. Authors have noticed that within tight rock samples the effect of redistribution of water by changing stress could further decrease effective permeability (e.g. Al-Hinai et al., 2007).

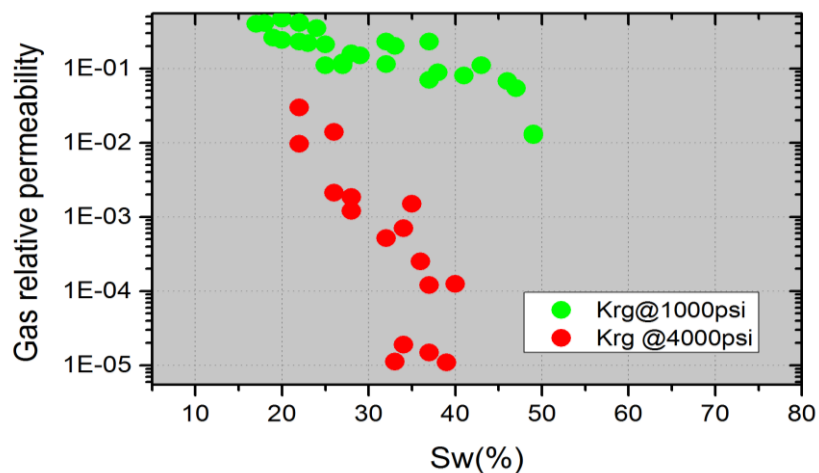


Figure 6.11 Diagram showing gas relative permeability results. The relative permeability measurements made at different stress conditions for sample sections of core samples.

The flow of gas as a non-wetting fluid more likely be blocked due to water redistribution as it can be seen from **Figure 6.12**. It should also be emphasized that the **Figure 6.12** is very simplified and might not reflect the actual grain particles deformation and brine redistribution. Although, during laboratory permeability measurements, as effective stress increases the pore diameter becomes smaller which forces grains to get closer hence a shift in pore throat diameter could occur that might be

expected resulting in smaller pore throat size. Therefore, it was thought that brine starts redistributing and occupies more pores potentially blocking some pore throats for gas flow resulting in lower gas relative permeability. Similar observations were also reported by Al-Hinai et al. (2008) who reported the effective permeability of partially saturated fault rock samples from the Clashach Quarry, Invernesshire UK and the Vale of Eden, Cumbria UK as well as tight rock samples. They thought that by increasing overburden stress the grain particles forced and were packed together, which resulted in reduction of the pore throat size and redistribution of water. The redistribution of water towards larger pores reduces the non-wetting fluid flow. Ali et al. (1987) conducted experiments of the effective permeability of partially saturated Berea sandstone cores at stresses of up to 6000psi. They reported decrease in oil relative permeability due to overburden stress. On theoretical grounds, they speculated that when stress increases the pore throats size decreases. Then, the wetting phase moves and occupies more pore spaces which disrupt the pore connectivity and tends to trap the no-wetting phase flow. Similarly the present study shows that permeability reduced at higher stresses because of water redistribution led to poor connectivity of pore throats.

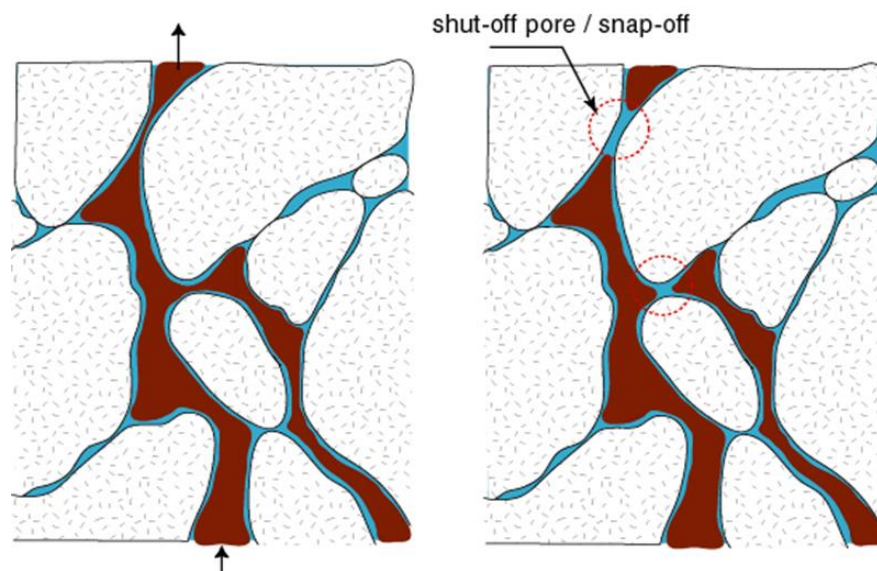


Figure 6.12 The illustration is the representation of water redistribution with increasing applied stress (taken from Al-Hinai et al. 2008).

In summary, the effective and relative gas permeabilities are very sensitive to stress in the laboratory. The gas relative permeabilities are sensitive to stress particularly to those samples which have lower absolute permeability. In low permeable samples there are more chances to form grain boundary micro-cracks due to stress relief during core

recovery process which were observed from polished thin sections within few samples that is why low permeable sample resulted in large decrease in effective and relative gas permeability at higher confining stress. The water redistribution due to stress increase presumably occupies more space which tended to block the flow of gas hence reduce the permeability. The effective gas permeability stress sensitivity discussed might not be exclusive however there might be other reasons that may impact need to be investigated. However, these results suggest that it is essential to understand both the relative permeability and its sensitivity to stress when assessing the quality of resources and their production performance.

### 6.4.2 Gas relative permeability controls and differences

**Figure 6.13** provides the gas relative permeability results from the samples analysed. The samples from North Sea group-B and Hopeman fault rock samples have lower absolute permeability than North Sea Group-A, therefore the lower absolute permeability samples appears to have lower relative permeability (**Figure 6.13**). The relative permeability plotted has shown scatter, the reason for such scatter in data is likely due to the problems with obtaining the water saturations within heterogeneous samples.

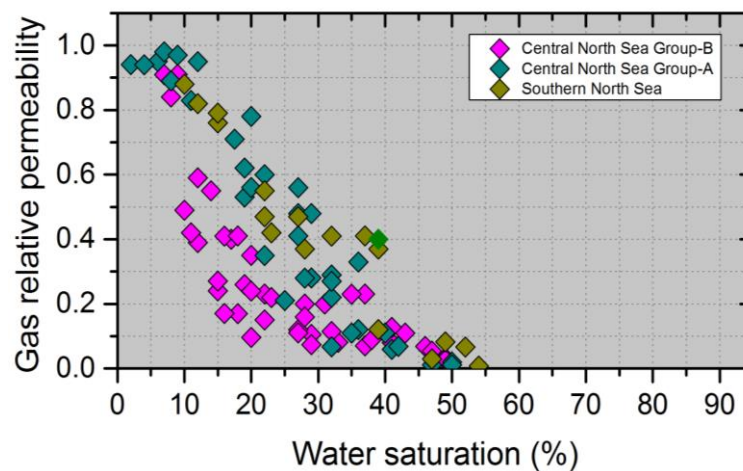


*Figure 6.13 Illustration is the combined gas relative permeability of samples versus water saturation from present study.*

The fault rocks itself occupy such a small volume compared to the host such that their water saturations are irrelevant in terms of volumetric calculations. Most likely the water saturation within the deformed bands might be higher than its associated undeformed host sandstones because the deformed band has smaller size pores that

might retain more fractions of water than its associated coarse grained host sediments. This might occur within fault rocks, because fault rocks have very small pore size which leads to high capillary attraction forces than its associated host sediments at similar capillary pressure. The gas relative permeability and capillary pressure data is plotted in **Figure 6.14** shows that samples with the higher absolute permeability appears to have higher gas relative permeability values at a given capillary pressures.

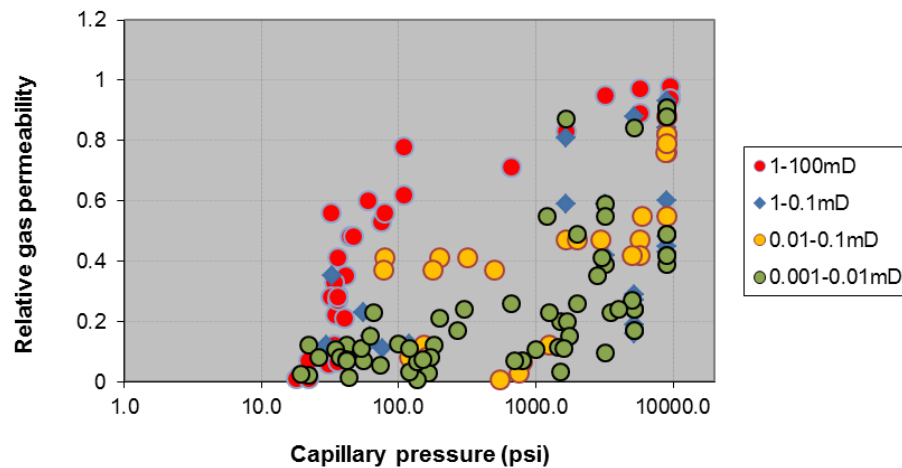


*Figure 6.14 The illustration is the semi-log plot of gas relative permeability versus capillary pressure for all samples. Data subdivided based on the range of measured absolute gas permeabilities is given in brackets.*

Furthermore, the geometry of the pore throats and their connectivity plays a significant role in controlling the permeability (e.g. Fetter, 1993; Motealleh and Bryant, 2009; Tiab and Donaldson, 2011). In **Figure 6.15** the data is subdivided into five groups based on the pore size of the samples studied, which shows that samples with lower relative permeability have smaller pore throat size, essentially the permeability is controlled by pore throat size. The relative permeability is more likely be affected by combination of factors such as pore geometry, interconnectivity of pores system, distribution of pore throat size and occurrence of clay minerals and other infilling minerals if they exists (e.g. Bennion et al., 2002). Authors have argued that the pore throat size and the number of pores occupied by phases depend on the distribution of pore size and the wetting tendency of the phase. If the interconnection of pores to pass the non-wetting phase is negligible, that shows that the hydraulic conductivity is lost and the relative permeability to that phase becomes negligible (e.g. Bachu and Bennion, 2008).

Several other authors have argued that the tight-rocks have very complex pore system that is dominated by different shapes of pores these might result in specific issues relating to multiphase flow. The existence of such a complex pore structure might result in reduced rate of effluent flow such as phase trapping. The explanations about favourable and unfavourable pore structures related to the phase trapping could be found in Bennion (2009) who demonstrated that a pore structure in which the effective permeability is controlled by moderately smaller fractions of the pore space, which comprises of interconnected meso- or macropores or little cracks and would not be sensitive to water-based trapping. These might be slightly more able to store the water without obstructing the major pores. A pore structure of a more uniformly distributed of micro-pores (1-10  $\mu\text{d}$ ) might be by a slight increment in water saturation result in stopping the flow by clogging the pores and in this manner a reduction in effective gas permeability occurs through the entire pore structure. Furthermore, he argues that this phenomenon of phase trapping might occurs in pore spaces which are very small with narrow pore throats openings. Similarly, the fault samples studied were phyllosilicate-framework faults with higher clay contents may have smaller size pore throats could be severely affected. Therefore, within narrow pore openings of rocks which are partially saturated with water may retain more water and trapping of water may occur (e.g. Lake, 2005) that will more likely result in reduction of sample permeability. It was also argued by Shanely et al. (2004) that within low permeability rock samples, water occupies more spaces and reduces the connection between pores, so the degree of connection between pore throats becomes less significant, which leads to the reduced flow of non-wetting phase. Hence, in water-wet rocks, water may have imbibed into the smallest pore-throats disrupting the continuity of the gas throughout the pore network. Most likely, water as a wetting phase occupies the smaller pore throats of the porous rock and the non-wetting fluid preferentially flow through larger size pore (e.g. Shanely et al., 2004). If pore spaces occupied by higher fractions of water covering the larger pores will disrupt the non-wetting fluid flow hence leads to lower relative permeability to gas. Similarly, within tight gas sandstones at higher water saturations a phenomenon might occur which is called permeability “jail”, at this saturation no any flow of wetting and non-wetting occurs (e.g. Cluff and Byrnes, 2010). Existence of “jail” phenomena depends upon the rock geometry and the saturations percentages, in some tight rock that occurs within the range of 55% to 80%, the tighter are the rocks wider saturation range

of Jail could be expected (e.g. Cluff and Byrnes, 2010). The fault rocks are heterogeneous, so it is very difficult to define the saturation percentages at which the “jail” phenomenon occurs. The “jail” permeability could not be specified for the fault rock samples as fault rocks are having variable microstructure so the idea of permeability “Jail” could not be defined for the samples studied. This should be further investigated by collecting more data on different fault rock types.

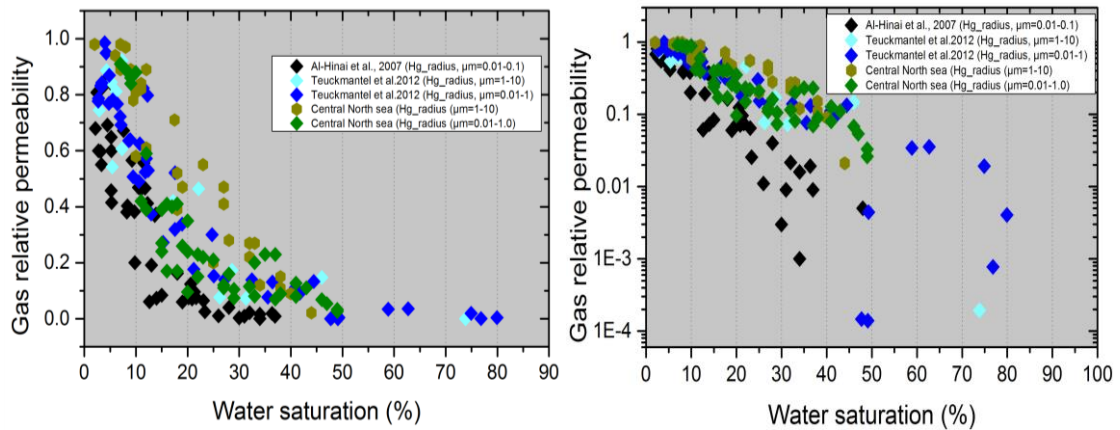


Figure 6.15 Plot of the gas relative permeability versus water saturations of fault rock samples based on pore radius data. The data plotted is from this study and collected from published studies of Al-Hinai et al. (2008) and Tueckmantel et al. (2012) respectively; the data were plotted on linear graph (left side) and semi-log graph (right-side).

In **Figure 6.16** the relative permeability data is subdivided into four groups based on absolute permeability which shows that the lower absolute permeability samples appears to have lower relative permeability at given water saturations. This shows that relative permeability of low permeable samples may not have a continuous interconnected pore network so these pores might not significantly contribute to gas flow (e.g. Benion et al., 2002). Similar observations have been reported within tight rocks gas relative permeability data based on range of absolute permeability values by Cluff and Byrnes (2010). **Figure 6.17** shows that at given saturation samples with lower absolute permeability have shown a downward shift in relative permeability curve.

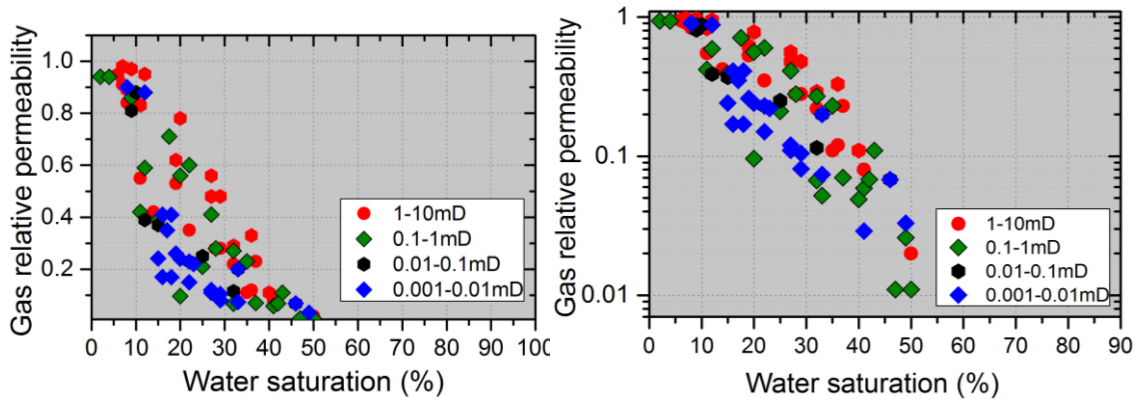


Figure 6.16 Illustration is the gas relative permeability of fault rock samples versus water saturation; the different colours indicate different ranges of absolute gas permeability. The data plotted on linear graph (left side) and semi-log graph (right-side).

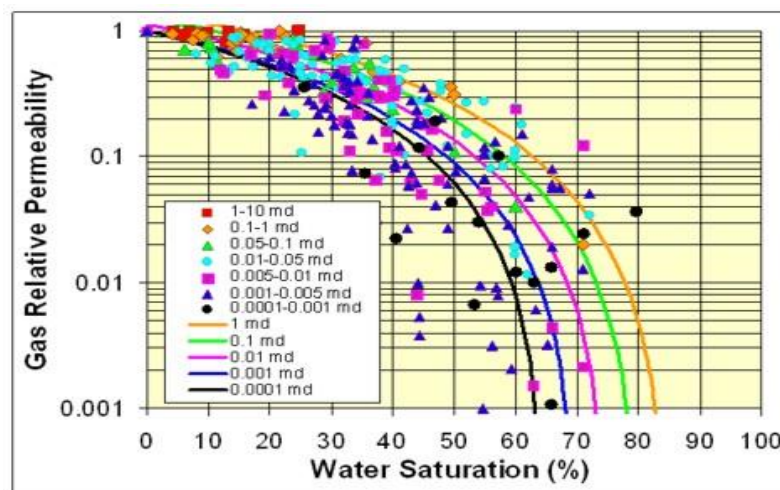


Figure 6.17 Gas relative permeability as a function of water saturation. The data represented with symbols are measured data and curves represent the predicted data (taken from Cluff and Byrnes, 2010)

Clay minerals has a major impact on permeability of samples, permeability could be controlled by the amount of clays present within samples (e.g. Khilar and Fogler, 1984). The cores samples might went under different processes of cementation or presence of authigenic clay minerals resulting in narrow pore throats, such rocks will certainly lead to lower permeabilities (e.g. Al-Hinai et al., 2006; Armitage et al., 2011). Sample containing clay mineral fractions, if interact with low salinity brines might result in pore size decrease due to creation of immobile bound water layer, hence that causes the reduction in permeability (e.g. Faulkner, 2004). Similar observations were made from present study data that higher the clay fractions lower will be the sample relative permeability (**Figure 6.18**). Land and Baptist (1965) reported that if sandstone samples containing different types of clay minerals their permeability might be sensitive if

exposed to water as a result of hydration. However, this should not be the case for the sample used in present study as these were saturated with (NaCl) brines. Land and Baptist (1965) also argued that in some situations the sandstone samples contains very small amounts of clays which might be found in traces, so this concept might not be generalized to all sandstone samples. The relative permeability of the samples studied does not show a simple relationship with clay fractions. Even though, few samples having higher percentages of clays appear to have higher relative permeability than those with lower clay contents. The samples with higher clay content and higher relative permeability appearing on the curve might have higher absolute permeability values. Therefore, the relative permeability could not necessarily be controlled simply with clay content. There might be several other factors that control the relative permeability such as the degree of cementation and cataclasis that need to be investigated by collecting more data on different fault rock types from different field locations, in particular, the faults formed in clay-rich sequences.

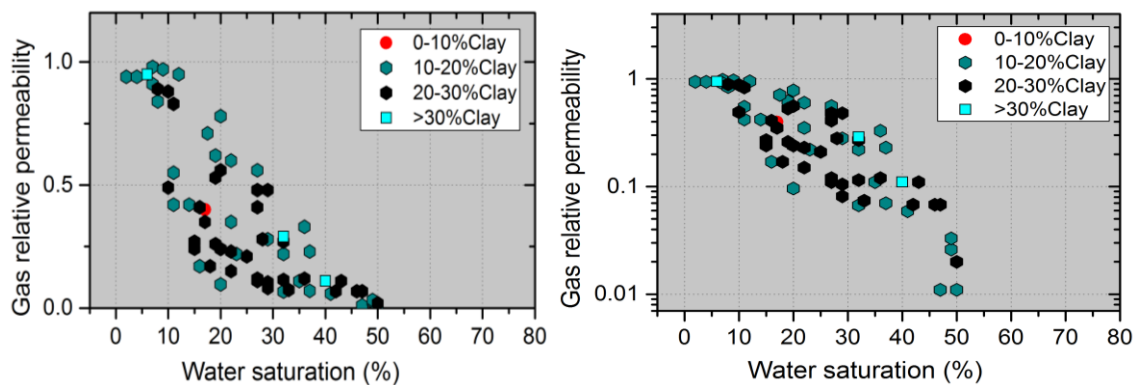


Figure 6.18 Plot of the gas relative permeability and water saturation relationship on linear and semi-log graph, the different colours indicate different ranges of clay content of host sediments.

As mentioned previously, the fault a rock comprises of small volume so the saturations calculations are irrelevant in terms of volumetric calculations. The highly heterogenous nature of fault rock samples means that their relative permeability relation with water saturation varies from sample to sample. Therefore, it would be more sensible to relate their relative permeability to capillary pressure. For this reason gas relative permeability of samples are plotted versus capillary pressure (**Figure 6.19**). It was observed that samples with higher gas relative permeability have higher capillary pressure. Similar observations from 90 Fathom faults two-phase flow measurements were also made by

Tueckmantel et al. (2011). The scatter in relative permeability and capillary pressure could be the samples heterogeneity.

Moreover, the two-phase flow has importance to control flow across faults. Suppose that fault is sealing to the columns of hydrocarbon height that could be supported by height of fault and that is related to the fault rock pore throat radius (e.g. Schowalter, 1987). Based on the empirical relations of Pitman (1992) pore throat radius could be obtained corresponding to (capillary) entry or threshold pressures of faults. The values of pore throat radius of 0.18  $\mu\text{m}$  and 13.3 $\mu\text{m}$  has been reported by Gibson (1998) and Ogilvie and Glover (2001) which were corresponding to the heights of 137 and 2m respectively. Knott (1993) demonstrated that within the North Sea reservoirs 30% of seals are formed due to the sand to sand juxtapositions. Gibson (1994) found that hydrocarbon column heights that were closely related to the fault throw for sand-sand juxtapositions and the throws were around 75 m (246 ft) based on his observations he found that these faults were potentially sealing faults. These studies suggest that fault formed in these situations could be potential barrier to fluid flow in case of two phase hydrocarbon flow. Similar to these studies, present study data showed that the Central North Sea group-B samples and samples from Hopeman cataclastic faults having low permeabilities and poorly sorted fine-grained sands with small pore-throat size could be able to act as a capillary seal in two-phase flow situations. This might be the reason to history match the production data of fault compartmentalized reservoirs by incorporating the two-phase flow properties of fault rocks. As an example, Zijlstra et al. (2007) showed a good history match of Rotliegend reservoirs, as the faults identified within these reservoirs were formed in low permeability cataclastic faults and were modelled by taking account of multiphase flow properties of fault rocks.

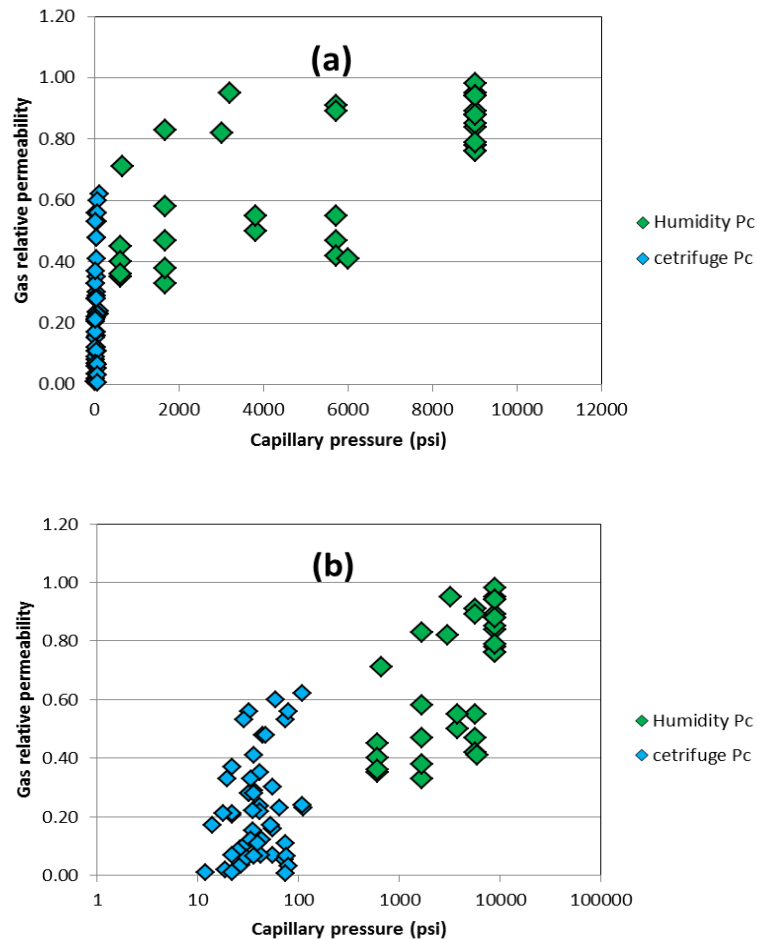


Figure.6.19 The relative gas permeability versus capillary pressure plotted on (a) linear graph (b) semi-log graph. The data presented is obtained during this study from North Sea fields core samples. The different colours indicate different techniques used for saturation alterations.

### 6.4.3 Capillary pressure

The capillary pressure curves of all plugs were experimentally obtained using the different techniques discussed in **section 3.5**. The capillary pressure versus saturation graph shows that data obtained using the ultracentrifuge technique does not follow the trend with the data obtained from humidity chambers and Hg injection methods (**Figure 6.20**). It was observed that capillary pressure data from different rock samples follows the different trends at given water saturation. Even though exceptional estimates of equilibriums at each rotational speed were obtained and that is required for calculations to obtain the capillary pressure curve. From production measurements the capillary pressures were obtained by applying known mathematical solutions (Forbes, 1997). The mismatches were observed in plotting capillary pressures for different samples. These mismatches could be the results of the samples heterogeneity as samples used were composed of deformed and undeformed sediments of varying microstructure. Another

possibility was the different saturation monitoring techniques used to achieve saturation equilibrium. The centrifuge methods results in irregular changes in water saturation along the core sample length because the centrifugal force gradually increases with distance from the centre of rotation (Hagroot, 1980).

In conducting centrifuge capillary pressure measurements there is a common error that is not to achieve good calculations of the average saturation at equilibrium in each rotational speed (O'Meara Jr.et al., 1992). In centrifuges tests the equilibrium at a certain rotation speed is defined the condition where there is no more any further production of fluid was noticed (e.g. Fernø, 2008). Although, many authors have discussed about the concern in attaining time to reach equilibration within the centrifuge experiments (e.g. Hoffman, 1963, Slobod and Prehn, 1951, Ward and Morrow, 1987).

In general the high permeable samples greater than five mD to several hundreds of mD could reach equilibrium in 1 to 2 hrs of rotation, hence within the low permeability samples fluid production could be observed for longer periods and with slow decrease in saturation. Slobod and Prehn Jr. (1951) reported about the equilibrium times for samples with 2mD permeabilities to hundreds of mD. They achieved equilibrium very quickly in high permeability samples in few hours; on the other hand the low permeability samples after 20hrs at speed of 18000rpm showed that the saturations were still decreasing. Several others authors have also attempted monitor saturation and obtain the capillary pressure curve. Such as, Hoffman (1963) using centrifuge method attempted to measure capillary pressure of the sample which were more than 60mD permeability. The criterion set by Hoffman (1963) to achieve equilibrium for samples used for capillary pressure measurement was that if there is no further production occurs after at least one hour from the last noted production. Fernø (2008) argued that there is no such case in which samples reach equilibrium in less than 24 hour.

The likely explanation about variable time to reach equilibrium and the possible reason of difficulties in reaching equilibrium could be found in Ward and Morrow (1987). Ward and Morrow (1987) from experimental observations reported that possible reason is the high degree of fluid discontinuity within the rock pores and fluid retained within the edges of pore spaces. Another possible reason could be the lack of pore network connectivity which causes the lack of capillary equilibrium (Morrow, 1970). Similarly, the fault rocks are composed of different zone of deformed and undeformed formations

having variable pore structure and pore connectivity between host and fault formations could be the possible reason of the scatter in data. In **Figure 6.20** there were few data points which were not fitting well on curve generated were removed.

A part from discussion about the capillary pressure measurement and its interpretation issues, capillary pressure plays a significant role in trapping oil and water within narrow pore spaces of rock (e.g. Berg, 1975). The factors responsible for trapping hydrocarbons includes the radius of the pore throats, oil and water interfacial tension and wettability and is quantified by the relationship of flow through rock pores (Purcell, 1948). Detailed discussions about capillary pressures and could be found in Berg (1975) and Schowalter (1987).

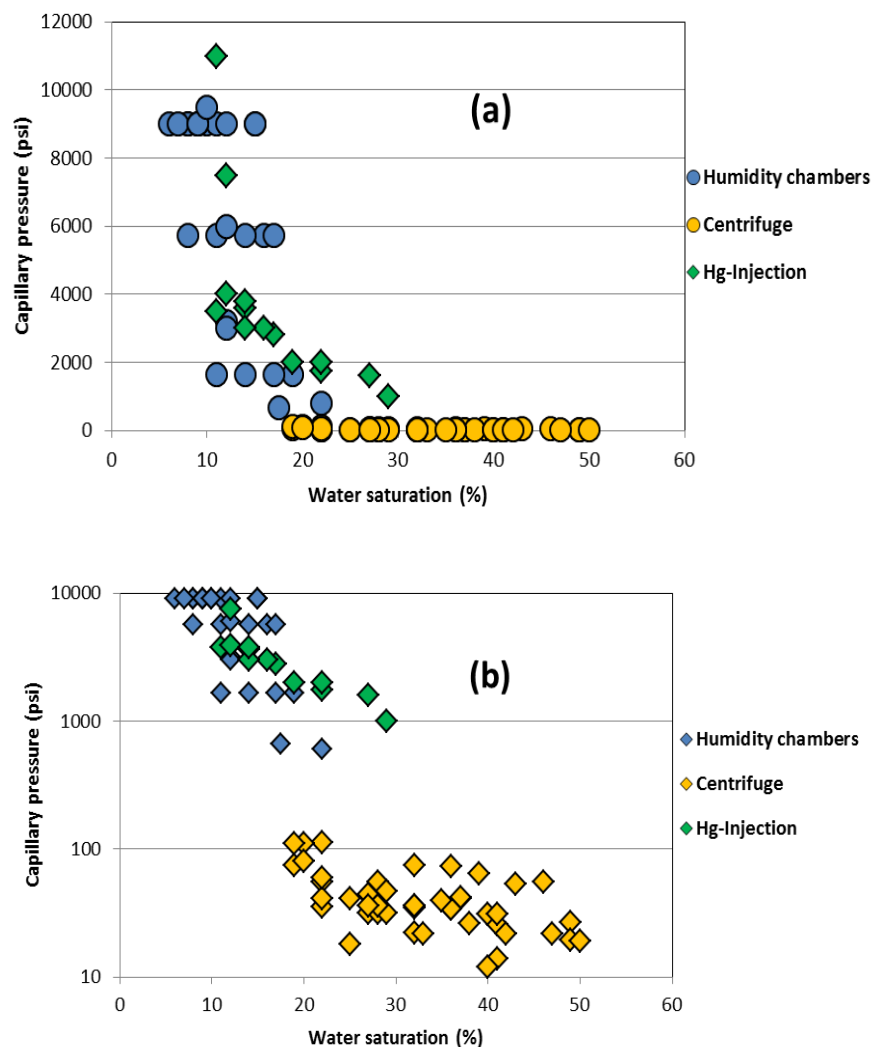


Figure 6.20 Plot is the capillary pressure versus water saturation. (a) The plotted data is on linear chart and (b) semi-log plot. The capillary pressure was obtained with three different techniques.

#### 6.4.4 Comparison of result with published two-phase flow properties of fault rock

The reason for collecting and comparing data on fault rock relative permeability is twofold: 1) the interest in modelling fault rock two-phase flow behaviour has only evolved after it was recognized by several authors that it is essential to incorporate the multiphase flow properties (relative permeability and capillary pressure) of fault rocks into simulations models (e.g. Fisher and Knipe, 2001; Fisher et al., 2001; Manzocchi et al., 2002 and 2010; Al-Busafi et al., 2005; Zijlstra et al., 2007). 2) The workers in simulation have almost resorted to use pseudo-properties (relative permeabilities and capillary pressures) when actual core data were unavailable (Manzocchi et al., 2002, 2008). Another reason was that due to lack of fault rock multiphase flow data authors also attempted to model fault rocks by using tight gas sands data as an analogue (e.g. Zijlstra et al., 2007). However, as per author's knowledge, there are two published experimental data on fault rock relative permeability and capillary pressure (e.g. Al-Hinai et al., 2008; Tueckmantel et al., 2012) have provided a sound basis for using relative permeabilities and capillary pressures for fluid flow simulations and modelling of fault compartmentalized reservoirs. The availability of fault rock relative permeability is yet in scarcity because measurements of such a low permeable samples are very difficult to obtain and are time consuming. However, the availability of data on relative permeability has provided a foundation of evidence base and that can be used to quantify the fault sealing behavior.

The gas relative permeability and capillary pressure results from present study and those collected from published sources are summarized in **Figure 6.21**. Al-Hinai et al. (2008) was the first who had reported the cataclastic fault rock relative permeability capillary pressure. The absolute permeability of their studied samples ranges from 0.01md to 0.2mD for Vale of Eden samples and from 0.001mD to 0.005mD for the Clashach fault samples. The second data set on two phase flow properties of fault rock comes from the work of Tueckmantel et al. (2012) who published two phase flow properties on small and large scale faults of 90 Fathom fault. The relative permeability data plotted together with other published fault rock data sets, the data from central North Sea group-B samples appears to be the lowest and follows the similar trend as of the 90 Fathom fault samples from Tueckmantel et al. (2012). The relative permeability data from central

North Sea group-A samples and the data from Al-Hinai et al. (2008) appear to follow the same declining trend. On the other hand the central North Sea group-B samples data and the data from Tueckmantel et al. (2012) appears to be lower than Al-Hinai et al. (2008) relative permeability data. This reflects that samples with lower absolute permeability have lower relative permeabilities at the similar saturations. The data presented here and that reported by Byrnes et al. (2003) have shown similar behaviour as the tight gas samples considered as an undeformed low permeability sandstone samples. The slip-surface cataclasite fault rocks from 90 Fathom and samples from Hopeman fault rock virtually consists of major part of faults resulted in low permeability and these might have resemblance with undeformed tight gas sands (e.g. Tueckmantel et al. (2012)).

It should also be noted that there is a large variation in data, which reflects the samples heterogeneity. Another concern is that the different studies have conducted effective permeability measurements at different stress conditions. Tueckmantel et al. (2012) conducted experiments at an effective stress of 1500psi, while the data from Al-Hinai et al. (2008) measured using an effective stress of 500psi. The present study relative permeability data points of 1000psi confining stress used for comparison with the Al-Hinai et al. (2008) and Tueckmantel et al. (2012). To better understand the controls and difference of the different data sets it is essential to consider the conditions under which these properties were measured. The stress differences must be taken into account while comparing the relative permeability data of fault rock samples for assessment to use for fault sealing behavior.

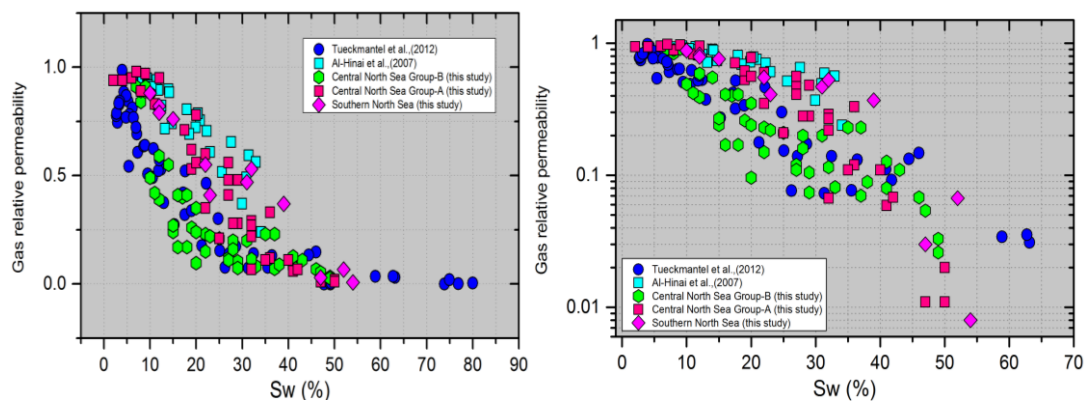


Figure 6.21 Plot of the fault rock gas relative permeability versus water saturation for all samples used during the present study as well as that obtained in the studies of Al-Hinai et al. (2008) and

Tueckmantel et al. (2012) respectively (left side data are on linear graph). The same data of relative permeability versus water saturation are plotted on semi-log graphs (right-side plot).

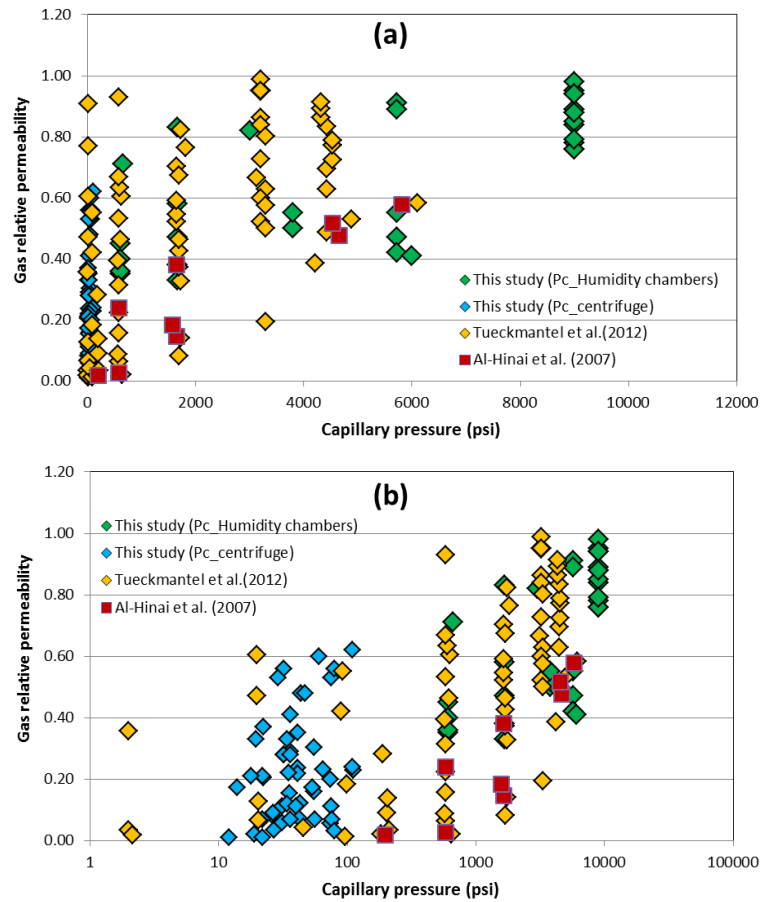


Figure 6.22 Plot showing the relationship between relative permeability and capillary pressure from this study, and collected from Al-Hinai et al. (2008) and Tueckmantel et al. (2012).The data is presented (a) linear graph and (b) semi-log graph.

### 6.4.5 Implications

The laboratory results on fault rock two phase flow properties presented here are incorporated into a specific example of simulation model into **chapter 7** to evaluate effects across fault. Considering the impact of faults on subsurface flow, here a general discussion is provided.

Samples effective and relative gas permeability measurements demonstrated more sensitivity to the stress than the single phase gas permeability values, particularly at higher stress conditions. Samples with low absolute permeabilities were observed that their relative permeabilities were likely to be more sensitive to stress. The reduction in rock permeability at lower stress may not reflect the in-situ reservoir conditions due to core damage effects. So the permeability reduction effects should be taken into account

at higher levels of stress around 2000psi up to 5000psi, this might vary and depends upon the type of fault rock and diagenesis.

Cataclastic fault rock having absolute permeabilities  $<0.12\text{mD}$  have gas relative permeabilities values in range of 0.40 down to 0.02 at a capillary pressures  $>606$  psi. The capillary pressure of 606 psi measured under laboratory conditions is equivalent to  $\sim 380$  psi at reservoir conditions based on gas-water interfacial tension of  $72\text{mN/m}$  at ambient conditions and  $45\text{mN/m}$  at reservoir conditions of  $100^\circ\text{C}$  and 3000 psi pressure (e.g. Firoozabadi and Ramey, 1988). McCrone et al. (2003) reported a large gas column of 400m within one of the North Sea field (Indefatigable field) which would generate buoyancy force of only 540 psi even though it has large gas column. Therefore, if the fault rocks were present there would be expected to have relative permeability to gas of  $<0.02$ . Essentially the transmissibility multipliers calculated based on the single phase gas permeability values would overestimate cross-fault transmissibility multipliers by many orders of magnitude.

On the other hand, mercury injection data suggests that few samples from central North Sea at 20% water saturation have capillary pressure of around 10psi. The relative permeability indicates that the samples at that saturation would have a gas relative permeability  $k_{rg}$  of around 0.50. Assuming the water wet rock an oil water interfacial tension of  $25\text{dynes/cm}$ , brine and water densities of 1.0 and 0.7 respectively, at this water saturation  $S_w$  can only generate oil column of 15m.

The transmissibility multipliers calculated for fault rock based on their single phase permeability could be high just by factors of 2 for the segments of fault that is 15m above the water-oil contact. This implies that it may be essential to take into account of multiphase flow properties where there is very low absolute permeability fault rocks ( $<0.01\text{mD}$ ) are present within the central North Sea reservoirs. On the other hand it might not be so important to consider the multiphase flow properties where there is fault rocks with high absolute permeability ( $>0.1\text{mD}$ ) and low capillary threshold pressure are present. Interestingly, few recent publications have shown different concepts about the success of production history matching using single- and two-phase fault rock fault properties into production simulation models. For example, Zijlstra et al. (2007) showed how history match of Rotliegend reservoirs, which contain low permeability cataclastic faults similar to those analysed during this study were improved by incorporation

multiphase flow properties of fault rocks. On the other hand, Jolley et al. (2007) showed that good history matches of a Brent-type reservoir, in that low permeability fault rocks are not likely to be as continuous as in the Rotliegend. The history matching in such reservoirs could be achieved by calculating transmissibility multipliers based on their single phase permeability values without taking into account multi-phase flow behaviour. Therefore, these shows that fault rock should be carefully modelled by assigning appropriate flow properties.

## 6.5 Conclusion

This chapter has presented the first ever measurements of the relative permeability and air-brine capillary pressures of fault rocks from North Sea reservoirs. The main findings from work are:

- The stress sensitivity of effective gas permeability increases with decreasing absolute permeability. The effective gas permeability measured at different stress conditions is far more stress sensitive than is the absolute gas permeability under the similar stress conditions.
- The effective gas permeability from cataclastic faults and many of the phyllosilicate framework faults showed a significant reduction at higher stress of 4000psi and there was hardly any flow to gas at 5000psi effective stress. This indicates that fault rocks may act as effective barriers within southern North Sea.
- The gas relative permeability values of low permeability (<0.01mD) fault rocks are most likely to be <0.012. Therefore, if low permeability cataclastic faults are present within the reservoirs it may be necessary to take account of multiphase flow for simulation and modelling. Otherwise, transmissibility multipliers calculated based on the single phase gas permeability values would overestimate cross-fault flow in such reservoirs.
- Clay contents content has shown effect on permeabilities (effective and relative permeability). As clay percentages increases the effective permeability as well as relative permeability both decreases. This also depends on the samples absolute permeability.

# 7 Modelling the influence of fluid flow across fault

---

## 7.1 Introduction

Reservoirs often behave in rather unexpected ways during production. For example, Zijlstra et al. (2007) described a situation from the southern North Sea where the gas-water contact rose in a producing compartment relative to one that was not under production. In this case, it was interpreted that the fault was sealing to gas but not water. In another example, van der Molen et al. (2003) described a reservoir in which  $p/z$  vs cumulative production fell far more dramatically than expected. The authors interpreted this to be a result of fault compartmentalization. Several studies have claimed that reservoir simulations in which the impact of faults on fluid flow have been incorporated into the simulation models based on the absolute permeability of fault rocks have provided a good history match to production data (e.g. Knai and Knipe, 1998; Sverdrup et al., 2003; Jolley et al., 2007; Zijlstra et al., 2007; Irving et al., 2010). Other studies have suggested that fault permeabilities need to be reduced by several orders of magnitude to achieve a history match of production data (e.g. Sperrevik et al., 2002; and Fisher et al., 2005). However, changing properties without any strong justification is not recommended because history matches are inherently non-unique and by arbitrarily changing a property to achieve a history match may mean that one is not correctly modelling another important control on production. This situation is eloquently described by Dake (1994): *“Reservoir engineering is a complex subject for two reasons. In the first place, we never see enough of the reservoir we are trying to describe. Therefore, it is difficult to define the physics of the system and, therefore, select the correct mathematics to describe the physics with any degree of certainty. The second*

*problem is that even having selected a sensible mathematical model there are never enough equations to solve the number of unknowns*". Essentially, great care must be taken when drawing conclusions from different case studies, no matter how confidently the argument is reported.

Jolley et al. (2007) presented fault seal analysis studies on several fields from the Brent Province (including the Brent and North Cormorant Fields), which showed how faults could act as barriers on a production time-scale and that history matches to simulation models could be improved by incorporating realistic fault permeability values. It appears that in Brent Group fields fault-related compartmentalisation is not a major issue where there is clear juxtaposition of clean sand against clean sand (e.g. self juxtaposition of the Etive Formation in the Brent, Gullfaks and Ninian fields).. This is consistent with the dominant fault rock type being disaggregation zones, which have very similar petrophysical properties to their host sandstone. On the other hand, faults that deform sediments within higher clay content tend to act as barriers to fluid flow over production time-scales. This is consistent with presence of clay smears or phyllosilicate-framework fault rocks (e.g. Fisher and Knipe, 2001). In those situations, however it might not be justifiable to dramatically reduce cross-fault transmissibility below that calculated from single phase permeability values. For example, Al Hinai et al. (2008) produced a simple simulation model of the reservoir described by van der Molen et al. (2003) and showed that production could not be matched using a traditional fault seal analysis in which only the single phase permeability of the fault rock was incorporated into the model. A good match of the production data was, however, achieved when the multiphase flow behaviour of the fault rock was incorporated into the simulation model. The failure to take into account multiphase flow properties of fault rocks is a not the only reason why cross-fault transmissibility might need to be reduced far more than would be expected based on published values of single phase fault permeability. In particular, as shown in the previous chapters, fault permeabilities maybe stress sensitive so permeabilities in the reservoir could be orders of magnitude lower than measured in laboratory conditions. Incorporating multiphase flow properties of faults into simulations models is not straightforward (Manzocchi et al. 2008). So in reality engineers generally model faults in a fairly simple manner. This might change if simple rules-

of-thumb could be provided that would provide a guide as to when it is worth investing the time into incorporating multiphase flow and single phase flow properties into simulation models. Conducting sensitivity studies is a potentially valuable way to construct such guidelines. This chapter attempts to fill some of these knowledge gaps, by incorporating the results reported in **chapter 6** obtained on fault rock two-phase flow properties (i.e. relative permeability and capillary pressures) into simulation to model cross fault flow behavior.

The chapter starts by describing the existing methods of fault rock flow modelling and also discusses the importance and impact of two-phase flow properties for fault modelling (**Section 7.2**). The new data sets obtained on single and two-phase flow properties of fault rock to model flow across the fault are presented in **Section 7.3**. Then model input parameters and geometry is described in detail in **Section 7.4**. The results from different cases of simulations run by assigning fault rock properties derived from laboratory data of single and two-phase flow are presented in **Section 7.5**. Finally, the results are discussed and main findings are summarized in the **sections 7.6 and section 7.7** of this chapter.

## **7.2 Methods of fault modelling**

The influence of flow across fault considering the two compartments of reservoir has been modelled using the Eclipse software. In simulation model the fluid flow between neighbour cells is controlled by the cell-cell transmissibility as a function of the cell properties and cell geometry. Although, if there is fault rock that would have smaller permeability than its associated host sands and will impede the fluid flow across juxtaposed sands. The influence of reduction rate of flow due to fault would be taken into consideration using fault transmissibility multipliers, that would be calculated from fault rock permeability and thickness (**Figure 7.1**). Modelling the faults in the simulation involves the calculation of transmissibility multipliers by modifying the flow between juxtaposed cells (Knai and Knipe, 1998; Manzocchi et al., 1999). After the work of Manzocchi et al. (1999), if there is no fault, then transmissibility separated by two grid blocks can be calculated using following relation,

$$\text{Trans}_{i,j} = \frac{2}{\frac{L_i}{k_i} + \frac{L_j}{k_j}} \quad (7-1)$$

where,  $L_i$  and  $L_j$  are the cell lengths,  $k_i$  and  $k_j$  are the permeabilities of the undeformed cells. If there is fault present, then the transmissibility between two grid-block centers,  $\text{TransF}_{i,j}$ , separating fault of thickness  $t_f$  can be calculated using following equation:

$$\text{TranF}_{i,j} = \left( \frac{2}{\frac{L_i - t_f}{k_i} + \frac{2t_f}{k_f} + \frac{L_j - t_f}{k_j}} \right) \quad (7-2)$$

where and  $k_f$  is the fault rock permeability,  $t_f$  is the fault rock thickness. To account for the effect of fault rock in the Eclipse simulation a  $TM$  was applied to the face of grid-blocks adjacent to the fault; the  $TM$  is calculated using,

$$TM = \frac{\text{TransF}_{i,j}}{\text{Trans}_{i,j}}$$

The following equation was used to calculate the fault transmissibility multipliers (Manzocchi et al., 1999).

$$TM_{abs} = \left( 1 + \frac{t_f \left( \frac{2}{k_f} - \frac{1}{k_1} - \frac{1}{k_2} \right)}{\frac{L_1}{k_1} + \frac{L_2}{k_2}} \right)^{-1} \quad (7-3)$$

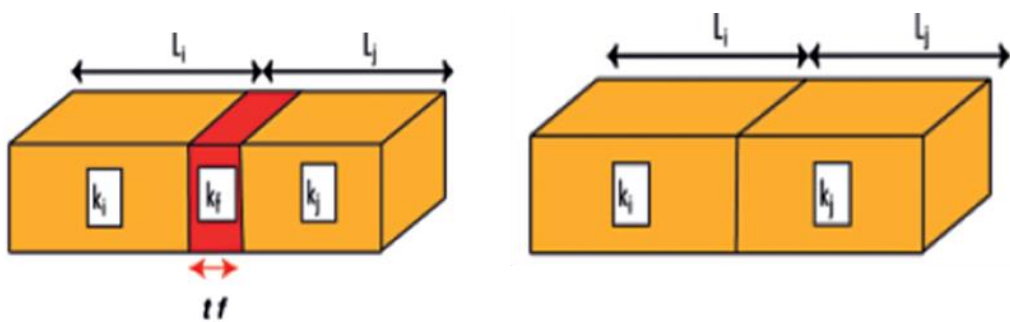


Figure 7.1 illustrations is the methods of representing the transmissibility multipliers within within faulted and unfaulted cells of the reservoirs (taken from Zijlstra et al. 2007)

The shortcoming of the above methods of fault modelling is that it does not capture the multiphase flow properties of fault rocks. In the past, authors have adopted different methods of fault modelling to take into account of two-phase flow

properties. According to Manzocchi et al. (2010) two phase flow properties of fault rocks could be assigned in two distinct ways. One simple method of fault modelling is the local grid refinements, in this method the two-phase flow properties (i.e. relative permeability and capillary pressure) of the fault rocks can be assigned explicitly in the simulation models (e.g. Manzocchi et al., 1998, 2002; Al-Busafi et al., 2005; Berg and Øian 2007, Al-Hinai et al., 2008, Teuckmantel et al., 2012). Alternatively, a method of fault modelling called the ‘capillary entry height model’, to incorporate the multi-phase flow properties of faults in Rotliegend reservoirs in the southern North Sea was proposed by Zijlstra et al. (2007). This method of reservoir modelling divides the fault into three regions in accordance to the free water level. In this the fault is divided into three different regions. In first region where only the water is present whose transmissibility multipliers will be calculated using **equation 7.3** presented above. However, in second region as shown in **Figure 7.2**, the hydrocarbons immediately above the free water level, where the buoyant force in hydrocarbon column is not enough to exceed the fault rock threshold entry pressure, therefore the relative permeability to hydrocarbon is zero and the fault will be acting as a sealing fault that would be treated with transmissibility multiplier of  $TM=0$ , to height above free water level relative to fault entry pressure. The data from mercury injection was used to calculate the fault sealing height and buoyancy forces.

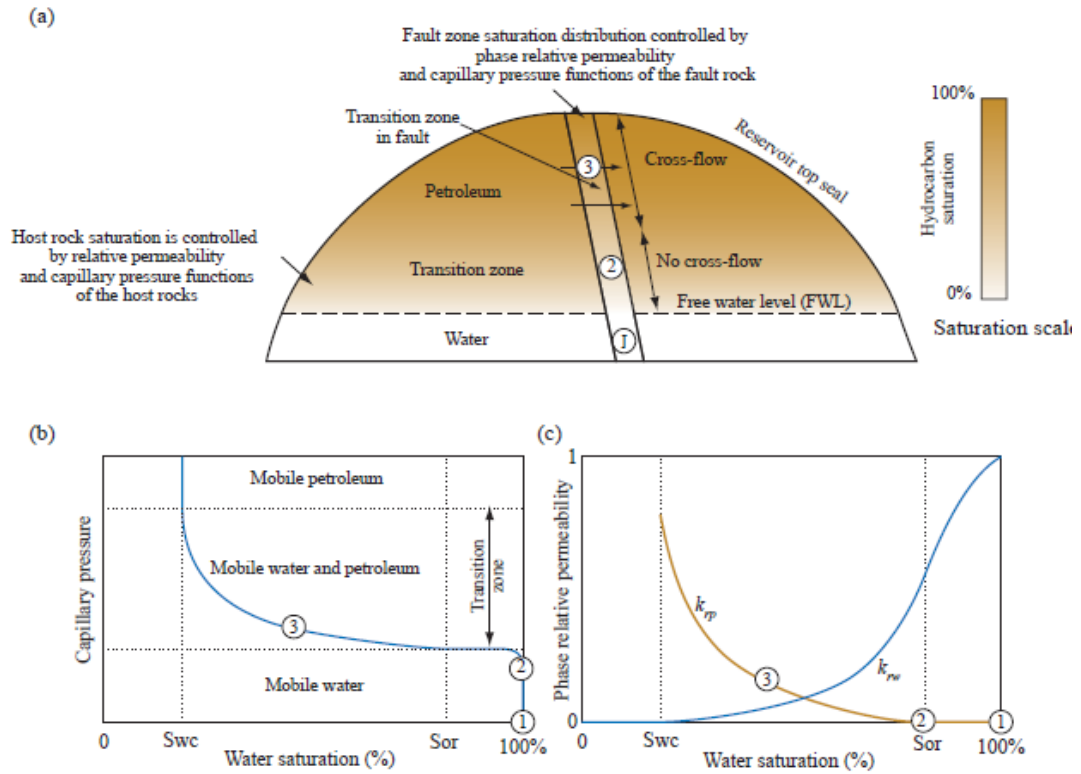


Figure 7.2 A reservoir model representing hydrocarbon saturation within fault zones. In this model the fault is divided into three different zones, below free water level the fault will be assigned TMs, which will be determined from fault rock and host rock single phase permeabilities. within the zone 2, fault is immediately above the free water level, where capillary threshold pressure could not be exceeded by hydrocarbon, that would be considered as sealing fault for hydrocarbon (TMs=0). The zone 3 represents that the fault rock entry pressure has been exceeded so it is essential to calculate the TMs to consider the relative permeability of the fault rock (taken from Al-Hinai PhD thesis).

In third region (**Figure 7.2**) in case of the height above free water level (FWL), where the buoyancy force in the hydrocarbon column goes above the capillary entry pressure of the fault rock. In that situation, the fault rock will be permeable to hydrocarbon which will be associated to fault rock capillary entry pressure and its relative permeability. Hence, in that case, the relative transmissibility multipliers will be required to model the fault rock by taking into account multi-phase flow behaviour. Therefore, the modified transmissibility between gridblocks will be obtained using following relation:

$$TM_{abs} = \left( 1 + \frac{t_f \left( \frac{2}{K_f(Krg)} - \frac{1}{K_1} - \frac{1}{K_2} \right)}{\frac{L_1 + L_2}{K_1 + K_2}} \right)^{-1} \quad (7 - 4)$$

In above equation the  $k_{rg}$  is the gas relative permeability required for calculation of modified transmissibility multipliers.

### 7.3 Incorporating host and fault rock properties into flow simulation model

The fault rock properties incorporated into Eclipse2013 simulation software and the flow properties (single and two-phase flow) were measured in the laboratory during the present study and are presented in previous chapters. The transmissibility multipliers were calculated based on arithmetic averages of fault rock absolute permeability (**Table 7.1**). The arithmetic average permeability and porosity from host and fault rock were assigned during fluid flow modelling and are given in **Table 7.1**.

*Table 7.1 The absolute fault and host permeabilities and porosities assigned to simulation models that based on data presented in chapter 5*

	Low	Average	High
Host rock absolute permeability (mD)	120	120	500
Fault from central North Sea reservoirs absolute permeability (mD)	0.0053	0.0087	0.0125
Fault from southern North Sea reservoirs absolute permeability (mD)	0.0015	0.0015	0.0015
Porosity (%) central North sea reservoir	5	7	12
Porosity (%) Host	12	15	20

The relative permeability data before use into simulations were fitted with Brooks and Corey equations to generate the relative permeability and capillary pressure curves to use for simulation. The water relative permeability and relative gas permeability was expressed as a function of water saturation,  $S_w$ . The following equations of Brooks and Corey (1964, 1966) were used,

$$K_{rw}(S_w) = K_{rw,gr} \left( \frac{S_w - S_{cw}}{1 - S_{wc} - S_{gr}} \right)^{n_w} \quad (7-3)$$

$$K_{rg}(S_w) = K_{rg,wc} \left( \frac{1 - S_w - S_{gr}}{1 - S_{wc} - S_{gr}} \right)^{n_g} \quad (7-4)$$

where  $n_w$  and  $n_g$  are the Corey exponents for water and gas respectively. The capillary pressure function is written in the following form,

$$P_c = P_e \left( \frac{S_w - S_{wc}}{1 - S_{wc} - S_{gr}} \right)^{-1/\lambda} \quad (7-5)$$

Where,  $P_e$  is the entry pressure and  $\lambda$  is an exponent, which is used to fit the curve on data. The exponents  $n_w$  and  $n_o$  control the shape of the relative permeability curves once the end points have been fixed. The exponents and other different parameters fitted on the laboratory data are presented in **Table 7.2**. The relative permeability and capillary pressure curves generated for incorporation into simulation model are graphically presented in **Figure 7.3. and Figure 7.4**. The water relative permeability data was assigned using Tueckmantel et al. (2012) because the fault rocks analyzed in the present study had similar absolute permeability as reported by Tueckmantel et al. (2012). Only gas relative permeability data of host rock sample were measured in the laboratory. The gas-water relative permeability of the host rock samples can be obtained on typical homogenous porous sandstone samples (C. Grattoni, pers. communication) and the curves can be generated using Brooks and Corey equations. Therefore, the water relative permeability curves used for host sandstones were generated using Brooks and Corey equation with similar range of absolute permeability of the host sandstones. It should be noted that the gas-water permeability was considered to model oil water system the samples used for measurement were strong water-wet. Therefore, the oil relative permeability could be treated as a non-wetting similar to gas and water remains as wetting phase. Simulation run for different cases for explicit fault modelling were given same relative permeability curves, which are shown in **Figure 7.3**.

It should be noted that laboratory capillary pressure data generated by centrifuge or by mercury injection techniques cannot be compared directly to each other or to reservoir conditions. Therefore the laboratory data was converted to reservoir conditions prior to incorporation into simulation modelling. The equations used for converting the laboratory data to reservoir is, (e.g. Schowalter, 1979)

$$P_{c\text{ res}} = P_{c\text{ lab}} \left( \frac{\gamma \text{Cos}\theta_{\text{res}}}{\gamma \text{Cos}\theta_{\text{lab}}} \right) \quad (7-6)$$

The conversion of the data from laboratory to subsurface reservoirs requires values for the contact angle,  $\theta$ , of the fluids and interfacial tension ( $\gamma$ ) between the two fluids;  $\theta$  is a reflection of wettability. This information is often needed to calculate an equivalent buoyancy pressure in the reservoir. Therefore, the Hg-injection data for capillary pressure has been converted to air-water values assuming interfacial tension of 70 dynes/cm and 480 dynes/cm for air- water and Hg-injection respectively. Contact angles of  $0^\circ$  and  $140^\circ$  were considered for air-water and Hg-injection respectively. The LGR assigned with threshold pressure of fault rock was 77psi considered based on the laboratory air-water measurements.

Table 7.2 The table below shows the input variables for generating fault and host rock relative permeability and capillary pressure curves using equation of Brooks and Corey (1964).

Input parameters	Fault rock		
	Low	Average	High
$S_{gr}$	0	0.09	0.12
$S_{cw}$	0.08	0.06	0.11
$K_{rg}$	0.79	0.82	0.89
$K_{rw}$	1	1	1
$n_g$	2	6.5	8.5
$n_w$	12	16	20
Pt	1.2	177	200
$\lambda$	0.63	0.69	0.84

Input parameters	Host rock		
	Low	Average	High
$S_{gr}$	0	0.12	0.15
$S_{cw}$	0.12	0.06	0.08
$K_{rg}$	0.89	0.82	0.68
$K_{rw}$	1	1	1
$n_g$	2.5	4.2	5.5
$n_w$	3.5	4.8	5.6
Pt	2	10	22
$\lambda$	0.79	0.69	0.62

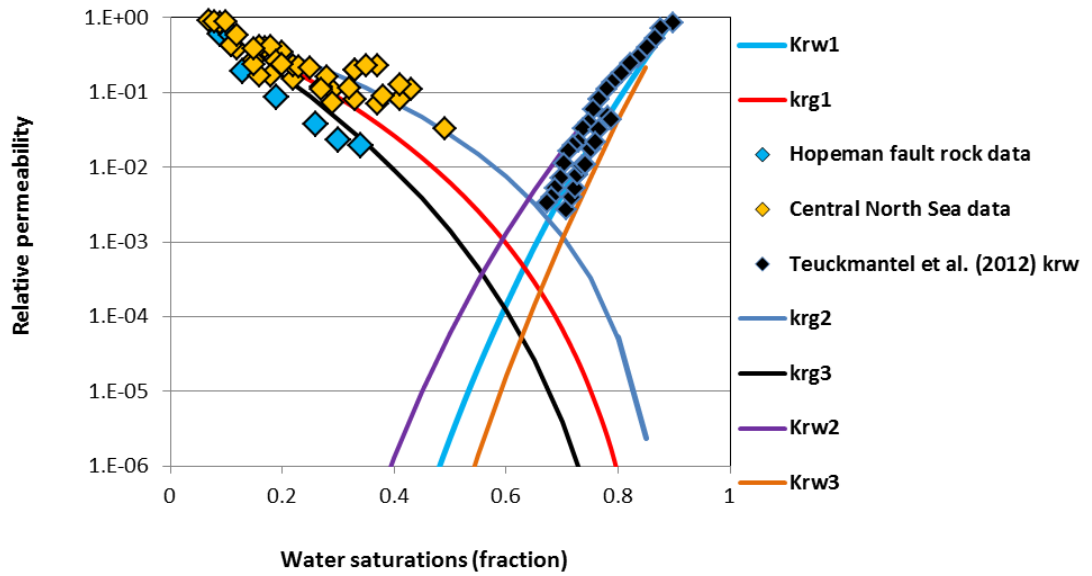


Figure 7.3 Illustration is the relative permeability data used for reservoir modelling.

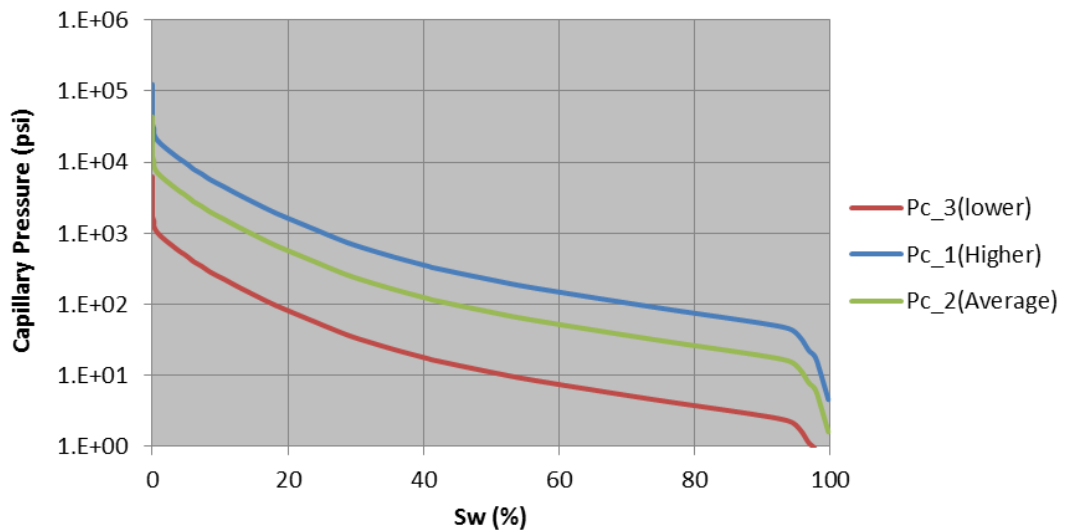


Figure 7.4 Capillary pressure curves from mercury injection data used for simulation models and was fitted with Brooks and Corey empirical equation. The data was converted from laboratory to reservoir water-oil capillary pressure and is from central North Sea reservoir core samples.

#### 7.4 Model set-up

To quantify the effect of flow across faults and to make predictions for hydrocarbon reservoirs, synthetic reservoir models were generated and simulations of different cases were run on reservoir scale. A synthetic model of fault reservoir was created

using ECLIPSE™2013. The model consisted of 71 x 25 x 3 cells and was 1020ft in length, 500ft wide and 150ft in thickness. The fault thickness of 2.02 feet (0.615m) was assumed which is accommodated by 9 grid cells and the cells are logarithmically increasing from centre of fault towards left and right. Fault is located at the centre of reservoir and is dividing reservoir into two segments (**Figure 7.5**). The grid cells accommodating fault were assigned similar absolute permeability values as used to determine the TMs described in **section 7.2** above. The fault thickness assumed is also consistent with Hull (1989) correlation. The geometry of the model is shown in **Figure 7.5** for two model cases run. The drive mechanism is the depletion drive where there is no injector and no aquifer support - reservoir has its own energy.

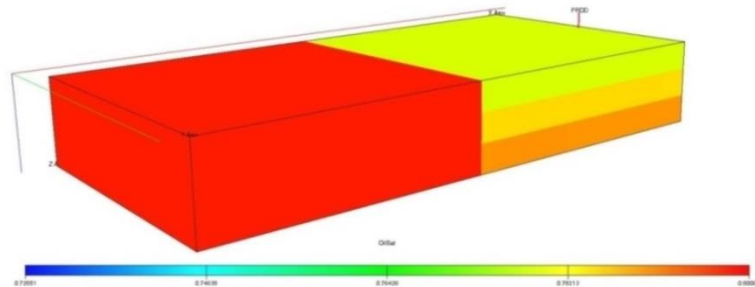
To investigate the effect of fault cross flow within gas reservoir, similar fault rock multi-phase flow properties were used that were measured in the laboratory as shown in **Figure 7.3**. The modelling of oil-water and gas-water reservoirs were performed by assigning with different ranges of capillary pressure curves that were obtained from mercury injection data to quantify the impact of having high and low threshold pressures. The models run for oil-water and gas- water system are summarized in **Table 7.3** and **Table 7.4 respectively**. Production in the oil reservoir was controlled by oil rate, while for the gas reservoir; the production of the reservoir was controlled by bottom hole pressure limit (BHP) that was set to 500psi. In the case of water injection, the injection rate was controlled by the same rate as the production for the oil reservoir. The initial pressure of the reservoir was set as 4000psi.

The model containing oil and water two-phase system was idealised as a black oil system with dissolved gas which produces below the bubble point. In oil-water model water properties used in a numerical simulation consist of brine with brine compressibility of  $2.6E-6 \text{ psi}^{-1}$  and the viscosity of water was 0.47 cp. The reservoir temperature was 60 °C. The producing period of reservoir was 30 years, where the well was producing at a constant rate of 15stb/day per producing well and was perforated throughout the entire formation.

Two types of the model geometries were adapted for grid construction, which vary only the way the properties were incorporated. In the first simulation model the impact of fault rock flow properties was taken into account by assigning (TMs)

transmissibility multipliers to the faces of grid-blocks (**Figure 7.5a**). The base case was considered such that it was assigned with transmissibility multiplier of (TM=1). The second model was fine grid model geometry using (LGR) local grid refinement approach as shown in **Figure 7.5b**. The cell thicknesses in LGR models were set such that it was logarithmically increasing away from fault. The fault transmissibility multipliers were calculated using the procedure described by Manzocchi et al. (1999), in which the relative permeability or capillary pressure were not taken into account. In the later case, faults were modelled explicitly by assigning two phase flow properties (relative permeability and capillary pressure curves) (**Figure 7.5**) using LGR. The LGR used were tested for any numerical dispersion and instability due to the changing properties between the fault and its associated host rocks. Several simulation models were also run to make sure that the results obtained might not be the artefacts effect from the gridding used. Their output was then compared with LGR model results by assigning similar properties both showed identical result which implies that there was no any numerical instability.

5) **TM**



6) **LGR**

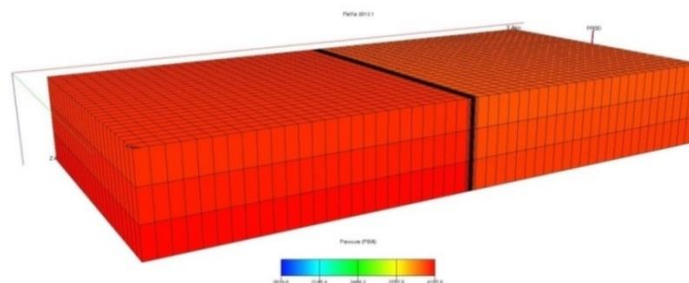


*Figure 7.5 The flow simulation model geometries and their configuration adapted during modelling. (a) Fault modelled by assigning TMs between juxtaposed faults (b) the fault modelling was performed discretely by assigning its own cells and properties as (LGR) local grid refinements.*

Table 7.3 The summary of the different case scenarios of water-oil simulations run during the study.

Case	Water injection	Producers	Fault Modelled
<b>Case study 1</b>			
CP1	No	One Prod. in Compart2	TM=1 (No fault)
CP2	No	One Prod. in Compart2	TM Case 1
CP3	No	One Prod. in Compart2	LGR case 1 (high Pc)
CP4	No	One Prod. in Compart2	LGR case 2 (low Pc)
<b>Case study 2</b>			
HP1	One INJ. Compart 1	One Prod. in Compart2	TM=1 (No fault)
HP2	One INJ. Compart 1	One Prod. in Compart2	TM Case 1
HP3	One INJ. Compart 1	One Prod. in Compart2	LGR case 1 (high Pc)
HP4	One INJ. Compart 1	One Prod. in Compart2	LGR case 2 (low Pc)
<b>Case study 3</b>			
CS1	No	One Prod. in each Compart	(No fault)
CS2	No	One Prod. in each Compart	TM
CS3	No	One Prod. in each Compart	LGR

#### 7.4.1 Simulation modelling results (Oil-water Model)

This section presents the results from different model cases of oil-water model were run, the difference in these models were only in assigning the flow properties of the faults and the way the properties were incorporated into the model. Initially the simulation was performed using TMs then the fault was explicitly modelled using LGRs in which the fault was assigned its own relative permeability and capillary pressure.

**Model CP** has only one producer without any aquifer support and injector. The results presented in **Figure 7.6** predicts that pressure drop could be observed within TM=1 as oil is produced in that there is no fault. The TMs case showed that there is flow across fault, which appears that the fault is acting as a partial barrier. From TM case, it was observed that oil in left compartment across the fault starts communicating with right side oil producing compartment, as the pressure decreases due to oil production. As production starts from right compartment, the pressure increases across the fault as well as in the un-drained oil compartment. When the

pressure reaches the fault threshold pressure, the oil from the left compartment of reservoir enters into the barrier and then flows across the fault. The difference is not significant in TM case and the base case in which there was no fault. However, when flow across fault was explicitly modelled using LGRs assigning fault rock its own two-phase properties, the results from TM and LGR are clearly different. In LGR both cases, it was observed that there was hardly any flow across fault and the fault seems to be acting almost as barrier. The LGR cases of high and low capillary pressure predict lower oil production as compared to base case and TMs case. The effect of fault was observed after 22years of production.

**Model HP** has one producer in right compartment and one injector on its opposite compartment. The results presented (**Figure 7.8**) predicts that fault has a large impact in case of using LGR of high capillary pressure case. There was a large pressure difference in between two compartments observed, which shows that the fluid was injected at the opposite side of producing compartment has not communicated across the fault. Although, there was no any difference observed within the TMs and the Base case model. As in this model there was injector well, so the oil produced predicts the similar results of cumulative production for all cases irrespective of the TM or high and low threshold pressures were used for fault modelling.

In performing simulations, unlike former models, the **Model CS** has one producer in each compartment. The simulation results showed that the fault properties assigned based on TM multipliers has no any impact on the oil production (**Figure 7.9**). This would be expected that both compartments were behaving in the similar manner, so the both compartments were producing at same rate. It was observed that if both compartments are producing at same rate their depletion behaviour will be virtually identical and the fault will not play any role in retarding fluid flow in this case.

The oil saturation maps are presented in **Figure 7.7** for HP model from TM case and LGR and base case model at the end of model production period of 30 years. In TM case, the change in saturation during production was observed as oil started migrating towards the wellbore and across the fault from left compartment. However, in case of LGR model, the only saturation change was observed was within right compartment, which shows that there was a producing well in that compartment and there was hardly any change in left compartment saturation during

the production period, that reflects the fault is acting as a strong barrier in this case. The saturation maps shows two different depletion trends as it is obvious that in fault sealing case there is faster depletion compared to non-sealing cases (**Figure 7.7**). The depletion stage was controlled by the depletion rates that were set as a minimum pressure of 500psi. As pressure of the right compartment depletes due to oil production, the oil from left compartment across the fault is not flowing and the fault is almost acting as barrier.

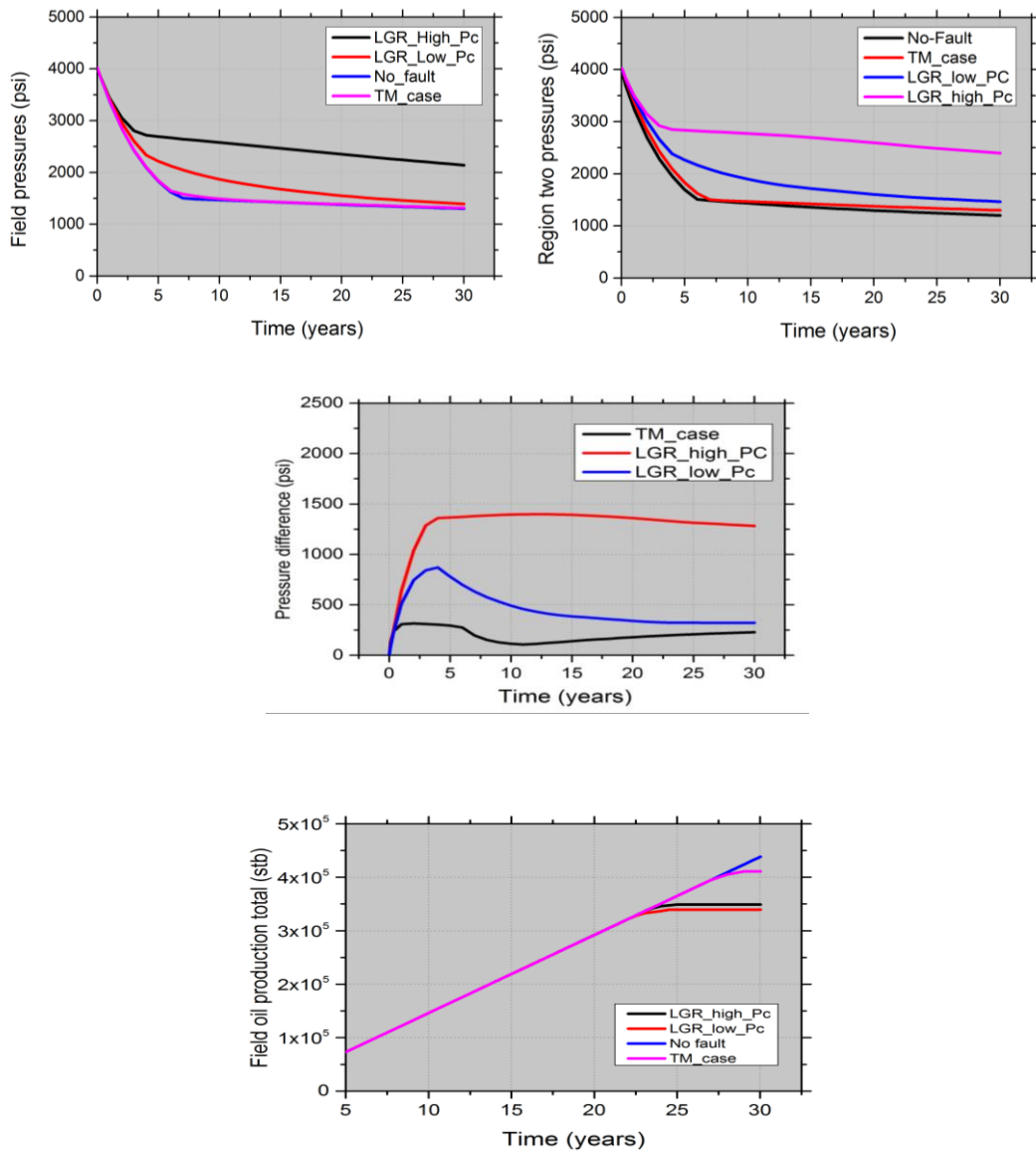
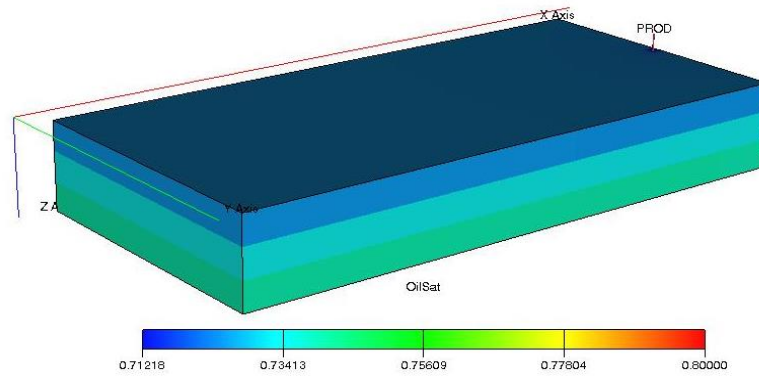
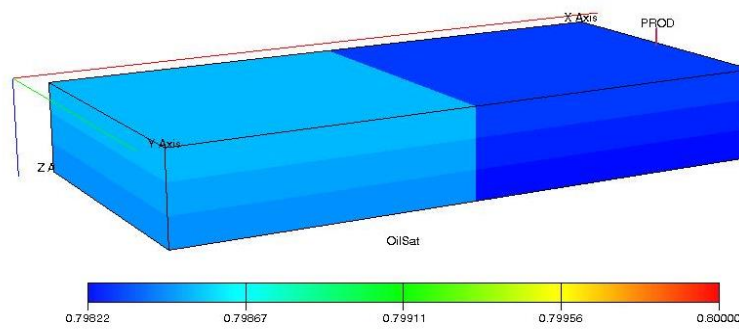


Figure 7.6 Simulation results and their comparison from **CP-oil-water model** that has one producer in right compartment with no injector. The results presented for different cases where there was no fault case, TM case and the fault was modelled by LGR by assigning high and low capillary pressure curves. The results show, the total production from field, the filed pressure, region pressures and difference of pressures in between compartmented.

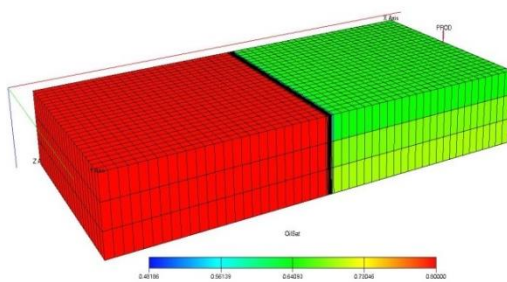
**(a) Host rock base case**



**(b) TM case**



**(c) LGR case1**



**(c) LGR case2**

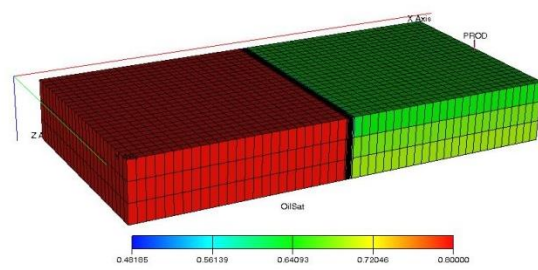


*Figure 7.7 Illustrations are the oil saturation distribution of the model at the end of simulation runs. (a) Base case-no fault (b) TM transmissibility multipliers case and (c) is LGR case explicitly modelling fault rock by giving its own relative permeability and capillary pressures. The fault cuts the entire model splitting it into two compartments.*

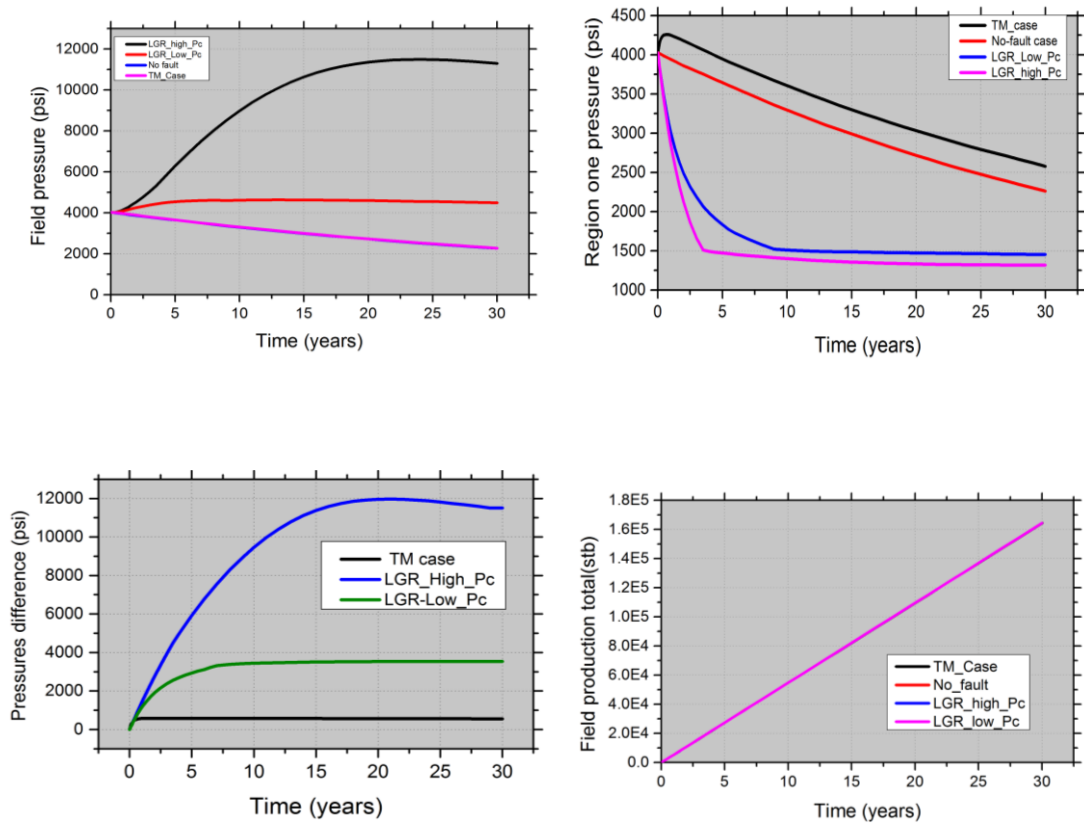


Figure 7.8 The illustrations are the comparison of results from **HP model** case of simulation run, which has one injector and one producer in each compartment. The results presented are compares different cases, where the fault was modelled by assigning ( $TM=1$ ) no fault case, the fault modelled by assigning transmissibility multipliers which were calculated from fault rock properties and the third model in that the fault was given its own properties relative permeability and capillary pressures curves of two different ranges of high and low caapillary pressures. The results from all simulation runs were compared are the cumulative production of oil, field pressures, compartment pressures and pressure difference within the compartments as a function of producing time of the reservoir.

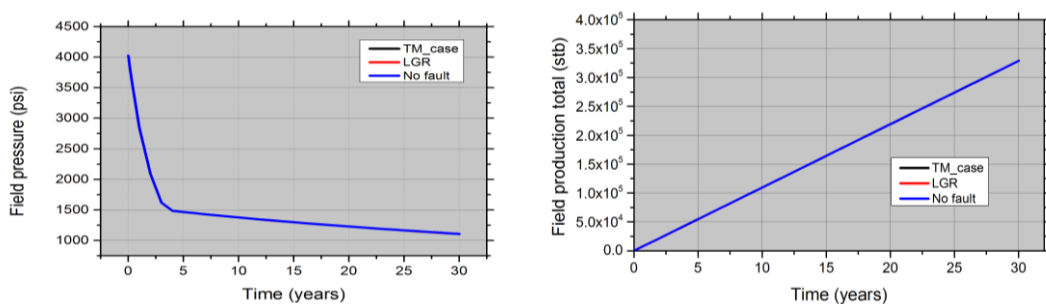


Figure 7.9 Comparisons of simulation results from **CS model**, where fault rock properties were assigned by transmissibility multipliers and by giving fault its own relative permeability and capillary pressure. The results show that the both of the compartments are depleting at same rate, so the model response in all case is identical.

#### 7.4.2 Simulation modelling results (Gas-water model)

For gas-water system two different model types were run as shown in **Table 7.4**. In first case reservoir model BP, the reservoir exhibits only one producer, without any injector and aquifer support. In GP model there is one producer and one injector at the opposite side of the producer. In both cases the fault was modelled by assigning relative transmissibility multipliers, absolute TM and by assigning fault its own two phase flow properties by explicitly.

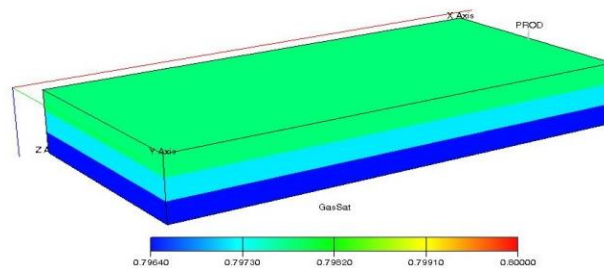
The results predicted from Model BP are shown in **Figure 7.11**. This model shows that the production is overestimated in case of the fault rock properties that were modelled by assigning transmissibility multipliers that were calculated from single phase permeability and it is obvious that the gas production predicted by TM case assumes that there is cross flow across fault and the compartments are in communication. However, that is opposite to the two phase flow case (LGR) when fault was explicitly modelled by assigning relative permeability and capillary pressures. The method of TM case1 was different from TM case 2, in that the TMS were calculated based on the modified approach, the formula for calculation of such TMs are presented above. In that case, model results were nearly close to those predicted by LGR and of the modified TMs case1. The graphs show two different depletion trends, as a sealing fault and high fault transmissibility as non-sealing faults. It is obvious that fault sealing cases are depleted faster than the non-sealing cases (**Figure 7.11**). The depletion stage is controlled by the depletion rates that were set and a minimum pressure of 500psi.

*Table 7.4 The summary of the different case scenarios of gas-water system simulations run during the study.*

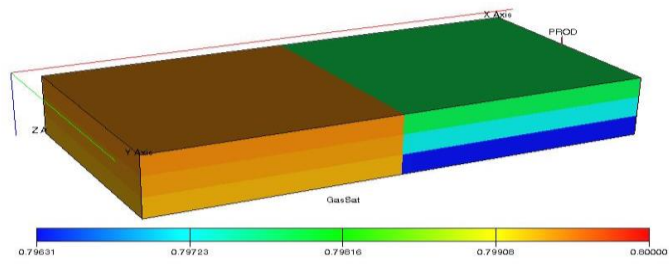
Case	Water injection	Producers	Fault treatment
<b>Case study 1</b>			
BP1	No	One Prod. Compart2	TM=1 (No fault)
BP2	No	One Prod. Compart2	TM Case 1
BP4	No	One Prod. Compart2	TM Case 2
BP4	No	One Prod. Compart2	LGR case
<b>Case study 2</b>			
GP1	One INJ. Compart 1	One Prod. Compart2	TM=1 (No fault)
GP2	One INJ. Compart 1	One Prod. Compart2	TM Case 1
GP3	One INJ. Compart 1	One Prod. Compart2	TM case 2
GP4	One INJ. Compart 1	One Prod. Compart2	LGR case 2 (low Pc)

The results from **model GP** presented in **Figure 7.12** shows importance of considering the fault rock two-phase flow properties. As in this model there is an injector well which maintains the pressure of reservoir and there is very less change in gas saturation was observed (**Figure7.13**) the injector in TM case equilibrates the pressure of compartments. The only saturation change was around the injector well. The effect of fault was observed after ten years of cumulative production in case of LGR model. The TM case 2 and base case in which there is no fault exhibits the similar behavior and the cumulative production from these cases are nearly identical.

a) **Base case**



b) **TM case**



c) **LGR model**

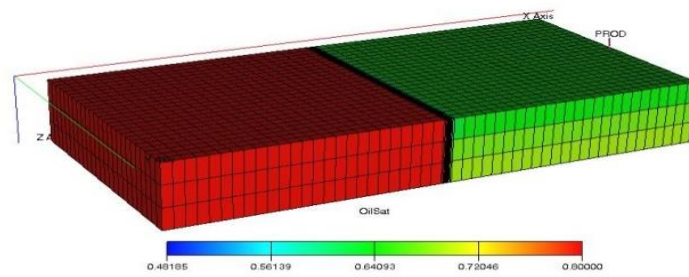


*Figure 7.10 Illustrations are the gas saturation distribution of the model at the end of simulation runs. (a) Base case-no fault (b) TM transmissibility multipliers case and (c) is LGR case explicitly modelling fault rock by giving its own relative permeability and capillary pressures. The fault cuts the entire model splitting it into two compartments.*

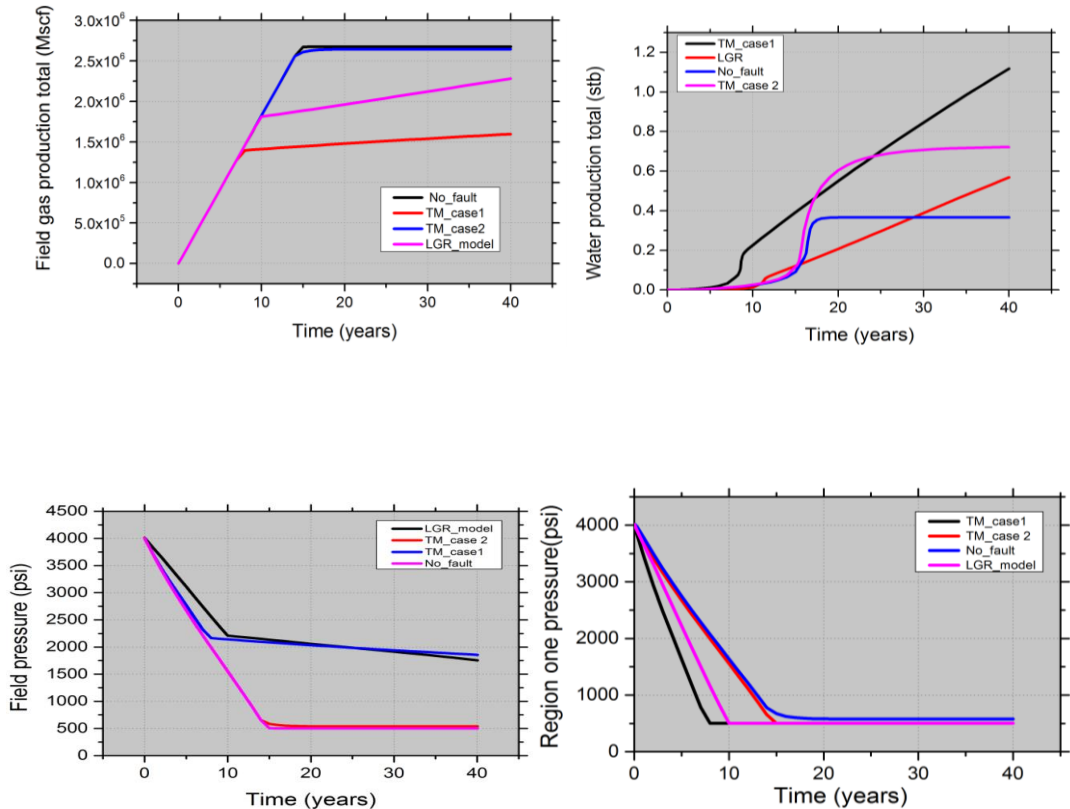


Figure 7.11 Comparisons of simulation results from BP model, different model cases were run, such as no fault as a base case, a TMs case where fault rock properties were assigned by transmissibility multipliers and LGR by giving fault its own relative permeability and capillary pressure. The simulations results resented compares the different responses such as cumulative field production, field pressures and water production as well as region one pressures.

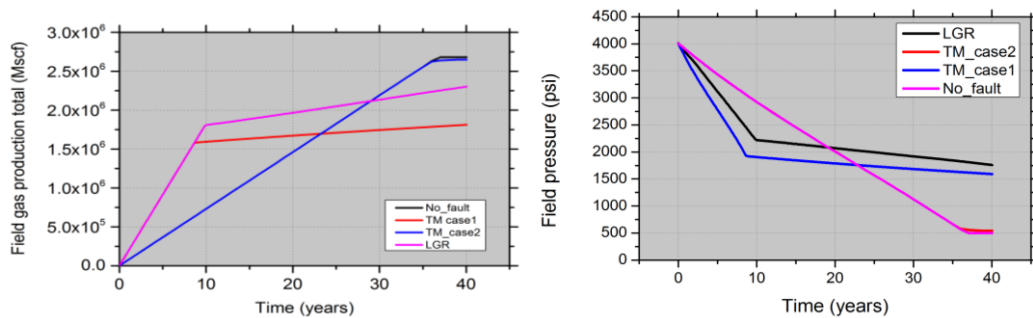
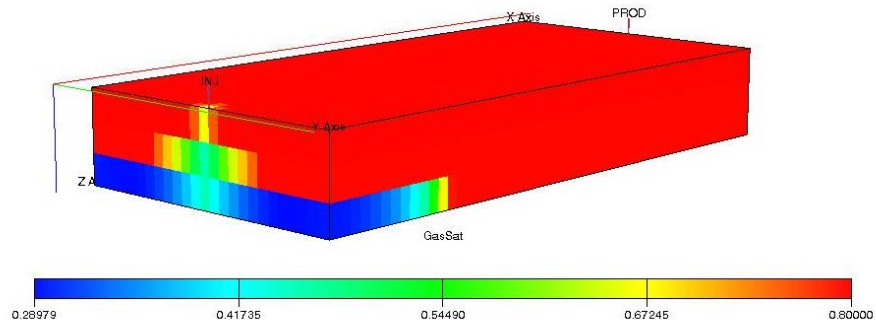
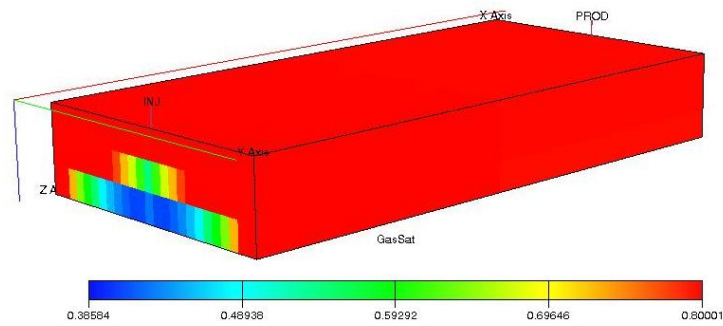


Figure 7.12 GP simulation model results for the gas reservoir that has one injector and one producer which are opposite side to each other. Comparisons of different cases, in which there was a base case (no fault), a model in that the fault rock properties were assigned by TM and explicit model (LGR) in that the fault was assigned with its own two-phase flow properties.

**a) Base case**



**b) TM Case**



**c) LGR model**

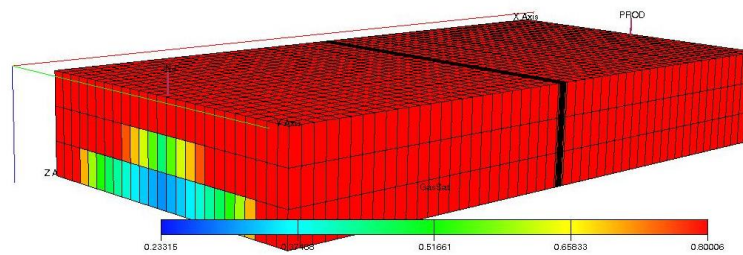


*Figure 7.13 Illustrations are showing the maps of gas saturation distribution of the GP model at the end of simulation runs in which there is a one injector and the producer is in the opposite side of injector. (a) Base case-no fault (b) TM transmissibility multipliers case and (c) is LGR case explicitly modelling fault rock by giving its own relative permeability and capillary pressures.*

## **Simulation results based on high fault rock relative permeability range:-**

In following section water-oil simulations were performed considering four different scenarios that were compared using low fault rock relative permeability curves. Similar model geometry and other input parameters were considered as in previous cases, two different ranges of capillary pressures used. The TMs of high and low range were assigned to run the sensitivities, the TMs values were calculated based on the absolute permeability data presented in **Table 7.1** . The results are presented in **Figure 7.14**.

In this simulation run , there is only one producer without any aquifer support and injector. The results presented predicts that pressure drop could be observed within TMs case showed that there is flow across fault, which appears that the fault is acting as a partial barrier. From TM case, it was observed that oil in left compartment across the fault starts communicating with right side oil producing compartment, as the pressure decreases due to oil production. As production starts from right compartment, the pressure increases across the fault as well as in the un-drained oil compartment. When the pressure reaches the fault threshold pressure, the oil from the left compartment of reservoir enters into the barrier and then flows across the fault. The difference is not significant in TM case and the base case in which there was no fault. However, when flow across fault was explicitly modelled using LGRs assigning fault rock its own two-phase properties, the results from TM and LGR are clearly different. In LGR both cases, it was observed that there was hardly any flow across fault and the fault seems to be acting almost as barrier.

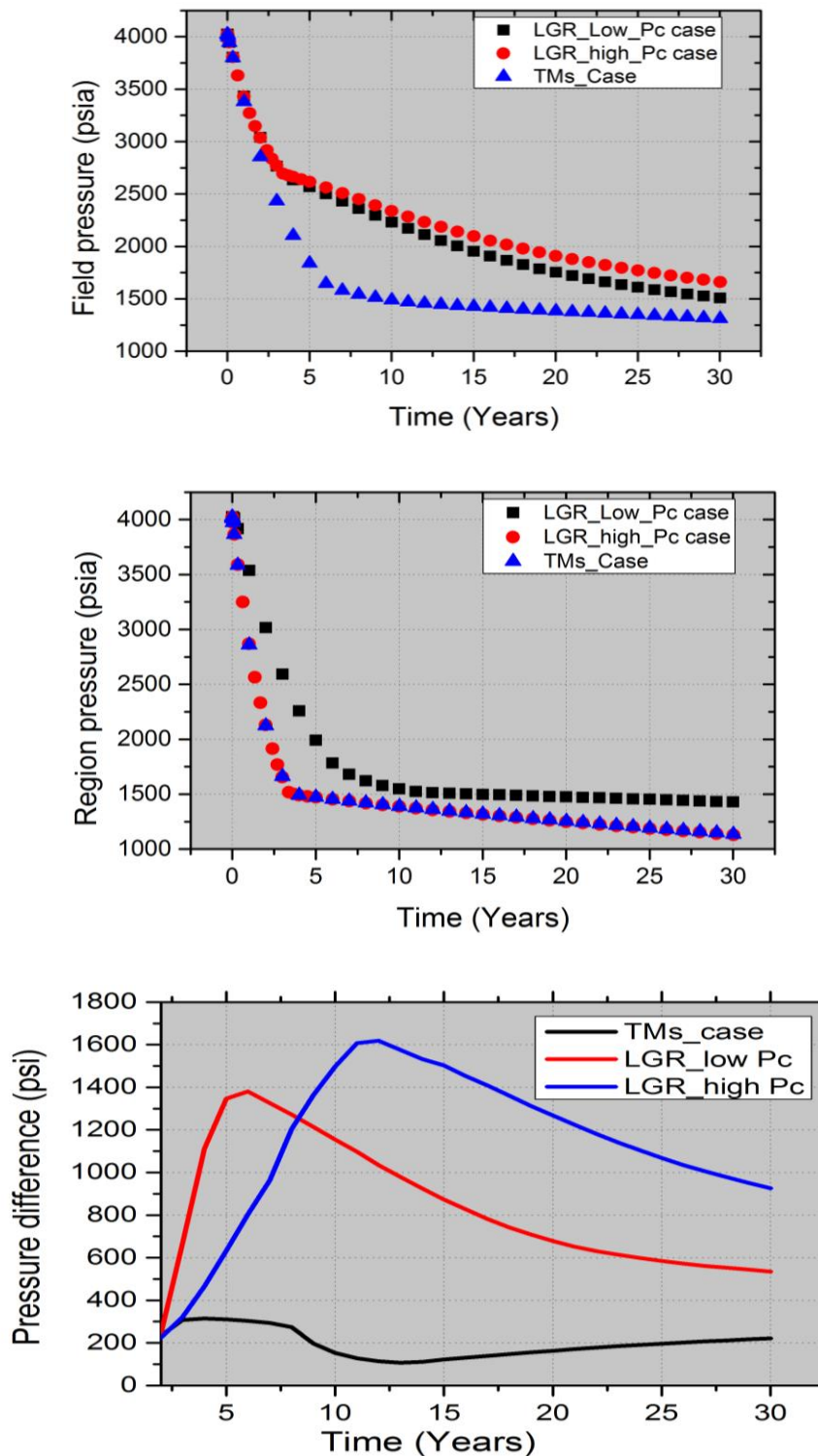


Figure 7.14 The illustrations are the comparison of results from **high relative permeability range** of simulation run, which has one injector and one producer in each compartment. The results presented are compares different cases, where the fault modelled by assigning transmissibility multipliers which were calculated from fault rock properties and the third model in that the fault was given its own properties relative permeability and capillary pressures curves of two different ranges of high and low caapillary pressures. The results from all simulation runs were compared are the cumulative production of oil, field pressures, compartment pressures and pressure difference within the compartments as a fuction of producing time of the reservoir.

## **Simulation results based on low fault rock relative permeability range:-**

In following section series of simulations were performed considering different scenarios that were compared considering low fault rock relative permeability. Similar model geometry and other input parameters were considered as in previous cases, different ranges of capillary pressures of high and low were used. Transmissibility multipliers of high and low range were also assigned to study the impact of fluid flow across fault. The results are presented in **Figure 7.15**.

In low relative permeability simulation Model run that has only one producer without any aquifer support and injector. The result presented **Figure 7.15** predicts that pressure drop within TMs simulation case could show that there is a flow across fault, which appears that the fault is acting as a partial barrier. It was also observed that oil in left compartment across the fault starts communicating with right side oil producing compartment, as the pressure decreases in both of the compartments due as the oil starts producing. As production starts from right compartment, the pressure increase observed across the fault as well as in the opposite compartment. When the pressure reaches the fault threshold pressure, the oil from the left compartment of reservoir enters into the barrier (fault) and then flows across the fault. The pressure difference is not significant in TM case. However, when flow across fault was explicitly modelled using LGRs assigning fault rock its own two-phase properties, the results from TM and LGR are clearly different. In LGR both cases, it was observed that there was hardly any flow across fault and the fault seems to be acting almost as barrier.

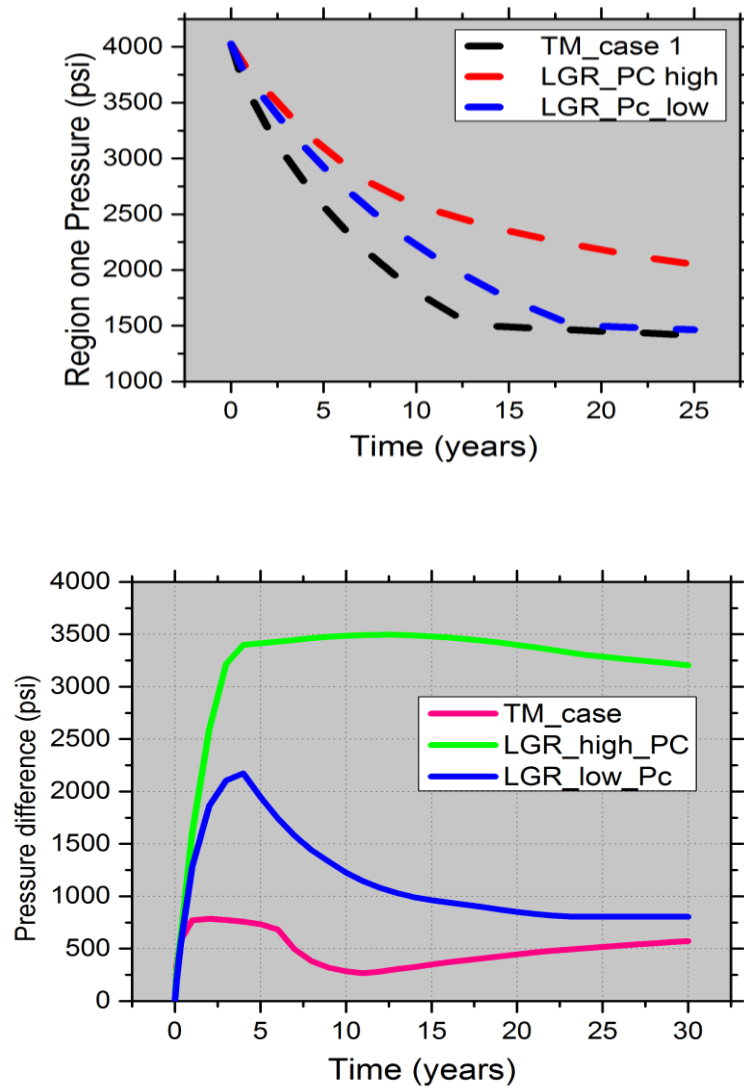


Figure 7.15 The illustrations are the comparison of results from **low permeability** case of simulation run, which has one injector and one producer in each compartment. The results presented are compares different cases, where the fault modelled by assigning transmissibility multipliers which were calculated from fault rock properties and model in which the fault was assigned with its own properties relative permeability and capillary pressures curves of two different ranges of high and low capillary pressures. The results from all simulation runs were compared are the field pressures, compartment pressures and pressure difference within the compartments as a function of producing time of the reservoir.

## Simulations performed using relative transmissibility multipliers

One of the alternate approach of transmissibility multipliers for incorporating fault rock properties have been adopted to produce results in combination with the existing methods; the details could be found in Al-Hinai, et al. (2008) Fisher, Harris and Al-Busafi (2006). In previous simulations, the transmissibility multipliers calculations were performed using single-phase properties of the fault, and therefore the relative permeability needs to be included in such calculations. This has been done by scaling the transmissibility multiplier by the end-point gas relative permeability and by deriving the capillary pressure from mercury injection data.

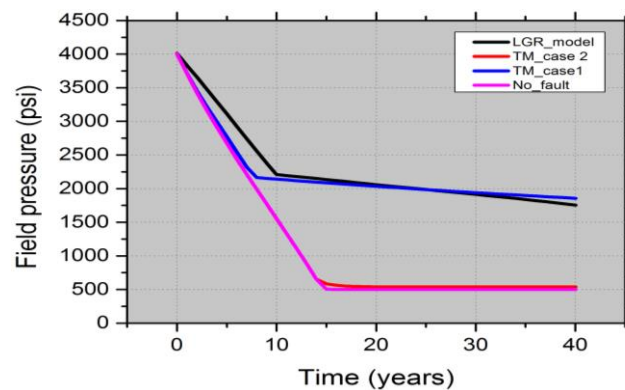


Figure 7.16 The illustrations are the comparison of results from **relative TMs** case of simulation run, which has one injector and one producer in each compartment. The results presented are compared with different cases, where the fault was modelled by assigning ( $TM=1$ ) no fault case, the fault modelled by assigning transmissibility multipliers which were calculated from fault rock properties and the third model in that the fault was given its own properties relative permeability and capillary pressures curves of two different ranges of high and low capillary pressures. The results from all simulation runs were compared are the cumulative production of oil, field pressures, compartment pressures and pressure difference within the compartments as a function of producing time of the reservoir.

Results from relative transmissibility multiplier (**TMs case 1**) compared with all other different simulation cases run. The results from relative TMs approach are significantly improved and reproduce results similar to those when fault rock properties effects modelled by using LGRS. Although this approach has worked on basic models, this could be evaluated in other situations, suppose the reservoir is being produced by water flooding. Although, this methods of TMs calculation and the existing methods of accounting for the effects of faults on fluid provides a sound

basis to incorporate fault rock properties into simulation models that is adequately easy to implement that could also be acceptable to the practising reservoir engineers.

The above cases of fault modelling were solely based on the existence of oil in both compartments however; another case of fault modelling was performed. In that one compartment was totally full of water phase i.e. the left compartment and the right compartment was containing oil phase. The grid geometry and all other properties of the model were same as previous case of LGR model, similar size and number of the LGR considered and the fault thickness. The model has only one producer without any aquifer support or injection well. The sensitivity study conducted to test that effect of flow across fault that is separated by water on other side of oil producing compartment.

The results of cumulative oil and water production from the model are summarized in **Figure 7.14**. These results show that the fault has a large impact on flow; it almost acts as a total sealing fault with most of the production coming from compartment one. Cumulative water production is also very small until the end of simulation period, which also reflects that there is no communication between compartments. The simulation results from pressure versus time and pressure difference between two compartments are presented in **Figure 7.15**. The pressure gradually decreases within the right compartment as reservoir starts depleting; however there is very small change in left compartment pressure. The simulation results show that there is higher pressure difference in between two compartments. The graphs show two different pressures depletion trends of two compartments, which show that fault acting almost as a sealing fault. It is obvious that fault sealing cases are depleted faster (**Figure 7.16**). The depletion stage is controlled by the depletion rates that were set and a minimum pressure of 500psi. As pressure of the right compartment depletes due to oil production it might be expected that water from left compartment across the fault is not flowing and the fault that is acting as barrier. Generally, the capillary pressure increases across the fault within the undrained compartment. If capillary pressure exceeds the fault rock threshold pressure then flow of water from left compartment starts invading into the fault then the flow across fault could occur towards the producing compartment. However, this was not the case within this

model. Instead, it was observed there was no flow across fault and the fault is acting almost barrier. The saturation profiles are presented for this case at the end of simulation period as shown in **Figure 7.16**. The saturation within the left compartment does not change even at the end of simulation that reflects that the fault rock is acting almost barrier to water.

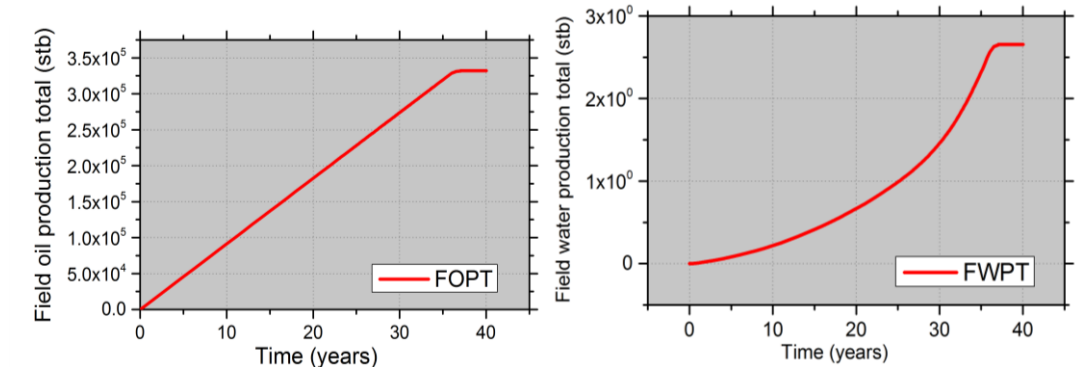


Figure 7.15 Field cumulative oil production total from the LGR model.

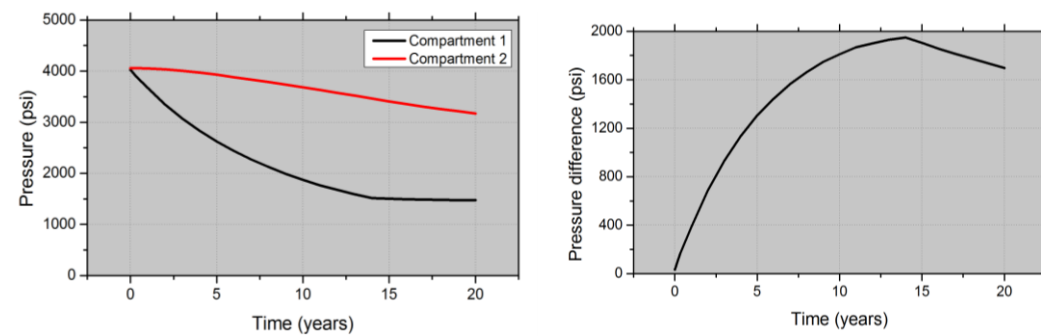
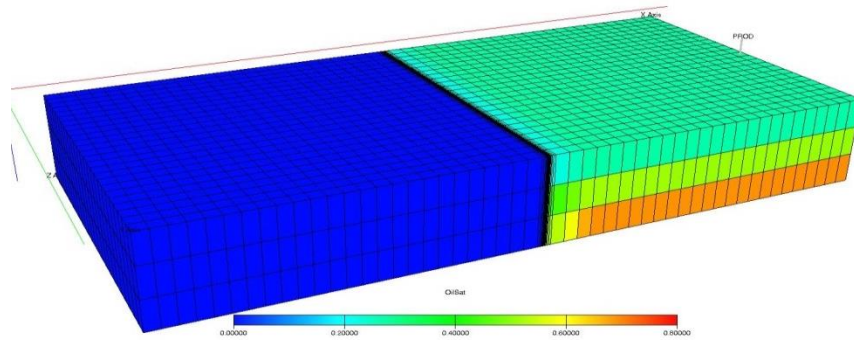


Figure 7.16 Illustration is the pressure in (LGR case) compartment 1 and compartment 2. The producer is in the compartment 1 and model results from pressure difference between compartment 1 and compartment 2 at the end of simulation period.

## 1. LGR model



*Figure 7.17 Oil saturation map of the model containing water and oil in left and right compartments (LGR case) at the end of simulation run.*

## 7.5 Discussion

The fault rocks from central North Sea fields and Hopeman outcrop studied both had very low permeability and high capillary threshold pressure. The fault samples from Hopeman were relatively homogenous compared to samples from central North Sea reservoir cores, which shows that measured average water saturations are only relevant for the fault rock itself.

The simulations performed during present study showed that if the faults have low permeability it is necessary to incorporate their multi-phase flow properties in the production simulation models to predict their behaviour; otherwise modelling the flow behaviour by assigning TM will overestimate the cross fault flow. The transmissibility multipliers (calculated based on fault rock single phase permeability and its thickness) response was nearly identical to the case where there was no fault. The number of simulation cases performed during present study has shown that the fault rocks having low permeability similar to that of the faults formed within the Rotliegend gas reservoirs of the southern North Sea fields of offshore UK reservoirs where high compartmentalization was observed and their behaviour could not be accurately modelled based on their single phase flow properties. In contrast, the cases where fault rock formed within clean sands, the impact of fault modelling by explicit method using LGR assigning their own relative permeability and capillary pressure is not important, in those cases of high permeable faults with lower threshold pressure pressures could be modelled by assigning TM. However, the faults formed in low permeability have high capillary threshold pressures need to be modelled their behaviour by assigning their own two phase flow properties. The fault was also modelled by an alternative approach that was different from traditional way of calculation of transmissibility multiplier TMs based on single phase permeability of the fault rock. However, the alternative method of fault modelling that has been also reported by authors such as Zijlstra et al. (2007) in which relative permeability was used to scale the transmissibility multiplier. The results obtained from this approach and from explicit method of fault modelling using LGR by assigning fault its own two-phase properties were very close to each other.

The authors have reported that faults sealing capacity depends on the fault rock permeability, thickness and threshold pressures, the flow across fault is depend upon the average of these properties (e.g. Manzocchi et al. 2010). Davies et al. (2003) argues that

the petroleum within low pressure region and the water pressure gradient in fault supports the column in high pressure region, when the high pressure of compartment depletes, so the capillary pressure within fault increase until it exceeds the entry pressure of the fault and to enter into fault, in that situation the fault rock turns to be permeable to oil. Essentially, this is the case of capillary seal failure of fault that takes place when there is a displacing fluid moves towards the fault and invades into the fault due to cross fault pressure differences (e.g. Manzocchi et al. 2010; Brown, 2013). The extent to which a fault rock acts as a barrier depends on permeability, threshold pressure and its thickness. Cross-fault flow can only happen if capillary pressure becomes higher than the fault threshold pressures (e.g. Fisher et al. 2001; Manzocchi et al., 2008; Brown, 2013). More recently, it has been argued that it might be possible at earliest to know the time for the failure of the barriers within producing reservoirs by relating the cross-barrier pressure difference to the permeability and threshold pressure (e.g. Brown, 2013).

The present study has modelled simple synthetic reservoir behaviour to understand the flow behaviour and impact of fault seal failure due to reservoir pressure depletion. The results from different simulation cases have suggested that in case of TM based on single phase fault rock properties, the flow exceeds the capillary threshold pressure and enters into the fault rock and cross flow occurs. This might overestimate the cross fault flow of those faults which were formed within low permeability impure sands. However, authors have suggested that low permeability faults need to be modelled explicitly by assigning two phase properties (e.g. Al-Hinai et al. 2008) similar to that present study has also observed that if two phase flow properties of faults ignored then there would be overestimation of cross-fault flow. Moreover, the introduction has provided several examples where history matches were achieved where cross fault flow was modelled based on single phase flow properties. It also gives examples where incorporating two-phase flow properties of the faults improved history matches. It might be relevant that the former examples were from reservoirs that deformed early in which faults in clean sandstones had a high permeability. On the other hand, the reservoirs in which history matches were improved using multiphase flow properties of faults deformed at deeper depths so had low permeability fault rock.

Many of the studies have tried to understand the importance of flow behaviour of fault in context of production during reservoir depletion process (e.g. Freeman et al., 2007; Harris et al. 2007; Manzocchi et al., 2008). Hence, no one have yet provided with any clear conclusion, as the behaviour of the fault is case specific, sometime it behaves very complex and some time is simple (e.g. Manzocchi et al., 2010). The modelling considerations are likely to be critical due to material properties of reservoir such as overburden stresses. Coupled fluid flow-geomechanical modelling of such processes by taking into account of the stress sensitivity of fault rocks is also important, particularly when processes such as stress arching (Segura et al., 2011) are occurring. Considering stress sensitivity in modelling fault compartmentalized reservoirs would provide a guide as to when it is worth investing the time into incorporating multiphase flow properties or stress sensitivity into simulation models. Clearly such analysis depends on the information on reservoir properties, regional hydraulic properties, structure and the fault rock properties as well as reservoir depletion in case of producing reservoirs and trapping mechanisms in case of injection. However, the oil and gas reservoirs data and other information related to field producing behaviour and the data of assets are confidential, so research based on real reservoir is difficult without industry partnership. So, it is recommended that the work need to be performed to develop methods that incorporate the stress sensitivity impact into the numerical simulation to accurately model the flow behaviour across faults based on real reservoir data.

## 7.6 Conclusions

Experimental data from reservoir core samples of central North Sea fields and Hopeman fault rock presented in **chapter 6** were incorporate into the synthetic reservoir simulation model as a realistic fault and host rock properties. The fault modelling was performed by either using local grid refinement by assigning fault its own two-phase flow properties or by assigning with transmissibility multipliers. The focus of present study was to investigate the effect of fault on fluid flow properties across the fault rocks. The main findings from this chapter are summarized below:

- Models have been constructed in which the low permeability fault cataclastic faults from Hopeman outcrop and from Central North Sea reservoirs have been used to estimate rates of cross-fault flow. The TM methods that use single phase permeability to model the impact of faults on fluid flow have overestimated the

cross fault flow compared to discrete representation, which uses LGR grids that are assigned two-phase flow properties.

- The experimental results of gas relative permeability of faults from Central North Sea-Group-A samples presented in chapters 6 were higher than Hopeman cataclastic fault. If these faults that are formed within high permeability have a less impact if capillary entry pressure of faults is low. As within some Brent reservoirs of North Sea, the history matching resulted by assigning fault with TMs, because of fault formed in clean sands having high permeability and low threshold pressures and it was possible for gas to flow across fault, this implies that the fault present was a low permeable (non-sealing) (e.g. Jolley et al. 2007).
- Ignoring the fault rock two-phase flow properties of Hopeman faults might result in a significant overestimation of production. If these faults were present within southern North Sea, whose relative permeability values would be less than 0.02. The results from this study explain that fault formed within Rotligend reservoirs of southern North Sea UK could not be easily modelled based on the single phase flow properties. Although, if these faults were modelled based on single phase flow might overestimates the cross fault flow by many orders of magnitude.
- The assessment based on existing methods of fault modelling to incorporate the fault rock properties into simulation models have suggested that there were different depletion trends related to incorporating the fault properties either using transmissibility multipliers and by giving faults its own two-phase flow properties. These showed that fault modelled by using LGR giving its own two-phase flow properties was almost acting as a sealing fault and the depletion was faster within the compartment where there was a producing well than the non-sealing cases which were modelled using transmissibility multipliers.

# 8

## Conclusions and recommendations for future work

---

### 8.1 Introduction

The main aim of this thesis has been to address challenges in estimating cross-fault fluid flow within fault compartmentalized reservoirs. Several experiments were conducted including:-

- X-ray CT tomography to assess the internal structure of samples.
- Microstructural analysis using scanning electron microscopy (SEM) to examine the rock texture and to relate with the rock permeability.
- Quantitative X-ray diffraction analysis (QXRD) to determine relative proportions of minerals present.
- Mercury porosimetry to obtain pore size distribution and capillary entry pressures.
- Absolute permeability using gas, distilled water and formation compatible brines NaCl at a range of stress conditions from ambient stress up to in-situ stress conditions were performed to assess the accuracy of existing fault rock permeability data.
- Relative permeability measurements and air brine capillary pressure experiments were conducted to assess the multiphase flow properties of fault rocks.

The work presented and summarized in this chapter is solely based upon the findings presented in the previous chapters. The chapter then provides possible future work for improving further understanding of the flow through complex heterogeneous fault rock systems.

## **8.2 Summary of experimental results**

As evidence in the literature review presented in **Chapter 2**, there have not been many published studies of fault rock permeability conducted at high stress conditions. Also, the data available on two-phase flow (relative permeability and capillary) properties of fault rocks are very limited. In addition, to the authors' knowledge no any other study has attempted to measure the fault rock liquid permeability stress sensitivity. The experimental work done and the data collected on fault rock flow properties during the present study are particularly useful as the data have been collected in conjunction with measurements of the mineralogy and microstructure of the samples. Therefore, this forms a sound basis for comparing the results with existing models and previous data sets to incorporate the data accurately to model the fluid flow through such complex fault rocks.

### **8.2.1 Conclusions from single phase permeability experiments (ambient stress)**

The physiochemical interactions and fine particles retention within the confined pore throats of fault rocks play significant role in controlling permeability. This chapter was aimed at understanding the impact of brine composition on fault rock permeability. The main conclusions arising from the experimental investigations, discussions and analysis are summarized below:

- Fault rock permeability measurements made with different pore fluids such as gas, distilled water and brine of different composition showed a gradual decrease in permeability by changing pore fluids from gas, to brine and then to distilled water. Essentially, the permeant used have a significant effect on fault rock permeability due to rock surface and mineral interactions.
- Microstructural and mineralogical observation of fault rocks has shown presence of variety of clay minerals including illite-smectite, kaolin and chlorite; the presence of clay minerals resulted to differences in permeability. Using gas permeability values to calculate transmissibility multipliers instead of using formation compatible fluids might lead to an overestimation of cross-fault fluid flow.

- The samples contained a variety of minerals such as quartz (dominant mineral), clay and on some extent cementing minerals (calcite). The presence of different minerals types in differing proportions has shown a contrasting permeability. The water adsorbed by the clay minerals surfaces possibly reduces the pore throat size due to interaction with swelling clays and hence reduces the permeability. Furthermore, the permeability results show that the difference in gas and liquid permeability might be the result of layer of bound water on mineral surfaces. This affects the narrow pore throat areas which might be reduced subsequently reducing the cross-sectional area for the fluid to flow and hence reducing the permeability of fault rock.
- The permeability of fault rocks plotted versus clay content resulted in scatter. Attempts were made to model the permeability based on the information of clay content using existing empirical correlations (e.g. Manzocchi et al. 1999; Sperrevik et al. 2002; Revil and Cathles 2001). The comparisons of empirical estimates for fault rock permeability suggested that Revil and Cathles (2001) model provides reasonable permeability estimation compared to aforementioned empirical relations. However, it is important to have information of sand-clay contents.
- The gas slippage factor calculated from following Klinkenberg procedure suggests that it would be far better either to measure the permeability of each sample or to conduct permeability measurements at high pore pressure therefore; the gas slippage effect could be compensated particularly for low permeable fault rocks.

### **8.2.2 Conclusions from fault rock permeability stress sensitivity experiments**

Experiments have been conducted to investigate the stress sensitivity of fault rock gas and liquid permeability; Klinkenberg corrections were applied to all gas permeability measurements. The combined effect of gas slippage and permeability reduction due to stress was analysed and the following are some of the important conclusions which evolve from stress sensitivity experiments conducted:

- At low confining stresses, the permeability of the fault rock core samples showed high stress sensitivity, whereas at higher confining stresses the permeability was less pronounced to stress. This might be due to core damage effects, and the micro fractures formed due to stress release, which were observed from SEM images of the samples. The pore radius calculated from gas slippage parameters at low confining pressures was of the same order of magnitude as the microfracture width observed in SEM. The pore radius was reduced at higher confining stresses, which reflects that microfractures are closed due to stress application. The permeability estimated from a simple fracture model also supported the idea that at ambient stress there was high flow as well as higher permeability due to microfractures. The permeability stress sensitivity results from outcrop and reservoir cores showed that outcrops samples are less stress sensitive than reservoir core samples. This potentially reflects the presence of microfractures formed as a result of stress release. The microfractures were observed from thin sections of core samples.
- It was also interesting to note that fault rock permeability data (e.g. Fisher and Knipe, 2001) compared with present study results and was found that the use of distilled water (which gave lower permeability than formation brines) and low stresses (which give higher permeability than high stress measurements) partially cancel one another out. Therefore it is still safe to use the data sets published by Fisher and Knipe (2001) for modelling and making predictions for fault seal analysis.
- At *in situ* stress, the pore pressure reduction initially reduced the measured permeability by increasing the net stress and thus reducing the absolute permeability. As the gas pressure was reduced further, the increased contribution of gas slippage increased in the measured permeability. This indicates that large pressure differences (drawdowns) would enhance the rate of gas production in these reservoirs without reducing fault permeability due to being stress sensitive.
- An attempt was made to find a relation between the stress sensitivity of permeability and rock mineralogy. However, it was found that mineral composition is not the primary reason to control the permeability stress sensitivity; the samples have shown different stress sensitivity even when having a similar mineral composition.

- The absolute gas and liquid permeability of fault rocks obtained from core and outcrop is sensitive to the stress conditions under which it is measured. Overall, the stress sensitivity of fault rocks is similar to that of the tight gas data of Byrnes et al. (2009). Although, some fault rocks have shown less stress sensitivity than tight gas sandstones.

### **8.2.3 Two-phase flow properties**

The two phase flow properties measurements were conducted, the reservoir core samples were supplied from different fields of North Sea reservoirs. The following conclusions were made from two-phase flow experiments.

- The samples having low absolute permeability have lower relative permeability compared to high absolute permeability samples at similar capillary pressures. The permeability of partially saturated samples were very sensitive to stress. The effective gas permeability in some cataclastic faults and many of the phyllosilicate framework faults is significantly reduced at higher stress, namely of 4000psi, and there was hardly any flow to gas at 5000psi effective stress. This indicates that fault rocks may act as effective barriers within the deep reservoirs.
- The gas relative permeability values of low permeability (<0.01mD) cataclastic fault rocks are most likely <0.02. Therefore, these results suggest that if low permeability cataclastic faults are present within the reservoirs it would be necessary to take into account the multiphase flow properties for simulation and modelling. Otherwise, transmissibility multipliers calculated based on the single phase permeability might overestimate cross-fault flow.
- The permeability of samples sub-divided based on the clay content that has shown an effect on permeabilities (effective and relative permeability). As clay percentage increases both the effective permeability and the relative permeability decrease. This also depends on the samples absolute permeability.

### **8.2.4 Modelling the impact of fault rock properties**

The fault rock properties obtained from central North Sea samples and Hopeman fault rock based on existing method of fault modelling were incorporated into a specific example of synthetic fault reservoir models. It was observed that the faults formed

within low permeability having higher threshold pressures need to be modelled by assigning with two-phase flow properties. By ignoring two phase flow properties will result in overestimation of cross fault flow. However, the faults formed in clean sands having high permeability and low capillary entry pressures could be modelled by assigning TM multipliers based on their single phase properties. An alternate method of was used to model the flow behavior of fault using relative permeability to scale the transmissibility multiplier. The results obtained from this approach and from explicit method of fault modelling using LGR by assigning fault its own two-phase properties resulted in close match to each other.

### **8.3 Implications of the results for fault seal analysis**

The purpose of conducting experiments at higher stresses and changing brine NaCl concentration to see how the permeability results differ from the published data (e.g. Fisher and Knipe, 2001) as these were measured under inappropriate experimental conditions i.e. measurement were made at low stresses using distilled water as permeant. The results obtained during the present study at in-situ stress were compared with those previously published by Fisher and Knipe (2001). An important observation was that the permeability measured at ambient stress using distilled water gave lower permeability values, whereas the permeability measured at in-situ stress with formation compatible fluid (i.e. brine NaCl) in turn gave higher values, therefore the effect of low stress distilled water measurements and high stress brine permeability measurements are partially cancelling out. Therefore, the present study findings suggested that the data reported by Fisher and Knipe (2001) could be reliable to use for analysis of fault seal.

The simulations performed using the data collected during present study have suggested that the fault rocks formed within low absolute permeability, it is essential to take account of their relative permeabilities and capillary pressures, when modelling their behaviour. However, the faults found within higher absolute permeability it might not be so important to model by assigning their two phase flow properties. The faults formed in high permeable reservoirs and low capillary threshold pressures could be modelled based on their single phase flow properties of faults.

## 8.4 Recommendations for future work

Although a number of achievements have been gained in fault rock characterization and modelling, there is still no universal method that could be applied to all types of fault rocks in all situations. These issues and problems require some further investigation. The following recommendations are suggested for future work.

### 8.4.1 Experimental work

- All fault rock samples studied during this research were from siliciclastic sediments. However, hydrocarbon reserves exist within the carbonate formations if faults found within carbonate reservoirs might have a different behaviour than sandstone to address the effects of fluid flow within such reservoirs would be an active area of research.
- Most of the data related to fault rock capillary threshold pressures comes from measurements performed under ambient stress conditions. This could be one of the important areas of research which needs to be further investigated, by performing experiments under realistic reservoir stress conditions which may alter results significantly.
- Since faults have such a major impact on the movement of fluids on both geological and production time-scales, it is likely that they will also have a significant impact on the movement of CO<sub>2</sub> in and around geological storage sites. A large proportion of the CO<sub>2</sub> projects are aimed to use numerical modelling and laboratory experiments to predict how faults will affect the long-term integrity of CO<sub>2</sub> storage sites such as depleted oil and gas reservoirs or deep saline aquifers. To the author's knowledge only one study has been conducted on fault rock CO<sub>2</sub> injection in saline aquifers (e.g. Tueckmantel et al., 2012). To better parameterise simulation studies of CO<sub>2</sub> injection and to reduce the uncertainties in storing CO<sub>2</sub> this needs to be further investigated by collecting data from those of the representative fault compartmentalized reservoirs fields and measurements should be conducted at reservoir stress conditions using CO<sub>2</sub> and brines. The attention should be paid to those sites which are potential candidates for CO<sub>2</sub> injection so the accuracy could be verified with experimental results.

### **8.4.2 Capillary end effects**

Capillary end effects within heterogeneous reservoirs are important to be investigated; the fault rocks are very tight than its associated host sandstones, though their capillary characteristics will be different from their host sandstone. At the interfaces of different core segments within composite core, the capillary contact might not be maintained between connecting segments. In general, if two phases wetting and non-wetting such as water and oil are present within the porous rock segments, the rocks neighbour to each other possessing high and low permeability, the saturation discontinuity exists and the capillary pressure is continuous this is called the capillary end effect (e.g. Bear, 1988). Capillary end effect has significance in fault rocks as these comprise alternate layers of high and low permeability deformation bands. This effect has been studied by Dale et al. (1997) that discusses this effect based on analytical solution within 1D steady state two phase flow as a function of pressure and saturation across heterogeneous rocks. The relative permeability within heterogeneous rocks composed of alternating bands of high and low permeability segments might be obtained through analytical solutions presented by Dale et al. (1997) and is an important area of research.

### **8.4.3 Field scale fault modelling**

There are two common methods of fault compartmentalized reservoirs modelling; the one which is routinely practiced within the industry is the TMs method (e.g. Manzocchi et al., 1999). The other method of fault modelling is representing fault as LGR local grid refinement, the explicit method of fault modelling and is performed by assigned fault rock two-phase flow (relative permeability and capillary pressure) properties discretely (e.g. Rivenæs and Dart, 2002; Al-Busafi et al., 2005; Berg and Øian, 2007, Al-Hinai et al., 2008). However, the modelling considerations are likely to be critical due to material properties of reservoir such as overburden stresses. Coupled fluid flow-geomechanical modelling of such processes by taking into account of the stress sensitivity of fault rocks is also important, particularly when processes such as stress arching (Segura et al., 2011) are occurring. This might change simple rules of thumb that would provide a guide as to when it is worth investing the time into incorporating multiphase flow properties and stress sensitivity into simulation models. Therefore, for

coupling of stress sensitivity effects within complex field scale modelling is yet an important research area to be considered for fault modelling.

#### **8.4.4 Pore network modelling**

The fault rocks have diverse geological characteristics consisting of high and low permeability deformation bands associated with undeformed host sands. Most of the fault rocks are dominated by more or less uniform quartz cementation to heterogeneous distributions of authigenic clay minerals (Fisher and Knipe, 2001). The experimental characterisation of fault rocks is also difficult due to their low permeabilities and heterogeneities. The experimental analysis of such rocks is difficult to perform and is very time consuming. The empirical models of relative permeability and capillary pressure estimation often have little or no physical basis. Hence, the prediction could differ from one model to the other and there might be considerable differences in the laboratory measurements and prediction from empirical models (e.g. Blunt, 2000). The numerical pore scale modelling is fast compared to conventional laboratory experiments (e.g. Blunt, 2001). Although, there is no any standard workflow available to model fault rock properties using pore network modelling. Therefore, a next step could be the extraction of pore networks for fault rock multi-phase fluid flow.

## References

ABHIJIT Y. DANDEKAR, (2006) "Petroleum Reservoir Rock and Fluid Properties, Second Edition" ISBN-10: 1439876363 | 544 page.

Al-Busafi, B. (2005). Incorporation of fault rock properties into production simulation models. *PhD thesis, University of Leeds*

AL-BUSAFI, B., FISHER, Q. J., HARRIS, S. D. (2005) The importance of incorporating the multi-phase flow properties of fault rocks into production simulation models. *Marine and Petroleum Geology*, 22, 365-374.

Ali, H.S., Al-Marhoun, M.A., Abu-Khamsin, S.A. and Celik, M.S. (1987) The effect of overburden pressure on relative permeability SPE 15730 pp. 335–334.

AL-HINAI, S., FISHER, Q., AL-BUSAFI, B., GUISE, P., GRATTONI, C.A. (2006) "Recent application of special core analysis to fault rocks", paper SCA 2006-15, presented at the 2006 Int. Symp of Soc. Core Analysts.

AL-HINAI, S., FISHER, Q. J., AL-BUSAFI, B., GUISE, P., GRATTONI, C. A. (2008) Laboratory measurements of the relative permeability of cataclastic fault rocks: An important consideration for production simulation modelling. *Marine and Petroleum Geology*, 25, 473-485.

Al-Hinai, S. (2007) Multiphase fluid flow properties of fault rocks: implications for production simulation models. PhD Thesis. University of Leeds.

AMAEFULE, J., WOLFE, K., WALLS, J., AJUFO, A. and PETERSON, E. (1986). Laboratory determination of effective liquid permeability in low-quality reservoir rocks by the pulse decay technique. SPE California Regional Meeting. Society of Petroleum Engineers.

API (1998) Recommended Practices for Core Analysis, API RP 40. Washington: American Petroleum Institute.

ARCHER, S., WARD, S., MENAD, S., SHAHIM, I., GRANT, N., SLOAN, H., & COLE, A. (2010). The Jasmine discovery, Central North Sea, UKCS. In *Geological Society, London, Petroleum Geology Conference series* (Vol. 7, pp. 225-243). Geological Society of London.

ANTONELLINI, M. and AYDIN, A. (1994). Effect of faulting on fluid flow in porous sandstones: petrophysical properties. AAPG bulletin, 78, 355-377.

ARTHUR, T. Mesozoic structural evolution of the UK Southern North Sea: insights from analysis of fault systems. Geological Society, London, Petroleum Geology Conference series, 1993. Geological Society of London, 1269-1279.

ARMITAGE P.J., FAULKNER, D.R., WORDEN, R.H., APLIN, A.C., BUTCHER, R., ILIFFE, J. (2011) Experimental measurement of, and controls on, permeability and permeability anisotropy of caprocks from CO<sub>2</sub> storage project at the Krechba Field, Algeria: Journal of geophysical research, vol. 116, b12208.

M. BAI; F. MENG; D. ELSWORTH; M. ZAMAN; J.-C. ROEGIERS. (1997) Numerical modeling of stress-dependent permeability. Int. J. Rock Mech. & Min. Sci. Vol. 34, No. 3-4, 1997 ISSN 0148-9062

BACHU, S., AND B. BENNION (2008), Effects of in-situ conditions on relative permeability characteristics of CO<sub>2</sub>-brine systems, Environ. Geol., 54, 1707–1722.

BARAKA-LOKMANE, S. (2002) Hydraulic versus pneumatic measurements of fractured sandstone permeability. Journal of Petroleum Science and Engineering 36, 183–192.

Bjorlykke, K. (2010) Petroleum Geoscience: From Sedimentary Environments to Rock Physics.

BARTON, C. A., ZOBACK, M. D. and MOOS, D. (1995). Fluid flow along potentially active faults in crystalline rock. Geology, 23, 683-686.

BESKOK, A., KARNIADAKIS, G.E. (1999) A model for flows in channels, pipes and ducts at micro and nano-scales. Micro-scale thermophys. Eng. 3(1), 43-77.

BENNION D.B., THOMAS F.B., SCHULMEISTER B.E., RUSHING J. (2002). Laboratory and field validation of the mechanism of establishment of very low initial water saturations in ultra-low permeability porous media. Petroleum society's canadian international petroleum conference 2002, calgary, alberta, canada, june 11 – 13, 2002.

BENTON M., COOK E., AND TURNER P., 2002. Permian and Triassic Red Beds and the Penarth Group of Great Britain. Geological Conservation Review Series, No. 24, p. 2-28.

BENSE, V. F., AND M. A. PERSON,(2006) Faults as conduit-barrier systems to fluid flow in siliciclastic sedimentary aquifers. *Water resources research* 2006

BLASINGAME T.A.(2008). the characteristic flow behaviour of low permeability reservoir system. SPE 114168, presented at 2008, SPE unconventional reservoirs conference held at Keystone colorado USA.

BLOOMFIELD, J.P., WILLIAMS, A.T. (1995). An empirical liquid permeability–gas permeability correlation for use in aquifer properties studies. *Q. J. Eng. Geol.* 28, 143–150.

BLUNT, M.J. 2001. Flow in porous media Pore network models and multiphase flow. *Curr. Opin. Colloid Interface Sci.*(3): 197–207. DOI: 10.1016/S1359-0294(01)00084X.

BLUNT, M. J. (1997). Effects of heterogeneity and wetting on relative permeability using pore level modeling. *SPE Journal*, 2(01), 70-87.

BRYANT, S., AND JOHNSON, A. (2003). Wetting phase connectivity and irreducible saturation in simple granular media. *Journal of colloid and interface science*, 263(2), 572-579.

BRACE, W., WALSH, J. and FRANGOS, W. (1968). Permeability of granite under high pressure. *Journal of Geophysical Research*, 73, 2225-2236.

BRITT, L., AND SCHOEFFLER, J., 2009, “The geomechanics of a shale play: What makes a shale prospective!,” SPE Eastern Regional Meeting , Charleston, West Virginia, September 23-25.

BROWER, K. R. AND MORROW, N.R. (1985) Fluid flow in cracks as related to low permeability gas sands. Society of Petroleum Engineers. Paper SPE 11623.

BROOKS, R. H., & COREY, T. (1964). Hydraulic properties of porous media.

BOUVIER, J., KAARS-SIJPESTEIJN, C., KLUESNER, D., ONYEJEKWE, C. & VAN DER PAL, R. (1989). Three-dimensional seismic interpretation and fault sealing investigations, Nun River Field, Nigeria. *AAPG bulletin*, 73, 1397-1414.

BYRNES, A. P., (1997). Reservoir characteristics of low-permeability sandstones in the Rocky Mountains: *The Mountain Geologist* v. 43, no. 1, p. 37-51.

BYRNES, ALAN P AND CASTLE, J. W. (2000) Comparison of core petrophysical properties between low-permeability sandstone reservoirs: Eastern U.S. Medina group and Western U.S. Mesaverde group and Frontier formation. Paper presented at SPE Rocky Mountain Regional Low -Permeability Reservoirs Symposium and Exhibition. 12-15 March, at Denver, CO. SPE: 1-10

BYRNES, A. P., CLUFF, R.M., WEB, J.C. (2009) Analysis of Critical Permeability, Capillary and Electrical Properties for Mesaverde Tight Gas Sandstones from Western U.S. Basins. DOE report DE-FC26-05NT42660.

BURHANNUDINNUR, M. and MORLEY, C. (1997). Anatomy of growth fault zones in poorly lithified sandstones and shales: implications for reservoir studies and seismic interpretation: part 1, outcrop study. *Petroleum Geoscience*, 3, 211-224.

CAINE, J.S., EVANS, J.P., FORSTER, C.B., 1996. Fault zone architecture and permeability structure. *Geology* 24, 1025-1028

CARDWELL, W. T. AND PARSONS, R. I. (1945) Average permeability of heterogeneous sands. *Transactions of the American Institute of Mining Engineers*, 160, 34-42.

CALHOUN JR, J. C., LEWIS JR, M. and NEWMAN, R. 1949. Experiments on the capillary properties of porous solids. *Journal of Petroleum Technology*, 1, 189-196.

CHADWICK, R. A., Holliday, D. W., HOLLOWAY, S. T., & Hulbert, A. G. (1993). The evolution and hydrocarbon potential of the Northumberland–Solway Basin. In *Geological Society, London, Petroleum Geology Conference series* (Vol. 4, pp. 717-726). Geological Society of London.

CHALMERS, G.R.L., ROSS, D.J.K. AND BUSTIN, R.M., (2012). Geological controls on matrix permeability of Devonian Gas shales in the Horn River and Liard basins, north eastern British Columbia, Canada. *International journal of coal geology* 103, 120-131.

CIVAN, F. (2010). Effective correlation of apparent gas permeability in tight porous media. *Transport in Porous Media*, 82(2), 375-384.

COLLIER, R. L. (1989). Tectonic evolution of the Northumberland Basin; the effects of renewed extension upon an inverted extensional basin. *Journal of the Geological Society*, 146, 981-989.

CHOWDIAH, P. (1987) Laboratory measurements relevant to two-phase flow in a tight gas sand matrix: paper SPE 16945-MS, Proceedings of the 62nd Annual Technical Conference and Exhibition of the Society of Petroleum Engineers, Dallas, Texas, September 27-30, 12 p. DOI: 10.2118/16945-MS.

CLUFF, R. M. and BYRNES, A. P. Relative Permeability In Tight Gas Sandstone Reservoirs-The " Permeability Jail" Model. SPWLA 51st Annual Logging Symposium, (2010). Society of Petrophysicists and Well-Log Analysts.

CHIERICI, G. L., ET AL. (1967) Effect of the overburden pressure on some petrophysical parameters of reservoir rocks." 7th World Petroleum Congress. World Petroleum Congress.

CRAWFORD, B. R., MYERS, R. D., MORROW, A., FAULKNER, D. R., RUTTER, E. H. (2002). Porosity–permeability relationships in clay-bearing fault gouge. Paper 78214 presented at the Society of Petroleum Engineers/International Society of Rock Mechanics Conference, Irving Texas.

CRAWFORD, B., FAULKNER, D., RUTTER, E. (2008) strength, porosity, and permeability development during hydrostatic and shear loading of synthetic quartz-clay fault gouge, *J. Geophys. Res.*, 113, B03207.

Dacy, J.M. (2010) Core tests for relative permeability of unconventional gas reservoirs. SPE 135427

DANDEKAR (2006). *Petroleum Reservoir Rock and Fluid Properties*, Second Edition

DAVIES, J. P. AND DAVIES, D. K. (1999) Stress-dependent permeability: Characterization and modeling. *Journal of petroleum technology*. Paper SPE 56813.

DAVIES, J. P. AND HOLDITCH, S. A. (1998) Stress-dependent permeability in low permeability gas reservoirs: Travis peak formation, East Texas. SPE Rocky

Mountain Regional Low-Permeability Reservoirs Symposium and Exhibition, pp. 117–128.

DAVID, C., WONG, T. F., ZHU, W., ZHANG, J. (1994) Laboratory measurement of compaction-induced permeability change in porous rocks: Implications for the generation and maintenance of pore pressure excess in the crust. *Pure and Applied Geophysics*, 143(1-3), 425-456.

DALATABAN, AND H. JOHNSON, EDS., Structural geology in reservoir characterization. . Geological Society (London) Special Publication , , 127, p. 83-97.

DE PAOLA, N., HOLDSWORTH, R. and MCCAFFREY, K. (2005). The influence of lithology and pre-existing structures on reservoir-scale faulting patterns in transtensional rift zones. *Journal of the Geological Society*, 162, 471-480.

DEWHURST, D.N., APLIN, A.C., SARDA, J. P., AND YANG, Y.L. (1998). Compaction-driven evolution of poroperm in natural mudstones: An experimental study, *J. Geophysics. Res.*, 103, 651-661.

DEWHURST, D.N., APLIN, A.C., SARDA, J. P., AND YANG, Y.L. (1998). Influence of clay fraction on pore-scale properties and hydraulic conductivity of experimentally compacted mudstones, *J. Geophysics. Res.*, 104, 29261-29274.

DICKER, A. AND SMITS, R. (1988). A practical approach for determining permeability from laboratory pressure-pulse decay measurements. International Meeting on Petroleum Engineering. Society of Petroleum Engineers.

DONG, J. J., HSU, J. Y., WU, W. J., SHIMAMOTO, T., HUNG, J. H., YEH, E. C., AND SONE, H. (2010). Stress-dependence of the permeability and porosity of sandstone and shale from TCDP Hole-A. *International Journal of Rock Mechanics and Mining Sciences*, 47(7), pp. 1141-1157.

DURLOFSKY, L.J.(2000). “An approximate model for well productivity in heterogeneous porous media,” *Mathematical Geology*, **32**, 421-438, 2000.

DULLIEN (1992), Porous media: fluid transport and pore structure. Academic Press, New York.

ELLEVSSET, S. O., KNIPE, R., OLSEN, T. S., FISHER, Q. and JONES, G. (1998). Fault controlled communication in the Sleipner Vest Field, Norwegian Continental Shelf; detailed, quantitative input for reservoir simulation and well planning. Geological Society, London, Special Publications, 147, 283-297.

EVANS, J. P., FORSTER, C. B. and GODDARD, J. V. (1997). Permeability of fault-related rocks, and implications for hydraulic structure of fault zones. *Journal of Structural Geology*, 19, 1393-1404.

FATT, I. (1953). The effect of overburden pressure on relative permeability. *Journal of Petroleum Technology*, 5(10), 15-16.

FAULKNER, D. AND RUTTER, E. (2000). Comparisons of water and argon permeability on natural clay-bearing fault gouge under high pressure at 20°C, *J. Geophys. Res.*, 105, 16, 415-426.

FAULKNER, D. R. (2004) - A model for the variation in permeability of clay-bearing fault gouge with depth in the brittle crust *Journal of Geophysical Research Letters*. JA - Geophys. Res. Lett. Vol - 31 IS - 19 SN - 1944-8007

FETTER, C. W. (1993). Contaminant hydrogeology (2<sup>nd</sup> edition). Prentice Hall international (UK) limited London

FIROOZABADI, A. & RAMEY, H. J. (1988). Surface-tension of a water-hydrocarbon system at reservoir conditions. *Journal of Canadian Petroleum Technology*, 27(3), 41-48.

FISHER, Q.J., and JOLLEY, S. (2007). Treatment of faults in production simulation models. Geological Society, London, Special Publications, 292, 219-233.

FISHER, Q. J. (2005) Recent advances in fault seal analysis as an aid to reservoir characterisation and production simulation modelling. 1757-1764.

FISHER, Q.J. and KNIPE, R. J. (1998). Fault sealing processes in siliciclastic sediments. Geological Society, London, Special Publications, 147, 117-134.

FISHER, Q. J. AND KNIPE, R. J. (2001) The permeability of faults within siliciclastic petroleum reservoirs of the North Sea and Norwegian Continental Shelf. *Marine and Petroleum Geology*, 18, 1063-1081.

FISHER, Q. J., CASEY, M., CLENNELL, M. B. and KNIPE, R. J. (1999). Mechanical compaction of deeply buried sandstones of the North Sea. *Marine and Petroleum Geology*, 16, 605-618.

FISHER, Q. J. and KNIPE, R. J. (2001). The permeability of faults within siliciclastic petroleum reservoirs of the North Sea and Norwegian Continental Shelf. *Marine and Petroleum Geology*, 18, 1063-1081.

FISHER, Q.J., F. KETS, A. CROOK (2013). Self-sealing of faults and fractures in argillaceous formations: Evidence from the petroleum industry.

FISHER, Q.J., HARRIS, S.D., MCALLISTER, E., KNIPE, R.J., BOLTON, A.J., 2001. Hydrocarbon flow across sealing faults: theoretical constraints. *Marine and Petroleum Geology* 18, 251–257.

FLODIN, E., GERDES, M., AYDIN, A., WIGGINS, W. D. (2005). Petrophysical properties and sealing capacity of fault rock, Aztec Sandstone, Nevada. *AAPG Memoir*, 197-217.

FLORENCE F.A., RUSHING, J.A., NEWSHAM, K.E., BLASINGAME, T.A. (2007) Improved permeability prediction relations for low permeability sands, Paper SPE 107954 presented at SPE Rocky Mountain Oil and Gas technology symposium, Denver Colorado USA, 16-18 April 2007.

FOWLES, J., AND BURLEY, S. (1994). Textural and permeability characteristics of faulted, high porosity sandstones. *Marine and Petroleum Geology*, 11(5), 608-623.

FORBES, P (1991) Simple and accurate method for converting centrifuge data into drainage and imbibition capillary pressure curves, in Proceedings of the Society of Core Analysts Annual Conference, San Antonio, pp. 20–22

FORBES, P.L. CHEN, Z. A. AND RUTH, D. W. (1994) Quantitative Analysis of Radial Effects on Centrifuge Capillary Pressure Curves, Society of Petroleum Engineers, Richardson, TX.

FORBES, P.L., ED.,(1997) Centrifuge Data Analysis Techniques: A Survey from the Society of Core Analysts, 1997

FRASER, S.I, ROBINSON, A M, JHONSON, HD, UNDERHILL, J R, KADOLSKY, D G , CONNELL,R, JOHANNESSON, P AND RAVNAS, R., (2003). Petroleum geology of the central and northern North Sea. (157-189), London geological society.

FUNK, J. J., CHOINSKI, M. C., SAXMAN, B. B., CALLENDER, C. A. (1989) Characterization of Carbonate Porosity Using Petrophysical Properties and Image Analysis. *Middle East Oil Show*.

GANGI. AF. (1978) Variation of whole and fractured porous rock permeability with confining pressure. *Int J Rock Mech Min Sci Geomech Abstr* 15(5):249–257

GHABEZLOO S, SULEM J, GUÉDON S, MARTINEAU F. (2008) Effective stress law for the permeability of a limestone. *International Journal of Rock Mechanics and Mining Science*, DOI 10.1016/j.ijrmms.2008.05.006.

GIBSON, R.G., (1998.) Physical character and fluid-flow properties of sandstone-derived fault zones. In: Coward, M.P., Daltaban, T.S., Johnson, H. (Eds.), *Structural Geology in Reservoir Characterization*, volume 127, Geological Society, London, Special Publications, pp. 83-97.

HAGOORT, J. (1980), Oil recovery by gravity drainage. *SPEJ*, 139-150.

GUPTA, V., HAMPTON, M.A., STOKES, J.R., NGUYEN, A.V. AND MILLER, J.D. (2011), “Particle interactions in kaolinite suspensions and corresponding aggregate structures,” *Journal of Colloid and Interface Science*, **359**, (1), 95-103.

HARRIS, D., YIELDING, G., LEVINE, P., MAXWELL, G. ROSE P.T. & NELL P. (2002) Using Shale Gouge Ratio (SGR) to model faults as transmissibility barriers in

reservoirs: an example from the Strathspey Field, North Sea. *Petroleum Geoscience*, 8, 167-176.

HEID, J.G., MCMAHON, J.J., NIELSEN, R.F., YUSTER, S.T. (1950) Study of the Permeability of Rocks to Homogeneous Fluids. American Petroleum Institute.

HILLIER, S. 1999. Use of an air brush to spray dry samples for X-ray powder diffraction. *Clay Minerals*, 34, 127-135.

HOLT, R.M. AND KENTER, C.J. (1992) : Laboratory simulation of core damage induced by stress release. In J.R.Tillerson and W.R.Waversik (eds.) Proc.33<sup>rd</sup> US Rock Mechanics Symposium, pp. 959-68.

HOLT, R.M., BRIGNOLI, M., FJAER, E., KENTER, C.J., AND UNANDER, T.E. (1994): Core damage effects on compaction behaviour. SPE/ISRM Paper 28027, pres. at EUROCK'94, Delft, Netherlands 29-31 August.

HØILAND, O., KRISTENSEN, K., AND MONSEN, T. (1993). Mesozoic evolution of the Jacren high area, Norwegian central North Sea. In J.R. Parker (Ed.), *Petroleum geology of Northwest Europe: Proceedings of the 4<sup>th</sup> Conference* (pp. 1189-1195). The Geological society, London.

HSIEH, P., TRACY, J., NEUZIL, C., BREDEHOEFT, J. and SILLIMAN, S., (1981). A transient laboratory method for determining the hydraulic properties of 'tight' rocks—I. Theory. *International Journal of Rock Mechanics and Mining Sciences & Geomechanics Abstracts*. Elsevier, 245-252.

HOSSAIN, Z., GRATTONI, C. A., SOLYMAR, M., AND FABRICIUS, I. L. (2011). Petrophysical properties of greensand as predicted from NMR measurements. *Petroleum Geoscience*, 17(2), pp. 111-125.

HOWER, T.L., LEWIS, D.R, AND OWENS, R.W. (1992) Recovery Optimization in a Multi-Reservoir Offshore Gas Field with Water Influx. SPE 24865.

HOFFMAN, R.N. "A technique for the determination of Capillary pressure curves using a constantly accelerated Centrifuge", SPEJ.3(3):pp.227-235, 1963

JING, X.D., ARCHER, J.S. AND DATABAN, T.S. (1992) Laboratory study of the electrical and hydraulic properties of rocks under simulated reservoir conditions. *Marine and Petroleum Geology* pp. 115–127.

JONES, J. M. and DEARMAN, W. (1967). *Geology of the coast section from Tynemouth to Seaton Sluice*, Natural History Society of Northumberland, Durham and Newcastle upon Tyne.

JONES J.M, (1967). The geology of coast section from Tynemouth to Seaton Sluice. *Trans. Nat. Hist. Soc. Northumberia*. 16, 153-192.

JONES, S. C. (1972) A rapid accurate unsteady – state Klinkenberg permeameter , *SPE Journal*, pp. 383–397.

JONES, F.O. AND OWENS, W.W. (1980) A Laboratory Study of Low-Permeability Gas Sands. *J Pet Technol* **32** (9): 1631–1640. SPE-7551-PA.

JONES, S. 1997. A technique for faster pulse-decay permeability measurements in tight rocks. *SPE formation evaluation*, 12, 19-26.

JONES, F. O. AND W.W. OWENS (1980) A laboratory study of low-permeability gas sands: paper SPE 7551-PA, *Journal of Petroleum Technology*, v. 32, no. 9, p.1631-1640. DOI: [10.2118/7551-PA](https://doi.org/10.2118/7551-PA).

JONES. S.C (1988) “Two-point determinations of permeability and PV vs net confining stress,”*SPE Formation Evaluation*,vol. 3, pp 235-241

KATZ, A. and THOMPSON, A. 1987. Prediction of rock electrical conductivity from mercury injection measurements. *Journal of Geophysical Research: Solid Earth (1978–2012)*, 92, 599-607.

KNAI, T.A. AND KNIPE, R.J. (1998) The impact of faults on fluid flow in the Heidrun Field. In: Jones, G., Fisher, Q.J. , Knipe, R.J. (eds) *Faulting, Fault Sealing and Fluid Flow in Hydrocarbon Reservoirs*. Geological Society, London, Special Publications, 147, 269–282.

KATZ, A. J. AND THOMPSON. A.H. (1986) Quantitative prediction of permeability in porous rock. *Physical review*. *Physical review B*, 34(11), 8179-8181.

KATZ, A. and THOMPSON, A. (1987). Prediction of rock electrical conductivity from mercury injection measurements. *Journal of Geophysical Research: Solid Earth* (1978–2012), 92, 599-607.

KARNIADAKIS, G., BESKOK, A. AND ALURU, N. (2005) *Micro flows and nanoflows: Fundamentals and simulation (interdisciplinary applied mathematics)*, 1 ed. Springer.

Klinkenberg, L.J. (1941) The Permeability of Porous Media to Liquids and Gases. *Drill. & Prod. Prac.* 200.

KEANEY, G.M., MEREDITH, P., MURRELL, S., BARKER, J., (2004). Determination of the effective stress laws for permeability and specific storage in a low porosity sandstone, in: North America Rock Mechanics Symposium. American Rock Mechanics Association, Houston, Texas

KEITH W. SHANLEY, ROBERT M. CLUFF, JOHN W. ROBINSON (2004). Factors controlling prolific gas production from low-permeability sandstone reservoirs: Implications for resource assessment, prospect development, and risk analysis. *AAPG Bulletin*, V. 88, No. 8 (August 2004), P. 1083-1121

KELLER, T., BAYES, R., AULD, H., & LINES, M. (2005). Judy Field: rejuvenation through a second phase of drilling. In *Geological Society, London, Petroleum Geology Conference series* (Vol. 6, pp. 651-661). Geological Society of London.

KIMBELL, G. S., CHADWICK, R. A., HOLLIDAY, D. W., & WERNGREN, O. C. (1989). The structure and evolution of the Northumberland Trough from new seismic reflection data and its bearing on modes of continental extension. *Journal of the Geological Society*, 146(5), 775-787.

KLINKENBERG, L. 1941. The permeability of porous media to liquids and gases. *Drilling and production practice*.

KHILAR, K.C., FOGLER, H.S., (1984). The existence of a critical salt concentration for particle release. *J.Colloid Interface Sci.*101, 214–224.

KHILAR, K. C., VAIDYA, R. N., & FOGLER, H. S. (1990). Colloidally-induced fines release in porous media. *Journal of Petroleum Science and Engineering*, 4(3), 213-221.

KWON, O., B. E. HERBERT, AND A. K. KRONENBERG (2004) Permeability of illite-bearing shale: 2. Influence of fluid chemistry on flow and functionally connected pores, *J. Geophys. Res., Solid Earth*, 109, B10206.

[LAKE, L.W., \(2005\) Enhanced oil recovery. Prentice Hall \(Englewood Cliffs, N.J\)](#)

LEKIA, S. D. L., & EVANS, R. D. (1990). A Water-Gas Relative Permeability Relationship for Tight Gas Sand Reservoirs. *Journal of Energy Resources Technology*, 112(4), 239-245.

LEVER A., AND DAWE, R.A. (1987) Clay migration and entrapment in synthetic porous media. *Marine and Petroleum Geology*, 4, 112-118.

LOVELOCK, P.E.R. (1977) Aquifer properties of Permo-Triassic sandstones in the United Kingdom. *Bull. Geol. Survey. G. B.* 56, 1–40.

LEVEILLE, G. P., KNIPE, R., MORE, C., ELLIS, D., DUDLEY, G., JONES, G., FISHER, Q. J. and ALLINSON, G. (1997). Compartmentalization of Rotliegendes gas reservoirs by sealing faults, Jupiter Fields area, southern North Sea. Geological Society, London, Special Publications, 123, 87-104.

LIN, W. (1982). Parametric analyses of the transient method of measuring permeability. *Journal of Geophysical Research: Solid Earth (1978–2012)*, 87, 1055-1060.

LUFFEL, D. L., HOPKINS, C. W., SHETTLER, P. D.(1993). “Matrix Permeability Measurement of Gas Productive Shales”, 68 th Annual Technical Conference and Exhibition of the Society of Petroleum Engineers, Houston, Texas,. SPE 26633.

LUFFEL, D., HERRINGTON, K., WALLS, J. (1993) Effect of Drying on Travis Peak Cores Containing Fibrous Illite. *SPE Advanced Technology Series*, 1, 188–194.

LUFFEL, D.L., HOWARD, W.E., AND HUNT, E.R. (1991) Travis Peak core permeability and porosity relationships at reservoir stress: paper SPE 19008. PA, Society of Petroleum Engineers Formation Evaluation, September, 1991, v. 6, n. 3, p. 310-319.

MELROSE, J. 1987. Role of capillary condensation in adsorption at high relative pressures. *Langmuir*, 3, 661-667.

MCDOWELL-BOYER, L., HUNT, J.R., AND SITTA, N. (1986), "Particle Transport Through Porous Media," *Water Resources Research*, **22**, 1901-1921.

MANZOCCHI, T., WALSH, J.J., NELL, P. & YIELDING, G. (1999) Fault transmissibility multipliers for flow simulation models. *Petroleum Geoscience*, 5, 53-63.

MANZOCCHI, T., HEATH, A.E., WALSH J.J. and CHILDS, C. (2002). The representation of two-phase fault-rock properties in flow simulation models. *Petroleum Geoscience*, 8, 119-132.

MANZOCCHI, T., CHILDS, C., and WALSH J.J. (2010). Faults and faults properties in hydrocarbon flow models. *Geofluids* 10(1-2), 94-113.

MCCRONE, C. W., GAINSKI, M., & LUMSDEN, P. J. (2003). The Indefatigable Field, Blocks 49/18, 49/19, 49/23, 49/24, UK North Sea. In J. G. Gluyas & H. M. Hitchens (Eds.), *United Kingdom Oil and Gas Fields, Commemorative Millennium Volume* (pp. 741-747). Geological Society, London.

MESRI, G., & OLSON, R. E. (1971). Mechanisms controlling the permeability of clays. In *From Soil Behavior Fundamentals to Innovations in Geotechnical Engineering@ sHonoring Roy E. Olson* (pp. 88-95). ASCE.

MERCER, J.W. AND R.M. COHEN. 1990. A review of immiscible fluids in the subsurface: properties, models, characterization and remediation. *J. Contam. Hydrol.*, **6**: 107- 163.

MCPHEE, C.A. AND ARTHUR, K.G., (1991) Klinkenberg permeability measurements: problems and practical solutions.

MIZOGUCHI, K., HIROSE, T., SHIMAMOTO, T. and FUKUYAMA, E. (2008). Internal structure and permeability of the Nojima fault, southwest Japan. *Journal of Structural Geology*, 30, 513-524.

MOHAN, K. AND FOGLER, H. (1997) Colloidally induced smectitic fines migration: Existence of microquakes, *AIChE J.*, 45, 565-576.

MONDOL, N. H. BJØRLYKKE, K., AND JAHREN, J. (2008) "Experimental compaction of clays: relationship between permeability and petrophysical properties in mudstones." *Petroleum Geoscience* 14 (4), 319-337.

MOORE, D., MORROW, C., AND BYERLEE, J. (1982) Use of swelling clays to reduce permeability and its potential application to nuclear waste repository sealing, *Geophys.Res. Letters*, 9, 1009-1012.

MORROW, C. A., SHI, L. Q., & BYERLEE, J. D. (1984). Permeability of fault gouge under confining pressure and shear stress. *Journal of Geophysical Research: Solid Earth (1978–2012)*, 89(B5), 3193-3200.

MORROW, C.A., SHI, L., BYERLEE, J.D. (1984) Permeability of fault gouge under confining pressure and shear stress. *J Geophys Res.* 89:3193-200.

MORROW, N.R. AND MELROSE, J.C. (1991). Application of Capillary Pressure Measurements to the Determination of Connate Water Saturation. In *Interfacial Phenomena in Petroleum Recovery*, 257-287, ed. N.R. Morrow. New York City: Marcel Dekker Inc

MORROW, N. R. (1976). Capillary pressure correlations for uniformly wetted porous media. *Journal of Canadian Petroleum Technology*, 15(04).

MORROW, N.R. (1970). Irreducible wetting-phase saturations in porous media. *Chem. Eng. Sci.* **25** (11): 1799–1818. [http://dx.doi.org/10.1016/0009-2509\(70\)80070-7](http://dx.doi.org/10.1016/0009-2509(70)80070-7)

MOTEALLEH, S., AND BRYANT, S. L. (2009). Quantitative mechanism for permeability reduction by small water saturation in tight-gas sandstones. *SPE Journal*, 14(02), 252-258.

MUSKAT, M., MERES, M.W., (1936). The flow of heterogeneous fluids through porous media. *Physics* 7, 346–363.

NEWSHAM, K., RUSHING, J., LASSWELL, P., COX, J. and BLASINGAME, T. A. (2004) comparative study of laboratory techniques for measuring capillary pressures in tight gas sands. SPE Annual Technical Conference and Exhibition. Society of Petroleum Engineers.

NEASHAM J.W. (1977). The morphology of dispersed clay in sandstone reservoirs and its effect on sandstone shallness, pore space and fluid flow properties. Soc. Petroleum Engineers of AIME, Denver, SPE 6858, 7 pp.

N.J.C. FARRELL, D. HEALY, C.W. TAYLOR, (2014) Anisotropy of permeability in faulted porous sandstones Journal of structural geology.

ODLING, N. E., HARRIS, S. D. AND KNIPE, R. J. (2004) Permeability scaling properties of fault damage zones in siliclastic rocks. Journal of Structural Geology, 26, 1727-1747.

OSTENSEN, R. W. (1983) December, Micro-crack Permeability in Tight Gas Sandstone. Society of Petroleum Engineers. doi:10.2118/10924-PA.

O'MEARAJR.,D.J.,HIRASAKI,G.J.ANDROHAN,J.A.(1992). Centrifuge measurements of capillary pressure: Part 1 - Outflow Boundary Condition ", SPE Reservoir Eng. 7(1):pp.133-142,1992

PATHI, V. S. M. (2008). Factors affecting the permeability of gas shales. Thesis Msc. University of British Columbia Vancouver Canada.

PINDER G. F. AND GRAY, W. G. (2008). Essentials of Multiphase Flow in Porous Media. Wiley-Blackwell 1<sup>st</sup> edition.

PINDER, G. F., AND CELIA, M. A. (2006). *Subsurface hydrology*. John Wiley & Sons.

PURCELL, W. R. (1949). Capillary pressures-their measurement using mercury and the calculation of permeability therefrom. *Journal of Petroleum Technology*, 1(02), 39-48.

RAWLING, G.C., GOODWIN, L.B., AND WILSON, J.L, (2001). Internal architecture, permeability structure, and hydrologic significance of contrasting fault zone types. *Geology* 27(1), 43-46.

REVIL, A. AND CATHLES, L.M. (1999) Permeability of shaly sands. *Water Resources Research*, 35, NO. 3, 651–662,

REVIL, A. HERMITTE, D., SPANGENBERG, E. AND COCHEME, J.J., (2002) Electrical properties of zeolitized volcanoclastic materials, *J. geophysics. Res.*, 107(B8), 2168.

RHETT, D. W., AND TEUFEL, L. W. (1992). Effect of Reservoir Stress Path on Compressibility and Permeability of Sandstones. Society of Petroleum Engineers. doi:10.2118/24756-MS

RONNY PINI, SAMUEL C.M. KREVER, SALLY M. BENSON, MARCH (2012). Capillary pressure and heterogeneity for the CO<sub>2</sub>/water system in sandstone rocks at reservoir conditions, *Advances in Water Resources*, Volume 38, March 2012, Pages 48-59, ISSN 0309-1708, <http://dx.doi.org/10.1016/j.advwatres.2011.12.007>.

ROSENBRAND, E., HAUGWITZ, C., JACOBSEN, P.S.M., KJØLLER, C., FABRICIUS, I.L. (2014). The effect of hot water injection on sandstone permeability. *Geothermics* 50, 155–166.

ROSENBRAND, E., HAUGWITZ, C., JACOBSEN, P.S.M., KJØLLER, C., FABRICIUS, I.L. (2014) The effect of hot water injection on sandstone permeability. *Geothermics* 50, 155–166.

ROTEVATN., A., SANDVE, T.H., KEILEGAVLEN, E., KOLYUKHIN, D. & FOSSEN, H. (2013). Deformation bands and their impact on fluid flow in sandstone reservoirs: the role of natural thickness variations. *Geofluids* 13, 359-371

RUSHING, J.A., NEWSHAM, K.E., LASSWELL, P.M., COX, J.C., AND BLASINGAME, T.A. (2004) Klinkenberg-corrected permeability measurements in tight gas sands: steady-state versus unsteady-state techniques. SPE 89867.

RUSHING, J.A., NEWSHAM, K.E., VAN FRAASSEN, K.C. (2003) Measurement of the two-phase gas slippage phenomenon and its effects on gas relative permeability in tight gas sands. Paper SPE 84297.

SAMPATH, K., & KEIGHIN, C. W. (1982). Factors affecting gas slippage in tight sandstones of cretaceous age in the Uinta basin. *Journal of Petroleum Technology*, 34(11), 2-715.

SCHLÖMER, S. AND KROOSS, B.M. (1997). Experimental characterisation of the hydrocarbon sealing efficiency of cap rocks. *Marine and Petroleum Geology*, 14, 565-580.

SCHOWALTER, T.T. (1979). Mechanics of secondary hydrocarbon migration and entrapment. *AAPG Bulletin*, 63, 723-760.

SEGURA, J. M., FISHER, Q. J., CROOK, A. J. L., DUTKO, M., YU, J. G., SKACHKOV, S., ANGUS, D. A., VERDON, J. P. AND KENDALL, J.-M. (2011). "Reservoir stress path characterization and its implications for fluid-flow production simulations." *Petroleum Geoscience* 17(4): 335-344.

SHANLEY, K.W., R.M. CLUFF, AND J.W. ROBINSON, (2004). Factors controlling prolific gas production from low-permeability sandstone reservoirs: Implications for resource assessment, prospect development, and risk analysis, *AAPG Bulletin*, v.88, no. 8, p. 1083-1121.

SHIPTON, Z.K., EVANS, J.P., ROBESON, K.R., FORSTER, C.B., SNELGROVE, S. (2002) Structural heterogeneity and permeability in faulted eolian sandstone: implications for subsurface modeling of faults. *AAPG Bulletin* 86 (5), 863-883.

SHIPTON, Z. K., AND P. A. COWIE (2003), A conceptual model for the origin of fault damage zone structures in high-porosity sandstone, *J. Struct. Geol.*, 25, 333-345.

SIGDA. J.M., L. B. GOODWIN, P.S. MOZLEY, AND J.L. WILSON, (1999). Permeability alteration in small-displacement faults in poorly lithified sediments: Rio Grande rifts, central New Mexico: *Geophysical Monograph*, v. 113, p. 51-68.

SOLYMAR, M., FABRICIUS, I.L. AND MIDDLETON, M. (2003) Flow characterization of glauconitic sandstones by integrated Dynamic Neutron Radiography and image analysis of backscattered electron micrographs. *Petroleum Geoscience*, 9, 175–183.

SPERREVIK, S., GILLESPIE, P.A., FISHER, Q.J., HALVORSEN, T. and KNIPE, R.J. (2002). Empirical Estimation of Fault Rock properties. *In: Koestler A.G. and Hunsdale R. (eds) Hydrocarbon Seal Quantification*. Norwegian Petroleum Society, Special Publication, 11, 109-125.

SAMPATH, K. AND KEIGHIN, C. W. (1982) Factors affecting gas slippage in tight sandstones of cretaceous age in the unita basin. *Society of Petroleum Engineers* pp. 235–241.

SERONT, B., WONG, T. F., CAINE, J. S., FORSTER, C. B., BRUHN, R. L., and FREDRICH, J. T. (1998). Laboratory characterization of hydromechanical properties of a seismogenic normal fault system. *Journal of structural geology*, 20(7), 865-881.

SHI T., C.Y. WANG (1986), Pore pressure generation in sedimentary basins: overloading versus aquathermal J.Geophys Res, 91 (B2) (1986), pp. 2153–2162

SPERREVIK, S, GILLESPIE, P., FISHER, Q.J., HALVORSEN T, KNIPE, R.J., (2002) Empirical estimation of fault rock properties, In: Koestler A.G., Hunsdale, R. (Eds) Hydrocarbon seal quantification: papers presented at the Norwegian Petroleum Society Conference, 16-18 October 2000, Stavanger, Norway, Norsk Petroleumsforening Special Publication, Elsevier, pp.109-125.

SLOBOD, R. L., CHAMBERS, A. and PREHN, W. L., JR. Use of Centrifuge for Determining Connate Water, Residual Oil, and Capillary Pressure Curves of Small Core Samples.

SMITH, D. A. (1966). Theoretical considerations of sealing and non-sealing faults. *AAPG Bulletin*, 50(2), 363-374.

SORKHABI, R. and HASEGAWA, S. 2005. Fault zone architecture and permeability distribution in the Neogene clastics of northern Sarawak (Miri Airport Road outcrop), Malaysia.

SOEDER, D.J., 1988, Porosity and Permeability of Eastern Devonian Gas Shale: Society of Petroleum Engineers, SPE Formation Evaluation, March, p. 116-124.

SORKHABI, R., & TSUJI, Y. (2005). The place of faults in petroleum traps.

STONE, H. L. (1973). Estimation of three-phase relative permeability and residual oil data. *Journal of Canadian Petroleum Technology*, 12(04).

THOMAS, R. D. AND WARD, D.C. (1972) Effect of overburden pressure and water saturation on gas permeability of tight sandstone cores, Paper SPE3634, pp. 120–124.

THOMAS FINKBEINER, M. Z., PETER FLEMINGS, AND BETH STUMP. (2001). Stress, pore pressure, and dynamically constrained hydrocarbon columns in the South Eugene Island 330 field, northern Gulf of Mexico. *AAPG bulletin*, 85, 1007-1031.

TANIKAWA W, SHIMAMOTO, T. (2006) Comparison of Klinkenberg-corrected gas permeability and water permeability in sedimentary rocks. *Int. J Rock Mech Min Sci*, 41:915-25.

TIAB, D., C. DONALDSON, E.C. (2004) *Petrophysics; second edition, "Theory and Practice of Measuring Reservoir Rock and Fluid Transport Properties"*. ELSEVIER.

Thomas, R. D. and Ward, D.C. (1972), Effect of overburden pressure and water saturation on gas permeability of tight sandstone cores SPE3634 pp. 120–124.

TUECKMANTEL, C., FISHER, Q. J., GRATTONI, C. A. and APLIN, A. C. 2012. Single-and two-phase fluid flow properties of cataclastic fault rocks in porous sandstone. *Marine and Petroleum Geology*, 29, 129-142.

TEUCKMANTEL, C., FISHER, Q.J., KNIPE, R.J., LICKORISH, H. and KHALIL, S.M. (2010). Fault seal prediction of seismic-scale normal faults in porous sandstone: a case study from the eastern Gulf of Suez rift, Egypt. *Marine and Petroleum Geology*, 27, 334-350.

TUECKMANTEL, C., FISHER, Q.J., MANZOCCHI, T., SKACHKOV, S., GRATTONI C.A. (2012) Two-phase fluid flow properties of cataclastic fault rocks: Implications for CO<sub>2</sub> storage in saline aquifer. *Geology*, 40, 39-42

TUECKMANTEL, C., FISHER, Q. J., GRATTONI, C. A. APLIN, A. C. (2012A) Single- and two-phase fluid flow properties of cataclastic fault rocks in porous sandstone. *Marine and Petroleum Geology*, 29, 129-142.

TUECKMANTEL, C., FISHER, Q. J., KNIPE, R. J., LICKORISH, H., KHALIL, S. M. (2010) Fault seal prediction of seismic-scale normal faults in porous sandstone: A case study from the eastern Gulf of Suez rift, Egypt. *Marine and Petroleum Geology*, 27, 334-350.

TUECKMANTEL, C., FISHER, Q. J., GRATTONI, C. A. and APLIN, A. C. (2012). Single-and two-phase fluid flow properties of cataclastic fault rocks in porous sandstone. *Marine and Petroleum Geology*, 29, 129-142.

Vaughan. J.,D.E.Moore,C.A.Morrow, and J.D. Byerlee, Role of cracks in progressive permeability reduction during flow of heated aqueous fluids through granite, *J.Geophys. Res.*, 91,7517-7530, 1986.

VAN DER MOLEN, I., ZIJLSTRA, E., OKERMAN, J., REEMST, P.,( 2003). Compartmentalization in Rotliegend gas fields, concepts and examples from the

offshore on shore Netherlands. In: "Fault and Top Seals – what do We know and Where Do We Go" EAGE Conference , Montpellier, France.

VAN DER ZEE, W. and URAI, J. L. (2005). Processes of normal fault evolution in a siliciclastic sequence: a case study from Miri, Sarawak, Malaysia. *Journal of Structural Geology*, 27, 2281-2300.

VERWEY, E.J.W. AND OVERBEEK, J.TH.G. (1948) Theory of the Stability of Lyophobic Colloids: The Interaction of Sol Particles Having an Electric Double Layer. Elsevier, Amsterdam.

WASHBURN, E.W. (1921). The Dynamics of Capillary Flow. *Physical Review*, 17, 273-283.

WATTS, N. (1987). Theoretical aspects of cap-rock and fault seals for single- and two-phase hydrocarbon columns. *Marine and Petroleum Geology*, 4, 274-307.

WALSH, J. B. (1965) The effect of cracks on the compressibility of rock, *J. Geophys. Res.*, 70, pp. 381–389.

WALLS, J.D. (1982). Tight gas sands- permeability, pore structure and clay. *Journal of petroleum technology*, pp. 2708–2714.

WELLS, J. D., AND AMAEFULE, J.O., (1985). "Capillary Pressure and Permeability Relationships in Tight Gas Sands," Paper SPE/DOE 13879, *Proceedings of the 1985 SPE/DOE Joint Symposium on Low Permeability Gas Reservoir*, Denver, Colo., May 19-22.

WEI, K. K., MORROW, N. R., AND BROWER, K. R. (AUGUST 1986). Effect of Fluid, Confining Pressure, and Temperature on Absolute Permeabilities of Low-Permeability Sandstones. Society of Petroleum Engineers.

WILSON, M.D. AND PITTMAN, E.D. (1977) Authigenic clays in sandstones; recognition and influence on reservoir properties and paleoenvironmental analysis. *Journal of Sedimentary Research*, 47, 3–31.

WIPRUT, D. and ZOBACK, M. D. (2002). Fault reactivation, leakage potential, and hydrocarbon column heights in the northern north sea. In: ANDREAS, G. K. & ROBERT, H. (eds.) *Norwegian Petroleum Society Special Publications*. Elsevier.

YALE, D.P. (1984) Network modeling of flow, storage and deformation in porous rocks. PhD thesis, Stanford University.

YIELDING, G., FREEMAN, B. and NEEDHAM, D. T. (1997). Quantitative fault seal prediction. *AAPG bulletin*, 81, 897-917.

YIELDING, G., BRETAN, P., & FREEMAN, B. (2010). Fault seal calibration: a brief review. *Geological Society, London, Special Publications*, 347(1), 243-255.

ZIJLSTRA, E., REEMST, P. and FISHER, Q. (2007). Incorporation of fault properties into production simulation models of Permian reservoirs from the southern North Sea. *Geological Society, London, Special Publications*, 292, 295-308.

ZHANG, S., TULLIS, T. E., SCRUGGS, V. J. (2001) Implications of permeability and its anisotropy in a mica gouge for pore pressures in fault zones. *Tectonophysics*, 335, 37-50.

ZHELEZNYI, B. V, ZORIN, Z.M., SOBOLEV, W.D. AND CHURAEV, N. V. (1972) Experimental study of properties of water in thin films and fine capillaries. *Bulletin of the International Association of Engineering Geology*, 5, 57–61.

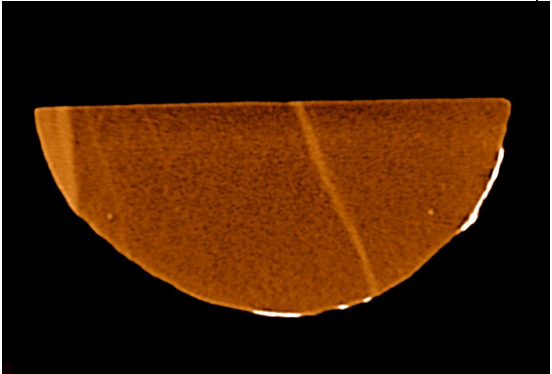
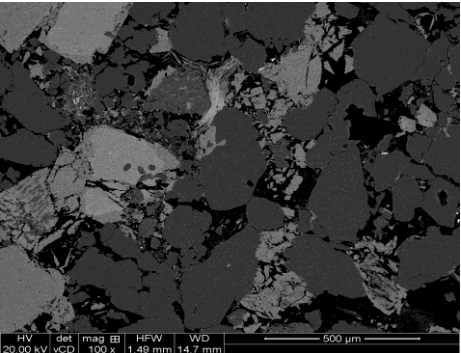
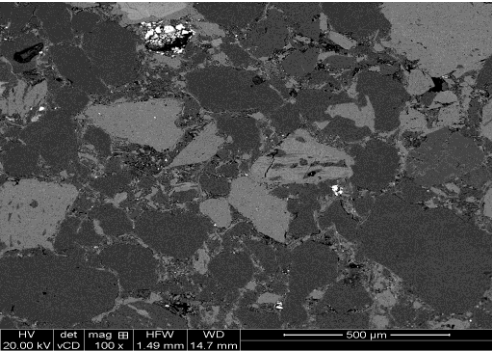
ZOBACK, D. M. AND BYERLEE, D. J. (1975). The effect of micro crack dilatancy on the permeability of westerly granite. *J. Geophys. Res.*, 80, pp. 752–755.

# Appendix-A

## Central North Sea Group-A

All samples supplied from a Triassic reservoir in the Central North Sea. Samples from four wells were analysed.

### Well CP1

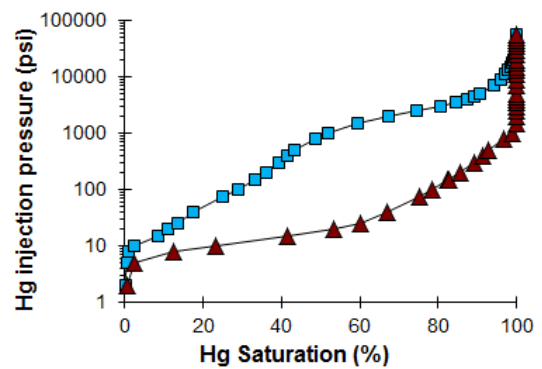
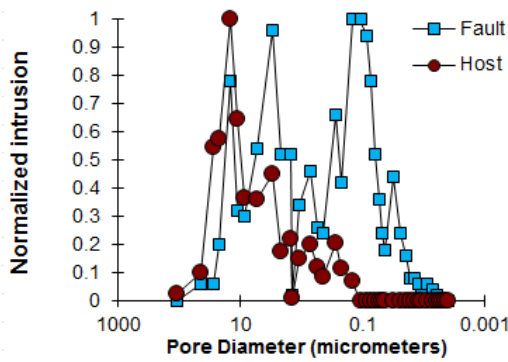
Well CP1: Triassic reservoir, central North Sea, UK	Depth: 11724.0-11724.4 m MD
Sample ID: CP1A	Cataclastic fault
	
	<p>Fault</p> 
<p>Host</p> 	<p>Fault</p> 

The undeformed sandstone is medium grained and moderately well sorted with a porosity of 25.2%. QXRD results indicate that it is composed of 38.2 % chlorite, 19.2 % quartz, 16.3 % microcline, 7.3 % albite, 3.8 % mica, and a porosity of 25.2 %. However, the sample taken for BSEM contains far less chlorite and more quartz and K-feldspar. The main diagenetic process to affect the sample were the precipitation of K-feldspar, chlorite, and quartz. The K-feldspar occurs as up to 50  $\mu\text{m}$  wide rhombs on detrital K-feldspar. The chlorite occurs as a grain coating clay. It is possible that it formed as a result of the recrystallization of early smectitic clay. The authigenic quartz is relatively abundant and occurs as both overgrowths and outgrowths.

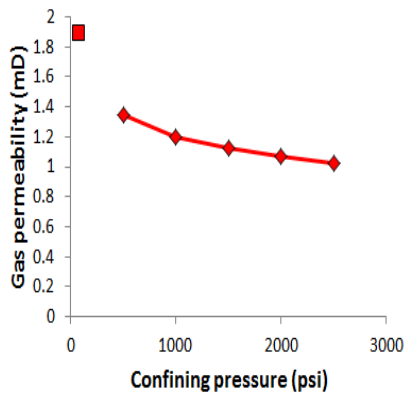
The fault has porosity of <5%, which is <20% that of the host sandstone. This reduction in porosity has occurred as a result of three processes. First, framework grains were fractured allowing enhanced mechanical compaction. Second, clays were mixed with fractured framework grains leading to enhanced mechanical compaction. Third, the fault appears to have undergone enhanced grain contact quartz dissolution.

Faulting occurred after the precipitation of K-feldspar overgrowths and chlorite (or its precursor) but before quartz.

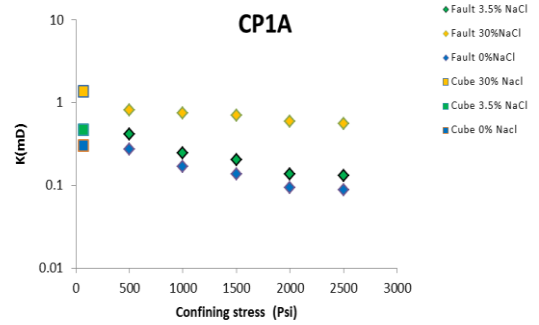
**Hg-injection (unstressed)**



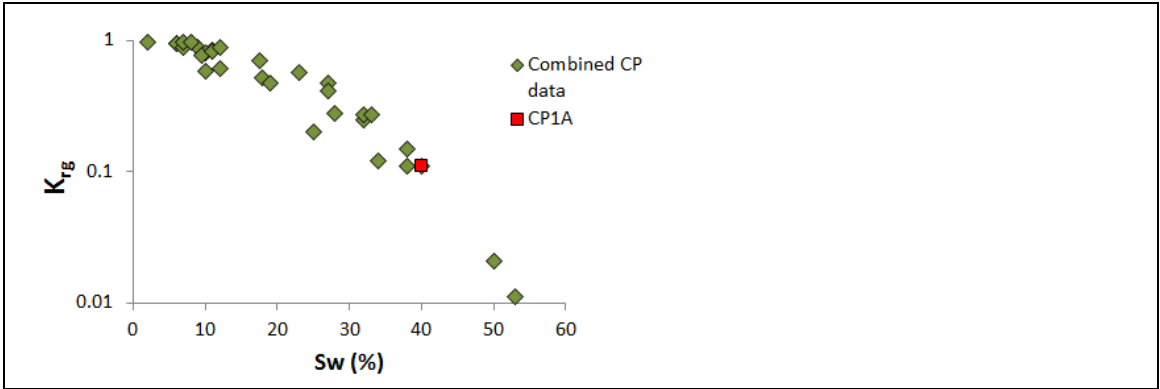
**Gas permeability vs stress: fault**



**Brine permeability**

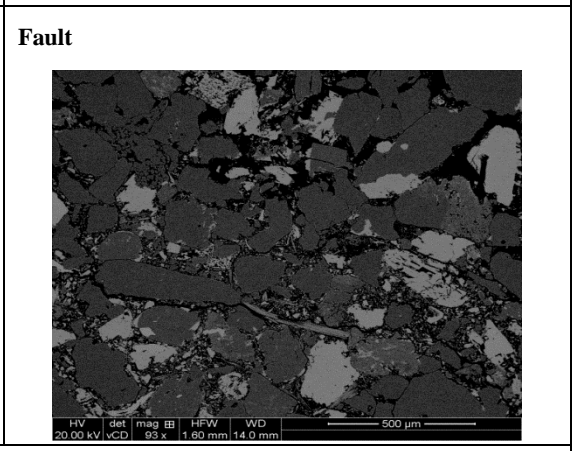
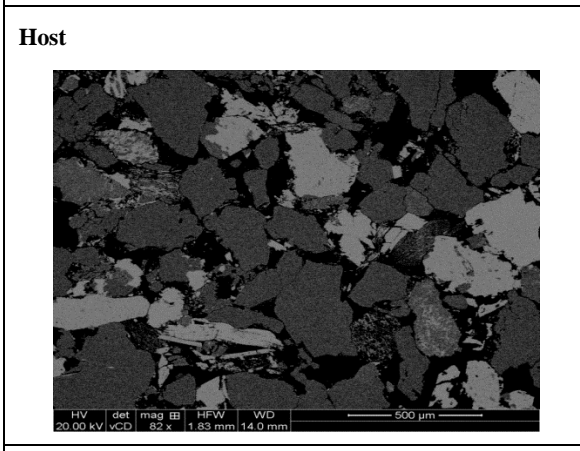
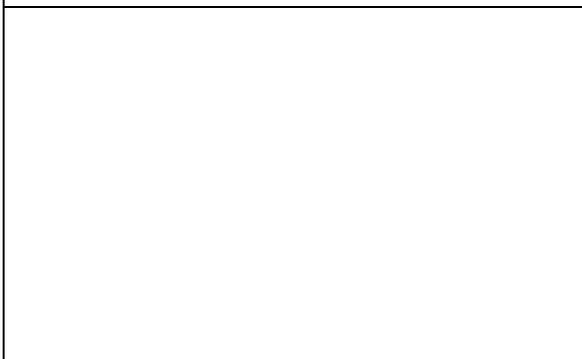
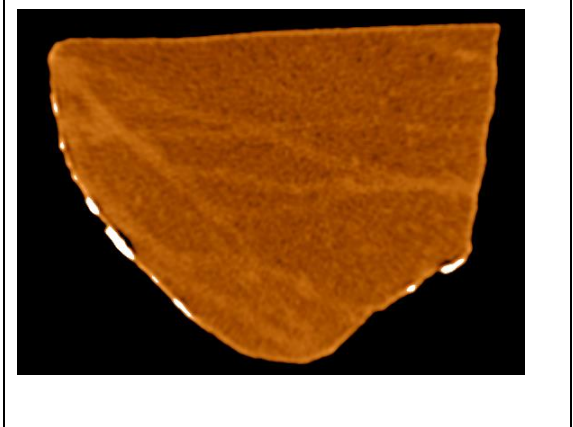


**Gas relative permeability**



<b>Well CP1: Triassic reservoir, central North Sea, UK</b>	<b>Depth: 11928.1-11928.5 mMD</b>
--	-----------------------------------

<b>Sample ID: CP1B</b>	<b>Cataclastic fault</b>
------------------------	--------------------------



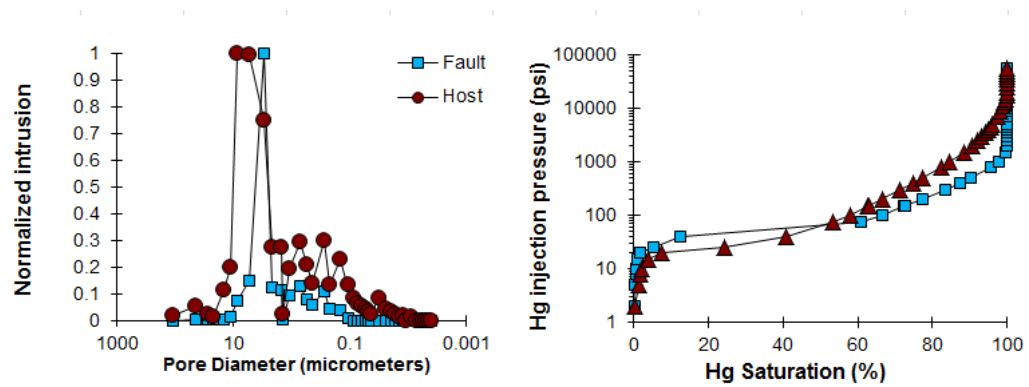
The undeformed sandstone is medium grained and well sorted and is composed 31.2 % quartz, 20.8 % microcline, 11.0 % chlorite, 8.7 % albite, 7.0 % mica, 2.2 % Illite-smectite, and a porosity of 22.9%. The main diagenetic process to affect the sample were the precipitation of K-feldspar, chlorite, and quartz. The K-feldspar occurs as up to

50  $\mu\text{m}$  wide rhombs on detrital K-feldspar. The chlorite occurs as a grain coating clay. It is possible that it formed as a result of the recrystallization of an early smectitic clay. The authigenic quartz is relatively abundant and occurs as both overgrowths and outgrowths.

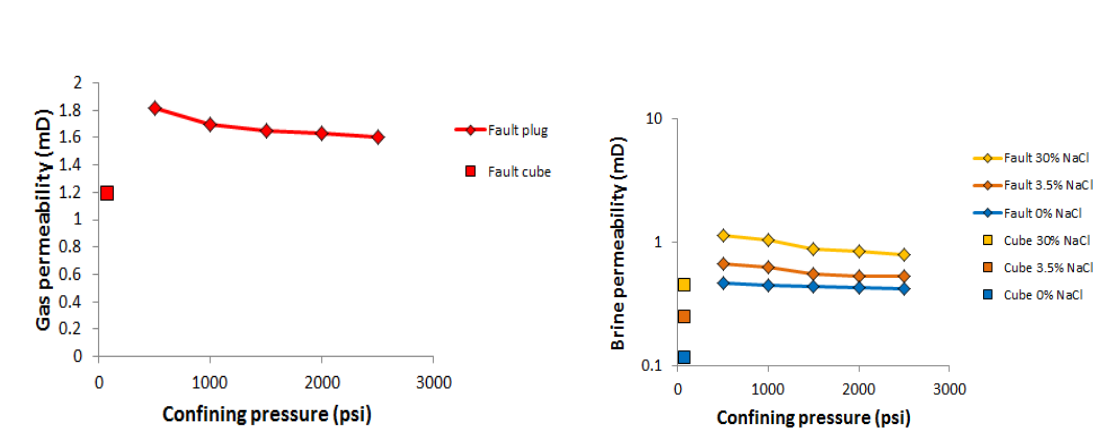
The fault has porosity of 8%, which is <40% that of the host sandstone. This reduction in porosity mainly occurred as a result of cataclastic deformation, which enhanced mechanical compaction.

Faulting occurred after the precipitation of K-feldspar overgrowths and chlorite (or its precursor) but before quartz.

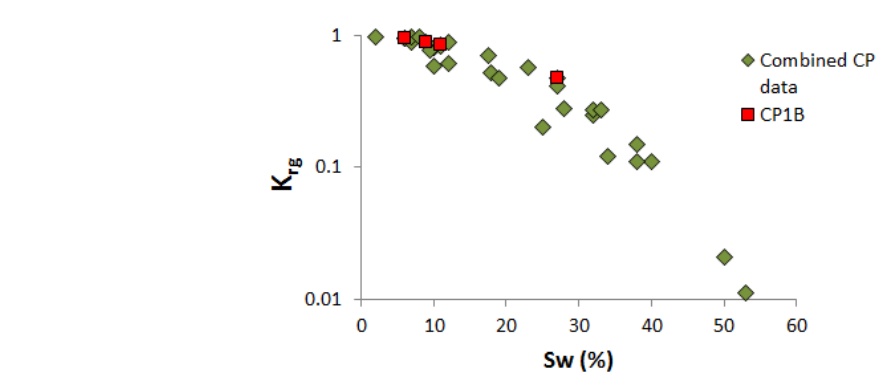
### Hg injection (unstressed)

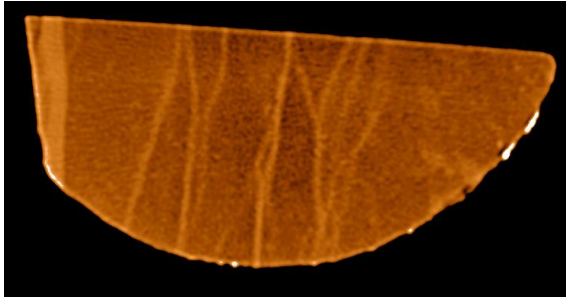
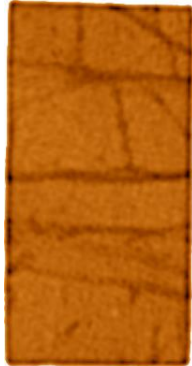
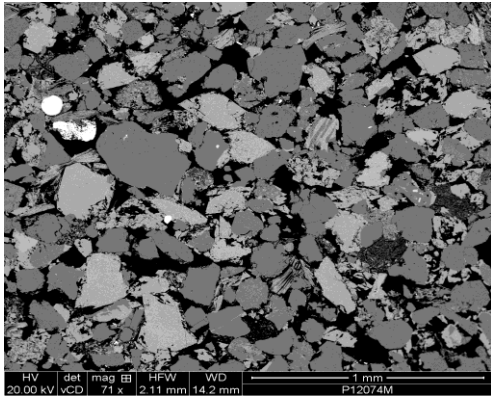
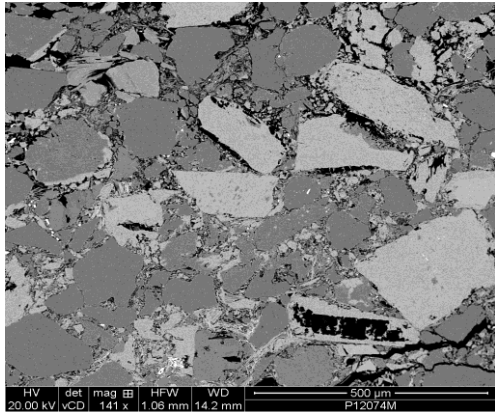


### Gas permeability vs stress Brine permeability: fault



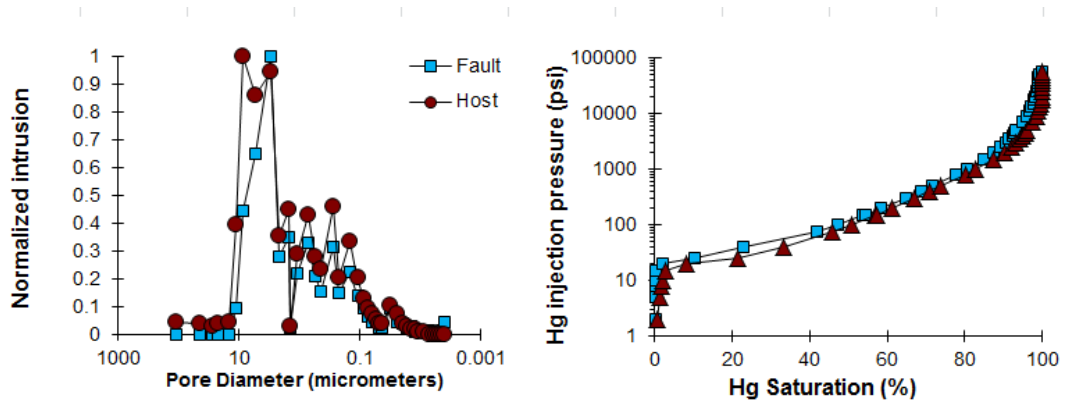
### Gas relative permeability



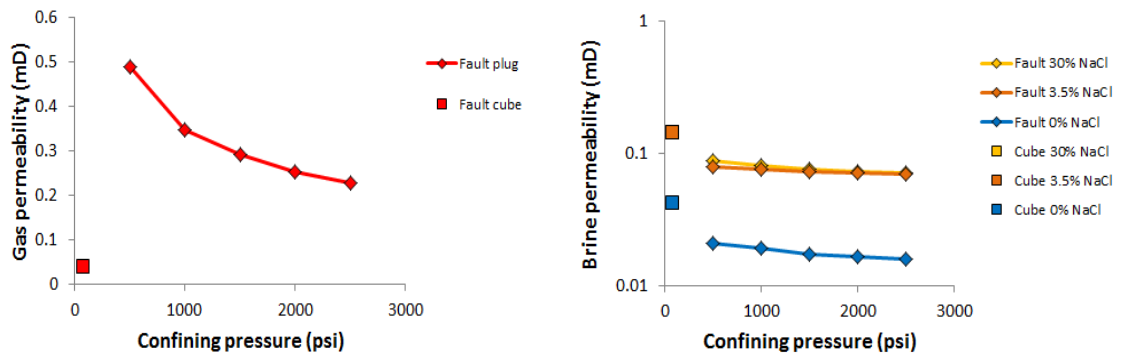
Well CP1: Triassic reservoir, central North Sea, UK	Depth: 11934.3-11934.7 mMD
Sample ID: CP1C	Cataclastic fault
	
	
<p><b>Host</b></p> 	<p><b>Fault</b></p> 
<p>The undeformed sandstone is fine grained (upper), moderately well sorted, composed of 28.9 % quartz, 16.9 % microcline, 15.2 % chlorite, 8.3 % albite, 4.5 % mica, 2.5 % Illite-smectite, 1.2 % kaolin, and a porosity of 23.7%. The main diagenetic process to affect the sample were the precipitation of K-feldspar, chlorite, and quartz as well as the partial dissolution of feldspar The K-feldspar occurs as up to 50 μm wide rhombs on detrital K-feldspar. The chlorite occurs as a grain coating clay. It is possible that it formed as a result of the recrystallization of an early smectitic clay. Secondary pores, surrounded by K-feldspar overgrowths are present. These probably formed as a result of feldspar dissolution. The authigenic occurs as both overgrowths and outgrowths.</p> <p>The fault has porosity of ~5%, which is &lt;25% that of the host sandstone. This reduction in porosity has occurred as a result of three processes. First, framework grains were fractured allowing enhanced mechanical compaction. Second, clays were mixed with fractured framework grains leading to enhanced mechanical compaction. Third, the fault appears to have undergone enhanced grain contact quartz dissolution.</p> <p>Faulting occurred after the precipitation of K-feldspar overgrowths and chlorite (or its precursor) but before quartz and</p>	

secondary porosity formation.

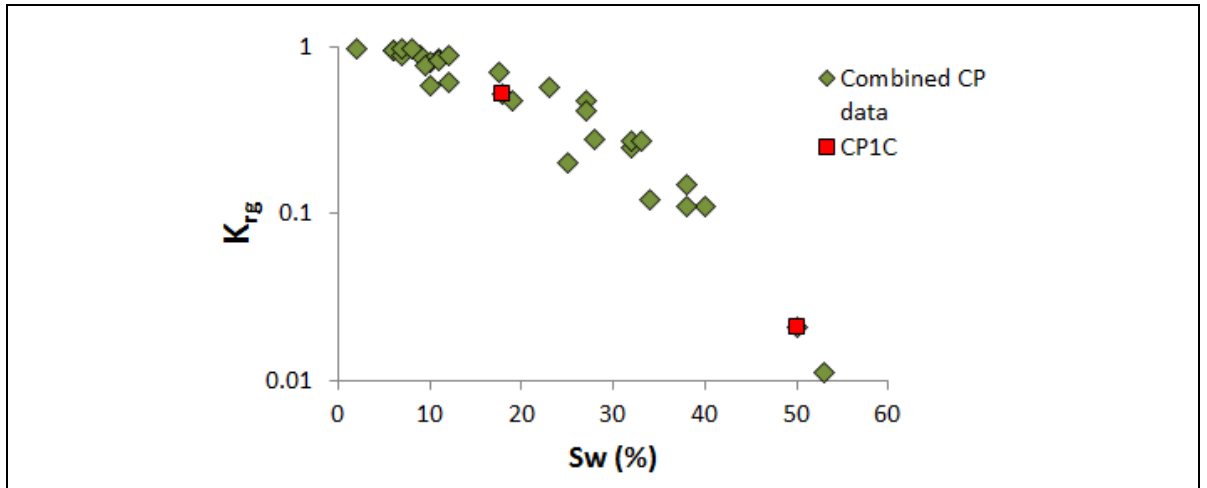
**Hg-injection (unstressed)**

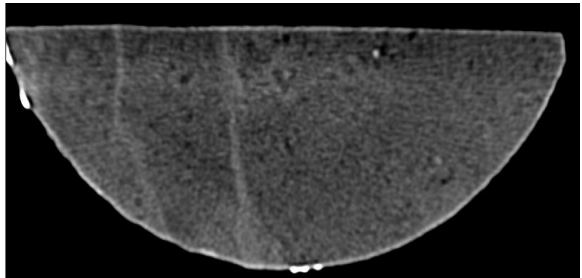


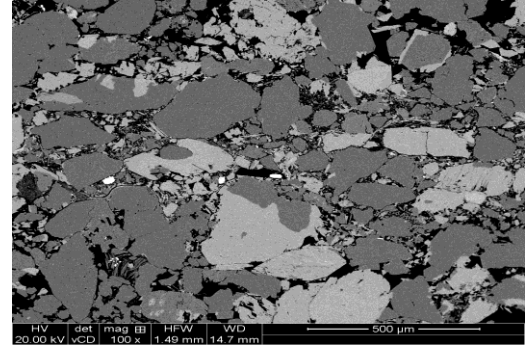
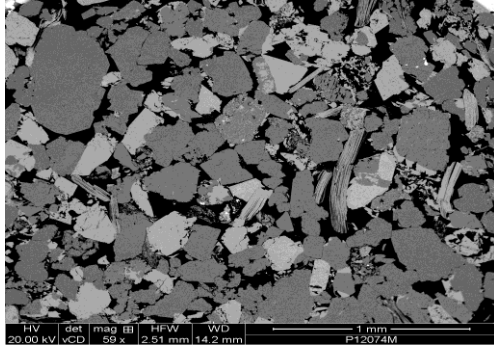
**Gas permeability vs stress: fault      Brine permeability vs stress: fault**



**Gas relative permeability**



Well CP1: Triassic Central North Sea	Depth: 11936.4-11937.0 m MD
Sample ID: CP1D	Cataclastic fault
	
	<p data-bbox="922 1227 981 1254"><b>Fault</b></p> 
<b>Host</b>	<b>Fault</b>

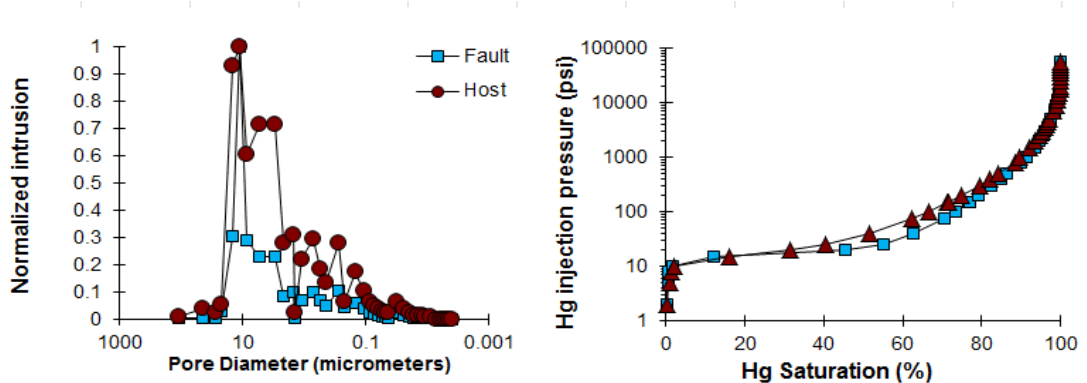


The undeformed sandstone is fine grained (upper), moderately well sorted, and is composed of 28.7 % quartz, 20.0 % microcline, 10.9 % albite, 9.4 % chlorite, 5.3 % Illite-smectite, 4.7 % mica, 5.3 % Illite-smectite, and a porosity of 21.0%. The main diagenetic processes to affect the sample were the precipitation of K-feldspar, chlorite, and quartz. The K-feldspar occurs as up to 50 μm wide rhombs on detrital K-feldspar and albite. The chlorite occurs as a grain coating clay. It is possible that it formed as a result of the recrystallization of early smectitic clay. The authigenic quartz occurs as both overgrowths and outgrowths.

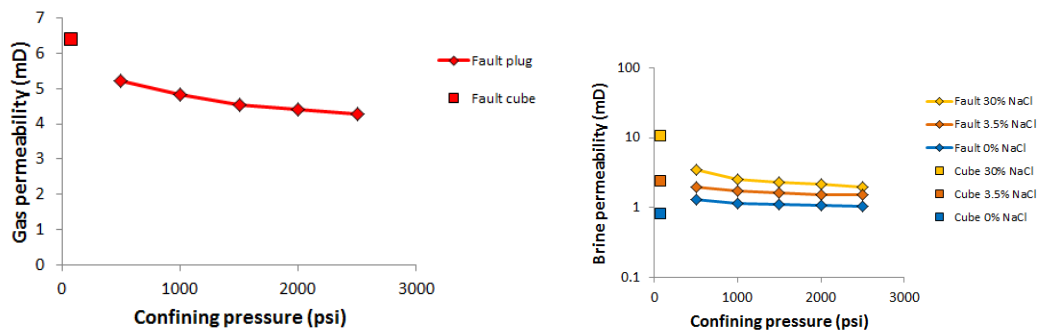
The fault has porosity of 9%, which is <50% that of the host sandstone. This reduction in porosity mainly occurred as a result of cataclastic deformation, which enhanced mechanical compaction.

Faulting occurred after the precipitation of K-feldspar overgrowths and chlorite (or its precursor) but before quartz.

**Hg-injection (unstressed)**

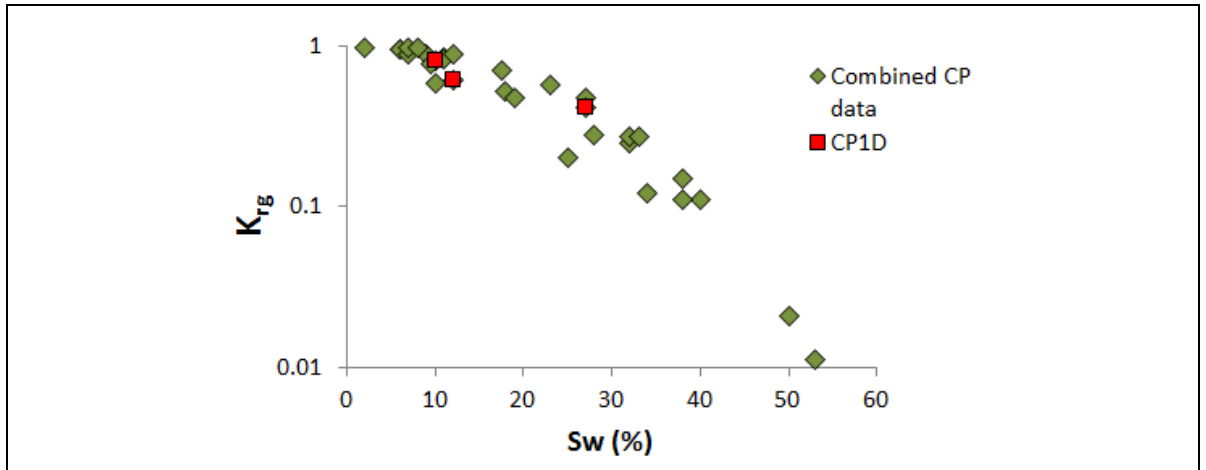


**Gas permeability vs stress: fault**

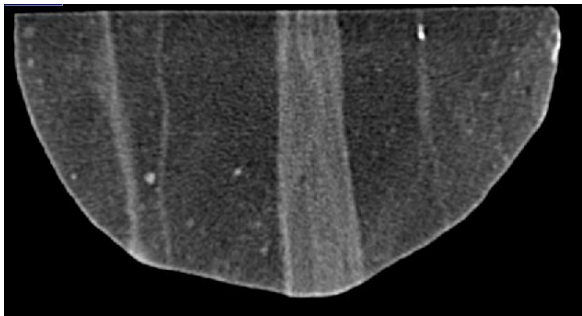
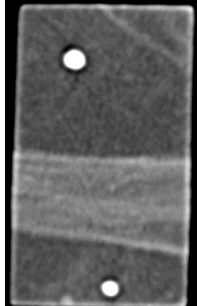


**Brine permeability: fault**

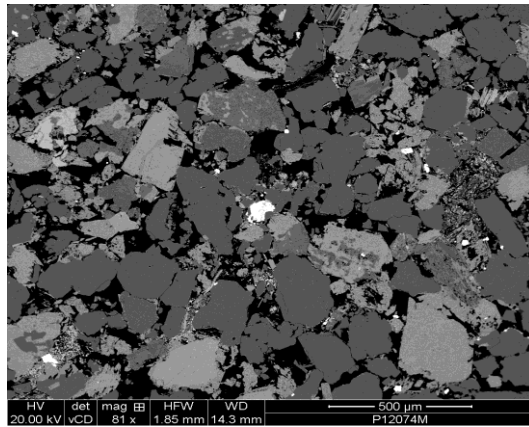
**Gas relative permeability**



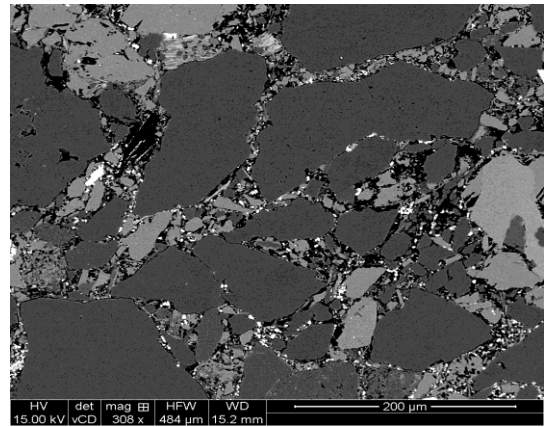
1.1.1.1 Well CP2

Well CP2: Triassic reservoir, central North Sea, UK	Depth 12984.0-12984.3 mMD
Sample ID: CP2A	Cataclastic fault
	
	<p>Faulted core</p> 

**Host**



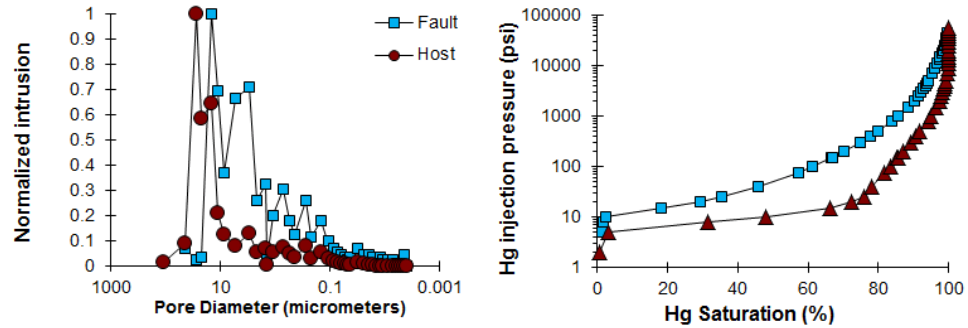
**Fault**



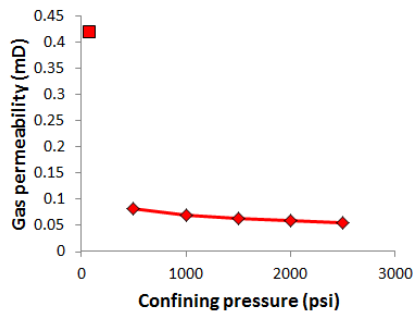
The undeformed sandstone is fine grained, moderately well sorted, and is composed of 25.5 % quartz, 20.4 % microcline, 9.7 % albite, 8.7 % chlorite, 4.4 % mica, 4.3 % Illite-smectite, 1.7 % pyrite and a porosity of 24.4%. The main diagenetic process to affect the sample were the precipitation of K-feldspar, chlorite, and quartz. The K-feldspar occurs as up to 50 μm wide rhombs on detrital K-feldspar and albite. The chlorite occurs as a grain coating clay. It is possible that it formed as a result of the recrystallization of early smectitic clay. The authigenic quartz occurs as both overgrowths and outgrowths.

The fault has porosity of 5%, which is ~25% that of the host sandstone. This reduction in porosity mainly occurred as a result of cataclastic deformation, which enhanced mechanical compaction. Mixing of clays with the grain fragments also added to the reduction in porosity. Faulting occurred after the precipitation of K-feldspar overgrowths and chlorite (or its precursor) but before quartz.

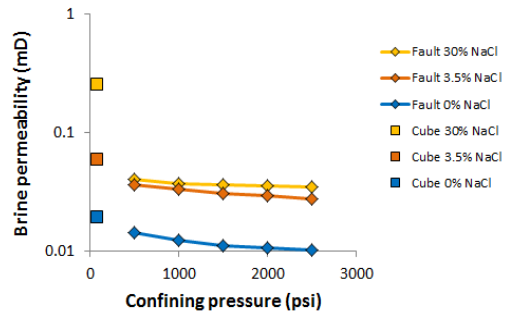
**Hg-injection (unstressed)**

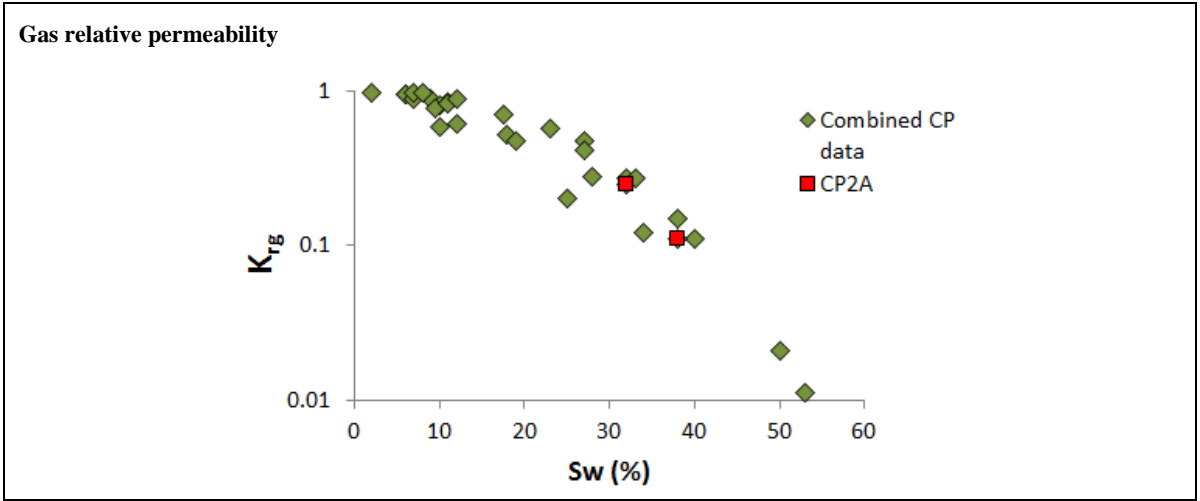


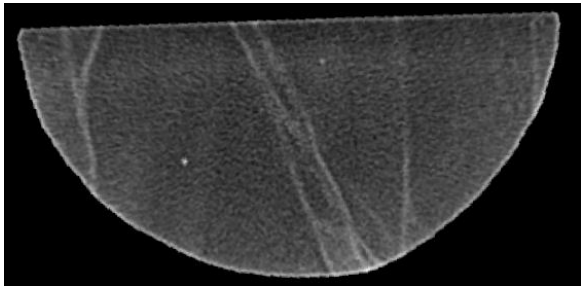
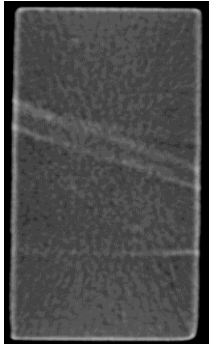
**Gas permeability vs stress: fault**

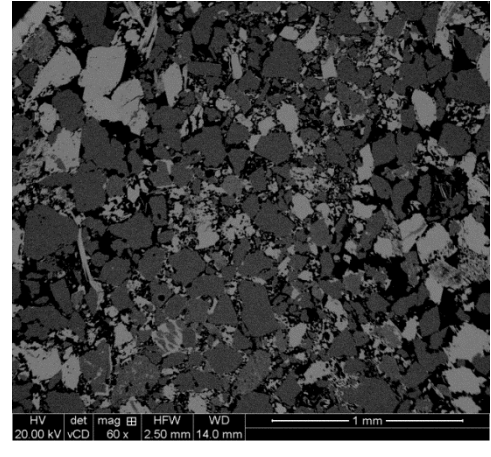
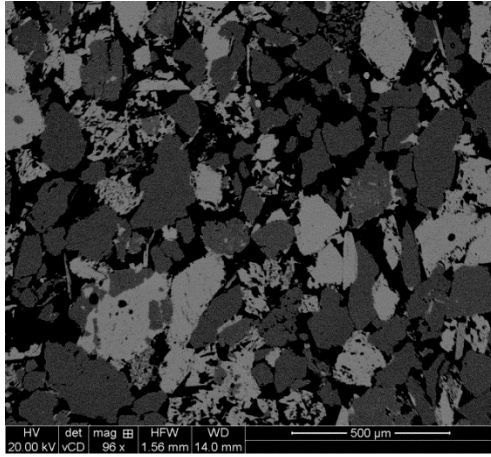


**Brine permeability vs stress: fault**





Well CP2: Triassic reservoir, central North Sea, UK	Depth 12996.6-12996.9 mMD
Sample ID: CP2B	Cataclastic fault
	
	
Host	Fault

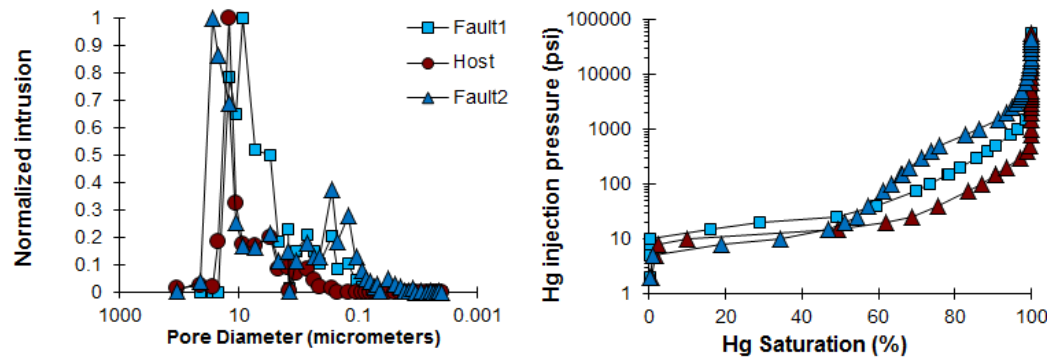


The undeformed sandstone fine grained, well sorted, and is composed of 23.9 % quartz, 8.2 % albite, 21.6 % microcline, 8.5 % chlorite, 6.9 % mica, 2.0 % Illite-smectite and a porosity of 28.4%. The main diagenetic process to affect the sample were the precipitation of K-feldspar, chlorite, and quartz. The K-feldspar occurs as up to 50 μm wide rhombs on detrital K-feldspar and albite. The chlorite occurs as a grain coating clay. It is possible that it formed as a result of the recrystallization of an early smectitic clay. The authigenic quartz occurs as both overgrowths and outgrowths.

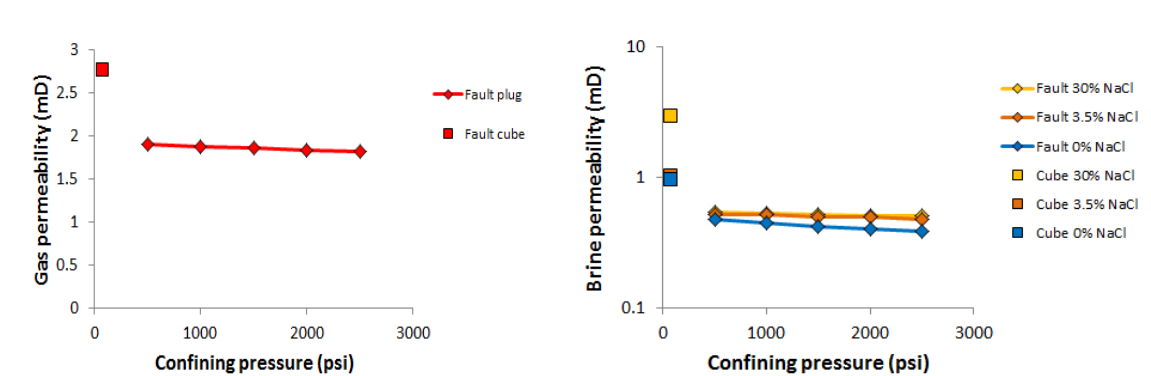
The fault has porosity of 9%, which is ~30% that of the host sandstone. This reduction in porosity mainly occurred as a result of cataclastic deformation, which enhanced mechanical compaction.

Faulting occurred after the precipitation of K-feldspar overgrowths and chlorite (or its precursor) but before quartz.

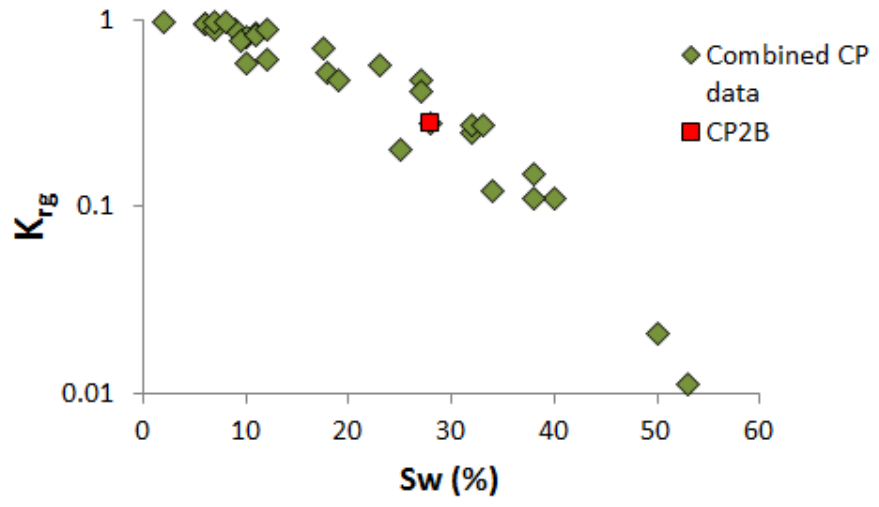
**Hg-injection (unstressed)**

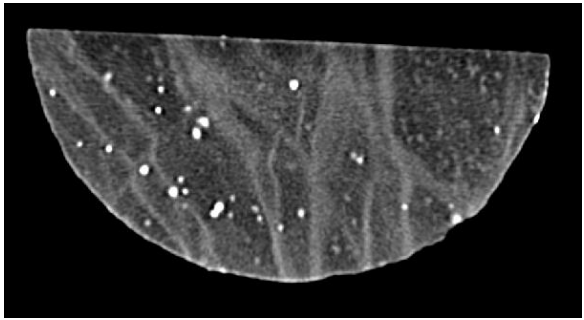
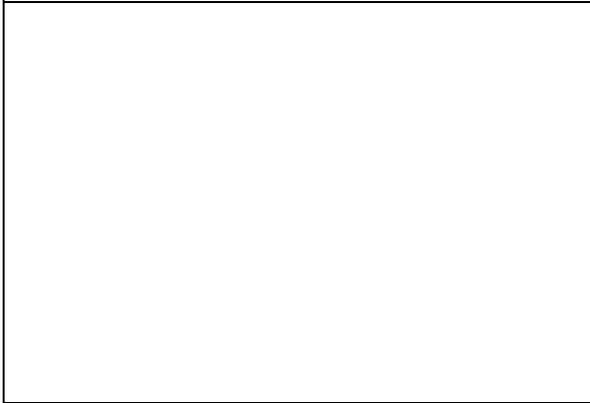
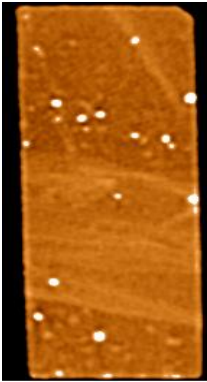
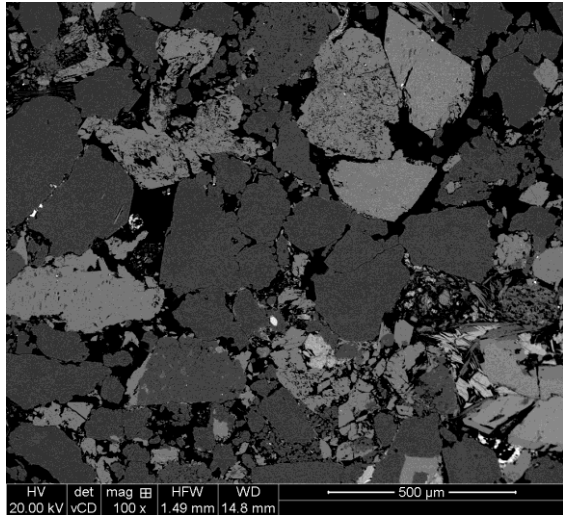
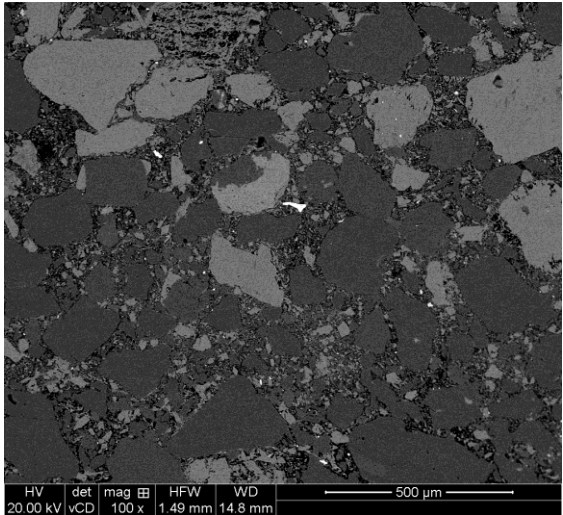


**Gas permeability vs stress: fault    Brine permeability vs stress: fault**



Gas relative permeability



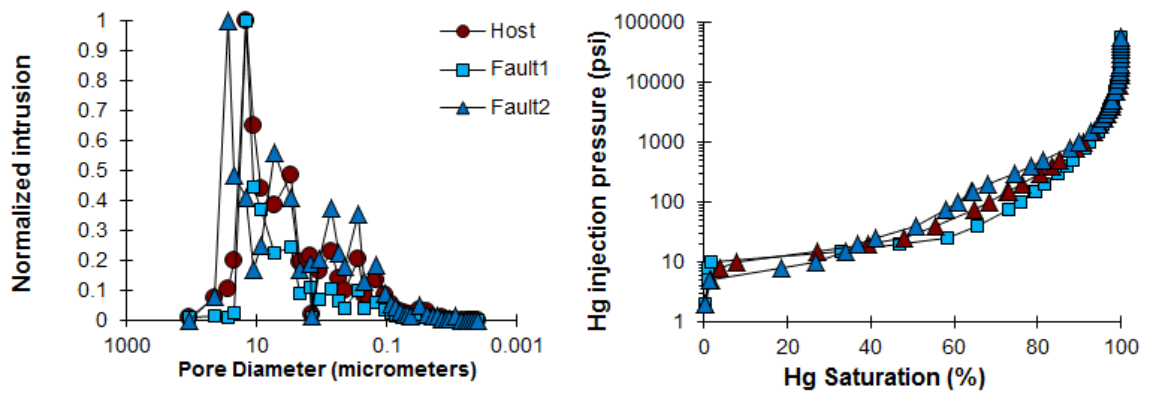
<p><b>Well CP2: Triassic reservoir, central North Sea, UK</b></p>	<p><b>Depth: 13023.3-13023.8 mMD</b></p>
<p><b>Sample ID: CP2C</b></p>	<p><b>Cataclastic fault</b></p>
	
	
<p><b>Host</b></p>	<p><b>Fault</b></p>
	

The undeformed sandstone is medium grained (lower) and moderately well sorted with a porosity of 25.7%. QXRD indicates the sample is composed of 24.2 % quartz, 22.7 % microcline, 8.1 % albite, 8 % chlorite, 2.9 % calcite, 4.8 % mica, and 3.2 % Illite-smectite. However, calcite was not observed in the sample prepared for SEM but poikilitic barite was identified. The main diagenetic processes to affect the sample were the precipitation of K-feldspar, chlorite and quartz, which subordinate quantities of barite. The K-feldspar occurs as up to 50  $\mu\text{m}$  wide rhombs on detrital K-feldspar and albite. The chlorite occurs as a grain coating clay. It is possible that it formed as a result of the recrystallization of an early smectitic clay. The authigenic quartz occurs as both overgrowths and outgrowths. The barite occurs as  $\sim 2$  mm wide poikilitic grains.

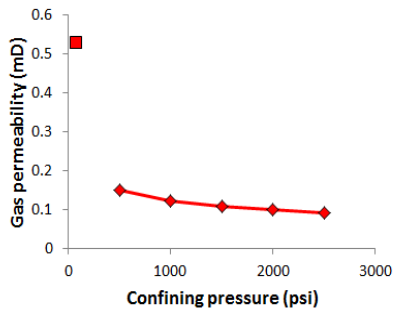
The fault has porosity of <5%, which is <20% that of the host sandstone. This reduction in porosity mainly occurred as a result of cataclastic deformation, which enhanced mechanical compaction.

Faulting occurred after the precipitation of K-feldspar overgrowths and chlorite (or its precursor) but before quartz and barite.

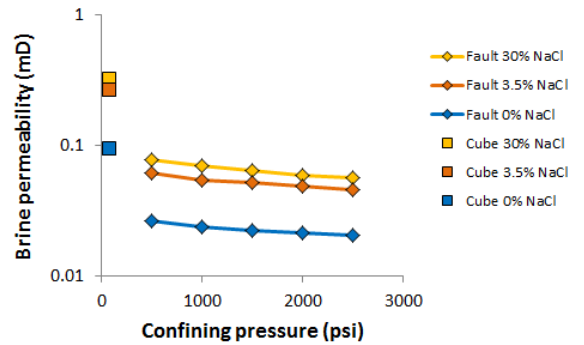
**Hg-injection (stressed)**



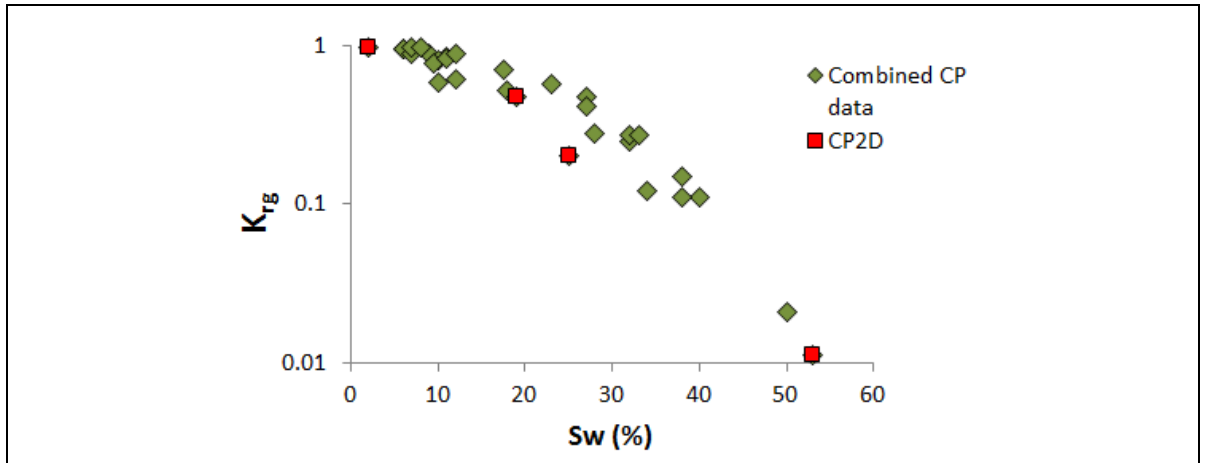
**Gas permeability vs stress: fault**

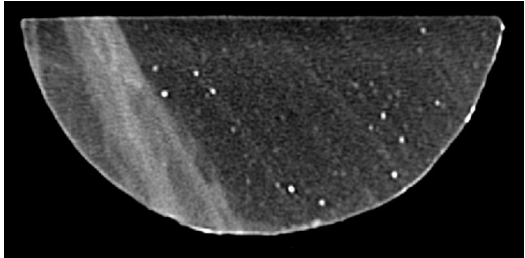
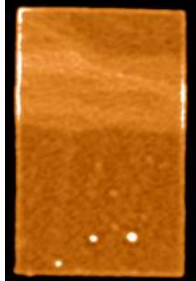
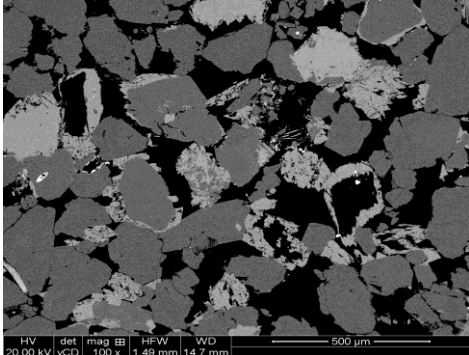
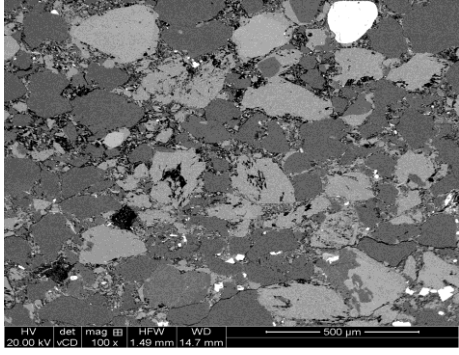


**Brine permeability vs stress: fault**



**Gas relative permeability**



Well CP2: Triassic reservoir, central North Sea, UK	Depth: 13024.3-13025 mMD
Sample ID: CP2D	Cataclastic fault
	
	
<p><b>Host</b></p> 	<p><b>Fault</b></p> 

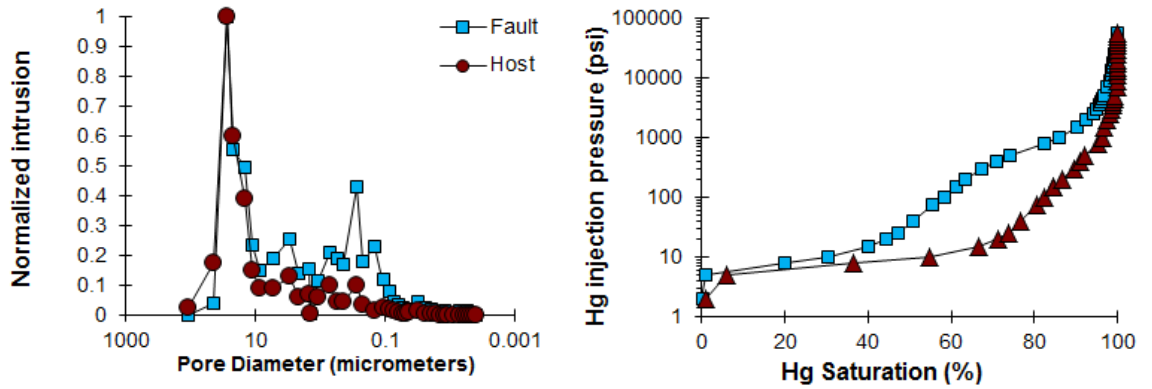
The undeformed sandstone is fine grained (upper), moderately well sorted, composed of 27.2 % quartz, 25.9 % microcline, 8.2 % albite, 7.7 % chlorite, 6.2 % mica, 1 % calcite, and a porosity of 23.4%. The main diagenetic process to affect the sample were the precipitation of K-feldspar, chlorite, and quartz as well as the partial dissolution of feldspar. The K-feldspar occurs as up to 50  $\mu$ m wide rhombs on detrital K-feldspar. The chlorite occurs as a grain coating clay. It is possible that it formed as a result of the recrystallization of an early smectitic clay. Secondary pores,

surrounded by K-feldspar overgrowths, are present, which probably formed as a result of feldspar dissolution. The authigenic quartz occurs as both overgrowths and outgrowths.

The fault has porosity of ~5%, which is <25% that of the host sandstone. This reduction in porosity has occurred mainly as a result of cataclastic deformation, which enhanced mechanical compaction

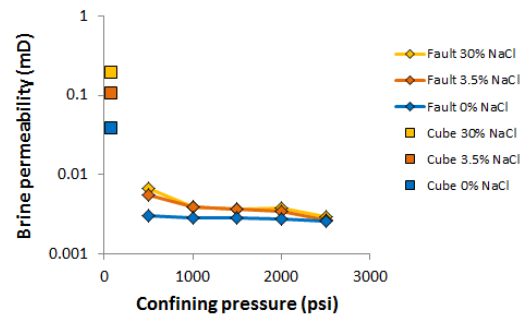
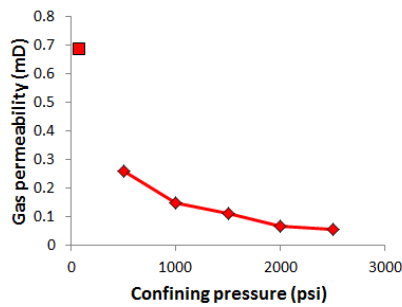
Faulting occurred after the precipitation of K-feldspar overgrowths and chlorite (or its precursor) but before quartz and secondary porosity formation.

**Hg-injection (stressed)**

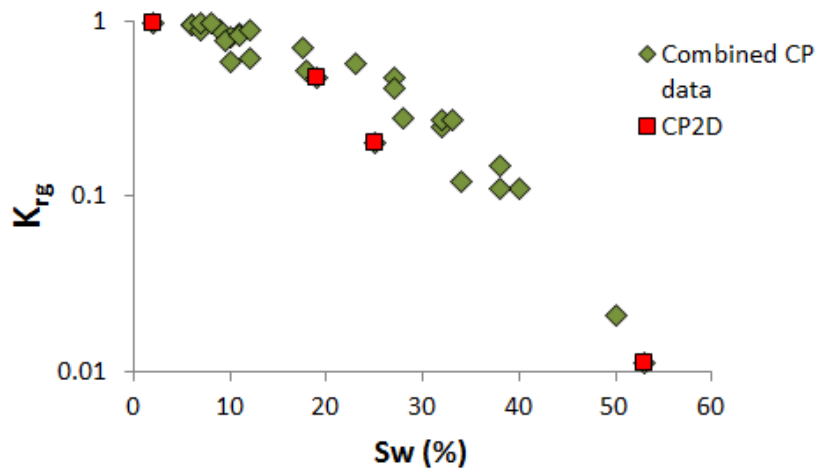


**Gas permeability vs stress: fault**

**Brine permeability: fault**

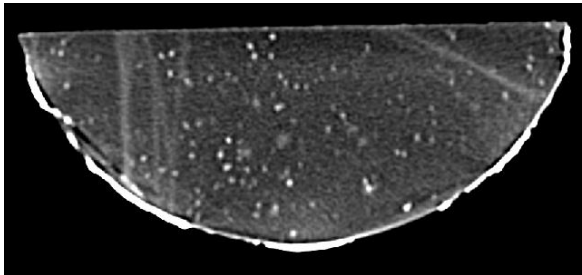
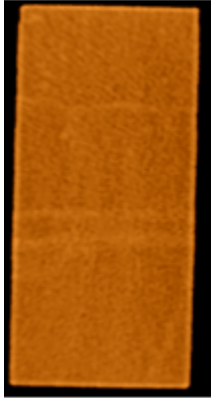
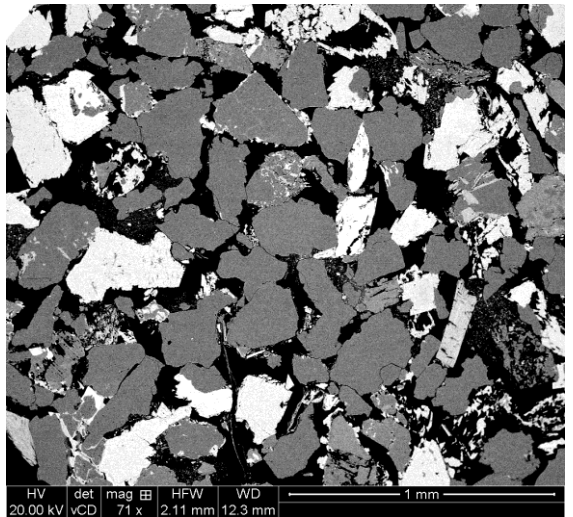
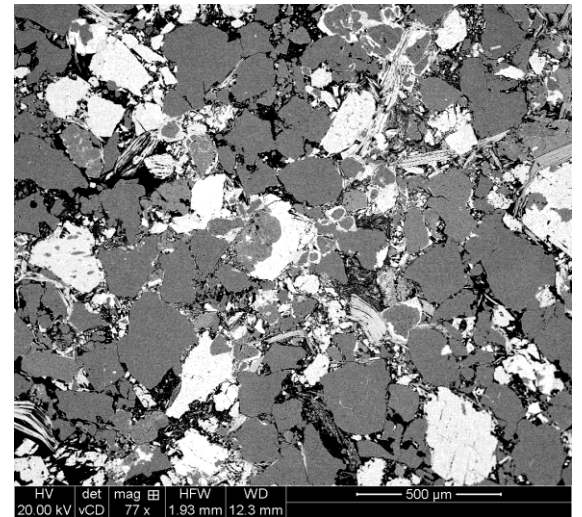


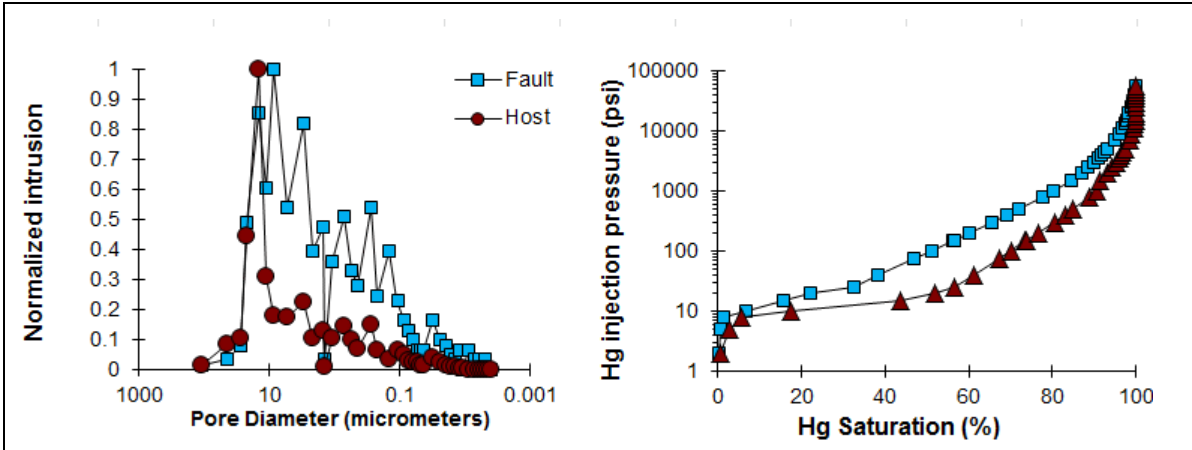
**Gas relative permeability**



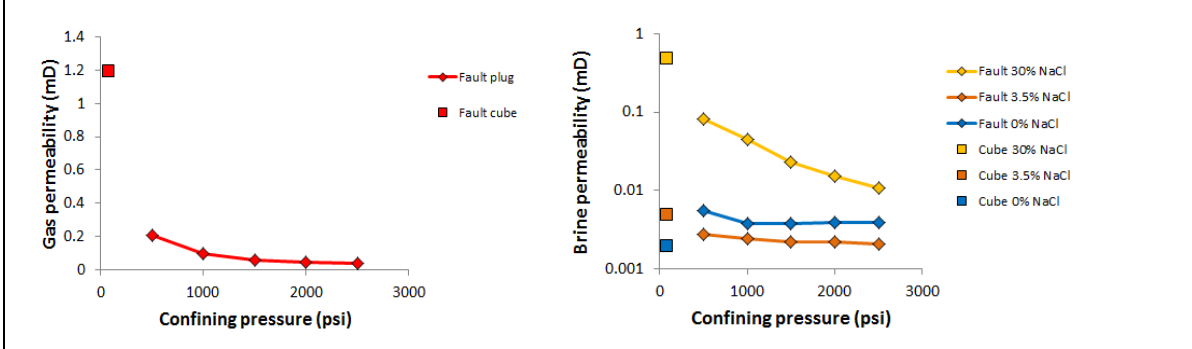
Well CP2: Triassic reservoir, central North Sea, UK

Depth: 13105.7 13106.3 mMD

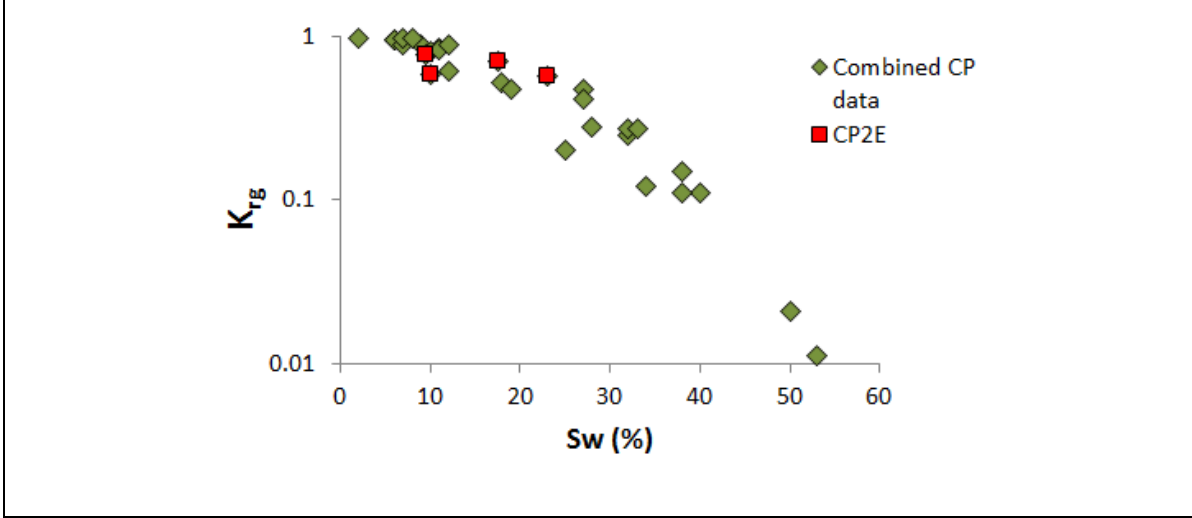
<b>Sample ID: CP2E</b>	
	
	
	
<p>The undeformed sandstone is fine grained (upper), well sorted, composed of 26.4 % quartz, 17.6 % microcline, 12.6 % albite, 8.8 % chlorite, 6.5 % mica, 3.9 % illite-smectite, and a porosity of 24.1%. The main diagenetic process to affect the sample were the precipitation of K-feldspar, chlorite, and quartz as well as the partial dissolution of feldspar. The K-feldspar occurs as up to 50 μm wide rhombs on detrital K-feldspar and albite. The chlorite occurs as a grain coating clay. Secondary pores, surrounded by K-feldspar overgrowths, are present, which probably formed as a result of feldspar dissolution. The authigenic quartz occurs as both overgrowths and outgrowths.</p> <p>The fault has porosity of ~8%, which is ~30% that of the host sandstone. This reduction in porosity has occurred mainly as a result of cataclastic deformation, which enhanced mechanical compaction. Faulting occurred after the precipitation of K-feldspar overgrowths and chlorite (or its precursor) but before quartz and secondary porosity formation.</p>	
<b>Hg-injection (unstressed)</b>	

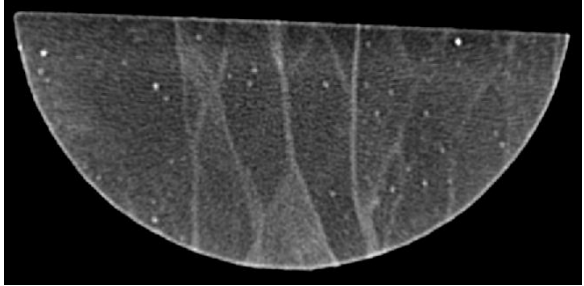
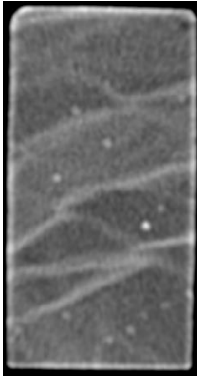
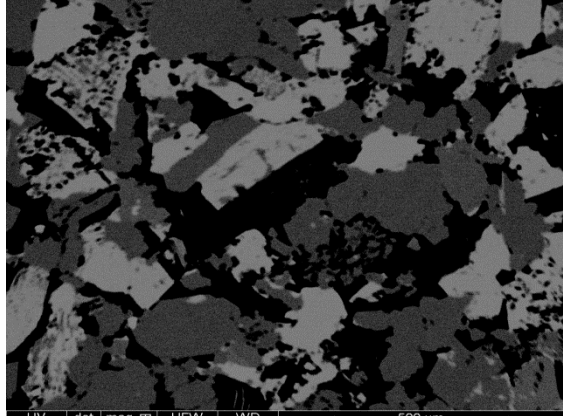
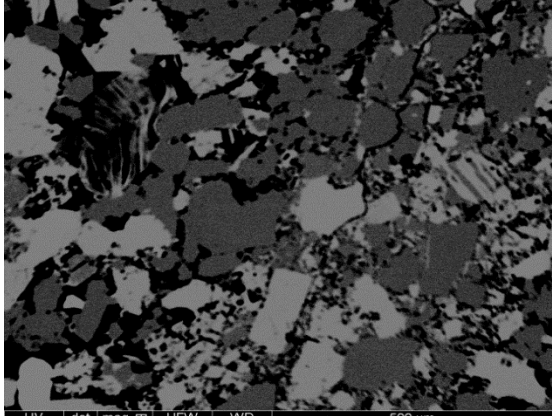


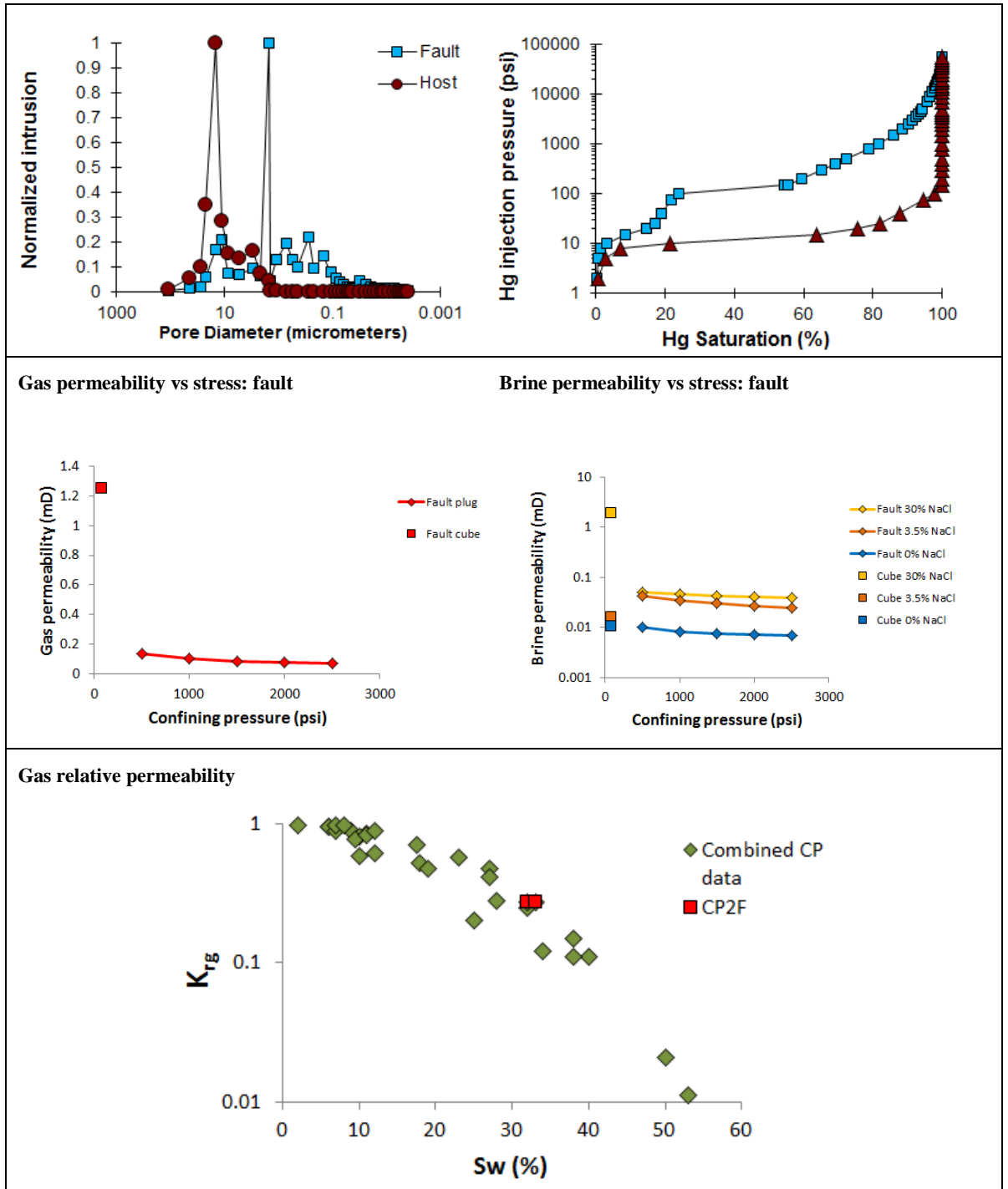
**Gas permeability vs stress: fault**      **Brine permeability: fault**



**Gas relative permeability**



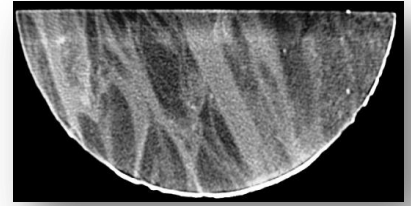
Well CP2: Triassic reservoir, central North Sea, UK	Depth: 13114.8-13115.2 mMD
Sample ID CP2F	
	
	
<b>Host</b>	<b>Fault</b>
 <p>HV 20.00 kV det vCD mag 93 x HFW 1.60 mm WD 14.0 mm 500 μm</p>	 <p>HV 20.00 kV det vCD mag 93 x HFW 1.60 mm WD 14.0 mm 500 μm</p>
<p>The undeformed sandstone is medium grained, well sorted, composed of 24.5 % quartz, 22.4 % microcline, 10.7 % albite, 10.8 % chlorite, 8.8 % mica, 1.7 % Illite-smectite, and a porosity of 21.1%. The main diagenetic process to affect the sample were the precipitation of K-feldspar, chlorite, and quartz as well as the partial dissolution of feldspar The K-feldspar occurs as up to 70 μm wide rhombs on detrital K-feldspar and albite. The chlorite occurs as a grain coating clay. Secondary pores are present, which probably formed as a result of feldspar dissolution. The authigenic quartz occurs as both overgrowths and outgrowths.</p> <p>The fault has porosity of ~9%, which is ~&lt;50% that of the host sandstone. This reduction in porosity has occurred mainly as a result of cataclastic deformation, which enhanced mechanical compaction Faulting occurred after the precipitation of K-feldspar overgrowths and chlorite (or its precursor) but before quartz and secondary porosity formation.</p>	
<b>Hg-injection (unstressed)</b>	



## Central North Sea –Group-B samples

All samples supplied were from a Triassic reservoir in the Central North Sea. Samples from four wells were analysed.

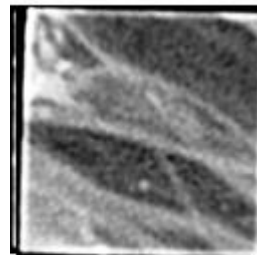
Well Shella: Triassic reservoir Central North Sea, UK	Depth: 14200.1-14200.8 m MD
Sample ID 3A	Cataclastic fault



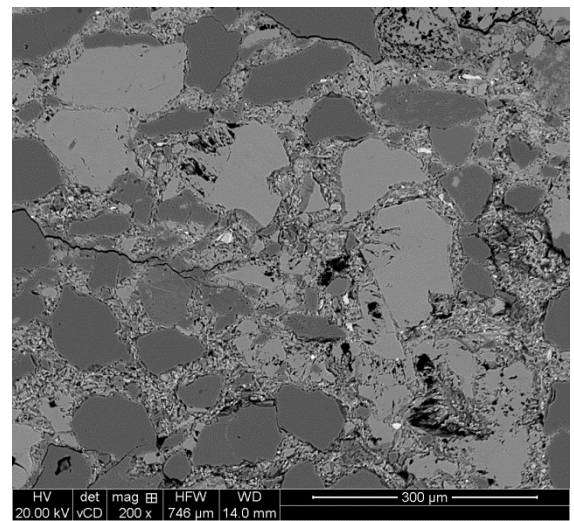
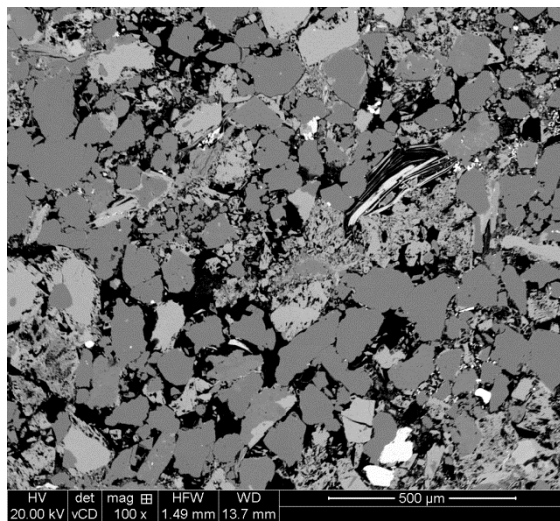
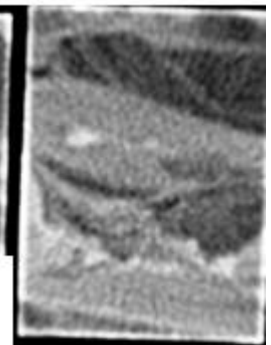
**Host sandstone**



**Fault 1**



**Fault 2**

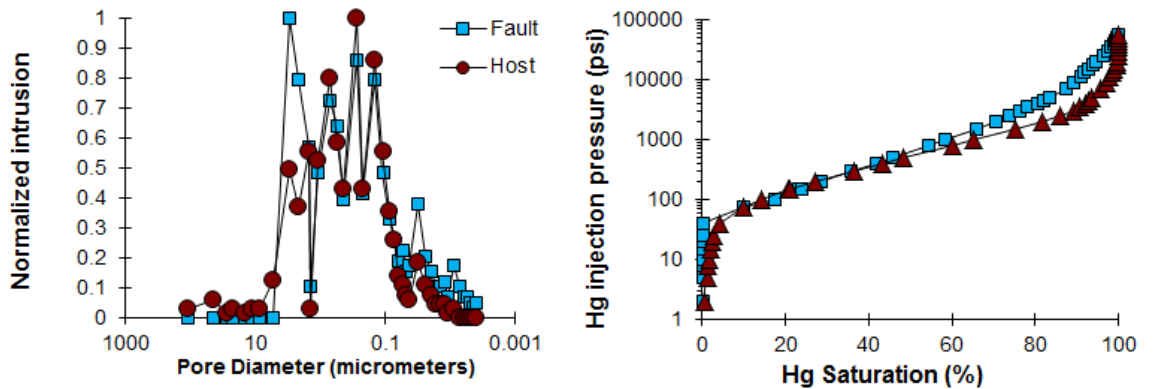


The undeformed sandstone very fine grained, moderately well sorted, composed of 26.4 % quartz, 19.0 % microcline, 12.0 % chlorite, 11.6 % albite, 3.4 % dolomite, 6.9 % mica, 2.9 % Illite-smectite, and has a porosity of 18.0%. The main diagenetic process to affect the sample were the precipitation of K-feldspar, dolomite, chlorite and small amounts of quartz. The K-feldspar occurs as thin (20 μm) wide overgrowths on detrital K-feldspar. The dolomite occurs as 50 μm rhombs that are compositionally zoned with put dolomite cores and ankerite rims. The chlorite occurs as a grain coating clay. It is possible that it formed as a result of the recrystallization of an early smectitic clay. The authigenic quartz occurs as outgrowths on detrital quartz.

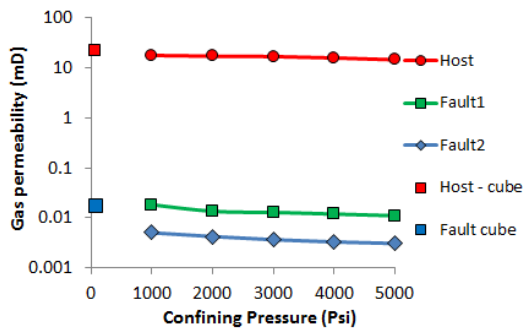
The fault has a porosity of <5%, which is around 25% that of the host sandstone. The reduction in porosity occurred as a result of three process. First, framework grains were fractured during faulting. Secondly, clays were mixed with the products of cataclasis allowing enhanced mechanical compaction. Third, the fault appears to have undergone enhanced

grain contact quartz dissolution. Faulting occurred after the precipitation of dolomite, K-feldspar overgrowths and chlorite (or its precursor) but before authigenic quartz.

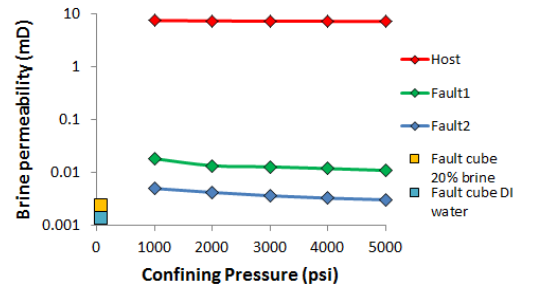
**Hg-injection (unstressed)**



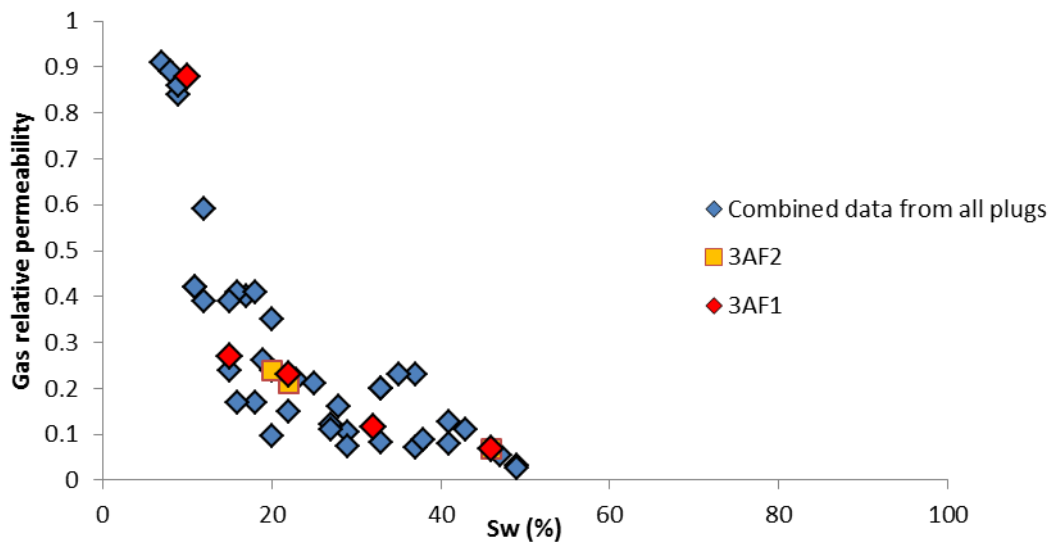
**Gas permeability vs stress:**



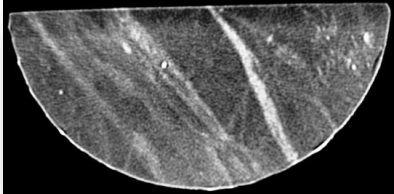
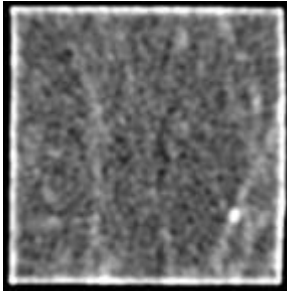
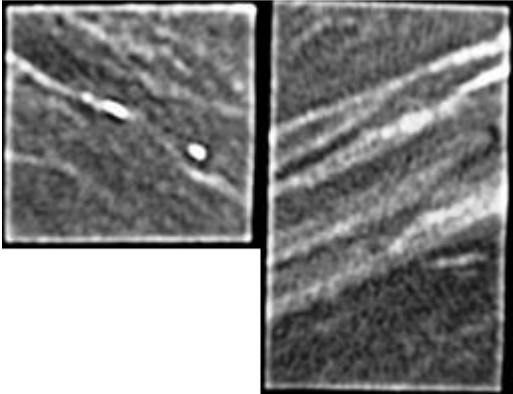
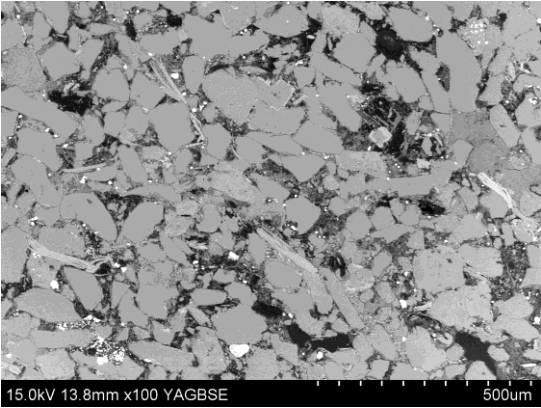
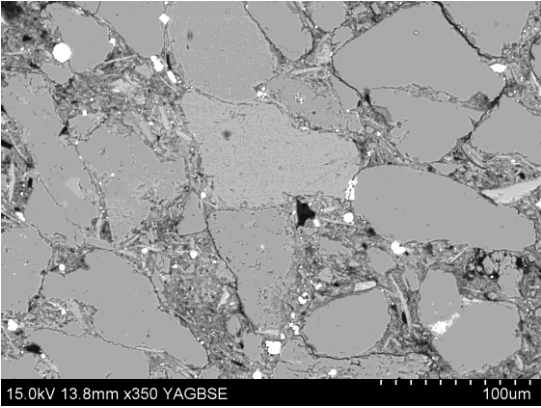
**Brine permeability vs stress (20% brine for stress measurements)**



**Gas relative permeability**

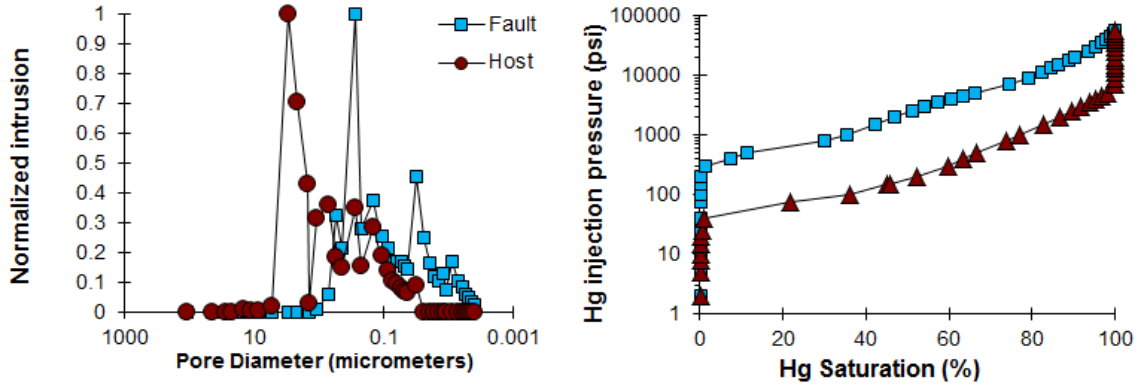


Sample ID: 5A

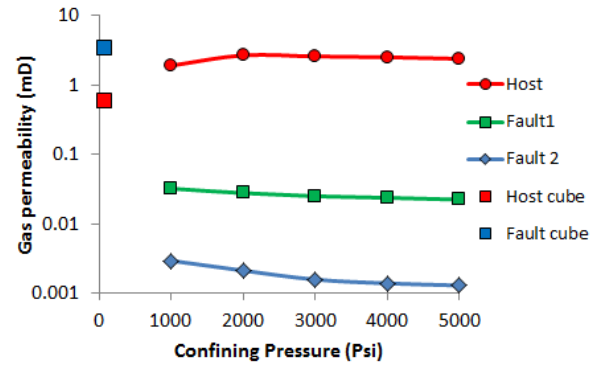
<p>Well ID: Triassic reservoir Central North Sea, UK</p>	<p>Depth 14359-14359.3 mMD</p>
<p>Sample ID: 5A</p>	<p>Phyllosilicate-framework fault rock</p>
	
<p>Host</p> 	<p>Fault 1      Fault 2</p> 
<p>Host</p> 	<p>Fault</p> 
<p>The undeformed sandstone fine grained, well sorted, composed of 41.7 % quartz, 16.8 % albite, 6.4 % mica, 5.4 % Illite-smectite, 4.4 % chlorite, 3.3 % dolomite, 1.1 % pyrite and a porosity of 21%. The main diagenetic process to affect the sample were the precipitation of dolomite, chlorite and small amounts of quartz. The dolomite occurs as 100 µm rhombs that are compositionally zoned with pure dolomite cores and ankerite rims. The chlorite occurs as a grain coating clay. It is possible that it formed as a result of the recrystallization of an early smectitic clay. The authigenic quartz occurs as outgrowths on detrital quartz.</p>	

The fault has a porosity of <5%, which is around 25% that of the host sandstone. The reduction in porosity occurred as a result of three process. First, clays were mixed with the products of cataclasis allowing enhanced mechanical compaction. Second, framework grains were fractured during faulting. Third, the fault appears to have undergone enhanced grain contact quartz dissolution. Faulting occurred after the precipitation of dolomite and chlorite (or its precursor) but before authigenic quartz.

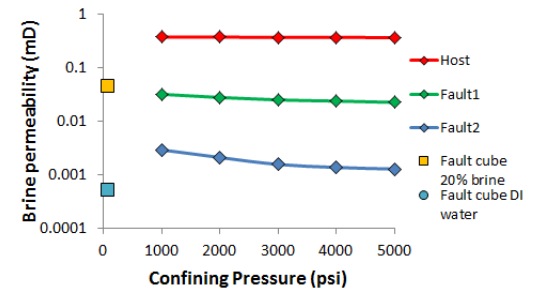
**Hg injection (unstressed)**

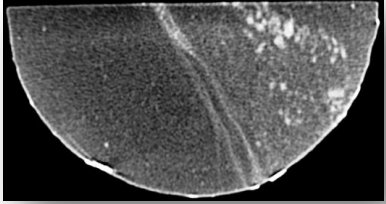


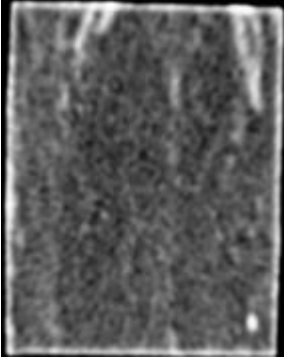
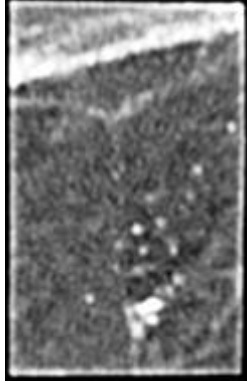
**Gas permeability vs stress:**

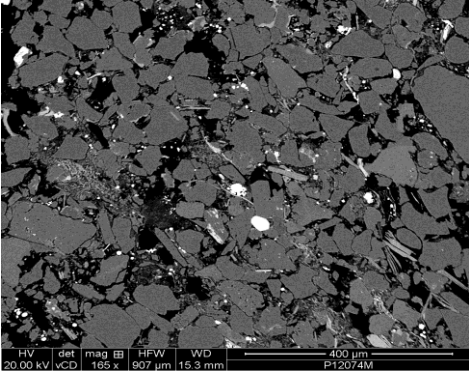
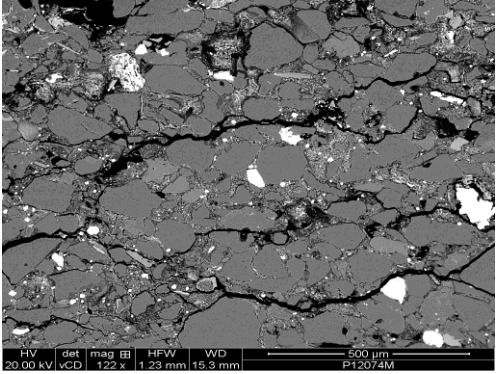


**Brine permeability vs stress (20% NaCl brine for the stressed measurements)**



<b>Well ID: Triassic reservoir Central North Sea, UK</b>	<b>Depth: 14359.3-14359.6 mMD</b>
<b>Sample ID 5B</b>	<b>Phyllosilicate-framework fault rock</b>
	

<b>Host sandstone</b>	<b>Faulted core</b>
	

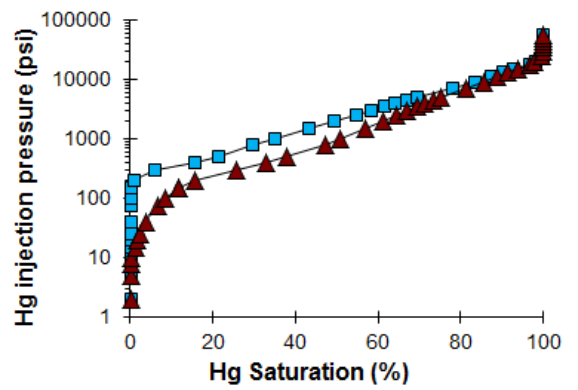
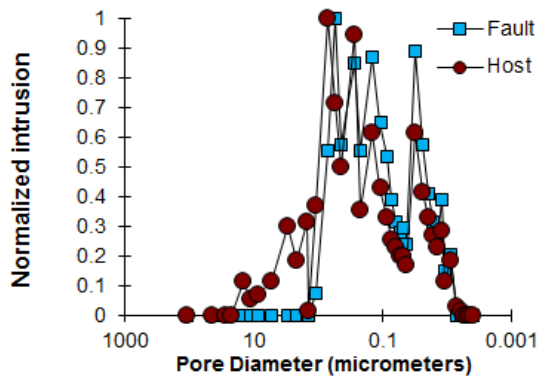
<b>Host</b>	<b>Fault</b>
	

The undeformed sandstone is very fine grained, well sorted, composed of 40.5 % quartz, 17.0 % albite, 8.4 % mica, 7.5 % Illite-smectite, 4.7 % chlorite, 4.1 % dolomite, 1.8 % pyrite and a porosity of 16.0%. The main diagenetic processes to affect the sample were mechanical compaction, the precipitation of dolomite, chlorite and small amounts of quartz and albite. Mechanical compaction is manifest by the presence of deformed mica through the sample. The dolomite occurs as 100 µm rhombs that are compositionally zoned with dolomite cores and thin ankerite rims. The chlorite occurs as a grain coating clay. It is possible that it formed as a result of the recrystallization of early smectitic clay. The authigenic quartz and albite occurs as thin outgrowths on detrital quartz.

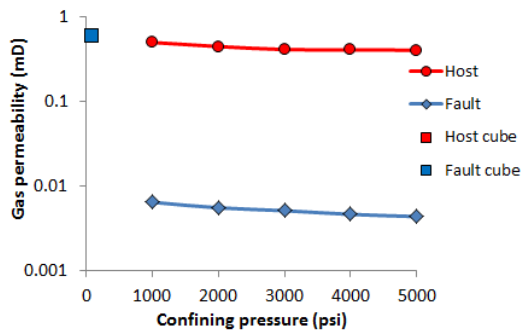
The fault has a porosity of <5%, which is around 25% that of the host sandstone. The reduction in porosity occurred as a result of two process. First, clays were mixed with the products of cataclasis allowing enhanced mechanical compaction. Second, the fault appears to have undergone enhanced grain contact quartz dissolution. Faulting occurred after the

precipitation of dolomite and chlorite (or its precursor) but before authigenic quartz and albite. There is no evidence of grain fracturing suggesting faulting occurred under low effective stress conditions.

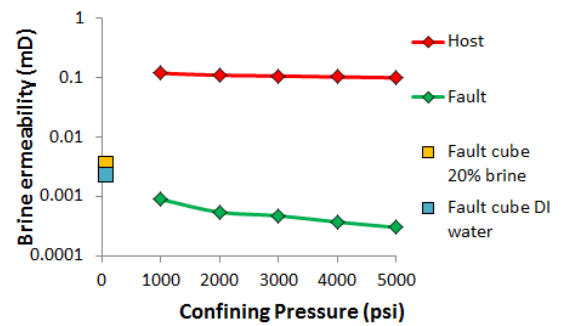
**Hg-injection (unstressed)**

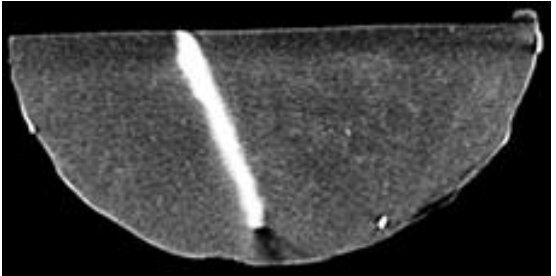
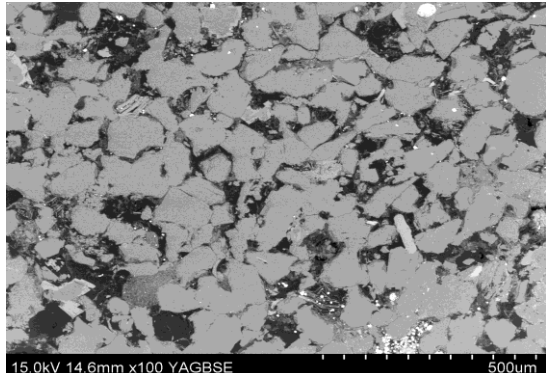
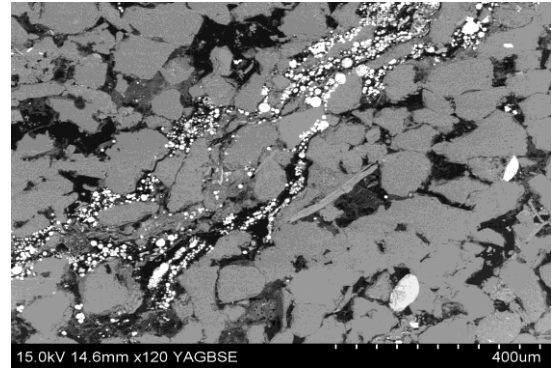


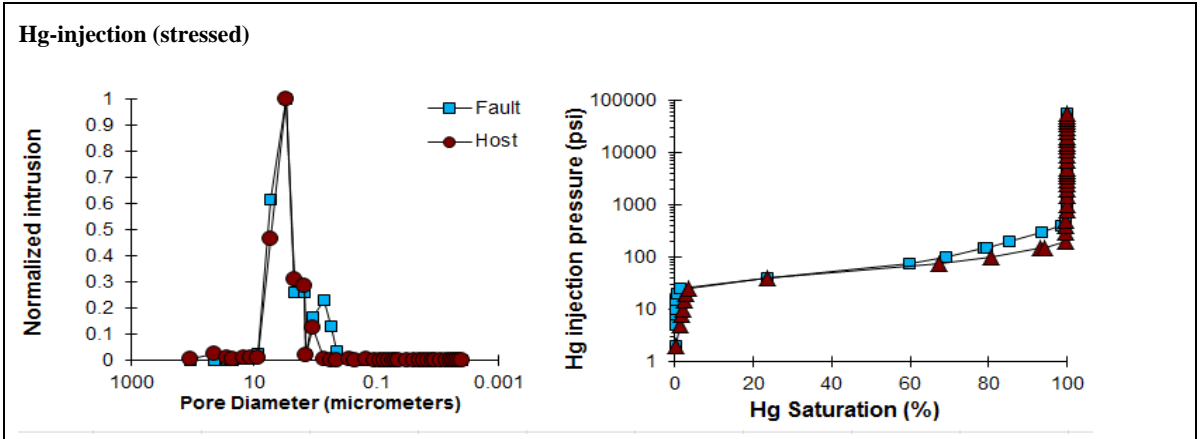
**Gas permeability vs stress**



**Brine permeability vs stress**



Well IB: Triassic reservoir Central North Sea, UK	Depth: 14360-14360.2 mMD
Sample ID 5C	Phyllosilicate-framework fault rock
	
	
<p>The undeformed sandstone is very fine grained, moderately well sorted, composed of 39.5 % quartz, 19.1 % albite, 3.7 % dolomite, 6.4 % mica, 5.3 % Illite-smectite, 4.1 % chlorite, 1.1 % pyrite and a porosity of 21.0%. The main diagenetic process to affect the sample were mechanical compaction, the precipitation of pyrite, dolomite, chlorite and small amounts of quartz and albite. The pyrite occurs as framboids in organic-rich layers and probably precipitated directly beneath the sediment-water interface soon after sediment deposition. The dolomite occurs as 70 <math>\mu\text{m}</math> rhombs that are compositionally zoned with dolomite cores and thin ankerite rims. The chlorite occurs as a grain coating clay. It is possible that it formed as a result of the recrystallization of an early smectitic clay. The authigenic quartz and albite occurs as thin outgrowths on detrital quartz.</p> <p>The fault has a porosity of &lt;5%, which is &lt;25% that of the host sandstone. The reduction in porosity occurred as a result of two process. First, clays were mixed with framework greains leading to enhanced mechanical compaction. Second, the fault appears to have undergone enhanced grain contact quartz dissolution. Faulting occurred after the precipitation of dolomite and chlorite (or its precursor) but before authigenic quartz and albite. There is no evidence of grain fracturing suggesting faulting occurred under low effective stress conditions.</p>	

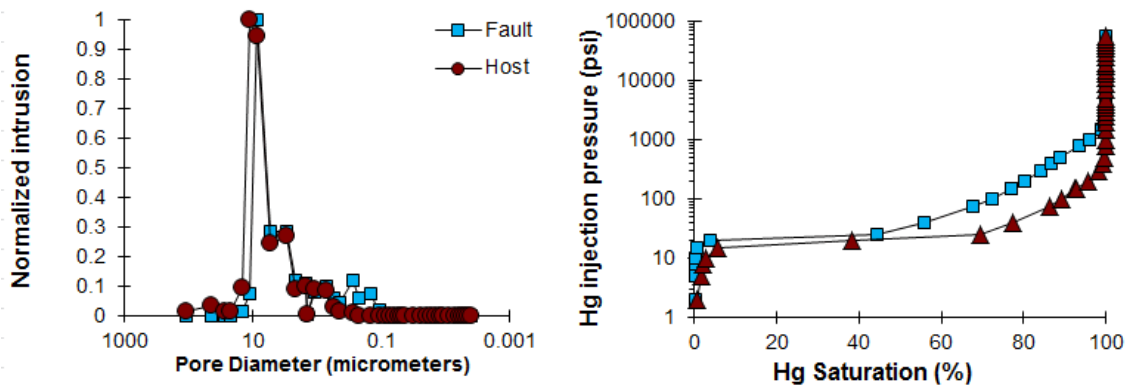


Well ID: Triassic reservoir Central North Sea, UK	Depth: 14363.1-14363.6 m MD
Sample ID 5D	Proto-cataclastic fault
<p><b>Host</b></p> <p>15.0kV 14.0mm x100 YAGBSE 500um</p>	<p><b>Fault</b></p> <p>15.0kV 14.0mm x150 YAGBSE 300um</p>

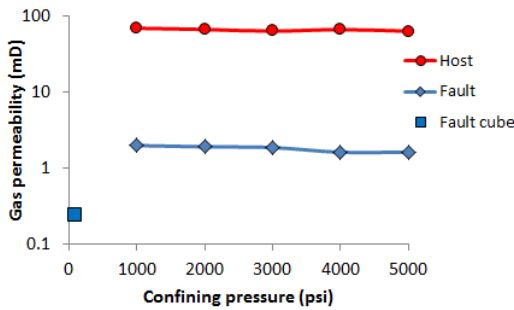
The undeformed sandstone is fine grained, well sorted, composed of 42.1 % quartz, 17.5 % albite, 5.8 % mica, 4.9 % pyrite, 2.7 % Illite-smectite, 2.4 % dolomite, 2.5 % chlorite, and a porosity of 22.0%. The main diagenetic process to affect the sample were mechanical compaction, the precipitation of pyrite, dolomite, chlorite and small amounts of quartz and albite. The pyrite occurs as framboids in organic-rich layers and probably precipitated directly beneath the sediment-water interface soon after sediment deposition. The dolomite occurs as 70  $\mu\text{m}$  rhombs that are compositionally zoned with dolomite cores and thin ankerite rims. The chlorite occurs as a grain coating clay. It is possible that it formed as a result of the recrystallization of an early smectitic clay. The authigenic quartz and albite occurs as thin outgrowths on detrital quartz.

The fault has a porosity of 8%, which is <40% that of the host sandstone. The reduction in porosity occurred as a result of cataclastic deformation which allowed enhanced mechanical compaction. Faulting occurred after the precipitation of dolomite and chlorite (or its precursor) but before authigenic quartz and albite.

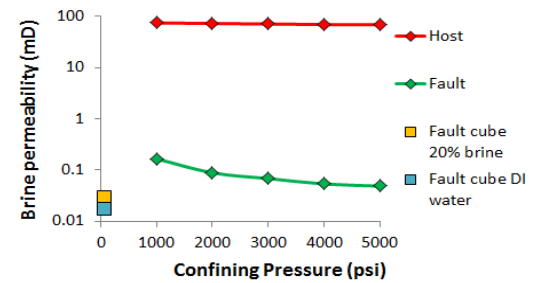
**Hg-injection (unstressed)**



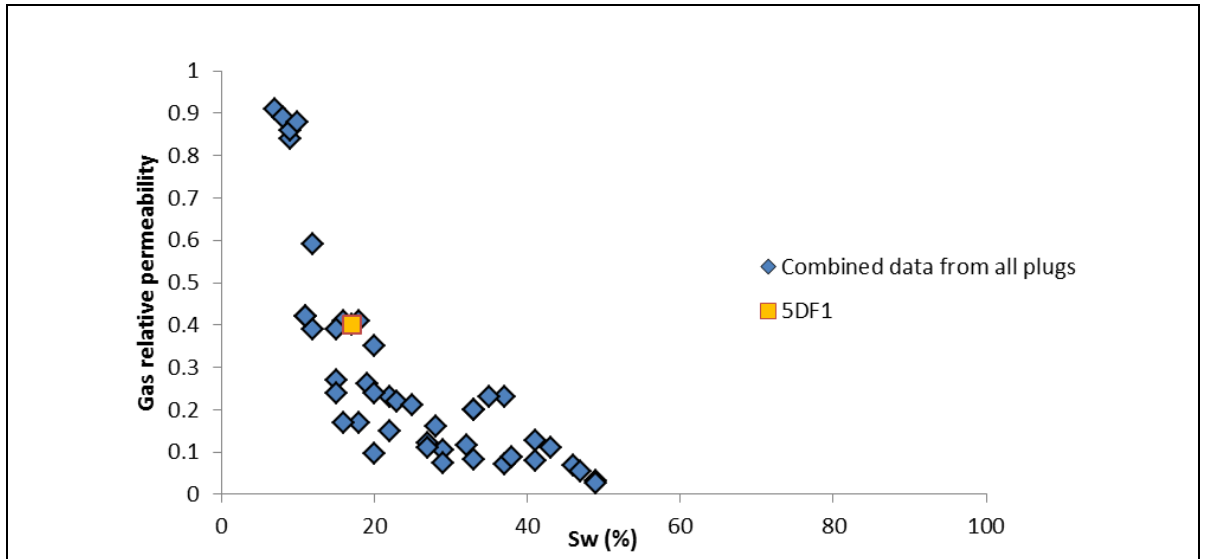
**Gas permeability vs stress**

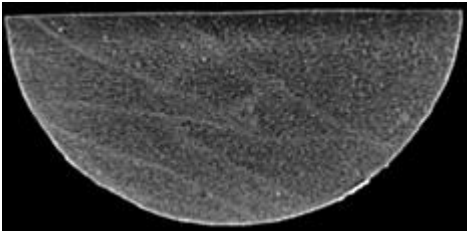
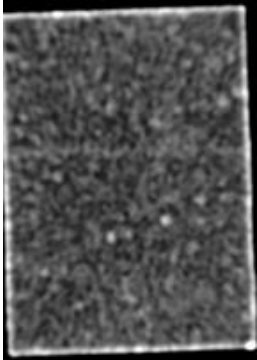
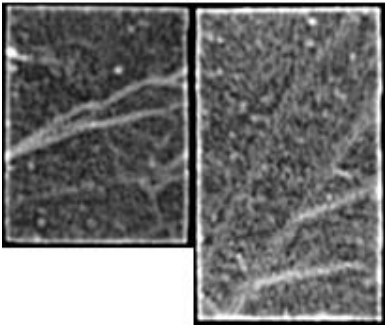


**Brine permeability vs stress (20% NaCl brine for stressed measurements)**

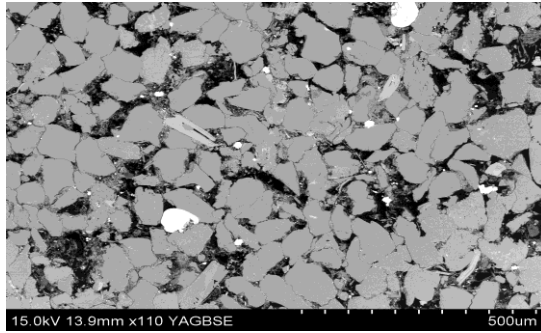


**Gas relative permeability**

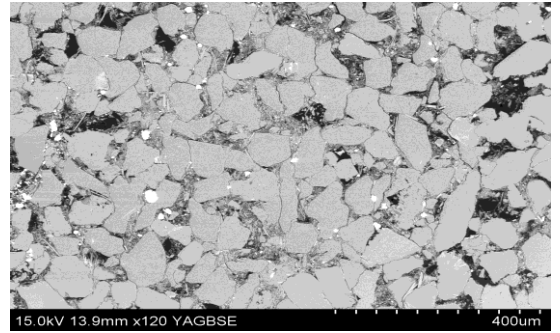


Well IB: Triassic reservoir Central North Sea, UK	Depth: 14367.9-14368.3 mMD
Sample ID 5E	Disaggregation zone/Phyllosilicate-framework fault rock
	
<p>Host sandstone</p> 	<p>Fault 1      Fault 2</p> 

**Host**



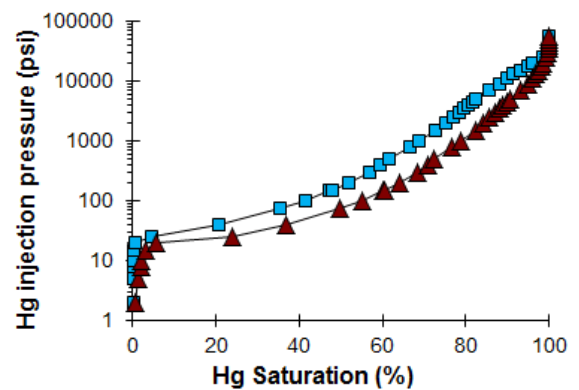
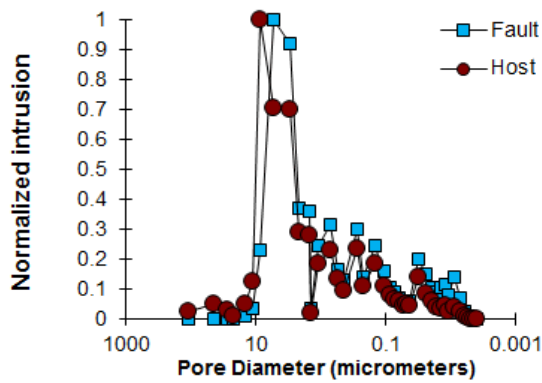
**Fault**



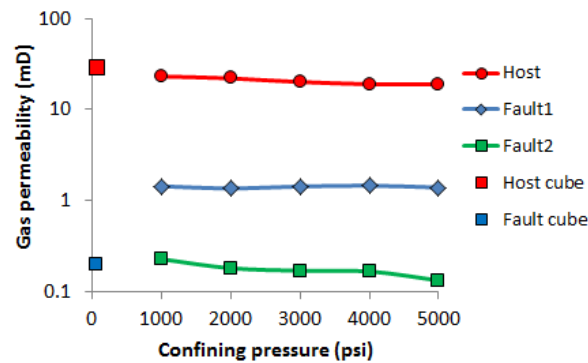
The undeformed sandstone is fine grained, well sorted, composed of 42.2 % quartz, 19.1 % albite, 6.0 % Illite-smectite, 3.5 % dolomite, 3.9 % mica, 3.1 % chlorite, and a porosity of 22.0%. The main diagenetic process to affect the sample were mechanical compaction, the precipitation of dolomite, chlorite and small amounts of quartz and albite. The dolomite occurs as 50  $\mu\text{m}$  rhombs that are compositionally zoned with dolomite cores and thin ankerite rims. The chlorite occurs as a grain coating clay. It is possible that it formed as a result of the recrystallization of an early smectitic clay. The authigenic quartz and albite occurs as think outgrowths on detrital quartz.

The fault has a heterogeneous microstructure. In some places, it is very similar to that of the host sandstone. Elsewhere it has experienced a slight reduction in porosity due to the deformation-induced mixing of clays with framework grains leading to enhanced mechanical compaction. There is no evidence of grain fracturing suggesting faulting occurred under low effective stress conditions.

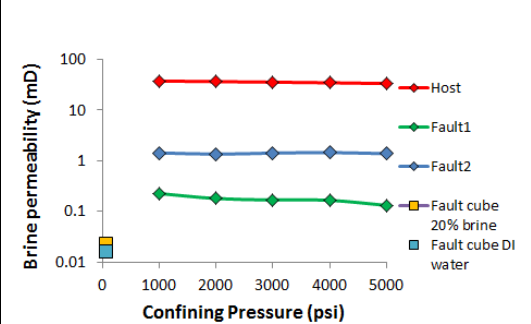
**Hg-injection (unstressed)**

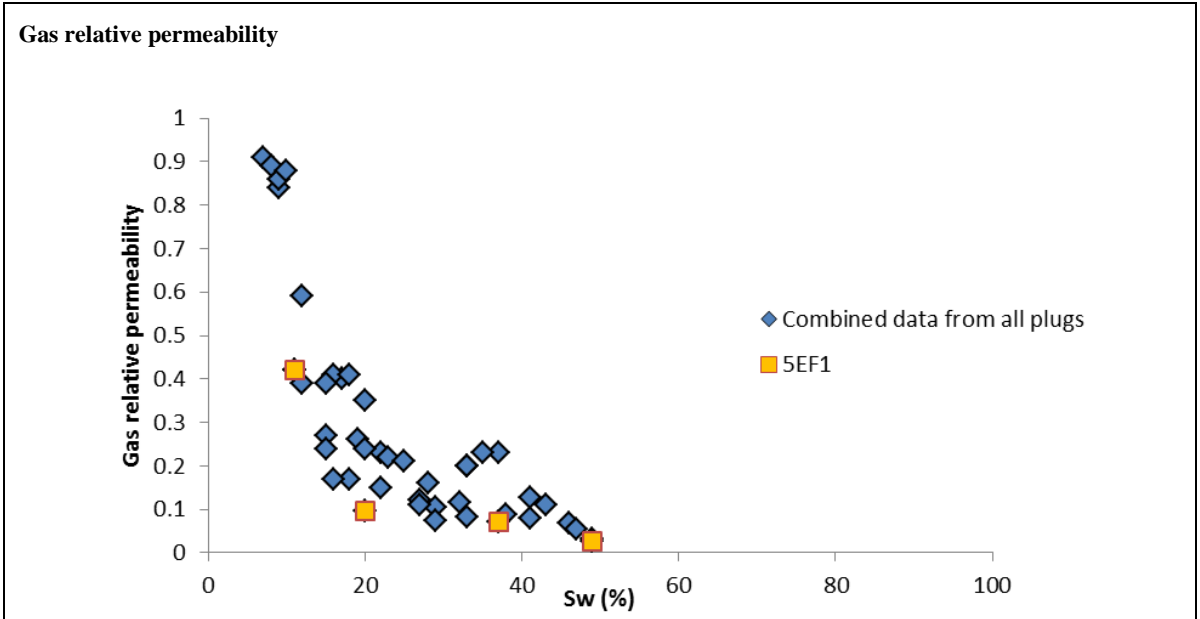


**Gas permeability vs stress**

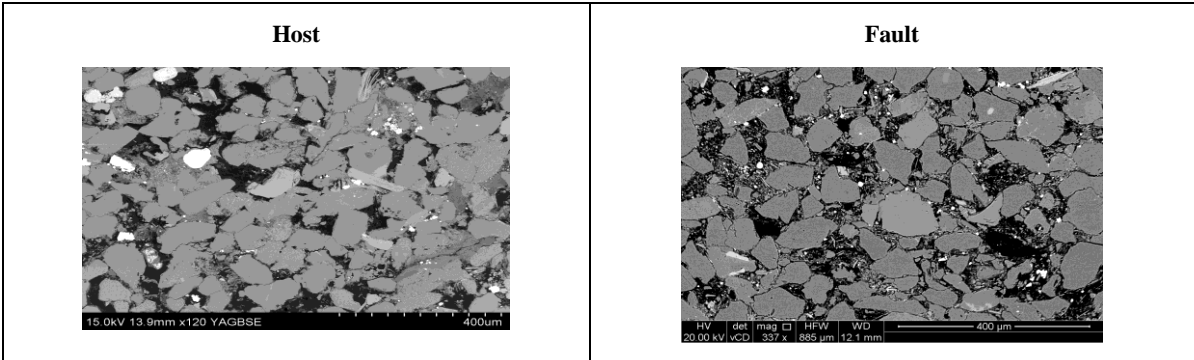


**Brine permeability vs stress (20% NaCl brine)**





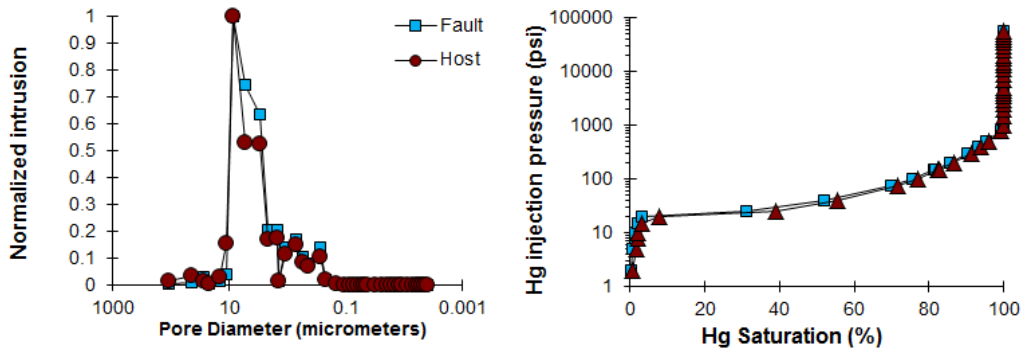
<b>Well IB: Triassic reservoir Central North Sea, UK</b>		<b>Depth: 14375-14375.4 m MD</b>	
<b>Sample ID 5F</b>		<b>Phyllosilicate-framework fault rock</b>	
<b>Host sandstone</b>		<b>Fault</b>	



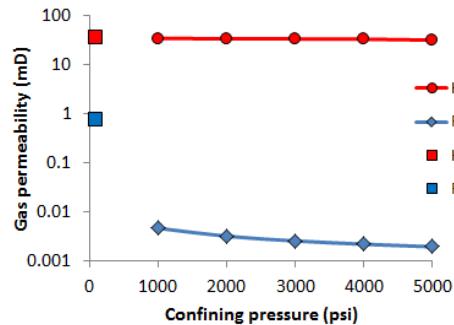
The undeformed sandstone is fine grained, well sorted, composed of 40.2 % quartz, 19.1 % albite, 5.3 % mica, 4.2 % pyrite, 4.1 % Illite-smectite, 4.3 % dolomite, 3.1 % chlorite, and a porosity of 20.7%. The main diagenetic process to affect the sample were mechanical compaction, the precipitation of pyrite, dolomite, chlorite and small amounts of quartz and albite. The pyrite occurs as framboids in organic-rich layers and probably precipitated directly beneath the sediment-water interface soon after sediment deposition. The dolomite occurs as 70  $\mu\text{m}$  rhombs that are compositionally zoned with dolomite cores and thin ankerite rims. The chlorite occurs as a grain coating clay. It is possible that it formed as a result of the recrystallization of an early smectitic clay. The authigenic quartz and albite occurs as thin outgrowths on detrital quartz.

The fault has a porosity of 9%, which is <40% that of the host sandstone. The reduction in porosity occurred as a result of the deformation-induced mixing of clays with framework grains leading to enhanced mechanical compaction. Faulting occurred after the precipitation of dolomite and chlorite (or its precursor) but before authigenic quartz and albite. There is no evidence of grain fracturing suggesting faulting occurred under low effective stress conditions.

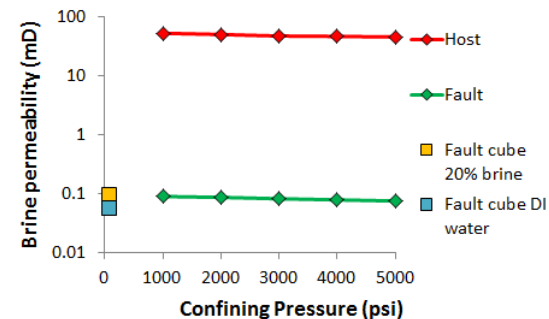
**Hg-injection (stressed)**

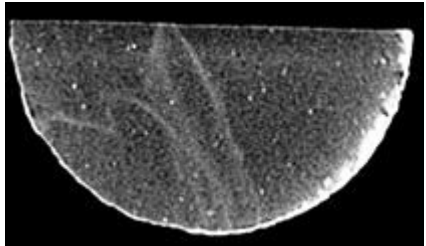
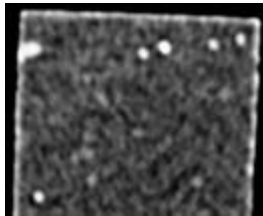
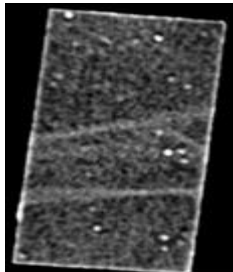
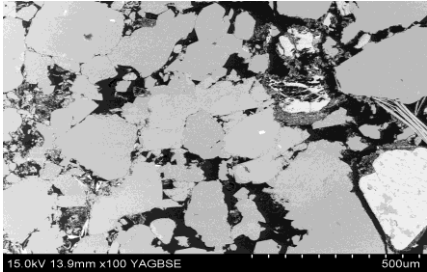
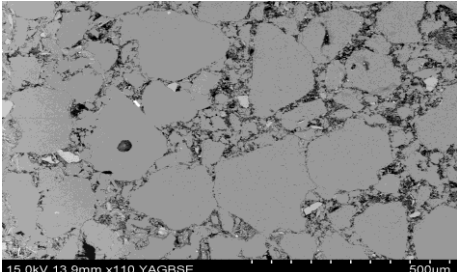


**Gas permeability vs stress**

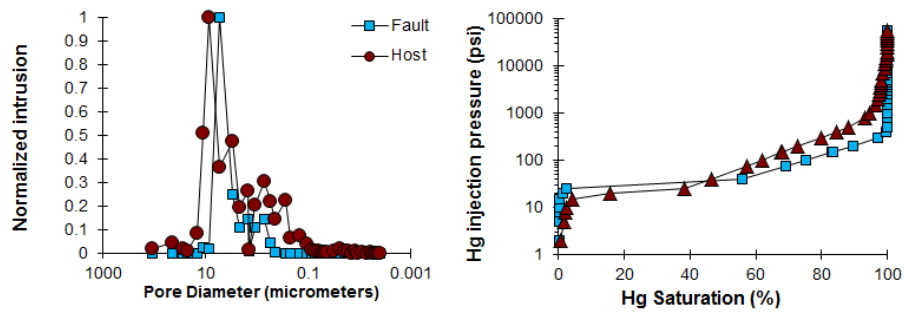


**Brine permeability vs stress (20% NaCl brine for stressed measurements)**

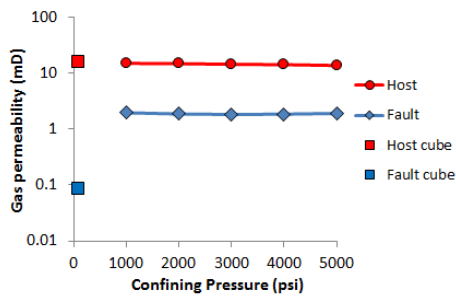


Well IC: Triassic reservoir Central North Sea, UK	Depth: 14507.1-14507.8 m MD
Sample ID 7A	Cataclastic fault
	
<p data-bbox="331 752 496 781"><b>Host sandstone</b></p> 	<p data-bbox="941 752 1075 781"><b>Faulted core</b></p> 
<p data-bbox="331 1108 387 1137"><b>Host</b></p> 	<p data-bbox="941 1108 997 1137"><b>Fault</b></p> 
<p data-bbox="331 1451 1509 1675">The undeformed sandstone is fine grained upper, moderately well sorted, composed of 40.2 % quartz, 14.7 % albite, 8.9 % microcline, 6.9 % dolomite, 5.6 % chlorite, 4.6 % mica, 3.0 % Illite-smectite, and a porosity of 16%. The main diagenetic process to affect the sample were mechanical compaction, the precipitation of dolomite, chlorite, quartz and small amounts of albite. The dolomite occurs as 100 µm rhombs that are compositionally zoned with dolomite cores and thin ankerite rims. The chlorite occurs as a grain coating clay. It is possible that it formed as a result of the recrystallization of an early smectitic clay. The authigenic quartz is relatively abundant and occurs as both overgrowths and outgrowths.</p> <p data-bbox="331 1691 1509 1785">The fault has a porosity of 6%, which is ~30% that of the host sandstone. The reduction in porosity occurred as a result of cataclastic deformation which allowed enhanced mechanical compaction. Faulting occurred after the precipitation of dolomite and chlorite (or its precursor) but before authigenic quartz and albite.</p>	

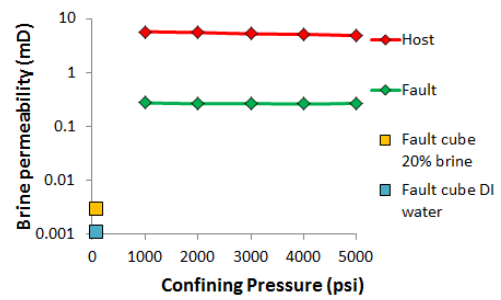
### Hg-injection (unstressed)



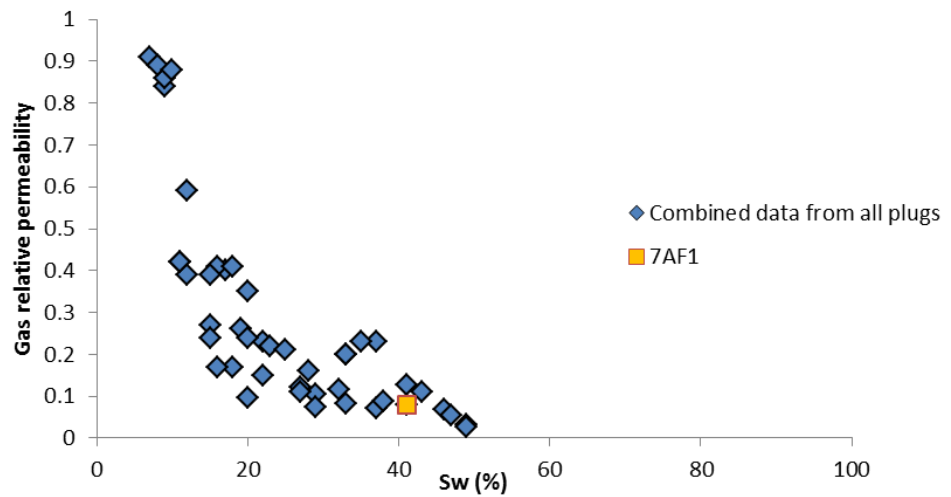
### Gas permeability vs stress

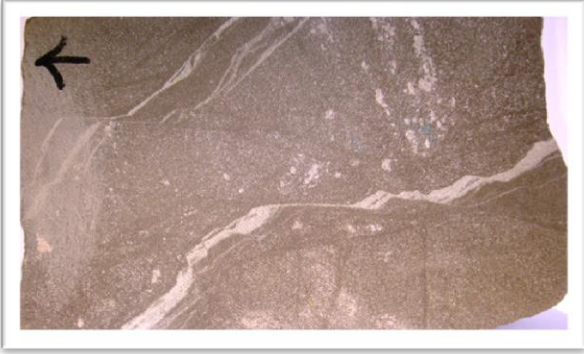
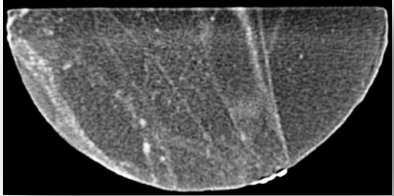
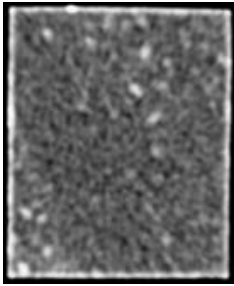
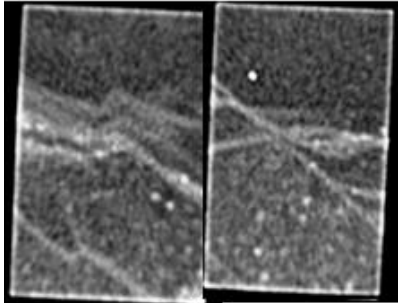
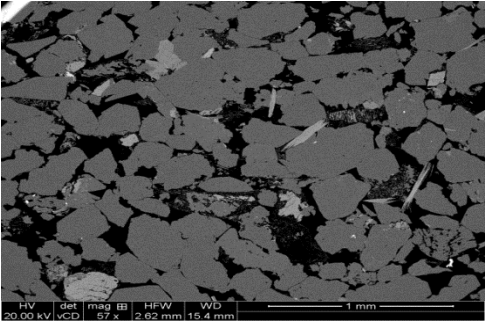
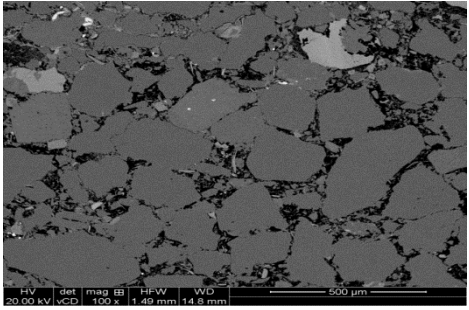


### Brine permeability vs stress (20% NaCl brine for stressed measurements)

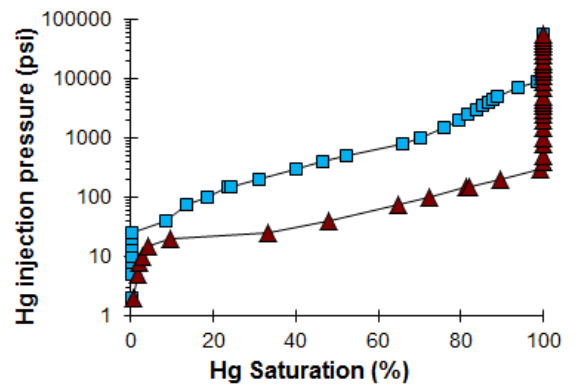
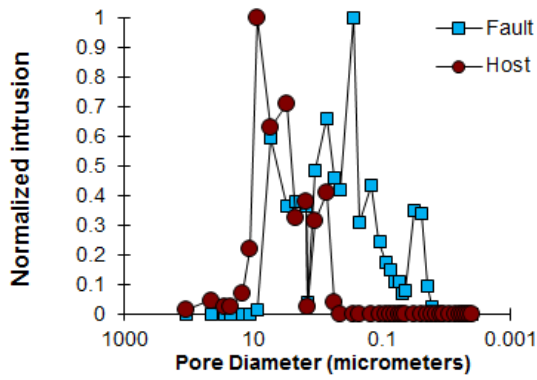


### Gas relative permeability

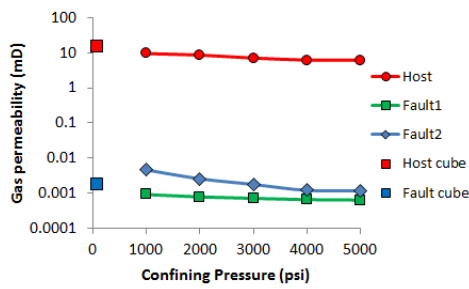


Well Sample ID 7B: Triassic reservoir Central North Sea, UK	Depth: 14519.2-14519.8 mMD
Sample ID 7B	Cataclastic fault
	
<p>Host</p> 	<p>Fault 1      Fault 2</p> 
<p>Host</p> 	<p>Fault</p> 
<p>The undeformed sandstone is medium grained, well sorted, composed of 37.4 % quartz, 13.7 % albite, 10 % microcline, 7.2 % dolomite, 6.1 % Illite-smectite, 4.4 % chlorite, 4.2 % mica, and a porosity of 17%. The main diagenetic process to affect the sample were mechanical compaction, the precipitation of dolomite, chlorite, quartz and small amounts of albite. The dolomite occurs as 100 μm rhombs that are compositionally zoned with dolomite cores and thin ankerite rims. The chlorite occurs as a grain coating clay. It is possible that it formed as a result of the recrystallization of an early smectitic clay. The authigenic quartz is relatively abundant and occurs as both overgrowths and outgrowths.</p> <p>The fault has a porosity of 7%, which is ~30% that of the host sandstone. The reduction in porosity occurred as a result of cataclastic deformation which allowed enhanced mechanical compaction. Faulting occurred after the precipitation of dolomite and chlorite (or its precursor) but before authigenic quartz and albite.</p>	

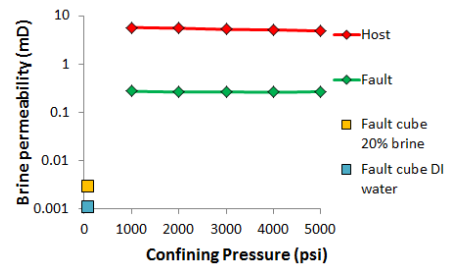
**Hg-injection (unstressed)**



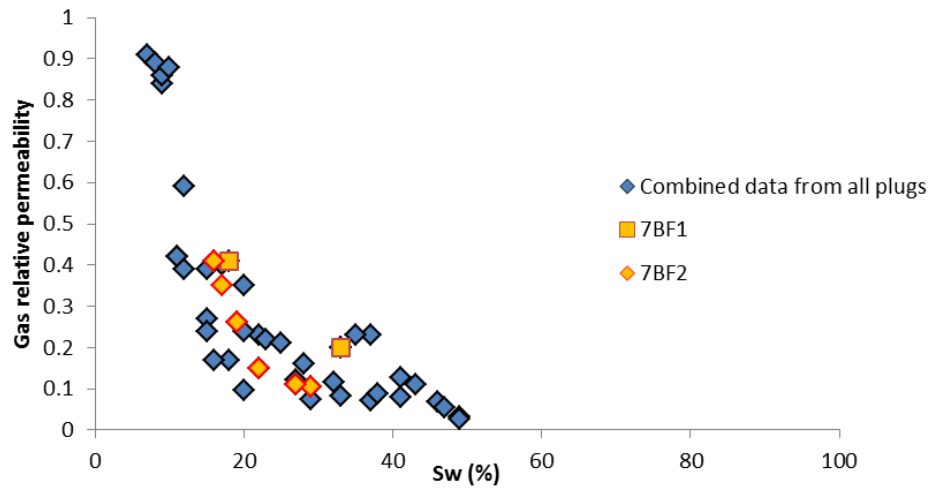
**Gas permeability vs stress:**

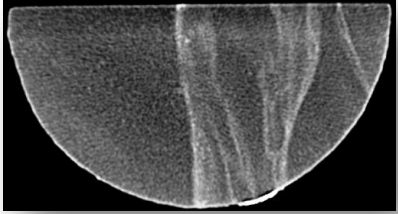
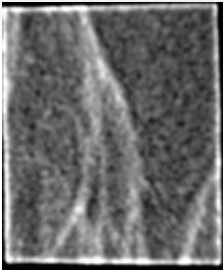
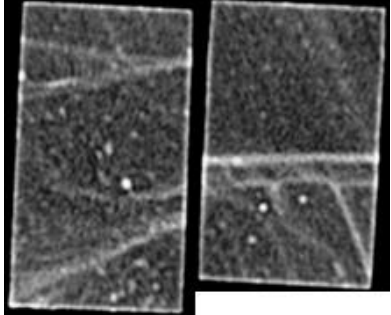
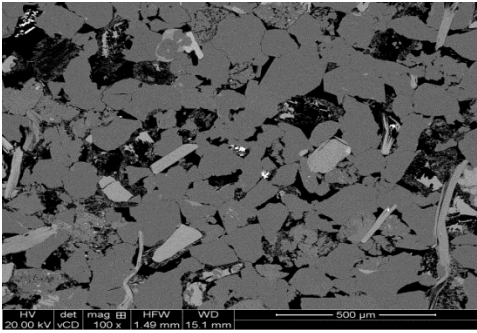
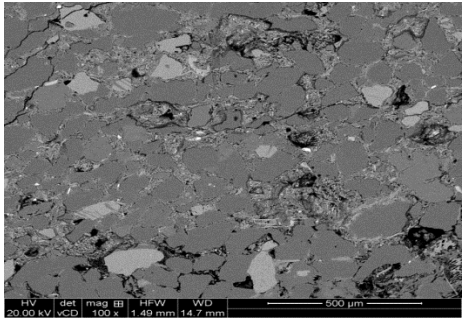


**Brine permeability vs stress (20% NaCl brine for stressed measurements)**

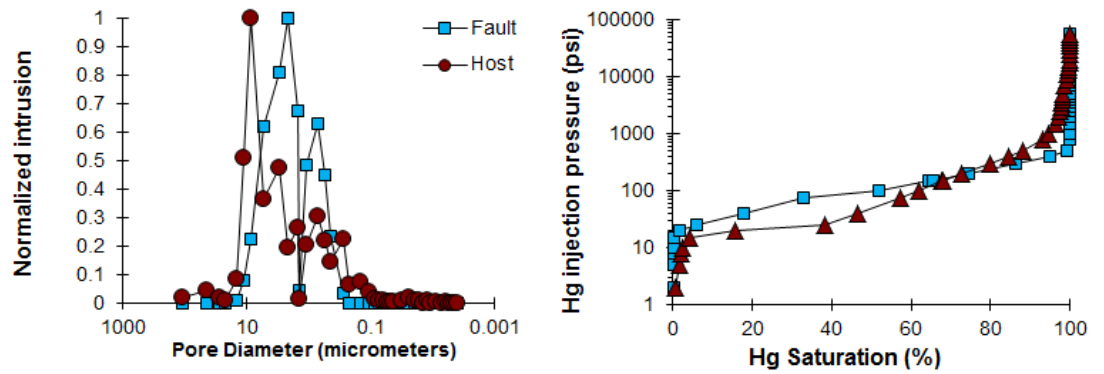


**Gas relative permeability**

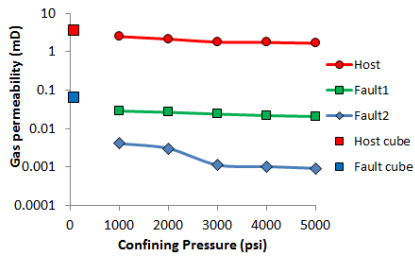


Well C: Triassic reservoir Central North Sea, UK	Depth: 14520.6-14521.0 m MD
Sample ID 7C	Phyllosilicate-framework fault rock
	
<p data-bbox="331 745 496 775">Host sandstone</p> 	<p data-bbox="1086 757 1182 786">Fault 1</p> <p data-bbox="1278 757 1374 786">Fault 2</p> 
 <p data-bbox="395 1435 874 1469">HV det mag B HFW WD 20.00 kV vCD 100 x 14.49 mm 15.1 mm 500 µm</p>	 <p data-bbox="1002 1435 1465 1458">HV det mag B HFW WD 20.00 kV vCD 100 x 14.49 mm 14.7 mm 500 µm</p>
<p data-bbox="331 1496 1508 1715">The undeformed sandstone is very fine grained, moderately well sorted, composed of 32.8 % quartz, 18.2 % albite, 11.7 % microcline, 7.7 % chlorite, 6.4 % Illite-smectite, 5.7 % mica, 3.5 % dolomite, and a porosity of 14.0%. The main diagenetic process to affect the sample were the precipitation of K-feldspar, dolomite, chlorite, quartz and albite. The K-feldspar occurs as µm overgrowths on detrital K-feldspar grains; it has been partially corroded during later burial. The dolomite occurs as 100 µm rhombs that are compositionally zoned with dolomite cores and thin ankerite rims. The chlorite occurs as a grain coating clay. It is possible that it formed as a result of the recrystallization of an early smectitic clay. The authigenic quartz and albite occurs as thin overgrowths on detrital quartz.</p> <p data-bbox="331 1733 1508 1886">The fault has a porosity of ~6%, which is ~40% that of the host sandstone. The reduction in porosity occurred as a result of two process. First, clays were mixed with framework grains leading to enhanced mechanical compaction. Second, the fault appears to have undergone enhanced grain contact quartz dissolution. Faulting occurred after the precipitation of dolomite and chlorite (or its precursor) but before the precipitation of quartz and albite or the dissolution of K-feldspar.</p>	

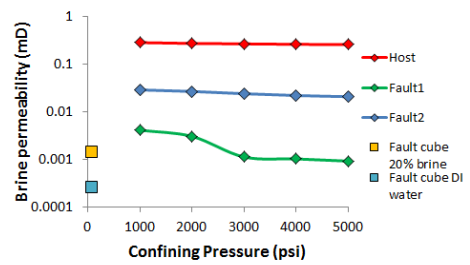
**Hg-injection (unstressed)**



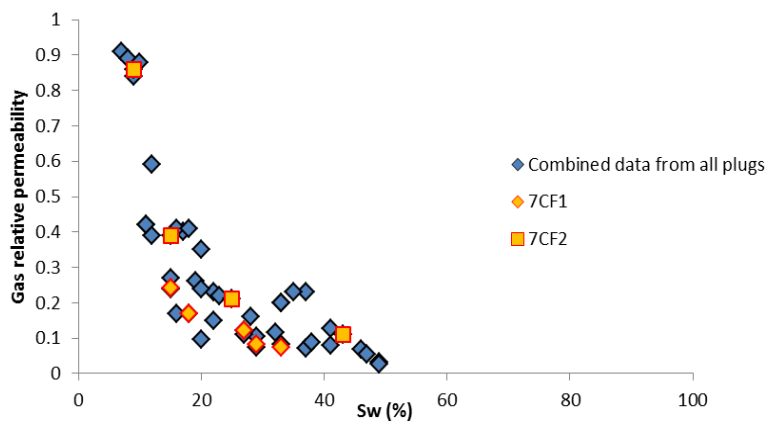
**Gas permeability vs stress**

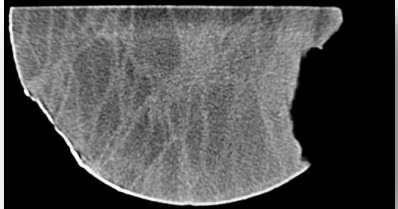
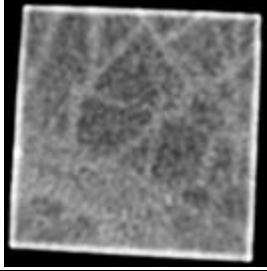
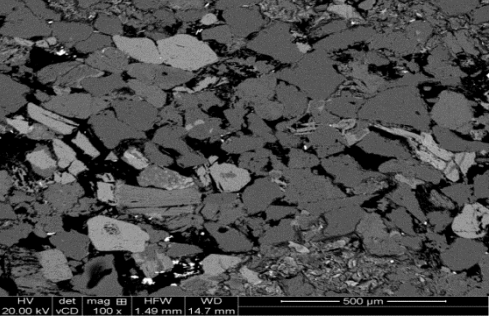
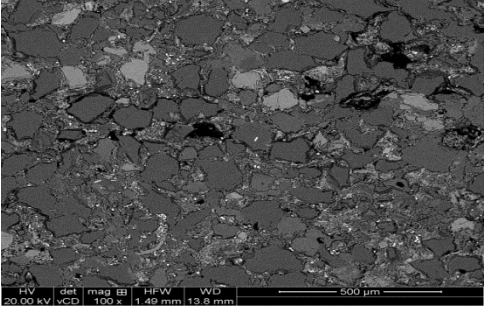


**Brine permeability vs stress (20% NaCl brine for stressed measurements)**

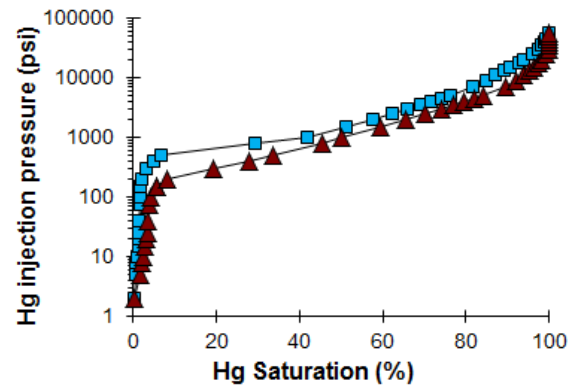
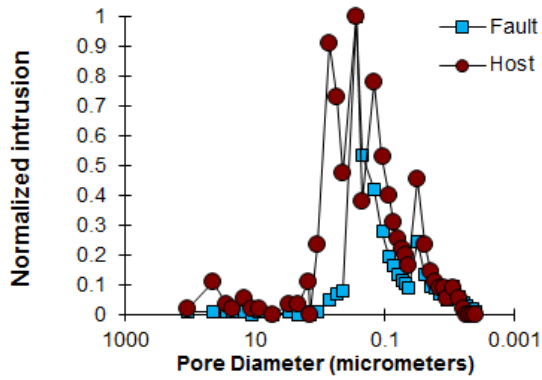


**Gas relative permeability**

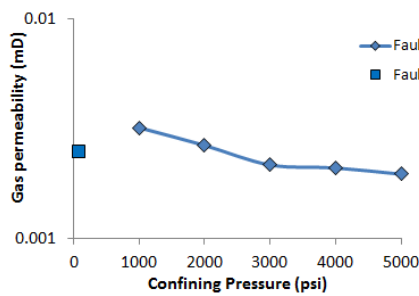


Well C: Triassic reservoir Central North Sea, UK	Depth: 14623-14623.3 m MD
Sample ID 7D	Phyllosilicate-framework fault rock
	
	<p data-bbox="906 869 963 898"><b>Fault</b></p> 
<p data-bbox="336 1205 389 1234"><b>Host</b></p> 	<p data-bbox="906 1205 963 1234"><b>Fault</b></p> 
<p data-bbox="336 1585 1513 1809">The undeformed sandstone is very fine grained, moderately well sorted, composed of 32.0 % quartz, 23.5 % albite, 8.9 % chlorite, 7.8 % microcline, 7.7 % Illite-smectite, 5.9 % dolomite, 2.3 % mica, and a porosity of 12%. The main diagenetic processes to affect the sample were the precipitation of K-feldspar, dolomite, chlorite, quartz and albite. The K-feldspar occurs as <math>\mu\text{m}</math> overgrowths on detrital K-feldspar grains; it has been partially corroded during later burial. The dolomite occurs as 200 <math>\mu\text{m}</math> rhombs that are compositionally zoned with dolomite cores and thin ankerite rims. The chlorite occurs as a grain coating clay. It is possible that it formed as a result of the recrystallization of an early smectitic clay. The authigenic quartz and albite occurs as thin overgrowths on detrital quartz.</p> <p data-bbox="336 1823 1513 1942">The fault has a far lower porosity than the host sandstone has a result of two processes. First, clays were mixed with framework grains leading to enhanced mechanical compaction. Second, the fault appears to have undergone enhanced grain contact quartz dissolution. Faulting occurred after the precipitation of dolomite and chlorite (or its precursor) but before the precipitation of quartz and albite or the dissolution of K-feldspar.</p>	

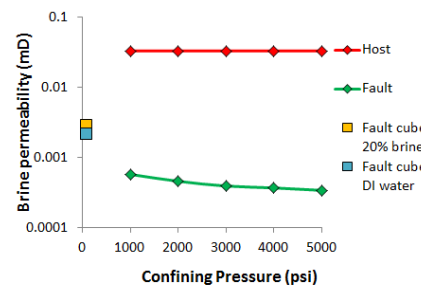
**Hg-injection (unstressed)**



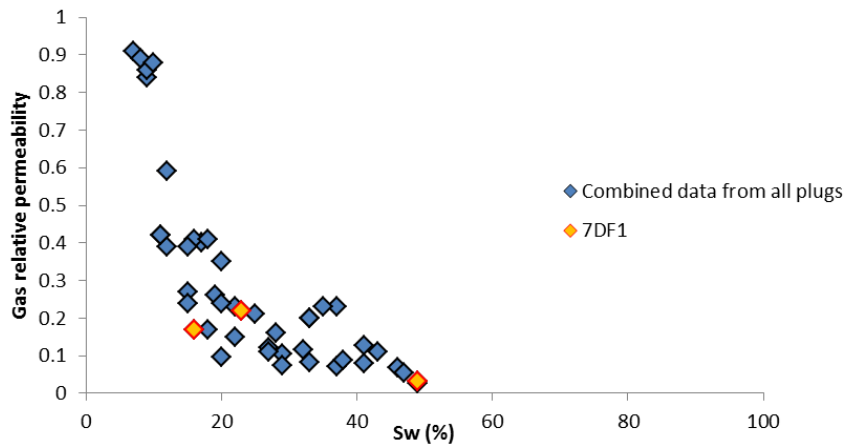
**Gas permeability vs stress:**

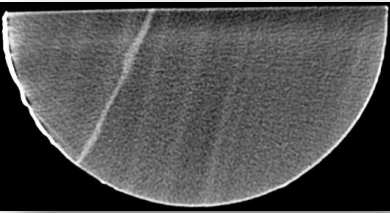
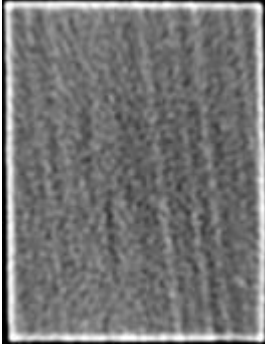
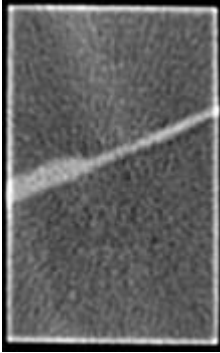
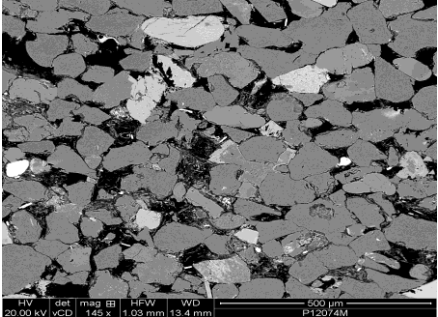
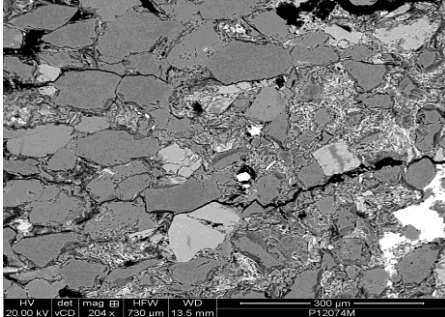


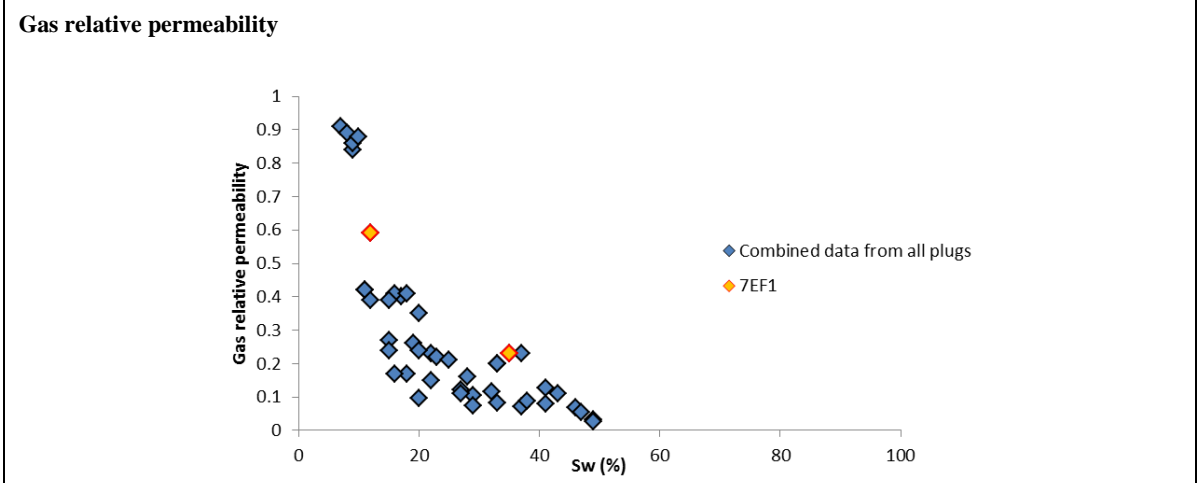
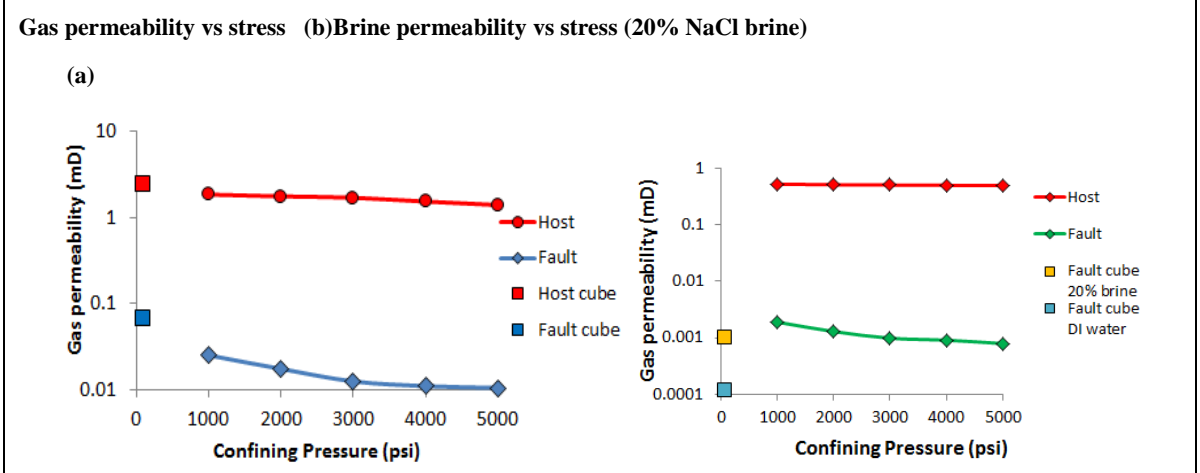
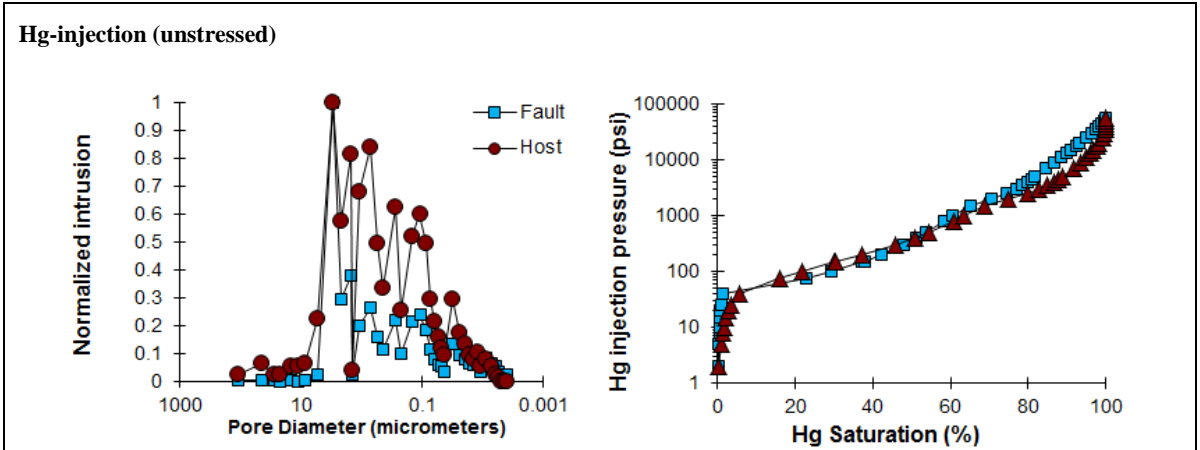
**Brine permeability vs stress (20% NaCl brine)**



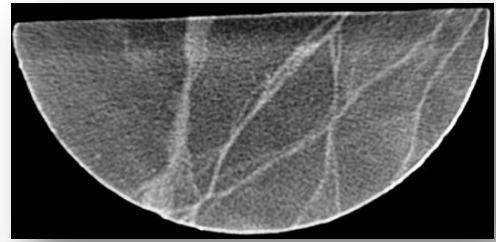
**Gas relative permeability**



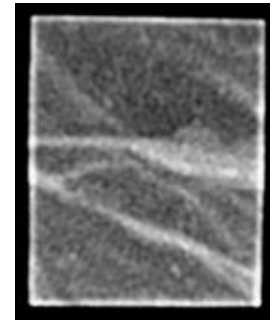
Well C: Triassic reservoir Central North Sea, UK	Depth: 14051.8-14052 mMD
Sample ID 7E	Phyllosilicate-framework fault rock
	
<p data-bbox="331 745 384 770"><b>Host</b></p> 	<p data-bbox="922 745 975 770"><b>Fault</b></p> 
<p data-bbox="331 1164 384 1189"><b>Host</b></p>  <p data-bbox="335 1507 774 1529">HV det mag B HFW WD 500 µm 20.00 kV vCD 145 x 1.03 mm 13.4 mm P12074M</p>	<p data-bbox="922 1164 975 1189"><b>Fault</b></p>  <p data-bbox="989 1507 1436 1529">HV det mag B HFW WD 300 µm 20.00 kV vCD 204 x 1.70 µm 13.5 mm P12074M</p>
<p data-bbox="331 1552 1508 1769">The undeformed sandstone is fine grained upper, well sorted, composed of 36.2 % quartz, 16.7 % albite, 9.5 % chlorite, 7.4 % Illite-smectite, 6.6 % microcline, 4.5 % mica, 4.0 % dolomite, and a porosity of 15%. The main diagenetic process to affect the sample were the precipitation of K-feldspar, dolomite, chlorite, quartz and albite. The K-feldspar occurs as 20 µm overgrowths on detrital K-feldspar grains. The dolomite occurs as 200 µm rhombs that are compositionally zoned with dolomite cores and thin ankerite rims; occasionally it exhibits a poikilitic texture. The chlorite occurs as a grain coating clay. It is possible that it formed as a result of the recrystallization of an early smectitic clay. The authigenic quartz and albite occurs as thin outgrowths on detrital quartz.</p> <p data-bbox="331 1787 1508 1912">The fault has a far lower porosity than the host sandstone has a result of two processes. First, clays were mixed with framework grains leading to enhanced mechanical compaction. Second, the fault appears to have undergone enhanced grain contact quartz dissolution. There appears to be more clay in the fault rock than in the host sandstone possibly indicating material was injected along the fault.</p> <p data-bbox="331 1930 1508 1989">Faulting occurred after the precipitation of dolomite and chlorite (or its precursor) but before the precipitation of quartz and albite or the dissolution of K-feldspar.</p>	



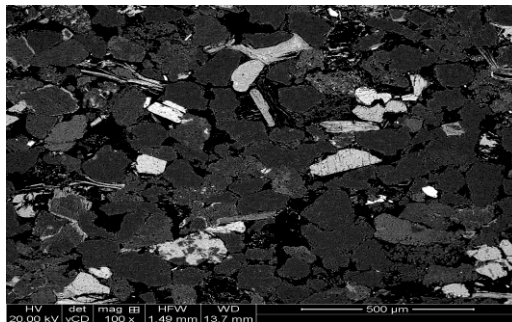
Triassic reservoir Central North Sea, UK	Depth: 14717.9-14718.2 mMD
Sample ID 7F	Phyllosilicate-framework fault rock



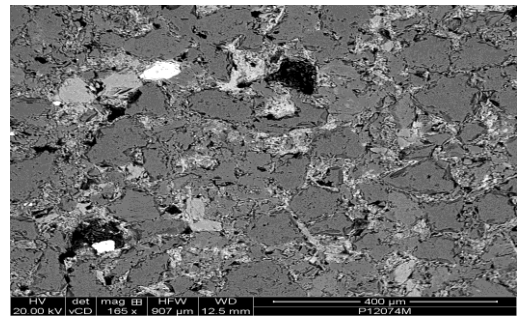
**Fault**



**Host**



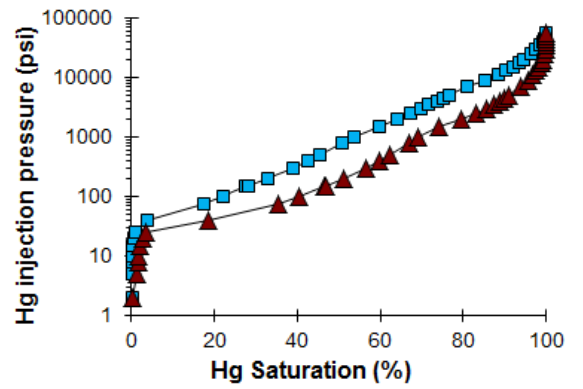
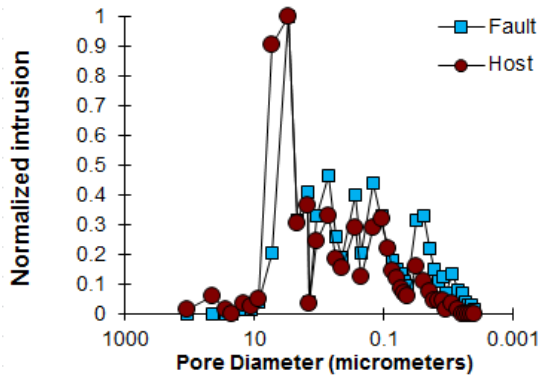
**Fault**



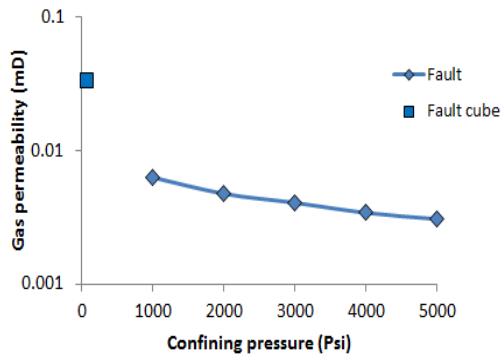
The undeformed sandstone is fine grained upper, well sorted, composed of 31 % quartz, 21.8 % albite, 12.5 % chlorite, 6.2 % microcline, 5.2 % dolomite, 4 % Illite-smectite, 3.4 % mica, and a porosity of 16.0%. The main diagenetic process to affect the sample were the precipitation of K-feldspar, dolomite, chlorite, quartz and albite. The K-feldspar occurs as 20  $\mu\text{m}$  overgrowths on detrital K-feldspar grains. The dolomite occurs as 100  $\mu\text{m}$  rhombs that are compositionally zoned with dolomite cores and thin ankerite rims. The chlorite occurs as a grain coating clay. It is possible that it formed as a result of the recrystallization of an early smectitic clay. The authigenic quartz and albite occurs as thin outgrowths on detrital quartz.

The fault has porosity than the host sandstone has a result of two processes. First, clays were mixed with framework grains leading to enhanced mechanical compaction. Second, the fault appears to have undergone enhanced grain contact quartz dissolution. There appears to be more clay in the fault rock than in the host sandstone possibly indicating material was injected along the fault. Faulting occurred after the precipitation of dolomite and chlorite (or its precursor) but before the precipitation of quartz and albite or the dissolution of K-feldspar.

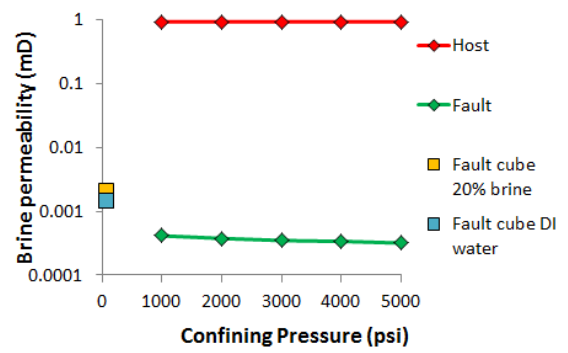
**Hg-injection (unstressed)**

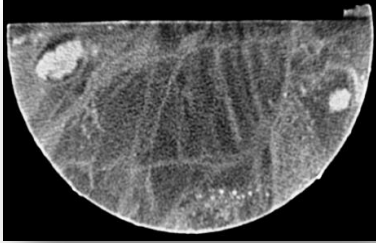
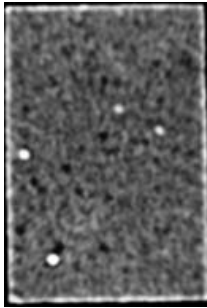
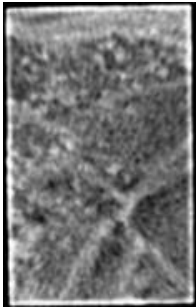
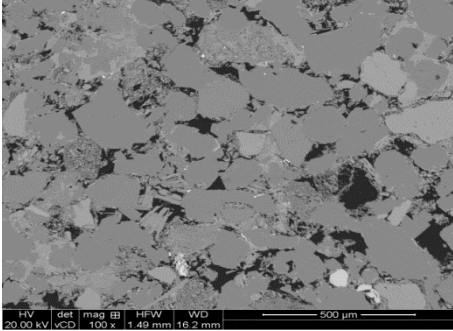
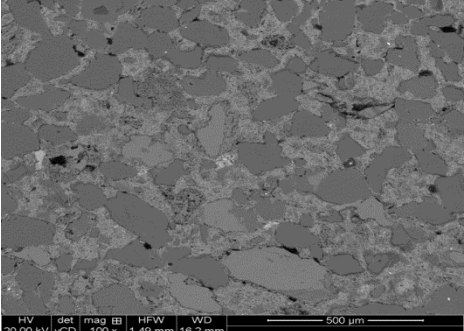


**(a) Gas permeability vs stress**

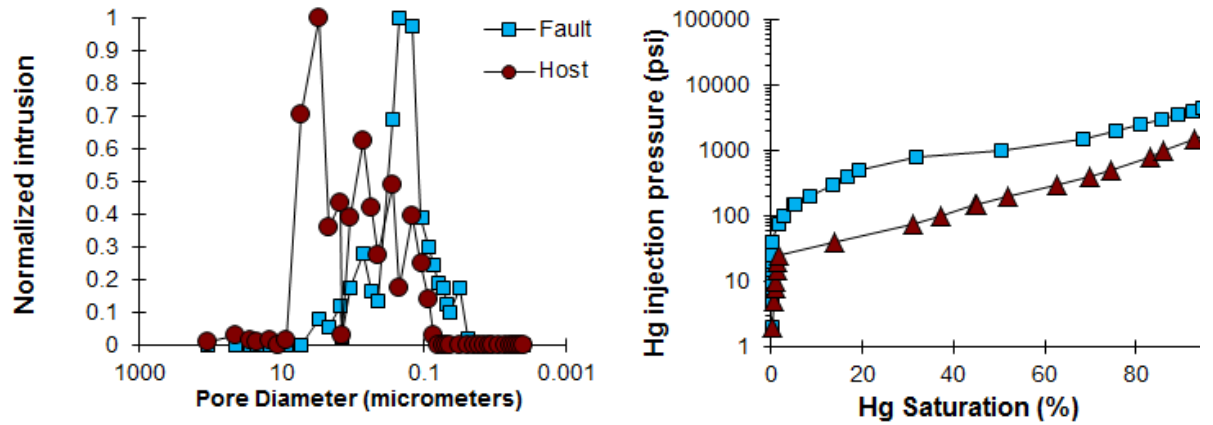


**(b) Brine permeability vs stress (20% NaCl brine)**

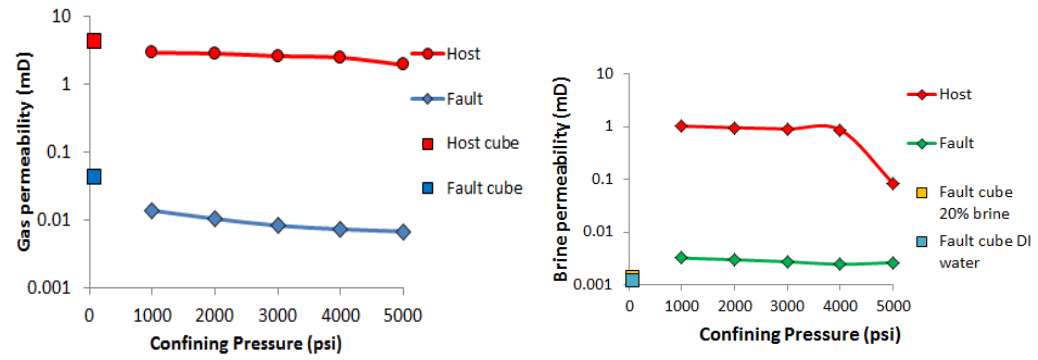


Well D: Triassic reservoir Central North Sea, UK	Depth: 14638.1-14638.4 mMD
Sample ID 10/3A	Phyllosilicate-framework fault rock
	
<p data-bbox="331 745 384 772"><b>Host</b></p> 	<p data-bbox="943 745 995 772"><b>Fault</b></p> 
<p data-bbox="600 1122 652 1149"><b>Host</b></p> 	<p data-bbox="1193 1122 1246 1149"><b>Fault</b></p> 
<p data-bbox="331 1525 1508 1742">The undeformed sandstone is medium grained, moderately well sorted, composed of 49.4 % quartz, 15.8 % albite, 7.4 % microcline, 6.3 % chlorite, 3.7 % Illite-smectite, 2.7 % dolomite, 2.7 % mica, and a porosity of 12%. The main diagenetic process to affect the sample were the precipitation of K-feldspar, dolomite, chlorite, quartz and small amounts of albite. The K-feldspar occurs as up to 40 μm wide rhombs on detrital K-feldspar and plagioclase. The dolomite occurs as 30 μm rhombs that are compositionally zoned with dolomite cores and thin ankerite rims. The chlorite occurs as a grain coating clay. It is possible that it formed as a result of the recrystallization of an early smectitic clay. The authigenic quartz is relatively abundant and occurs as both overgrowths and outgrowths.</p> <p data-bbox="331 1765 1508 1883">The fault has porosity than the host sandstone has a result of two processes. First, clays were mixed with framework grains leading to enhanced mechanical compaction. Second, the fault appears to have undergone enhanced grain contact quartz dissolution. There appears to be more clay in the fault rock than in the host sandstone possibly indicating material was injected along the fault.</p> <p data-bbox="331 1906 1508 1960">Faulting occurred after the precipitation of dolomite and chlorite (or its precursor) but before the precipitation of quartz and albite or the dissolution of K-feldspar.</p>	

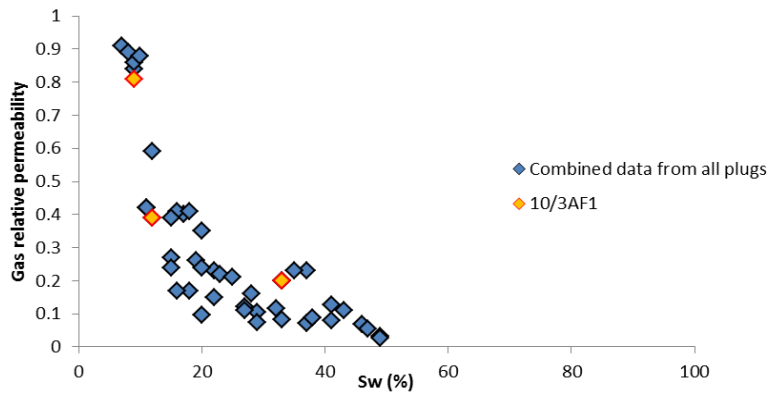
**Hg-injection (unstressed)**

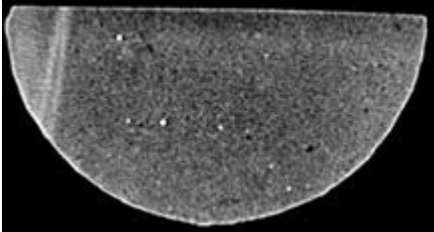
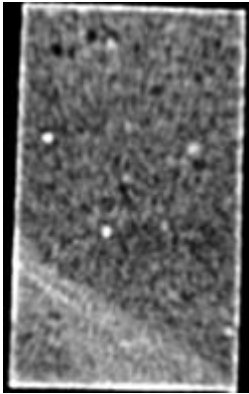
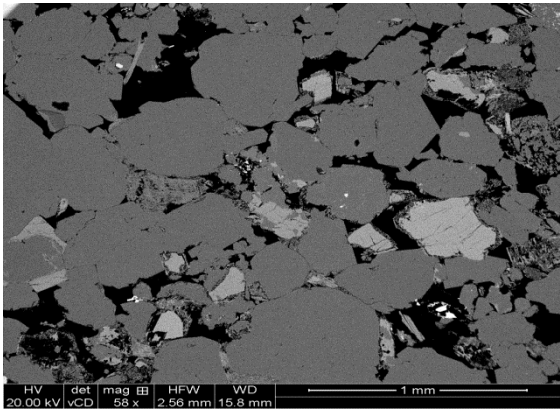
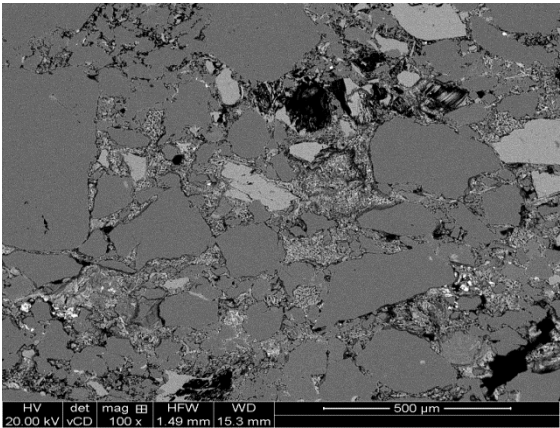


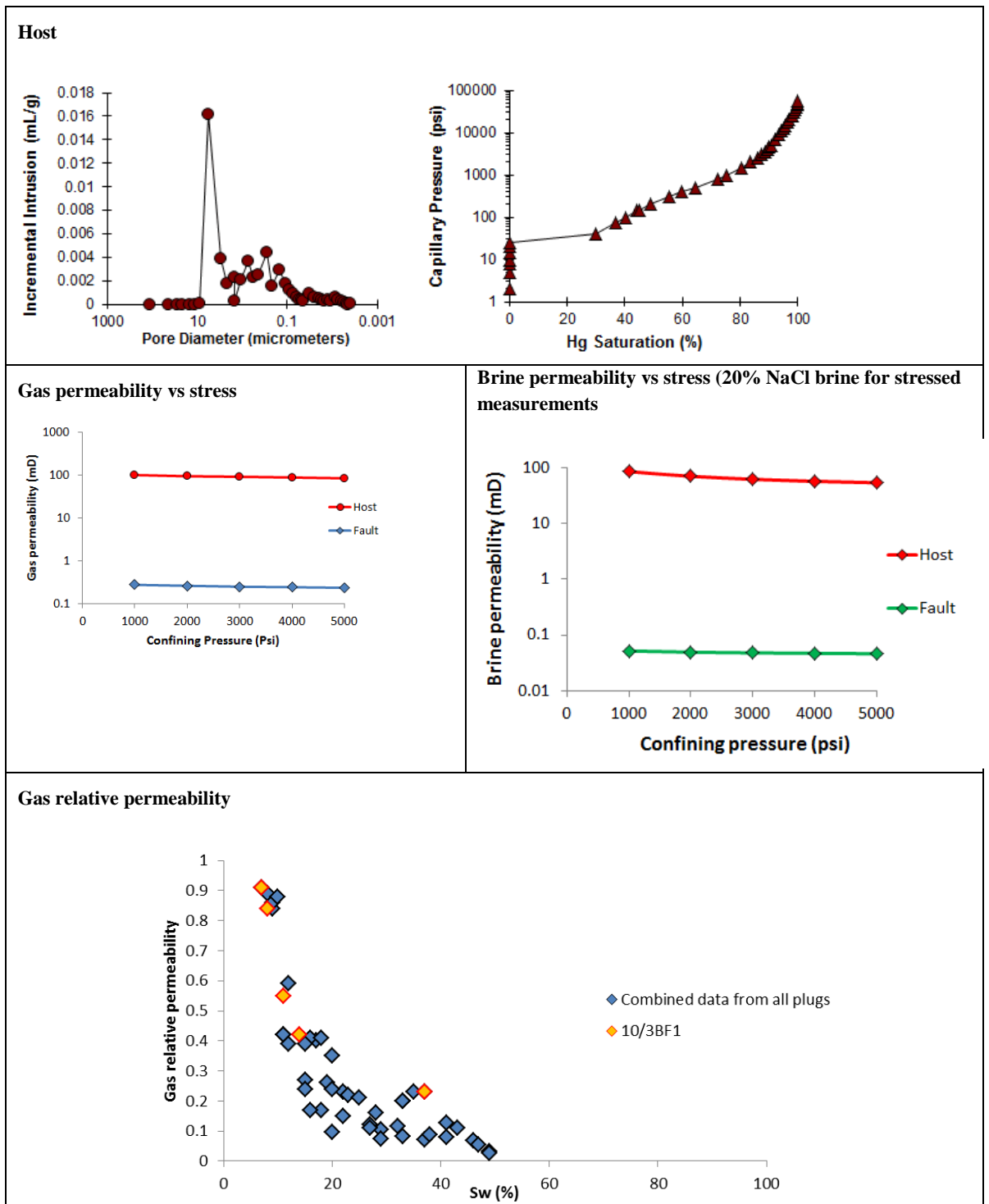
**Gas permeability vs stress:**



**Gas relative permeability**

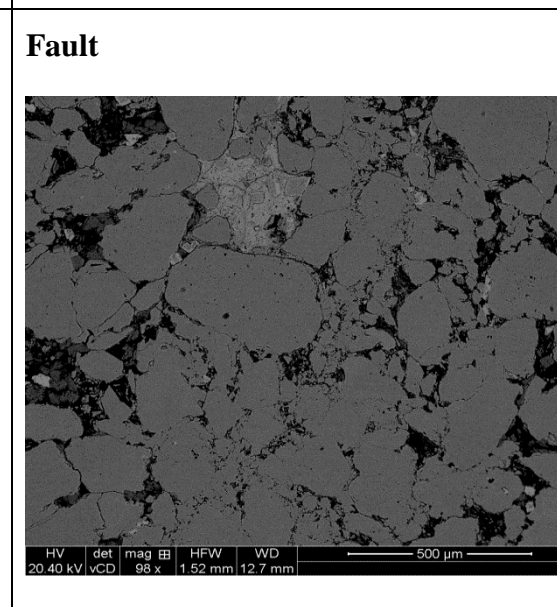
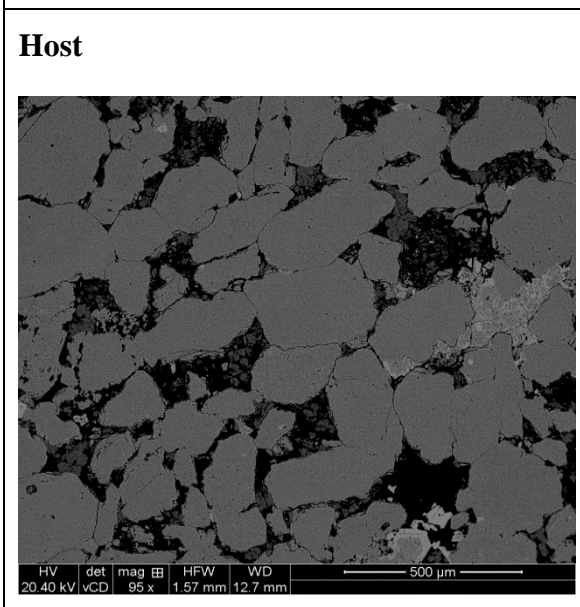
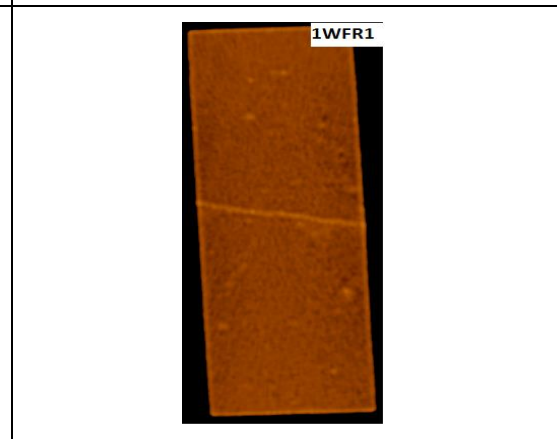
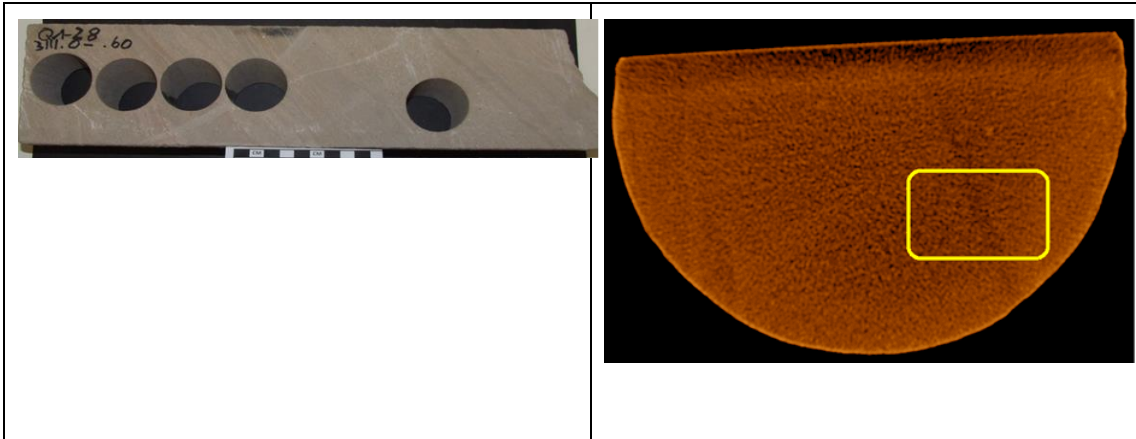


Well ID: Triassic reservoir Central North Sea, UK	Depth 14718.1-14718.7 mMD
Sample ID 10/3B	Cataclastic fault
	
<p data-bbox="331 651 384 678"><b>Host</b></p> 	<p data-bbox="943 651 995 678"><b>Fault</b></p> 
<p data-bbox="331 1111 384 1137"><b>Host</b></p> 	<p data-bbox="943 1111 995 1137"><b>Fault</b></p> 
<p data-bbox="331 1603 1509 1821">The undeformed sandstone is medium grained, moderately well sorted, composed of 47.6 % quartz, 9.0 % albite, 11.1 % microcline, 6.4 % chlorite, 4.7 % Illite-smectite, 2.1 % mica, and a porosity of 19%. The main diagenetic process to affect the sample was the precipitation of K-feldspar, dolomite, chlorite, quartz and small amounts of albite. The K-feldspar occurs as up to 20 μm wide rhombs on detrital K-feldspar. The dolomite occurs as 200 μm rhombs that are compositionally zoned with dolomite cores and thin ankerite rims. The chlorite occurs as a grain coating clay. It is possible that it formed as a result of the recrystallization of an early smectitic clay. The authigenic quartz is relatively abundant and occurs as both overgrowths and outgrowths.</p> <p data-bbox="331 1839 1509 1933">The fault has porosity than the host sandstone has a result of three processes. First, framework grains were fractured allowing enhanced mechanical compaction. Second, clays were mixed with fractured framework grains leading to enhanced mechanical compaction. Third, the fault appears to have undergone enhanced grain contact quartz dissolution.</p> <p data-bbox="331 1951 1509 2007">Faulting occurred after the precipitation of dolomite and chlorite (or its precursor) but before the precipitation of quartz and albite or the dissolution of K-feldspar.</p>	



**Southern North Sea samples**

<b>Well WIN1:</b>	<b>Depth: 3111.00-3111.60</b>
<b>Sample WIN1A</b>	<b>Cataclastic fault</b>

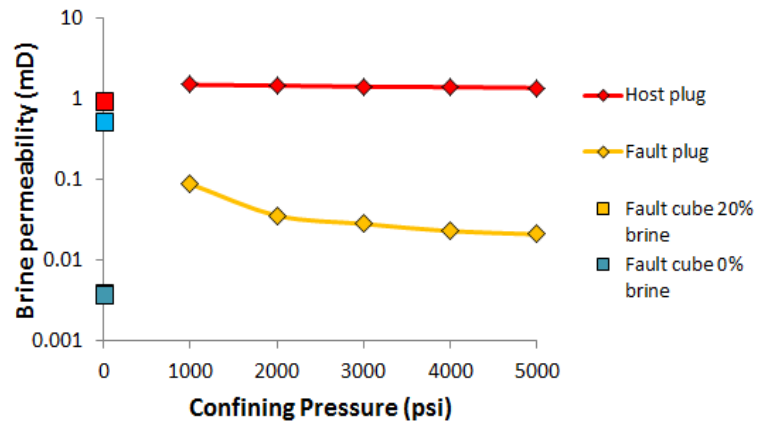
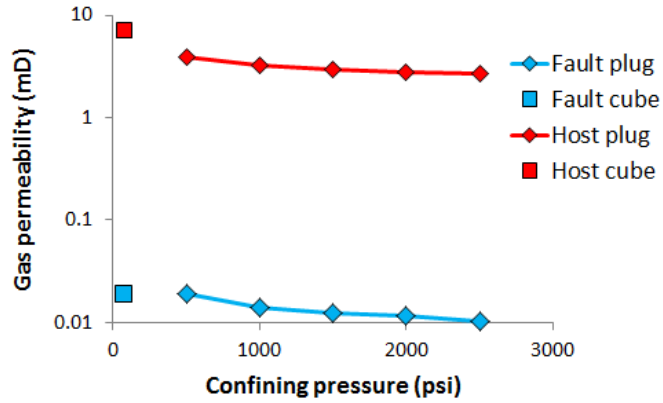


The undeformed sandstone is medium grained, well sorted with a porosity of 15.4%. QXRD analysis indicates that it is composed of 49.1 % quartz, 21.2 % kaolin, 5.8 % albite, 5.6 % mica, 1.1 % calcite, and 1.5 % illite-smectite. Although, the sample analyzed by SEM does not contain calcite, has <10% kaolin but does contains small amounts (<1%) of dolomite. The main diagenetic process to affect the sample was the precipitation of kaolin and quartz; there are also the occasional secondary pores. The kaolin occurs as ~50 μm booklets and appears to have precipitated during early burial but may have recrystallized. The authigenic quartz occurs as outgrowths and can occasionally be observed

overgrowing the kaolin.

The fault has porosity of ~8%, which is ~50% that of the host sandstone. This reduction in porosity has occurred mainly as a result of cataclastic deformation, which enhanced mechanical compaction. Faulting occurred after the precipitation of kaolin and dolomite but before the quartz.

**Gas permeability vs stress:**



**Well WIN1:**

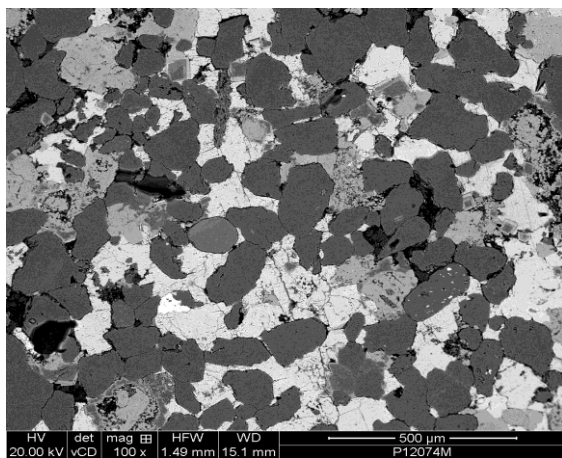
**Depth: 3133.10-3133.2 m**

**Sample WIN1B**

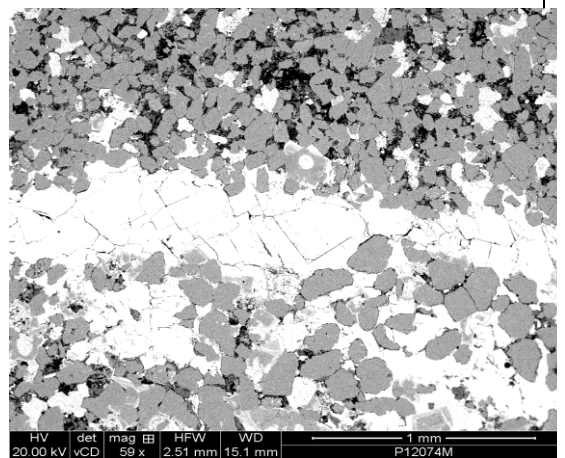
**Juxtaposition fault with anhydrite cement**



**Host**

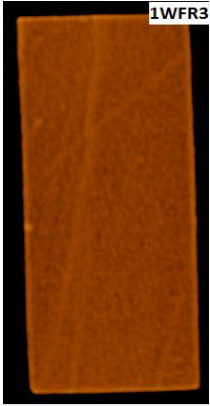
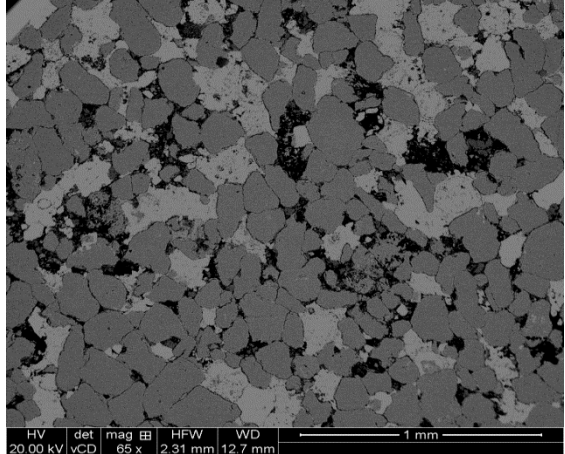
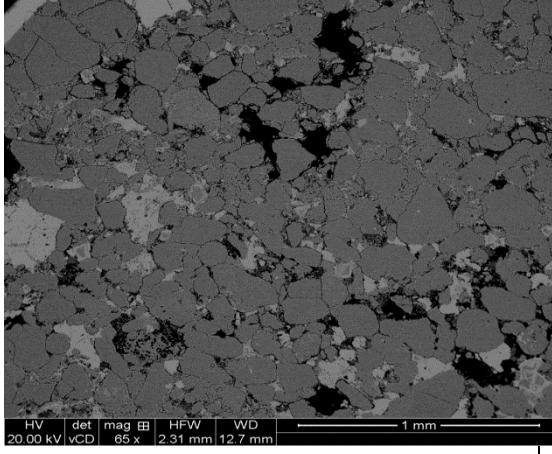


**Fault**



Examination of the hand specimen revealed it to be extremely heterogeneous so several samples were taken for SEM analysis. One sample was composed of ~31.4% quartz, 18.4% dolomite/ferroan dolomite, 15.1% kaolin, 13.2% calcite, 6.4% albite, 5.2% mica, 4% siderite, 3.5% anhydrite and a porosity of 4%. Another sample, had far less authigenic cements and was composed of ~46.2% quartz, 12.1% kaolin, 9.4% albite, 4.2% dolomite/ferroan dolomite, 4.6% mica, 2.9% calcite, and a porosity of 17%. The first mineral to precipitate was ferroan dolomite, which occurs as up to 100μm rhombs overgrown by ferroan dolomite. The next mineral to precipitate was kaolin, which occurs as 50um booklets that are partially overgrown by kaolin. During deeper burial the sample then experienced the precipitation of ferroan calcite, quartz, siderite and finally anhydrite.

The fault is a juxtaposition fault but in places it has dilated and been cemented by anhydrite. It is possible that the fault formed relatively early and that the dilation occurred due to late stage reactivation.

Well WIN1:	Depth: 3133.35 – 3133.55
Sample WIN1C	
	
	
Host	Fault
	
<p>The undeformed sandstone is fine grained, well sorted with a porosity of 12%. QXRD analysis indicates that it is composed of 35.3 % calcite, 25.8 % quartz, 17.2 % kaolin, 5.1 % mica, 3.8 % albite, and 1.3 % dolomite. Although, the sample analyzed by SEM contains far less calcite. The main diagenetic process to affect the sample were the precipitation of kaolin and calcite; dolomite and quartz cement are also present but in small quantities. The kaolin occurs as ~50 μm booklets and appears to have precipitated during early burial but may have recrystallized. The calcite occurs is pore filling and</p>	

occasionally poikilitic. The authigenic quartz occurs as outgrowths and can occasionally be observed overgrowing the kaolin.

The fault has porosity of ~8%, which is ~75% that of the host sandstone. This reduction in porosity has occurred mainly as a result of cataclastic deformation, which enhanced mechanical compaction. Faulting occurred after the precipitation of kaolin and dolomite but before the calcite and quartz.

### Gas permeability vs stress

